AMAP 2021 Assessment: Air Pollution in the Arctic with a Focus on Short-Lived Climate Forcers (SLCFs)

National Data Check

The following pages comprise the v0 (ca. 18 March 2020) compiled draft of substantive chapters of the AMAP 2021 AMAP 2021 Assessment of Air Pollution in the Arctic with a Focus on Short-Lived Climate Forcers (SLCFs).

The purpose of the national data check is to ensure completeness and correctness of national data and information included in the assessment, and to identify any relevant missing data/information or studies so that these can be introduced before the peer review stage. As far as possible, the check should also ensure that national data and studies presented in the current draft have been correctly interpreted.

This version of the assessment is missing the following:

- Chapter 9 Conclusion of the Assessment (not yet produced); please note: any conclusions/recommendations in the current chapter drafts reflect only very preliminary conclusions; these parts of the assessment will be revised and further developed as appropriate.
- Chapter 7 and some sections of Chapters 4, 5, 8, and 9.

Content of chapters 7, 8 and 9, in particular have yet to be drafted, for example when further results from modelling effort have been compiled. The preliminary drafts of chapters 8 and 9 circulated for national data check are therefore incomplete; however, they do incorporate notes and tables that provide an overview of the models and data that have been identified and will be addressed in the final versions. Models that will be summarized in Chapter 7 are listed in chapter 6. This will hopefully be sufficient to allow any gaps or omissions in national data to be identified during the national data check.

All materials compiled for this national data check are still under development and chapter structure, etc. may be adjusted following a drafting meeting that will take place in June; the assessment chapters will also be subjected to comprehensive peer review and linguistic/technical editing at a later stage. As such the drafts have not yet been through any editing; cited references may still be incomplete; graphics are often preliminary, and the chapter drafts include notes describing suggestions for work still to be undertaken. It is not the intention that the current round of checking addresses e.g. linguistic/technical editing issues.

The goal of the assessment is to produce a 'scientifically independent' assessment, so any comments should be with respect this objective, i.e., comments should be scientific and not attempt to insert or reflect national political views, etc.

<u>Note that these draft chapters are confidential and should not be cited, copied or circulated outside the context of this review.</u>

The deadline for responding on the national data check is <u>15 June</u>; however, if responses could be received by <u>5 June 2020</u> (in time for the SLCF drafting meeting) that would be

much appreciated. Please refer any comments to the line numbers added to the draft circulated for the national data check.

Table of contents of the drafts circulated for National Data Check

(yellow highlight indicates numbering provisionally inserted; green section missing in circulated PDF)

3. Open biomass burning

3.1 Policy questions:

- 3.1.1 Impact of climate change on fire risk and fire emissions
- 3.1.2 Fire management and open biomass burning emissions in the Arctic
- 3.1.3 Long term emissions from open biomass burning
- 3.1.4 Emissions from 'natural' fires
- 3.1.5 Human-caused open biomass burning emissions
- 3.1.6 Climate change will increase 'natural' fire emissions in the Arctic

3.2 Uncertainties in future open biomass burning emissions

- 3.2.1 Satellite-based fire emissions
- 3.2.2 Lack of agreement between official statistics and satellite-based emission inventories
- 3.2.3 Climate-driven ignitions, vegetation shifts, and fuel conditions
- 3.2.4 Constraining fire intensity and plume injection height for fire emissions
- 3.2.5 More future fires in Arctic peatlands, but where and how much?
- 3.2.6 Uncertainties in permafrost degradation
- 3.2.7 The role of people in future Arctic fire regimes

4. Advances in measurement techniques and observational capacity

4.0 Introduction

4.1 Particulate matter

- 4.1.1 BC in the atmosphere
  - 4.1.1.1 BC measurements using SP2
  - 4.1.1.2 Measurements of BC by instruments other than SP2
- 4.1.2. Measurement method of BC in snow/ice and rain
  - 4.1.2.1 Measurements of BC by instruments other than SP2
  - 4.1.2.2 Measurements of BC by SP2

4.2 Mineral dust

5. Observations, origins and trends of Arctic aerosols

5.2 Mineral dust

5.3 Ozone and precursors

- 5.3.1 Ozone sources and sinks
  - 5.3.1.1 Ozone sources (incomplete – missing natural sources, VOCs):
  - 5.3.1.2 Ozone sinks
- 5.3.2 Observed concentrations
  - 5.3.2.1 Surface site and ship in-situ observations
  - 5.3.2.2 Vertical profiles
  - 5.3.2.3 Satellite data
- 5.3.3 Observed trends in ozone
  - 5.3.3.1 Observed trends in ozone (and precursors)
  - 5.3.3.2 Vertical profile trends
- 5.3.4 Open questions (DRAFT): Observations, origins and trends
- 5.3.5 Summary

5.4 Methane

5.5 Clouds

5.6 Conclusions and Recommendations

6. Modeling of short-lived climate forcers, climate, and air quality

6.1 Introduction

6.2 Models for simulations of short-lived climate forcers and radiative forcing

- 6.2.1 CanAM5-PAM
- 6.2.2 CESM
- 6.2.3 CIESM-DESS
- 6.2.4 CMAM
- 6.2.5 DEHM
- 6.2.6 ECHAM-SALSA
- 6.2.7 EMEP-MSC-W
- 6.2.8 FLEXPART

6.3.4.2 Simulated aerosol optical depth trend vs AVHRR

6.4 Summary of SLCF models and their evaluation

Appendix

7. Simulated impacts on climate and air quality

7.1 Introduction

7.2 Future changes in global and Arctic climate systems

7.2.1 Summary of Type 3 simulations

7.2.2 CO2 impacts (either via ARTP or Type3 analysis)

7.2.3 PM2.5, ozone, and methane trends

7.3 Impacts of regional emissions on Arctic temperature, SLCFs, and air quality

7.3.1 Radiative forcings and absolute Arctic temperature change potentials

7.3.2 Comparison with Earth System Model projections and historic changes

7.3.3 Changes in burdens and concentrations of short-lived climate forcers in the Arctic

7.3.3.1 Methane

7.3.3.2 Black carbon

7.3.3.3 Ozone

7.3.3.4 Sulphate and OC

7.3.3.5 PM2.5,

7.3.3.6 Exceedance of AQ standards

7.3.4 Changes in radiative forcing within the Arctic

7.3.4.1 Methane

7.3.4.2 Black carbon

7.3.4.3 Ozone precursors

7.3.4.4 Sulphate and OC

7.3.4.5 CO2

7.3.5 Equilibrium temperature changes

7.3.6 Historic changes in Arctic temperature and air quality

7.3.7 Mitigation scenario impacts on Arctic temperature and air quality

7.4 Conclusions

7.4.1 Summary of uncertainty

7.4.2 Answers to policy-relevant science questions

8. Health and Ecosystem Impacts

8.1. Introduction

8.2 Review of evidence on air quality related health impacts

8.2.1 Health effects of PM2.5 and ozone

8.2.2. Burden of disease estimates in Arctic nations

8.2.3. Arctic and Nordic-specific emissions sources and health studies

8.2.3.1. Local emissions sources:

8.2.3.2 Arctic and Nordic-specific epidemiological studies

8.3. Review of evidence on air pollution impacts on ecosystems and crops

8.3.1 Deposition and Critical Loads:

8.3.2 Crop Impacts

8.4 Modeled impacts of SLCP emissions on health, depositions and crops in Arctic Council nations & observers

8.4.1 Models and Methods

8.4.2 Data and Methods for Health Impact Analysis (HIA)

8.4.3 Present-day (2015) impacts of air quality on health, critical loads and crops

8.4.3.1 PM2.5 and ozone health impacts

8.4.3.2. Sulfur and Nitrogen deposition and Critical loads

8.4.3.3. Crop impacts

8.4.4. Future benefits of emission mitigation on health, deposition and crops (2030, 2050)

8.4.4.1 PM2.5 and ozone health Impacts

8.4.4.2 Acidifying and eutrophying depositions

8.4.4.3 Crop Impacts

8.4.5 Uncertainties and sensitivity analyses

8.5. Conclusions

9. Conclusions and Recommendations

1. Introduction

1.1 Background

In 2015, AMAP expert groups published comprehensive scientific reports about the impacts of black carbon and tropospheric ozone (AMAP, 2015a) and methane (AMAP, 2015b) on atmospheric chemistry and climate in the Arctic. AMAP (2015a) expanded on and superseded a prior assessment focused only on black carbon (AMAP, 2011). The 2015 assessments clearly acknowledged the dominant role of anthropogenic carbon dioxide emissions in driving Arctic climate change, but estimated that the climate change mitigation potential from short-lived climate forcers (SLCFs) is approximately 0.5 degrees in the Arctic by 2050, if all technically feasible emission reduction measures targeted specifically to address the warming species, specifically black carbon and methane, are implemented. Substantial uncertainties remain, however. To provide a better scientific underpinning for policy decisions, more work is needed in Earth System modeling and monitoring capabilities in the Arctic, and also in the development of emission inventories, including of anthropogenic and natural emissions at present and associated with future mitigation options.

Additional call for robust scientific information comes from the Arctic Council Framework for Action on Black Carbon and Methane Emissions Reductions document adopted in 2015, which calls for "continuing monitoring, research and other scientific efforts, with the inclusion of traditional and local knowledge, to improve the understanding of black carbon and methane emissions, emission inventories, Arctic climate and public health effects, and policy options" and supports "a four-year cycle of periodic scientific reporting, including the assessment of status and trends of short-lived climate pollutants such as black carbon and methane with a focus on the impacts of anthropogenic emissions on Arctic climate and public health. This should include estimates of associated costs of mitigation, as well as enhancing our state of knowledge regarding natural sources."

In the ministerial declaration from Fairbanks in 2017 the Arctic Council "Adopt[ed] the first Pan-Arctic report on collective progress to reduce black carbon and methane emissions by the Arctic States and numerous Observer States and its recommendations, including an aspirational collective goal, acknowledge[d] the importance of implementing those recommendations as nationally appropriate, recognizing that Arctic communities are entitled to develop in accordance with their needs and interests…". The aspirational collective goal presented in the first Pan-Arctic report on collective progress to reduce black carbon and methane emissions states that the "black carbon emissions be further collectively reduced by at least 25-33 percent below 2013 levels by 2025". This goal provides a relevant setting for further scientific analyses on emission reduction strategies.

In 2016, the two expert groups focusing on methane and black carbon + tropospheric ozone were merged into the new AMAP SLCF expert group (EG). The AMAP Working Group (WG) tasked the SLCF EG to provide a new comprehensive assessment on the state of the science of Arctic impacts from SLCFs in advance of the 2021 Arctic Council ministerial meeting.

1.2. Introduction to SLCFs and scope of this assessment

SLCFs include all agents that have the potential to directly or indirectly alter Earth's radiative energy budget, and which also have relatively short residence times in the atmosphere. SLCFs include gaseous species such as ozone, methane, and nitrous oxides, and also aerosols (either in solid or liquid form) such as black carbon, sulphate, and mineral dust. There is not a universally agreed-upon lifetime threshold for agents to be considered "short-lived", but all agents included in the SLCF basket have lifetimes shorter than that of carbon dioxide. Indeed, methane, which has a lifetime of ~12 years, is considered an SLCF in some communities but not others. Because atmospheric methane concentrations are chemically influenced by species which are clearly short-lived, however, it is reasonable to explore its climate impacts consistently with other SLCFs. Key properties of some of the SLCFs considered in this assessment are listed in Table 1.

SLCFs influence climate through various mechanisms. The gaseous SLCFs like methane and ozone amplify Earth's greenhouse effect by absorbing infrared radiation. Ozone also warms the stratosphere by absorbing ultraviolet radiation from the sun, though this assessment focuses primarily on tropospheric ozone, whose dominant influence is as a greenhouse gas. Methane also absorbs a small amount of solar radiation, as indicated in recent upward adjustments to its global warming potential (Etminan et al., 2016). In considering the radiative and climate impacts from both of these species, we must consider emissions of precursor species that alter their atmospheric concentrations. Species that can strongly affect tropospheric ozone concentrations through chemical reactions include nitrous oxides (NO_x), carbon monoxide (CO) and volatile organic compounds (VOCs). These species also influence methane, though its atmospheric concentration is governed more strongly by direct emissions of methane.

Aerosols mostly affect climate by altering the amount of solar energy absorbed by Earth. Black carbon, a product of incomplete combustion, absorbs a high proportion of incident sunlight and therefore warms the climate system. Sulphate, which is formed primarily through oxidation of sulphur dioxide gas, absorbs very little sunlight and cools climate by scattering solar radiation back to space that would otherwise have been absorbed. Organic carbon, which is co-emitted with black carbon during combustion, absorbs an intermediate proportion of sunlight and causes cooling in some environments and warming in others. Highly reflective regions such as the Arctic are more likely to experience warming effects from these aerosols (e.g., Myhre et al, 2013). Mineral dust and volcanic ash can also warm or cool climate depending on the content of light-absorbing minerals (especially those

containing iron) in the soil or rocks from which they are derived. Because some dust and volcanic ash particles are quite large, they can also absorb an appreciable amount of infrared radiation and warm Earth by enhancing its greenhouse effect (e.g., Miller and Tegen, 1998, Flanner et al., 2014). Large particle size also, however, reduces the atmospheric lifetime of these aerosols. Typical lifetimes for sulphate, BC and OC are on the order of days to weeks, whereas lifetimes of larger dust and ash particles are of order one to several days.

Aerosols also influence climate via indirect mechanisms. After depositing to snow and ice surfaces, dark particles like black carbon can hasten ice melt by increasing solar heating at the surface. This is an especially important consideration for Arctic climate impacts of SLCFs (e.g., AMAP, 2015a). Aerosols also affect cloud properties, including their droplet size, lifetime, and vertical extent, thereby influencing both the shortwave cooling and longwave warming effects of clouds. Globally, this indirect cloud forcing from aerosols is likely larger than their direct forcing, though the indirect effects are more uncertain and difficult to accurately assess. Moreover, Arctic cloud impacts are different than global cloud impacts, owing to the extreme seasonality of sunlight in the Arctic and unique characteristics of Arctic clouds (e.g., high frequency of mixed-phase occurrence).

When quantifying Arctic climate impacts of SLCFs, it is also important to consider how SLCFs residing outside the Arctic influence the poleward heat flux and thereby influence Arctic climate. This consideration is especially important in the Arctic, where poleward heat flux constitutes a substantial portion (roughly 100 W/m^2) of the energy budget. AMAP (2015a), for example, found that SLCF emissions from key regions like East Asia caused greater perturbations to Arctic climate via their alteration of poleward heat flux than through their direct radiative impact within the Arctic. Emissions from high-latitude regions like Russia and Canada, on the other hand, were found to primarily affect the Arctic via their influence within the Arctic, and they did so with greater effectiveness because of their greater likelihood to deposit to snow and ice surfaces and heat the lower troposphere (AMAP, 2015a; Sand et al., 2016).

Many of the SLCFs that are of interest for climate purposes also adversely influence air quality and human health. These include all components of particulate matter, especially contributors to smaller sized particles, and precursors of ozone. Furthermore, whereas the climate impacts of SLCFs may be positive or negative, the air quality impacts of SLCFs are nearly universally negative. This is one reason why policies to reduce emissions of SLCFs have also been justified perhaps sometimes more by air quality concerns than climate concerns. Recognition that knowledge of both climate and air quality impacts is important for policy considerations has led to an expansion of this assessment, relative to AMAP (2015a; 2015b), to include air quality impacts.

Almost all SLCF species have both anthropogenic and naturally occurring emissions, though with different proportions. Black carbon, for example, is emitted mostly from anthropogenic combustion of fossil fuel and biofuel, though some is emitted from naturally occurring fires. Volcanic ash, on the other hand, is entirely natural. In cases where the human influence on emissions is indirect, the proportion of natural and anthropogenic emissions can be quite uncertain. These grey areas exist for (e.g.,) mineral dust aerosols, which derive both from natural desert soils and from soils made erodible by human activity, and methane, which can be created from naturally-occuring biota whose prevalence has changed due to anthropogenically-induced warming or hydration of soils. Understanding how these indirectly-affected emissions will change in the future is a matter of even greater uncertainty. This assessment focuses more on emissions that are clearly anthropogenic, as it is within human capacity to mitigate climate change and improve air quality via alterations of these emissions. In assessing climate and air quality perturbations from anthropogenic emissions, however, it is often important to know the background quantities of naturally-occurring agents. To the extent possible, this assessment incorporates this knowledge, though significant gaps remain in this and other key areas.

Finally, the Arctic environment is changing rapidly and this also has consequences for how SLCFs affect the Arctic. Diminishing sea ice, thawing of permafrost, expansion of shrubs, humidification of the Arctic troposphere, and increasing prevalence of liquid clouds are all examples of changing environmental conditions that can affect the emissions of SLCFs and also the lifetime and radiative forcing of SLCFs within the Arctic.

Due to the emphasis of this assessment on anthropogenic SLCFs and the limited number of experts within the EG, the scope of this assessment is necessarily limited, though it has broadened somewhat relative to the 2015 assessments. SLCF species considered here include methane, tropospheric ozone and its associated precursors including NOx, CO and to a lesser extent VOCs, and a suite of aerosol species that includes black carbon, organic carbon, sulphate (and its precursor SO2 emissions), and mineral dust. Volcanic and fire-derived ash are also discussed, though they are not treated comprehensively. Halocarbons are not treated in this assessment. Nitrate and secondary organic aerosols are treated in some of the models applied in the assessment, but impacts from these species are not rigorously explored here. Finally, considerable attention has been brought recently to snow and ice algae living on the Greenland Ice Sheet. We discuss these biological impacts in the context of incremental darkening caused by black carbon and dust deposition.

The assessment is outlined as follows… To the extent possible, the assessment focuses on new results and knowledge obtained since the AMAP 2015 assessments. We refer readers to these assessments for additional background information.

Table 1.1 SLCFs considered in this assessment				
	Atmospheric Lifetimes	*Major Precursors*	*Spectrum of Action (Solar or IR)*	*Indirect Effects*
Gases				
Methane	~12 years		IR (dominant), Solar	
Tropospheric Ozone	~1 month	NOx, VOCs, CO	IR (dominant), Solar	
Aerosols				
Black Carbon	~1 week		Solar	snow/ice albedo, clouds
Mineral Dust	~1 week or less		Solar, IR	snow/ice albedo, clouds
Primary Organic Carbon	~1 week		Solar	snow/ice albedo, clouds
Sulphate	~1 week	SO2, DMS	Solar	clouds
Volcanic Ash	~1 week or less		Solar, IR	snow/ice albedo, clouds
PM2.5 (for air quality)	~1 week	dust, BC, OC, sulphate		

[Figure ?] Radiative balance of the Arctic (atmospheric and ocean heat transport into the Arctic, clouds, ...)

References:

AMAP Assessment (2015): Black carbon and ozone as Arctic climate forcers. Arctic Monitoring and Assessment Programme (AMAP), Oslo, Norway. vii + 116 pp.

AMAP (2011): The Impact of Black Carbon on Arctic Climate, P. K. Quinn, A. Stohl, A. Arneth, T. Berntsen, J. F. Burkhart, J. Christensen, M. Flanner, K. Kupiainen, H. Lihavainen, M.

1176 Shepherd, V. Shevchenko, H. Skov, and V. Vestreng. Arctic Monitoring and Assessment
1177 Programme (AMAP), Oslo. 72 pp.

1178 Etminan, M., Myhre, G., Highwood, E. J., and Shine, K. P. (2016), Radiative forcing of carbon
1179 dioxide, methane, and nitrous oxide: A significant revision of the methane radiative
1180 forcing, Geophys. Res. Lett., 43, 12,614– 12,623, doi:10.1002/2016GL071930.

1181 Flanner, M. G., A. S. Gardner, S. Eckhardt, A. Stohl, J. Perket (2014), Aerosol radiative forcing
1182 from the 2010 Eyjafjallajökull volcanic eruptions, J. Geophys. Res. Atmos., 119, 9481-
1183 9491, doi: 10.1002/2014JD021977.

1184 Miller, R. L., and I. Tegen (1998), Climate response to soil dust aerosols, J. Clim., 11(12),
1185 3247–3267, doi:10.1175/1520-0442(1998)011<3247:CRTSDA>2.0.CO;2

1186 Myhre, G., D. Shindell, F.-M. Bréon, W. Collins, J. Fuglestvedt, J. Huang, D. Koch, J.-F.
1187 Lamarque, D. Lee, B. Mendoza, T. Nakajima, A. Robock, G. Stephens, T. Takemura and H.
1188 Zhang, 2013: Anthropogenic and Natural Radiative Forcing. In: Climate Change 2013: The
1189 Physical Science Basis. Contribution of Working Group I to the Fifth Assessment Report of
1190 the Intergovernmental Panel on Climate Change [Stocker, T.F., D. Qin, G.-K. Plattner, M.
1191 Tignor, S.K. Allen, J. Boschung, A. Nauels, Y. Xia, V. Bex and P.M. Midgley (eds.)].
1192 Cambridge University Press, Cambridge, United Kingdom and New York, NY, USA.

1193 Sand, M., T. K. Berntsen, K. von Salzen, M. G. Flanner, J. Langner, and D. G. Victor (2016),
1194 Response of Arctic temperature to changes in emissions of short-lived climate forcers,
1195 Nature Clim. Change, 6, 286-290, doi: 10.1038/nclimate2880.

2. Emissions of short-lived climate forcers in an Arctic context

(Tentative list of authors and contributors, not ordered: K. Kupiainen, , Z. Klimont, V.-V. Paunu, J. Christensen, J. Fu, L. Höglund-Isaksson, M. Crippa, V. Vestreng?, S. Anenberg?,...)

2.1 Introduction

This section presents emission data and scenarios used in the modelling work for this Assessment (Chapter X). The estimates of historical emissions are compared with the most recent available emission datasets, including national reporting data. While the focus is on providing background information about the assumptions behind the scenarios and respective development of short-lived climate pollutants (SLCFs) including black carbon (BC) and methane (CH4) emissions, there is also information about other key species included in the modelling work, especially SO2.

This section also provides background material supporting answers to the emission related Policy Relevant Science Questions (PRSQs) which can be found in Chapter X where explicit references to sections in this chapter are made.

2.2 Defining scenarios for the assessment

The scenarios developed for this assessment need to consider new (since the previous assessment (AMAP, 2015)) data on energy and emission sources, further established environmental legislation, and new perspectives on how the energy system might develop in the near future. Furthermore, there have been advancement in tools and methods applied to estimate emissions, distribute them spatially and temporally, as well as revisions of officially reported emissions.

As for the 2015 Assessment, the emission scenarios have been developed with the GAINS model (Amann et al., 2011). They are an update and extension of the previously used dataset providing an overview of historical emissions until the year 2015 and a projection extending to 2050. They include all key air pollutants (SO2, NOx, BC, OC, NMVOC, CO, NH3, PM2.5) and greenhouse gases (CO2, CH4) at a global scale. The overview and a more detailed description of assumptions and scenarios' characteristics will be published in

Klimont et al. (in preparation) while methane has been already documented in Hoglund-Isaksson et al. (2020).

Box 2.1 provides an overview of the key sources and assumptions about the energy data and projections used as well as evolution and comparison of CO2 emissions to scenarios developed for the sixth cycle of the IPCC report (AR6), the so called Shared Socioeconomic Pathways (SSPs) (Riahi et al., 2017). The three underlying activity scenarios implemented in GAINS for use in AMAP Assessment provide a wide range of possible future development from the high fossil fuel case to a scenario similar to rapid decarbonization necessary to constrain additional warming to below 2oC, globally.

Box 2.1 **Key assumption behind anthropogenic emission scenarios**

The energy data originates from the statistics of the International Energy Agency (IEA) and the projections rely on the 2018 World Energy Outlook (IEA, 2018) that were translated and incorporated into the GAINS model framework. The agricultural projections are derived from Food and Agriculture Organization (FAO) (Alexandratos and Bruinsma 2012). The IEA (2018) macro-economic assumptions include a 25% growth in global population and a 90% increase of GDP by 2050. The baseline (_base) scenario assumes implementation of national energy programs and commitments of the Nationally Determined Contributions (NDCs) towards Paris goals; its CO2 emissions appear comparable to SSP2-45 evolution. Two additional activity scenarios were developed where, (i) NDCs are not included resulting in higher fossil fuel use (_CPS) and CO2 emission trajectory resembling SSP4-60, and (ii) a sustainable development scenario (_SDS) which resembles a SSP1-26 decarbonization scenario with quick transformation away from fossil fuels, access to clean energy for cooking and achieving several other Sustainable Development Goals (SDGs). Charts below compare the CO2 emissions in GAINS ECLIPSE scenarios to the key SSP cases and show CO2 emissions for the aggregate of Arctic Council countries.

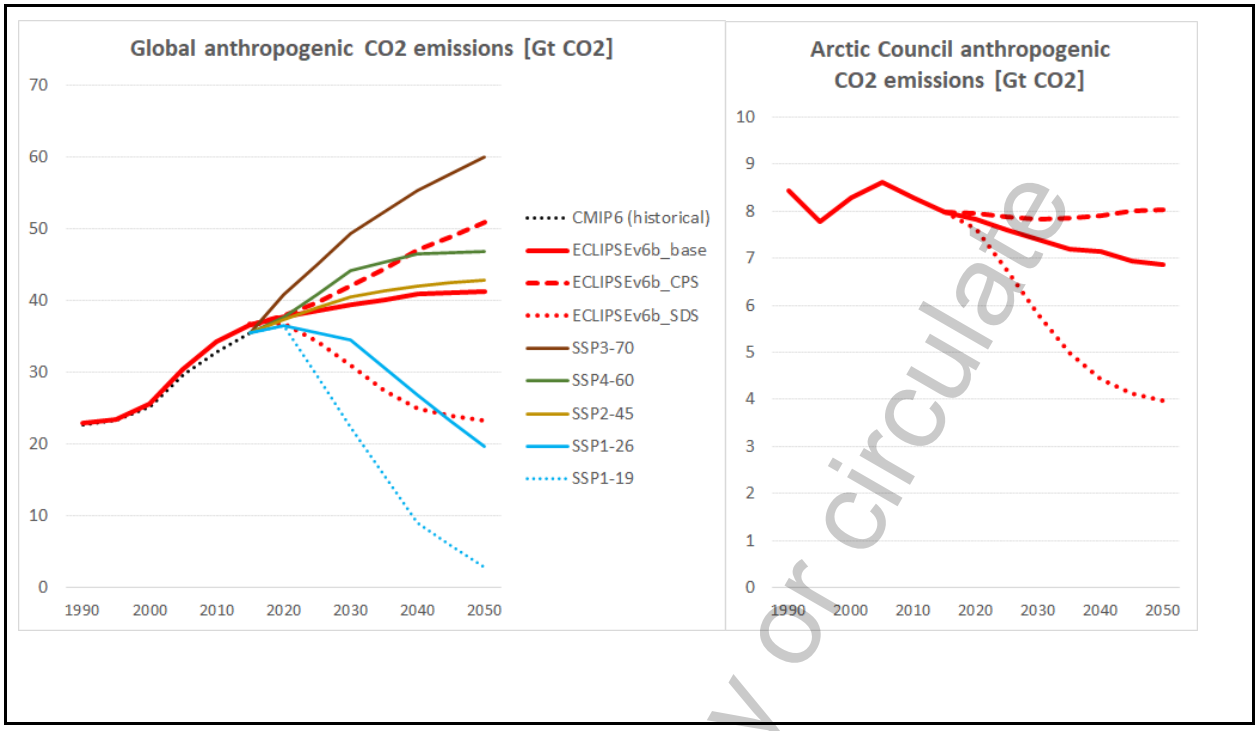

With support of the European Commission Action on Black Carbon in the Arctic, the GAINS model was updated to include statistical data for 2015, review assumptions on new policies and their implementation, improve spatial gridding of emissions, and finally to develop and implement several new scenarios for use in the assessment.

One particular aspect worth highlighting are improvements in spatial distribution of emissions. The spatial proxies for many sources have been revised including residential sector, shipping, power plants, oil and gas operations including flaring, transportation. In all cases new data was used either providing higher resolution or more up to date representation of source location. Two particular elements that appear to make a visible difference is new distribution of residential (heating) emissions as well as flaring of associated gas. Fig 2.2.1 below shows not only higher granularity of emissions in many regions but also identifies more emissions in high latitudes in sparsely populated areas, which has been identified as a problem in the past (e.g., Winiger et al., 2019). The new dataset has implications for distribution of all species, not only BC as shown below, and should allow for improved modelling.

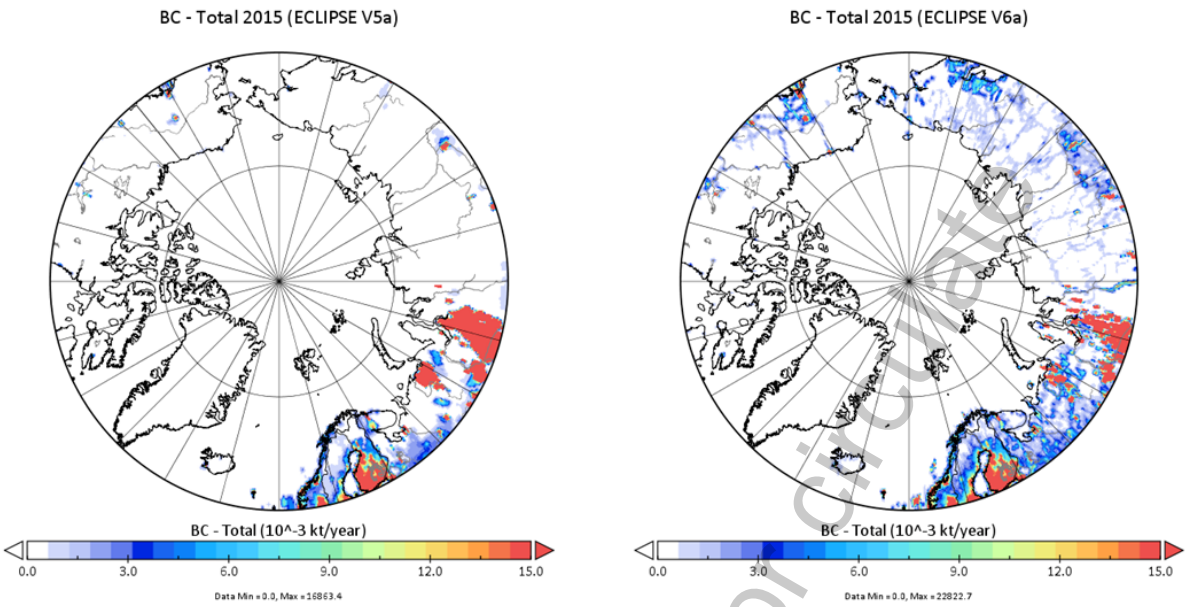

Figure 2.2.1 Spatial distribution of total 2015 BC emissions beyond 60oN in ECLIPSE V5a set (left, used in AMAP 2015 assessment) and the new ECLIPSE V6b (right).

The developed scenarios can be categorized into three types: (i) baseline, (ii) mitigation, and (iii) failure.

- **Baseline** (CLE): Assumes *base* (see BOx 2.1) energy projection and efficient implementation of the current air pollution legislation committed before 2018
- **Mitigation**: Dedicated reduction of all or specific pollutants is envisaged; there are two categories here:
    - Maximum technically feasible reduction (MFR) case where implementation of best available technologies defined in the GAINS model is included. The introduction of measures is not constrained by their costs but there are limitations on how quickly certain measures achieve high market penetration, i.e. no premature scraping of equipment is assumed. Two scenarios were developed (i) MFR for baseline activity data (base_MFR), and (ii) MFR for the sustainable development case (SDS_MFR)
    - Mitigation of short-lived climate forcers (SLCF) case where focus is on further (beyond CLE) reduction of emissions applying technologies which result in lower climate forcing of net emissions after abatement. Principally, this means MFR type of mitigation for CH4 and near MFR reduction of BC where also additional reductions of cooling species (OC, SO2, and NOx) occur as

these are necessary to achieve full BC mitigation. Additionally, CO and NMVOC are reduced strongly, while ammonia (NH3) remains at the level of CLE. This type of scenarios have been developed to allow comparison with the mitigation simulations performed in the AMAP 2015 assessment as well as to explore futures with less pronounced reduction of colling species while warming SLCFs reach minimum. Two scenarios were developed: (i) SLCF reduction for base case (base_SLCF), and (ii) SLCF for SDS case (SDS_SLCF).

- **Failure**: No further control (NFC) - this scenario attempts to demonstrate the importance of current policies and assumes a failure in implementation of policies in recent years and so freezes the level of implementation of laws at the level of pre 2015 legislation. Two scenarios developed: (i) NFC for baseline (NPS_NFC), and (ii) NFC for the higher fossil fuel case, the so called CPS (see BOx 2.1), assuming that both national energy efficiency and structural goals established in the post Paris process as well as recent air pollution laws are not implemented (CPS_NFC).

Further text provides analysis of the trends of emissions for Arctic Council and Observer countries as well as available mitigation potential.

2.3 Recent trends in Arctic Council and observers' SLCF emissions

- *Shipping - both Arctic and global and legislation on sulfur (reference to the detailed section)*
- *Discussion includes baseline and how important it is to achieve baseline (failure scenarios)*
    - *Evaluation of development towards the AC BC goal*
    - *Discuss CH4 - incl AC vision to significantly reduce emissions (which is not happening according to CLE.*

Figure 2.3.1 shows the different baseline developments of human made BC, SO2 and CH4 emissions in 2010 to 2050 in the Arctic Council and its Observer countries as estimated by the IIASA institute's GAINS model. All analysed emission scenarios indicate a declining trend for black carbon emissions in the Arctic Council with the scenarios with existing policies and

also point out that the voluntary Arctic Council black carbon goal can almost be achieved already with current policies in the baselines.

The "v5a base"-scenario indicates the evaluation of the emission pathway with air pollutant legislation as estimated in the AMAP 2015 assessment and the "base CLE"-scenario reflects the evaluation of the emission pathway with current policies targeting air pollutants. A comparison of these scenarios indicates legislative changes and adoption of new policies aimed at emission reductions of air pollutants. In the case of black carbon emissions, the Arctic Council member countries the updated scenario (base CLE) follows relatively similar emission development as the scenario used in the 2015 assessment (v5a base). However, in the Arctic Council Observer countries the current evaluation of the black carbon emission scenario indicates that "base CLE"-scenario is significantly lower than the 2015 situation, which is a result of the development of new clean air policies in Asia. The AC Observer countries are on a declining emission pathway for black carbon in all baselines. SO2... CH4...

Base_NFC and CPS_NFC show how failure to meet the already decided emission mitigations will put the BC emission trajectory further from the Arctic Council 2025 target. This highlights the importance of applying the decided commitments.

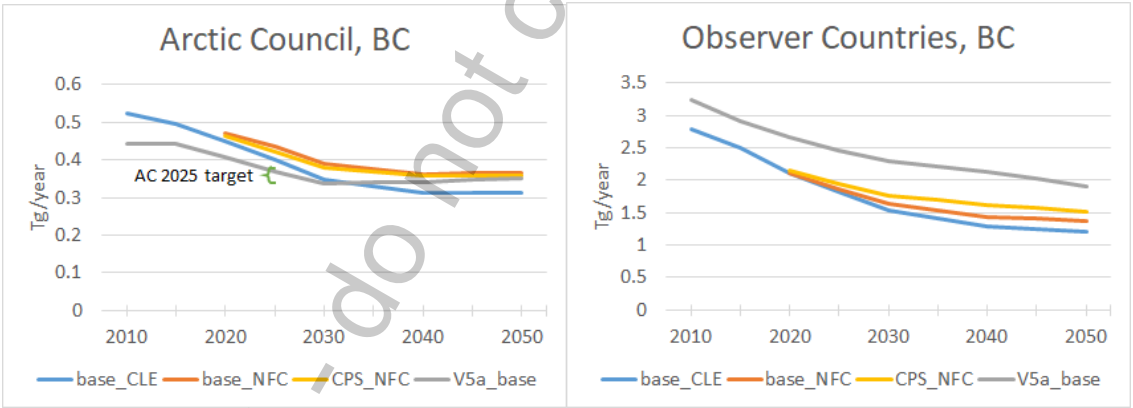

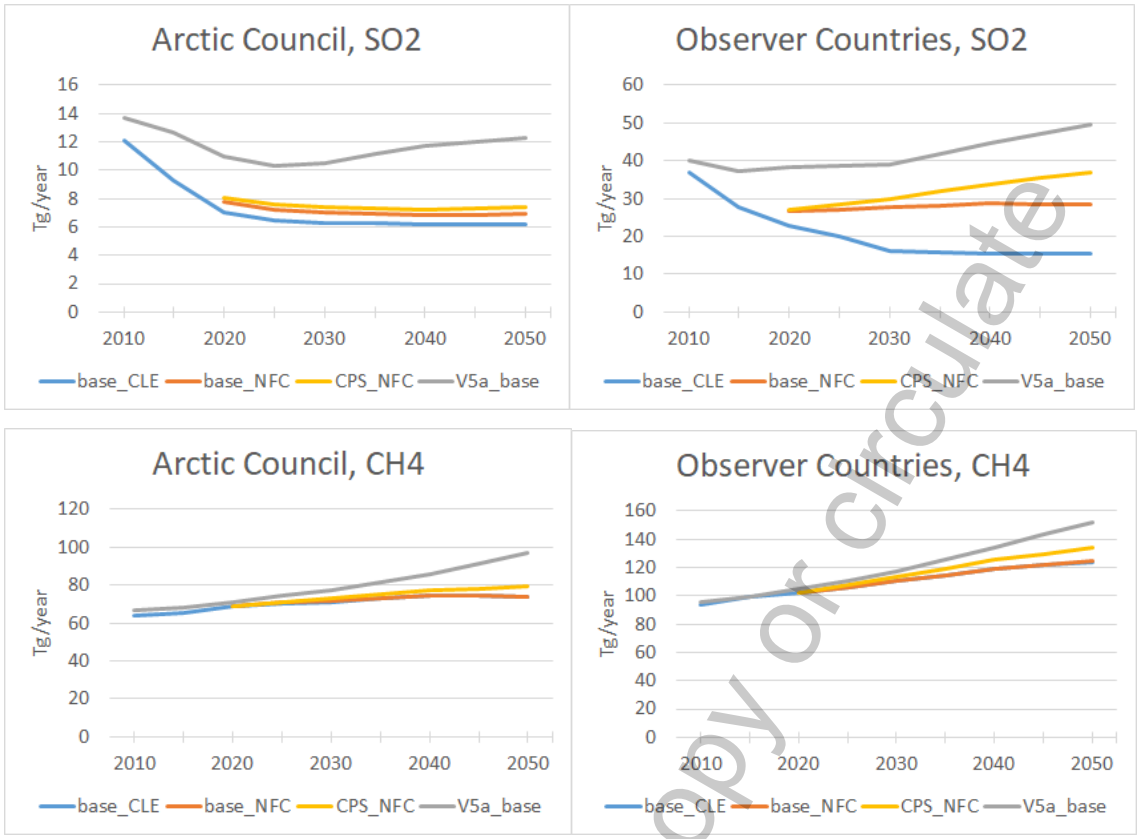

Figure 2.3.1 BC, SO2 and CH4 emissions in the baseline scenarios and ECLIPSE V5a baseline, which was used in the AMAP assessment 2015.

[*NFC and CPS lines will be connected to 2015 in the next version.*]

Figure 2.3.2 shows the sectoral shares of BC, SO2 and CH4 emissions in 2015 for the current and AMAP 2015 assessment baselines. For BC in Arctic Council countries, the *traffic* sector has increased its share from the 2015 assessment, and the *domestic* sector reduced almost with the same amount. In the AC Observer countries there has been a similar development, although change in the *traffic* sector is smaller and in the *domestic* larger. Also, there is an increase in the share of the *waste* sector. The reasons for these changes are..

SO2… CH4...

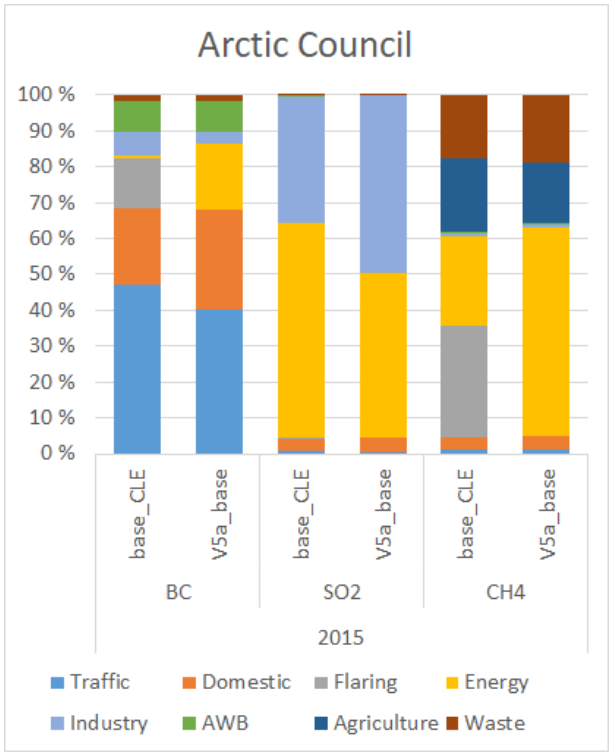

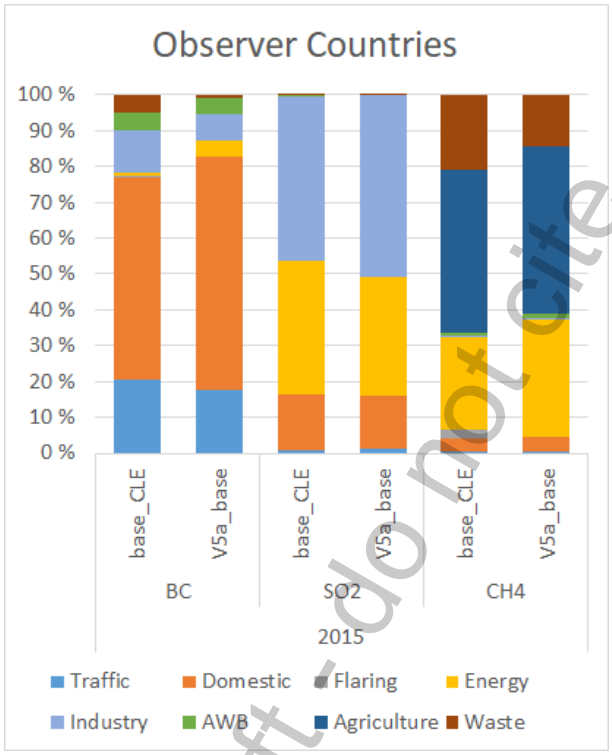

Figure 2.3.2 Share of BC, SO2 and CH4 emissions by major sectors. In V5a (AMAP 2015 assessment baseline) flaring is part of the energy sector.

[*"Traffic" could be renamed to "Surface transport" or similar.*]

Figure 2.3.3 presents relative changes in the emissions in the baseline scenarios compared to the base_CLE 2015 emissions. AMAP 2015 assessment baseline V5a_base is compared to its own 2015 emissions. In the Arctic Council countries the net reduction in 2030 and 2050 for BC emissions was slightly larger than in the AMAP 2015 assessment in the base_CLE. In base_NFC and CPS_NFC the net reductions were similar or slightly smaller in 2030 and slightly larger in 2050. The majority of the emission reduction comes for the *traffic* sector. In the AC Observer countries current scenarios show larger net reductions than AMAP 2015 assessment in 2030, and similar, although smaller difference, in 2050. Main reductions come from the *domestic* sector, and some from the *traffic* sector. The differences are caused by...

SO2… CH4...

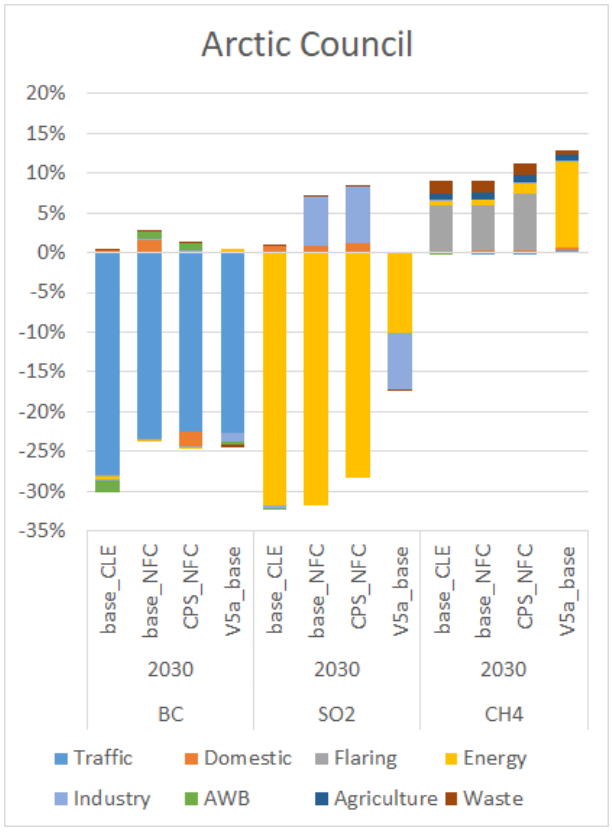

2164

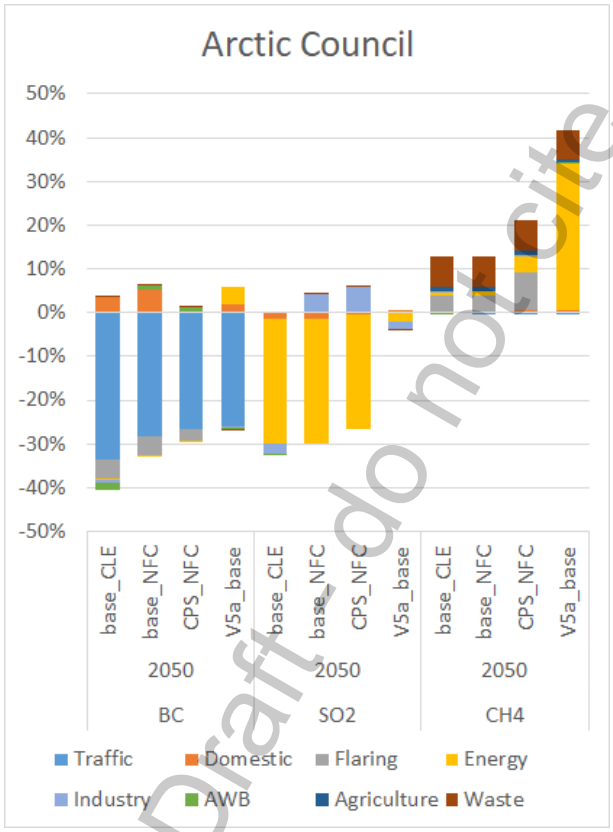

2165

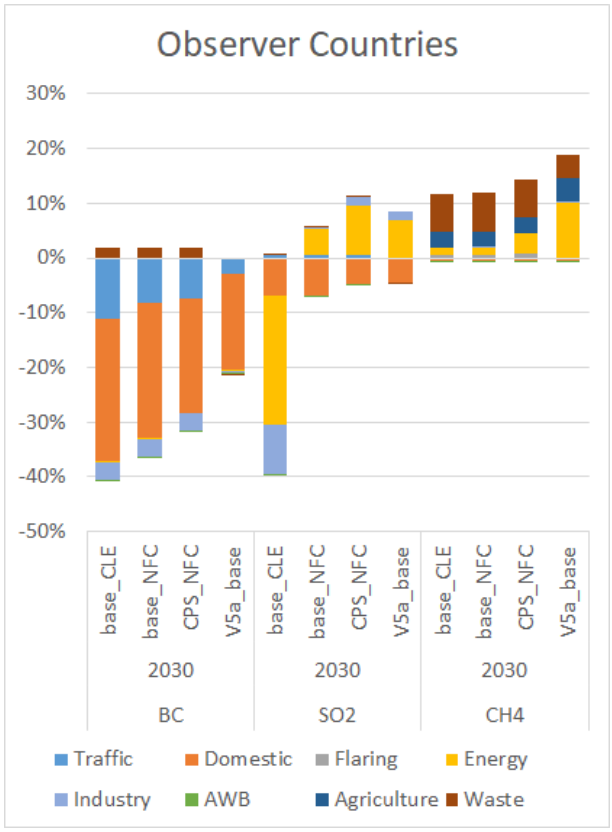

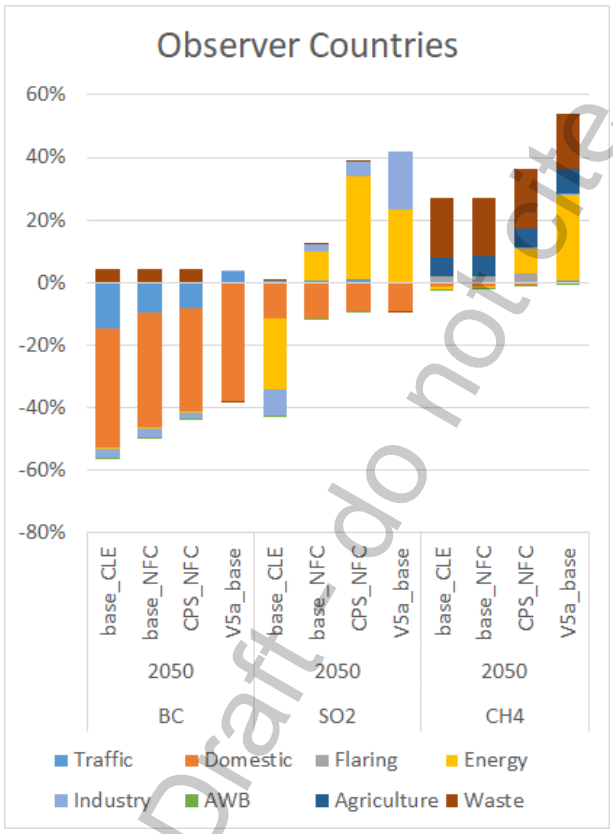

Figure 2.3.3 Relative change in emissions from 2015 to 2030 and 2050 under the baseline scenarios. All changes are to base_CLE scenario 2015 emissions, except V5a_base, which is compared to its own 2015 emissions.

[*"Net changes added as points later."*]

Global share of BC, SO2 and CH4 emissions are presented in table 2.3.1.

Table 2.3.1 Share of global BC, SO2 and CH4 emissions for the Arctic Council Member and Observer countries and the rest of the world for 2015, 2025 and 2050 in base_CLE. Global share of AC Observer countries BC emissions are expected to reduce from 2015 to 2050 due to… AC Members country shares are expected to remain almost similar. SO2 and CH4 emission shares are expected to remain similar to the 2015 situation without mitigation actions.

Although the share of Arctic Council member countries of the global BC emissions is a bit below 10 %, the emissions occur within and close to the Arctic area, increasing their impact on the Arctic climate to the emission from southern sources. Furthermore, Arctic Council has an important role in demonstrating the BC emission mitigation options and feasibility of said actions.

2015 Gg a^{-1}	Arctic Council Members	Arctic Council Observers	Rest of the world
BC	495	2511	3205
	8 %	40 %	52 %
SO2	9239	27782	33170
	13 %	40 %	47 %
CH4	65523	99245	162865
	20 %	30 %	50 %

2025 Gg a^{-1}	Arctic Council Members	Arctic Council Observers	Rest of the world
BC	400	1816	3313

	7 %	33 %	60 %
SO2	6482	19859	23446
	13 %	40 %	47 %
CH4	70612	105966	181656
	20 %	30 %	51 %

2189

2050 Gg a^{-1}	Arctic Council Members	Arctic Council Observers	Rest of the world
BC	313	1209	3680
	6 %	23 %	71 %
SO2	6207	15261	28666
	12 %	30 %	57 %
CH4	73925	124179	236736
	17 %	29 %	54 %

2190

2191 Graph on the failure scenario vs. baseline to highlight importance of baseline commitments.

2192

2193 **2.4 High-Arctic emission sources and communities [could be a BOX?]**

2194 - *...general text about the importance and specific aspects of this region and particular*
2195 *sources with a focus on: shipping, distributed electricity, lack of waste management,*
2196 *oil and gas as an important economic sector. Mention the spatial distribution and*
2197 *refer to the uncertainty discussion.*
2198 - *Could consider also adding a map showing spatial distribution of shipping based on*
2199 *the recent data*

2200

2201 **2.4.1 Arctic shipping**

2202 Since the last 2015 assessment there have been developed several emissions inventories,
2203 which covers the Arctic. Common for these inventories is that the spatial and temporal
2204 information about shipping are based on the Automatic Identification System (AIS) data for

the assessment of shipping emissions. The AIS data are mainly retrieved from AIS satellite receivers and for some inventories from terrestrial base stations. The AIS system is very useful because it provides information about the ships and continuously automatic information on the positions of the ships and their speeds. It is possible by combining this information with ship engine power functions and emission factors for different ship types to construct the emissions from individual ships in a realistic way in order to make a reliable bottom-up emission inventories. In the 2015 assessment the Arctic inventory described in Winther et al. (2014), referred to as 'W2014', was made by using this methodology. Furthermore, there has been more focus on emissions factors, especially for BC.

In Johansson et al. (2017)), referred to as 'J2017, a comprehensive global shipping emission inventory and the global activities of ships for the year 2015 have been published. The emissions were estimated using the Ship Traffic Emission Assessment Model (STEAM3) that uses AIS data. The STEAM3 model is a comprehensive model with special treatment of input data, path generation of ship routes, taking into account meteorological conditions, etc. This inventory has a relatively large emissions factor for BC of 0.47g/kg fuel, which has been estimated from emissions of BC and CO_2, compared to the other inventories.

ICCT published in 2017, referred to as ICCT2017, a report with a global emission inventory of BC for shipping based on combined terrestrial and satellite based AIS data and IHS ship registry data. Gaps in AIS were linear interpolated. The report has a detailed discussion of the emissions factor for BC. The mean emission factor globally is 0.25 g/kg fuel. According to report, 0.7% of the global BC emissions of 67kT/y are North 60°N

The global ECLIPSE_v6b emissions (see Klimont et al (in preparation), referred as K2017) which are used in the model calculations in this assessment also include ship emissions. The emissions for 2015 are based on activity data developed on the basis of FMI data with a BC emission factor of about 0.11 g/kg for shipping outside ECA (similar to assumptions in Winther et al (2017)) and <0.05 g/kg within ECA. Since emission factors are independently assumed for various fuels (HFO, LFO, LNG) and their shares change over time and also are different in the ECA the actual implied emission factors are regionally specific and change over time.

In the report by Winther et al (2017), referred to as W2017, there has been an update of the original Arctic emission inventory on a domain defined as north of 60°N, and described in W2014 and in the old 2015 assessment. In this work, AIS data for 2012 -2016 instead for only 2012 have been used. There is some variability between the years, see fig 1. A mean emissions inventory representing the year 2016 based on 5 years AIS data has been constructed and this mean inventory has a total fuel consumption which is 20% higher than the original 2012. Furthermore, there has been a focus on updating the emissions factors based on new studies, especially for BC. The mean BC emissions factor for 2016 is 0.10 g/kg Fuel, which is a factor 3.5 lower than the old factor. Furthermore, the mean BC emissions factor for the future scenario is decreasing to 0.074 g/kg fuel in 2050 due to expected changes in the used fuel. In the old work, it was assumed that this factor was constant on 0.35 g/kg Fuel for all scenarios as in emissions inventories as described in Corbett (2010).

In fig. 1 the total fuel consumption for the area north of 60°N for the 5 years 2012-2016a re shown. The trend shown at the figure is not significant. In PAME – Arctic Shipping Status Report #1 (2020) there is published data about the current shipping in areas covered by the Polar Code Area. The information about the shipping activities are based on PAME's Arctic Ship Traffic Data (ASTD) project, which has been developed in response to a growing need to collect and distribute accurate, reliable, and up-to-date information on shipping activities in the Arctic. The ASTD System collects a wide range of historical information, including ship tracks by ship type, information on number of ships in over 60 ports/communities across the Arctic, detailed measurements on emissions by ships, shipping activity in specific areas. In the report there are published data for the sailed distance for the period 2013-2019, and they show a monotone increasing trend with a 75% increase between 2013 and 2019. This is not completely consistent with results from W2017, which are shown in fig. 1. The reason could be that Polar Code Area is a subdomain of the area north of 60°, which are used in W2017, and there are large shipping activities outside the Polar Code Area. According to the 2015 assessment only 10-15% of total traffic amount north of 60°N took place inside the Polar Code Area.

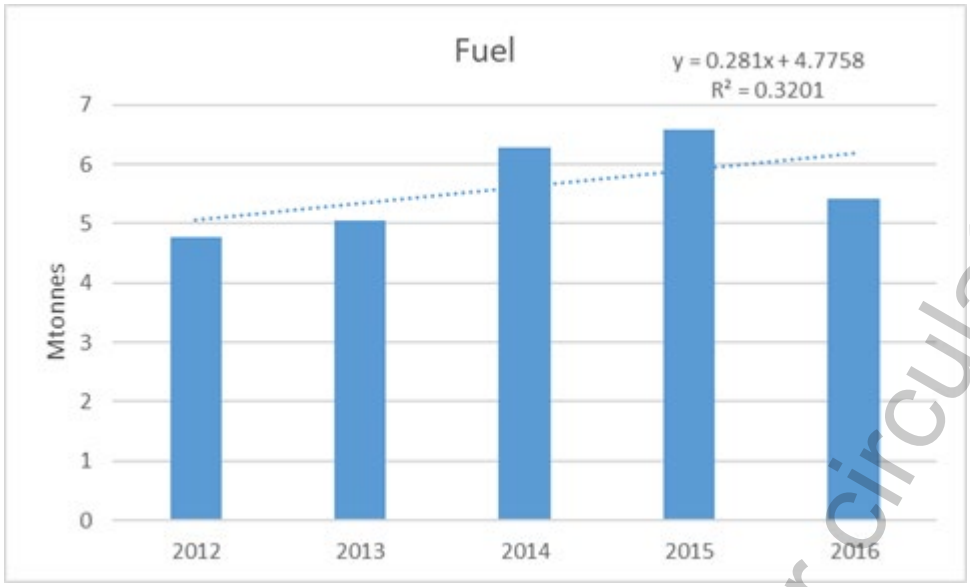

Fig. 1. Total Fuel consumption for the area North of 60°N (see W2017)

Fig. 2 shows emissions of SO2, NOx and BC in Mg/y for the year 2015 for K2017, J2017 and ICCT2017 and for 2016 for W2017, for the area North of 60N.

For SO_2 K2017 has the highest emission estimate with about 50% higher emissions than W2017 and 85% higher than J2017. The SO2 emissions are lower than the emissions given in the old 2015 assessment mainly due to changed sulfur content in the fuel.

For the NOx emissions W2017 has the highest emissions with about 80-100% higher than K2017 and J2017. The main reasons for this is that total estimated fuel consumption is 85% higher compared to J2017 based on the CO_2 emissions. These NOx emissions are comparable with results in 2015 assessment.

For BC emissions J2017 have the highest emission, approximately between 150-240% higher than the other three mainly due to a relatively high emission factor for BC. K2017, W2017 and ICCT2017 are quite similar in their estimates of the Arctic BC emission. Compared to old 2015 assessment the BC emissions estimates have decreased considerably. The new W2017 BC emissions are a factor 3 lower than the previous estimate in W2014 and presented in old 2015 assessment.

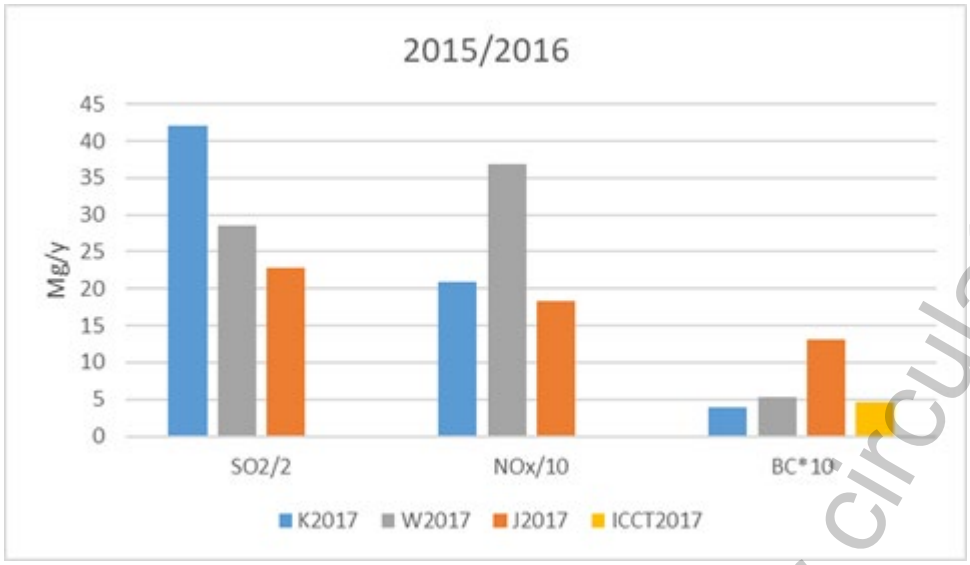

Fig. 2 Emissions SO_2, NO_x and BC in Mg/y for the year 2015/2016 for the area north of 60N for the four different emissions inventories

Only K2017 and W2017 have made projections of the shipping emissions for the 2020-2050. The projections of K2017 have been used in the model simulations in this assessment. Both projections are based on projections of the future shipping activities based on the activities in 2015.

In W2017 there are used the same scenarios of different ship type activities as in C2010, which also was used in W2014. The only difference between W2014 is the using of a mean inventory for 2016 and the updated emissions factors. Two projections, Business-as-Usual and High-Growth, have been made. Here only results from the BAU scenario will be presented, because the current changes in shipping activities indicate that High-Growth is an unrealistic scenario. In the BAU scenario the total use of fuel will increase 14% between 2016 and 2050 for the 2016 shipping activities, e.g. without additional fuel consumption from diversion, quite similar to the old W2014.

In the emissions scenarios by K2017 the future shipping activities are increasing 60% from 2015 to 2050 (reflecting the trend of international shipping in the WEO2018 projections (IEA, 2018)), and includes no additional shipping activities from diversion routes. More about that?

It is expected that in the future an increase in shipping activity and emissions is due to the shift in global traffic away from the traditional routes into Arctic waters when the Arctic are getting more ice-free, which also was described in the 2015 assessment report. W2017 have made an update of these emissions from shipping activities by using C2010 estimates of total CO2 emissions combined with the updated emissions factors for 2020 to 2050 due to expected changes in ships and changes in sulfur content in the fuel. The estimates of the CO_2 emissions from the diversion by C2010 is based on the global shipping activities in 2004, which was projected to 2050 by assumption of a constant increase of 2.1%/year for the BAU scenario. By using newer data for the global emissions for shipping, f.ex. from J2017 for the year 2015, together with expected future shipping activities taken from K2017, the emissions is expected to be reduced with 45% compared to the updated diversion data in W2017.

In fig 3 there shown are shown projected emission for the area North of 60°N of SO_2, NOx and BC in Mg/y for the year 2050 for K2017 and W2017 and also the expected emissions from diversion in W2017 (W2017_div) and the updated emission based on J2017 global CO_2 emissions and the projections of shipping activities in K2017(W2017_div_u).

The two projections of the current arctic shipping activities made by K2017 and W2017 are quite similar for SO_2, NO_x and BC. Furthermore the contribution from diversion based on C2010 future BAU CO_2 emissions (W2017_div) will increase the emissions by about 100% and with updated CO2 estimates about 50%.

Compared to the BAU scenario in the old assessment the projected emissions for 2050 of the current shipping activities are about 80% lower for SO_2, 50-75% lower for NO_x and 80-90% lower for BC.

Comparing the BAU scenarios including projected emissions form diversion the SO_2 emissions 90-95% lower, 80-85% lower for NO_x and

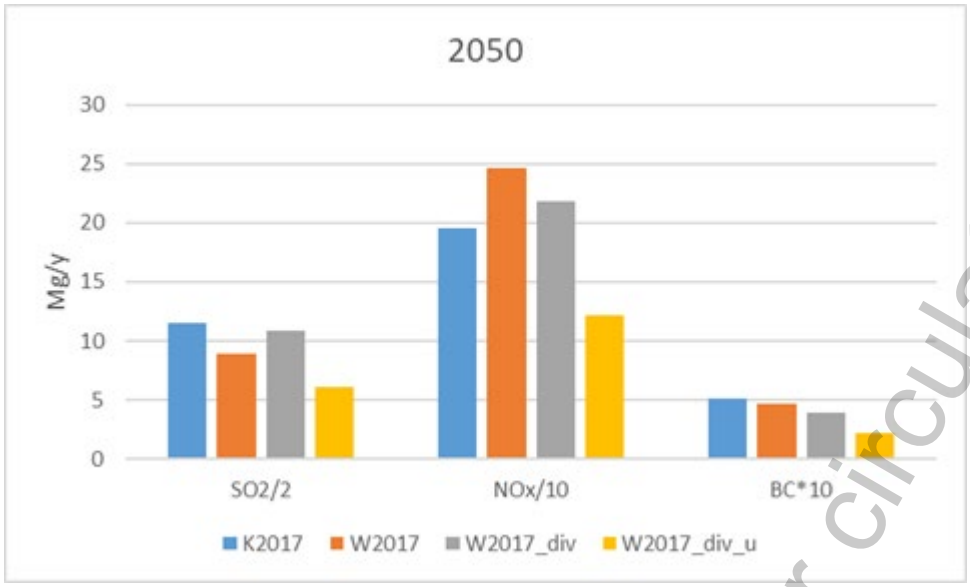

Fig 3. Emissions for the area North of 60N of SO_2, NO_x and BC in Mg/y for the year 2050 for projections of the current shipping activities, K2017 and W2017, and the expected emissions from diversion in W2017 (W2017_div) and the updated emission based on J2017 and the projections in K2017(W2017_div_u).

2.4.2 Oil and gas activities in the Arctic (Lena, Zig, Joshua, Carbon Limits) - probably in separate section - might say a word about updated data for the last few years on oil and gas production and new outlook from WEO2018. Possibly a link to the report done by Carbon Limits within the EU BC Action reviewing technical measures (published in 2020)

2.4.3 Any information on specific challenges in Arctic communities? (waste management, heating and electricity incl. diesel generators, stoves, transport,...) Alternatively focus on local community air pollution/exposure and include the text to the section on health impacts. We could add here a map with location of communities/townships that are off-grid and discuss briefly what the consequences or gaps in terms of emissions and impacts could be; eventually something for further work

2.5 Policy scenarios

- *Further mitigation scenarios (MFR, SDS/SDG, SLCF) - highlight what the SDS (incl SDG) energy scenario is and what 'structural' measures are behind [I can check the total region dimension in term of key species]*

- *Measures/options in MFR/SDS/SLCF*
- *How the policy scenarios/recommendations compare to the 2015 report (or earlier too?)? What is new? What has moved into the current policy basket? Where challenges are better understood?*

Significant BC emission reduction potential remains with already existing technologies. In the Arctic Council additional efforts could be taken in several sectors indicated in the slide and particular attention should also be paid on sources emitting directly in the Arctic, particularly flaring of APG and Arctic shipping activities.

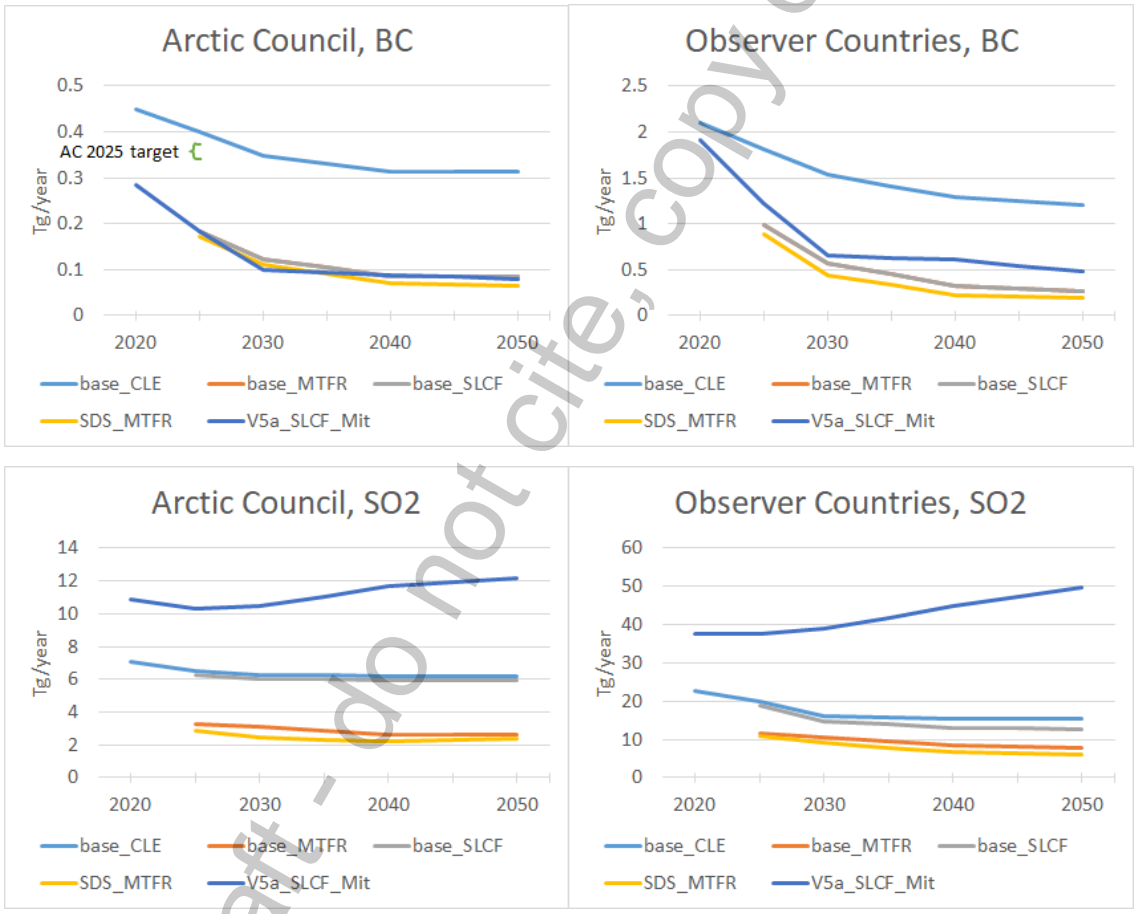

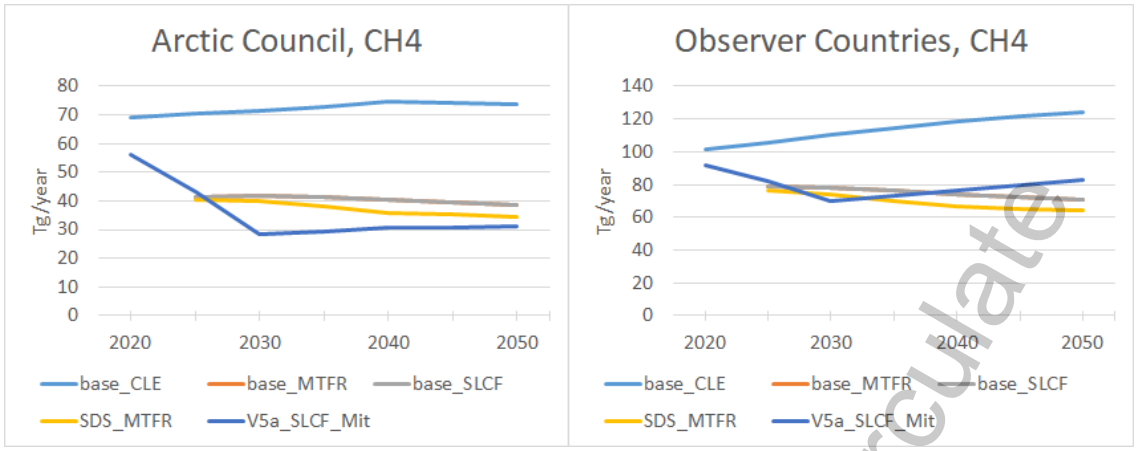

Figure 2.5.1 BC, SO2 and CH4 emissions in the current legislation baseline and mitigation scenarios and ECLIPSE V5a SLCF mitigation scenario, which was used in the AMAP assessment 2015.

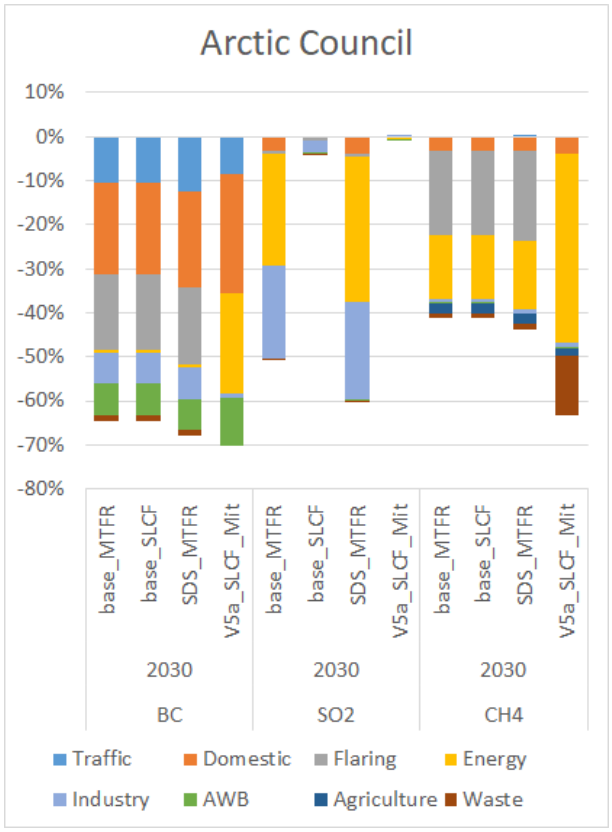

2361

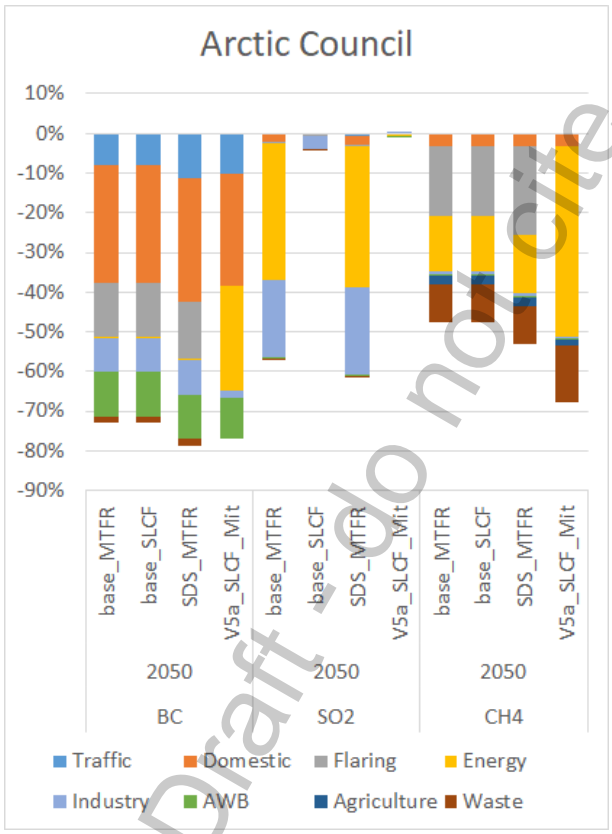

2362

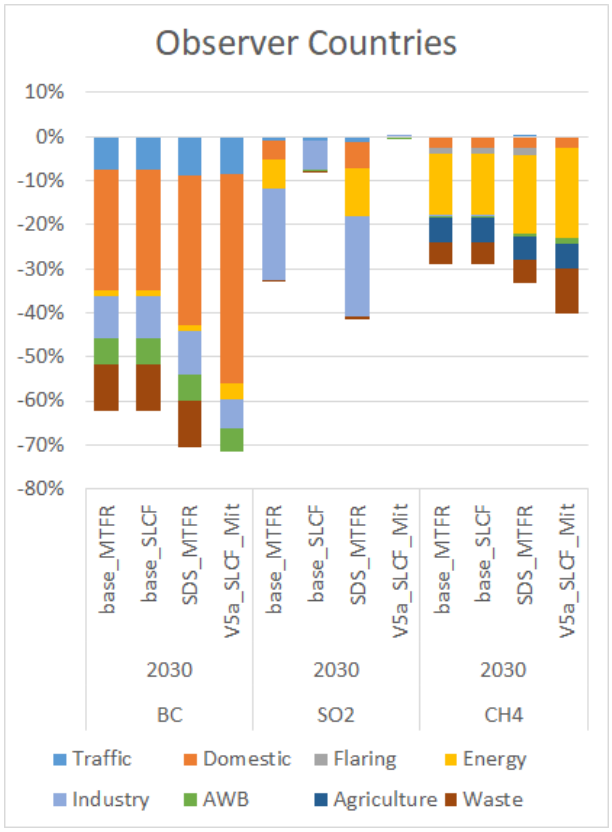

2363

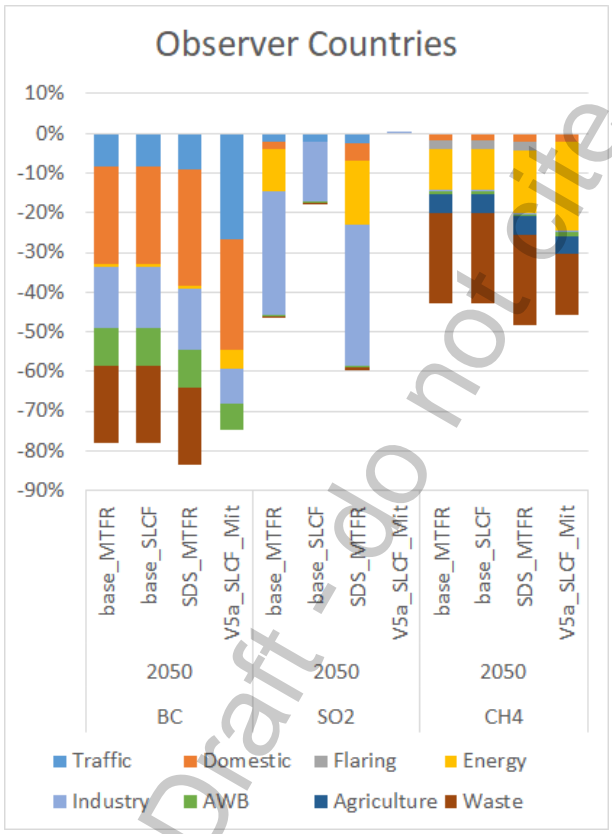

2364

2365 **Figure 2.5.2** Relative change in emissions in 2030 and 2050 under the mitigation scenarios
2366 compared to the base_CLE scenario. V5a_SLCF_Mit mitigation scenario is compared to
2367 V5a_base emissions.

[*"Net changes added as points later."*]

Comparison to 2015 report. Maybe no graphs, just by text highlighting the main points.

2.6. Comparisons to other inventories and national LRTAP/UNFCCC reporting

2.6.1 Black carbon

Table 3.10 Total black carbon emissions for 2010 (unless marked otherwise) in kilotons.

Country	CLRTAP	EDGAR 4.3.2	TNO MACC-III[a]	ECLIPSEv5a	GAINS
Canada	43.0[b]	26.1		48.0	49.7
China		1304.9		1914.3	1308.6
Denmark	5.6	2.4	7.9	4.8	4.6
Finland	6.3	5.1	15.3	6.9	7.6
France	48.3	22.9	75.0	60.7	56.4
Germany	20.8	18.6	45.2	30.3	27.5
Iceland	0.2	0.1	0.1	0.1	0.2
India		597.3		1030.7	1065.0
Italy	32.7	18.7	42.0	31.9	41.0
Japan	22.0[c]	23.1		29.4	23.6
Republic of Korea	13.4[b,c]	15.7		29.1	21.2
Netherlands	5.4	2.8	7.0	6.3	5.7
Norway	4.6	3.5	8.1	3.8	6.5
Poland	23.3	18.9	108.0	57.1	60.6
Russia		27.3	187.1	171.2	152.8
Singapore		1.9		3.7	2.2
Spain	43.9	18.0	33.7	33.3	34.4
Sweden	3.9	3.0	11.7	4.9	4.5
Switzerland	1.7	2.1	5.6	1.6	2.01
United Kingdom	27.2	14.0	23.3	20.4	28.2
United States	315.0[b]	137.9		200.8	217.7
Total		2264.3		3689.3	3098.6
Europe		157.3	569.7	433.4	431.9
Arctic Council		205.3		440.4	443.5
Observers		2058.9		3248.9	2655.2

[a]2011 emissions; [b]2014 emissions; [c]from national reports for the Arctic Council.

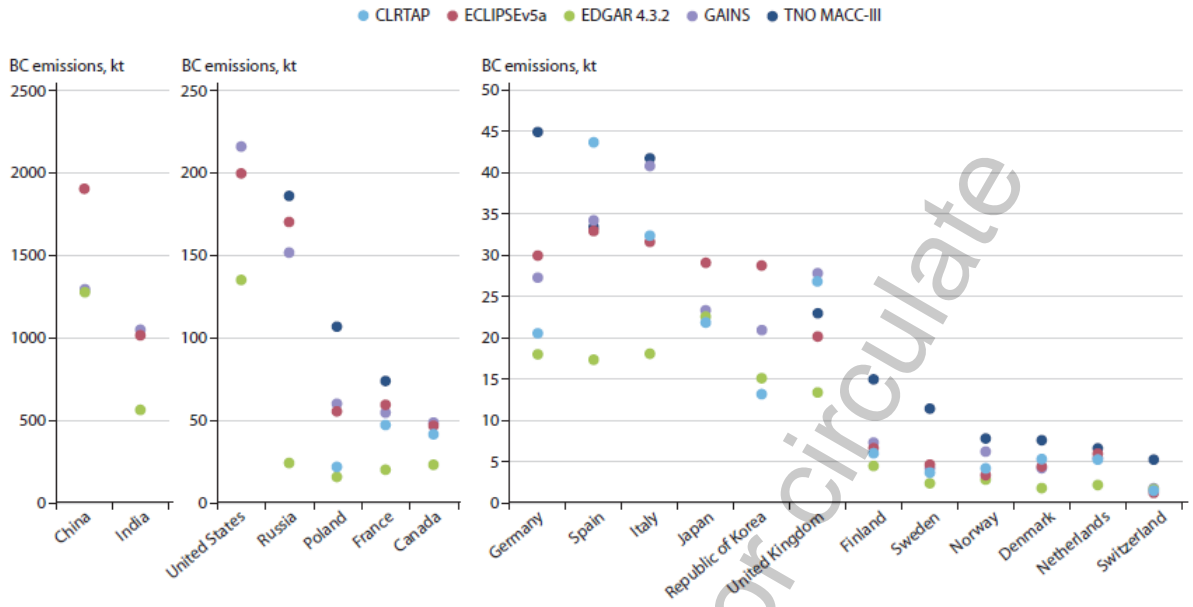

Figure 3.17 Total black carbon emissions. The data are for 2010, except for TNO MACC-III which used 2011 data and Canada and the Republic of Korea under CLRTAP which are for 2014. The United States CLRTAP value for 2014 (315 kt) is not shown on the graph.

[*Table and graph from Review of Reporting Systems for National Black Carbon Emissions Inventories:EU Action on Black Carbon in the Arctic - Technical Report 2. Similar table and graph with updated numbers for BC and CH4 from CLRTAP/UNFCCC and EDGAR v5.0 will be produced for this report.*]

The Review of Reporting Systems for National Black Carbon Emissions Inventories (EU Action on Black Carbon in the Arctic, 2019) report compared BC emissions from independent inventories to CLRTAP national submissions. The comparison showed that there was variation in the inclusion and handling of important emission sectors between the inventories. Of the main source sectors, road transport emissions showed the smallest variation between inventories. Non-road machinery showed higher variation than road transport. For residential combustion (household heating, cooking, lighting, commercial and agricultural heating) the inventories showed a range of methods to estimate the activity (amount of combusted fuel) and allocation between technologies, causing differences in the emissions. CLRTAP reported emissions for residential combustion were close to ECLIPSEv6b numbers used in this assessment. Flaring showed the largest variation between the inventories.

2.6.2. Methane

[*Similar analysis as for BC.*]

2.7 Section on uncertainties

- *Joshua Fu provides text*
- *Subsection on spatial distribution (How well we know where the emissions occur…?, Focus on high latitude relevant sectors)*

2.x Natural releases of methane and selected other species

Main focus on methane, but qualitatively also VOCs and DMS, iodic species (Henrik)

- *Is this covered in another chapter (discussions in Ann Arbor)*

2.8 Discussion and summary

2.8.1 Remaining challenges and recommendations for further work

emissions of particular sectors, mitigation potential, spatial info

2.8.2 Follow-up of recommendations from the 2015 assessment

AMAP 2015 assessment included recommendations to support and guide further development of anthropogenic emission datasets particularly in the Arctic area. This section provides a follow-up on these recommendations and specifically how the datasets used in this assessment take these into account.

- *Recommendation 1 (BC and O3 report): A comparison of several global emission inventories has shown that relative uncertainties in the total emissions per latitude band increase with latitude and are largest in the Arctic. The global inventories thus need improvement, especially at high latitudes. This could be achieved by including information from regional and Arctic Council national inventories.*

The spatial representation of emissions in the Arctic area has been improved in the anthropogenic emission datasets used and assessed in this study. Since the AMAP 2015 assessment a new population pattern has been introduced to allocate activities correctly to Arctic communities. Attention has been paid on datasets representing the Arctic shipping, including the within Arctic traffic and rivers. Road networks, pipelines, power plants and industrial facilities including oil and gas activities flaring APG,...

- *Recommendation 2 (BC and O3 report): Further analysis of observed and modeled historical trends of SLCFs should be made.*

This recommendation does not directly address anthropogenic emission datasets. However, emissions are a key driver in explaining the trends of SLCFs in atmospheric concentrations and thus such comparisons can provide important insight into further improvements of emission datasets. In this assessment we have continued, as in previous assessments, to analyse and compare observed and modeled historical trends of SLCFs. Chapter 5 of this assessment addresses trends in observations and Chapter 6 evaluates the performance of models used in this assessment against observations.

- *Recommendation 3 (BC and O3 report): Future work should develop emission scenarios that describe a strong increase in anthropogenic activities within the Arctic and quantify the projected impacts these activities would have on the Arctic climate and environment.*

An emission scenario representing high-growth in activities in the Arctic area still remains an interesting topic for further work. However, the scenario representing the situation if no further controls would be introduced (NAME OF THE SCENARIO) addresses some potential aspects of such development.

- *Recommendation 1 (CH4 report): Undertake additional direct or on-site source measurements (at scales that support extrapolation), harmonize development and*

application of emission factors internationally, and improve the temporal (interannual) resolution of reported emissions in order to improve estimation of anthropogenic methane emissions.

To be filled in.

- *Recommendation 2 (CH4 report): Subsequent assessment efforts should focus on fugitive emissions from all aspects of oil and gas systems from exploration through production and distribution.*

To be filled in.

3. Open biomass burning

(Jessica, Justin, Sabine, Nikos, Juha, Ari, Lin, Zig, Kaarle, Jesper, HC, Joshua; authors and author order TBD) (klimont@iiasa.ac.at;sec@nilu.no;ne@nilu.no;Kaarle.Kupiainen@ym.fi; jsfu@utk.edu; jmccarty@miamioh.edu; fainjj@miamioh.edu; juha.aalto@fmi.fi; jc@envs.au.dk; hc@aces.su.se; lin.huang@canada.ca; Ari.Venalainen@fmi.fi)

Recent evidence suggests that northern and Arctic ecosystems will become more susceptible to biomass burning as the climate warms (York et al., 2017; Figure 1). Open biomass burning is a known disturbance in the Arctic Council region. Krylov et al. (2014) found that stand- replacement wildfires, fires that kill most aboveground vegetation and trigger ecological succession, are ~66% of total forest disturbance in the Russian Federation. In terms of burned area, 2015 was the largest fire year for the Alaskan tundra ecoregion (Michaelides et al., 2019). Broadly speaking, wildfire regimes are driven by climate and weather, fuels and fuel conditions, and people as ignition sources (Silva and Harrison, 2010; de Groot et al., 2013). Human-caused fires are driven by management needs and sometimes cultural practices (Granström & Niklasson, 2008; Bowman et al., 2011). Fuels and anthropogenic ignition sources can be managed to reduce open biomass burning. Along those lines, Astrup et al. (2018) argue that boreal forests should be managed to increase broad-leaved stands to reduce wildfire risk, fire emissions, and increase surface albedo. Management strategies should be defined by regional needs. This report will focus on three biophysical regions of the Arctic: North America and Greenland, Fennoscandia and European Russia, and Siberia and the Russian Far East.

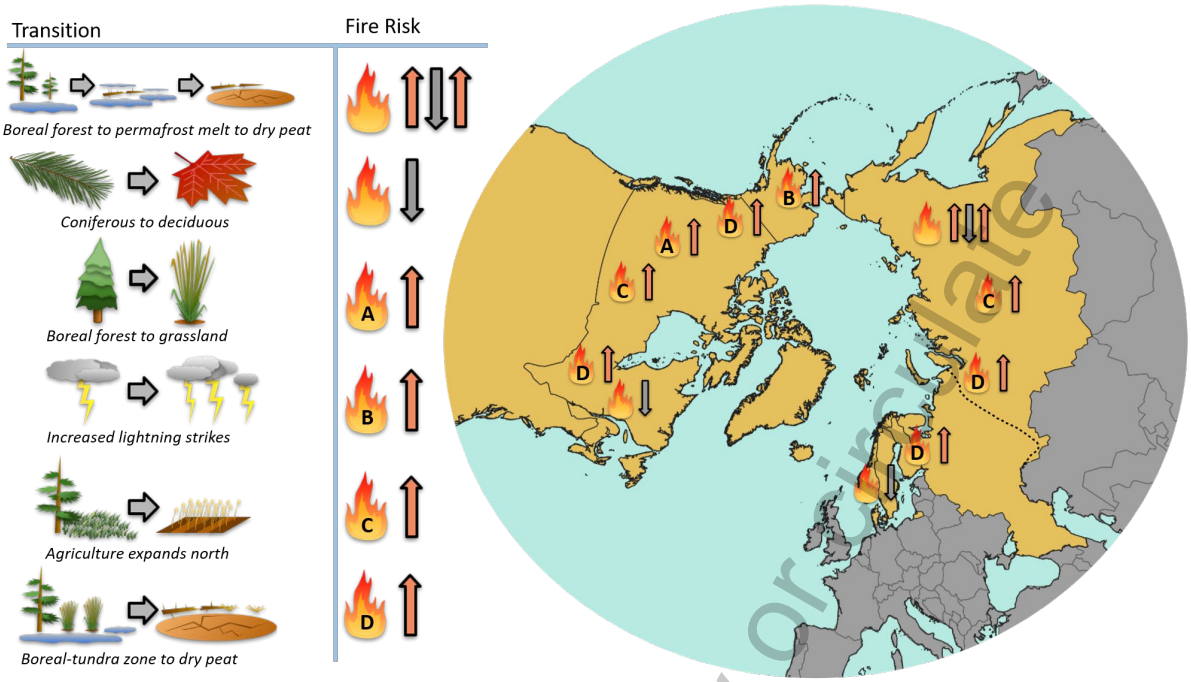

Figure 1. A sample of peer-reviewed future Arctic fire risk variables due to expected ecological and meteorological transitions by mid- and late 21st century climate change for Arctic Council member nations; 'up arrows' indicate increase in fire risk and 'down arrows' indicate a decrease in fire risk; the dashed line indicates the start of the Siberia and Far East region.

Figure 2. Conceptual framework for drivers of fire risk in the Arctic Council region: climate, fuels, and people.

Open biomass burning, as defined in this chapter, includes both wildland fires (i.e., wildfires, forest fires) and fires in human-dominated landscapes. Reported statistics and geospatial methods from Earth observations were used to quantify and differentiate open biomass burning as human-caused fires, i.e., agricultural open burning, timber and agroforestry, and natural fires, i.e., lightning-caused fires. Fire risk in the Arctic regions is often driven by climate and fire weather, fuels type, availability, and condition, and presence of people as ignition sources (Figure 2).

Many future fire modelling approaches use Representative Concentration Pathways (RCPs) developed for IPCC AR5, to contextualize the impact of climate change on future temperature and precipitation - both influencing fuel conditions and availability of fuels for ignition and subsequent burning (Veira et al., 2016). RCP4.5 (~650 ppm CO_2 eq.) and RCP8.5 (~1370 ppm CO_2 eq.) are commonly used for sub-national, national, and regional studies (Krause et al., 2014; Sherstyukov and Sherstyukov, 2014; Girardin and Terrier, 2015; Lehtonen et al., 2016; Wotton et al., 2017), often due to the lack of downscaled climate scenarios for RCP2.6 and RCP6.0 needed for future fire modelling (Davis et al., 2017). While the overall modelling work for this assessment relies on biomass burning emissions evolution represented in the newly developed Shared Socioeconomic Pathways (SSPs) for IPCC AR6, comparable assessment for the biomass burning conditions and impacts have not been published yet. For a detailed description of the SSPs, and their relation to the RCPs, see Riahi et al. (2019).

The 2015 AMAP assessment on black carbon (BC) and ozone as Arctic forcers noted key characteristics of open biomass burning. In this 2021 assessment, many of the open biomass burning characteristics remain constant, including human influence on both ignition and fuels management, significant interannual variation of fire events and emissions, and spatial and seasonal clustering of burning related to active land management as well as fuel conditions (AMAP, 2015). Since 2015, evidence of direct climate change influence on early season megafires has increased (Wang et al., 2017) as well as fueling extreme wildfires in more populated areas and not just remote boreal forests and Arctic tundra (Abatzoglou and Williams, 2016; Kirchmeier-Young et al., 2019). An increasing trend in fires above 60°N is documented in global fire emission databases for years 2005 to 2018, including a case study of a novel fire regime in Greenland with two documented fire seasons in 2017 and 2019. Further this assessment provides clarification of the concept of what is open biomass burning for the Arctic Council region and specific language of fire emission sources, attributing landscape-scale determination of fire types in the Arctic to wildland (boreal forest, hemiboreal forest, taiga, tundra, grasslands and steppe, peatlands) or anthropogenic (croplands, pasture and rangeland, timber and agroforestry). Ignition sources are classified as natural or human-caused, providing needed context for policy recommendations. Finally,

current uncertainties of quantifying future emissions from open biomass burning in the Arctic Council region are noted.

New Novel Arctic Fire Regime Case Study: Greenland

Unusual open fires were observed in western Greenland and also confirmed by satellites between 31 July and 21 August 2017, after a period of warm, dry and sunny weather. The fires burned > 2,000 ha of high carbon soils - most likely peat due to smouldering and fire spread behavior - that became vulnerable due to permafrost degradation (Daanen et al., 2011). Work by Evangeliou et al. (2019) estimated the 2017 wildfire consumed a fuel amount of about 117 kt C and emitted about 23.5 t of BC (Black Carbon) and 731 t of OC (Organic Carbon), including 141 t of BrC (Brown Carbon). Although these fires were small compared to fires burning at the same time in North America and Eurasia, a large fraction of the BC, OC and BrC emissions (30%) was deposited on the Greenland ice sheet. Measurements of aerosol optical depth in western Greenland showed that the air was strongly influenced by the Canadian forest fires. Even so, the Greenland fires had an observable impact, doubling the column concentrations of BC. The spatiotemporal evolution and, in particular, the top height of the plume was also confirmed using the vertical cross section of total attenuated backscatter (at 532 nm) from Cloud-Aerosol Lidar and Infrared Pathfinder Satellite Observations (CALIOP) Lidar. The maximum albedo change due to BC and BrC deposition from the Greenland fires was 0.007 at maximum, while the average instantaneous BOA (Bottom Of the Atmosphere) radiative forcing over Greenland at noon on 31 August 2017 (post-fire) was between 0.03 and 0.04 W m-2, with locally occurring maxima up to 0.77 W m-2. The summer 2017 fires in Greenland had a small impact on the Greenland ice sheet, causing almost negligible extra radiative forcing. This was due to the – in a global context – still rather small size of the fires. However, ***the 30% fraction of the emissions was deposited on the Greenland ice sheet, making the 2017 Greenland wildfires very efficient climate forcers on a per unit emission basis***. Thus, while the fires in 2017 were still relatively small on a global scale, if the expected future warming of the Arctic (IPCC, 2013) produces more and larger fires in Greenland (Keegan et al., 2014), this could indeed cause substantial albedo changes and, in turn, contribute to accelerated melting of the Greenland ice sheet.

3.1 Policy questions:

3.1.1 Impact of climate change on fire risk and fire emissions

Near-term warming means more ignitions from lightning (Veraverbeke et al., 2017) and degraded permafrost increasing dry ground fuels and fire severity (Teufel and Sushama, 2019). By the end of the century, wildland fire risk is expected to increase, with length of fire seasons - measured in terms of daily severe fire weather occurrence - predicted to expand by much as 20 days globally (Flannigan et al., 2013). Similarly, Sherstyukov and Sherstyukov (2014) predict an increase of > 50 days of high fire risk days for Russia under RCP 8.5 scenario, with a potential to double annual forest fire burned area. Using CMIP5 model intercomparisons, Lehtonen et al. (2016) estimate large (≥ 10 ha) boreal forest fires in Finland to increase by 1.9 times under RCP 4.5 and 2.3 times under RCP 8.5 by mid-century. Robust predictions of future burned area in wildland and human-dominated landscapes for the Arctic require an understanding and quantitative simulation of the major drivers of fire (specifically climate and fire weather, ignition, fuels, and humans), including coupled dynamics between and among these drivers (Riley et al., 2019).

The climate-induced vegetation shifts, which would also drive fire risk and related emissions, present a complex matrix for the Arctic Council member nations. Predictions of boreal forest transition to deciduous forest stands would decrease fire risk in eastern Canada and interior Alaska (Terrier et al., 2013; Foster et al., 2019; Mekonnen et al., 2019). Wang et al. (2020) found these trends are already occurring in Alaska and Northwestern Canada using three decades' worth of 30 m Landsat imagery, as climate drives grass and shrub expansion in the Arctic and wildfires drive most of the evergreen forest reduction and expansion of deciduous forests in the Boreal. Further work in mature deciduous forests of Interior Alaska show that current canopy gaps are related to ecological shifts to evergreen shrubs, lichens, and mosses, thus increasing fire risk of these gaps within low flammability deciduous stands transitioning from high flammability coniferous species (Alexander and Mack, 2017). Under RCP 8.5, Stralberg et al. (2018) estimated that by 2100, grasslands will replace much of the upland conifer, mixed forests, and deciduous forests for a large area of the boreal forest zone of northern Alberta. Shorter fire return intervals combined with climate change-induced drought will reduce the resiliency of evergreen and broadleaf

species to re-seed and/or establish after wildfires, leading to expansion of grassland ecosystems in what is now Northern Canadian forests (Whitman et al., 2019). Increased grass-dominated landscapes would create a new fire regime of frequent but low severity fires, with the likelihood of SLCP/SLCFs transport to the Arctic most likely in the spring months of March through May (Hall and Loboda, 2018). Grassland fires produce less energy, with smoke plumes more similar to crop residue burning, and are unlikely to breach the tropopause for consistent transport of smoke to the Arctic (Hall and Loboda, 2017), unlike the current observed deposition from boreal forest fires in the Arctic (Thomas et al., 2017).

3.1.2 Fire management and open biomass burning emissions in the Arctic

McWethy et al. (2019) argue that active "fuels management, prescribed fires and allowing wildfires to burn under moderate fire weather conditions will protect and promote ecological and cultural resources, and communities" more effectively than to through management of fire risk via suppression and/or efforts to eliminate all fire from the landscape, including novel fire landscapes caused by warming in the Arctic. In dried and degraded peatlands of the Arctic region, fuels management will be more complicated outside the boreal forest and forest-tundra gradient, where mulching treatments that convert canopy and surface fuels to a masticated fuel bed can limit peat burn depth in Black Spruce (Picea mariana) stands (Wilkinson et al., 2018). Privately-owned grassy tussock tundra and dwarf shrub tundra vegetation types are more likely to burn than low shrub tundra in Alaska (Hu et al., 2015), showing relatively rapid vegetation re-greening within a decade after burning (Rocha et al., 2012). Prescribed burning could be effective in fuels management for tussock and dwarf shrub landscapes of the tundra.

Prescribed burning effectiveness for peatlands is less clear. Peat fire risk and burn depth, however, is less influenced by canopy and ground vegetation and more by soil bulk density (impacting air availability in soils), the water table depth, and precipitation (Kieft et al., 2016). After the devastating 2010 fires in the Moscow region, the regional government undertook an ambitious 70,000 ha peatland rewetting project to reduce fire risk (Sirin et al., 2014), a landscape-scale process that can be monitored using existing Earth observation sensors at the moderate resolution (30 m Landsat to 10 m Sentinel-2; Sirin et al., 2018). To date, the effectiveness of this campaign is unclear but in practical terms should reduce fire

risk. In the larger context of CH_4, Günther et al. (2020) used a radiative forcing model to determine that methane emissions from peatland rewetting are less significant in the short-term when compared to the CO_2 emissions from degraded or drained peatlands increasing long-term warming when rewetting is postponed.

Adaptive management strategies of the timber industry in Fennoscandia could also reduce fire risk. Intensive management via ditch network maintenance and fertilization of drained peatlands will increase timber values while also rewetting the peat (Ahtikoski and Hökkä, 2019). Prescribed burning for silvicultural retention and maintaining and regenerating pure stands can also reduce fuel loadings while increasing biodiversity (Lindberg et al., 2020).

The variable with the highest uncertainty is people - as ignition sources and determining how demographic, migration, and/or development patterns into these changing landscapes will impact fire activity and related emissions (Robinne et al. 2016; Reilly et al. 2019). For example, consider agricultural landscapes as one source of fire. Expanding climate-driven agricultural frontiers in the high northern latitudes under RCP 8.5 scenario for 2060-2080 could add 8.5 million km^2 of new croplands in Canada and Russia alone, expanding wheat and maize production into areas with carbon-rich or peat soils (Lee et al., 2020). Further, Parfenova et al. (2019) found crop growing conditions would be established in the permafrost zone of West Siberia under RCP 2.6 and 8.5 by 2080, favorable for wheat and maize production. These crops are commonly managed via open burning practices in Canada, the U.S., eastern Europe, and Russia (Kutcher and Malhi, 2010; McCarty et al., 2017; Theesfeld and Jelinek, 2017; Shiwakoti et al., 2019). Thus, seasonality of burns and management of croplands, grasslands, and deciduous forests may occur at times when transport to the Arctic is likely, i.e., late winter/early spring (Hall and Loboda, 2018).

3.1.3 Long term emissions from open biomass burning

Comparison of five biomass burning emission models include the Global Fire Emissions Database (GFED; van der Werf et al., 2017); the Fire Inventory from NCAR (FINN; Wiedinmyer et al., 2011); the Global Fire Assimilation System (GFAS; Kaiser et al., 2012); the Quick Fire Emissions Dataset (QFED; Koster et al., 2015); and the Fire Energetics and

Emissions Research (FEER; Ichoku and Ellison, 2014) was completed for 2005 through 2018. This builds on the previous work of the 2015 AMAP assessment of BC and ozone (AMAP, 2015), which included 2005 biomass burning emissions from GFAS, GFED, and FINN. It should be noted that GFED is used in the CMIP5 and CMIP6 inventories and analyses (van Marle et al., 2017). For each global fire emissions model, the area of interest was defined roughly as 45° to 80° North (N) globally, split by latitude ranges of 45° to 50° N, 50° to 60° N, 60° to 70° N, and 70° to 80° N. Average annual emissions from open biomass burning from all sources (agriculture, boreal forest, tundra, peat, etc.) were calculated for 2005-2018 for black carbon (BC), methane (CH_4), carbon monoxide (CO), and particulate matter ($PM_{2.5}$). A custom AMAP open biomass burning emissions inventory was developed for this report by co-authors McCarty and Fain (Supplemental Figure 3). VIIRS active fire from day and night detections (Oliva and Schroeder, 2015) were assumed to completely burn each 375 m^2 pixels. A 'best-guess' land cover was created from three different land cover products, with a sample (n = 30 locations) validation of land cover type performed for each country. Ultimately, the 750 m VIIRS Surface Type land cover product (Zhang et al., 2018) was used for North America, Greenland, and the Russian Federation, augmented by the revised 1 km Circumpolar Arctic Vegetation Map (Raster CAVM; Raynolds et al., 2019) for missing values in the High Northern Latitudes. For Norway, Sweden, and Finland, the 10 m Land Cover Map of Europe 2017 from the Sentinel-2 Global Land Cover Project (Gromny et al., 2019) was used. All land cover maps were reclassified into the International Geosphere-Biosphere Program (IGBP) classes (Loveland et al., 1999) for ease of emission calculations. Fuel loadings and combustion completeness were taken from Van Leeuwen et al. (2014), with tundra values used for Greenland. Emission factors were taken from Akagi et al. (2011), with updates from Andreae (2019).

Most fire activity and emissions occur between 50° and 60° N, with very few open biomass burning emissions between 70° and 80° N and zero satellite observations of fire above 80° N (Figure 3). The latitude band of 50° to 60° N corresponds to the southern extents of the Boreal region, an area experiencing increasing fires due to climate change (de Groot et al., 2013) and includes the largest wildfires in British Columbia's history, burning 1.2 million ha in summer 2017 (Kirchmeier-Young et al., 2019).

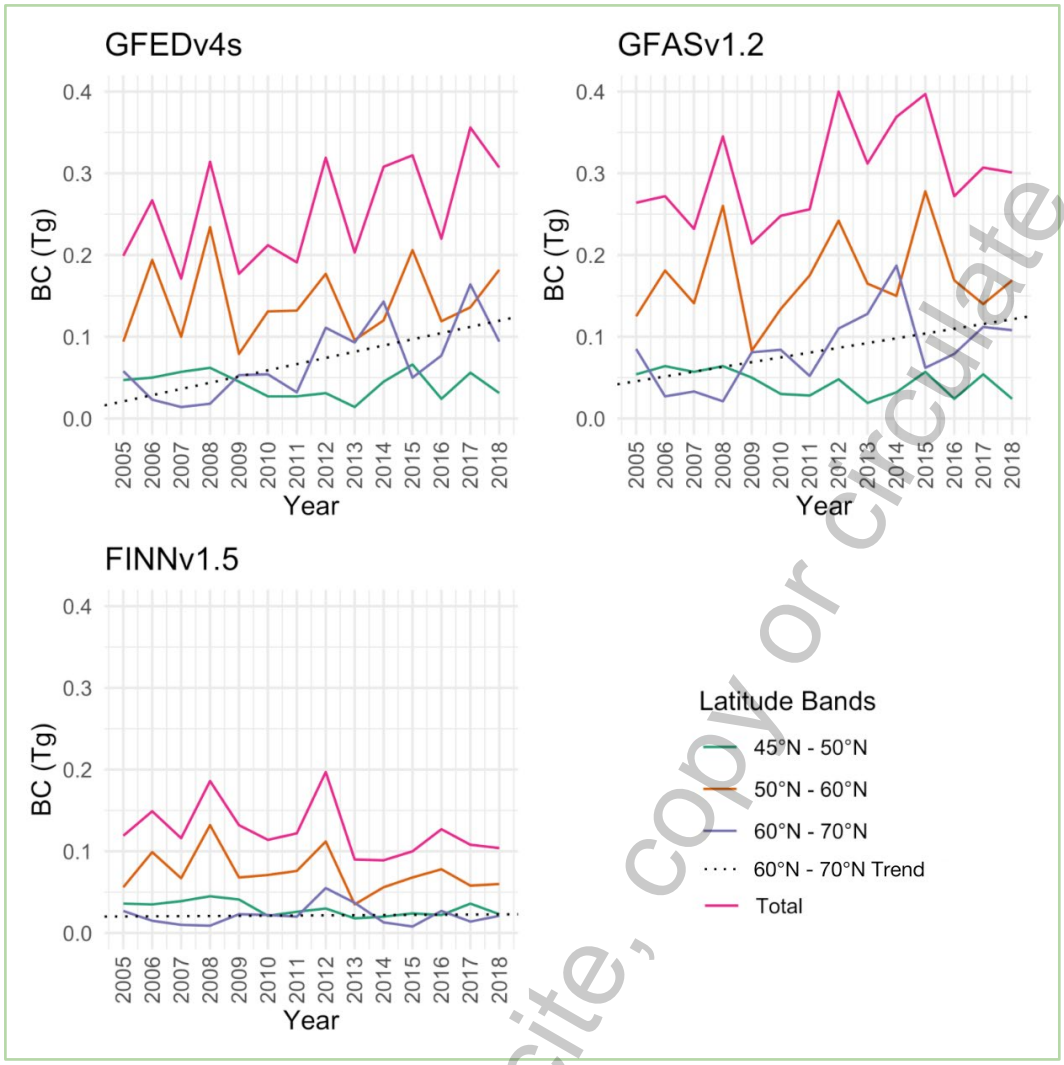

Figure 3. Annual black carbon (BC) emissions in Tg from three commonly used global fire emissions models split by latitude ranges for the Arctic Council Region, 2005 - 2018; note the y-axis has been standardized for each model for ease of comparison; dotted line is the trend for BC emissions from open biomass burning for 50° to 70° N.

In the 14-year emissions estimates from GFAS, GFED, and FINN, a clear shift has occurred since the mid-2000's where more fire is occurring above 60° N than in the temperate zone of 45° to 50° N, where large amounts of human-caused burning and wildfires throughout North America, Europe, and Eurasia (Figure 3). This trend is more pronounced in GFED and GFAS than in FINN, respectively, though all models show a positive trend (note the dotted line in Figure 3). The 2005 to 2018 multi-model annual average black carbon emissions from all open biomass burning sources in the Arctic (60° to 80° N) and adjacent regions known to impact smoke transport into the Arctic (45° to 60° N) is 340,000 tonnes. The years with the

highest multi-model average are 2012, 2008, and 2015 with BC emissions of 450,000 tonnes, 440,000 tonnes, and 410,000 tonnes, respectively. The lowest annual average BC emission from the five global fire emissions models are 2008 and 2013, with 270,000 tonnes. The fire emissions model with the consistently highest BC emissions is QFED, with an annual average of 680,000 tonnes (Figure 3). FEER, GFAS, and GFED have more agreement, with annual BC emission averages of 320,000 (± 70,000) tonnes, 300,000 (± 71,800) tonnes, and 250,000 (± 61,000) tonnes, respectively. FINN has the lowest annual average BC emissions of 130,000 tonnes, with higher emissions in outlier years in 2012 (197,000 tonnes) and 2008 (186,000 tonnes). The custom AMAP model produced emission estimates slightly higher than FINN (Figure 4) for year 2018. The AMAP model predicts BC emissions of 129,000 metric tonnes and CH_4 emissions of 1,390,000 metric tonnes, compared to FINN's 105,000 metric tonnes of BC and 1,190,000 metric tonnes of CH_4. Compared for 2018 only, GFED has marginally higher BC emissions than GFAS, while methane emission estimates from GFAS are substantially higher than GFED.

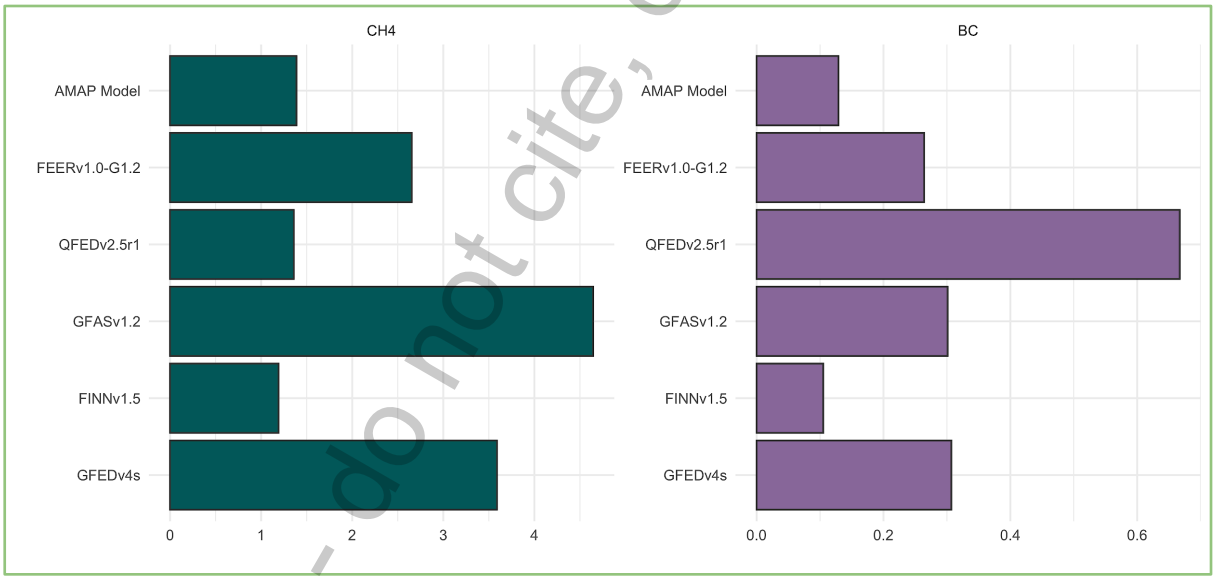

Figure 4. Annual 2018 BC and CH_4 emissions in Tg from five global fire emissions models and a custom AMAP fire emissions model for the Arctic Council Region.

Ground-based official statistics vary greatly by country or sub-region (i.e., Alaska and Greenland) for circa 2019 (Table 1). The Russian Federation has the highest burned area, with over 100,00 km^2 burned, resulting in ~25.6 tonnes of BC. In 2019, open biomass burning in European Russia - comprising Northwestern, Central, Southern, North Caucasus,

and Volga Federal Districts - accounted for only 190 km^2 of burned area (ФБУ "АВИАЛЕСООХРАНА", 2019). Approximately 98.2% of burned area in Russia occurred in the Urals, Siberia, and Far East Federal Districts. In general, Fennoscandia and European Russia is the region with the lowest burned area and open biomass burning emissions (Figure 5), with all regions experiencing the most burning in 50° to 60°N and the second most burning in the latitudinal band of 60° to 70°N. Alaska (USA) and Canada account for approximately 29,000 km^2 of total pan-Arctic biomass burning and 22% of the BC emissions. Greenland is a novel fire regime in the Arctic, with two relatively significant wildfires in 2017 and 2019, but accounted for more burned area and emissions than Norway or Finland. In 2019, the majority of open biomass burning and related emissions for the Arctic Council nations originated in Siberia and the Russian Far East.

Country/ Region	Year	Official Burned Area (km^2)	BC (metric tonne)	$PM_{2.5}$ (metric tonne)	CH_4 (metric tonne)	SO_2 (metric tonne)
USA/ Alaska	2019	10,481[a]	2.660	81.40	31.71	5.85
Canada	2019	18,389[b]	4.667	142.81	55.63	10.27
Denmark/ Greenland	2019	8[c]	1.27E-04	2.88E-02	6.59E-02	1.27E-03
Norway	2019	0.03[d]	7.61E-06	2.33E-04	9.08E-05	1.68E-05
Sweden	2018	250[e]	0.063	1.94	0.76	0.14
Finland	2019	6[f]	0.002	0.05	0.02	0.003
Russia	2019	100,785[g]	25.579	782.72	304.90	56.27
	Total	129,919	32.97	1,008.95	393.09	72.53

Table 1. Summary table of BC, $PM_{2.5}$, CH_4, and SO_2 emissions from reported statistics on burned area in the Arctic member nations; sources for burned area from [a](Alaska Division of Forestry, 2020); [b](CIFFC, 2020) ; [c](Markuse, 2019); [d] (DSB, 2020); [e](Betänkande av 2018 års skogsbrandsutredning, 2019); [f](Ketola, 2020); [g](ФБУ "АВИАЛЕСООХРАНА", 2019); fuel loadings and combustion completeness from Van Leeuwen et al. (2014) for boreal forests, with tundra values used for Greenland; emission factors taken from GFED with 0.5 g/kg assigned to boreal forest ecosystems and 0.04 g/kg assigned to peat for Greenland.

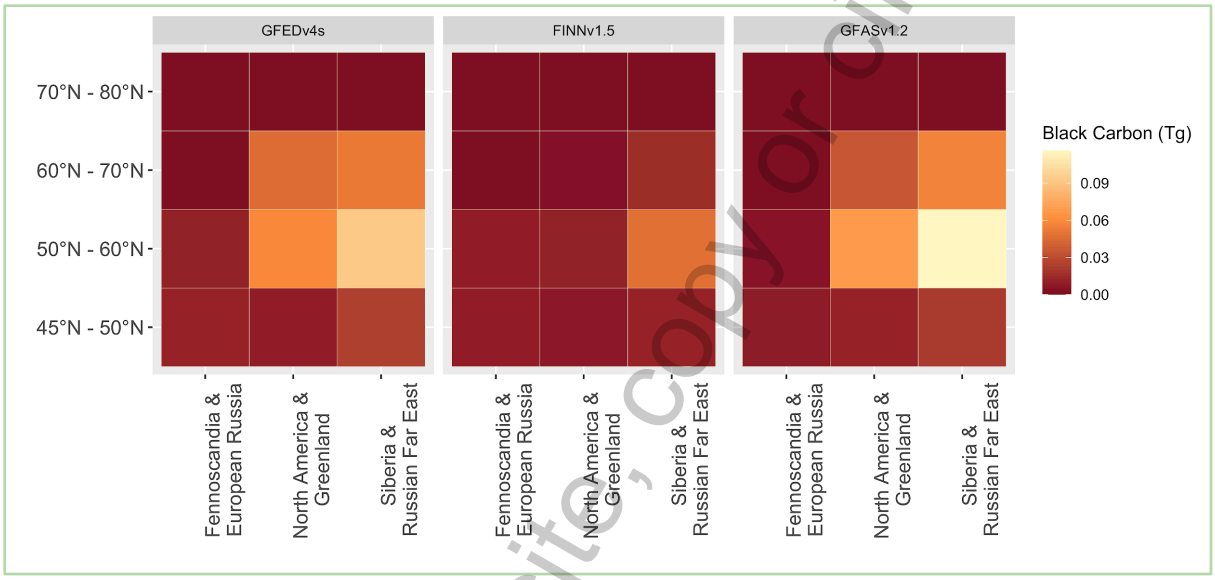

Figure 5. Average black carbon (BC) emissions in Tg for 2015 to 2018 from three global fire emissions models split by latitude ranges for the three biomass burning regions.

Elemental Carbon Concentrations Case Study: Arctic & Boreal Canada

A case study of Arctic and boreal sites by Environment & Climate Change Canada (ECCC), illustrates long-term observed elemental carbon (EC) concentrations at Alert (82°27'N, 62°31'W) and East Trout Lake (54°21'N,104°59'W). Figure 6 shows the relative locations of these two sites, which were also compared with corresponding assembled GFED/CMIP6 biomass burning emissions for Northwest Canada over the same period. Alert is mainly influenced by emission sources from Northern Eurasia and North America, depending on the season (Hirdman, et al., 2010; Stohl et al., 2013; Xu, et al., 2017). Biomass burning from North America influences Alert more during summer than winter. East Trout Lake is located, a

boreal forest site, largely impacted in the summertime from the widespread fires across Canada, particularly in western Canada.

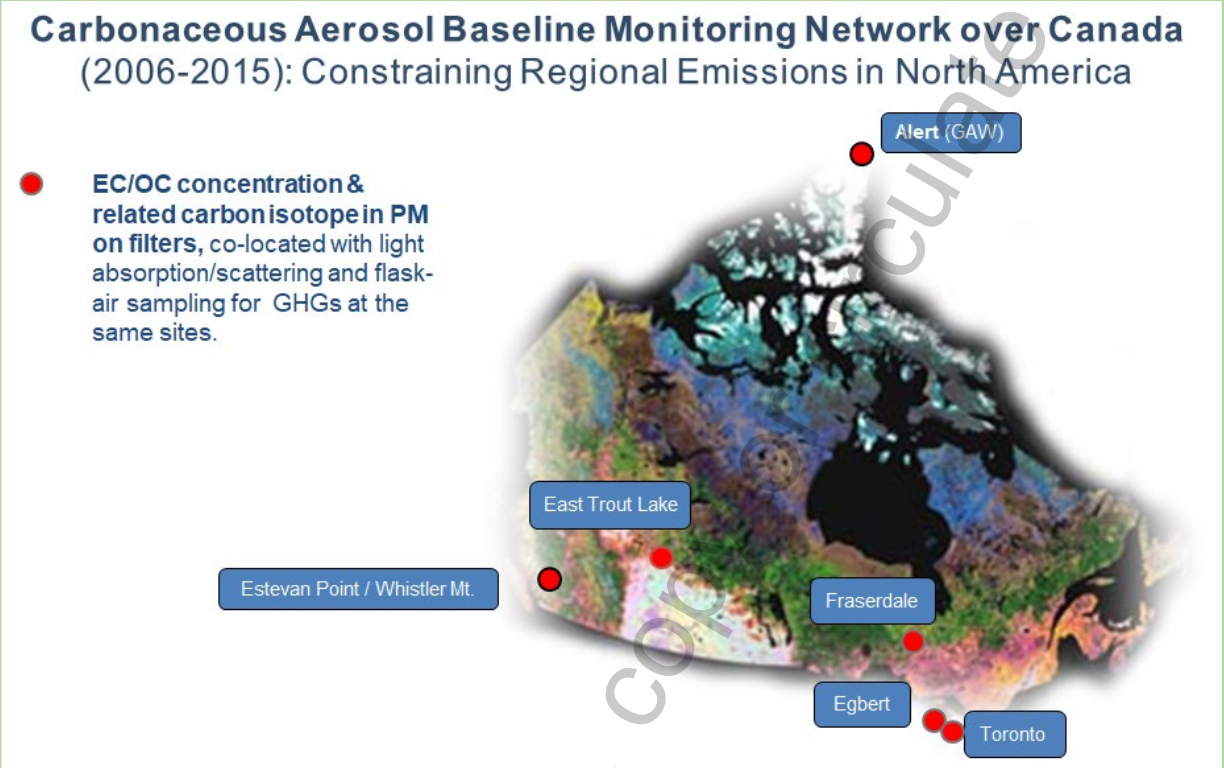

Figure 6. The carbonaceous aerosols sampling network for EC/OC and carbon isotope measurements by ECCC for characterizing the impacts of the major emission or transported sources over Canada; results from Alert and East Trout Lake are described in the text.

Comparing the time series and seasonal variation of EC from these two sites provides insight on the impacts of biomass burning from North America on the EC transported to the Canadian Arctic. Figure 7 shows EC six-month means time series (dark gray bars: November to April; light gray bars: May to October) over 2006 to 2015 at Alert in the top panel, corresponding results from East Trout Lake in the middle panel (dark gray bars: November to April; light gray bars: May to October), and the six-month means time series of assembled biomass burning from GFED emissions in CMIP6 (van Marle et al., 2017) from the upwind area of East Trout Lake from 2006 to 2015 in the bottom panel. It is obvious that the inter-annual variation of EC in the middle panel is well correlated with the changes of biomass burning emissions in the bottom panel (R^2 = 0.89), indicating that about 90% of the inter-annual changes in atmospheric EC at boreal East Trout Lake can be explained by the changes

of biomass burning emissions from the upwind area, i.e., Northwestern Canada. It is also noticeable that the inter-annual variations of EC at Alert from the top panel look largely different than those observed at East Trout Lake in both winter-spring and summer-fall seasons. This may imply that the inter-annual variations of EC at Alert were not due to the biomass burning impacts from North America.

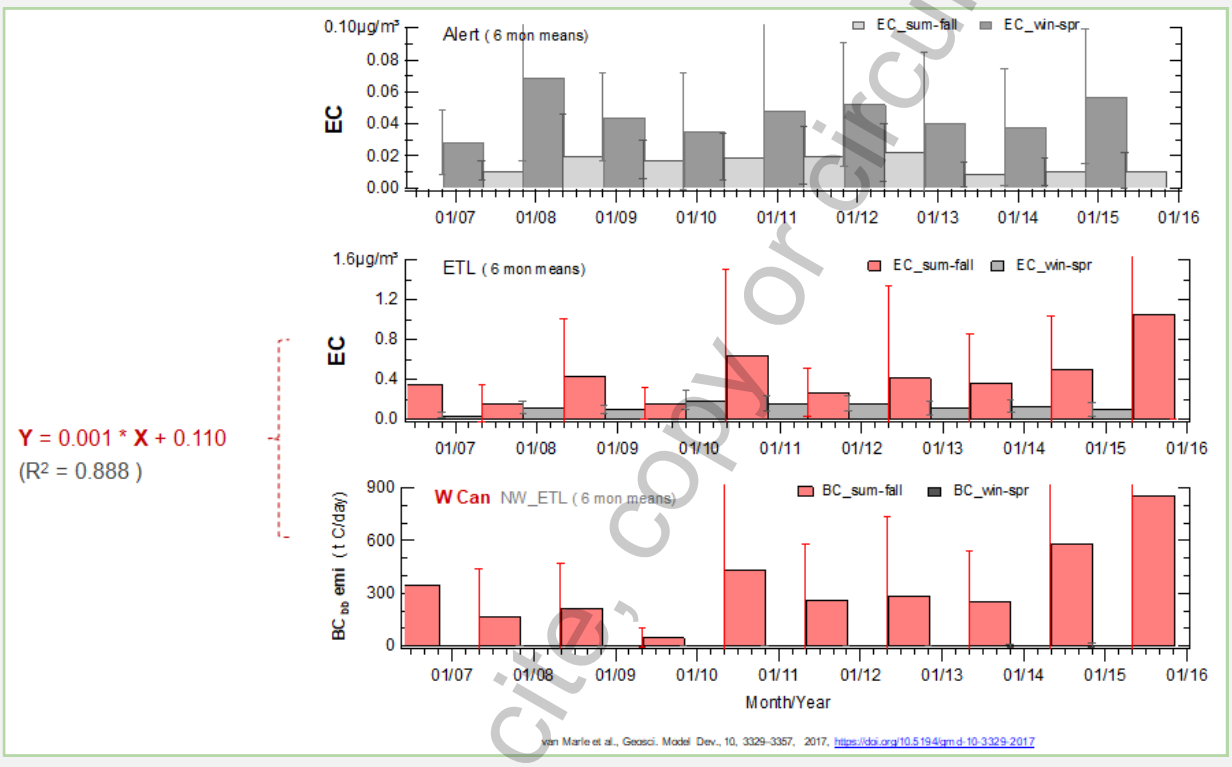

Figure 7. Comparison between the observed EC inter-annual seasonal trends at Alert (top panel) and at East Trout Lake (middle panel), with corresponding assembled GFED/CMIP6 emissions from upwind area (bottom panel) over the period of 2006-2015. *Y* in the regression equation is EC concentrations in the middle panel, whereas *X* in the equation is the BC emission in the bottom panel.

Comparing the seasonal profile of EC monthly means from East Trout Lake with biomass burning emissions, Figure 8 shows that the seasonal variation of atmospheric EC at this boreal site is well correlated with the corresponding profile of GFED/CMIP6 biomass burning emissions (R^2 = 0.93). This suggests that more than 90% of the EC seasonal profile at East Trout Lake was caused by the biomass mass emissions from the upland wind area. Seasonal variation of EC at Alert (top panel) shows an opposite pattern from East Trout Lake (middle

panel), with the relatively higher concentrations during winter-spring months and relatively lower concentrations during summer-fall months. With a small peak in July implying that while biomass burning-emitted EC from North America are not the main sources to the EC concentration in the Arctic overall, the influence of the biomass burning-emitted EC during summer seasons from North America could not be ruled out. To further quantify the relative fraction of biomass burning transferred to the Arctic region, ^{14}C measurements are required in conjunction with the Lagrangian dispersion model.

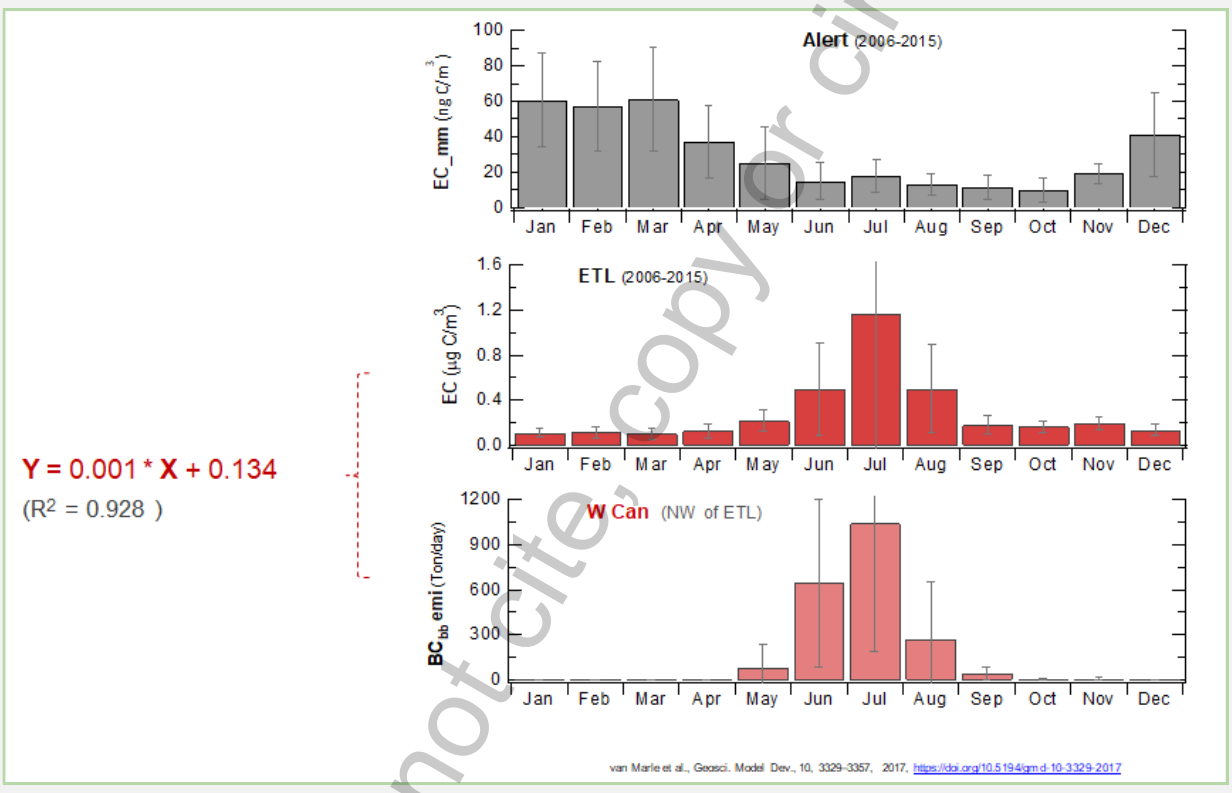

Figure 8. The comparison of the observed EC mass seasonal variations at Alert (top panel) and at ETL (mid panel) and the corresponding assembled GFED/CMIP6 emissions from up-wind area (bottom panel) over the period of 2006-2015; *Y* in the regression equation is EC concentrations in middle panel, whereas *X* in the equation is the BC emission in the bottom panel, indicating that there is a good correlation between the two variables.

3254

3255

3.1.4 Emissions from 'natural' fires

Lightning strikes, fire weather, and fuels conditions are the controlling processes for 'natural' fires, i.e. fires not caused directly by human activity. Box et al. (2019) note that ***increased wildfires in the Arctic will likely be driven by drier conditions, increased maximum temperatures, and lightning-caused ignitions***. Increased convective cloud formation has been documented in the Russian Arctic (Chernokulsky and Esau, 2019) and the North American boreal forest (Veraverbeke et al., 2017), with a 5% increase in convective storms in Northern Europe by end of century (Púčik et al., 2017). Krause et al. (2014) predict burned area to increase 40 to 50% in the high latitudes under climate-forcing scenario 8.5 given predicted changes in fuel loads, fuel moisture, and increased lightning frequency. End of century modeled fire-climate interactions under RCP 6.0 for Alaska found that summer temperature and annual moisture are the most important climatic thresholds driving the likelihood of new novel wildland fire regimes in tundra and the boreal forest-tundra boundary (Young et al., 2016). In general, lightning frequency is expected to increase over areas north of 50°N. The strongest relative increase is approximately 100% across far northern Europe under RCP 8.5 scenario by the end of the century (Groenemeijer et al., 2016). Moreover, since summers are expected to become drier in the future, the role of lightning as an ignition source for wildfires may increase for northern Europe. These future models align with lessons learned from historical controlling processes of natural fires in the Arctic region. Paleofire meta analysis of boreal biomass burning during the Holocene (4,000 to 200 years BP) for the boreal zone of North America and Fennoscandia general trends in boreal biomass burning were primarily controlled by climatic changes, mainly mean annual precipitation in Alaska, northern Quebec, and northern Fennoscandia and summer temperatures in central Canada and central Fennoscandia (Molinari et al., 2018). Boreal needleleaf evergreen fuel composition at the landscape-level across Alaska and central and southern Fennoscandia was secondary to climatic controls.

3.1.5 Human-caused open biomass burning emissions

Open biomass burning from anthropogenic activities like agriculture, timber, and energy extraction will increase in the Arctic as climate change expands human-dominated landscapes northward, increasing potential ignition sources (Figure 1). For the case of Greenland, the 2019 wildfire was caused when an outdoor smoke over ignited dry ground near a public camping site of the world-renowned Arctic Circle Trail (McGwinn, 2019), indicating that tourism will need to adapt to increased fire risk in tundra landscapes. Greenland wildfires in 2017 and 2019 occurred east of Sisimiut in tundra areas with low vegetative cover and degraded permafrost, but high carbon soils, during warm, dry, and sunny summers (Evangeliou et al., 2019). Timber extraction and site preparation currently cause large wildfires in the Arctic region, including the 2014 Västmanland fire - the largest single wildfire event in Sweden's history (Lidskog et al., 2019). Northward agricultural expansion will likely increase human-caused open burning as wheat and maize establish in previously permafrost areas of West Siberia (Parfenova et al., 2019).

3.1.6 Climate change will increase 'natural' fire emissions in the Arctic

An overall increase in natural fire risk is expected in the Arctic, as well as associated emissions. Natural fires, i.e., lightning-caused fires, are estimated to increase as lightning strikes are predicted to increase (Púčik et al., 2017; Veraverbeke et al. 2017). Using the RCP 8.5 scenario, Teufel and Sushama (2019) estimate a 2.0°C threshold will be reached around 2031, causing 42% of pan-Arctic permafrost to abruptly degrade and increase fire severity in Russia, Canada, and Alaska (Figure 1). Under RCPs 4.5 and 8.5, wildfire emissions could exceed anthropogenic emissions in northeastern Europe by 2090, including Sweden and Finland (Knorr et al., 2016). There is a clear consensus that longer fire seasons will increase in the eastern boreal forests of Canada (Boulanger et al., 2013); central and northwestern Canada (Boulanger et al., 2014); and European Russia (particularly Karelia and Leningradskaya), West Siberia, and the Far East (Sherstyukov and Sherstyukov, 2014). Wang et al. (2017) note that a recent increase in the fire season in Canada has led to the increase in the total number of fire spread days, leading to large increases in total fire size and emissions for early season fires like the Fort McMurray megafire in Alberta. Lengthening the fire season means increased potential for more and larger fire emissions throughout the fire

season, starting earlier in spring and lasting later into autumn. Further, suppression of wildfire in Canadian boreal communities has increased their likelihood of flammability (Parisien et al., 2020), calling into question what other willand-urban interfaces in the Arctic region may have similar risks due to long term aggressive fire suppression.

3.2 Uncertainties in future open biomass burning emissions

3.2.1 Satellite-based fire emissions

Uncertainties in emission inventories are driven by availability and quality of fire activity data from satellite- and ground-based sources. Current global fire emission inventories rely on satellite-derived fire activity from active fire detections, burned area mapping, and fire radiative power (Liu et al., 2020). ***Satellite-based observations of fire in the Arctic underestimate open burning in agricultural landscapes, surface fires in boreal forests, and smouldering peat fires***. For example, current emission inventories, like GFEDv4, based on satellite-derived products of burned area underestimate human-caused burning in agricultural landscapes and mixed forests in Eurasia between 50° to 65° N by ~2,100 km^2 annually for 12 regions of interest (Zhu et al., 2017), indicating that actual burned area from anthropogenic sources in the Eurasian boreal zone is currently underestimated by as much as 16%.

Surface fires under forest canopies dominate fire regimes in much of Northern Eurasia, which are not well quantified in current satellite-based burned area products (Duncan et al., 2020) and thus emission inventories. Smouldering fires in carbon-rich humus and peat landscapes will be difficult to detect, as smouldering combustion occurs at much lower temperatures than flaming combustion; 500 °C to 700 °C versus 1500 °C to 1800 °C, respectively (Rein et al. 2008). Daily, global observations of low-intensity fire from existing satellite systems are limited currently to the Visible Infrared Imaging Spectroradiometer (VIIRS) (Johnston et al., 2018). Smouldering fires in the Arctic can be mapped via regionally-tuned algorithms designed to ingest daily active fire detections from multispectral VIIRS (Waigl et al., 2017) and hyperspectral Hyperion (Waigl et al., 2019). In general, satellite and

drone detections (Burke et al., 2019) of smouldering peat fires are difficult because these ground fires are low temperature and can burn underground and re-emerge in new locations (Rein, 2016), with additional existing detection constraints from coarse resolution (> 1 km) global satellite sensors, canopy cover, and cloud cover (Johnston et al., 2018). A further complication is that peat fires can smoulder for months, years, and even decades (Hu et al., 2018), burning laterally and vertically below surface, appearing to be extinguished, but releasing smoke at the surface in a different location than the original ignition site. In Alaska, this phenomenon is referred to as holdover, overwintered, and/or zombie fires, difficult to allocate as a single - but complex - fire event from cumulative satellite active fire and burned area pixels. For example, in April 2020, the Alaska Division of Forestry was monitoring several active smoldering peat fires from the ~ 5 km^2 Deshka Landing Fire of August 2019 that had overwintered near Willow, Alaska despite heavy snow melt (Alaska Wildland Fire Information, 2020). Preliminary results by Scholten and Veraverbeke (2020), indicate that overwintering fires are more likely to be holdovers from high severity fires, emerging more frequently in lowland black spruce-dominated forests.

3.2.2 Lack of agreement between official statistics and satellite-based emission inventories

Earth observations from satellite products are powerful tools for forecasting (Pickell et al., 2017), improving rapid response post-fire modelling (Miller et al., 2017), and quantifying fire in the boreal and Arctic regions (Hislop et al., 2020). Consistently, however, ***there has been little correlation between satellite-derived and official estimates of burned area*** (Fusco et al., 2019). Loepfe et al. (2012) found that multiple satellite fire products had high correlation with official reports of burned areas for Sweden, but little to no correlation with official statistics for Finland. Agreement of official Russian burned area statistics from fires in Siberian forests was less than 10% when compared to four satellite-based burned area products (Kukavskaya et al., 2013). The Global Wildfire Information System (GWIS; https://gwis.jrc.ec.europa.eu/), a joint program between the Group on Earth Observations (GEO; https://www.earthobservations.org/geoss_wp.php), the Copernicus (https://www.copernicus.eu/en/services/emergency), and NASA (https://www.nasa.gov/), uses the MODIS MOD64A1 Collection 6 Burned Area product (Giglio et al., 2018) to create

country-level burned area statistics. GWIS satellite-derived burned area overestimates open biomass burning in both Norway and Finland by 199% and 129%, respectively, when compared to official statistics. GWIS underestimates by approximately 48% for total open biomass burning in Sweden. Future open biomass burning emissions will need improved satellite fire methodologies for the Arctic region and also shorter latency in ground reports and statistics from official agencies.

Country	Year	Official Burned Area (km^2)	GWIS Burned Area (km^2)	BC (metric tonne) from official stats	BC (metric tonne) from GWIS
Norway	2019	0.03	13	7.61E-06	3.30E-03
Sweden	2018	250	154	0.063	0.039
Finland	2019	6	28	0.002	0.007

Table 2. Burned area and black carbon emissions from official burned area statistics compared to GWIS satellite-derived burned area and calculated BC emissions; emission calculations use the same fuel loadings, emission factor, and combustion completeness from Table 1.

3.2.3 Climate-driven ignitions, vegetation shifts, and fuel conditions

Ignition likelihood is often modeled by considering the moisture conditions of ground fuels (i.e., litter) and the organic layer (i.e., forest canopy), whereby humans are the most likely source of fire on the ground and lightning the source for canopy fires (Wotton et al. 2003). Veraverbeke et al. (2017) introduced ***a positive feedback loop between climate, lightning, fires and northward forest expansion, whereby surface energy fluxes from forests appeared to be statistically increasing the probability of lightning*** in Alaska: "warming may increase treeline lightning and fires; increased treeline fires may facilitate northward

expansion of forest; increased high-latitude forest may feedback to further increase local lightning."

Climate change may have both positive and negative impacts on boreal forests and forestry (Reyer et al., 2017). In the near future, these changes may be positive but become negative in the mid- and long-term. In general, climate change accelerates forest growth at high northern latitudes due to a longer growing season. Moreover, elevated CO_2 concentration decreases transpiration and increases photosynthetic rate and thus enhances forest growth (Peltola et al., 2002; Ellsworth et al., 2012; Kellomäki et al., 2018). However, abiotic and biotic damages in particular may have opposite effects on forest growth (Seidl et al., 2014). For example, drought increases the risk of forest fires, but also negatively impacting the growth of Norway spruce (*Picea abies)* and exposing trees to biotic damages. Snow damages are estimated to increase in northeastern Europe but decrease elsewhere in Europe by end-of-century under scenarios 4.5 and 8.5 (Gronemeijer et al., 2016). Wind damage risk is expected to increase due to the shortening of soil frost period (Venäläinen et al., 2020).

Future climate conditions are expected to become more favourable for forest fires in the Boreal zone, even highly managed regions. By integrating the seasonal severity rating index (SRI) with the Canadian Fire Weather Index, Lehtonen et al. (2016) found that climate change increases the probability of large forest fires in Finland under scenario RCP 4.5. Finland can expect an increase in the number of days of very flammable conditions by approximately 13% for 2019–2039, 40% for 2040–2069, and 55% for 2070–2100 when compared with 1980 to 2010. Here, the increase of fire risk is expected to be caused only by climate warming.

Many forest insects responsible for bug kill of trees will benefit from climate change due to established linkage of increased habitat range and increased winter temperatures (Pureswaran et al., 2018). Climate-driven bug kill increases the amount of easily burnable material in forests and can influence fire risk. For example, a large-scale bark beetle invasion could increase the amount of fuels via dead wood, increasing ignition risk and crown fire risk as well as increasing the need, danger, and cost of fuels and fire management of insect attacked forests (Jenkins et al., 2014). According to Venäläinen et al. (2020), a warming

climate is likely to increase the risk of bark beetle outbreaks and wood decay caused by *Heterobasidion spp*. root rot in Finland's coniferous forests. Moreover, the probability of forest-damaging cascading and compounding events, i.e., large-scale wind damage followed by a widespread bark beetle outbreak, may increase remarkably in the future for the High Northern Latitudes.

3.2.4 Constraining fire intensity and plume injection height for fire emissions

Future fire emissions in the boreal zone must consider fire intensity. Wotton et al. (2017) found that by mid- and late-century under both RCP 4.5 and RCP 8.5, the number of days where fire intensity of wildfires (i.e., crown fires) in the Canadian boreal zone will be practically unmanageable by ground crews and/or aerial support, like water bombers. For instance, Canadian wildland firefighters operationally use several key thresholds to guide fire operations based on fire intensity. Wotton et al. (2017) report that at 2 MW m^{-1} fire line intensity, ground resources request aerial firesupport to hold fireline; at 4 MW m^{-1} aerial fire suppression via air tankers lose effectiveness at directly controlling a fire line; at 10 MW m^{-1} heavy air tankers are not effective for holding or suppressing a fire line. Emissions from functionally uncontrollable fires, i.e., megafires, in boreal forests are not well quantified due to uncertainties in combustion efficiency observations and estimates (Xu et al., 2020) and lack of fine-scale burned area products that account for small waterbodies, with a capacity to map combustion in "wet", intermediate drainage soils with high soil carbon often dominated by species like black spruce (*Picea mariana*) (Walker et al., 2018). However, fire intensity does not always prohibit vegetation recovery. Shvetsov et al. (2019) found that high fire frequency in the Zabaikal region of southern Siberia, when combined with positive surface temperature anomalies, is more likely to negatively impact the post-fire reforestation process than severe burns - which actually had higher vegetation recovery rates.

Smoke injection height and smoke detrainment height is critical to estimate the transport of smoke plumes (Sokolik et al., 2019). Detrainment occurs when turbulence moves smoke particles beyond plume boundaries or when the smoke plume is weak enough to be torn apart by turbulence of the surrounding air. Current satellite-based injection height models

must model smoke detrainment (Val Martin et al., 2018), whereas direct observations of detrainment height are important to determine the transport and deposition capacity of a smoke plume to (Sokolik et al., 2019). Yu et al. (2019) found that an August 2017 wildfire fire in British Columbia, Canada produced a pyrocumulonimbus (pyroCb) event that injected smoke into the stratosphere, with an initial smoke injection height of 12 km but eventually rising to 23 km in the atmosphere due to solar heating of BC over a two month period.

3.2.5 More future fires in Arctic peatlands, but where and how much?

Peat smouldering can emit large quantities of smoke, contributing to hazardous air quality (Hu et al., 2018). Current global fire emissions inventories underestimate peat fires, as forest fuel types currently drive fuels maps and profiles (Liu et al., 2020). Boreal zone peatland fires are not well quantified in terms of fuel loadings (Van Leuwen et al., 2014). High uncertainty in emission factors for boreal peat fires (Hu et al., 2018) has led to improved laboratory-derived emission factors from sampled peat from Russia and Alaska (Watson et al., 2019).

With a warming climate, there is a risk of increasing peatland and "legacy carbon" fires (Ingram et al., 2019) in boreal forests, particularly in stands younger than 60 years where drying limits the resilience of the carbon rich soils (Walker et al., 2019) and in drying fen watersheds near large settlements, like the costliest wildfire in Canada's history - the May 2016 Horse River/Fort McMurray fire (Elmes et al., 2018). Future emission estimates from peat fires will need to know where and in what condition these carbon-rich soils are, particularly as predicted moderate and severe drought in boreal peatlands western Canada are expected to increase fire size by over 500% (Thompson et al., 2019). ***Pan-Arctic maps of peatlands are still incomplete*** (Yu et al., 2010; Wu et al., 2017; Xu et al., 2018).

Climate mitigation efforts, like restoration or rewetting of peatlands, do not eliminate the role of fire as a management tool (Davies et al., 2016) nor the risk of wildland fire in peat landscapes. Thus, ***future fire emission inventories will need to include complex peat fuels conditions and loadings***. For example, restoration of peat is not a linear process, with previous results in Canada showing one to two decades needed for restoration and

rewetting of degraded peatlands that have residual peat and vegetation to 'seed' the sites (Nugent et al., 2019). Until these restored peatlands have sufficient moisture and vegetation cover, they are still susceptible to fire risk (Gewin, 2020). Burn depth in peat can be limited in naturally wet and rewetted peatlands if the surface maintains a high moisture content via hydrological and vegetation processes (Granath et al., 2016). Maintaining these needed hydrogelogical processes is difficult for degraded, unmanaged peatlands. In Alberta, wildland peat sites lacking constant sources of water and depositional inputs experienced severe burning on margins (Ingram et al., 2019) while Wilkinson et al. (2019) found forested peatland margins were extremely vulnerable to peat smouldering combustion, especially in previously burned areas with > 60 years since fire. Ronkainen et al. (2013) expect a warmer climate to lower water tables via evapotranspiration for unmanaged peatlands in Finland, thus increasing wildfire risk. Producing more complete fuel loadings for peatlands across the Arctic region can follow methodologies set by Johnston et al. (2015) to augment the dynamic boreal and taiga fuel loadings, e.g. Ivanova et al. (2019).

3.2.6 Uncertainties in permafrost degradation

While not all permafrost is confined to peatlands, ***many discontinuous permafrost sites are dominated by peatlands*** in Canada (Estop-Aragonés et al., 2018; Gibson et al., 2018), Russia (Hugelius et al., 2014), and Sweden (Chang et al., 2019). Further, current climate models may be missing the link between melting soil ice, sometimes referred to as thermokarst processes, and potential permafrost degradation of the currently stable and carbon-rich northeast Siberian Arctic lowlands (NESAL). Nitzbon et al. (2020) indicate that we can expect a threefold increase of permafrost melt in the NESAL region under RCP 4.5 by 2100 when thermokarst processes are combined with increased temperature projections in numerical modelling, potentially increasing the amount of peat fuels in an already high fire activity region. Combining current peatland distribution maps with newer modeled datasets of predicted mid-century and late-century permafrost extent and geohazard indices under climate-forcing scenarios (Karjalainen et al., 2019) can reduce uncertainties to determine where 1) increased peat fire risk and locations due to permafrost melt and 2) decreased

capability to deploy ground-level wildland firefighting, thus limiting ability to control future peat fires and fire emissions in the Pan-Arctic.

Permafrost areas, especially at their southern distributions, are being disturbed by wildfires (Holloway et al., 2020). In Alaska and northwestern Canada the impacts of wildfire disturbances on permafrost has been well quantified. For instance, post-fire permafrost change in Alaska showed surface warming greater in boreal sites than tundra, with surface temperatures higher for previously burned sites than at unburned sites, even after vegetation recovered for one to four decades (Jiang et al., 2017). Though the vast majority of fires in the continuous and discontinuous permafrost zones occur in deciduous needleleaf forests (Loranty et al., 2016), ***knowledge gaps on post-fire permafrost resiliency exist for larch-dominated forests*** (Larix spp.) in Siberia. Likewise, ***uncertainties persist for post-fire permafrost resiliency in the boreal forests*** of eastern Canadian, like Quebec and Labrador (Holloway et al., 2020).

3.2.7 The role of people in future Arctic fire regimes

Determining the impact of humans on fire risk is dependent on local- to national-scale actions that may increase fire and emissions via deforestation, transportation networks, energy extraction, and agricultural open burning as well as decrease fire and fire emissions via active suppression. Riley et al. (2019) note that humans on a global scale have been able to disrupt and sometimes uncouple the direct relationship between temperature and biomass burning, asking "[I]s there a threshold in the magnitude of climate change after which humans will no longer be able to affect this relationship?"

On a practical level, ***people are the main ignition sources for fires in the Arctic region, while lightning ignitions tend to lead to larger fire sizes***. In interior Alaska, where lightning-caused fires account for 95% of total burned area (Veraverbeke et al. 2017), 52% of total ignitions were human in origin but occured in areas of high fire suppression resulting in only 5% of total burned area from 1990 to 2016 (Calef et al. 2017). Archard et al. (2008) estimated 65% of all forest fires in the Russian Federation to be caused by human ignition, and a more recent study finding approximately half of all fires in Sakha Republic are caused

by anthropogenic activities (Kirillina et al., 2020). Throughout boreal Canada, anthropogenic factors increase fire probability (Parisien et al., 2016), with humans igniting most fires close to roads while lightning-caused fires are responsible for the majority of burned area in remote areas (Gralewicz et al., 2012). Blouin et al. (2016) found that 45% of wildfires in Alberta were started by lightning, but responsible for 71% of burned area. In Finland, lightning-caused fires account for less than 15% of forest fires (Larjavaara et al., 2005). Machines used for forestry operations in stony areas of Sweden account for 330 to 480 annual ignitions and 40% of total burned area (Sjöström et al., 2019). For the 19 European countries reporting fires and ignition sources to the European Forest Fire Information System (EFFIS; https://effis.jrc.ec.europa.eu/), de Rigo et al. (2017) determined only 4% of fires were from natural sources, with half of the fire records lacking a verified cause.

References (APA)

Abatzoglou, J. T., & Williams, A. P. (2016). Impact of anthropogenic climate change on wildfire across western US forests. *Proceedings of the National Academy of Sciences*, *113*(42), 11770-11775.

Achard, F., Eva, H. D., Mollicone, D., & Beuchle, R. (2008). The effect of climate anomalies and human ignition factor on wildfires in Russian boreal forests. *Philosophical Transactions of the Royal Society B: Biological Sciences*, *363*(1501), 2329-2337.

Ahtikoski, A., & Hökkä, H. (2019). Intensive forest management—does it pay off financially on drained peatlands?. *Canadian Journal of Forest Research*, *49*(9), 1101-1113.

Akagi, S. K., Yokelson, R. J., Wiedinmyer, C., Alvarado, M., Reid, J. S., Karl, T., ... & Wennberg, P. O. (2011). Emission factors for open and domestic biomass burning for use in atmospheric models. *Atmospheric Chemistry and Physics*, *11*(9), 4039.

Alaska Division of Forestry (2020). *2019 EOY handout*. http://forestry.alaska.gov/Assets/pdfs/firestats/2019%20Alaska%20Fire%20Statistics.pdf

Alaska Wildland Fire Information. (2020). *Despite heavy snow melt, Deshka Landing hot spots still smoldering.* https://akfireinfo.com/2020/04/24/despite-heavy-snow-melt-deshka-landing-hot-spots-still-smoldering/

Alexander, H. D., & Mack, M. C. (2017). Gap regeneration within mature deciduous forests of Interior Alaska: Implications for future forest change. *Forest Ecology and Management*, *396*, 35-43.

AMAP Assessment 2015. (2015). *Black carbon and ozone as Arctic climate forcers*. Arctic Monitoring and Assessment Programme (AMAP), Oslo, Norway. vii + 116 pp. http://hdl.handle.net/11374/1607.

Astrup, R., Bernier, P. Y., Genet, H., Lutz, D. A., & Bright, R. M. (2018). A sensible climate solution for the boreal forest. *Nature Climate Change*, *8*(1), 11-12.

Betänkande av 2018 års skogsbrandsutredning. (2019). Skogsbränderna sommaren 2018 [Forest fires in summer 2018, in Swedish]. Statens offentliga utredningar (SOU) 2019:7, Stockholm. 334 p.

Blouin, K. D., Flannigan, M. D., Wang, X., & Kochtubajda, B. (2016). Ensemble lightning prediction models for the province of Alberta, Canada. *International Journal of Wildland Fire*, *25*(4), 421-432.

Boulanger, Y., Gauthier, S., Gray, D. R., Le Goff, H., Lefort, P., & Morissette, J. (2013). Fire regime zonation under current and future climate over eastern Canada. *Ecological applications*, *23*(4), 904-923.

Boulanger, Y., Gauthier, S., & Burton, P. J. (2014). A refinement of models projecting future Canadian fire regimes using homogeneous fire regime zones. *Canadian Journal of Forest Research*, *44*(4), 365-376.

Bowman, D.M., Balch, J., Artaxo, P., Bond, W.J., Cochrane, M.A., D'antonio, C.M., DeFries, R., Johnston, F.H., Keeley, J.E., Krawchuk, M.A., & Kull, C.A. (2011). The human dimension of fire regimes on Earth. *Journal of Biogeography*, *38*(12), 2223-2236.

Box, J.E., Colgan, W.T., Christensen, T.R., Schmidt, N.M., Lund, M., Parmentier, F.J.W., Brown, R., Bhatt, U.S., Euskirchen, E.S., Romanovsky, V.E., & Walsh, J.E. (2019). Key

indicators of Arctic climate change: 1971–2017. *Environmental Research Letters*, *14*(4), p.045010.

Burke, C., Wich, S., Kusin, K., McAree, O., Harrison, M. E., Ripoll, B., ... & Longmore, S. (2019). Thermal-Drones as a Safe and Reliable Method for Detecting Subterranean Peat Fires. *Drones*, *3*(1), 23.

Calef, M. P., Varvak, A., & McGuire, A. D. (2017). Differences in human versus lightning fires between urban and rural areas of the boreal forest in interior Alaska. *Forests*, *8*(11), 422.

Chang, K. Y., Riley, W. J., Crill, P. M., Grant, R. F., Rich, V. I., & Saleska, S. R. (2019). Large carbon cycle sensitivities to climate across a permafrost thaw gradient in subarctic Sweden. *The Cryosphere*, 13(2), 647– 663.

Chernokulsky, A., & Esau, I. (2019). Cloud cover and cloud types in the Eurasian Arctic in 1936–2012. *International Journal of Climatology*, *39*(15), 5771-5790.

CIFFC. (2020) *Canadian Interagency Forest Fire Centre: Fire Hectares by Year.* https://ciffc.net/en/ext/hectares-by-year

Daanen, R. P., Ingeman-Nielsen, T., Marchenko, S. S., Romanovsky, V. E., Foged, N., Stendel, M., ... & Hornbech Svendsen, K. (2011). Permafrost degradation risk zone assessment using simulation models. *The Cryosphere*, *5*(4), 1043-1056.

Davies, G. M., Kettridge, N., Stoof, C. R., Gray, A., Ascoli, D., Fernandes, P. M., ... & McMorrow, J. (2016). The role of fire in UK peatland and moorland management: the need for informed, unbiased debate. *Philosophical Transactions of the Royal Society B: Biological Sciences*, 371(1696), 20150342.

De Groot, W. J., Flannigan, M. D., & Stocks, B. J. (2013). Climate change and wildfires. In *González-Cabán, Armando, tech. coord. Proceedings of the fourth international symposium on fire economics, planning, and policy: climate change and wildfires. Gen. Tech. Rep. PSW-GTR-245 (English). Albany, CA: US Department of Agriculture, Forest Service, Pacific Southwest Research Station: 1-10* (Vol. 245, pp. 1-10).

de Rigo, D., Libertà, G., Houston Durrant, T., Artés Vivancos, T., & San-Miguel-Ayanz, J. (2017). *Forest fire danger extremes in Europe under climate change: variability and*

uncertainty. Publication Office of the European Union, Luxembourg, 71 pp. ISBN:978-92-79-77046-3, https://doi.org/10.2760/13180.

Duncan, B. N., Ott, L. E., Abshire, J. B., Brucker, L., Carroll, M. L., Carton, J., ... & Gregg, W. W. (2020). Space-Based Observations for Understanding Changes in the Arctic-Boreal Zone. *Reviews of Geophysics*, 58(1), e2019RG000652. https://doi.org/10.1029/2019RG000652.

DSB. 2020. *Direktoratet for samfunnssikkerhet og beredskap*. Personal communication, March 2020. https://www.dsb.no/.

Ellsworth, D. S., Thomas, R., Crous, K. Y., Palmroth, S., Ward, E., Maier, C., ... & Oren, R. (2012). Elevated CO 2 affects photosynthetic responses in canopy pine and subcanopy deciduous trees over 10 years: a synthesis from D uke FACE. *Global Change Biology*, *18*(1), 223-242.

Elmes, M. C., Thompson, D. K., Sherwood, J. H., & Price, J. S. (2018). Hydrometeorological conditions preceding wildfire, and the subsequent burning of a fen watershed in Fort McMurray, Alberta, Canada. *Natural Hazards & Earth System Sciences*, *18*(1).

Estop-Aragonés, C., Czimczik, C. I., Heffernan, L., Gibson, C., Walker, J. C., Xu, X., & Olefeldt, D. (2018). Respiration of aged soil carbon during fall in permafrost peatlands enhanced by active layer deepening following wildfire but limited following thermokarst. *Environmental Research Letters*, 13(8), 085002.

Evangeliou, N., Kylling, A., Eckhardt, S., Myroniuk, V., Stebel, K., Paugam, R., ... & Stohl, A. (2019). Open fires in Greenland in summer 2017: transport, deposition and radiative effects of BC, OC and BrC emissions. *Atmospheric Chemistry Physics*, 19, 1393–1411, 10.5194/acp-19-1393-2019.

Flannigan, M., Cantin, A. S., De Groot, W. J., Wotton, M., Newbery, A., & Gowman, L. M. (2013). Global wildland fire season severity in the 21st century. *Forest Ecology and Management*, *294*, 54-61.

Foster, A.C., Armstrong, A.H., Shuman, J.K., Shugart, H.H., Rogers, B.M., Mack, M.C., Goetz, S.J., & Ranson, K.J. (2019). Importance of tree-and species-level interactions with wildfire, climate, and soils in interior Alaska: Implications for forest change under a warming climate. *Ecological Modelling*, *409*, 108765.

3662 Fusco, E. J., Finn, J. T., Abatzoglou, J. T., Balch, J. K., Dadashi, S., & Bradley, B. A. (2019).
3663 Detection rates and biases of fire observations from MODIS and agency reports in the
3664 conterminous United States. *Remote Sensing of Environment*, *220*, 30-40.

3665 Gewin, V. (2020). How peat could protect the planet. *Nature*, 578(7794), 204.

3666 Gibson, C. M., Chasmer, L. E., Thompson, D. K., Quinton, W. L., Flannigan, M. D., & Olefeldt,
3667 D. (2018). Wildfire as a major driver of recent permafrost thaw in boreal peatlands.
3668 *Nature communications*, 9(1), 1-9.

3669 Giglio, L., Boschetti, L., Roy, D. P., Humber, M. L., & Justice, C. O. (2018). The Collection 6
3670 MODIS burned area mapping algorithm and product. *Remote sensing of environment*,
3671 *217*, 72-85.

3672 Girardin, M. P., & Terrier, A. (2015). Mitigating risks of future wildfires by management of
3673 the forest composition: an analysis of the offsetting potential through boreal Canada.
3674 *Climatic Change*, *130*(4), 587-601.

3675 Gralewicz, N. J., Nelson, T. A., & Wulder, M. A. (2012). Factors influencing national scale
3676 wildfire susceptibility in Canada. *Forest Ecology and Management*, *265*, 20-29.

3677 Granath, G., Moore, P. A., Lukenbach, M. C., & Waddington, J. M. (2016). Mitigating wildfire
3678 carbon loss in managed northern peatlands through restoration. *Scientific reports*, 6(1),
3679 1-9.

3680 Granström, A., & Niklasson, M. (2008). Potentials and limitations for human control over
3681 historic fire regimes in the boreal forest. *Philosophical Transactions of the Royal Society*
3682 *B: Biological Sciences*, *363*(1501), 2351-2356.

3683 Groenemeijer, P., Vajda, A., Lehtonen, I., Kämäräinen, M., Venäläinen, A., Gregow, H.,
3684 Becker, N., Nissen, K., Ulbrich, U., Paprotny, D., & Morales Napoles, O. (2016). *Present*
3685 *and future probability of meteorological and hydrological hazards in Europe.* Final report
3686 of Deliverable 2.5 for the Risk Analysis of Infrastructure Networks in response to extreme
3687 weather (RAIN) project. http://rain-project.eu/wp-
3688 content/uploads/2016/09/D2.5_REPORT_final.pdf

3689 Gromny, E., Lewiński, S., Rybicki, M., Malinowski, R., Krupiński, M., Nowakowski, A., &
3690 Jenerowicz, M. (2019, November). Creation of training dataset for Sentinel-2 land cover

classification. In *Photonics Applications in Astronomy, Communications, Industry, and High-Energy Physics Experiments 2019* (Vol. 11176, p. 111763D). International Society for Optics and Photonics. Data available: http://s2glc.cbk.waw.pl/

Günther, A., Barthelmes, A., Huth, V., Joosten, H., Jurasinski, G., Koebsch, F., & Couwenberg, J. (2020). Prompt rewetting of drained peatlands reduces climate warming despite methane emissions. *Nature Communications*, 11, 1644. https://doi.org/10.1038/s41467-020-15499-z.

Hall, J. V., & Loboda, T. V. (2017). Quantifying the Potential for Low-Level Transport of Black Carbon Emissions from Cropland Burning in Russia to the Snow-Covered Arctic. *Frontiers in Earth Science*, *5*, 109.

Hall, J., & Loboda, T. (2018). Quantifying the variability of potential black carbon transport from cropland burning in Russia driven by atmospheric blocking events. *Environmental Research Letters*, *13*(5), 055010.

Hannah, L., Roehrdanz, P.R., KC, K.B., Fraser, E.D., Donatti, C.I., Saenz, L., Wright, T.M., Hijmans, R.J., Mulligan, M., Berg, A., & van Soesbergen, A., 2020. The environmental consequences of climate-driven agricultural frontiers. *PLoS One*, *15*(2), p.e0228305. https://doi.org/10.1371/journal.pone.0228305.

Hlásny, T., Krokene, P., Liebhold, A., Montagné-Huck, C., Müller, J., Qin, H., ... & Viiri, H. (2019). *Living with bark beetles: impacts, outlook and management options* (No. 8). European Forest Institute.

Hislop, S., Haywood, A., Jones, S., Soto-Berelov, M., Skidmore, A., & Nguyen, T. H. (2020). A satellite data driven approach to monitoring and reporting fire disturbance and recovery across boreal and temperate forests. *International Journal of Applied Earth Observation and Geoinformation*, *87*, 102034.

Holloway, J. E., Lewkowicz, A. G., Douglas, T. A., Li, X., Turetsky, M. R., Baltzer, J. L., & Jin, H. (2020) Impact of wildfire on permafrost landscapes: A review of recent advances and future prospects. *Permafrost and Periglacial Processes*. https://doi.org/10.1002/ppp.2048.

3719 Hu, Y., Fernandez-Anez, N., Smith, T. E., & Rein, G. (2018). Review of emissions from
3720 smouldering peat fires and their contribution to regional haze episodes. *International*
3721 *Journal of Wildland Fire*, 27(5), 293-312.

3722 Hugelius, G., Strauss, J., Zubrzycki, S., Harden, J. W., Schuur, E. A. G., Ping, C. L., ... &
3723 O'Donnell, J. A. (2014). Estimated stocks of circumpolar permafrost carbon with
3724 quantified uncertainty ranges and identified data gaps. *Biogeosciences*, 11(23), 6573-
3725 6593.

3726 Ichoku, C., & Ellison, L. (2014). Global top-down smoke-aerosol emissions estimation using
3727 satellite fire radiative power measurements. *Atmospheric Chemistry Physics*, 14, 6643-
3728 6667, 10.5194/acp-14-6643-2014.

3729 Ingram, R. C., Moore, P. A., Wilkinson, S., Petrone, R. M., & Waddington, J. M. (2019).
3730 Postfire soil carbon accumulation does not recover boreal peatland combustion loss in
3731 some hydrogeological settings. J*ournal of Geophysical Research: Biogeosciences*, 124(4),
3732 775-788.

3733 IPCC: Climate Change 2013: The Physical Science Basis. Contribution to the Fifth Assessment
3734 Report of the Intergovernmental Panel on Climate Change, edited by: Stocker, T. F., Qin,
3735 D., Plattner, G.-K., Tignor, M., Allen, S.K., Boschung, J., Nauels, A., Xia, Y., Bex, V. and
3736 Midgley, P.M., 2013.

3737 Ivanova, G. A., Kukavskaya, E. A., Ivanov, V. A., Conard, S. G., & McRae, D. J. (2019). Fuel
3738 characteristics, loads and consumption in Scots pine forests of central Siberia. *Journal of*
3739 *Forestry Research*, 1-18.

3740 M. M. B., Allen, S. K., Boschung, J., Nauels, A., Xia, Y., Bex, V., and Midgley, P. M., Cambridge
3741 University Press, 2013.

3742 Jenkins, M. J., Runyon, J. B., Fettig, C. J., Page, W. G., & Bentz, B. J. (2014). Interactions
3743 among the mountain pine beetle, fires, and fuels. *Forest Science*, *60*(3), 489-501.

3744 Jiang, Y., Rocha, A. V., O'Donnell, J. A., Drysdale, J. A., Rastetter, E. B., Shaver, G. R., &
3745 Zhuang, Q. (2015). Contrasting soil thermal responses to fire in Alaskan tundra and boreal
3746 forest. *Journal of Geophysical Research: Earth Surface*, *120*(2), 363-378.

3747 Johnston, D. C., Turetsky, M. R., Benscoter, B. W., & Wotton, B. M. (2015). Fuel load,
3748 structure, and potential fire behaviour in black spruce bogs. *Canadian Journal of Forest*
3749 *Research*, *45*(7), 888-899.

3750 Johnston, J. M., Johnston, L. M., Wooster, M. J., Brookes, A., McFayden, C., & Cantin, A. S.
3751 (2018). Satellite detection limitations of sub-canopy smouldering wildfires in the North
3752 American Boreal Forest. *Fire*, *1*(2), 28.

3753 Kaiser, J.W., Heil, A., Andreae, M.O., Benedetti, A., Chubarova, N., Jones, L., Morcrette, J.J.,
3754 Razinger, M., Schultz, M.G., Suttie, M., & Van Der Werf, G.R. (2012). Biomass burning
3755 emissions estimated with a global fire assimilation system based on observed fire
3756 radiative power. *Biogeosciences*, *9*(1), 527-554.

3757 Karjalainen, O., Aalto, J., Luoto, M., Westermann, S., Romanovsky, V. E., Nelson, F. E., ... &
3758 Hjort, J. (2019). Circumpolar permafrost maps and geohazard indices for near-future
3759 infrastructure risk assessments. *Scientific data*, 6, 190037.

3760 Keegan, K. M., Albert, M. R., McConnell, J. R., & Baker, I. (2014). Climate change and forest
3761 fires synergistically drive widespread melt events of the Greenland Ice Sheet. *Proceedings*
3762 *of the National Academy of Sciences*, *111*(22), 7964-7967.

3763 Kellomäki, S., Strandman, H., Heinonen, T., Asikainen, A., Venäläinen, A., & Peltola, H.
3764 (2018). Temporal and spatial change in diameter growth of boreal Scots pine, Norway
3765 spruce, and birch under recent-generation (CMIP5) global climate model projections for
3766 the 21st century. *Forests*, *9*(3), 118.

3767 Ketola, J. (2020). Forest fire activity and burned area for Finland, Emergency Services
3768 Academy. [Personal communication to Henrik Lindberg, based on rescue service
3769 database PRONTO].

3770 Kieft, J., Smith, T., Someshwar, S., & Boer, R. (2016). Towards Anticipatory Management of
3771 Peat Fires to Enhance Local Resilience and Reduce Natural Capital Depletion. In
3772 *Ecosystem-Based Disaster Risk Reduction and Adaptation in Practice* (pp. 361-377).
3773 Springer, Cham.

3774 Kirchmeier-Young, M. C., Gillett, N. P., Zwiers, F. W., Cannon, A. J., & Anslow, F. S. (2019).
3775 Attribution of the Influence of Human-Induced Climate Change on an Extreme Fire
3776 Season. *Earth's Future*, *7*(1), 2-10.

3777 Kirillina, K., Shvetsov, E. G., Protopopova, V. V., Thiesmeyer, L., & Yan, W. (2020).
3778 Consideration of anthropogenic factors in boreal forest fire regime changes during rapid
3779 socio-economic development: case study of forestry districts with increasing burnt area
3780 in the Sakha Republic, Russia. *Environmental Research Letters*, *15*(3), 035009.

3781 Knorr, W., Dentener, F., Hantson, S., Jiang, L., Klimont, Z., & Arneth, A. (2016). Air quality
3782 impacts of European wildfire emissions in a changing climate. *Atmospheric Chemistry and*
3783 *Physics*, *16*(9), 5685-5703.

3784 Koster, R. D., Darmenov, A. S., & da Silva, A. M. (2015). *The Quick Fire Emissions Dataset*
3785 *(QFED): Documentation of Versions 2.1, 2.2 and 2.4*. Volume 38; Technical Report Series
3786 on Global Modeling and Data Assimilation.
3787 https://ntrs.nasa.gov/search.jsp?R=20180005253.

3788 Krause, A., Kloster, S., Wilkenskjeld, S., & Paeth, H. (2014). The sensitivity of global wildfires
3789 to simulated past, present, and future lightning frequency. *Journal of Geophysical*
3790 *Research: Biogeosciences*, *119*(3), 312-322.

3791 Krylov, A., McCarty, J. L., Potapov, P., Loboda, T., Tyukavina, A., Turubanova, S., & Hansen,
3792 M. C. (2014). Remote sensing estimates of stand-replacement fires in Russia, 2002–2011.
3793 *Environmental Research Letters*, *9*(10), 105007.

3794 Kutcher, H. R., & Malhi, S. S. (2010). Residue burning and tillage effects on diseases and yield
3795 of barley (Hordeum vulgare) and canola (Brassica napus). *Soil and Tillage Research*,
3796 *109*(2), 153-160.

3797 Kukavskaya, E. A., Soja, A. J., Petkov, A. P., Ponomarev, E. I., Ivanova, G. A., & Conard, S. G.
3798 (2013). Fire emissions estimates in Siberia: evaluation of uncertainties in area burned,
3799 land cover, and fuel consumption. *Canadian journal of forest research*, *43*(5), 493-506.

3800 Larjavaara, M., Kuuluvainen, T., & Rita, H. (2005). Spatial distribution of lightning-ignited
3801 forest fires in Finland. *Forest ecology and management*, *208*(1-3), 177-188.

3802 Lehtonen, I., Venäläinen, A., Kämäräinen, M., Peltola, H., & Gregow, H. (2016). Risk of large-
3803 scale fires in boreal forests of Finland under changing climate. *Natural Hazards & Earth*
3804 *System Sciences Discussions*, 16, 239–253.

3805 Lidskog, R., Johansson, J., & Sjödin, D. (2019). Wildfires, responsibility and trust: public
3806 understanding of Sweden's largest wildfire. *Scandinavian Journal of Forest Research*,
3807 *34*(4), 319-328.

3808 Lindberg, H., Punttila, P., & Vanha-Majamaa, I. (2020). The challenge of combining variable
3809 retention and prescribed burning in Finland. *Ecological Processes*, *9*(1), 4.

3810 Liu, T., Mickley, L. J., Marlier, M. E., DeFries, R. S., Khan, M. F., Latif, M. T., & Karambelas, A.
3811 (2020). Diagnosing spatial biases and uncertainties in global fire emissions inventories:
3812 Indonesia as regional case study. *Remote Sensing of Environment*, *237*, 111557.

3813 Loepfe, L., Lloret, F., & Román-Cuesta, R. M. (2012). Comparison of burnt area estimates
3814 derived from satellite products and national statistics in Europe. *International journal of*
3815 *remote sensing*, *33*(12), 3653-3671.

3816 Loranty, M. M., Lieberman-Cribbin, W., Berner, L. T., Natali, S. M., Goetz, S. J., Alexander, H.
3817 D., & Kholodov, A. L. (2016). Spatial variation in vegetation productivity trends, fire
3818 disturbance, and soil carbon across arctic-boreal permafrost ecosystems. *Environmental*
3819 *Research Letters*, *11*(9), 095008.

3820 Loveland, T. R., Zhu, Z., Ohlen, D. O., Brown, J. F., Reed, B. C., & Yang, L. (1999). An analysis
3821 of the IGBP global land-cover characterization process. *Photogrammetric engineering and*
3822 *remote sensing*, *65*, 1021-1032.

3823 Markuse, P. (2019). *Before/After Comparison of the July/August 2019 Greenland Wildfire:*
3824 *Analysis from Sentinel-2*. https://pierre-markuse.net/2019/08/19/before-after-
3825 comparison-of-the-july-august-2019-greenland-wildfire/

3826 McCarty, J. L., Krylov, A., Prishchepov, A. V., Banach, D. M., Tyukavina, A., Potapov, P., &
3827 Turubanova, S. (2017). Agricultural fires in European Russia, Belarus, and Lithuania and
3828 their impact on air quality, 2002–2012. In *Land-Cover and Land-Use Changes in Eastern*
3829 *Europe after the Collapse of the Soviet Union in 1991* (pp. 193-221). Springer, Cham.

McGwinn, K. (2019). Hikers warned as Greenland wildfire burns out of control. *Arctic Today*, 16 July 2019. https://www.arctictoday.com/hikers-warned-as-greenland-wildfire-burns-out-of-control/

McWethy, D. B., Schoennagel, T., Higuera, P. E., Krawchuk, M., Harvey, B. J., Metcalf, E. C., ... & Virapongse, A. (2019). Rethinking resilience to wildfire. *Nature Sustainability*, *2*(9), 797-804.

Michaelides, R. J., Schaefer, K., Zebker, H. A., Parsekian, A., Liu, L., Chen, J., ... & Schaefer, S. R. (2019). Inference of the impact of wildfire on permafrost and active layer thickness in a discontinuous permafrost region using the remotely sensed active layer thickness (ReSALT) algorithm. *Environmental Research Letters*, *14*(3), 035007.

Miller, M. E., Billmire, M., Bourgeau-Chavez, L., Elliot, W. J., Robichaud, P. R., & MacDonald, L. (2017). *Rapid response tools and datasets for post-fire modeling in Boreal and Arctic Environment*s. Spring 2017 AFSC Remote Sensing Workshop: Opportunities to Apply Remote Sensing in Boreal/Arctic Wildfire Management and Science. Retrieved from: https://digitalcommons.mtu.edu/mtri_p/290

Molinari, C., Lehsten, V., Blarquez, O., Carcaillet, C., Davis, B. A., Kaplan, J. O., ... & Bradshaw, R. H. (2018). The climate, the fuel and the land use: Long-term regional variability of biomass burning in boreal forests. *Global Change Biology*, 24(10), 4929-4945.

Nitzbon, J., Westermann, S., Langer, M., Martin, L. C., Strauss, J., Laboor, S., & Boike, J. (2020). Fast response of cold ice-rich permafrost in northeast Siberia to a warming climate. *Nature Communications*, *11*(1), 1-11.

Nugent, K. A., Strachan, I. B., Roulet, N. T., Strack, M., Frolking, S., & Helbig, M. (2019). Prompt active restoration of peatlands substantially reduces climate impact. *Environmental Research Letters*, 14(12), 124030.

Oliva, P. and Schroeder, W., 2015. Assessment of VIIRS 375 m active fire detection product for direct burned area mapping. *Remote Sensing of Environment*, *160*, pp.144-155.

Parfenova, E., Tchebakova, N., & Soja, A. (2019). Assessing landscape potential for human sustainability and 'attractiveness' across Asian Russia in a warmer 21st century. *Environmental Research Letters*, *14*(6), 065004.

3859 Parisien, M. A., Miller, C., Parks, S. A., DeLancey, E. R., Robinne, F. N., & Flannigan, M. D.
3860 (2016). The spatially varying influence of humans on fire probability in North America.
3861 *Environmental Research Letters*, *11*(7), 075005.

3862 Parisien, M. A., Barber, Q. E., Hirsch, K. G., Stockdale, C. A., Erni, S., Wang, X., ... & Parks, S.
3863 A. (2020). Fire deficit increases wildfire risk for many communities in the Canadian boreal
3864 forest. *Nature Communications*, *11*(1), 1-9.

3865 Peltola, H., Kilpeläinen, A., & Kellomäki, S. (2002). Diameter growth of Scots pine (Pinus
3866 sylvestris) trees grown at elevated temperature and carbon dioxide concentration under
3867 boreal conditions. *Tree physiology*, *22*(14), 963-972.

3868 ФБУ «Авиалесоохрана». (2019). Сведения о лесопожарной обстановке на территории
3869 субъектов РФ на 31.12. https://bit.ly/3c8R6KR

3870 Pickell, P. D., Coops, N. C., Ferster, C. J., Bater, C. W., Blouin, K. D., Flannigan, M. D., & Zhang,
3871 J. (2017). An early warning system to forecast the close of the spring burning window
3872 from satellite-observed greenness. *Scientific reports*, *7*(1), 1-10.

3873 Púčik, T., Groenemeijer, P., Rädler, A.T., Tijssen, L., Nikulin, G., Prein, A.F., van Meijgaard, E.,
3874 Fealy, R., Jacob, D. & Teichmann, C. (2017). Future changes in European severe
3875 convection environments in a regional climate model ensemble. *Journal of Climate*,
3876 *30*(17), 6771-6794.

3877 Pureswaran, D. S., Roques, A., & Battisti, A. (2018). Forest insects and climate change.
3878 *Current forestry reports*, *4*(2), 35-50.

3879 Raynolds, M. K., Walker, D. A., Balser, A., Bay, C., Campbell, M., Cherosov, M. M., ... &
3880 Jedrzejek, B. (2019). A raster version of the Circumpolar Arctic Vegetation Map (CAVM).
3881 Remote Sensing of Environment, 232, 111297.

3882 Rein, G., Cleaver, N., Ashton, C., Pironi, P., & Torero, J. L. (2008). The severity of smouldering
3883 peat fires and damage to the forest soil. Catena, 74(3), 304-309.

3884 Rein, G. (2016). "Smoldering combustion," in *SFPE Handbook of Fire Protection Engineering*,
3885 eds M. J. Hurley, D. Gottuk, J. R. Hall, K. Harada, E. Kuligowski, M. Puchovsky, J. Torero, J.
3886 M. Watts, and C. Wieczoreks (New York, NY: Springer New York, 581–603.

Reyer, C. P., Bathgate, S., Blennow, K., Borges, J. G., Bugmann, H., Delzon, S., ... & Gracia, C. (2017). Are forest disturbances amplifying or canceling out climate change-induced productivity changes in European forests?. *Environmental Research Letters*, *12*(3), 034027.

Riahi, K., Van Vuuren, D. P., Kriegler, E., Edmonds, J., O'neill, B. C., Fujimori, S., ... & Lutz, W. (2017). The shared socioeconomic pathways and their energy, land use, and greenhouse gas emissions implications: an overview. *Global Environmental Change*, *42*, 153-168.

Riley, K. L., Williams, A. P., Urbanski, S. P., Calkin, D. E., Short, K. C., & O'Connor, C. D. (2019). Will Landscape Fire Increase in the Future? A Systems Approach to Climate, Fire, Fuel, and Human Drivers. *Current Pollution Reports*, *5*(2), 9-24.

Robinne, F. N., Parisien, M. A., & Flannigan, M. (2016). Anthropogenic influence on wildfire activity in Alberta, Canada. *International Journal of Wildland Fire*, *25*(11), 1131-1143.

Rocha, A. V., Loranty, M. M., Higuera, P. E., Mack, M. C., Hu, F. S., Jones, B. M., ... & Shaver, G. R. (2012). The footprint of Alaskan tundra fires during the past half-century: implications for surface properties and radiative forcing. *Environmental Research Letters*, *7*(4), 044039.

Ronkainen, T., Väliranta, M., & Tuittila, E.-S. (2013). Fire pattern in a drainage-affected boreal bog. *Boreal Environment Research*, 18, 309–316.

Scholten, R., & Veraverbeke, S. (2020) Alaska Fire Science Consortium: Spatiotemporal patterns of overwintering fire in Alaska. https://akfireconsortium.files.wordpress.com/2020/03/fsh_2020mar25_holdoverfires-1.pdf.

Seidl, R., Schelhaas, M. J., Rammer, W., & Verkerk, P. J. (2014). Increasing forest disturbances in Europe and their impact on carbon storage. *Nature climate change*, *4*(9), 806-810.

Sherstyukov, B. G., & Sherstyukov, A. B. (2014). Assessment of increase in forest fire risk in Russia till the late 21st century based on scenario experiments with fifth-generation climate models. *Russian Meteorology and Hydrology*, *39*(5), 292-301.

3915 Shiwakoti, S., Zheljazkov, V. D., Gollany, H. T., Kleber, M., Xing, B., & Astatkie, T. (2019).
3916 Micronutrients in the Soil and Wheat: Impact of 84 Years of Organic or Synthetic
3917 Fertilization and Crop Residue Management. *Agronomy*, 9(8), 464.

3918 Shvetsov, E. G., Kukavskaya, E. A., Buryak, L. V., & Barrett, K. (2019). Assessment of post-fire
3919 vegetation recovery in Southern Siberia using remote sensing observations.
3920 *Environmental Research Letters*, *14*(5), 055001.

3921 Silva, J. S., & Harrison, S. P. (2010). Humans, Climate and Land Cover as Controls on
3922 European Fire Regimes. In J.S. Silva, F.C. Rego, P. Fernandes & E. Rigolot (Eds.), T*owards*
3923 *integrated fire management-Outcomes of the European project Fire Paradox* (pp. 49-59).
3924 European Forest Institute.

3925 Sirin, A., Maslov, A., Medvedeva, M., Vozbrannaya, A., Valyaeva, N., Tsyganova, O., ... &
3926 Makarov, D. (2014). Multispectral remote sensing data as a tool for assessing the need
3927 and the effectiveness for peatland restoration. In *Proceedings of the 9th European*
3928 *Conference on Ecological Restoration, Oulu, Finland* (pp. 3-8).

3929 Sirin, A., Medvedeva, M., Maslov, A., & Vozbrannaya, A. (2018). Assessing the Land and
3930 Vegetation Cover of Abandoned Fire Hazardous and Rewetted Peatlands: Comparing
3931 Different Multispectral Satellite Data. *Land*, *7*(2), 71.

3932 Sjöström, J., Plathner, F. V., & Granström, A. (2019). Wildfire ignition from forestry machines
3933 in boreal Sweden. *International Journal of Wildland Fire*, 28(9), 666-677.

3934 Sokolik, I. N., Soja, A. J., DeMott, P. J., & Winker, D. (2019). Progress and Challenges in
3935 Quantifying Wildfire Smoke Emissions, Their Properties, Transport, and Atmospheric
3936 Impacts. *Journal of Geophysical Research: Atmospheres*.
3937 https://doi.org/10.1029/2018JD029878

3938 Stralberg, D., Wang, X., Parisien, M.A., Robinne, F.N., Sólymos, P., Mahon, C.L., Nielsen, S.E.,
3939 & Bayne, E.M. (2018). Wildfire-mediated vegetation change in boreal forests of Alberta,
3940 Canada. *Ecosphere*, *9*(3), p.e02156.

3941 Terrier, A., Girardin, M. P., Périé, C., Legendre, P., & Bergeron, Y. (2013). Potential changes
3942 in forest composition could reduce impacts of climate change on boreal wildfires.
3943 *Ecological Applications*, *23*(1), 21-35.

3944 Teufel, B., & Sushama, L. (2019). Abrupt changes across the Arctic permafrost region
3945 endanger northern development. *Nature Climate Change*, *9*(11), 858-862.

3946 Theesfeld, I., & Jelinek, L. (2017). A misfit in policy to protect Russia's black soil region. An
3947 institutional analytical lens applied to the ban on burning of crop residues. *Land use*
3948 *policy*, *67*, 517-526.

3949 Thomas, J. L., Polashenski, C. M., Soja, A. J., Marelle, L., Casey, K. A., Choi, H. D., ... & Pelon,
3950 J. (2017). Quantifying black carbon deposition over the Greenland ice sheet from forest
3951 fires in Canada. *Geophysical Research Letters*, *44*(15), 7965-7974.

3952 Thompson, D. K., Simpson, B. N., Whitman, E., Barber, Q. E., & Parisien, M. A. (2019).
3953 Peatland hydrological dynamics as a driver of landscape connectivity and fire activity in
3954 the boreal plain of Canada. *Forests*, 10(7), 534.

3955 Val Martin, M., Kahn, R. A., & Tosca, M. G. (2018). A Global Analysis of Wildfire Smoke
3956 Injection Heights Derived from Space-Based Multi-Angle Imaging. *Remote Sensing*,
3957 *10*(10), 1609.

3958 Van Der Werf, G.R., Randerson, J.T., Giglio, L., Van Leeuwen, T.T., Chen, Y., Rogers, B.M.,
3959 Mu, M., Van Marle, M.J., Morton, D.C., Collatz, G.J., &Yokelson, R.J. (2017). Global fire
3960 emissions estimates during 1997-2016. *Earth System Science Data*, *9*(2), 697-720.

3961 Van Leeuwen, T. T., Van der Werf, G. R., Hoffmann, A. A., Detmers, R. G., Rücker, G., French,
3962 N. H., ... & Hély, C. (2014). Biomass burning fuel consumption rates: a field measurement
3963 database. *Biogeosciences*, 11, 7305–7329.

3964 van Marle, M. J. E., Kloster, S., Magi, B. I., Marlon, J. R., Daniau, A. L., Field, R. D., Arneth, A.,
3965 Forrest, M., Hantson, S., Kehrwald, N.M., & Knorr, W. (2017). Historic global biomass
3966 burning emissions for CMIP6 (BB4CMIP) based on merging satellite observations with
3967 proxies and fire models (1750–2015), *Geosci. Model Dev.*, 10, 3329–3357.

3968 Veira, A., Lasslop, G., & Kloster, S. (2016). Wildfires in a warmer climate: emission fluxes,
3969 emission heights, and black carbon concentrations in 2090–2099. *Journal of Geophysical*
3970 *Research: Atmospheres*, *121*(7), 3195-3223.

Veraverbeke, S., Rogers, B. M., Goulden, M. L., Jandt, R. R., Miller, C. E., Wiggins, E. B., & Randerson, J. T. (2017). Lightning as a major driver of recent large fire years in North American boreal forests. *Nature Climate Change*, 7(7), 529-534.

Waigl, C. F., Stuefer, M., Prakash, A., & Ichoku, C. (2017). Detecting high and low-intensity fires in Alaska using VIIRS I-band data: An improved operational approach for high latitudes. *Remote Sensing of Environment*, *199*, 389-400.

Waigl, C. F., Prakash, A., Stuefer, M., Verbyla, D., & Dennison, P. (2019). Fire detection and temperature retrieval using EO-1 Hyperion data over selected Alaskan boreal forest fires. *International Journal of Applied Earth Observation and Geoinformation*, *81*, 72-84.

Walker, X. J., Rogers, B. M., Baltzer, J. L., Cumming, S. G., Day, N. J., Goetz, S. J., ... & Mack, M. C. (2018). Cross-scale controls on carbon emissions from boreal forest megafires. *Global Change Biology*, 24(9), 4251-4265.

Walker, X. J., Baltzer, J. L., Cumming, S. G., Day, N. J., Ebert, C., Goetz, S., ... & Turetsky, M. R. (2019). Increasing wildfires threaten historic carbon sink of boreal forest soils. *Nature*, *572*(7770), 520-523.

Wang, X., Parisien, M. A., Taylor, S. W., Candau, J. N., Stralberg, D., Marshall, G. A., ... & Flannigan, M. D. (2017). Projected changes in daily fire spread across Canada over the next century. *Environmental Research Letters*, *12*(2), 025005.

Wang, J. A., Sulla-Menashe, D., Woodcock, C. E., Sonnentag, O., Keeling, R. F., & Friedl, M. A. (2019). Extensive land cover change across Arctic–Boreal Northwestern North America from disturbance and climate forcing. *Global change biology*, 26(2), 807-822.

Watson, J. G., Cao, J., Chen, L. W. A., Wang, Q., Tian, J., Wang, X., ... & Chow, J. C. (2019). Gaseous, PM2. 5 mass, and speciated emission factors from laboratory chamber peat combustion. *Atmospheric Chemistry and Physics*, 19(22), 14173.

Whitman, E., Parisien, M. A., Thompson, D. K., & Flannigan, M. D. (2019). Short-interval wildfire and drought overwhelm boreal forest resilience. *Scientific Reports*, *9*(1), 1-12.

Wiedinmyer, C., Akagi, S. K., Yokelson, R. J., Emmons, L. K., Al-Saadi, J. A., Orlando, J. J., & Soja, A. J. (2011). The Fire INventory from NCAR (FINN): A high resolution global model to estimate the emissions from open burning. *Geoscientific Model Development*, *4*(3), 625.

4000 Wilkinson, S. L., Moore, P. A., Thompson, D. K., Wotton, B. M., Hvenegaard, S., Schroeder,
4001 D., & Waddington, J. M. (2018). The effects of black spruce fuel management on surface
4002 fuel condition and peat burn severity in an experimental fire. *Canadian Journal of Forest*
4003 *Research*, *48*(12), 1433-1440.

4004 Wilkinson, S. L., Moore, P. A., & Waddington, J. M. (2019). Assessing Drivers of Cross-Scale
4005 Variability in Peat Smoldering Combustion Vulnerability in Forested Boreal Peatlands.
4006 *Frontiers in Forests and Global Change*, *2*, 84.

4007 Wotton, B. M., Martell, D. L., & Logan, K. A. (2003). Climate change and people-caused
4008 forest fire occurrence in Ontario. *Climatic Change*, *60*(3), 275-295.

4009 Wotton, B. M., Flannigan, M. D., & Marshall, G. A. (2017). Potential climate change impacts
4010 on fire intensity and key wildfire suppression thresholds in Canada. *Environmental*
4011 *Research Letters*, *12*(9), 095003.

4012 Wu, Y., Chan, J. R., & Verseghy, D. L. (2017). A map of global peatland distribution created
4013 using machine learning for use in terrestrial ecosystem and earth system models.
4014 *Geoscientific Model Development Discussions*, *7*(13), 1-21.

4015 Xu, J., Morris, P. J., Liu, J., & Holden, J. (2018). PEATMAP: Refining estimates of global
4016 peatland distribution based on a meta-analysis. *Catena*, *160*, 134-140.

4017 Xu, W., He, H. S., Hawbaker, T. J., Zhu, Z., & Henne, P. D. (2020). Estimating burn severity
4018 and carbon emissions from a historic megafire in boreal forests of China. *Science of The*
4019 *Total Environment*, 136534.

4020 York, A., Bhatt, U., Thoman, R., & Ziel, R. (2017). *Arctic Essays: Wildland Fire in High*
4021 *Latitudes*. NOAA Arctic Program, Arctic Report Card: Update for 2017.
4022 https://arctic.noaa.gov/Report-Card/Report-Card-
4023 2017/ArtMID/7798/ArticleID/692/Wildland-Fire-in-High-Latitudes.

4024 Young, A. M., Higuera, P. E., Duffy, P. A., & Hu, F. S. (2016). Climatic thresholds shape
4025 northern high-latitude fire regimes and imply vulnerability to future climate change.
4026 *Ecography*, 40(5), 606-617.

4027 Yu, P., Toon, O. B., Bardeen, C. G., Zhu, Y., Rosenlof, K. H., Portmann, R. W., ... & de Gouw, J.
4028 (2019). Black carbon lofts wildfire smoke high into the stratosphere to form a persistent
4029 plume. *Science*, *365*(6453), 587-590.

4030 Yu, Z., Loisel, J., Brosseau, D. P., Beilman, D. W., & Hunt, S. J. (2010). Global peatland
4031 dynamics since the Last Glacial Maximum. *Geophysical Research Letters*, *37*(13).

4032 Zhang, R., Huang, C., Zhan, X., Jin, H., & Song, X. P. (2018). Development of S-NPP VIIRS
4033 global surface type classification map using support vector machines. *International*
4034 *Journal of Digital Earth*, 11(2), 212-232.

4035 Zhu, C., Kobayashi, H., Kanaya, Y., & Saito, M. (2017). Size-dependent validation of MODIS
4036 MCD64A1 burned area over six vegetation types in boreal Eurasia: Large underestimation
4037 in croplands. *Scientific reports*, *7*(1), 1-9.

4038

4039 Supplemental Materials for Chapter 3. Open biomass burning

4040

Country/ Region	Year	Official Burned Area (km^2)	Fuel Loading (kg/km^2)	Black Carbon Emission Factor (g/kg)	Combustion Completeness (%)	Black Carbon Emission (g converted to metric tonne)
USA/ Alaska	2019	10,481[a]	1080	0.5	47	2.660
Canada	2019	18,389[b]	1080	0.5	47	4.667
Denmark/ Greenland	2019	8[c]	1650	0.04	24	1.27E-04
Norway	2019	0.03[d]	1080	0.5	47	7.61E-06
Sweden	2018	250[e]	1080	0.5	47	0.063
Finland	2019	6[f]	1080	0.5	47	0.002
Russia	2019	100,785[g]	1080	0.5	47	25.579

4041 **Supplementary Table 1**. Black carbon emissions from reported statistics on burned area in
4042 the Arctic member nations; sources for burned area from [a](Alaska Division of Forestry,
4043 2020); [b](CIFFC, 2020) ; [c](Markuse, 2019); [d] (DSB, 2020); [e](Betänkande av 2018 års
4044 skogsbrandsutredning, 2019); [f](Ketola, 2020); [g](ФБУ "АВИАЛЕСООХРАНА", 2019); fuel
4045 loadings and combustion completeness from Van Leeuwen et al. (2014) for boreal forests,
4046 with tundra values used for Greenland; emission factors for BC taken from GFEDv4s with 0.5
4047 g/kg assigned to boreal forest ecosystems and 0.04 g/kg assigned to peat for Greenland.

4048

Comparison of five biomass burning emission models, including the Global Fire Emissions Database (GFED; van der Werf et al., 2017); the Fire Inventory from NCAR (FINN; Wiedinmyer et al., 2011); the Global Fire Assimilation System (GFAS; Kaiser et al., 2012); the Quick Fire Emissions Dataset (QFED; Koster et al., 2015); and the Fire Energetics and Emissions Research (FEER; Ichoku and Ellison, 2014), was completed for the entire Pan-Arctic region. Supplemental Figures 1 - 4 show details of the variation of these peer-reviewed satellite-based emissions inventories. It should be noted that GFED is used in the current CMIP runs and analyses (van Marle et al., 2017).

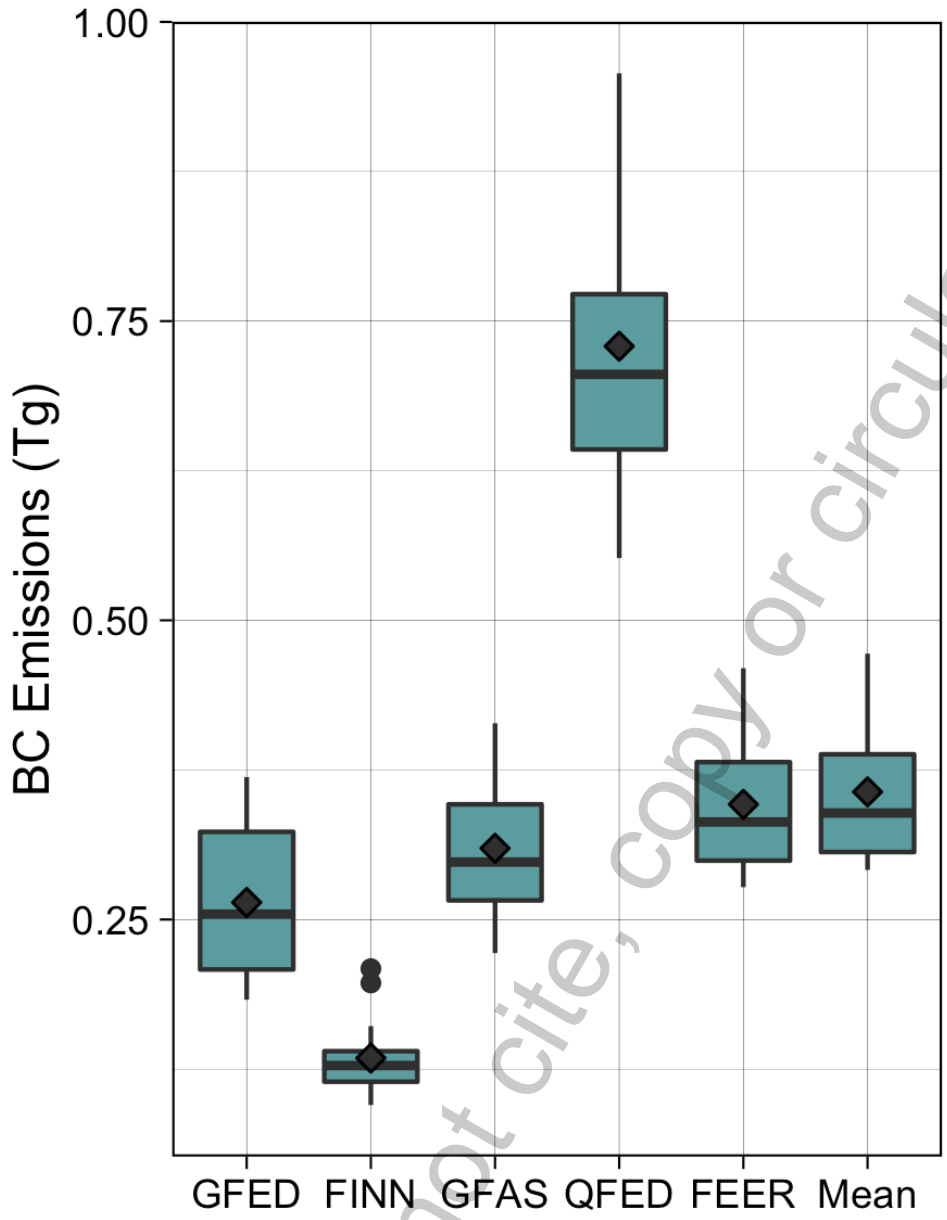

4058

4059 **Supplementary Figure 1.** Boxplot summaries of total annual emissions of BC in teragrams
4060 for 45° to 80° N from 2005 to 2018. Emissions from GFED, FINN, GFAS, QFED, and FEER plus
4061 an average of the five models is included. The horizontal bar is the median, with the mean
4062 indicated as a diamond. The box shows the 25th to the 75th percentile, and the whiskers
4063 show 1.5 times the interquartile range. Points outside the interquartile range are shown as
4064 dots; the FINN outliers are for years 2008 and 2012.

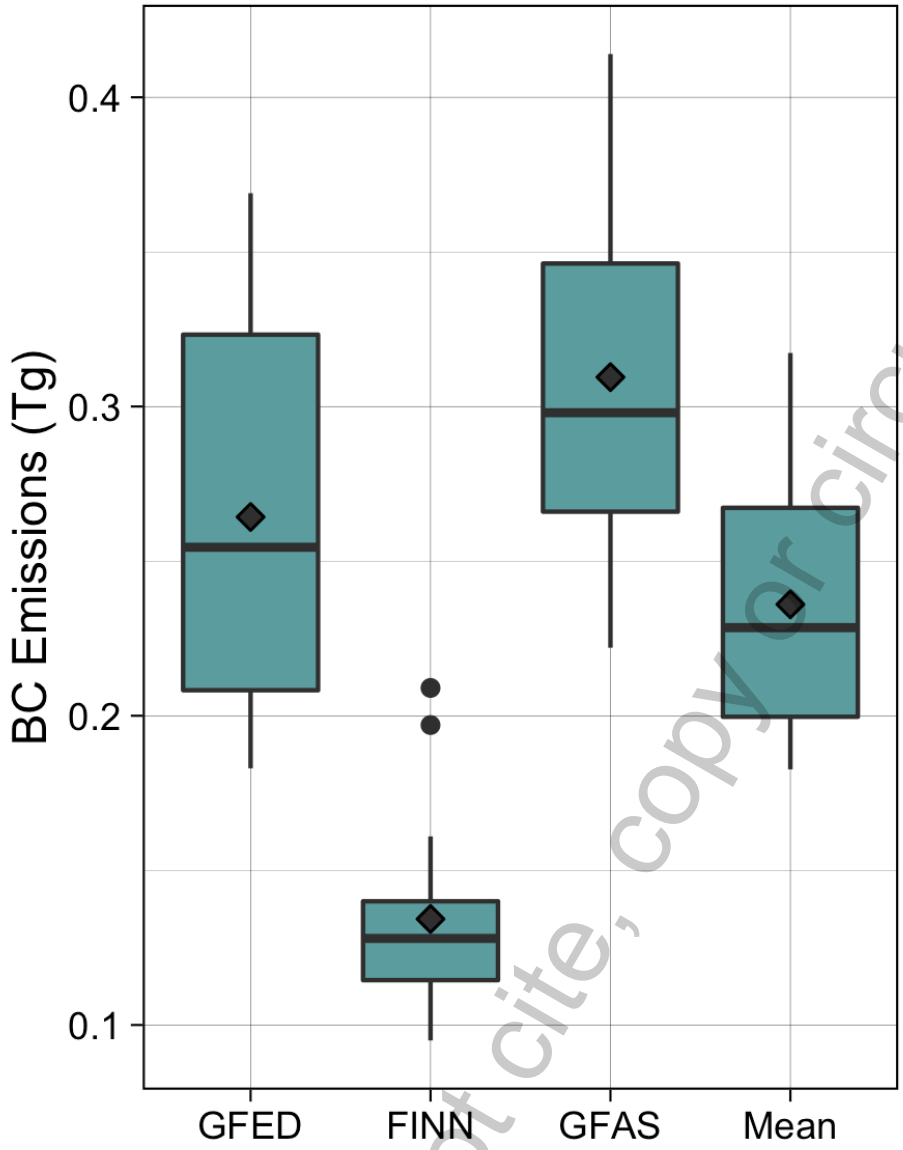

4065

4066 **Supplementary Figure 2.** Boxplot summaries of total annual emissions of BC in teragrams
4067 for 45° to 80° N from 2005 to 2018 as calculated by GFED, FINN, GFAS,and an average of the
4068 three fire emissions models. The horizontal bar is the median, with the mean indicated as a
4069 diamond. The box shows the 25th to the 75th percentile, and the whiskers show 1.5 times
4070 the interquartile range. Points outside the interquartile range are shown as dots; the FINN
4071 outliers are for years 2008 and 2012.

4072

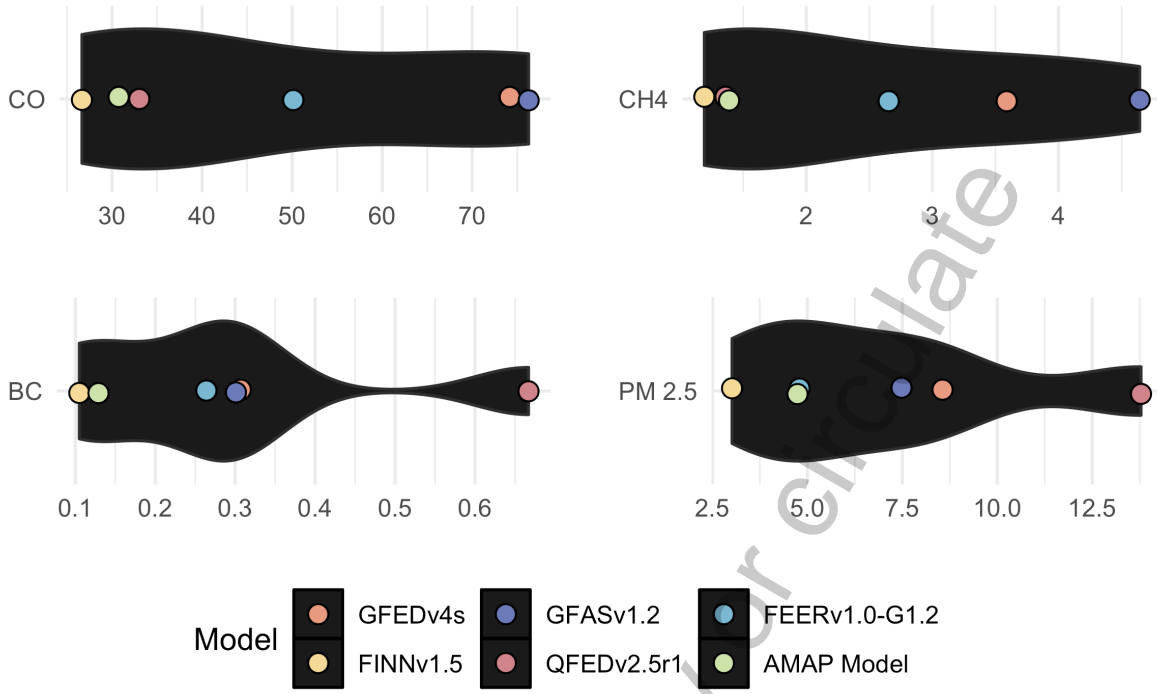

Supplementary Figure 3. Density plot of the 2018 annual emissions (Tg) for CH_4, CO, BC, and $PM_{2.5}$ from six satellite-based global biomass burning emission models: GFED v.4s, GFAS v1.2, FEER v1.0-G1.2, FINN v1.5, and a custom AMAP SLCF model produced by chapter co-authors McCarty and Fain (2020) for 45° to 80° N.

The current satellite-based fire emissions models are not consistent in their ranking of which produces the highest overall emission estimates, particularly when considering emissions from CH_4, CO, and $PM_{2.5}$ (Supplementary Figure 3). Fire emission calculations are not linear calculations and thus we expect to see these differences. Consistently, FINN is the model with the lowest emission estimates.

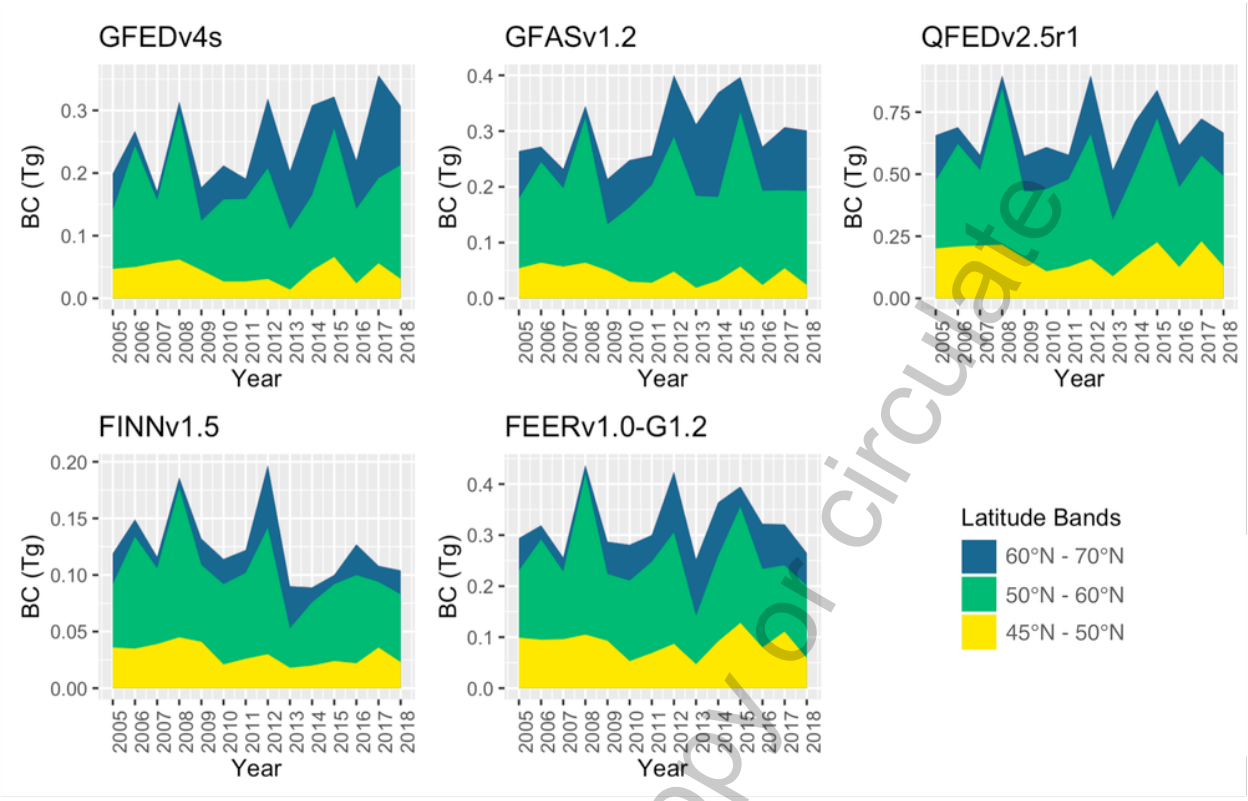

4085

4086 **Supplementary Figure 4.** Area plots of annual BC emissions in teragrams (Tg) from five
4087 global fire emissions models split by latitude ranges, 2005 - 2018; note each latitude break is
4088 a cumulative sum and each panel has different y-axis.

4. Advances in measurement techniques and observational capacity

(note – this draft is a compilation of files located in the assessment C4 google drive)

Policy-relevant science question:

- Are the current monitoring activities (of atmospheric concentrations) sufficient to capture anticipated source changes?
- Why do we need long-term observations?

4.0 Introduction

(Julia et al.) : Why do we need long-term observations? … Is the current network sufficient to be representative…

4.1 Particulate matter

(Kondo et al.)

4.1.1 BC in the atmosphere

(Kondo and Koike; Last revised on April 7, 2020)

This section provides an overview of methods used to measure mass concentration of BC. Accurate measurements of BC are crucial for understanding of behaviors of BC, assessing and improving emission inventories and transport models, and mitigation strategies designed to reduce the warming of the Arctic. Development and assessment of BC measurements need to be made not only for the Arctic but from viewpoint of global BC studies.

4.1.1.1 BC measurements using SP2

Size distribution of BC have been measured by single particle soot photometer (SP2), based on the laser induced incandescence (LII) technique with a typical accuracy of about 10%. More details of SP2 are given in section 4.1.1.2. SP2 is regarded to have a number of advantages over other techniques (Bond et al., 2013). 1) It is not influenced by the mixing state of BC. 2) It is not influenced by non-BC particles. 3) Calibration standard is well established. 4) By integrating size distributions, total mass concentrations of BC (M_{BC}) can be

derived accurately. Considering these advantages, SP2 is recognized as the most reliable in measuring BC mass concentrations. SP2 instruments have been used for ground based, ship-borne, and airborne measurements. These measurements were made mainly on a campaign basis due to a difficulty in the maintenance of the system.

In addition to mass of individual BC particles, SP2 can provide information on the mixing state of BC, namely coating thickness and way of internal mixing (coating or attached).

4.1.1.2 Measurements of BC by instruments other than SP2

Most autonomous and continuous measurements of BC mass concentrations in ambient air (M_{BC}) have been made by filter- based optical technique (AMAP 2015). At many locations, particle soot absorption photometer (PSAP; Radiance Research, Seattle, WA, USA), Aethalometer (Magee Scientific, Berkeley, CA, USA) and multi-angle absorption photometer (MAAP; Thermo ESM Andersen Instruments, Erlangen, Germany) (Petzold and Schönlinner, 2004) have been used. However, the accuracies of the MBC values derived from these measurements have not been critically evaluated in the Arctic. There are two major uncertainties in these filter-based absorption techniques that are caused by non-BC aerosol compounds.

First, absorption coefficients b_{abs} (m^{-1}) must be derived from measured attenuation (absorption and scattering) of light by subtracting the scattering contributions from non-BC aerosols in the filter medium based on the empirical relationship using independent measurements of aerosol scattering coefficients (b_{scat}). For MAAP, measuring reflectance at two angles as well as transmittance with which radiative transfer is solved across the filter, insensitivity to the co-existing light-scattering particles has been evaluated (Petzold and Schönlinner, 2004).

Second, M_{BC} (g m^{-3}) is derived as $M_{BC} = b_{abs}$ /MAC, where MAC (m^2 g^{-1}) is the mass absorption cross section of BC. The MAC value is affected by non-BC aerosol compounds coating the BC particles, which produce a lensing effect. Previous studies have

recommended a wide range of MAC values (10 – 29 m^2 g^{-1}) for individual locations and seasons (Eleftheriadis et al., 2009; Hirdman et al., 2010; Sharma et al., 2006).

The COSMOS instrument was designed to overcome these deficits of the previous filter-based optical technique (Kondo et al., 2011). It uses a heated inlet to evaporate major fractions of non-BC aerosol components in the incoming air sample. As a result, one does not need to subtract a scattering contribution of non-BC particles and can use a constant MAC value of about 10 m^2 g^{-1}, which depends only (and slightly) on the size distribution of bare BC particles. In fact, an agreement within 10% was found between COSMOS and SP2 measurements at Ny-Ålesund and Asia (Ohata et al., 2019), indicating that COSMOS is traceable to SP2.

In general, M_{BC} (PSAP) was highly correlated with M_{BC} (COSMOS) at Barrow, Ny-Ålesund, and Alert (Sinha et al., 2017; Sharma et al., in preparation) and M_{BC} (MAAP) at Pallas in Finland (Hyvärinen et al., in preparation). Rescaling of the M_{BC} (PSAP) and M_{BC} (MAAP) data by M_{BC} (COSMOS) is possible at these sites. However, some cautions are needed in this scaling procedures. Correlations between M_{BC} (COSMOS) and M_{BC} (PSAP) have not been evaluated in regions outside the Arctic. Second, individual b_{abs} for PSAP, Aethalometer, and MAAP instruments are not fully calibrated (WMO/GAW, 2016), whereas b_{abs} for each COSMOS is calibrated using atmospheric BC particles (Kondo et al., 2011). Therefore, it is desirable to determine MAC of PSAP, Aethalometer, and MAAP by comparison of COSMOS.

M_{BC}, so called EC, were measured also by the thermal-optical transmittance (TOT) methods in the Arctic (Sharma et al., 2017; Sinha et al., 2017). Further comparisons with other techniques such as SP2 and COSMOS will provide improved estimates of the accuracy of this method.

4.1.2. Measurement method of BC in snow/ice and rain

(Kondo and Koike (Last revised: April 8, 2020)

Because BC in snowpack lowers their albedo and potentially accelerates ice-albedo feedback, accurate measurements are crucial for understanding of evaluation of their

impacts and improving transport models. As described in section 4.1, currently most reliable measurement technique of atmospheric BC is SP2. Progresses have been made on the use of SP2 for measurements of BC in snowpack and precipitation since the last AMAP report.

4.1.2.1 Measurements of BC by instruments other than SP2

Mass concentrations of BC in snow (C_{MBC}) in Arctic regions have been measured mainly by the Integrating Sphere/Integrating Sandwich spectrometer (ISSW) method (AMAP 2015: Doherty et al., 2010). In this method, C_{MBC} measured by ISSW is estimated from spectrally resolved measurements of the absorption coefficient of solid particles collected on a filter, by assuming a unitary absorption Ångstrom exponent for BC and associating most long-wavelength (650–700 nm) absorption to BC. However, these techniques have large measurement uncertainties attributed mainly to interference from co-existing non-BC solid particles, such as mineral dust, and filter undercatch (Doherty et al., 2010, 2016; Schwarz et al., 2012).

C_{MBC} has also been measured by the thermal-optical transmittance (TOT) method (Aamaas et al., 2011; Forsström et al., 2009, 2013). Lim et al. (2014) reported both overestimations and underestimations of C_{MBC} measured by the TOT method, depending on the sample origin.

4.1.2.2 Measurements of BC by SP2

Recent studies have shown that the size distributions of BC in snow and rain water can be measured accurately by a single-particle soot photometer (SP2) based on a laser-induced incandescence technique, combined with a nebulizer (Jaobi et al., 2019; Kaspari et al., 2011; Lim et al., 2014; Macdonald et al., 2017; McConnell et al., 2007; Mori et al., 2016, 2019; Sinha et al., 2018; Wendl et al., 2014).

Melted snow samples are injected into a concentric pneumatic nebulizer to generate airborne BC particles, which are introduced into an SP2 for the detection of BC. The detectable mass equivalent diameter of BC is typically 70-600 nm (Lim et al., 2014). The

upper limit of detectable BC size has been expanded to about 4170 nm and the overall accuracy of the measured BC concentrations in water was estimated to be about 16% (Mori et al., 2016). BC size distributions in snow samples obtained in the Arctic have been shown to be stable for 10-42 months after they were melted and stored in glass bottles at about 4°C. This indicates that BC losses due to adhesion on the inner walls of the glass bottles are small.

C_{MBC} measured by ISSW from Alaska, Greenland, and Ny-Ålesund are higher than those measured by SP2 by a factor of 13 (Mori et al., 2019), suggesting that these values were significantly overestimated, although the two studies differ in their sampling locations and dates, consistent with laboratory measurements (Schwarz et al., 2012). The magnitude of the discrepancy revealed in this study indicates that the SP2 should be preferred for measuring BC in snowpack.

4.2 Mineral dust

(Outi, Antti et al.)

4.2.1 Single-particle measurement of FeO_x

(Kondo and Koike; Last revised on April 8, 2020)

The laser-induced incandescence (LII) method utilizes incandescent light from strongly light-absorbing and refractory particles passing through the laser beam, such as refractory BC, silicon, nickel, and tungsten. The single-particle soot photometer (SP2) is an instrument implementing LII technique with an intracavity Nd:YAG laser (λ = 1064 nm). Among incandescent particles, BC has been shown to be generally the most numerous in the atmosphere. Thus, the SP2 has been used for the measurement of BC. Moreover, because the SP2 detects individual particles in real-time, it can be used for rapid real-time measurements of BC mass and mixing state (Schwarz et al., 2015).

However, iron oxide (FeO_x) is also refractory, and some species, such as magnetite and hematite, are strong light-absorbers. Recent studies have demonstrated that the LII technique can be used to measure light-absorbing iron oxide particles quantitatively (Moteki et al., 2017; Yoshida et al., 2016, 2020). Detailed analyses of the light signals obtained by the LII have shown that individual light-absorbing iron oxide particles can be identified and quantified. LII signals can be used to distinguish iron oxide particles arising either from natural or anthropogenic sources. An evaluation of the mixing state of iron oxide particles is also possible.

The LII technique have important advantages over the filtration technique for FeO_x measurements. 1) Time resolutions for number and mass concentration are greatly improved. 2) Size distributions can be obtained. The fundamental limitation of the LII technique compared with filtration techniques is difficulty of unambiguous chemical speciation of ambient FeO_x. In smaller particle size, FeO_x incandescence efficiency may decrease from ~100% in a way depending on the operating laser power and FeO_x composition. In particle size larger than ~1000 nm, FeO_x measurement by LII technique will be primarily limited by the size dependent transmission efficiency of FeO_x particles thorough the aerosol sampling system. Depending on the purpose, a complemental use of the LII technique and filtration techniques is recommended for ambient FeO_x observations.

4.3 Ozone

4.3.1 Introduction

This section discusses different measurements of ozone and its precursors, in particular NOx, CO and VOCs including in-situ techniques used to make observations at the surface and vertical profiles using airborne platforms and sondes. Remote sensing measurements by lidar and from satellite are also discussed. Methane is a key precursor for tropospheric ozone, via its oxidation in the presence of sufficient. Anthropogenic CH4 emissions have been estimated to be responsible for around half of pre-industrial to present-day O3 radiative forcing (Stevenson et al. 2013). The current status of observational capacity to

provide adequate information about the distribution of ozone and its precursors, and changes in ozone concentrations (trends) and budgets is also addressed.

Radiative properties (to be moved to Report Introduction): Ozone radiative forcing in the Arctic is highly sensitive to the altitude at which ozone produced from a particular emission source or region perturbs the O3 profile. Different sources/regions will contribute different magnitudes at different altitudes to ozone abundances and forcing (Wespes et al., 2012; Monks et al., 2015). Radiative forcing responses to emission perturbations in different regions are dependent on source attribution (i.e. how much mid-latitude emission reaches the Arctic or is produced from a local Arctic emission) as well as photochemical O3 production sensitivities to emissions from different regions. Forcing due to changes in Arctic surface O3 may be most sensitive to European or local sources, whereas emissions from North American and Asian sources are more important in the mid- and upper troposphere (Monks et al., 2015; Wespes et al., 2012).. The presence of temperature inversions in the Arctic lower troposphere may result in negative local forcing (Rap et al., 2015), in particular for local sources such as shipping (Marelle et al., 2018). Based on parameterised source-receptor sensitivities for a range of CMIP6 SSP scenarios, Turnock et al. (2019) illustrated the significant contribution of methane to future O3 concentration reductions globally (including the high latitudes) and global radiative forcing (see Fig. X).

4.3.2 Measurement techniques

4.3.2.1 In-situ ozone and precursors: surface data

Surface O3 is generally measured using optical methods, where air samples are continuously drawn through a UV-lamp chamber, where it is measured by UV absorption at 254 nm. The stability of the instruments is ensured by addition of known concentrations of ozone from an internal ozone generator traceable to a primary standard. The uncertainty of the UV is within 7 % on a 95% confident interval following EN 14625 standard (e.g. Skov et al. 2020). Lately, the absorption cross section of O3 has been evaluated and most likely the absorption cross section will be decreased by 1.23% leading to higher O3 concentrations (Tarasick et al., 2019 and references in there). The UV absorption instruments are robust and provide

accurate measurements with only minor interferences from other compounds (e.g. Ollison et al. 2013). Other types of instruments are less frequently used in the Arctic. In the past, the chemiluminescence of O3 with methylene has been used. Differential Optical absorption spectroscopy (DOAS) is also used in the Arctic. It uses an open pass of typically of a few kilometers path length and Xe lamp as light source (e.g. Lorenzen-Schmidt et al. 1998).

Ozone precursors:

In the Arctic, NOx and NMVOC concentrations are generally low, posing additional difficulties compared to more southerly latitudes, where pollution levels are higher. NOx is most often measured with monitors using chemiluminescence. Sample air is split into two sub-streams, where the first leads directly to the analytical chamber where NO is detected by the chemiluminescence reaction of NO with O3. The other sample stream passes over a catalyst (e.g. gold) where NO2 is reduced to NO and followed by the detection of the sum of NO and NO2 (NOx). The catalysts are not specific for NO2 but reduces also PAN, N2O5, HOONO2 and other reactive nitrogen species (e.g. Skov et al. 1996). Instruments are available that can measure with low interference from other compounds e.g. NOx monitors using a photolytical converter, DOAS, cavity ring down, Cavity Attenuated Phase Shift (e.g. Kebabian et al. (2005). CO has been measured by NOAA at Alert, Barrow and Ny Ålesund by grap sampling approximate once a week in 1989, 1992 and 1994 onwards (www. esrl.noaa.gov). Online technologies for CO measurement are available today e.g. FTIR using a white cell, cavity ring down techniques or on-line gas chromatography (www. ebas.nilu.no). Gautrois et al. (2003) reported long-term VOC concentrations for Alert, where a 7 year time-series of VOC mixing ratios was determined using off-line techniques (GC-MS) and with a time resolution of 9 days. A few campaigns at specific stations focused on measurements with high time resolution of VOCs (Gao et al., 2012; Hornbrook et. al, 2016; Mungall et al., 2017; Mungall et al., 2018) and shipborne measurements (Sjosted et al., 2012). Lately, oxidized and aromatic VOCs were measured with high time resolution (April 2018 to October 2018) (Pernov et al. 2020) using Proton Transfer Reaction Time of Flight Mass Spectrometer.

4.3.2.2 Vertical profiles (ozonesondes, lidar, aircraft)

Ozone soundings provide a long-term record of Arctic O3 through the depth of the troposphere. Since 1990 regular soundings for longer time periods (years) are available from ~10 stations north of 60ºN. The measurements are mainly conducted using the balloon-borne Electrochemical Concentration Cell (ECC) ozonesonde, reaching an altitude of about 30 km. Biases in tropospheric measurements are reported to be 1.0±4.4% in the lower troposphere and 5.3±4.4% in the upper troposphere (Tarasick et al., 2019).
Tropospheric measurements of ozone using ground-based differential absorption lidar (DIAL) has become available for shorter periods in the Arctic, e.g. at Eureka (Seabrook and Whiteway,2016). DIAL measurements offer temporal resolution down to minutes and vertical resolution comparable to ozonesonde measurements depending on operation setup. Precision and bias in tropospheric measurements are reported to be better than 10% and 1±8% respectively (Tarasick et al., 2019).
Similar techniques as used in ground based monitoring are also deployed on aircraft based observation platforms. Since AMAP (2015) additional observation campaigns with aircraft data in the Arctic are available including the campaigns AToM (Brune et al., 2019) and PAMARCMIP 2018 (ref?).

4.3.2.3 Satellite data

An increasing number of space-borne sensors retrieve tropospheric trace-gas distributions, offering regular, continuous coverage in poorly observed regions, such as the Arctic. Polar orbiting and sun-synchronous orbiting satellites give global coverage with regular overpass times. Many instruments have accumulated long-term multiannual datasets with which to assess inter-annual variability and trends in tropospheric composition. Tropospheric ozone column amounts and some profile information are available from sensors in the ultra-violet (UV)/visible (GOME-1, GOME-2, OMI) and infra-red (IR) (TES) wavelength ranges. Limb sounders such as the IR AIRS and TES instruments and MLS microwave instrument offer improved vertical profile resolution at the expense of spatial coverage and horizontal resolution (Pittman et al., 2009). In addition, satellite sensors retrieve information on ozone precursor species and oxidants, including NO2, CO, CH4 and BrO. The recently launched TROPOMI instrument allows broad spectral retrieval across UV, visible and infra-red wavelengths, allowing measurement of a range of pollutants (NO2, O3, HCHO, methane,

CO) with a spatial resolution of less than 7km. Profiles of PAN have been retrieved from the MIPAS and TES IR instruments (Pope et al., 2016; Zhu et al., 2015), and the ACE FTIR instrument provides information on a wide range of species (see model evaluation in Chapter XX) in the upper troposphere (UT) region.

Despite the potential for extensive Arctic data coverage from satellite sensors, there are challenges in the reliable use of satellite observations to inform our understanding of tropospheric ozone and precursor distributions at high latitudes. Vertical sensitivity is limited, and varies according to environmental factors, meaning that fully resolving vertical profiles and layers of different composition and source influence is difficult. At Arctic latitudes, the sampled altitude range of limb instruments can often be within the lower stratosphere, limiting information available on tropospheric ozone and precursors. UV / visible wavelength instruments are unable to retrieve data in darkness, negating their use during polar winter. Retrievals may also have limited reliability at high latitudes, due to problems with lower surface-atmosphere thermal contrast for IR retrievals (Clerbaux et al., 22009), extensive Arctic cloud cover, and high surface albedo. Finally, a paucity of in-situ observations for satellite data evaluation may lead to poor confidence in retrieved abundances in the Arctic troposphere, and make it difficult to assess the impacts of instrument drift and inter-comparability between satellite platforms for the region (for example between different ozone sensors).

4.3.3 Recommendations

- Only a very limited number of stations provide long-term monitoring of surface ozone and related precursors/oxidants, and in many cases records are not continuous and large data gaps exist, especially in the eastern Arctic, Arctic Ocean and terrestrial locations. In particular, measurements of CO, NOx, VOCs, PAN and halogenated species are needed to allow better source characterization especially in a changing Arctic where local emission sources are increasing. Long-term monitoring of atmospheric composition at existing stations is essential for accurate determination of trends and needs to be continued and integrated into a Pan-Arctic observation network, building e.g. on IASOA and WMO GAW. Opportunities exist to make continuous measurements on commercial shipping.

- Sites collecting vertical ozone profiles using ozonesondes/lidar are limited and in many cases, records are not continuous. There is still a lack of vertical ozone measurements in the eastern part of the Arctic. The development of new techniques provides additional opportunities for regular monitoring (e.g., tethered balloons, unmanned aerial vehicles, measurements on commercial aircraft). Airborne campaigns provide detailed vertical information about Arctic chemical composition, origins and processes. However, very few campaigns have focused on ozone since AMAP 2015.
- Satellite data can provide spatial information about ozone and certain precursors/oxidants, and some limited vertical information, but more attention is needed to improve retrievals, understand biases and instrument limitations at high latitudes.

4.4 Methane

(Frans-Jan, Lise Lotte et al.)

4.5 Cloud properties from satellite observations

(Abhay Devasthale, Manu Anna Thomas, Joakim Langner, Makoto Koike, Yutaka Kondo et al.)

4.5.1 Introduction

The impact of clouds on the Arctic climate is multifaceted (Kay et al., 2016). Clouds exercise radiative and dynamical control on the Arctic environment and also interact with other components of the Arctic climate system. The importance of monitoring clouds and evaluating them in the chemistry transport and climate models in the context of AMAP can be justified due to the following reasons.

a) Cloud properties and cloud radiative effects respond to the changes in aerosols and their precursor gases. Indirect effects of aerosols on clouds and also aerosol processing by clouds in a pristine Arctic environment is highly sensitive to the changes in concentration and type of cloud condensation or ice nuclei (CN) (Garrett and Zhao, 2006; Lubin and Vogelmann, 2006; Mauritsen et al., 2011; Loewe et al., 2017; Lohmann, 2017; Zamora et al., 2017; Eirud

et al., 2019). The availability of CNs is primarily driven by the transport of pollutants from the southerly latitudes when the Arctic Ocean is locked by sea-ice during polar winters, while the CN contribution from the ocean additionally plays a role when the sea-ice melts during polar summers.

b) The net surface radiative impact of clouds in the Arctic is positive (i.e. warming) due to the dominance of longwave warming, except during few summer months (Kay and L'Ecuyer, 2013). This implies that the changes in clouds (and thus the surface longwave warming) could have an impact on seasonal sea-ice evolution in the Arctic Ocean and snow-covered land surfaces, which in turn has an impact on aerosol availability, optics and dynamics. This intrinsic coupling of clouds to the large-scale atmospheric dynamics (primary driver for cloud distribution), local meteorology (e.g. control by temperature and humidity inversions), aerosols (CCN-limited regimes), and other climate components demands that clouds should be monitored along with other climate variables in the context of AMAP.

c) Through liquid and ice precipitation processes, clouds influence wet deposition of pollutants in the Arctic (Yamagata et al., 2009).

4.5.2 Available suite of satellite based cloud climate data records

Monitoring clouds in the Arctic using the network of in-situ measurement stations or from the dedicated campaign measurements is challenging due to harsh environmental conditions and due to the fact that the central Arctic consists of ocean. The space based satellite observations therefore offer a practical and economically viable alternative in this context. An enormous progress has been made in the last decade in improving our understanding of clouds globally, including in the Arctic, from the space based observations. The polar orbiting meteorological satellites carrying passive imaging sensors that are capable of providing cloud description have been flying since 1978. These primarily NOAA and EUMETSAT satellites have flown the Advanced Very High Resolution Radiometer (AVHRR) instrument onboard, the data from which are currently available for nearly four decades. This has led to the compilation of several global cloud climate data records (CDRs).

Here, the Arctic cloud properties from the four longest CDRs are presented. The climatological averages are obtained over the 35-year period from 1982 to 2016. The first CDR investigated is the most recent version from the pioneering International Satellite Cloud Climatology Project (ISCCP-HGM, Young et al., 2018). The second CDR is the second edition of EUMETSATs Climate Monitoring Satellite Application Facility (CM SAF) Cloud, Albedo and surface Radiation dataset from AVHRR data (CLARA-A2, Karlsson et al., 2017). The third CDR is from the NOAAs Pathfinder Atmosphere Extended Program (PATMOS-x, Heidinger et al., 2014). The fourth CDR is from the framework of the European Space Agency (ESA) Climate Change Initiative (CCI) program (Stengel et al., 2017). It is to be noted that CLARA-A2, Cloud-CCI and PATMOS-x are AVHRR-based CDRs and employ the same AVHRR (inter)calibration. However, they differ in their cloud property retrieval approach. The active lidar and radar sensors onboard CALIPSO and CloudSat satellites, which are a part of the NASA's A-Train constellation, have proven instrumental in training, evaluating and improving these CDRs in the last decade. These active sensors have revolutionized our views of clouds globally. However, the data records from the active sensors are still not long enough to provide a climatological perspective. The strengths and limitations of the four CDRs and their retrieval approaches are documented in the respective publications (Heidinger et al., 2014; Karlsson et al., 2017; Stengel et al., 2017; Young et al., 2018) and their global intercomparison is documented in Karlsson and Devasthale (2018). Note that the uncertainties and differences in the retrievals of cloud microphysical properties, including liquid and ice water paths, among these CDRs which are based on passive sensors are high in the central Arctic, limiting the quantitative climate quality comparisons.

4.5.2.1 Climatological overview of cloud amount and cloud top pressure

The large-scale atmospheric circulation patterns primarily govern the spatial distribution and variability of clouds in the Arctic (Cesana et al., 2012; Kay et al., 2016; Lenaerts et al., 2017; Devasthale et al., 2020). The transport of heat and moisture in to the Arctic occurs mainly from the Atlantic and pacific sectors, bringing about changes in the thermodynamical conditions that influence cloud processes over the ocean areas. This transport often favours high cloudiness throughout the year over the Atlantic and Pacific sectors, as visible in the

climatological distribution of cloud fraction in all four CDRs (Fig. 4.1). The cloudiness in the parts of Greenland and Norwegian Seas is about 80-90% in annual average. The persistent cloudiness is also usually observed over the Barents and Kara Seas. The Canadian Archipelago and Beaufort Sea, on the other hand, show the lowest cloudiness, which is also represented in all four CDRs. Over the Central Arctic (north of 70N), the local thermodynamical conditions (e.g. temperature and humidity inversions) govern cloudiness. The cloudiness there is generally in the order of 60-70%. However, the areas that have highly reflective and cold surfaces (e.g. permanently sea covered parts of the Arctic Ocean, Greenland, parts of Siberia etc) present challenge while detecting clouds from the passive sensors and thus the CDRs have largest uncertainties and differences in cloudiness over these areas.

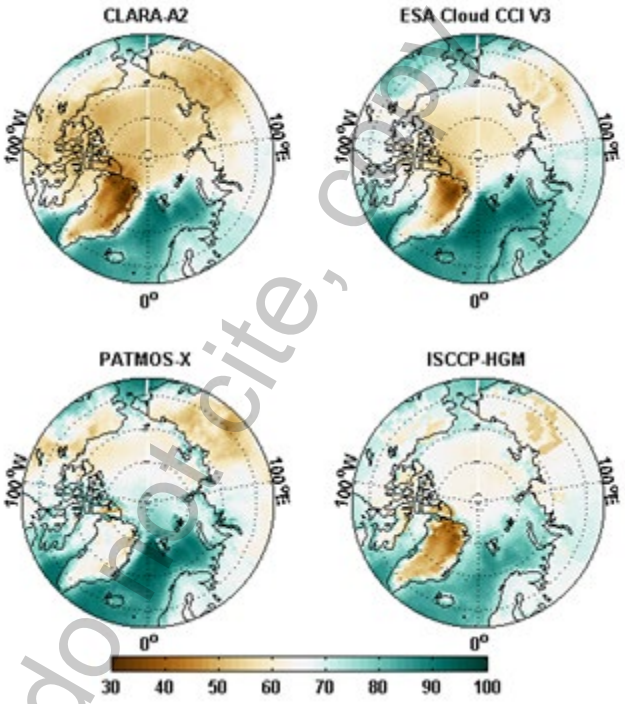

Fig. 4.1 Climatological mean total cloud fraction (in %) from the four satellite based CDRs.

One of the dominant meteorological phenomena in the Arctic is temperature inversion (Bradley et al., 1992; Serreze et al., 1992; Kahl et al., 1996; Devasthale et al., 2010). Inversions are persistent in all seasons, including in the summer, and exert control on the cloud top properties (Sedlar and Tjernström, 2009; Sedlar et al., 2012; Shupe et al., 2013). The majority of clouds in the Arctic are low level stratus and stratocumulus, often capped by inversions as the boundary layer height, cloud top entrainment and vertical mixing are

limited by these inversions. Over the ice-free parts of the oceans, all four CDRs broadly agree with one another and show cloud top pressures larger than 700 hPa in the regions dominated by the stratus and stratocumulus clouds (Fig. 4.2). Over the ice-covered regions, however, the differences among the four CDRs are larger. The cloud top heights (pressures) in PATMOS-x and ISCCP CDRs are clearly higher (lower) compared to the other two CDRs. This is due to many reasons. For example, the fraction of high clouds is higher in PATMOS-x and ISCCP as the separability between the cold surfaces and cloud tops as well as cloud typing in the retrieval algorithms is different over the ice-covered regions. The handling of the cold surface temperatures and the reliance and the usage of atmospheric temperature profiles from the reanalyses is also different among these CDRs. The evaluation of CDRs using active sensors shows that the passive retrievals in general overestimate cloud top heights in the Arctic. In the lower troposphere, the presence of near isothermal vertical structure often poses a challenge which assigning accurate cloud top heights in the retrievals.

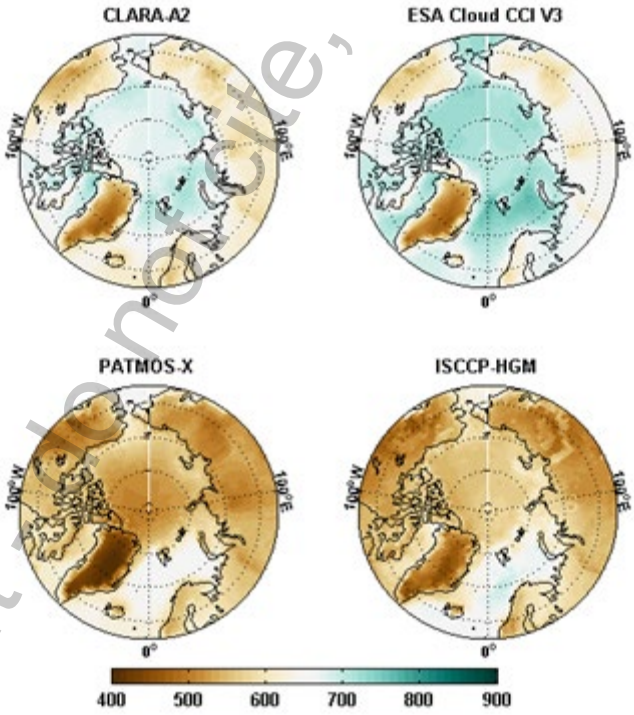

Fig. 4.2 Climatological mean cloud top pressure (in hPa) from the four CDRs.

4.5.2.2 Cloud radiative effects

The seasonality in incoming solar radiation primarily drives the seasonality in cloud radiative effects in the Arctic. As the optically thick low clouds are dominant over the ocean areas, their high reflection of insolation over otherwise optically black ocean areas results into the net cooling effect at the surface during the summer months, when the sea-ice is also retreating towards the seasonal minimum in September. In the absence of insolation, the longwave radiative effects dominate (Curry et al., 1996; Walsh and Chapman, 1998; Shupe and Intrieri, 2004; Wang and Key, 2005; Kay and L'Ecuyer, 2013; Kay et al., 2016, Lenaerts et a., 2017). The optically thick clouds capped by stronger inversions absorb and reradiate longwave radiation to the surface, thus exerting positive CRE at the surface during the majority of the year (Fig. 4.3).

The monthly spatial distribution of net CREs at the surface (Fig. 4.4) shows that over the permanently ice covered ocean areas and Greenland, the CREs remain positive throughout the year. Over the marginal sea-ice zones and open water northward of 60N, net CREs at the surface are follow seasonality in the insolation. The estimates of CREs constrained by the active CALIOP and CPR/CloudSat sensors show that the clouds only over the ocean areas in the Arctic warm the surface by 10 W/m2 in annual average and cool the top of the atmosphere (TOA) by -12 W/m2 (Kay and L'Ecuyer, 2013).

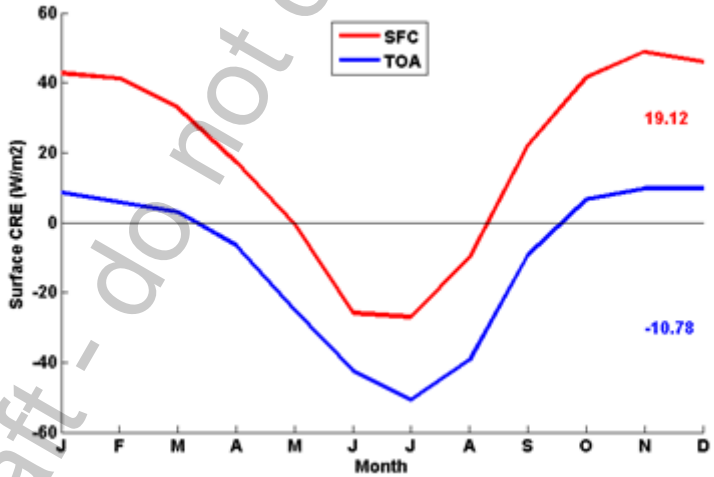

Fig. 4.3 Monthly CREs at the surface and top of the atmosphere over the Arctic (60N-90N). The numbers show annual average of CRE at the TOA and the surface. The results are based on 15 years of data (2003-2017) from the NASA's CERES instrument onboard Aqua satellite.

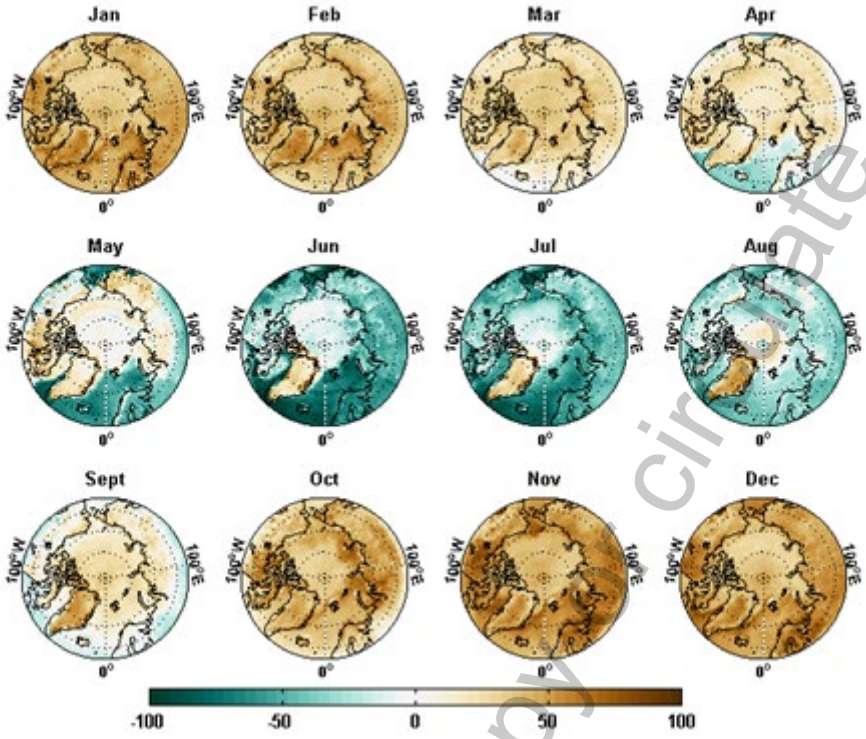

Fig. 4.4: Climatological spatial distribution of CREs at the surface. The results are based on 15 years of data (2003-2017) from the NASA's CERES instrument onboard Aqua satellite.

4.5.3 In-situ measurements of cloud microphysical properties

Changes in anthropogenic aerosol emissions can affect clouds in the Arctic that play fundamental roles for the Arctic climate. Reductions of Arctic sea ice and ice cover on the land surface can also increase emissions of natural aerosols which affect clouds. In the Arctic, in situ measurements of cloud microphysical properties have been made using the light scattering, imaging, and hot-wire techniques, which have also been used for other parts of the world (Baumgardner et al., 2017; McFarquhar et al., 2017). Although a continuous in situ measurement is a challenge in the Arctic, the first year-round in situ measurements of cloud microphysical properties in the Arctic were made at a mountain site (Koike et al., 2019). More advanced cloud probes have also been developed in recent years, primarily to discriminate between liquid and ice particles as well as to derive information of morphologies of ice particles. Some of them have been used in Arctic researches. They include probes measuring polarization in scattered light (CAS-DPOL, Baumgardner et al.,

2014, Costa et al., 2017), spatial intensity distribution of near-forward scattered light (SID-3 or PPD-HS, Vochezer et al., 2016; Mahrt et al., 2019), polar light scattering function and stereo images (PHIPS-HALO, Abdelmonem et al., 2011; Schnaiter et al., 2018), holographic images (HOLODEC or HOLIMO II, Fugal and Shaw, 2009; Henneberger et al., 2013), and interferometric laser image (ILIDS, Porcheron et al., 2015).

In addition to in situ measurements, vertical profiles of cloud microphysical properties were estimated using combined measurements of 94 GHz cloud radar, ceilometer, and microwave radiometer using Cloudnet algorithm (Nomokonova et al., 2019). The ground-based remote sensing is a powerful tool also for validating satellite measurements over the Arctic.

In the Arctic, in situ measurements of cloud microphysical properties have been made using the light scattering, imaging, and hot-wire techniques, which have also been used for other parts of the world (Baumgardner et al., 2017; McFarquhar et al., 2017). Although a continuous in situ measurement is a challenge in the Arctic, the first year-round in situ measurements of cloud microphysical properties in the Arctic were made at a mountain site (Koike et al., 2019). More advanced cloud probes have also been developed in recent years, primarily to discriminate between liquid and ice particles as well as to derive information of morphologies of ice particles. Some of them have been used in Arctic researches. They include probes measuring polarization in scattered light (CAS-DPOL, Baumgardner et al., 2014, Costa et al., 2017), spatial intensity distribution of near-forward scattered light (SID-3 or PPD-HS, Vochezer et al., 2016; Mahrt et al., 2019), polar light scattering function and stereo images (PHIPS-HALO, Abdelmonem et al., 2011; Schnaiter et al., 2018), holographic images (HOLODEC or HOLIMO II, Fugal and Shaw, 2009; Henneberger et al., 2013), and interferometric laser image (ILIDS, Porcheron et al., 2015).

In addition to in situ measurements, vertical profiles of cloud microphysical properties were estimated using combined measurements of 94 GHz cloud radar, ceilometer, and microwave radiometer using Cloudnet algorithm (Nomokonova et al., 2019). The ground-based remote sensing is a powerful tool also for validating satellite measurements over the Arctic.

4.6 Recommendations

References

Section 4.1.1 (BC in atmosphere)

Bond T. C., et al. (2013), Bounding the role of black carbon in the climate system: A scientific assessment, J. Geophys. Res., 118, 5380–5552, doi:10.1002/jgrd.50171.

Eleftheriadis, K., S. Vratolis, and S. Nyeki (2009), Aerosol black carbon in the European Arctic: Measurements at Zeppelin station, Ny-Ålesund, Svalbard from 1998–2007, Geophys. Res. Lett., 36, L02809, 5, doi:10.1029/2008GL035741.

Hirdman D., H. Sodemann, S. Eckhardt, J. F. Burkhart, A. Jefferson, T. Mefford, P. K. Quinn, S. Sharma, J. Ström, and A. Stohl (2010), Source identification of short-lived air pollutants in the Arctic using statistical analysis of measurement data and particle dispersion model output, Atmos. Chem. Phys., 10, 669–693.

Kondo, Y., L. Sahu, N. Moteki, F. Khan, N. Takegawa, X. Liu, M. Koike, T. Miyakawa (2011), Consistency and traceability of black carbon measurements made by laser-induced incandescence, thermal-optical transmittance, and filter-based photo-absorption techniques, Aerosol Sci. Tech., 45, 295-312, DOI: 10.1080/02786826.2010.533215.

Ohata, S., Y. Kondo, N. Moteki, T. Mori, A. Yoshida, P. R. Sinha, and M. Koike (2019), Accuracy of black carbon measurements by a filter-based absorption photometer with a heated inlet, Aerosol Sci. Technol., doi: 10.1080/02786826.2019.1627283.

Petzold, A. and M. Schönlinner (2004), Multi-angle absorption photometry—a new method for the measurement of aerosol light absorption and atmospheric black carbon, J. Aerosol. Sci., 35, 421-441.

Sinha, P. R., Y. Kondo, M. Koike, J. Ogren, A. Jefferson, T. Barrett, R. Sheesley, S. Ohata, N. Moteki, H. Coe, D. Liu, M. Irwin, P. Tunved, P. K. Quinn, and Y. Zhao (2017), Evaluation of ground-based black carbon measurements by filter-based photometers at two Arctic sites, J. Geophys. Res., 122, doi:10.1002/2016JJD025843.

Sharma, S., E. Andrews, L. A. Barrie, J. A. Ogren, and D. Lavoué (2006), Variations and sources of the equivalent black carbon in the high Arctic revealed by long-term

observations at Alert and Barrow: 1989-2003, J. Geophys. Res., 111 (D14208). doi:10.1029/2005JD006581.

WMO/GAW Aerosol measurement procedures, guidelines and recommendations, 2nd edition, 103, WMO-No. 1177, 2016 (http://library.wmo.int/opac/index.php?lvl=notice_display&id=19622).

Section 4.1.2 (BC in precipitaiton)

Arctic Monitoring and Assessment Programme (AMAP) (2015). AMAP Assessment 2015: Black carbon and ozone as Arctic climate forcers, (p. 116). Oslo, Norway. vii: Arctic Monitoring and Assessment Programme (AMAP). Retrieved from http://www.amap.no/documents/doc/AMAP-Assessment-2015-Black-carbon-andozone-as-Arctic-climate-forcers/1299

Doherty, S. J., Hegg, D. A., Johnson, J. E., Quinn, P. K., Schwarz, J. P., Dang, C., & Warren, S. G. (2016). Causes of variability in light absorption by particles in snow at sites in Idaho and Utah. Journal of Geophysical Research: Atmospheres, 121, 4751–4768. https://doi.org/10.1002/2015JD024375

Doherty, S. J., Warren, S. G., Grenfell, T. C., Clarke, A. D., & Brandt, R. E. (2010). Light-absorbing impurities in Arctic snow. Atmospheric Chemistry and Physics, 10, 11647–11680. https://doi.org/10.5194/acp-10-11647-2010

Jacobi, H.-W., Obleitner, F., Da Costa, S., Ginot, P., Eleftheriadis, K., Aas, W., & Zanatta, M. (2019). Deposition of ionic species and black carbon to the Arctic snowpack: combining snow pit observations with modeling. Atmospheric Chemistry and Physics, 19, 10,361–10,377. https://doi.org/10.5194/acp-19-10361-2019

Kaspari, S., Schwikowski, M., Gysel, M., Flanner, M. G., Kang, S., Hou, S., & Mayewski, P. A. (2011). Recent increase in black carbon concentrations from a Mt. Everest ice core spanning 1860–2000 AD. Geophysical Research Letters, 38(4), L04703. https://doi.org/10.1029/2010GL046096

5584 Katich, J. M., Perring, A. E., & Schwarz, J. P. (2017). Optimized detection of particulates from
5585 liquid samples in the aerosol phase: Focus on black carbon. Aerosol Science and
5586 Technology, 51(5), 543–553. https://doi.org/10.1080/02786826.2017.1280597

5587 Lim, S., Faïn, X., Zanatta, M., Cozic, J., Jaffrezo, J.-L., Ginot, P., & Laj, P. (2014). Refractory
5588 black carbon mass concentrations in snow and ice: Method evaluation and inter-
5589 comparison with elemental carbon measurement. Atmospheric Measurement
5590 Techniques, 7, 3307–3324. https://doi.org/10.5194/amt-7–3307–2014

5591 Macdonald, K. M., Sharma, S., Toom, D., Chivulescu, A., Hanna, S., Bertram, A. K., et al.
5592 (2017). Observations of atmospheric chemical deposition to high Arctic snow.
5593 Atmospheric Chemistry and Physics, 17(9), 5775–5788. https://doi.org/10.5194/acp-17-
5594 5775-2017

5595 McConnell, J. R., Edwards, R., Kok, G. L., Flanner, M. G., Zender, C. S., Saltzman, E. S., et al.
5596 (2007). 20th-century industrial black carbon emissions altered Arctic climate forcing.
5597 Science, 317, 1381–1384. https://doi.org/10.1126/science.1144856

5598 Mori, T., Moteki, N., Ohata, S., Koike, M., Goto-Azuma, K., Miyazaki, Y., & Kondo, Y. (2016).
5599 Improved technique for measuring the size distribution of black carbon particles in liquid
5600 water. Aerosol Science and Technology, 50(3), 242–254.
5601 https://doi.org/10.1080/02786826.2016.1147644

5602 Moteki, N., & Mori, T. (2015). Theoretical analysis of a method to measure size distributions
5603 of solid particles in water by aerosolization. Journal of Aerosol Science, 83, 25–31.
5604 https://doi.org/10.1016/j.jaerosci.2015.02.002

5605 Schwarz, J. P., Doherty, S. J., Li, F., Ruggiero, S. T., Tanner, C. E., Perring, A. E., et al. (2012).
5606 Assessing single particle soot photometer and integrating sphere/integrating sandwich
5607 spectrophotometer measurement techniques for quantifying black carbon concentration
5608 in snow. Atmospheric Measurement Techniques, 5(11), 2581–2592.
5609 https://doi.org/10.5194/amt-5-2581-2012

5610 Sinha, P. R., Kondo, Y., Goto-Azuma, K., Tsukagawa, Y., Fukuda, K., Koike, M., et al. (2018).
5611 Seasonal progression of the deposition of black carbon by snowfall at Ny-Ålesund,
5612 Spitsbergen. Journal of Geophysical Research: Atmospheres, 123, 997–1016.
5613 https://doi.org/10.1002/2017JD028027

Wendl, I. A., Menking, J. A., Färber, R., Gysel, M., Kaspari, S. D., Laborde, M. J. G., & Schwikowski, M. (2014). Optimized method for black carbon analysis in ice and snow using the Single Particle Soot Photometer. Atmospheric Measurement Techniques, 7, 2667–2681. https://doi.org/10.5194/amt-7-2667-2014

Section 4.2.1 (FeOx)

Moteki, N., Adachi, K., Ohata, S., Yoshida, A., Harigaya, T., Koike, M., & Kondo, Y. (2017). Anthropogenic iron oxide aerosols enhance atmospheric heating., Nature Communications, 8, 15329, doi:10.1038/ncomms15329

Schwarz, J. P., Perring, A. E., Markovic, M. Z., Gao, R. S., Ohata, S., Langridge, J., ... & Fahey, D. W. (2015). Technique and theoretical approach for quantifying the hygroscopicity of black-carbon-containing aerosol using a single particle soot photometer. Journal of Aerosol Science, 81, 110-126.

Yoshida, A., Moteki, N., Ohata, S., Mori, T., Tada, R., Dagsson-Waldhauserová, P., & Kondo, Y. (2016). Detection of light-absorbing iron oxide particles using a modified single-particle soot photometer, Aerosol Science and Technology, 50(3), 1–4, doi:10.1080/02786826.2016.1146402

Yoshida, A., N. Moteki, S. Ohata, T. Mori, M. Koike, Y. Kondo, H. Matsui, N. Oshima, A. Takami, and K. Kita (2020), Abundances and microphysical properties of light-absorbing iron oxide and black carbon aerosols over the East Asian and Arctic regions, submitted to J. Geophys. Res.: Atmospheres.

Section 4.3 (ozone)

Ancellet, G., Daskalakis, N., Raut, J. C., Tarasick, D., Hair, J., Quennehen, B., Ravetta, F., Schlager, H., Weinheimer, A. J., Thompson, A. M., Johnson, B., Thomas, J. L., and Law, K. S.: Analysis of the latitudinal variability of tropospheric ozone in the Arctic using the large number of aircraft and ozonesonde observations in early summer 2008, Atmos. Chem. Phys., 16, 13341–13358, https://doi.org/10.5194/acp-16-13341-2016, 2016.

5642 Arnold, S. R., Emmons, L. K., Monks, S. A., Law, K. S., Ridley, D. A., Turquety, S., Tilmes, S.,
5643 Thomas, J. L., Bouarar, I., Flemming, J., Huijnen, V., Mao, J., Duncan, B. N., Steenrod, S.,
5644 Yoshida, Y., Langner, J., and Long, Y., (2015), Biomass burning influence on high-latitude
5645 tropospheric ozone and reactive nitrogen in summer 2008: a multi-model analysis based
5646 on POLMIP simulations, Atmos. Chem. Phys., 15, 6047-6068, doi:10.5194/acp-15-6047-
5647 2015.
5648 Bahramvash Shams, S., Walden, V. P., Petropavlovskikh, I., Tarasick, D., Kivi, R., Oltmans, S.,
5649 Johnson, B., Cullis, P., Sterling, C. W., Thölix, L., and Errera, Q.: Variations in the vertical
5650 profile of ozone at four high-latitude Arctic sites from 2005 to 2017, Atmos. Chem. Phys.,
5651 19, 9733–9751, https://doi.org/10.5194/acp-19-9733-2019, 2019.
5652 Burd, J. A., P. K. Peterson, S. V. Nghiem, D. K. Perovich, and W. R. Simpson, Snowmelt onset
5653 hinders bromine monoxide heterogeneous recycling in the Arctic, J. Geophys. Res.
5654 Atmos., 122, 8297–8309, doi:10.1002/2017JD026906, 2017.
5655 Christiansen, B., Jepsen, N., Kivi, R., Hansen, G., Larsen, N., and Korsholm, U. S.: Trends and
5656 annual cycles in soundings of Arctic tropospheric ozone, Atmos. Chem. Phys., 17, 9347–
5657 9364, https://doi.org/10.5194/acp-17-9347-2017, 2017.
5658 Christian, K. E., Brune, W. H., and Mao, J.: Global sensitivity analysis of the GEOS-Chem
5659 chemical transport model: ozone and hydrogen oxides during ARCTAS (2008), Atmos.
5660 Chem. Phys., 17, 3769–3784, https://doi.org/10.5194/acp-17-3769-2017, 2017.
5661 Clerbaux, C., Boynard, A., Clarisse, L., George, M., Hadji-Lazaro, J., Herbin, H., Hurtmans, D.,
5662 Pommier, M., Razavi, A., Turquety, S., Wespes, C., and Coheur, P.-F.: Monitoring of
5663 atmospheric composition using the thermal infrared IASI/MetOp sounder, At- mos.
5664 Chem. Phys., 9, 6041–6054, doi:10.5194/acp-9-6041-2009, 2009.
5665 Fadnavis, S., Müller, R., Kalita, G., Rowlinson, M., Rap, A., Li, J.-L. F., Gasparini, B., and
5666 Laakso, A.: The impact of recent changes in Asian anthropogenic emissions of SO2 on
5667 sulfate loading in the upper troposphere and lower stratosphere and the associated
5668 radiative changes, Atmos. Chem. Phys., 19, 9989–10008, https://doi.org/10.5194/acp-19-
5669 9989-2019, 2019.
5670 Fiore, A. M., J. J. West, L. W. Horowitz, V. Naik, and M. D. Schwarzkopf (2008),
5671 Characterizing the tropospheric ozone response to methane emission controls and the
5672 benefits to climate and air quality, J. Geophys. Res., 113, D08307,
5673 doi:10.1029/2007JD009162.

Gaudel, A, et al. 2018. Tropospheric Ozone Assessment Report: Present-day distribution and trends of tropospheric ozone relevant to climate and global atmospheric chemistry model evaluation. Elem Sci Anth, 6: 39. DOI: https://www.elementascience.org/articles/10.1525/elementa.291

Herrmann, M., L. Cao, H. Sihler, U. Platt, and E. Gutheil, On the contribution of chemical oscillations to ozone depletion events in the polar spring, Atmos. Chem. Phys., 19, 10161–10190, 2019, https://doi.org/10.5194/acp-19-10161-2019

Huang, Y., Wu, S., Kramer, L. J., Helmig, D., and Honrath, R. E.: Surface ozone and its precursors at Summit, Greenland: comparison between observations and model simulations, Atmos. Chem. Phys., 17, 14661–14674, https://doi.org/10.5194/acp-17-14661-2017, 2017.

Kanaya, Y., Miyazaki, K., Taketani, F., Miyakawa, T., Takashima, H., Komazaki, Y., Pan, X., Kato, S., Sudo, K., Sekiya, T., Inoue, J., Sato, K., and Oshima, K.: Ozone and carbon monoxide observations over open oceans on R/V Mirai from 67◦ S to 75◦ N during 2012 to 2017: testing global chemical reanalysis in terms of Arctic processes, low ozone levels at low latitudes, and pollution transport, Atmos. Chem. Phys., 19, 7233–7254, https://doi.org/10.5194/acp-19-7233-2019, 2019.

Jiang, Z., J. R. Worden, V. H. Payne, L. Zhu, E. Fischer, T. Walker, and D. B. A. Jones (2016), Ozone export from East Asia: The role of PAN, J. Geophys. Res. Atmos., 121, 6555–6563, doi:10.1002/2016JD024952.

Kebabian, P. L., S. C. Herndon and A. Freedman (2005). "Detection of nitrogen dioxide by cavity attenuated phase shift spectroscopy." Analytical Chemistry 77(2): 724-728.

Lorenzen-Schmidt, H., S. Wessel, W. Unold, S. Solberg, H. Gernandt, F. Stordal and U. Platt (1998). "Ozone measurements in the European Arctic during the ARCTOC 1995 campaign." Tellus Series B-Chemical and Physical Meteorology 50(5): 416-429.

Marelle, L., Raut, J.-C., Law, K., & Duclaux, O. (2018). Current and future arctic aerosols and ozone from remote emissions and emerging local sources—Modeled source contributions and radiative effects. Journal of Geophysical Research: Atmospheres, 123, 12,942–12,963. https://doi.org/10.1029/2018JD028863

McNamara, S. M., A. R. W. Raso, S. Y. Wang, S. Thanekar, E. J. Boone, K. R. Kolesar, P. K. Peterson, W. R. Simpson, J. D. Fuentes, P. B. Shepson and K. A. Pratt (2019). "Springtime

Nitrogen Oxide-Influenced Chlorine Chemistry in the Coastal Arctic." Environmental Science & Technology 53(14): 8057-8067.

Mills G, Pleijel H, Malley CS, Sinha B, Cooper OR, Schultz MG, Neufeld HS, Simpson D, Sharps K, Feng Z, Gerosa G, Harmens H, Kobayashi K, Saxena P, Paoletti E, Sinha V, Xu X, Tropospheric Ozone Assessment Report: Present-day tropospheric ozone distribution and trends relevant to vegetation. Elem Sci Anth. 2018;6(1):47. DOI: http://doi.org/10.1525/elementa.302

Monks, S. A., Arnold, S. R., Emmons, L. K., Law, K. S., Turquety, S., Duncan, B. N., Flemming, J., Huijnen, V., Tilmes, S., Langner, J., Mao, J., Long, Y., Thomas, J. L., Steenrod, S. D., Raut, J. C., Wilson, C., Chipperfield, M. P., Diskin, G. S., Weinheimer, A., Schlager, H., and Ancellet, G., (2015), Multi-model study of chemical and physical controls on transport of anthropogenic and biomass burning pollution to the Arctic, Atmos. Chem. Phys., 15, 3575-3603, doi:10.5194/acp-15-3575-2015.

Mungall, E. L., Abbatt, J. P. D., Wentzell, J. J. B., Wentworth, G. R., Murphy, J. G., Kunkel, D., Gute, E., Tarasick, D. W., Sharma, S., Cox, C. J., Uttal, T., and Liggio, J.: High gas-phase mixing ratios of formic and acetic acid in the High Arctic, Atmos. Chem. Phys., 18, 10237–10254, https://doi.org/10.5194/acp-18-10237-2018, 2018.

Peterson, P. K., K. A. Pratt, W. R. Simpson, S. V. Nghiem, L. X. P. Perez, E. J. Boone, D. Pohler, J. Zielcke, S. General, P. B. Shepson, U. Friess, U. Platt and B. H. Stirm (2016). "The role of open lead interactions in atmospheric ozone variability between Arctic coastal and inland sites." Elementa-Science of the Anthropocene 4: 1-9, missing doi.

Peterson, P.K., D. Pöhler, J. Zielcke, S. General, U. Frieß, U. Platt, W.R. Simpson, S.V. Nghiem, P.B. Shepson, B.H. Stirm and K.A. Pratt, Springtime Bromine Activation over Coastal and Inland Arctic

Snowpacks ACS Earth Space Chem. 2018, 2, 1075−1086, DOI: 10.1021/acsearthspacechem.8b00083

Pittman, J. V., L. L. Pan, J. C. Wei, F. W. Irion, X. Liu, E. S. Maddy, C. D. Barnet, K. Chance, and R.-S. Gao (2009), Evaluation of AIRS, IASI, and OMI ozone profile retrievals in the extratropical tropopause region using in situ aircraft measurements, J. Geophys. Res., 114, D24109, doi:10.1029/2009JD012493.

Pope, R. J., Richards, N. A. D., Chipperfield, M. P., Moore, D. P., Monks, S. A., Arnold, S. R., Glatthor, N., Kiefer, M., Breider, T. J., Harrison, J. J., Remedios, J. J., Warneke, C., Roberts,

J. M., Diskin, G. S., Huey, L. G., Wisthaler, A., Apel, E. C., Bernath, P. F., and Feng, W., (2016), Intercomparison and evaluation of satellite peroxyacetyl nitrate observations in the upper troposphere-lower stratosphere, Atmos. Chem. Phys., 16, 13541-13559, doi:10.5194/acp-16-13541-2016.

Rap, A., N.A.D. Richards, P.M. Forster, S.A. Monks, S.R. Arnold, and M.P. Chipperfield, (2015), Satellite constraint on the tropospheric ozone radiative effect, Geophys. Res. Lett., 42, 5074-5081. doi: 10.1002/2015GL064037.

Seabrook, J., and J. Whiteway (2016), Influence of mountains on Arctic tropospheric ozone, J. Geophys. Res. Atmos., 121, 1935–1942, doi:10.1002/2015JD024114.

Sharma, S., L. A. Barrie, E. Magnusson, G. Brattstrom, W. R. Leaitch, A. Steffen and S. Landsberger, "A Factor and Trends Analysis of Multidecadal Lower Tropospheric Observations of Arctic Aerosol Composition, Black Carbon, Ozone, and Mercury at Alert, Canada." Journal of Geophysical Research-Atmospheres 124(24): 14133-14161, 2019.

Skov, H. Egeløv, A.H. Granby, K. and Nielsen, T. “The Relation of ozone with other Photochemical Products at Ll. Valby, Denmark". Atm. Environ. 1997, vol. 31 No. 5, p 685-691.

Skov, H., J. Hjorth, C. Nordstrøm, J. B., C. C., P. M.B., L. J.B. and M. Dall’Osto (2020). "The variability in Gaseous Elemental Mercury at Villum Research Station, Station Nord in North Greenland from 1999 to 2017." ACPD doi.org/10.5194/acp-2019-912.

Simpson, W. R., Frieß, U., Thomas, J. L., Lampel, J., & Platt, U. (2018). Polar nighttime chemistry produces intense reactive bromine events. Geophysical Research Letters, 45, 9987–9994. https:// doi.org/10.1029/2018GL079444

Tarasick, D. W., Davies, J., Smit, H. G. J., and Oltmans, S. J.: A re-evaluated Canadian ozonesonde record: measurements of the vertical distribution of ozone over Canada from 1966 to 2013, Atmos. Meas. Tech., 9, 195–214, https://doi.org/10.5194/amt-9-195-2016, 2016.

Tarasick, D., I. E. Galbally, O. R. Cooper, M. G. Schultz, G. Ancellet, T. Leblanc, T. J. Wallington, J. Ziemke, X. Liu, M. Steinbacher, J. Staehelin, C. Vigouroux, J. W. Hannigan, O. Garcia, G. Foret, P. Zanis, E. Weatherhead, I. Petropavlovskikh, H. Worden, M. Osman, J. Liu, K. L. Chang, A. Gaudel, M. Y. Lin, M. Granados-Munoz, A. M. Thompson, S. J. Oltmans, J. Cuesta, G. Dufour, V. Thouret, B. Hassler, T. Trickl and J. L. Neu (2019). "Tropospheric Ozone Assessment Report: Tropospheric ozone from 1877 to 2016,

observed levels, trends and uncertainties." Elementa-Science of the Anthropocene 7: 72. Missing doi.

Turnock, S.T., O. Wild, A. Sellar and F.M. O'Connor, 300 years of tropospheric ozone changes using CMIP6 scenarios with a parameterised approach, Atmos. Environ., https://doi.org/10.1016/j.atmosenv.2019.07.001, 2019.

Van Dam, B., D. Helmig, P. V. Doskey,and S. J. Oltmans (2016), Summertime surface O3 behavior and deposition to tundra in the Alaskan Arctic, J. Geophys. Res. Atmos., 121, 8055–8066, doi:10.1002/2015JD023914.

Wang, S. Y., S. M. McNamara, C. W. Moore, D. Obrist, A. Steffen, P. B. Shepson, R. M. Staebler, A. R. W. Raso and K. A. Pratt (2019). "Direct detection of atmospheric atomic bromine leading to mercury and ozone depletion." Proceedings of the National Academy of Sciences of the United States of America 116(29): 14479-14484.

Wang, X., Jacob, D. J., Eastham, S. D., Sulprizio, M. P., Zhu, L., Chen, Q., Alexander, B., Sherwen, T., Evans, M. J., Lee, B. H., Haskins, J. D., Lopez-Hilfiker, F. D., Thornton, J. A., Huey, G. L., and Liao, H.: The role of chlorine in global tropospheric chemistry, Atmos. Chem. Phys., 19, 3981–4003, https://doi.org/10.5194/acp-19-3981-2019 , 2019.

Wespes, C., Emmons, L., Edwards, D. P., Hannigan, J., Hurt- mans, D., Saunois, M., Coheur, P.-F., Clerbaux, C., Cof- fey, M. T., Batchelor, R. L., Lindenmaier, R., Strong, K., Wein- heimer, A. J., Nowak, J. B., Ryerson, T. B., Crounse, J. D., and Wennberg, P. O.: Analysis of ozone and nitric acid in spring and summer Arctic pollution using aircraft, ground-based, satellite observations and MOZART-4 model: source attribution and par- titioning, Atmos. Chem. Phys., 12, 237–259, doi:10.5194/acp- 12-237-2012, 2012.

Yang, X. Blechschmidt, A.-M. Bognar, K. McClure–Begley, Morris, S. Petropavlovskikh, I. Richter, A. Skov, H. Strong, K. Tarasick, D. Uttal, T. Vestenius, M. Zhao, X. (2020) The pan-Arctic surface ozone: modelling vs measurements. ACPD. doi.org/10.5194/acp-2019-984.

Young, P. J., V. Naik*, A. M. Fiore, A. Gaudel, J. Guo, M. Y. Lin, J. L. Neu, D. D. Parrish, H. E. Rieder, J. L. Schnell, S. Tilmes, O. Wild, L. Zhang, J. R. Ziemke, J. Brandt, A. Delcloo, R. M. Doherty, C. Geels, M. I. Hegglin, L. Hu, U. Im, R. Kumar, A. Luhar, L. Murray, D. Plummer, J. Rodriguez, A. Saiz-Lopez, M. G. Schultz, M. T. Woodhouse and G. Zeng (2018), Tropospheric Ozone Assessment Report: Assessment of global-scale model performance for global and regional ozone distributions, variability, and trends, Elem Sci Anth. 2018;6(1):10. DOI: http://doi.org/10.1525/elementa.265

Yeung, L.Y., L.T. Murray, P. Martinerie, E. Witrant, H. Hu, A. Banerjee, A. Orsi and J. Chappellaz, Isotopic constraint on the twentieth-century increase in tropospheric ozone, Nature, 570 (7760) 224, doi: 10.1038/s41586-019-1277-1, 2019.

Zhu, L., E. V. Fischer, V. H. Payne, J. R. Worden, and Z. Jiang (2015), TES observations of the interannual variability of PAN over Northern Eurasia and the relationship to springtime fires, Geophys. Res. Lett., 42, 7230–7237, doi:10.1002/ 2015GL065328.

Section 4.4 (methane)

Section 4.5 (clouds)

Abdelmonem, A., M. Schnaiter, P. Amsler, E. Hesse, J. Meyer, and T. Leisner (2011), First correlated measurements of the shape and light scattering properties of cloud particles using the novel Particle Habit Imaging and Polar Scattering (PHIPS) probe. *Atmos. Meas. Tech., 4*, 2125–2142, doi:10.5194/amt-4-2125-2011.

Mahrt, F., Wieder, J., Dietlicher, R., Smith, H. R., Stopford, C., and Kanji, Z. A. (2019), A high-speed particle phase discriminator (PPD-HS) for the classification of airborne particles, as tested in a continuous flow diffusion chamber, *Atmos. Meas. Tech., 12*, 3183–3208, https://doi.org/10.5194/amt-12-3183-2019.

Baumgardner, D., Newton, R., Krämer, M., Meyer, J., Beyer, A., Wendisch, M., and Vochezer, P. (2014), The Cloud Particle Spectrometer with Polarization Detection (CPSPD): A next generation open-path cloud probe for distinguishing liquid cloud droplets from ice crystals, *Atmos. Res., 142*, 2–14, https://doi.org/10.1016/j.atmosres.2013.12.010.

Baumgardner, D., Abel, S. J., Axisa, D., Cotton, R., Crosier, J., Field, P., Gurganus, C., Heymsfield, A., Korolev, A., Krämer, M., Lawson, P., McFarquhar, G., Ulanowski, Z., and Um, J. (2017), Cloud Ice Properties: In Situ Measurement Challenges, *Meteor. Mon., 58*, 9.1–9.23, https://doi.org/10.1175/AMSMONOGRAPHS-D-16-0011.1

Boeke, R. C., and P. C. Taylor (2016), Evaluation of the Arctic surface radiation budget in CMIP5 models, *J. Geophys. Res. Atmos., 121*, 8525–8548, doi:10.1002/2016JD025099.

5830 Bradley, R. S., Keimig, F. T., and Diaz, H. F.: Climatology of surface based inversions in the
5831 North American Arctic, J. Geophys. Res., 94, 15699–15712, 1992.

5832 Cesana, G., Kay, J. E., Chepfer, H., English, J. M., and de Boer, G. (2012), Ubiquitous low-
5833 level liquid-containing Arctic clouds: New observations and climate model constraints
5834 from CALIPSO-GOCCP, Geophys. Res. Lett., 39, L20804, doi:10.1029/2012GL053385.

5835 Costa, A., and Coauthors, (2017), Classification of Arctic, midlatitude and tropical clouds in
5836 the mixed-phase temperature regime. *Atmos. Chem. Phys.*, *17*, 12 219–12 238,
5837 https://doi.org/10.5194/acp-17-12219-2017.

5838 Curry, J. A., Rossow, W. B., Randall, D., & Schramm, J. L. (1996). Overview of Arctic cloud and
5839 radiation characteristics. Journal of Climate, 9, 1731–1764.

5840 Devasthale, A., J Sedlar, M Tjernström, A Kokhanovsky: A Climatological Overview of Arctic
5841 Clouds, Physics and Chemistry of the Arctic Atmosphere, 331-360, Springer Cham, 2020.

5842 Devasthale, A., Willén, U., Karlsson, K.-G., and Jones, C. G.: Quantifying the clear-sky
5843 temperature inversion frequency and strength over the Arctic Ocean during summer and
5844 winter seasons from AIRS profiles, Atmos. Chem. Phys., 10, 5565–5572,
5845 https://doi.org/10.5194/acp-10-5565-2010, 2010.

5846 Eirund, G. K., Possner, A., and Lohmann, U.: Response of Arctic mixed-phase clouds to
5847 aerosol perturbations under different surface forcings, Atmos. Chem. Phys., 19, 9847–
5848 9864, https://doi.org/10.5194/acp-19-9847-2019, 2019.

5849 Fugal, J. P. and Shaw, R. A. (2009), Cloud particle size distributions measured with an
5850 airborne digital in-line holographic instrument, Atmos. Meas. Tech., 2, 259–271,
5851 doi:10.5194/amt-2-259-2009.

5852 Garrett, T. J., and C. Zhao, 2006: Increased Arctic cloud longwave emissivity associated with
5853 pollution from mid-latitudes. Nature, 440, 787–789, doi:10.1038/nature04636.

5854 Heidinger, A.K.; Foster, M.J.; Walther, A.; Zhao, Z. The Pathfinder Atmospheres Extended
5855 (PATMOS-x) AVHRR climate data set. Bull. Am. Meteorol. Soc. 2014, 95, 909–922.

5856 Henneberger, J., Fugal, J. P., Stetzer, O., and Lohmann, U. (2013), HOLIMO II: a digital
5857 holographic instrument for groundbased in situ observations of microphysical properties

of mixed-phase clouds, Atmos. Meas. Tech., 6, 2975–2987, https://doi.org/10.5194/amt-6-2975-2013.

Kahl, J. D. W., Martinez, D. A., and Zaitseva, N. A.: Long-term variability in the low-level inversion layer over the Arctic Ocean, Int. J. Climatol., 16, 1297–1313, 1996.

Karlsson, K.-G., Anttila, K., Trentmann, J., Stengel, M., Fokke Meirink, J., Devasthale, A., Hanschmann, T., Kothe, S., Jääskeläinen, E., Sedlar, J., Benas, N., van Zadelhoff, G.-J., Schlundt, C., Stein, D., Finkensieper, S., Håkansson, N., and Hollmann, R.: CLARA-A2: the second edition of the CM SAF cloud and radiation data record from 34 years of global AVHRR data, Atmos. Chem. Phys., 17, 5809–5828, https://doi.org/10.5194/acp-17-5809-2017, 2017.

Karlsson, K. and Devasthale, A. Inter-Comparison and Evaluation of the Four Longest Satellite-Derived Cloud Climate Data Records: CLARA-A2, ESA Cloud CCI V3, ISCCP-HGM, and PATMOS-x. Remote Sens. 2018, 10, 1567.

Kay, J. E., and L'Ecuyer, T. (2013), Observational constraints on Arctic Ocean clouds and radiative fluxes during the early 21st century, J. Geophys. Res. Atmos., 118, 7219– 7236, doi:10.1002/jgrd.50489.

Kay, J. E., L'Ecuyer, T., Chepfer, H., Norman, L., Ariel, M. and Gregory, C.:Recent Advances in Arctic Cloud and Climate Research, Current Climate Change Reports, 2016, 2, 159-169.

Koike, M., Ukita, J., Ström, J., Tunved, P., Shiobara, M., Vitale, Lupi, V., Baumgardner, A., D., Ritter, C., Hermansen, O., Yamada, K., and Pedersen, C. (2019), Year-round in situ measurements of Arctic low-level clouds: Microphysical properties and their relationships with aerosols. *J. Geophys. Res. Atmos., 124*, 1798-1822. https://doi. org/10.1029/2018JD029802.

Lenaerts, J. T. M., K. Van Tricht,S. Lhermitte, and T. S. L'Ecuyer (2017),Polar clouds and radiation in satelliteobservations, reanalyses, and climatemodels,Geophys. Res.Lett.,44, 355–3364,doi:10.1002/2016GL072242.

Loewe, K., Ekman, A. M. L., Paukert, M., Sedlar, J., Tjernström, M., and Hoose, C.: Modelling micro- and macrophysical contributors to the dissipation of an Arctic mixed-phase cloud

during the Arctic Summer Cloud Ocean Study (ASCOS), Atmos. Chem. Phys., 17, 6693–6704, https://doi.org/10.5194/acp-17-6693-2017, 2017.

Lohmann, U. Anthropogenic Aerosol Influences on Mixed-Phase Clouds. Curr Clim Change Rep 3, 32–44 (2017). https://doi.org/10.1007/s40641-017-0059-9

Lubin, D., and A. M. Vogelmann, 2006: A climatologically significant aerosol longwave indirect effect in the Arctic. Nature, 439, 453–456, doi:10.1038/nature04449.

Mauritsen, T., Sedlar, J., Tjernström, M., Leck, C., Martin, M., Shupe, M., Sjogren, S., Sierau, B., Persson, P. O. G., Brooks, I. M., and Swietlicki, E.: An Arctic CCN-limited cloud-aerosol regime, Atmos. Chem. Phys., 11, 165–173, https://doi.org/10.5194/acp-11-165-2011, 2011.

McFarquhar, G. M., et al. (2017), Processing of Ice Cloud In Situ Data Collected by Bulk Water, Scattering, and Imaging Probes: Fundamentals, Uncertainties, and Efforts toward Consistency. *Meteorological Monographs, 58*, 11.1-11.33.

Mioche, G., Jourdan, O., Ceccaldi, M. & Delanoe, J. Variability of mixed-phase clouds in the Arctic with a focus on the Svalbard region: a study based on spaceborne active remote sensing. *Atmos. Chem. Phys.* **15**, 2445–2461 (2015).

Nomokonova, T., Ebell, K., Löhnert, U., Maturilli, M., Ritter, C., and O'Connor, E. (2019), Statistics on clouds and their relation to thermodynamic conditions at Ny-Ålesund using ground-based sensor synergy, *Atmos. Chem. Phys., 19*, 410–4126, https://doi.org/10.5194/acp-19-4105-2019.

Porcheron, E., P. Lemaitre, J. Van Beeck, R. Vetrano, M. Brunel, and G. Grehan (2015), Development of a spectrometer for airborne measurement of droplet sizes in clouds. *J. Eur. Opt. Soc. Rapid Publ., 10*, 15030, doi:10.2971/jeos.2015.15030.

Sedlar, J., M. D. Shupe and MT, 2012: On the relationship between thermodynamic structure and cloud top, and its climate significance in the Arctic. Journal of Climate, 25, 2374-2393, DOI 10.1007/s00382-010-0937-5.

Sedlar, J. and Tjernström, M.: Stratiform cloud-inversion characterization during the Arctic melt season, Bound-Lay. Meteorol., 132, 455–474, doi:10.1007/s10546-009-9407-1, 2009.

5915 Serreze, M. C., Kahl, J. D., and Schnell, R. C.: Low-level temperature inversions of the
5916 Eurasian Arctic and comparisons with Soviet drifting stations, J. Climate, 5, 615–630,
5917 1992

5918 Shupe, M. D., Persson, P. O. G., Brooks, I. M., Tjernström, M., Sedlar, J., Mauritsen, T.,
5919 Sjogren, S., and Leck, C.: Cloud and boundary layer interactions over the Arctic sea ice in
5920 late summer, Atmos. Chem. Phys., 13, 9379–9399, https://doi.org/10.5194/acp-13-9379-
5921 2013, 2013.

5922 Shupe, M.D., and J.M. Intrieri (2004), Cloud radiative forcing of the Arctic surface: The
5923 influence of cloud properties, surface albedo, and solar zenith angle. J. Climate, 17, 616-
5924 628.

5925 Stengel, M.; Stapelberg, S.; Sus, O.; Schlundt, C.; Poulsen, C.; Thomas, G.; Christensen, M.;
5926 Carbajal Henken, C.; Preusker, R.; Fischer, J.; et al. Cloud property datasets retrieved from
5927 AVHRR, MODIS, AATSR and MERIS in the framework of the Cloud_cci project. Earth Syst.
5928 Sci. Data 2017, 9, 881–904.

5929 Stohl, A. (2006). Characteristics of atmospheric transport into the Arctic troposphere.
5930 Journal of Geophysical Research, 111, D11306.

5931 Schnaiter, M., Järvinen, E., Abdelmonem, A., and Leisner, T. (2018), PHIPS-HALO: the
5932 airborne particle habit imaging and polar scattering probe – Part 2: Characterization and
5933 first results, *Atmos. Meas. Tech., 11*, 341–357, https://doi.org/10.5194/amt-11-341-2018.

5934 Vochezer, P., Järvinen, E., Wagner, R., Kupiszewski, P., Leisner, T., and Schnaiter, M. (2016),
5935 In situ characterization of mixed phase clouds using the Small Ice Detector and the
5936 Particle Phase Discriminator, *Atmos. Meas. Tech., 9*, 159–177,
5937 https://doi.org/10.5194/amt-9-159-2016.

5938 Walsh, J. E., & Chapman, W. L. (1998). Arctic cloud-radiation-temperature associations in
5939 observational data and atmospheric reanalyses. Journal of Climate, 11, 3030–3045.

5940 Wang, X., & Key, J. (2005). Arctic surface, cloud, and radiation properties based on the
5941 AVHRR polar pathfinder data set. Part I: Spatial and temporal characteristics. Journal of
5942 Climate, 18(14), 2558–2574.

5943 Wu, D. L., and J. N. Lee (2012), Arctic low cloud changes as observed by MISR and CALIOP:
5944 Implication for the enhanced autumnal warming and sea ice loss, J. Geophys. Res., 117,
5945 D07107, doi:10.1029/2011JD017050.

5946 Yamagata, S., Kobayashi, D., Ohta, S., Murao, N., Shiobara, M., Wada, M., Yabuki, M.,
5947 Konishi, H., and Yamanouchi, T.: Properties of aerosols and their wet deposition in the
5948 arctic spring during ASTAR2004 at Ny-Alesund, Svalbard, Atmos. Chem. Phys., 9, 261–
5949 270, https://doi.org/10.5194/acp-9-261-2009, 2009.

5950 Young, A. H., Knapp, K. R., Inamdar, A., Hankins,W., & Rossow,W. B. (2018). The
5951 international satellite cloud climatology project H-series climate data record product.
5952 Earth System Science Data, 10, 1–11.

5953 Zamora, L. M., Kahn, R. A., Eckhardt, S., McComiskey, A., Sawamura, P., Moore, R., and
5954 Stohl, A.: Aerosol indirect effects on the nighttime Arctic Ocean surface from thin,
5955 predominantly liquid clouds, Atmos. Chem. Phys., 17, 7311–7332,
5956 https://doi.org/10.5194/acp-17-7311-2017, 2017.

5957

5958 ***Additional references to section 4.5.3***

5959 (cloud microphysics – inserted grey highlighted paragraphs)

5960 Abdelmonem, A., M. Schnaiter, P. Amsler, E. Hesse, J. Meyer, and T. Leisner (2011), First
5961 correlated measurements of the shape and light scattering properties of cloud particles
5962 using the novel Particle Habit Imaging and Polar Scattering (PHIPS) probe. Atmos. Meas.
5963 Tech., 4, 2125–2142, doi:10.5194/amt-4-2125-2011.

5964 Baumgardner, D., Newton, R., Krämer, M., Meyer, J., Beyer, A., Wendisch, M., and Vochezer,
5965 P. (2014), The Cloud Particle Spectrometer with Polarization Detection (CPSPD): A next
5966 generation open-path cloud probe for distinguishing liquid cloud droplets from ice
5967 crystals, Atmos. Res., 142, 2–14, https://doi.org/10.1016/j.atmosres.2013.12.010.

5968 Baumgardner, D., Abel, S. J., Axisa, D., Cotton, R., Crosier, J., Field, P., Gurganus, C.,
5969 Heymsfield, A., Korolev, A., Krämer, M., Lawson, P., McFarquhar, G., Ulanowski, Z., and
5970 Um, J. (2017), Cloud Ice Properties: In Situ Measurement Challenges, Meteor. Mon., 58,
5971 9.1–9.23, https://doi.org/10.1175/AMSMONOGRAPHS-D-16-0011.1

5972 Boeke, R. C., and P. C. Taylor (2016), Evaluation of the Arctic surface radiation budget in
5973 CMIP5 models, J. Geophys. Res. Atmos., 121, 8525–8548, doi:10.1002/2016JD025099.

5974 Costa, A., and Coauthors, (2017), Classification of Arctic, midlatitude and tropical clouds in
5975 the mixed-phase temperature regime. Atmos. Chem. Phys., 17, 12 219–12 238,
5976 https://doi.org/10.5194/acp-17-12219-2017.

5977 Fugal, J. P. and Shaw, R. A. (2009), Cloud particle size distributions measured with an
5978 airborne digital in-line holographic instrument, Atmos. Meas. Tech., 2, 259–271,
5979 doi:10.5194/amt-2-259-2009.

5980 Henneberger, J., Fugal, J. P., Stetzer, O., and Lohmann, U. (2013), HOLIMO II: a digital
5981 holographic instrument for groundbased in situ observations of microphysical properties
5982 of mixed-phase clouds, Atmos. Meas. Tech., 6, 2975–2987, https://doi.org/10.5194/amt-
5983 6-2975-2013.

5984 Koike, M., Ukita, J., Ström, J., Tunved, P., Shiobara, M., Vitale, Lupi, V., Baumgardner, A., D.,
5985 Ritter, C., Hermansen, O., Yamada, K., and Pedersen, C. (2019), Year-round in situ
5986 measurements of Arctic low-level clouds: Microphysical properties and their
5987 relationships with aerosols. J. Geophys. Res. Atmos., 124, 1798-1822. https://doi.
5988 org/10.1029/2018JD029802.

5989 Mahrt, F., Wieder, J., Dietlicher, R., Smith, H. R., Stopford, C., and Kanji, Z. A. (2019), A high-
5990 speed particle phase discriminator (PPD-HS) for the classification of airborne particles, as
5991 tested in a continuous flow diffusion chamber, Atmos. Meas. Tech., 12, 3183–3208,
5992 https://doi.org/10.5194/amt-12-3183-2019.

5993 McFarquhar, G. M., et al. (2017), Processing of Ice Cloud In Situ Data Collected by Bulk
5994 Water, Scattering, and Imaging Probes: Fundamentals, Uncertainties, and Efforts toward
5995 Consistency. Meteorological Monographs, 58, 11.1-11.33.
5996 Mioche, G., Jourdan, O., Ceccaldi, M. & Delanoe, J. Variability of mixed-phase clouds in
5997 the Arctic with a focus on the Svalbard region: a study based on spaceborne active
5998 remote sensing. Atmos. Chem. Phys. 15, 2445–2461 (2015).

5999 Nomokonova, T., Ebell, K., Löhnert, U., Maturilli, M., Ritter, C., and O'Connor, E. (2019),
6000 Statistics on clouds and their relation to thermodynamic conditions at Ny-Ålesund using

ground-based sensor synergy, Atmos. Chem. Phys., 19, 410–4126, https://doi.org/10.5194/acp-19-4105-2019.

Porcheron, E., P. Lemaitre, J. Van Beeck, R. Vetrano, M. Brunel, and G. Grehan (2015), Development of a spectrometer for airborne measurement of droplet sizes in clouds. J. Eur. Opt. Soc. Rapid Publ., 10, 15030, doi:10.2971/jeos.2015.15030.

Schnaiter, M., Järvinen, E., Abdelmonem, A., and Leisner, T. (2018), PHIPS-HALO: the airborne particle habit imaging and polar scattering probe – Part 2: Characterization and first results, Atmos. Meas. Tech., 11, 341–357, https://doi.org/10.5194/amt-11-341-2018.

Vochezer, P., Järvinen, E., Wagner, R., Kupiszewski, P., Leisner, T., and Schnaiter, M. (2016), In situ characterization of mixed phase clouds using the Small Ice Detector and the Particle Phase Discriminator, Atmos. Meas. Tech., 9, 159–177, https://doi.org/10.5194/amt-9-159-2016.

5. Observations, origins and trends of Arctic aerosols

Policy-relevant science questions:

What are the current abundance of short-lived climate forcers such as black carbon and other particulates and ozone in the Arctic atmosphere? Or What is our current understanding of the abundance of these components?

What role do the natural sources play in emissions and concentrations?

Are the current monitoring activities (of atmospheric concentrations) sufficient to capture anticipated source changes?

5.1 Particulate matter: black carbon, dust, inorganic and organic aerosols

(main authors) Julia Schmale, Sangeeta Sharma, Andreas Massling, Marco Zanatta, Outi Meinander, Stefano Decesari, David Cappelletti, Hans Christen Hansson.

(contributing authors) Lin Huang, Joe, McConnell, Yutaka Kondo, Peter Tunved, Rita Traversi, Silvia Becagli, Christian Zdanowicz, Elena Barbaro.

5.1.1. Significance of aerosols for the Arctic and new observations since the last report

Arctic amplification, a phenomenon observed as enhanced atmospheric warming compared to other parts of the world, is expected to be also strongly influenced by short-lived climate forcers as aerosols, specifically black carbon and dust and their depositions on snow- and ice-covered surfaces. In addition, various feedback mechanisms e.g. surface albedo feedback or temperature feedback have been identified as strong contributors to Arctic warming (Boy et al. 2019). Also, the contribution of climate feedback to the net aerosol radiative effect in the Arctic is expected to increase in the future as the rate of climate change accelerates amplifying feedback mechanisms.

The availability of full yearly records of BC concentrations for observatories located in both the western and eastern regions of the Arctic has now increased (Tørseth et al., 2020) and has enabled models to better constrain key parameters controlling aerosol transport, cloud scavenging and deposition (Eckhardt et al., 2015).

The increasing emissions of dust particles caused by the retreat of snow surfaces over land has become a frontier research topic. Extensive data on this topic are still missing and important as dust significantly can modify the surface albedo of ice- and snow-covered surfaces and thus contribute to the radiative balance of the Arctic atmosphere. Dust and BC after atmospheric ageing are also potentially strong contributors to changes in cloud cover. New observations have been carried out and continued on other inorganic aerosol compounds including anthropogenic substances co-emitted with BC. But year-round particulate organic carbon (OC) measurements are only available for specific sites, although the modification of biogenic aerosol production as a consequence of marine and terrestrial ecosystem changes needs further intense research to clear the picture of how feedbacks of Arctic temperature change affect regional aerosol production.

Aerosol physical parameters as particle number size distributions, scattering and absorption coefficients, number of CCN or INP active particles have only partly been established in monitoring programs (Freud et al., 2017; Schmeisser et al., 2018; Jung et al., 2018). Long term series of these parameters are key to evaluate the role of aerosols as short-lived climate forcers on the climatic changes of the sensitive Arctic regions.

A detailed overview of aerosols observed in Arctic environments with a great potential for climate effects is given below. The description includes BC, dust, aerosols of inorganic and organic composition and their physical properties responsible for anticipated radiative changes of the atmosphere. The subchapter divides into atmospheric near-surface and vertical observations as well as such in ice and snow spanning from their origin and seasonal cycles to historical and present day trends.

5.1.2. Concentrations, seasonal cycles and origin

The stratified burden in aerosols concentrations measured in the Arctic are long range transported along the pathways of isentropic synoptic scale circulation from the anthropogenic emissions source regions in the south (Barrie 1986; Stone et al., 2014; Sharma et al., 2013; Law and Stohl, 2007). Seasonal variation with lower aerosol measurements during the summer are due to decrease in the frequency of this synoptic transport from the south, as the pressure systems change between October-April (Arctic haze) and May-September (summer). The depositional losses also increase with efficient wet scavenging during summer. During the Arctic haze, surface locations have direct influence from anthropogenic sources in the Eurasian regions i.e. Siberia, > 2km from Europe and North America and from deserts, biomass burning regions and Asia aloft, > 3km. (Koch and Hansen 2005; Sharma et. al., 2013; others?). Local natural sources become dominant during the summer at the surface and long range transport of dust (Dagsson-Waldhauserova et al., 2014; Groot Zwaaftink et al., 2017) and forest fires aloft (Evangeliou et. al., 2019).

5.1.2.1 Surface aerosol observations

The state of **black carbon (BC)** observations has been recently thoroughly reviewed in a dedicated technical report of the EU Action on Black Carbon in the Arctic (Tørseth et al., 2020). Figure 5.1.2.1.1 shows the monthly mean concentrations of equivalent black carbon (eBC) at the five observatories in the high Arctic carrying on year-round long-term monitoring. Nevertheless, continuous eBC measurements in Tiksi (Russia) have been performed since 2009 while periodical observations are hosted at Cape Baranova. At Villum in North Greenland measurements of eBC started in 2017. The Siberian observatories are located relatively close to strong emission sources and exposed to low-level atmospheric transport from the continent toward the Arctic ocean during winter. The monthly mean eBC concentrations in Tiksi exceed 100 ng m^{-3} in winter, more than four times higher than in the western and European Arctic. Conversely, in the summer months mean BC levels range between 5 and 12 ng/m^3 at all stations indicating comparable effects of large-scale transport and efficient wet scavenging in all geographical regions. Average BC concentrations peak in late winter or early spring in correspondence with the Arctic haze advection (Eckhardt et al., 2015; Gilardoni et al. 2019) with the exception of Summit which –

by reason of its elevation – is normally not impacted by low-level transport. However, the highest concentrations at Summit (>95-percentiles) are also observed in winter and early spring, indicating that Arctic haze can occasionally reach the top of the Greenland plateau. The climatology of the highest 5% of BC monthly concentrations show a second peak in mid-summer at all observatories which can linked to fire activity. The other main patterns in the yearly cycle of BC concentrations – as summarized by Eckhardt et al. (2015) – are the more pronounced seasonality at Alert with respect to the other stations in the western Arctic, and the delayed ramp-up period in late fall and winter at Zeppelin, indicating that for most of the dark season the Svalbard are relatively well protected inside the polar dome from the advection of pollutants from southerly regions. In addition to the stations considered here, Tørseth et al. (2020) report eBC measurements performed over periods of 1 to 3 years at other eight stations in North America and Europe. Periodical observations of eBC and EC are also hosted at Cape Baranova (Popovicheva et al., 2019) and complemented by further eBC measurements in the Russian Arctic seas in research ship experiments (Popovicheva et al., 2017). Additional BC measurements in the central Arctic ocean are provided by the MOCCHA research cruise (https://polarforskningsportalen.se/en/arctic/expeditions/arctic-ocean-2018) and are carried out in the frame of MOSAIC.

The determination of source-diagnostics for BC represents a new frontier of BC monitoring in the Arctic. The best established techniques for BC source attribution are based on the analysis of carbon isotopes (δ13C and Δ14C) in elemental carbon (EC) samples. According to the radiocarbon data discussed by Winiger et al. (2016, 2019), the biomass burning fraction of EC in the pan-Arctic region was on average 39 ± 10%. All sites are characterized by a pronounced seasonality with a higher biomass burning fraction in the summer when fire activity in the boreal forest is the highest (Mouteva et al., 2015). The stable isotopic carbon fingerprints (δ13C) presented by Winiger et al. (2019) indicate that the combustion of liquid fuel represented the major fraction of fossil EC at all sites for the period considered (2011 – 2015) (Fig. 5.1.2.1.2). However, on the basis of the long-term record of δ13C determinations carried out at Alert, a significant contribution to EC from gas flaring cannot be ruled out.

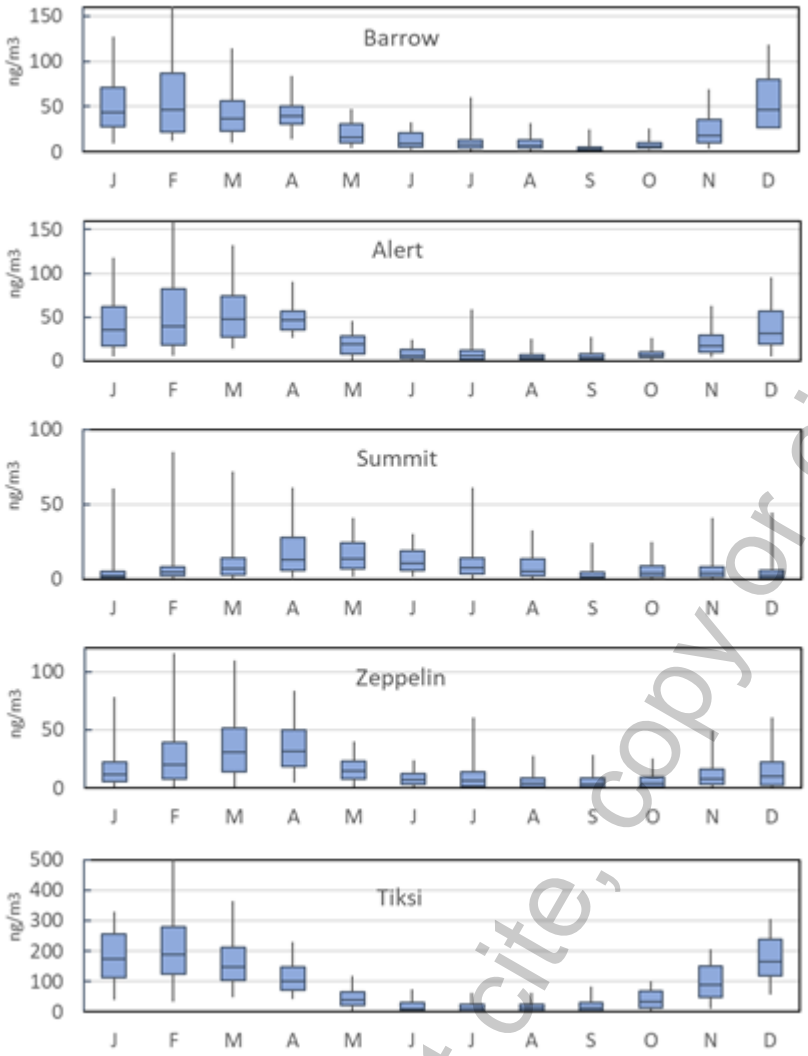

7123

7124 Figure 5.1.2.1.1. Seasonal cycles of eBC at five observatories in the high Arctic. A mass
7125 absorption coefficient of 10 m^2/g was used to convert absorption coefficients into mass of
7126 BC when not internally set by the BC instruments. Data source: EBAS.

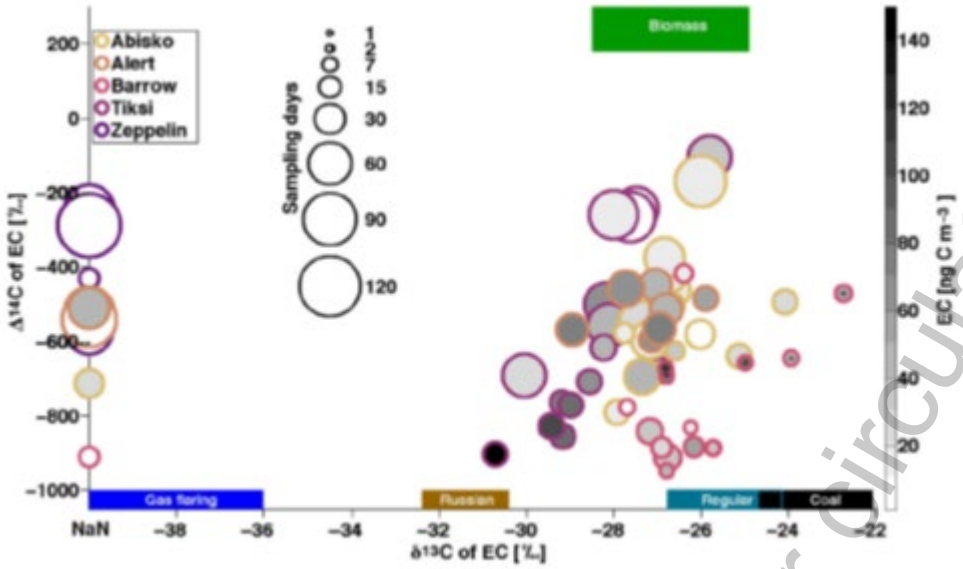

Figure 5.1.2.1.2. Source attribution of EC (mass-based analogue of BC) by dual carbon isotopic analysis (Winiger et al., 2019).

The recent observations of atmospheric dust have highlighted the importance of previously neglected sources at high latitudes. The locations of such **high latitude dust (HLD)** sources were identified in Bullard et al. (2016), as presented in Fig. 5.1.2.1.3. The authors have identified and compared the main sources and drivers of dust emissions in the Northern hemisphere including Alaska, Canada, Greenland, and Iceland. They found an overlap between HLD areas and cold deserts (Passarge, 1921) or Polar deserts which Péwé (1974) defines as areas where the mean air temperature of the warmest month is <10°C and mean annual rainfall <250 mm.

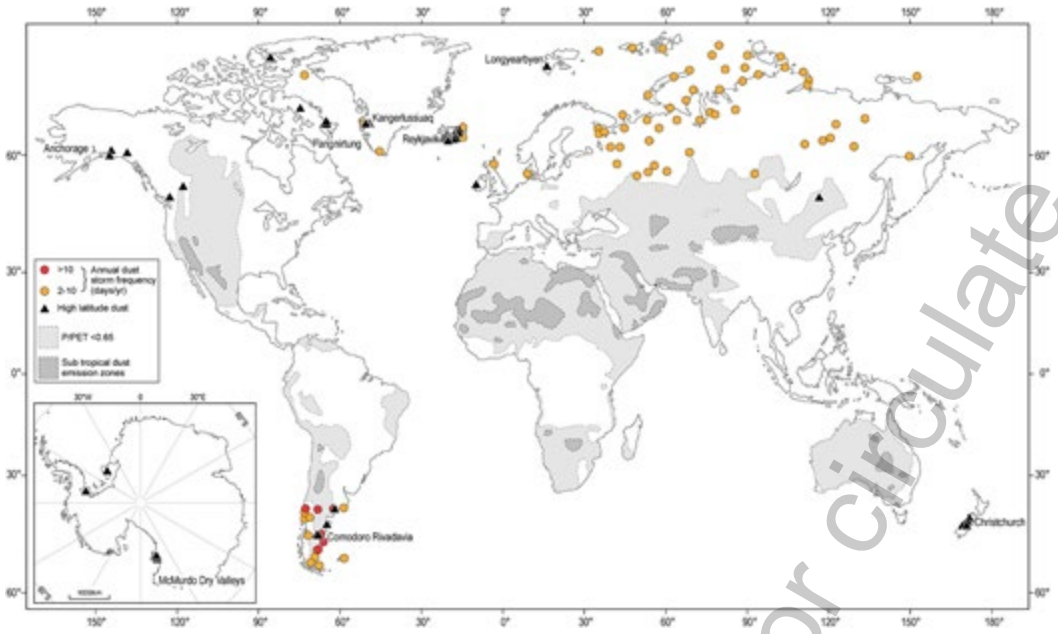

Figure 5.1.2.1.3. "Global observations of high-latitude dust where filled circles indicate dust storm frequency based on visibility data, and black triangles indicate georeferenced published observations of dust storms (see text for details). Areas where the precipitation: potential evapotranspiration ratio <0.65 (aridity index) [United Nations Environment Programme, 1997] and subtropical dust emission zones are included for reference." (Figure 3 of Bullard et al. 2016).

Dust has temporal and spatial variability, as well as episodic nature (Kaspari et al. 2014; Di Mauro et al. 2015). For example, in Iceland, the median annual PM_{10} dust concentration during the dust events in northeast Iceland in 1949–2011 was calculated as 106 µg m^{-3}, with maxima of 122 µg m^{-3} in May and September (Dagsson-Waldhauserova et al. 2017). About 50 % of the annual dust events in the southern part of Iceland take place at sub-zero temperatures, when dark dust may be mixed with snow (Dagsson-Waldhauserova et al. 2015). Icelandic dust contains iron (Fe). Iron aerosols are emitted to the atmosphere by both natural and anthropogenic processes. Natural aerosols with iron content (mineral dust) are emitted by wind erosion (surface creep, saltation, and suspension) of soil in arid and semi-arid regions (Acosta-Martinez et al., 2015) but iron is also used for production and power generation. Long-term measurements of geogenic elements (like Al, Fe and Ca) provide important information on the concentrations and variability of atmospheric dust in the high Arctic. The corresponding datasets are at least partially available on EBAS or other databases (such as NAtChem) for the stations of Villum, Alert and Zeppelin. The climatology

of Al concentrations compiled for Villum by Fan (2013) indicates a seasonal cycle with maxima in spring and fall and overlapping with the months of highest frequency of dust storms in Iceland (Dagsson-Waldhauserova et al., 2014). Similarly, the concentrations of geogenic elements in Ny Alesund show a maximum in March and April, when the ground is almost covered by snow and dust must be transported from lower latitudes (Conca et al., 2019). In summertime, local sources (resuspension from bare glacial soils) can sustain dust concentrations (Tobo et al. 2019). Finally, observations of aerosol iron, which can be used as a tracer for light-absorbing dust, have been performed over the Arctic ocean during intensive field campaigns (Gao et al., 2019; Yoshida et al., 2020).

Aerosol sulfate and nitrate found in the Arctic environment are transported from industrial and transportation sources situated in the south. However, sulfate also has a natural component such as the Volcanos and release of dimethyl sulfide (DMS) gas from oceans, oxidation of DMS in the atmosphere to give sulfate and primary production by sea-salt. Gaseous SO_x and NO_x oxidize in the atmosphere forming H_2SO_4 and HNO_3, respectively. These could readily condense onto pre-existing airborne particles or react with other compounds to form new particles. The contribution of sources of sulfate and nitrate are important towards the energy balance for understanding Arctic climate change. Meteorology governs the seasonality in the Arctic aerosol sulfate and nitrate concentrations measured at 6 Arctic surface stations that includes Alert, Utqiaġvik and Zeppelin and Gruvebadet in Ny-Ålesund, Thule and Villum (Figure 5.1.2.1.4 a and b). The patterns in seasonality for aerosol nitrate and sulfate concentrations are followed at all locations. Concentrations of sulfate and nitrate maximize in April due to buildup of Arctic haze, start to decline and minimize during the summer.

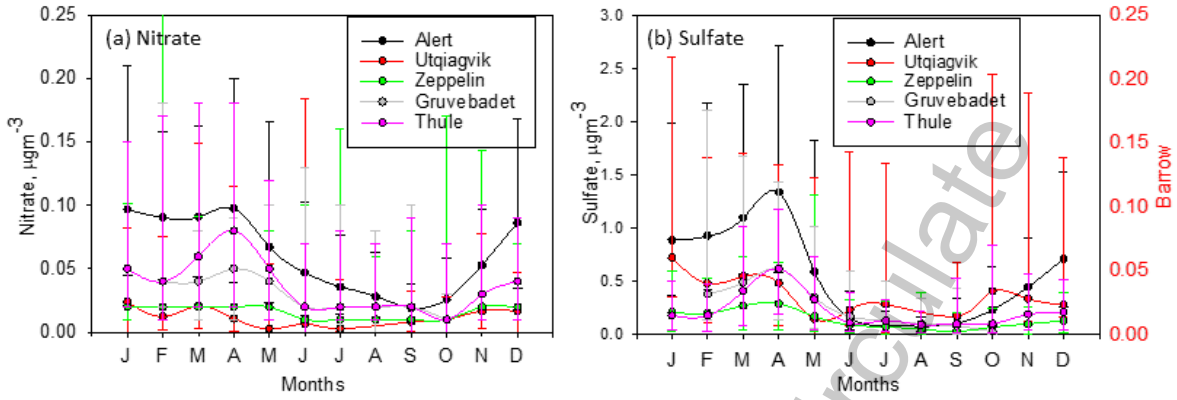

Figure 5.1.2.1.4: Seasonal variation of decadal or longer median aerosol nitrate(a) and sulfate (b) concentrations at Alert, Utqiaġvik, Zeppelin and Gruvebadet in Ny-Ålesund, Thule and Villum measurement stations (Villum to be added here!). The error bars are 5th and 95th percentile concentrations. (data source: EBAS and personal communication with PI of the station).

The comparison in concentrations among all measurements at all locations are very visible. Aerosol nitrate and sulfate median concentrations measure higher at locations Alert, Thule and Gruvebadet with the exception of Zeppelin which is at an altitude of 500m asl. Measurements of nitrate and sulfate are minimum at Utqiaġvik.

Several studies have estimated the source apportionment of various sulfate sources. Anthropogenic sources are predominant during winter/spring the anthropogenic input at Ny-Ålesund location (calculated as the differences between total sulfate and the sum of sea-salt, crustal and biogenic contributes) was found to be the most relevant contribution to the sulfate budget in summer and, especially, in spring 2014; crustal, sea-salt, biogenic and anthropogenic sources accounted for 3.3, 12.0, 11.5 and 74.8 % (Yang et al., 2018).

However, the biogenic sulfate fractions up to 70%, become dominant during the summer as the anthropogenic component declines at various locations in the Arctic including Alert (Norman et al., 1999). During July 2014, results along the ship track of Amundsen showed 70% of fine aerosols (<0.49 µm) and 86% of SO_2 were from biogenic sources (Ghahremaninezhad et al., 2016).

Organic aerosols (OAs) are characterized by a large diversity of sources, atmospheric transformations and compositions. By reason of such complexity, the current knowledge of the atmospheric lifecycle of organic aerosols in the Arctic is still very limited. Nevertheless, observations of concentrations and properties of OA have significantly intensified in the recent years. Organic compounds are deemed to be important in several processes involving climate feedbacks on the biogenic emissions to the atmosphere, with a potential impact on new particle formation, CCN number and cloud formation (Abbatt et al., 2018; Boy et al., 2019). Organic aerosols are also associated with wildfire emissions and other anthropogenic sources and can serve to trace BC emissions as well (Stohl et al., 2006).

Currently, the only long-term record of aerosol total organic carbon (OC) measurements in the high Arctic stations is available – since 2006 – for Alert (Leaitch et al., 2018), but multi-year observations are also available for Ny Alesund (from 2011 to 2015 at Gruvebadet and since 2017 at Mt. Zeppelin) and since 2008 at Villum. The seasonal trends of OC highlight anthropogenic inputs during Arctic haze months (Figure 5.1.2.1.5). However, the summer minimum is much less deep than for BC (Figure 5.1.2.1.1). On the contrary, OC concentrations are sustained or even find a second maximum in mid-summer and find the minimum only in September. The contribution to OC provided in summertime by sources other than fossil fuel combustion (hence biomass burning or biogenic) is supported by recent studies conducted in Tiksi and at Utqiaġvik on the basis of seasonal changes in the OC/EC ratios (Popovicheva et al., 2019) and, for Utqiaġvik, also in the OC Δ14C fingerprints (Barrett and Sheesley 2017).

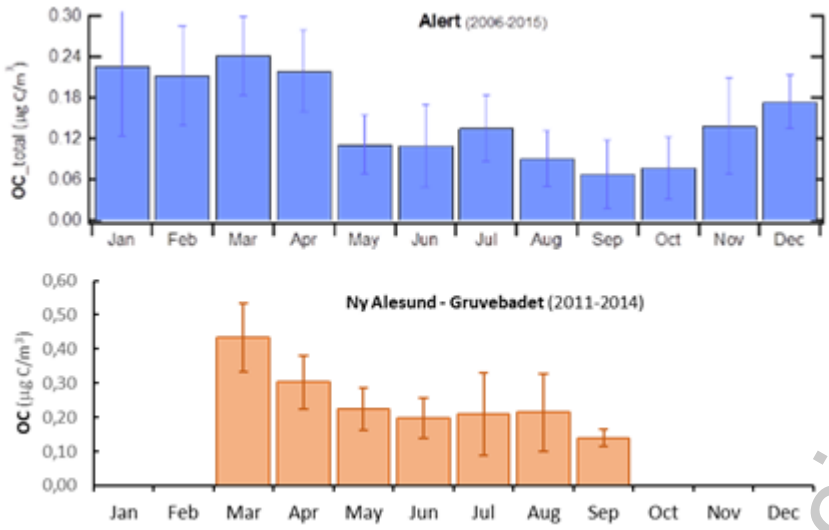

Figure 5.1.2.1.5. OC concentrations (monthly) means from Alert and Gruvebadet (Ny Alesund). Data from Gruvebadet are not available for the dark season (Oct to Jan). Source: unpublished data by Lin Huang (Climate Change Canada) and Rita Traversi (Uni. Florence).

Apportionment of OC mass to specific sources can be attempted with the employ of chemical tracers such as levoglucosan and phenolic compounds for biomass burning (Zangrando et al., 2013; Stohl et al., 2006; Yttri et al.. 2014; von Schneidemesser et al. 2009) and, more recently, by means of online aerosol mass spectrometry (Jaatinen et al. 2014; Willis et al., 2017; Tremblay et al. 2019; Nielsen et al. 2019). Most of the available observations of organic chemical composition have been carried out in the frame of intensive field campaigns at the observatories or involving measurements onboard research ships (Fu et al., 2009, 2013, 2015; Hu et al., 2013; Fu et al., 2013; Ferrero et al., 2019). The results have highlighted the seasonal change of OA composition from the haze period – when the oxidation state of organic matter points to a long-range transport and organic markers are clearly of anthropogenic origin – to the late spring and early summer season when biogenic sources become dominant (Fu et al. 2015; Nielsen et al. 2019). The analysis of the seasonal cycles of methanesulfonate (MSA) based on eight years of observations in Ny Alesund (Svalbard) and Thule (Greenland) (Becagli et al., 2019) provides confirmation of significant OA sources in the open ocean as well as from the biota colonizing the sea ice in its marginal zone (Mungall et al., 2017; Dall`Osto et al., 2017, 2018). Recently, continuous measurements of organic tracers and OA concentrations have been established at Mt. Zeppelin (Karl et al., 2019).

Measurements of chemical components started in the Arctic in the early 1980's while **physical aerosol properties** started during the late 1990ties. There is about 5 sites, Ny Ålesund with the Zeppelin Mountain site at Svalbard, Tiksi in the Lena river delta, Barrow in Alaska, Eureka and Alert in Canada and Villum Research Station (Station Nord) in northernmost Greenland around the Arctic, However only NyÅlesund has been measuring particle size distribution since about 2000 without any longer interruption while others are established later or has longer periods of interruption. From Ny Ålesund measurements (Tunved et. al, 2013, see figure 3.1.5.1) the seasonality is clearly observable with large submicrometer particles, accumulation mode, in the spring that during the summer is exchanged with about the same number but very much smaller, Aitken mode particles. Which is followed by a slow buildup of accumulation mode particle concentration during winter to the peak during the spring. The spring peak is since long identified as the Arctic Haze period due to long distance transported air pollution mainly from the Eurasian continent. The summer aerosol has lately been identified as regionally most likely natural particle formed through new particle formation in the atmosphere.

For the period 2013-2015 Freud et al., 2017, found quite similar seasonality for the other sites circumference the Arctic. However with some consistent differences between the sites that are beyond the year-to-year variability due to differences in the proximity to anthropogenic source regions and to the Arctic Ocean sea-ice edge, as well as in the exposure to free tropospheric air and in precipitation patterns. One important conclusion is that aerosol observations from a single Arctic site cannot fully represent the entire Arctic region. Addressing the question of the natural Arctic aerosol sources Dall'Osto et al., 2019, finds 6 different types of size distributions are related to natural sources and processes while only 2 related to anthropogenic sources. Natural particles dominate the summer while the anthropogenic contribution grow during the fall to dominate during the winter and spring as shown in Figure 5.1.2.1.7. Schmeisser et al, 2018, analyzed observations of annual mean scattering and absorption coefficients at 6 Arctic sites finding a seasonality for all sites clearly related to the seasonal variation of particle mass and chemistry (Figure 5.1.2.1.8). Studying the particle influence on clouds. Jung et al, 2018, presents 5 years of measurements from Zeppelin at Svalbard of the number of cloud condensation nuclei at different supersaturation. A clear seasonal dependence is seen, however different at a low

and a high supersaturation (Figure 5.1.2.1.9). At low supersaturation the Arctic Haze period with high concentrations of accumulation particle rich in sulfate show the highest number of CCN, while at higher supersaturation the equally high concentrations during the summer of much smaller particles of mainly biogenic origin show equally high CCN concentrations. Lange et al, 2019 conclude from a similar study on the hygroscopic properties that the long distance pollution aerosol dominate the CCN in Arctic cloud formation during the winter while the natural dominate the summer (see figure 5.1.2.10).

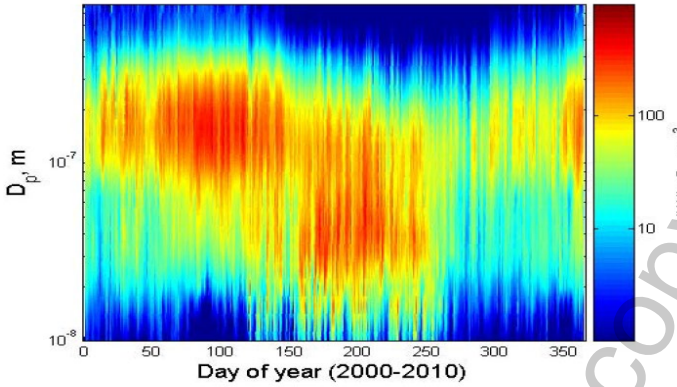

Figure 5.1.2.1.6. Spectral plot of daily average aerosol number size distributions, March 2000–December 2010, measured at the Zeppelin mountain site in Ny Ålsund, Svalbard. Units on x-axis as day of year. (Tunved et al., 2013)

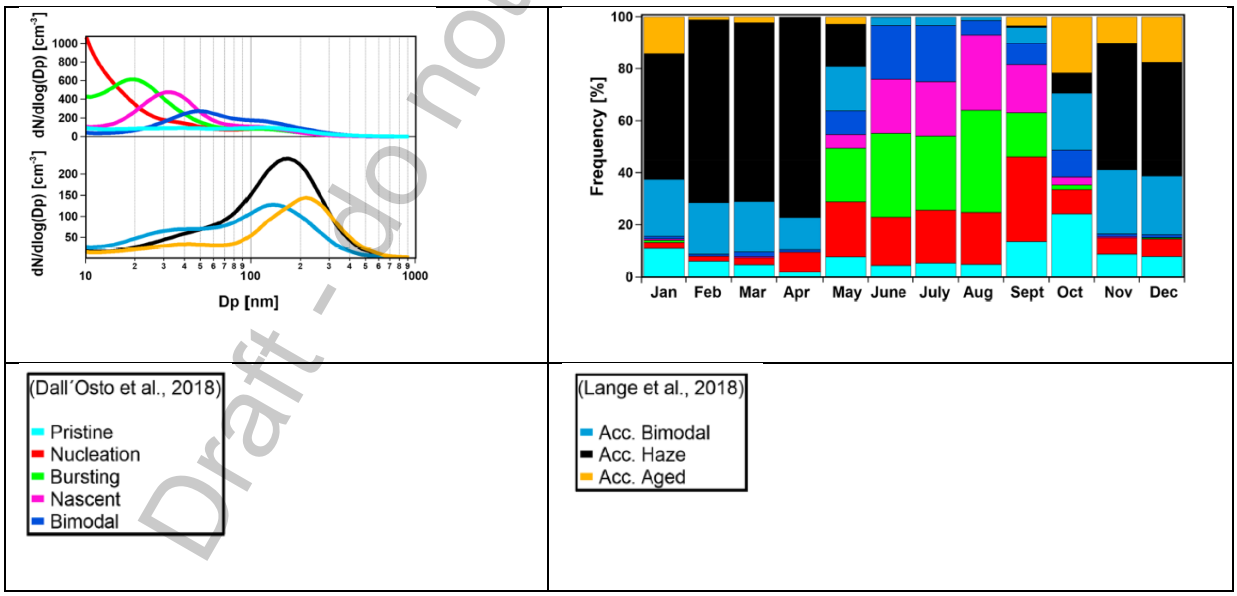

Figure 5.1.2.1.7. Cluster particle size distributions found by k-means analysis. The top left panel are ultrafine aerosol clusters (as reported in Dall'Osto, Geels, et al., 2018), while the

lower left panel show accumulation aerosol mode clusters (as reported in Lange et al., 2018). The right panel show monthly frequency of occurrence of all eight ultrafine and accumulation aerosol clusters. The haze and aged aerosol is interpreted as of air pollution origin while the others are natural.

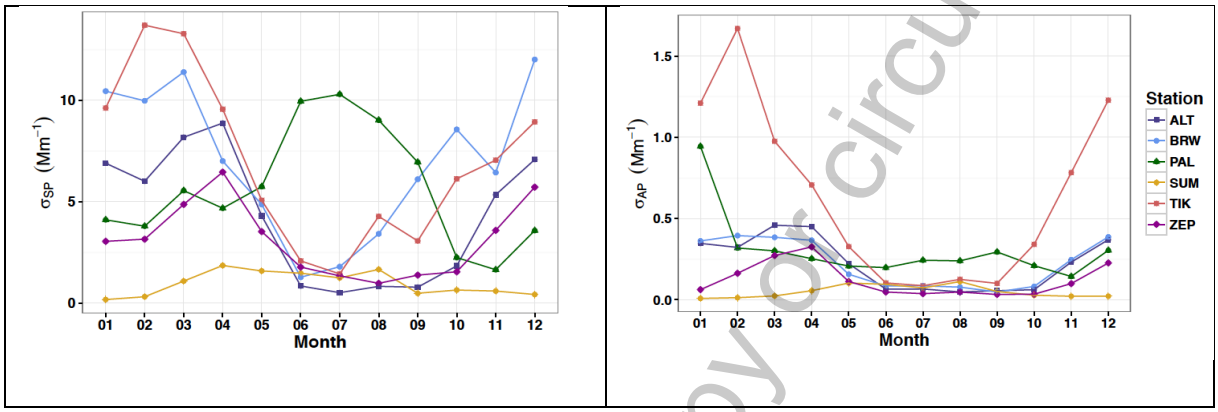

Figure 5.1.2.1.8. Seasonality of the aerosol light-scattering and absorption coefficients (σ_{sp} and σ_{ap}) at 550 nm at Alert (Canada), Barrow (Alaska), Pallas (Finland), Summit (Greenland), Tiksi (Russia) and Zeppelin (Svalbard) shown by monthly medians of scattering and absorption per megameter (Mm^{-1}). Schmeisser et al., 2018

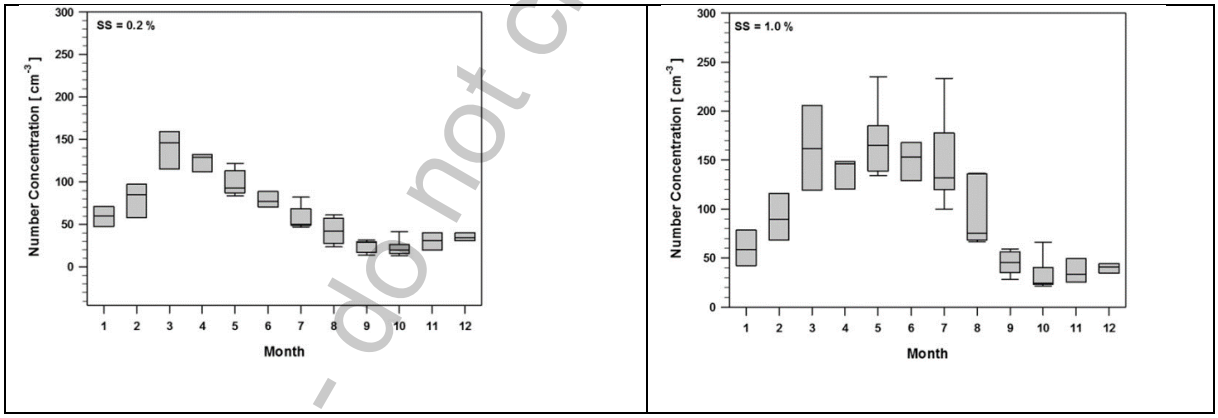

Figure 5.1.2.1.9. Box plot of Monthly median CCN number concentration at various supersaturations (SS): April 2007–March 2013. Jung et al, 2018

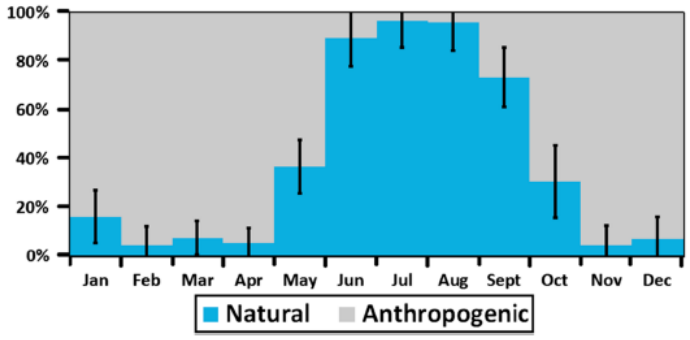

Figure 5.1.2.1.10. Extrapolated monthly contribution of natural and anthropogenic clusters to total ambient cloud condensation nuclei concentration at 0.4% supersaturation. Lange et al., 2019

5.1.2.2 Vertical distribution

Integrated along the entire atmospheric column, aerosol particle load and size distribution not only change as function of location and season, but have been showing decadal changes, indicating a variable influence of emerging sources and transport patterns (Stone et al., 2014). The marked vertical variability of the Arctic Amplification is in part controlled by distribution of the different atmospheric forcers, including aerosol particles (Stjern et al., 2019). It is thus important to understand the processes controlling the distribution of the Arctic aerosol along the atmospheric column. Remote sensing observations, both satellite and ground based, indicate that the highest aerosol concentration in all sectors of the High Arctic and all seasons is observed in the lowest kilometer of the atmosphere (Devasthale et al., 2011; Tomasi et al., 2015; Shibata et al., 2018). However, the seasonal peak of aerosol concentration changes as a function of altitude, indicating the influence of different sources and transport at different altitudes (Pierro et al., 2013; Tomasi et al., 2015; Shibata et al., 2018; Thomas et al., 2019). If remote sensing observations are fundamental tools to monitor the vertical variability of atmospheric aerosol on large spatial and long temporal scale, in-situ airborne aerosol observations provide insights on aerosol physics and chemistry. Validation of remote sensing (lidar) data with in-situ (tethered balloons) experiments has been recently proposed (Ferrero et al. 2019) and paved the way for future developments. More than 20 airborne campaigns focusing on aerosol have been performed since 2007 across the Arctic (Table S1). The spatial coverage of such observations includes the

European Arctic, Greenland, The Canadian Arctic, Alaska, the Arctic Ocean, Iceland and Russia. However, the spatial coverage is not homogeneous, with most of the surveys covering the European and North American Arctic sectors. Only two airborne observations are currently available for the Russian Arctic and Subarctic. Besides the spatial coverage, also the temporal coverage is quite inhomogeneous, with the majority of the observations occurring in April and March. 9 airborne surveys are performed between May and September, while only 3 observations are available in the winter period.

During the Arctic haze period, **black carbon** concentration tends to increase with altitude already within the first kilometer (Ferrero et al., 2016; Markowicz et al., 2017) showing consistent plumes at mid altitudes (McNaughton et al., 2011; Schulz et al., 2019). These plumes, however, appear to have a significantly smaller magnitude and vertical extent compared with the first airborne campaigns performed in the 80' (Stone et al., 2014). It must be noted that improvement of BC-measuring instruments might significantly bias any comparison between recent and more dated observations. The correlation of BC with sulfate and organic aerosol decrease and increase, respectively with altitude (Marelle et al., 2015; Willis et al., 2019) and might indicate differences in source regions. As a matter of fact, long range transport from easterner and southern Asia influences preferentially BC concentration in the mid and high troposphere, while transport from northern Asia (Siberia) increases at lower altitude (Liu et al., 2015; Xu et al., 2017). Moreover, the same studies report that almost the entirety of BC concentration was associated with anthropogenic emission located in the Asian continent rather than open biomass burning. This recent finding is partially in contrast with previous studies reporting open biomass burning episodes to be more important during the Arctic spring (Stohl A., 2006; Kondo et al., 2011; Matsui H. et al., 2011). In fact, biomass burning episodes might control the aerosol concentration and chemical composition at mid altitudes in the European Arctic (Marelle et al., 2015). The mass concentration and number fraction of BC decreases abruptly along the troposphere from spring to summer (Schulz et al., 2019). This is caused by a combination of processes including preferential wet scavenging of BC between source regions and the Arctic (Liu et al., 2015) and inhibited transport from mid latitudes (Bozem et al., 2019). As a consequence, Arctic sources, both anthropogenic and natural, might control the summer BC population. Arctic anthropogenic sources such as shipping and oil-gas extraction have been

shown to enhance BC concentration above the natural background in the lowest atmospheric layer on local and regional scale (Roiger et al., 2015; Ferrero et al., 2016; Law et al., 2017).

Nevertheless, injection of biomass burning in the free troposphere can episodically lead to elevated BC concentration at high altitudes (Roiger et al., 2015; Köllner et al., 2017; Sobhani et al., 2018). Only two aircraft campaigns in the Pacific Arctic sector (HIPPO1 and HIPPO2; Schwarz et al., 2013) and tethered balloon measurements in Svalbard (BC3D; Cappelletti et al., 2020) provides insufficient data to fully assess the influence of source type-region or transport in the Arctic winter.

Mineral dust is a ubiquitous species of the Arctic aerosol population and can be observed from the lowest to the highest layers of the troposphere. In spring, the mass concentration of mineral dust tends to increase with altitude, contributing by more than 80% to the total aerosol mass concentration above 4 km of altitude in the Western Arctic (McNaughton et al., 2011). A similar vertical increase is reported for the winter season in the Svalbard region (Biagio et al., 2018). This vertical trend is mostly caused by the efficient high altitude transport of mid latitude desert dust suspended above Africa and Asia (Groot Zwaaftink et al., 2016). Pure mineral dust plumes have been observed in the north Atlantic above 2.5 km (McAuliffe and Ruth, 2013) and associated with Saharan dust injections above 6 km of altitude over Africa and subsequent northward transport (Francis et al., 2018). Besides long range transport, Arctic and marginal-Arctic dust sources such as glacial and volcanic sediments are becoming more important in recent years (Crusius et al., 2011; Bullard et al., 2016; Groot Zwaaftink et al., 2016). Due to its relatively northern latitude and to its vast desert surface, Iceland represents one of the major sources of high latitude dust (Blechschmidt et al., 2012). Contrary to transported dust, Icelandic aeolian dust, not injected in the free troposphere during volcanic eruptions, has been observed to control the aerosol number concentration in the lowest kilometer of the atmosphere on local scale and regional (Blechschmidt et al., 2012; Groot Zwaaftink et al., 2016, 2017). These Icelandic winter dust storms can lead to dust concentration similar to Saharan conditions (Dagsson-Waldhauserova et al., 2019). However, the largest dust particles, and thus most of their mass, remain confined in the lowest atmospheric layer. Moreover, the episodic occurrence

of rain or snow precipitation can drastically change the intensity and vertical distribution of these dust storms (Dagsson-Waldhauserova et al., 2019). Icelandic dust can, nevertheless, be transported over long distances within the Atlantic Arctic sector (Groot Zwaaftink et al., 2017) and be observed in the lowest atmospheric kilometer over Svalbard (Moroni et al., 2018).

Similar to black carbon, **organic aerosol** (OA) shows a strong vertical variability in both summer and spring. Here are reported the latest results obtained from airborne observations in the Canadian Arctic during the NETCARE project. In spring the concentration of OA increases with altitude, with the mass fraction of OA increasing from approximately 20% at the surface to 40% in the high polar dome (Willis et al., 2019). The correlation of OA with BC also increased from the surface to the free troposphere suggesting the combustion nature of high-altitude OA in spring. Nevertheless, it is impossible, at the moment, to clearly distinguish the influence of source region, source type, chemical processing and wet removal or cloud processing during transport in the spring period (Abbatt et al., 2018). Although recent studies indicates that natural Arctic emissions represent an important contributor to surface aerosol population in summer (Collins et al., 2017; Dall´Osto et al., 2017, 2018; Leaitch et al., 2018; Croft et al., 2019), little is known about the vertical extend of such emission. In pristine summer conditions, the enhanced concentration of ultrafine particles (Burkart et al., 2017) and organic aerosol, trimethylamine and methane sulfonic acid (Willis et al., 2016) in the marine boundary suggests the local and marine origin of these particles. As a matter of fact, dimethyl sulfide, the oxidation product of methane sulfonic acid, and trimethylamine are found to be enriched in the low marine boundary layer and to be associated with air masses with long residence time within the Arctic region (Ghahremaninezhad et al., 2017; Köllner et al., 2017). In the absence of coarse mode aerosol, organic-rich ultrafine particles are found to correlate with the concentration of cloud condensation nuclei, suggesting that particles of marine origin might play a relevant role into cloud activation (Willis et al., 2016; Leaitch et al., 2016; Burkart et al., 2017). Currently, no vertical observations of organic aerosol are available in winter time.

The **vertical observations of aerosol physical properties** such as size distribution, absorption and scattering coefficient, water and ice activation are not performed

systematically but mostly focus on case studies. Is, hence, difficult to differentiate the influence of anthropogenic and natural sources. Here, an overview of both old and recent studies reporting observations of aerosol physical properties are summarized. Remote sensing indicate that vertical distribution of aerosol particle diameter changes drastically during seasons (Shibata et al., 2018). Although, in spring, strong variability is observed already in the first kilometer as function of atmospheric stability (Ferrero et al., 2016), the mean diameter of both total aerosol and black carbon slightly decreases with altitude (Shantz et al., 2014; Schulz et al., 2019). Nevertheless, the episodic influence of biomass burning plumes leads to a shift of size distribution to larger diameters at high altitude (Brock et al., 2011; Matsui et al., 2011; Moore et al., 2011; Quennehen et al., 2012), while bimodal distributions have been reported for anthropogenic plumes, some with enhanced Aitken mode particles (Quennehen et al., 2012) other with enhanced coarse particles (Matsui et al., 2011). In summer, the combination of new particle formation and wet removal might be responsible for the enhancement and depletion of ultrafine and coarse mode particles in the boundary layer, respectively (Kupiszewski et al., 2013; Burkart et al., 2017). Although very limited, the studies investigating the vertical distribution of cloud activation nuclei (CCN) generally indicate a concentration increase with altitude in spring and early summer (Hegg et al., 1995; Yum and Hudson, 2001; Moore et al., 2011). The aerosol activated fraction is found to increase above 1 km altitude during the occurrence of pollution plumes of both anthropogenic and natural origin (Moore et al., 2011) and fresh biomass burning plumes (Lathem et al., 2013). Although Arctic aerosol of marine origin has been shown to be ice active, the observation of vertical distribution of arctic ice nucleating particles are currently limited to few airborne observations in Alaska and do not allow differentiate nor quantify the impact of anthropogenic and natural sources (Rogers et al., 2001; Prenni et al., 2009; McFarquhar et al., 2010).

5.1.2.3 Observations of aerosol components in snow

BC and dust measurements are of crucial interest in the snowpack and in ice as the interaction between the cryosphere and atmosphere is of high importance (Flanner et al. 2007, Boy et al. 2019) and can only be understood when relevant data in both compartments are available. Current understanding of the abundance and effects can be

put on firmer grounds also using modeling (Chapter 6 of this report), e.g., for their albedo and melt effects as well as for their origin (e.g., Evangeliou et al. 2018, Meinander et al. 2020), as assessed recently by IPCC (2019). One should also consider that BC and mineral dust may mutually interfere in various measurement techniques which poses a question on the ability to disentangle their individual effects and relative abundances. There is evidence for a high spatiotemporal variability in the observed concentrations of BC and dust in the Arctic cryosphere (Meinander et al. 2020, Spolaor et al. 2017). Mass concentration of BC in snowpack can be measured by the Integrating Sphere/Integrating Sandwich spectrometer (ISSW) method, by the SP2 combined with a nebulizer, or by recording the mass fraction of C evolved from sample filters (Elemental Carbon, EC) using the thermo-optical transmittance method (see Chapter 4 for a description of the methodologies). A systematic harmonization of the techniques and dataset is still missing and is highly recommended (Svensson et al. 2019) since the method-to-method variability can be as high as a factor 2.

Snow sampling for **BC content** has only been carried out at a limited number of locations. In North Greenland at Villum Research Station snow sampling has started in 2016 and carried out on a weekly basis to investigate for EC content. Starting in 2007, the NPI Stockholm University, have a program of snow monitoring for elemental carbon (EC) in snow at two locations on the outskirts of Ny Ålesund which was extended in the 2016 at 22 sites on 7 glaciers of Spitsbergen and Nordauslandet (Zdanowicz et al., in preparation). No long-term trends between 2011–2018 were found. C_{snow}^{EC} near Ny Alesund can be reasonably predicted from BC aerosol data from Zeppelin Observatory by using modeled precipitation and BC snowfall washout ratios between 10–300, which are broadly consistent with values reported by Gogoi et al. (2018) for the area. The calculated mass loadings of EC in the late winter snowpack (L_{snow}^{EC}) were 0.1–16.2 mg m^{-2}, and close to, or lower than, those found by Forsström et al. (2009, 2013) at many of the same sites in 2007-09. There were no systematic variations in C_{snow}^{EC} with latitude or longitude across Svalbard. Mass accumulation of EC in snow appeared to be equal in autumn and spring months, and increased non-linearly with elevation and snow accumulation, with dry deposition likely playing only a minor role. The estimated area-averaged EC load across Svalbard was 1.8 mg EC m^{-2}, and the monthly mean accumulation rate was ~0.2 mg EC m^{-2} mo^{-1} for the winter 2015-16 (September to April). Comparing findings (see Figure 5.1.2.3.1, Zdanowicz et al., in

preparation) from this survey and from the NPI snow monitoring program near Ny Ålesund with data from earlier, comparable studies confirmed the existence of a longitudinal gradient in EC deposition across the Arctic and sub-Arctic, with the lowest C_{snow}^{EC} found in the western Arctic (Alaska, Yukon) and central Greenland, and the highest in northwestern Russia and Siberia. (***Pallas, Finland, a ten year record of continuous snow sampling???*** ref. Svensson et al.?) In Sodankylä, Finland, a five years record of weekly snow sampling and analysis of BC in surface snow is available (Meinander et al. 2020). These data, with a median value of 21 µg L^{-1}, show a large variability in surface snow BC concentrations from week to week and seasonally, due to deposition of long-range transported black carbon and post-depositional snow processes. In turn, the size distribution of BC in snowpack has been measured with the SP2 method . Systematic campaigns with SP2 were carried out in six Arctic regions (Finland, Alaska, North and South Siberia, Greenland, and Spitsbergen) in early spring during 2012–2016 (Fig. 5.1.2.3.2, Mori et al., 2019). Size distribution of BC in Greenland depended little on altitude and its lateral distribution of CMBC was largely uniform (average 0.81 ± 0.46 µg L^{-1}).

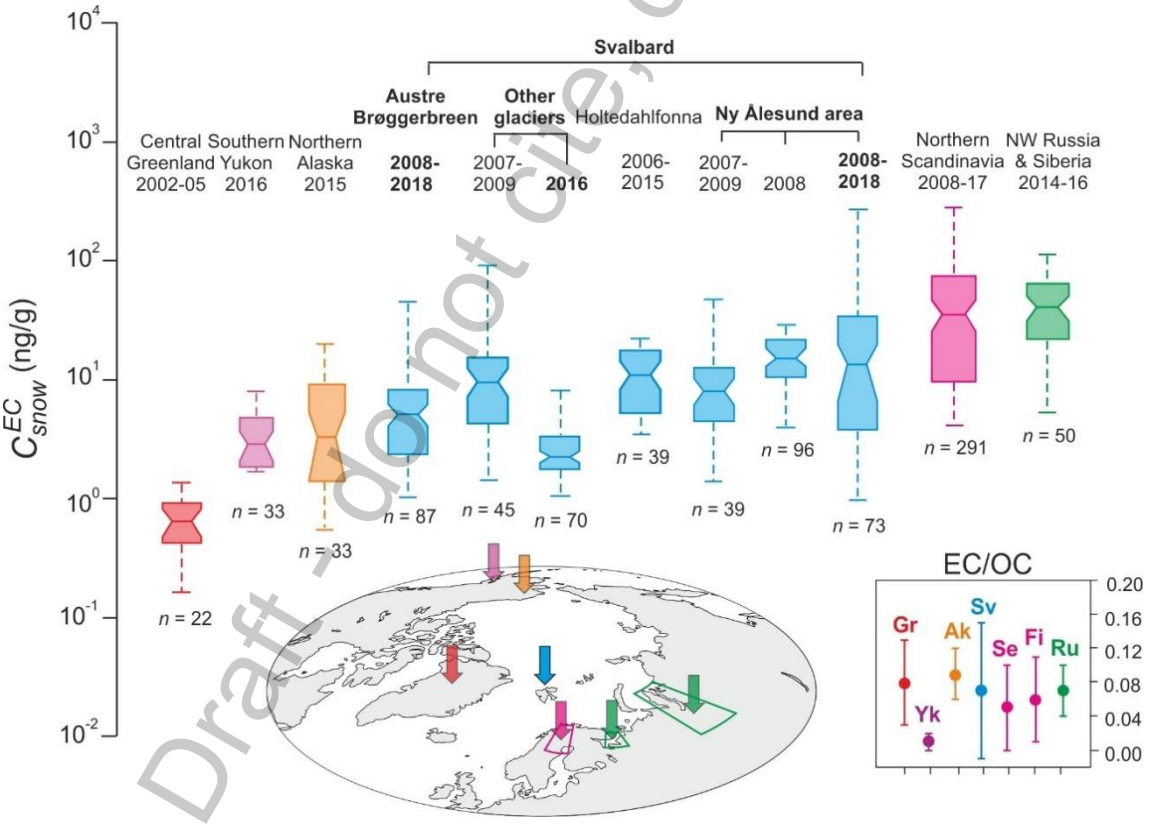

Figure 5.1.2.3.1. in winter/spring snow of Svalbard reported in (Zdanowicz et al., 2020) (bold headers; values >1 ng g^{-1}), compared with winter/spring snowpack data from other circum-Arctic sites, color-coded by region. Inset at far right: mean EC/OC (± s.d.) in snow from regions identified in the plot: Greenland (Gr), Yukon (Yk), Svalbard (Sv), Sweden (Se), Finland (Fi) and Russia (Ru). Only data obtained by thermo-optical analysis are included, although protocols differ between studies. Published data sources for Svalbard glaciers: Forsström et al. (2009, 2013) and Ruppel et al. (2017); Ny Ålesund and Longyearbyen: Aamaas et al. (2011); Greenland: Hagler et al. (2007); Alaska: Dou et al. (2007); northern Scandinavia: Forsström et al. (2013), Meinander et al. (2013), Svensson et al. (2013, 2018), and Zdanowicz, unpublished data; Russia and Siberia: Evangeliou et al. (2018); Yukon and Sweden: Zdanowicz, unpublished data. Data from Greenland and the Yukon span 3–6 years of accumulation in snow, while data from Holtedahlfonna span an estimated ~8 years (2006-14). Five samples with > 140 ng g^{-1} taken near Russian towns (Tomsk, Archangelsk) were excluded from the dataset by Evangeliou et al. (2018).

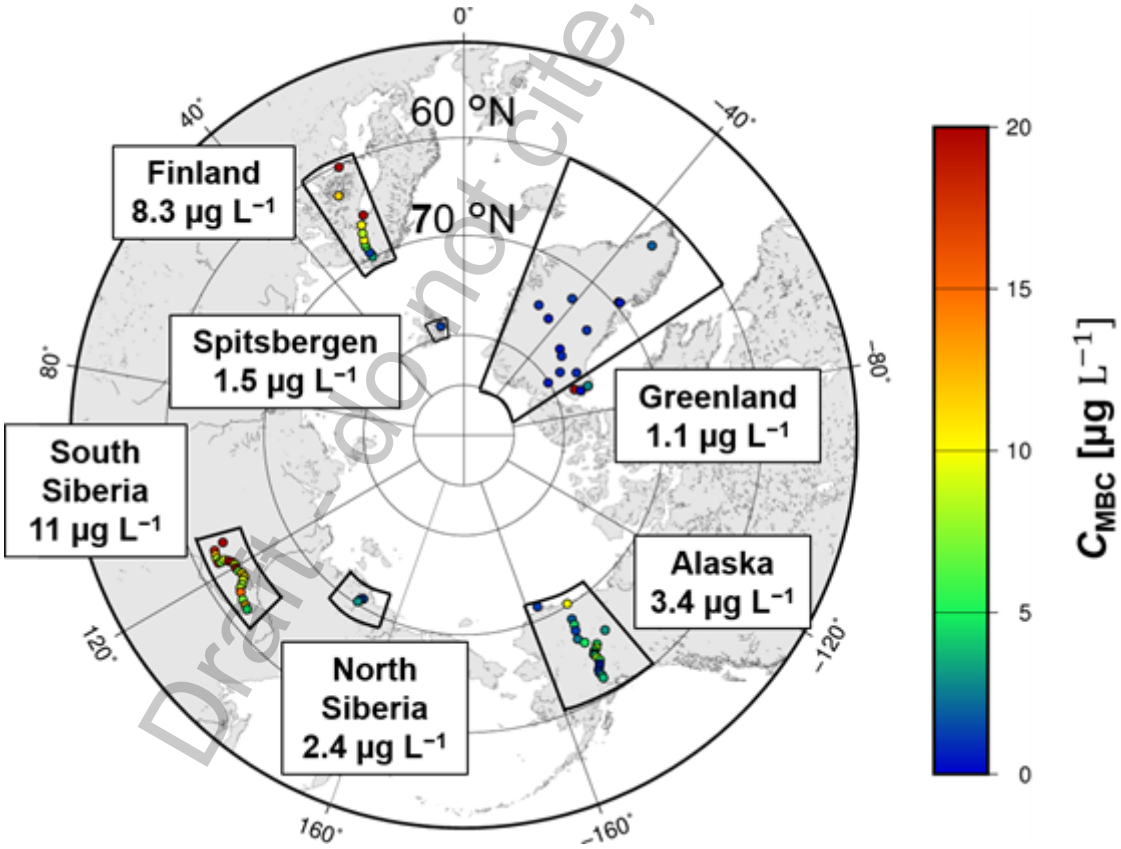

Figure 5.1.2.3.2. Map showing locations of snow samples. Circle color represents BC mass concentration in snowpack, CMBC. Median values of CMBC are also shown for each region. From Fig. 1 of Mori et al. (2019). Details of snow sampling conditions are given in Table 4 of Mori et al. (2019).

Kylling et al. (2018) estimate a surface radiative effect of 0.292 W m^{-2} caused by **dust deposition** (largely transported from Asia) to Arctic **snow** approximately half of the black carbon central scenario estimate of Flanner et al. (2007). Due to the temporal and spatial variability, **light absorbing dust particles** can contribute to interannual fluctuations of seasonal snow melt rate (Painter et al. 2018). Dust-cryosphere interactions in the Arctic have recently gained more and more attention (Boy et al. 2019, Dagsson-Waldhauserova & Meinander 2019, Dagsson-Waldhauserova & Meinander 2020, Dagsson-Waldhauserova et al. 2015, Meinander et al. 2014, Peltoniemi et al. 2015, Svensson et al.), where dust on snow most often increases melt, but can also insulate and decrease melt (Wittmann et al. 2016, Möller et al. 2016). Additionally, a reduction in snow density of surface snow due to light absorbing impurities has been documented (Meinander et al., 2014; Skiles and Painter 2017). In addition to natural dust, dust in Arctic snow can originate from anthropogenic sources, such as from an active mine (Khan et al., 2017). According to Dumont et al. (2014), the observed decline of Greenland's albedo over the past decade has been attributed to an enhanced growth of snow grains as a result of atmospheric warming but their analysis of remote sensing data indicates that the springtime darkening since 2009 stems from a widespread increase in the amount of light-absorbing impurities in snow, as well as in the atmosphere. They suggest that the transport of dust from snow-free areas in the Arctic that are experiencing earlier melting of seasonal snow cover as climate warms may contribute to sources of impurities. Medium evidence and high agreement to support the melt rate effect of light absorbing particles of **BC, OC and dust** has been recently recognized (IPCC 2019).

5.1.3. Historical and present day trends

5.1.3.1 Present day trends

(include a reference to the supplementary)

Long-term time series of eBC are available for stations, i.e. Utqiaġvik, Alert, Kevo and Zeppelin shown in Fig. 4.1.1. All four stations show a decline of eBC concentrations, mainly due to decline in emissions in the source regions specifically, Eurasian regions. Most evident changes have been measured at Alert and Kevo with 110 ng m^{-3} in 28 years (52%) and 188 ng m^{-3} in 47 years (72%) change during the haze season (January to April). The eBC measurements at Kevo are the longest since 1964 and measured highest among all locations. In the mid-sixties, higher concentrations of BC were due to wood burning, concentrations decreased sharply from 1970-1980 and systematic decline in the BC values until 2010 (Dutkiewicz et al., 2014). Kevo is also in closer proximity to the source regions than Alert and has greater influence from southern Russia and Kola Peninsula, regions of former soviet union and Europe (Dutkiewicz et al., 2014). Sharma et al. (2019) reported a 52 % decline in eBC concentrations since 1989. At Barrow, the decrease is about 39 ng m^{-3} in 28 years for the same season. It must be noted, however, that from 2008 onwards the eBC concentrations seemed to increase again at Barrow only. Concentration levels are still much below the ones in the 90s, but markedly higher than during the early 2000s. Haze period levels vary between 35 and 85 ng m^{-3} at all locations. These observations are in line with more vigorous emission reductions in the Former Soviet Union (FSU) and Europe in early 90s rather than later in the 2000s. Summer concentrations have decreased mildly at Barrow with 12 ng m^{-3} in 28 years. The increase in BC emission in Asia until 2010 due to increased economic development (reference) does not influence the eBC levels at all surface sites due to its influence in the upper layers. The aerosol burden as a measure of AOD showed declining trends over per year and values are around 10 ng m^{-3}. (Stone et al., 2014)
At Alert no significant change in eBC levels during summer can be observed. At Kevo, the decline is at 3 ng m^{-3} per year. At Zeppelin, there is no decline in eBC during the haze season between 2001 and 2017, with values ranging around 35 ng m^{-3}. Summer values decreased by about 1.5 ng m-3 per year, now staying below 10 ng m^{-3}. The eBC concentrations are generally lower at Zeppelin compared to Barrow and Alert. At Gruvebadet, the time series of eBC are short but we still calculated trends. But the eBC concentrations measured around 70 ng m^{-3}, while summer values are around 30 ng m^{-3}. Values at Zeppelin are much lower despite the close proximity of Zeppelin to Gruvebadet but the former is about 400 m higher. Potentially more local influence can be observed at Gruvebadet. For Tiksi, we also provided

7602 temporal trends in spite of the short time series. What is noteworthy are the generally
7603 higher concentration of eBC (note the different scale) and seasonal differences are most
7604 pronounced at this station. Summer levels are between 10 and 40 ng m^{-3}, comparable to the
7605 haze levels at the other stations.

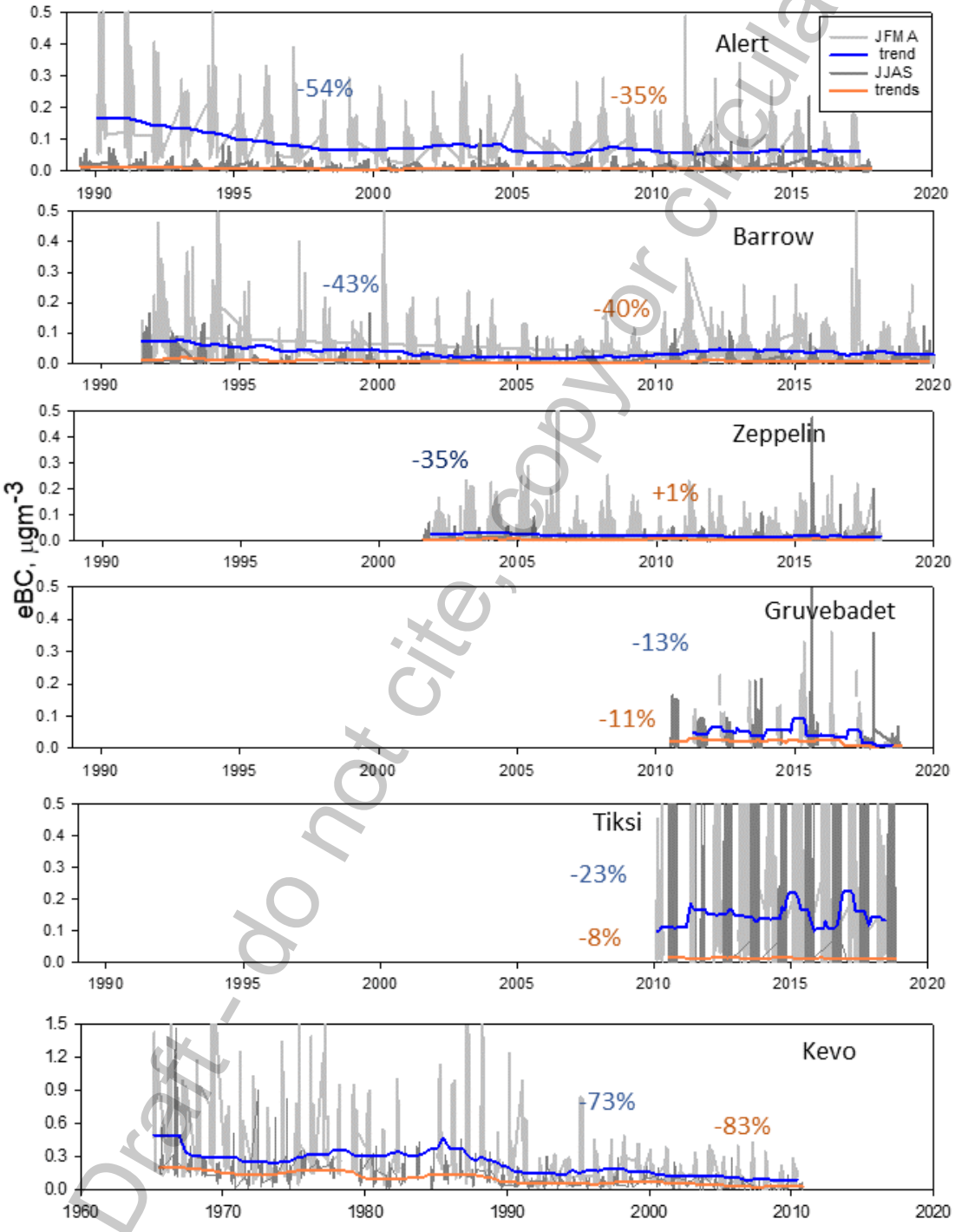

7606

7607 Figure 5.1.3.1.1: Long term trends in eBC at various Arctic locations (data source: EBAS +...).

7608

The **long-term frequency of atmospheric dust** observations in Iceland during 1949–2011, based on conventionally used synoptic codes for dust observations together with re-suspension of volcanic materials and dust haze (Dagsson-Waldhauserova et al. 2014), indicated 135 dust days annually (Fig. 5.1.3.1.2). The position of the Icelandic Low determined whether dust events occurred in the NE (16.4 dust days annually) or in the southern (S) part of Iceland (about 18 dust days annually). The decade with the most frequent dust days in S Iceland was the 1960s, but the 2000s in NE Iceland. A total of 32 severe dust storms (visibility < 500 m) were observed in Iceland with the highest frequency of events during the 2000s in S Iceland. The Arctic dust events (NE Iceland) were typically warm, occurring during summer/autumn (May-September) and during mild southwesterly winds. The subarctic dust events (S Iceland) were mainly cold, occurring during winter/spring (March-May) and during strong northeasterly winds. About half of the dust events in S Iceland occurred in winter or at sub-zero temperatures. The study showed that Iceland is among the dustiest areas of the world and that dust is emitted year-round (Dagsson-Waldhauserova et al. 2014).

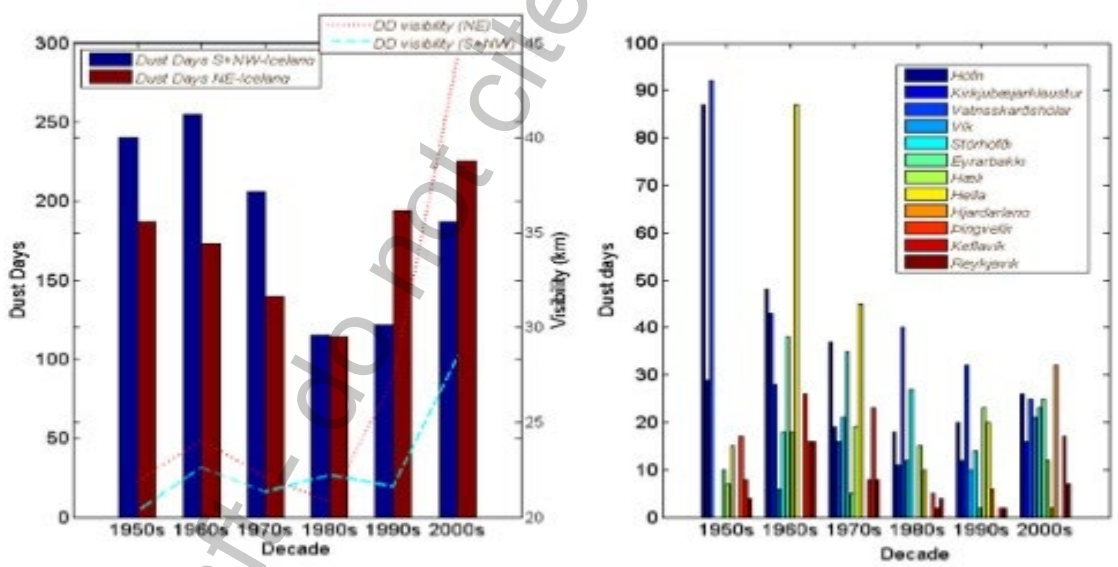

Figure 5.1.3.1.2. Icelandic data on dust events for 1949-2011.Left panel: total number of dust days, all stations combined (blue bars for southern and northwestern Iceland, brown bars for northeastern Iceland). Lines represent mean visibility (blue for S, brown for NE Iceland). Right panel: individual stations in south Iceland sorted by decade. (Fig.2 of Dagsson-Waldhauserova et al. 2014).

During the haze season, particulate **sulfate** concentrations, Figure 4.1.3.1 at Alert have decreased steadily until the end of the nineties, in line with North American and Eurasian emission policies (Sharma et al., 2019) and then kept constant between 0.6 and 1.0 ug m^{-3} since then. Overall, particulate sulfate has decreased by about 0.035 ug m^{-3} per year (49%) since 1980. Other locations have also shown declined sulfate levels by as much as 53% at Zeppelin with the greatest change occurring in the 2000s. Other changes are by -37% Utiquavig and Villum since the 1990s and around -20% at Gruvebadet and Thule locations. Summer time sulfate values have also declined at Alert(-12%), Thule (-39%) and Villum (-54%) while the trend in sulfate was positive at Utquagvik (18%), Gruvebadet (27%) and Zeppelin(10%). Note that the enhancement of sulfate in 2014 at Alert and Barrow originated from a Holuhraun Fissure volcanic eruption in Iceland that started in Sept and lasted until May 2015. At Villum research station concentrations are similar to Barrow and there seems to be a decline for the haze season since 2008.

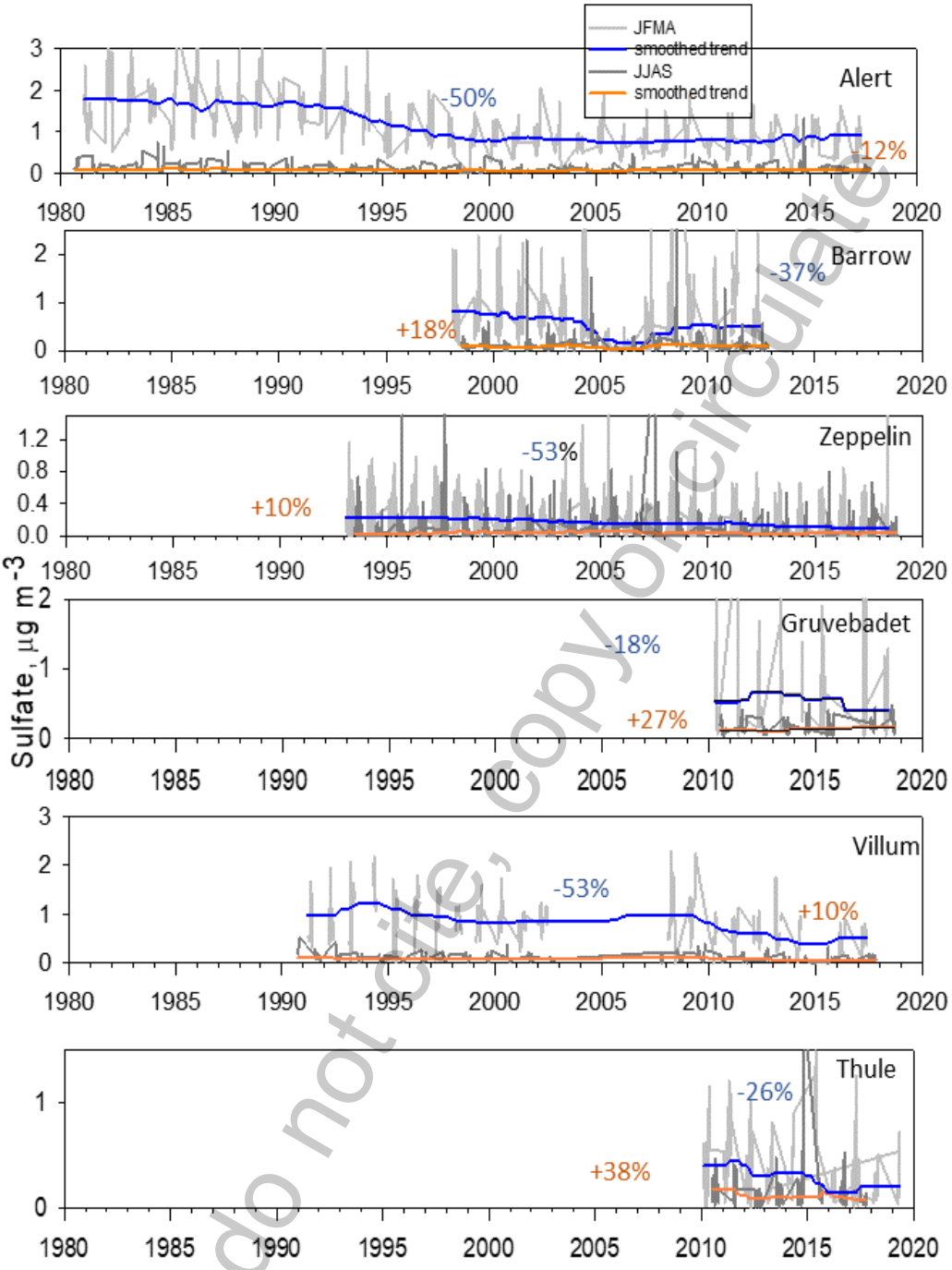

Figure 5.1.3.1.2: Long term trends in the aerosol sulfate concentrations at various Arctic stations with different time-periods. Data source: EBAS and personal communication with the PI of the station.

Particulate **nitrate** measured a positive trend different from sulfate and eBC at Alert, as shown in Figure 4.1.3.2. There was a change at Alert of +25% and Utqagvik of +47.5% in nitrate during the haze season. These positive trends in nitrate were also measured during

the summer time at all locations except for at Thule. While emissions of nitrogen oxides have declined by 40% since the early 80s in Eurasia, the higher particulate nitrate can be explained by decreasing aerosol acidity, i.e. less particulate sulfate, and hence enhanced partitioning of gaseous nitric acid into the particle phase (e.g. Sharma et al., 2019). Also during the cold season, nitrate partitions more readily onto the particle phase than during the warmer season because of volatility dependence on the temperature. At Villum the overall trend is positive and nitrate levels began to decline slightly since 2008 from early 2000 values.

A consequent change in aerosols acidity due decline in sulfate aerosol concentrations and ammonium concentrations have significant influence on the neutralization capability of the Arctic atmosphere (e.g. Sharma et al., 2019). There has been a shift in neutralization from sulfuric acid to ammonium sulfate particles, due to decline in SO_2 emissions relative to ammonium emissions in the source regions.

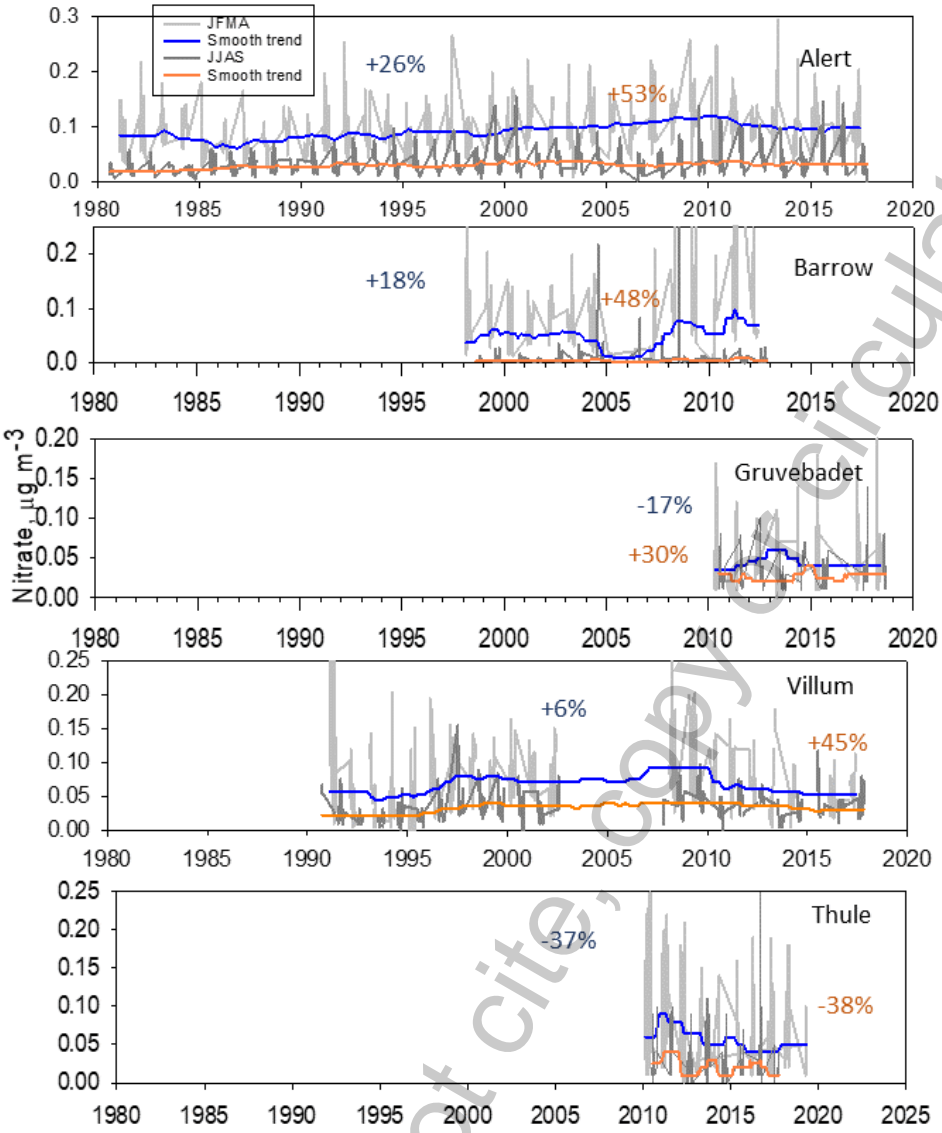

Figure 5.1.3.1.3 Trends in the aerosol nitrate concentrations at various Arctic stations. (data source: EBAS and personal communication with the PI of the stations as mentioned in the acknowledgement).

Mt. Zeppelin provides a unique long time record for **aerosol size distribution** since 2000 which can be used for long term trends. It shows a clear decrease of particles slight larger than 100 nm, i.e. accumulation mode particles typical for an aged pollution aerosol, during the Arctic Haze period, showing a decrease of up to 9% year. This reflects the significant decrease in sulfur emissions from the Eurasian sources also seen in the sulfur concentrations. Similar but less decrease show in the winter aerosol reflecting as well a decrease in emissions. While during the summer an increase in the nucleation and Aitken

size particles, i.e. particles less than 50 nm in size. This is interpreted as an increase of production of natural particles probably due to larger open sea areas providing precursor gases and particles. Sharma et al., 2012 observed increasing MSA concentrations at Ny Ålesund, Alert and Barrow since about 2000 implying higher production of sulfuric acid which is an important agent for new particle formation.

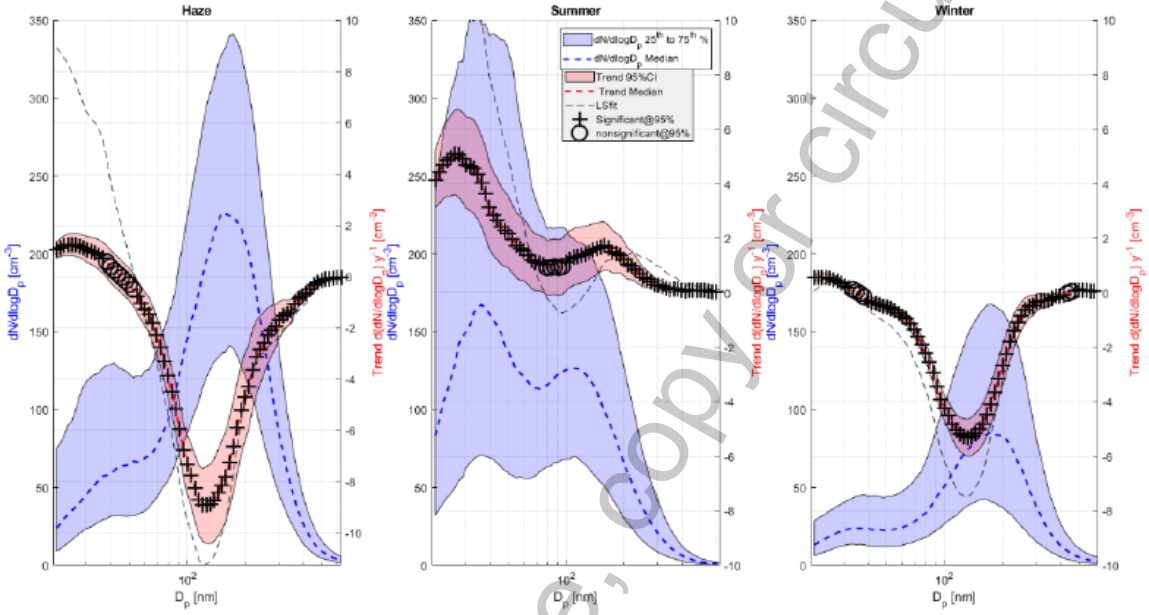

Figure 5.1.3.1.4 analysis of 20+ years of data from Zeppelin (unpublished data by Peter Tunved).

Aerosol optical properties are relevant parameters that determine the radiative forcing of the particulate matter. In-situ ground based measurements of the longest time series of light absorption, aerosol scattering, and single scattering albedo - the ratio of light scattered to total light extinction are presented here. The scattering values depend on the aerosol physical properties, chemistry and relative humidity while absorption depends on the amount of absorbing components present (black carbon, dust and other absorbing components) in the sample as it is the filter based measurement.

20 years of observations at ZEP of scattering and the Ångström exponent reveals an increase in scattering and a decrease in the ångström exponent (Figure xxx). This exponent depends on the size distribution such the small it is the more of coarse particles contribute to the

7699 scattering. So the observed trends show that more particle and especially more large
7700 probably super micron particles contribute to the scattering.
7701
7702
7703

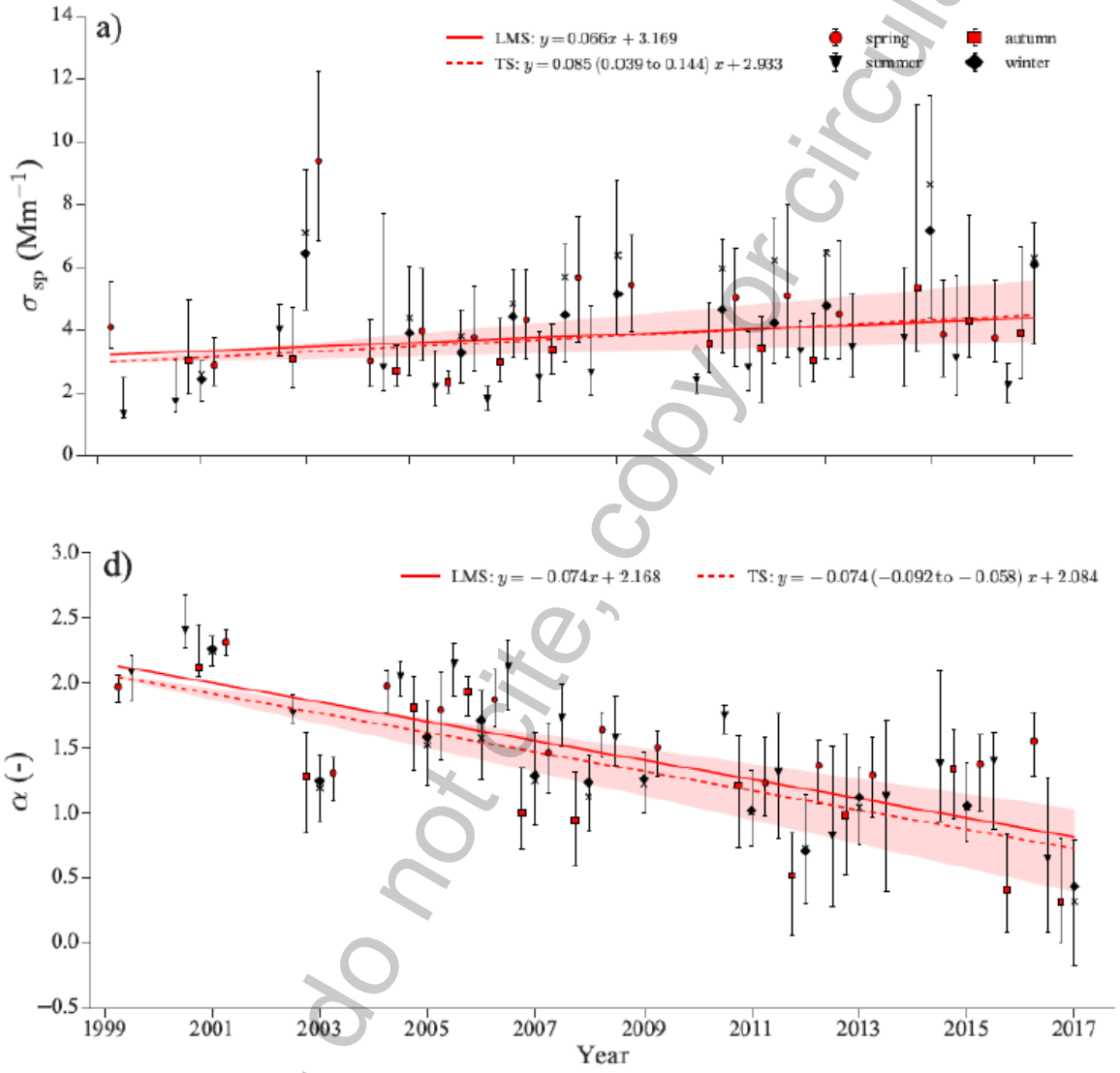

7704

7705 Figure 5.1.3.1.5. Long-term trends of the seasonal medians for a) the particle light scattering
7706 coefficient (_ = 550 nm) b) the particle light backscattering coefficient (_ = 550 nm) c) the
7707 hemispheric backscattering fraction (_ = 550 nm) d) the scattering Ångström exponent (_1 =
7708 450 nm, _2 = 550 nm). The seasonal medians are denoted by their respective symbols. The
7709 error bars denote the length of the 25th and 75th percentile values. The seasonal mean is
7710 given by the cross. The solid and dashed red lines represent the least mean square (LMS)
7711 and Theil-Sen slope (TS) of the seasonal medians, respectively. The red shaded area denotes

the associated 90% confidence interval of the TS slope. (Heslin-Rees et al., 2020, From a polar to a marine environment: has a changing Arctic led to a shift in aerosol optical properties? Manuscript to be published)

Heslin-Rees et al, 2020, have through a trajectory analysis for the same time period found a shift to higher windspeeds and more prevalent SW winds found an possible explanation for the increase in supermicron particles in that the air masses pass over more open sea area picking up more sea spray. This shift in air mass history fits with a more prevalent air mass transport into the Arctic with climate change as suggested by climate models (Krishnan et al., 2020).

The seasonal **scattering coefficients** are measured (Figure 4.5.1) higher during the Arctic haze season at Utqiaġvik (Barrow), Tiksi, and Alert, while found higher in the summer at Pallas and Summit. At Summit, the influence of forest fires could be a plausible cause (ref) and at Pallas, one hypothesis is signal enhancement from increased secondary organic aerosol production from the boreal forest with warmer temperatures in recent years (need a ref).

Aerosols scattering have had decreasing trends in the haze season (JFMA) at all locations except at Zeppelin and Summit stations over the past decade, Figure 4.1.5.1. Both of these stations are at higher elevation (500m and 3000m). Positive (up to 28%) and statistically significant (ss) trends are found for all the stations during summer except for Pallas location. Collaud Coen et al. (2020) recently showed different trends in scattering measured over global stations that showed positive trends are in the minority, that makes change in scattering and hence aerosol properties important in the Arctic.

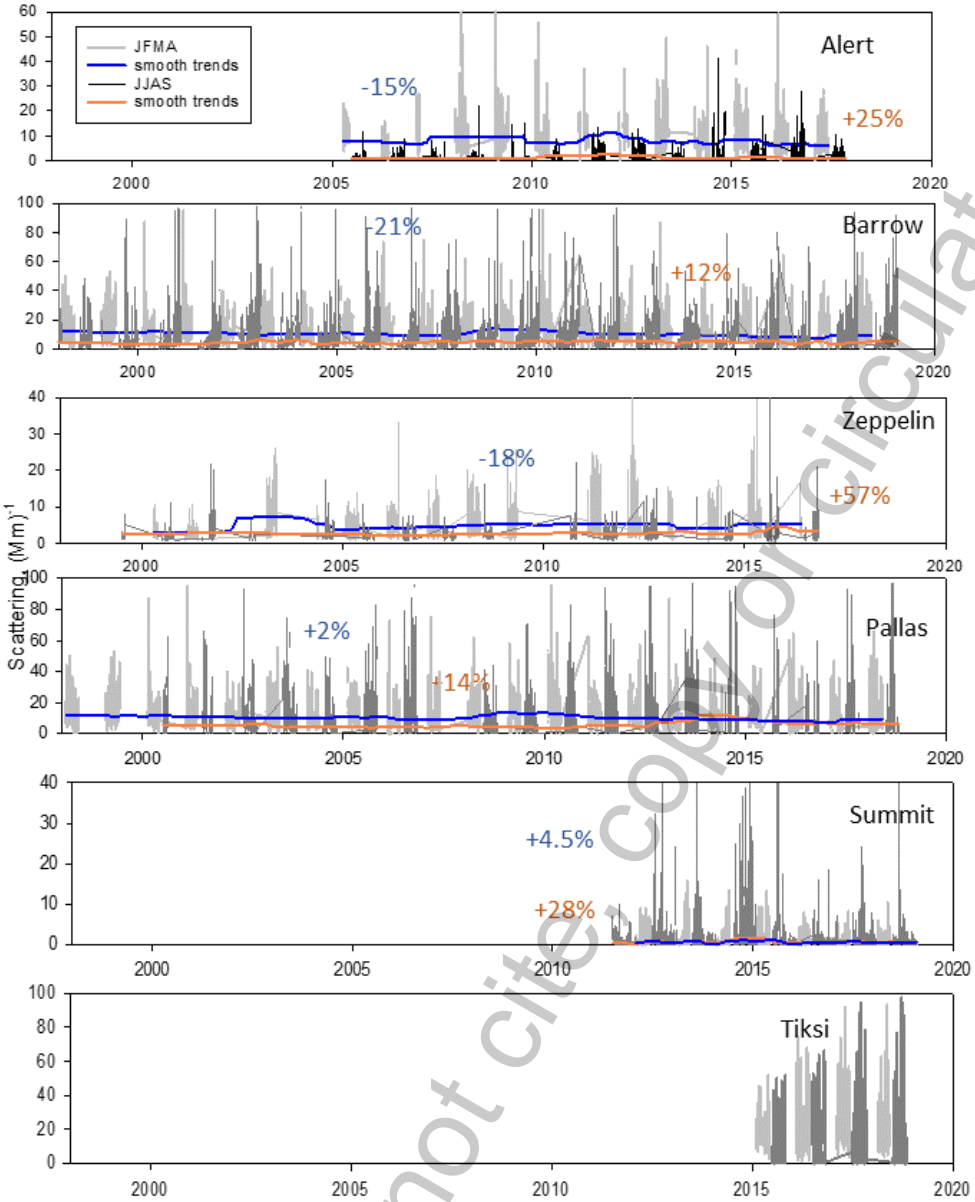

Figure 5.1.3.1.5. Seasonal scattering coefficients for six Arctic stations at 550 nm in Mm^{-1}. Haze is Jan – Apr and summer Jun – Sep. (Data source: EBAS and personal communication with the PI of station).

The seasonal amplitude of **absorption coefficients** as shown in Figure 4.1.5.2 vary at all locations and have a maximum during JFMA and minimum during the summer JJAS for all stations except for Summit possibly due to forest fires influence which is dominant at an altitude between 3-4 km (ref). At Zeppelin, the seasonal cycle has become less intense since 2007 and there are hence smaller absorptions coefficients measured now and greatest change during summer (-43%) than about 10 years ago.

Our analysis indicate that ss trends in absorption coefficients are negative during haze season at Alt, Utqiaġvik, Summit (-27%, -22%, and -3%) while positive trends Tiksi location (10%). During summer (JJAS) period absorption has decreased at all locations with largest decline at Zeppelin station.

For all year data, Collaud Cohen et al. (Submitted) showed that trends are negative at Barrow between -0.02 and -0.002 Mm m^{-1} per year and positive for Alert between 0.002 and 0.02 Mm m^{-1} per year. Globally, Alert was the only location with a statistically significant positive trend not related to any separately seasonal trends in support. At Tiksi, absorption trends were negative (-0.08 $(Mm)^{-1}$ per year).

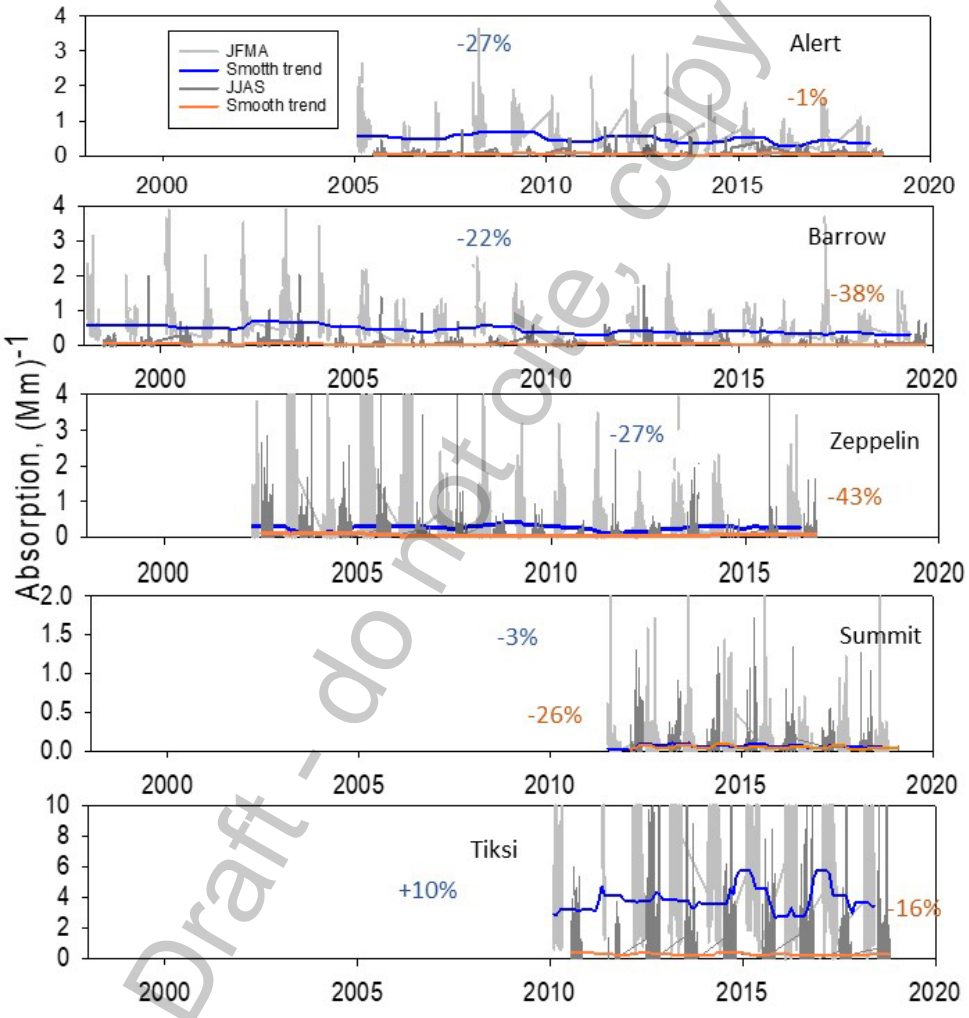

Figure 5.1.3.1.5: Seasonal trends in aerosol absorption coefficients at 550 nm measured at various Arctic locations.(Data source: EBAS and personal communications with the PI of the station).

The measurements of **single scattering albedo (SSA)** determine how absorbing an aerosol is with respect to its scattering components. A white aerosol measures SSA of 1 and this value decreases as the aerosol becomes more absorptive. Figure 4.1.5.3 shows trends in SSA for the haze and summer periods. The aerosols are less absorptive during Arctic haze period than in the summer time at all locations with an exception of Summit where the seasonality is opposite to other locations. The decadal change over the haze period is ss positive at Utqiaġvik, Alert, Summit and Zeppelin (0.0019, 0.033, 0.0013, 0.0115) and only show positive trends at Alert and Summit (0.0031 and 0.0035). This suggests that aerosol are becoming less absorptive at the four locations. In term of trends in 34 year so aerosol chemistry (Sharma et al.,2019), all aerosol components have decline at Alert except for NO_3 and sea-salt (NaCl) where there are increasing trends in both. This indicates that chemistry of the Arctic aerosol might be changing with decreasing acidity and increased sea-salt. This consequently could change the optical properties of the aerosol.

Collaud Cohen et al. (in prep) found a positive summer trend of SSA for the past 10 years, which seems to average too much about the marked variability in the past years. At Alert, the trend is positive for both seasons, and the eruption signal of the Holuraun volcano in 2014 stands out (Sept. 2014 to May 2015). Zeppelin shows extremely high variability in the SSA between 2001 and 2016 with rather lower values between 2004 and 2006. Summer SSA values are generally higher than haze period SSA values.

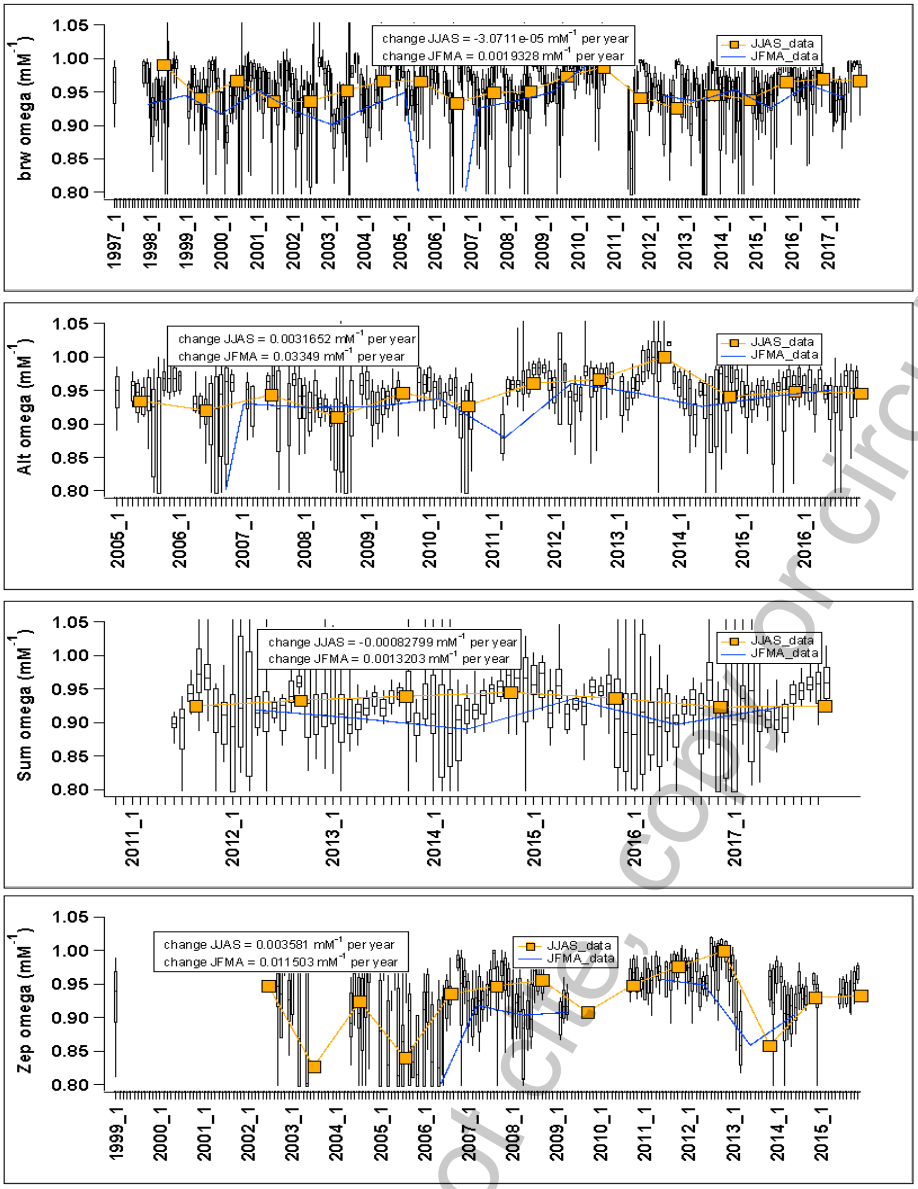

Figure 5.1.3.1.5: Seasonal trends in single scattering albedo of the aerosol at various Arctic measurement stations. (Data source same as for absorption and scattering measurements)

5.1.3.2 Ice cores

(include a reference to the table and map in the Supplementary)

Data from recent publications provide a regionally differentiated perspective on BC and sulfate deposition (Osmont et al., 2018;Zdanowicz et al., 2018;Ruppel et al., 2014;McConnell et al., 2007) across the Arctic. Figure 5.1.3.2.1 shows trends in concentrations (ng.g-1) and Figure 5.1.3.2.2 depositional fluxes in sulfate and refractory BC. Figure xx indicates the

geographical locations of the ice cores in Greenland (6 ice-cores), on Svalbard (1) and on Devon Island, Canada (1).

The ice-core concentrations of BC were more variable than sulfate during 1750 to 2000. All ice-cores from Greenland have similar common shape between 1880 and 1950 where **BC** concentrations increased followed by a sharp drop in BC concentrations until 2000, with exceptions for ACT11D where onset of higher BC concentrations were in early 1800s and NGT_B19 where levels remained higher until the 2000. The Summit 2010 and ACT2 ice cores feature a comparable trend. Humboldt core also had similar trends but with much smaller amplitude. The Lomonosovfonna ice core on Svalbard reveals a different pattern with increased BC concentrations between 1860 and 1910, and between 1940 until the early 2000s. Osmont et al (2018) hypothesize that the minimum at the beginning of the 20th century might be due to the Arctic warming in the early 20th century and hence artefacts from melting can play a role. Independently, the decline in concentrations after the end of the 20th century marks an important difference to the Greenland records. In the Canadian Arctic, the increase in BC concentrations were much more moderate between the late 19th and early 20th century and dropped much earlier. Melt-freeze cycles at Devon Ice Cap might have led to an underestimation of the rBC and make an overall interpretation more difficult. All cores show sporadic peaks in BC due to large forest or land deforestation fire events during the pre-industrial times. All cores however indicate that concentrations close to present day have decreased to a level similar to the preindustrial time, i.e. around 1800. The only exception is a record of EC concentration from the Holtedahlfonna ice core where a steady increase between 1970 and 2004 was found, while a similar peak deposition period was identified between 1850 and 1960. Ruppel et al. (2014) suggest that increased flaring emissions and enhanced wet scavenging of EC can explain this increase, while also taking into account the difference between the measurement methods (SP2 for rBC and thermos-optical detection for EC). Furthermore, four lake sediment records from an intense flaring region in arctic northwestern Russia show a consistent increase in BC deposition from 1850 to 2014, suggesting potentially underestimated and inaccurately portrayed BC emission trends for Russia in emission inventories, particularly after the fall of the USSR (Ruppel et al., in prep). Consequently, BC deposition trends variate in different parts of the Arctic and more data are urgently needed to get a more comprehensive view on geographical patterns.

The patterns in depositional values of BC and sulfate are different from the concentrations measured in the ice-core due to inclusion of amount of snowfall. Figure 5.1.3.2.2 show depositional fluxes of rBC and sulfate that exhibit very consistent trends among all ice-cores; some have higher depositional values i.e., D4, ACT2 and ACT11D while HUMBOLD, NEEM, NGT_B19 and TUNU2013 show lower magnitudes. The black carbon and sulfate depositions increased in early 1900s but black carbon started declining earlier than sulfate i.e., in 1950s at at all locations while sulfate deposition started decreasing in 1970s at D4, ACT2,ACT11D whereas remained consistent at other locations.

Generally, the different temporal patterns of BC and EC and sulfate depositions across the Arctic need to be associated to different source regions and atmospheric transport and scavenging patterns for interpretation. The Greenland cores reflect more long-range transported BC from North America. The Svalbard core is likely more representative of Eurasian activities, and the Canadian site is sensitive to emission from north-central and northwestern North America as well as from Russia and central Asia. In addition, during summer, a substantial contribution of BC comes from biomass burning which is partly a natural contribution and partly an anthropogenic source. It is possible that biomass burning will be responsible for most of the radiative forcing in the future (see section 3 on open biomass burning).

The trends in particulate sulfate concentrations are different from that of BC. Sulfate concentrations showed the similar trends with increase at the start of the 20th century peaking around 1920, followed by a small decrease after the great depression and another increase peaking in different decades depending on location. In Svalbard data the peak occurred before the 1970s, in Greenland in the 1970s and in Canada in the 1980s. Since then a decline is visible in agreement with the general anthropogenic emission trends. Sporadic peaks are due to natural volcanic eruptions that took place in various instances i.e., 1783 eruption of Laki volcano in Iceland; 1810 VEI-6 in South Pacific; 1815 Mount Tambora in Indonesia etc.

The CMIP6 data (Hoesly et al., 2018) provide long-term temporal BC and sulfur dioxide (precursor of sulfate) emissions information by region. In figure x the annual BC emissions for the Western and Easter Arctic are shown, as well as for the Rest of Europe, Asia and the

Rest of the World. Anthropogenic BC emissions from the Rest of Europe and Western Arctic started increasing around 1850 and peaked between 1900 and 1950 are now on the decline. Eastern Arctic emissions peaked around 1950 to 1990, while Asian emissions are still on the rise. This is consistent with the ice core records and atmospheric transport patterns. BC emissions from biomass burning are also shown, but given their sporadic nature and the need for favorable atmospheric transport a trend in the contribution to BC detected in ice cores is difficult to determine.

The here presented data suggest that trends in BC concentrations might be subject to greater regional variability across the Arctic than particulate sulfate. This is an important observation because it means that either emission patterns are more variable, or atmospheric processing plays a crucial role. Hence, comparing model performance against multiple ice core records becomes critical. Ice core records of BC and particulate sulfate can be used to constrain climate models (Fyfe et al. 2013) from which RF through direct radiation interactions of these aerosol components in the atmosphere and when deposited can be calculated. Deriving information for RF from aerosol-cloud interaction is much more difficult. Here, knowing the potential cloud condensation nuclei (CCN) and ice nucleating particles (INP) is important to correctly simulate the cloud water phase, which is an important factor for cloud radiative properties. There is only one study to date that has looked into the historical variability of INP in the Arctic from a Greenland and a Svalbard ice core (Hartmann et al., 2019). Analysis shows that no trend in INP concentrations could be observed for the time period between 1450 and 2000. INP are thought to be mostly made of **mineral dust** or biogenic material, hence from natural sources that could change in emission strength with a changing climate and retreating cryosphere (see section on mineral dust).

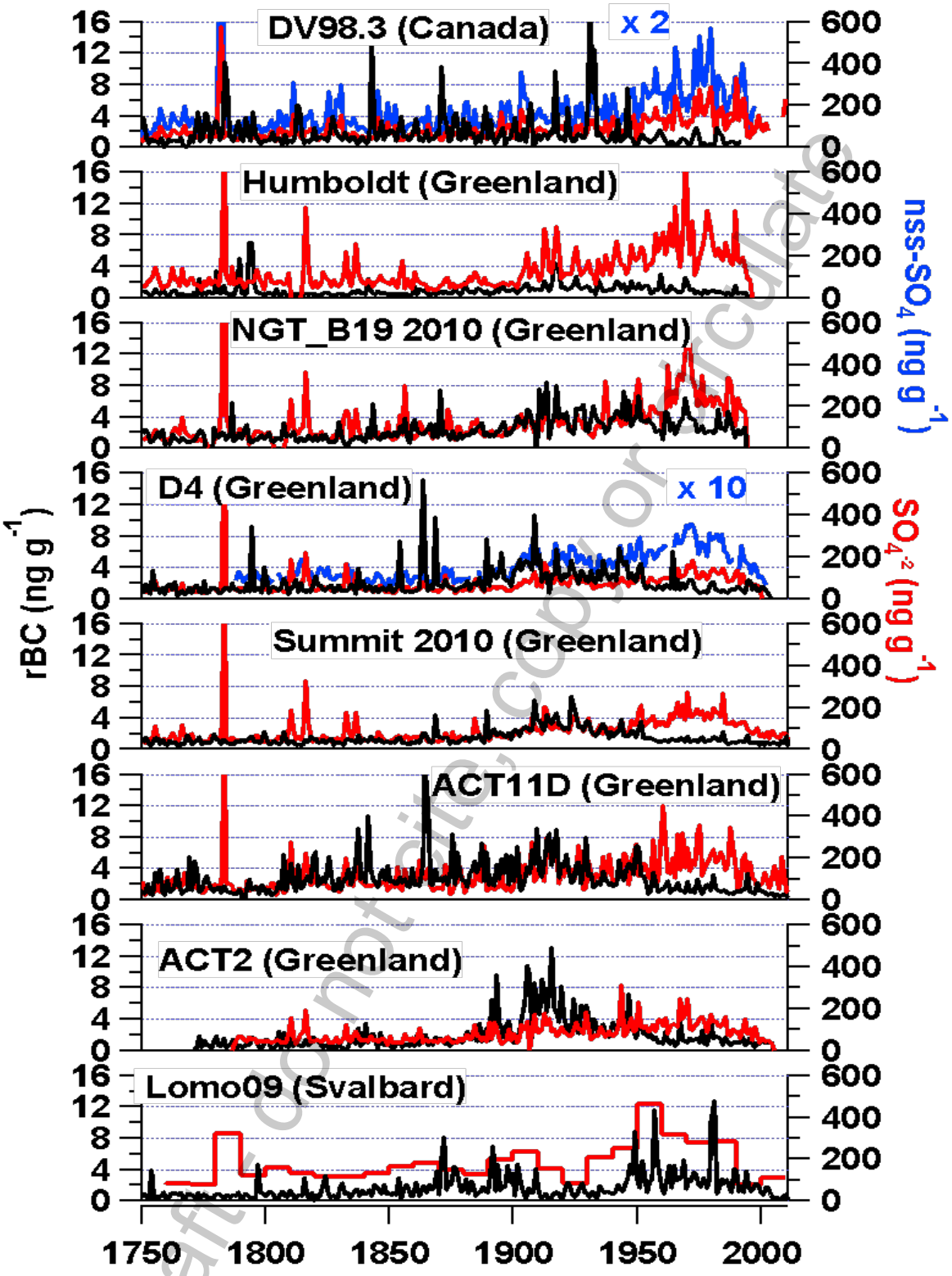

Figure 5.1.3.2.1: Trends in black carbon sulfate concentrations in various ice-cores in the Arctic. (Data source: Joe McConnell personal communication for all locations except for Devon PI (Christian Zdanowicz, Upsala U, Sweden) and Lomo09_11 (PI: Margit Schwikowski, PSI)

7892

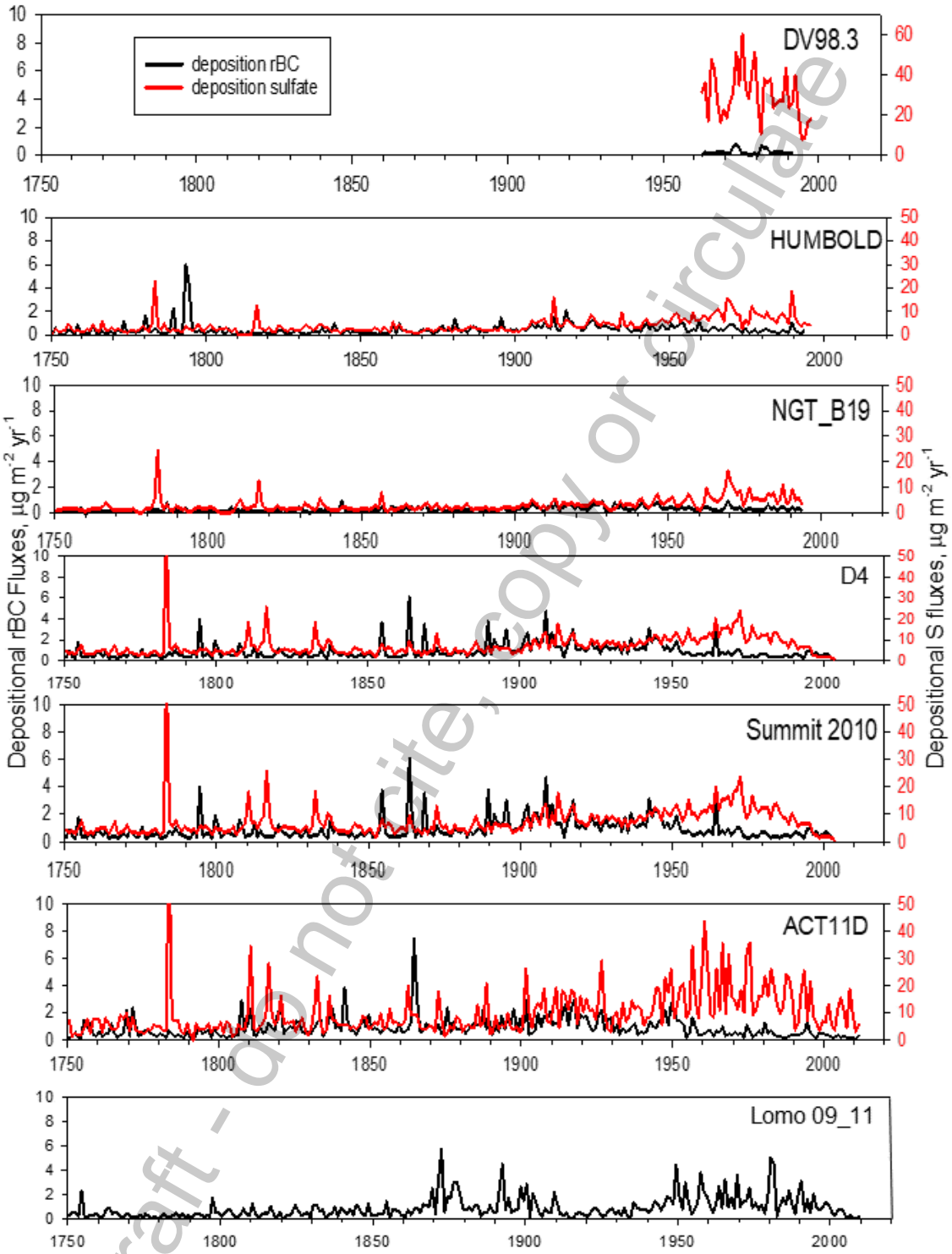

7893

7894 Figure 5.1.3.2.2: Trends in depositional fluxes of black carbon and sulfate at various Arctic
7895 locations. (Data source: McConnell et al., Science, 2007; McConnell and Edwards, PNAS,
7896 2008 and personal communication with Joe McConnell; Devon Ice-core (Christian
7897 Zdanowicz, Upsala U, Sweden) and Lomo09_11 (PI: Margit Schwikowski, PSI)

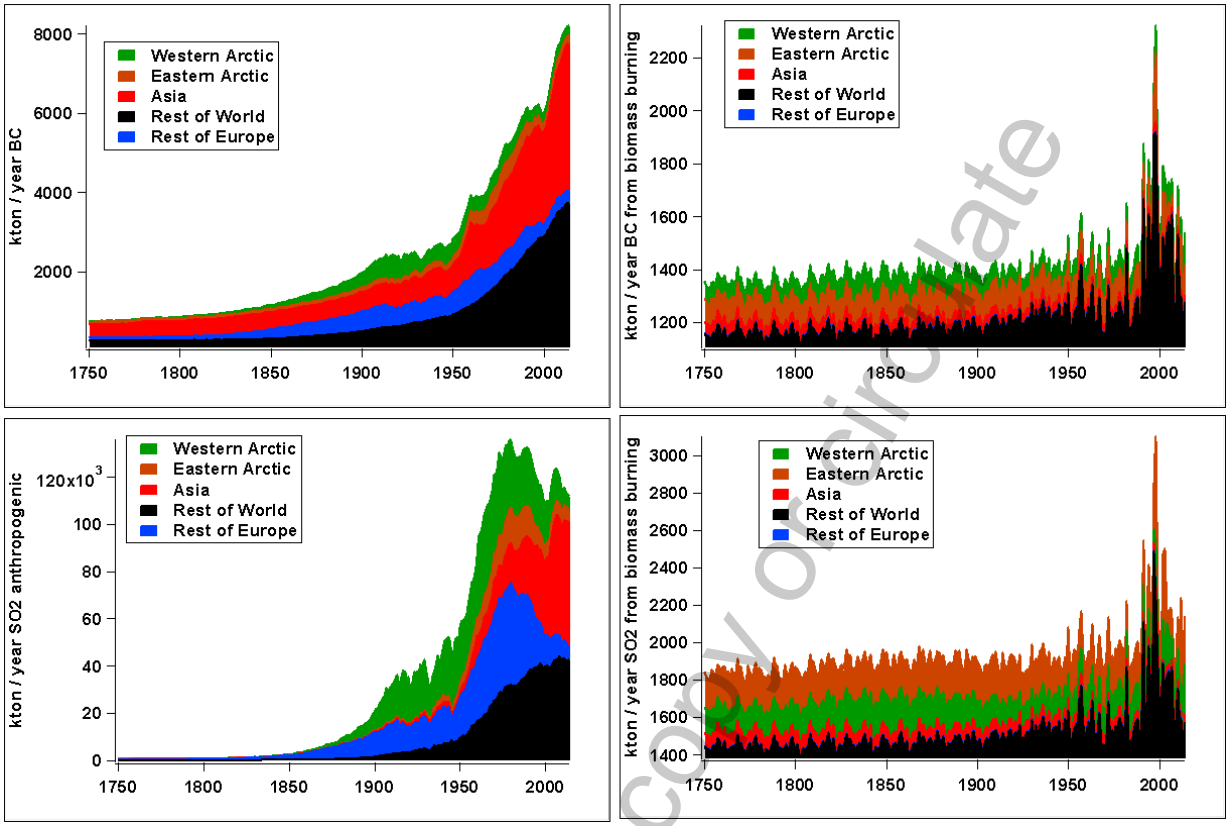

Figure 5.1.3.2.3: CMIP6 emission data after (Hoesly et al., 2018) split into regions used throughout this report.

The episodic nature of Icelandic dust events is demonstrated, for example, in a study by Wittmann (2017) using two 4.5 m deep firn cores on Brúarjökull, Iceland, drilled in 2015. The cores reached down to the year 2006 and showed distinct dust layers for the years 2008, 2011, 2012 and 2014 and only very small amounts for the years 2007 and 2013. McConnell ice-core concentrations and fluxes data include dust (Fig. 4.2.2.1). The concentrations are very different and it is important to include the depositional fluxes which includes the precipitation (snow) amount.

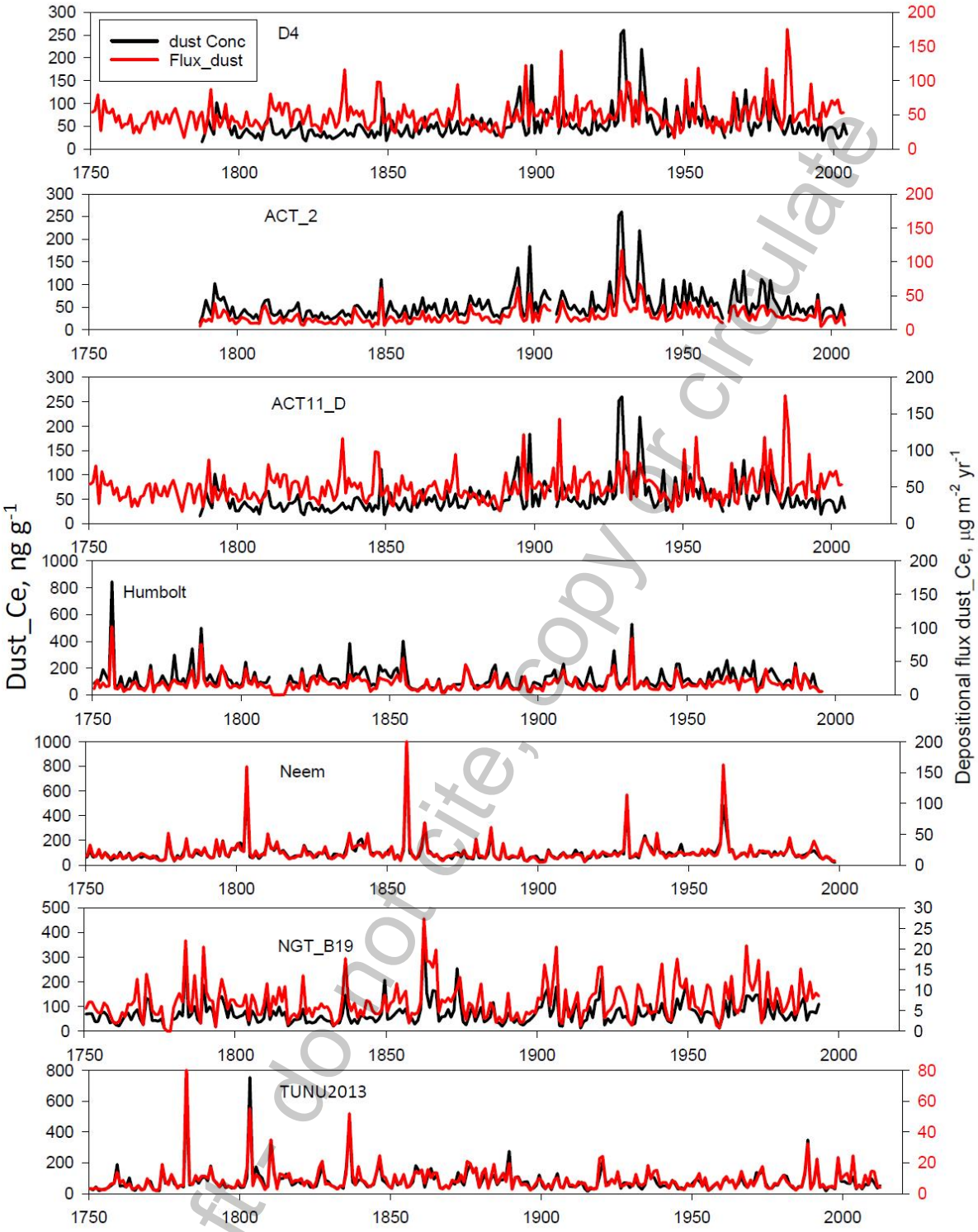

Figure 5.1.3.2.4. McConnell ice-core concentrations and fluxes data include dust (Fig. 4.2.2.1). The concentrations are very different and it is important to include the depositional fluxes which includes the precipitation (snow) amount. (Data source: McConnell et., PNAS, 2019)

The study of **organic tracers in Arctic ice cores** has provided detailed information on the variability of biomass burning in the boreal regions and on its dependence on large-scale climate anomalies (Legrand et al. 2016; Rubino et al. 2016). Specific organic markers for biomass burning encompass levoglucosan, phenolic compounds and dehydroabietic acid (Kehrwald et al., 2012; Kawamura et al., 2012). The analysis of ice core records from Svalbard (Grieman et al., 2018a), Greenland (Zennaro et al., 2014; Grieman et al., 2018b), Alaska (Pokhrel et al., 2020) and Russia (Grieman et al., 2017) indicate that fire activity in boreal regions in the last centuries was modulated by temperature and especially precipitation anomalies. Evidence for the general decline of biomass burning in the northern Hemisphere during XX century (Marlon et al, 2008) is scant in Arctic ice core records. This probably reflects the different trends in demographic growth, land use change and fire-management activities between the boreal regions and other areas of the Northern Hemisphere.

5.1.4 Summary, outlook and recommendations based on policy questions

The observations of the major aerosol components as inorganic and organic atmospheric components show dust, BC, S, NO3 and organics are abundant in low concentrations depended on natural and anthropogenic sources, but also meteorology. The atmospheric Arctic aerosol during the winter is still dominated by long distance transported air pollution while the summer seem to be similarly dominated by an natural aerosol mainly comprised of biogenic particles and sea spray which is clearly reflected in the optical and cloud formation properties. Long term observations of pollutants like S and BC have decreased for considerable time, more so during the first decades than the last decade. Nitrate is increasing due to changing atmospheric chemistry in spite of decreasing anthropogenic sources. The total aerosol concentrations and size distribution is also changing with a decreasing of aged submicron particle but increasing nanosized particles due to decreasing long distance pollution aerosol during winter and spring and with increasing natural particle formation during summer. The optical scattering observations show however an increasing trend both scattering and Ångström exponent implying higher coarse particle concentrations suggested due to an increased fraction of westerly air mass transport over open water into the Arctic giving higher concentration of supermicron seaspray particles

adding to the scattering. This is supported by increasing Na concentrations as measured at Alert (Sharma et al., 2019).

A first climatology of aerosol organic carbon (OC) concentrations in the high Arctic is emerging showing OC account for a significant fraction of aerosol mass especially in the summertime when they occur in large excess with respect to BC due to boreal forest fires and biogenic emissions.

The vertical distribution of aerosol are strongly dependent on the sources geographical position with long distant transported tending to show higher concentrations in elevated air masses. Black carbon particles are mostly transported from anthropogenic sources located at mid-latitudes causing intense plumes at mid altitudes. The seasonal and altitudinal influence of biomass burning is still controversial. Emerging anthropogenic sources within the Arctic have been causing intense summer plumes confined in the boundary layers and in proximity of the emission hotspot.

Observations of dust have increased as the influence on climate through scattering and snow melt has been recognized mainly showing an episodic but significant inflow and a possible increase with increasing snowfree land.

For a further understanding of BC and dust in snow and ice and corresponding interactions it is necessary to extend the snow sampling to more Arctic locations where in addition atmospheric data is available. A regular sampling and especially a scheme that covers the seasonality of this parameter is crucial to enhance the scientific background understanding of cryosphere - atmosphere interactions. In addition, a standardization of the analysis methods for BC and dust concentration in the snow and ice is needed.

The observations capacity has increased but also some of the time records now cover up to 20 years allowing not only a trend analysis but also to better see variability in seasonal behavior, thus revealing sources better. However it is also obvious that there is lacking coverage of the Arctic especially in the eastern and central parts revealed by the variability between existing sites. Besides the few well equipped observation sites, there is a major

need for expanding observations especially long term with new components as organics and dust.

Airborne in-situ observations of all aerosol species are still scattered both in space and time. While remote sensing observations provide the spatial and temporal coverage necessary to assess the vertical phenomenology of Arctic aerosol concentration, the chemical speciation and physical characterization of Arctic aerosol is still based on in-situ observations. Despite the technical challenge of measuring aerosol vertical distribution in the Arctic region, both remote sensing and in-situ measurements of aerosol vertical profiles indicate a very complex vertical phenomenology of Arctic aerosol. The clear outcome of the airborne studies is that ground observations are not representative of the atmospheric layers aloft. Moreover, the vertical distribution of aerosol particles varies as function of aerosol type, season and distance from the surface.

Recommendations:

GENERAL

· In general, we propose more extense observations that allow to evaluate the changes in the occurrence of natural Arctic aerosols which might be affected by climate change throughout complex feedback mechanisms.

BC

· Continuation of monitoring activities of BC mass concentrations at Arctic sites is strongly recommended.

· Improvement of monitoring of BC in snow samples to more Arctic sites and on more regular schemes is essential.

DUST

· Climatic significance of dust compared to BC as SLCF including seasonal variability in long-range transport of dust is important.

· Identification of dust sources, various methods of in situ observations, laboratory analysis (element composition and mineralogy), modeling and satellite approaches must contribute to narrowing down uncertainties.

· Wet and dry deposition rates and amounts (including accumulation in the cryosphere) must be determined.

· Effects of dust must be considered: influence on clouds as ice nucleation particles, cryospheric effects, health effects and its function as source of nutrients to ecosystems.

IO+ORG

· Continuation of existing monitoring activities of inorganic and organic aerosols is essential. A global comparison shows that Arctic stations are different and hence observations are key to understand the changes.

PHYSICS

· Enlarge the network for aerosol particle number size distribution measurements at Arctic stations worldwide especially in the eastern Arctic.

· Chemical records along with optical properties are the best combination to understand the drivers (natural or anthropogenic) of the changed Arctic atmospheric composition and corresponding consequences.

· Upgrade to monitoring of both (scattering and absorption) at stations where this is not yet the case is recommended. (Recent publications suggest changes in the SSA due to different aerosol properties in the North American Arctic - more absorbing aerosol - in contrast to the Southern European Arctic - more scattering - which might be linked to enhanced forest emissions.)

· More observations and especially time series on CCN (and maybe INP) numbers are relevant to understand the role of anthropogenic and natural (affected in a changing climate) aerosols on cloud and fog formation and corresponding climate effects.

References

5.1.1. Intro/New findings

Boy et al., 2019.

Tørseth, K. et al. in prep. (Assessment of observation capacities and data availability of Black Carbon in the Arctic region)

Eckhardt et al., ACP 15, 9413–9433, 2015.

Freud et al., ACP, 17, 8101–8128, 2017.

Schmeisser et al., ACP, 18, 11599-11622, 2018.

Jung et al., 2018.

5.1.2. Concentrations, seasonal cycles and origin

Barrie, L. A. (1986) Arctic air pollution: An overview of current knowledge, Atmos. Env., 20, 643-663, doi:10.1016/004-6981(86)90180-0.

Koch, D., and J. Hansen (2005), Distant origins of Arctic black carbon: A Goddard Institute for Space Studies Model Experiment,J. Geophys. Res.,110, D04204, doi:10.1029/2004JD005296.

Law, K. and Stohl, A. 2007. Arctic Air Pollution: Origins and Impacts, Science, Vol. 315, Issue 5818, pp. 1537-1540, DOI: 10.1126/science.1137695

Stone, S., S. Sharma, A, Herber, K Eleftheriadis, D. W. Nelson (2014), A characterization of Arctic aerosols on the basis of aerosol optical depth and black carbon measurements. Elementa: Science of the Anthropocene, 2:000027, doi:10.12952/journal.elementa.000027.

Evangeliou, N., A. Kylling, S. Eckhardt, V. Myroniuk, K. Stebel, R. Paugam, S. Zibtsev, and A. Stohl (2019): Open fires in Greenland in summer 2017: transport, deposition and radiative effects of BC, OC and BrC emissions. Atmos. Chem. Phys. 19, 1393-1411, doi:10.5194/acp-19-1393-2019. 321.pdf

Dagsson-Waldhauserova, P., Arnalds, O., and Olafsson, H.: Long-term variability of dust events in Iceland (1949–2011), Atmos. Chem. Phys., 14, 13411–13422, https://doi.org/10.5194/acp-14-13411-2014, 2014.

Groot Zwaaftink, C. D., O. Arnalds, P. Dagsson-Waldhauserova, S. Eckhardt, J. M. Prospero, and A. Stohl (2017): Temporal and spatial variability of Icelandic dust emissions and atmospheric transport. Atmos. Chem. Phys. 17, 10865-10878, doi:10.5194/acp-17-10865-2017. 301.pdf

5.1.2.1 Surface aerosol observations

8070 Arnalds, O.: The soils of Iceland, Springer, Dordrecht, the Netherlands, 160 pp., 2015.
8071 Arnalds, O., Gisladottir, F. O., and Sigurjonsson, H.: Sandy deserts of Iceland: an overview,
8072 J. Arid Environ., 47, 359–371, 2001.

8073 Arnalds, O., Olafsson, H., and Dagsson-Waldhauserova, P.: Quantificationofiron-
8074 richvolcanogenicdustemissionsanddeposition over the ocean from Icelandic dust sources,
8075 Biogeosciences, 11, 6623–6632, doi:10.5194/bg-11-6623-2014, 2014.

8076 Arnalds,O.,Dagsson-Waldhauserova,P.,andOlafsson,H.:TheIcelandic volcanic aeolian
8077 environment: Processes and impacts – A review, Aeolian Research, 20, 176–195, 2016.

8078 Barrett and Sheesley, Year-round optical properties and source characterization of Arctic
8079 organic carbon aerosols on the North Slope Alaska, J. Geophys. Res. Atmos., 122, 9319–
8080 9331, doi:10.1002/2016JD026194, 2017

8081 Becagli et al., Biogenic Aerosol in the Artic from Eight Years of MSA Data from Ny Ålesund
8082 (Svalbard Islands) and Thule (Greenland), Atmosphere, 10, 349;
8083 doi:10.3390/atmos10070349, 2019.

8084 Boy, M., Thomson, E.S., Acosta Navarro, J.-C., Arnalds, O., Batchvarova, E., Bäck et al. (2019).
8085 Interactions between the atmosphere, cryosphere, and ecosystems at northern high
8086 latitudes. Atmos. Chem. Phys. 19, 2015–2061.

8087 Brock et al., Characteristics, sources, and transport of aerosols measured in spring 2008
8088 during the aerosol, radiation, and cloud processes affecting Arctic Climate (ARCPAC)
8089 Project, Atmos. Chem. Phys., 11, 2423–2453, 2011

8090 Bullard, J.E., Baddock, M., Bradwell, T., Crusius, J., Darlington, E., Gaiero, D., Gassó, S.,
8091 Gisladottir, G., Hodgkins, R., McCulloch, R., McKenna-Neuman, C., Mockford, T., Stewart,
8092 H., and Thorsteinsson, T. (2016). High-latitude dust in the Earth system. Rev. Geophys.
8093 54, 447–485.

8094 Chang et al., Aerosol composition and sources in the central Arctic Ocean during ASCOS,
8095 Atmos. Chem. Phys., 11, 10619–10636, 2011.

8096 Conca et al., Source identification and temporal evolution of trace elements in PM10
8097 collected near to Ny-Ålesund (Norwegian Arctic), Atmos. Environ., 203, 153 – 165, 2019.

8098 Dagsson-Waldhauserova et al., Long-term variability of dust events in Iceland (1949–2011),
8099 Atmos. Chem. Phys., 14, 13411–13422, 2014

8100 Dall'Osto, M., Beddows, D. C., Tunved, P., Krejci, R., Ström, J., Hansson, H. C., et al. (2017).
8101 Arctic sea ice melt leads to atmospheric new particle formation. Scientific Reports, 7(1),
8102 3318–3310. https://doi.org/10.1038/s41598-017-03328-1

8103 Dall'Osto, M., Geels, C., Beddows, D. C. S., Boertmann, D., Lange, R., Nøjgaard, J. K., et al.
8104 (2018). Regions of open water and melting sea ice drive new particle formation in North
8105 East Greenland. Scientific Reports, 8(6109), 1–10. https://doi.org/10.1038/s41598-018-
8106 24426

8107 Dall'Osto, M., Beddows, D. C. S., Tunved, P., Harrison, R. M., Lupi, A., Vitale, V., Becagli, S.,
8108 Traversi, R., Park, K.-T., Yoon, Y. J., Massling, A., Skov, H., Lange, R., Strom, J., and Krejci,
8109 R.: Simultaneous measurements of aerosol size distributions at three sites in the
8110 European high Arctic, Atmos. Chem. Phys., 19, 7377–7395, https://doi.org/10.5194/acp-
8111 19-7377-2019, 2019.

8112 Eckhardt et al., Current model capabilities for simulating black carbon and sulfate
8113 concentrations in the Arctic atmosphere: a multi-model evaluation using a
8114 comprehensive measurement data set, ACP 15, 9413–9433, 2015.

8115 Fan, S-M., Modeling of observed mineral dust aerosols in the arctic and the impact on
8116 winter season low-level clouds, J. Geophys. Res., 118, 11,161–11,174,
8117 doi:10.1002/jgrd.50842, 2013.

8118 Ferrero et al., Chemical Composition of Aerosol over the Arctic Ocean from Summer ARctic
8119 EXpedition (AREX) 2011–2012 Cruises: Ions, Amines, Elemental Carbon, Organic Matter,
8120 Polycyclic Aromatic Hydrocarbons, n-Alkanes, Metals, and Rare Earth Elements,
8121 Atmosphere 2019, 10, 54; doi:10.3390/atmos10020054, 2019.

8122 Freud, E., Krejci, R., Tunved, P., Leaitch, R., Nguyen, Q. T., Massling, A., Skov, H., and Barrie,
8123 L.: Pan-Arctic aerosol number size distributions: seasonality and transport patterns,
8124 Atmos. Chem. Phys., 17, 8101–8128, https://doi.org/10.5194/acp-17-8101-2017, 2017.

8125 Frossard et al., Springtime Arctic haze contributions of submicron organic particles from
8126 European and Asian combustion sources, JGR 116, D05205, doi:10.1029/2010JD015178,
8127 2011.

8128 Fu, P., K. Kawamura, L. A. Barrie, Photochemical and Other Sources of Organic Compounds
8129 in the Canadian High Arctic Aerosol Pollution during Winter-Spring, Environ. Sci. Technol.
8130 43, 286–292, 2009.

8131 Fu et al., Organic molecular composition of marine aerosols over the Arctic Ocean in
8132 summer: contributions of primary emission and secondary aerosol formation,
8133 Biogeosciences, 10, 653–667, 2013.

8134 Fu et al., Fluorescent water-soluble organic aerosols in the High Arctic atmosphere, Sci.
8135 Rep., 5, 9845, DOI: 10.1038/srep09845, 2015

8136 Gao et al. Particle-Size Variability of Aerosol Iron and Impact on Iron Solubility and Dry
8137 Deposition Fluxes to the Arctic Ocean, Sci. Rep. 9:16653, doi:10.1038/s41598-019-52468-
8138 z 1, (2019)

8139 Ghahremaninezhad, Roghayeh, Norman, Ann-Lise, Abbatt, Jonathan, Levasseur, Maurice,
8140 Thomas, Jennie, 2016. Biogenic, anthropogenic, and sea salt sulfate size-segregated
8141 aerosols in the Arctic summer, Atmos. Chem. Phys., 16(8):1-27, DOi - 10.5194/acp-2015-
8142 1010

8143 Gilardoni et al. Atmospheric black carbon in Svalbard (ABC Svalbard) SESS report, 2019.

8144 Groot Zwaaftink et al. Substantial contribution of northern high-latitude sources to mineral
8145 dust in the Arctic, J. Geophys. Res. Atmos., 121, 13,678–13,697,
8146 doi:10.1002/2016JD025482, 2016.

8147 Hu, Q-H., Xie, Z-Q., Wang, X.M., Kang, H., Zhang, P., Levoglucosan indicates high levels of
8148 biomass burning aerosols over oceans from the Arctic to Antarctic, Sci. Rep., 3, 3119,
8149 DOI: 10.1038/srep03119, 2013.

8150 Huang et al., Short-cut transport path for Asian dust directly to the Arctic: a case study,
8151 Environ. Res. Lett., 10, 114018, 2015.

8152 IPCC, 2019. Summary for Policymakers. In: IPCC Special Report on the Ocean and
8153 Cryosphere in a Changing Climate [H.-O. Pörtner, D.C. Roberts, V. Masson-Delmotte, P.

8154 Zhai, M. Tignor, E. Poloczanska, K. Mintenbeck, M. Nicolai, A. Okem, J. Petzold, B. Rama,
8155 N. Weyer (eds.)]. In press.

8156 Jung, C. H., Yoon, Y. J., Kang, H. J., Gim, Y., Lee, B. Y., Ström, J., Krejci, R. & P. Tunved (2018)
8157 The seasonal characteristics of cloud condensation nuclei (CCN) in the arctic lower
8158 troposphere, Tellus B: Chemical and Physical Meteorology, 70:1, 1-13, DOI:
8159 10.1080/16000889.2018.1513291

8160 Karl et al., New insights in sources of the sub-micrometre aerosol at Mt. Zeppelin
8161 observatory (Spitsbergen) in the year 2015, Tellus B: Chemical and Physical Meteorology,
8162 71:1, 1613143, DOI: 10.1080/16000889.2019.1613143, 2019.

8163 Kylling, A., Groot Zwaaftink, C. D., & Stohl, A. (2018). Mineral dust instantaneous radiative
8164 forcing in the Arctic. *Geophysical Research Letters*, 45, 4290– 4298.
8165 https://doi.org/10.1029/2018GL077346

8166 Lange, R., Dall Osto, M., Skov, H., Nøjgaard, J. K., Nielsen, I. E., Beddows, D. C. S., et al.
8167 (2018). Characterization of distinct Arctic aerosol accumulation modes and their sources.
8168 Atmospheric Environment, 183, 1–10. https://doi.org/10.1016/j.atmosenv.2018.03.060

8169 Lange, R., Dall'Osto, M., Wex, H., Skov, H., & Massling, A. (2019). Large summer contribution
8170 of organic biogenic aerosols to Arctic cloud condensation nuclei. Geophysical Research
8171 Letters, 46. https://doi.org/10.1029/2019GL084142

8172 Leaitch et al., Organic functional groups in the submicron aerosol at 82.5° N, 62.5° W from
8173 2012 to 2014, Atmos. Chem. Phys., 18, 3269–3287, 2018.

8174 Matsui, H., Mahowald, N., Moteki, N., Hamilton, D., Ohata, S., Yoshida, A., Koike, M., Scanza,
8175 R., & Flanner, M. (2018). Anthropogenic combustion iron as a complex climate forcer,
8176 *Nature Communications*, 9(1), 1593, doi:10.1038/s41467-018-03997-0.

8177 Mouteva et al., Black carbon aerosol dynamics and isotopic composition in Alaska linked
8178 with boreal fire emissions and depth of burn in organic soils, Global Biogeochem. Cycles,
8179 29, doi:10.1002/2015GB005247, 2015.

8180 Mungall, E. L., Abbatt, J. P. D., Wentzell, J. J. B., Lee, A. K. Y., Thomas, J. L., Blais, M.,
8181 Gosselin, M., Miller, L. A., Papakyriakou, T., Willis, M. D., and Liggio, J.: Microlayer source
8182 of oxygenated volatile organic compounds in the summertime marine Arctic boundary

8183 layer, P. Natl. Acad. Sci. USA, 114, 6203, https://doi.org/10.1073/pnas.1620571114,
8184 2017.

8185 Nielsen et al., Biogenic and anthropogenic sources of aerosols at the High Arctic site Villum
8186 Research Station, Atmos. Chem. Phys., 19, 10239–10256, 2019.

8187 Norman AL, Barrie LA, Toom-Sauntry D, Sirois A, Krouse HR, LiSM, Sharma S (1999) Sources
8188 of aerosol sulphate at Alert:apportionment using stable isotopes. J Geophys Res
8189 104(D9):11619–11631

8190 Popovicheva et al., Black Carbon Sources Constrained by Observations in the Russian High
8191 Arctic, Environ. Sci. Technol., 51, 7, 3871-3879, 2017.

8192 Popovicheva et al., East Siberian Arctic background and black carbon polluted aerosols at
8193 HMO Tiksi. Science of The Total Environment, 655: 924-938, 2019.

8194 Prospero, J.M., Bullard, J.E., Hodgkins, R., 2012. High-latitude dust over the North Atlantic:
8195 inputs from Icelandic proglacial dust storms. Science 335, 1078–1082

8196 Quinn PK, Miller TL, Bates TS, Ogren JA, Andrews E et al (2002) Athree-year record of
8197 simultaneously measured aerosol chemical and optical properties at Barrow, Alaska. J
8198 Geophys Res. doi:10.1029/2001JD001248

8199 Quinn PK, Shaw G, Andrews E, Dutton EG, Ruoho-Airola T, GongSL (2007) Arctic haze:
8200 current trends and knowledge gaps.Tellus 59B:99–114

8201 Schmeisser, L., Backman, J., Ogren, J. A., Andrews, E., Asmi, E., Starkweather, S., Uttal, T.,
8202 Fiebig, M., Sharma, S., Eleftheriadis, K., Vratolis, S., Bergin, M., Tunved, P., and Jefferson,
8203 A.: Seasonality of aerosol optical properties in the Arctic, Atmos. Chem. Phys., 18, 11599–
8204 11622, https://doi.org/10.5194/acp-18-11599-2018, 2018.

8205 Stohl et al., Pan-Arctic enhancements of light absorbing aerosol concentrations due to North
8206 American boreal forest fires during summer 2004, JGR, 111, D22214,
8207 doi:10.1029/2006JD007216, 2006.

8208 Tobo et al. Glacially sourced dust as a potentially significant source of ice nucleating
8209 particles, Nature Geoscience, 12, 253–258, 2019.

8210 Tørseth et al., Review of Observation Capacities and Data Availability for Black Carbon in the
8211 Arctic Region: EU Action on Black Carbon in the Arctic – Technical Report 1, 2020.

8212 Tunved, P., Ström, J. and R. Krejci Arctic aerosol life cycle: linking aerosol size distributions
8213 observed between 2000 and 2010 with air mass transport and precipitation at Zeppelin
8214 station, Ny-Ålesund, Svalbard, Atmos. Chem. Phys., 13, 3643–3660, 2013, www.atmos-
8215 chem-phys.net/13/3643/2013/, doi:10.5194/acp-13-3643-2013.

8216 von Schneidemesser, Schauer, Hagler, Bergin, Concentrations and sources of carbonaceous
8217 aerosol in the atmosphere of Summit, Greenland, Atmos. Environ., 43, 4155–4162, 2009.

8218 Willis, M. D., et al. Evidence formarine biogenic influence on summertime Arctic aerosol,
8219 Geophys. Res. Lett., 44, 6460–6470, doi:10.1002/2017GL073359, 2017.

8220 Winiger et al., The sources of atmospheric black carbon at a European gateway to the Arctic,
8221 Nature Communications, 7:12776, DOI: 10.1038/ncomms12776, 2016.

8222 Winiger et al., Source apportionment of circum-Arctic atmospheric black carbon from
8223 isotopes and modeling, Sci. Adv. 5, eaau8052, 2019.

8224 Yang, Y, H Wang, S Smith, R Easter, and P Rasch. 2018. "Sulfate Aerosol in the Arctic:
8225 Source Attribution and Radiative Forcing." *Journal of Geophysical Research: Atmospheres*
8226 123(3): 1889 - 1918. https://doi.org/10.1002/2017jd027298.

8227 Yoshida, A., Moteki, N., Ohata, S., Mori, T., Koike, M., Kondo, Y., Matsui, H,m Oshima, N.,
8228 Takami, A., & Kita K. (2020). Abundances and microphysical properties of light-absorbing
8229 iron oxide and black carbon aerosols over East Asia and the Arctic, Journal of
8230 Geophysical Research: Atmospheres, under review.

8231 Yttri et al., Quantifying black carbon from biomass burning by means of levoglucosan – a
8232 one-year time series at the Arctic observatory Zeppelin, Atmos. Chem. Phys., 14, 6427–
8233 6442, 2014.

8234 Zangrando et al., Molecular Markers of Biomass Burning in Arctic Aerosols, Environ. Sci.
8235 Technol., 47, 8565−8574, 2013.

8236 Zhang, X. L., Wu, G. J., Zhang, C. L., Xu, T. L., & Zhou, Q. Q. (2015). What is the real role of
8237 iron oxides in the optical properties of dust aerosols? *Atmospheric Chemistry and Physics*,
8238 *15*(21), 12159-12177.

8239 Zubko, N., Muñoz, O., Zubko, E., Gritsevich, M., Escobar-Cerezo, J., Berg, J. (2019). Light
8240 scattering from volcanic-sand particles in deposited and aerosol form. Atmos. Env. 215,
8241 116813.

8242

8243 **5.1.2.2 Vertical distribution**

8244 Abbatt, J. P. D., Leaitch, W. R., Aliabadi, A. A., Bertram, A. K., Blanchet, J.-P., Boivin-Rioux, A.,
8245 Bozem, H., Burkart, J., Chang, R. Y. W., Charette, J., Chaubey, J. P., Christensen, R. J.,
8246 Cirisan, A., Collins, D. B., Croft, B., Dionne, J., Evans, G. J., Fletcher, C. G.,
8247 Ghahremaninezhad, R., Girard, E., Gong, W., Gosselin, M., Gourdal, M., Hanna, S. J.,
8248 Hayashida, H., Herber, A. B., Hesaraki, S., Hoor, P., Huang, L., Hussherr, R., Irish, V. E.,
8249 Keita, S. A., Kodros, J. K., Köllner, F., Kolonjari, F., Kunkel, D., Ladino, L. A., Law, K.,
8250 Levasseur, M., Libois, Q., Liggio, J., Lizotte, M., Macdonald, K. M., Mahmood, R., Martin,
8251 R. V., Mason, R. H., Miller, L. A., Moravek, A., Mortenson, E., Mungall, E. L., Murphy, J. G.,
8252 Namazi, M., Norman, A.-L., O'Neill, N. T., Pierce, J. R., Russell, L. M., Schneider, J., Schulz,
8253 H., Sharma, S., Si, M., Staebler, R. M., Steiner, N. S., Galí, M., Thomas, J. L., Salzen, K. von,
8254 Wentzell, J. J. B., Willis, M. D., Wentworth, G. R., Xu, J.-W. and Yakobi-Hancock, J. D.: New
8255 insights into aerosol and climate in the Arctic, Atmospheric Chem. Phys. Discuss., 1–60,
8256 doi:https://doi.org/10.5194/acp-2018-995, 2018.

8257 Antokhina, O. Yu., Antokhin, P. N., Arshinova, V. G., Arshinov, M. Yu., Belan, B. D., Belan, S.
8258 B., Davydov, D. K., Ivlev, G. A., Kozlov, A. V., Nédélec, P., Paris, J.-D., Rasskazchikova, T.
8259 M., Savkin, D. E., Simonenkov, D. V., Sklyadneva, T. K., Tolmachev, G. N. and Fofonov, A.
8260 V.: Vertical Distributions of Gaseous and Aerosol Admixtures in Air over the Russian
8261 Arctic, Atmospheric Ocean. Opt., 31(3), 300–310, doi:10.1134/S102485601803003X,
8262 2018.

8263 Biraud, S., Mei, F., Flynn, C., Hubbe, J., Long, C., Matthews, A., Pekour, M., Sedlacek, A.,
8264 Springston, S., Tomlinson, J. and Chand, D.: Campaign datasets for ARM Airborne Carbon
8265 Measurements (ARM-ACME-V), Atmospheric Radiation Measurement (ARM) Archive,
8266 Oak Ridge National Laboratory (ORNL), Oak Ridge, TN (US)., 2016.

8267 Brock, C. A., Cozic, J., Bahreini, R., Froyd, K. D., Middlebrook, A. M., McComiskey, A.,
8268 Brioude, J., Cooper, O. R., Stohl, A., Aikin, K. C., Gouw, J. A. de, Fahey, D. W., Ferrare, R.

A., Gao, R.-S., Gore, W., Holloway, J. S., Hübler, G., Jefferson, A., Lack, D. A., Lance, S., Moore, R. H., Murphy, D. M., Nenes, A., Novelli, P. C., Nowak, J. B., Ogren, J. A., Peischl, J., Pierce, R. B., Pilewskie, P., Quinn, P. K., Ryerson, T. B., Schmidt, K. S., Schwarz, J. P., Sodemann, H., Spackman, J. R., Stark, H., Thomson, D. S., Thornberry, T., Veres, P., Watts, L. A., Warneke, C. and Wollny, A. G.: Characteristics, sources, and transport of aerosols measured in spring 2008 during the aerosol, radiation, and cloud processes affecting Arctic Climate (ARCPAC) Project, Atmospheric Chem. Phys., 11(6), 2423–2453, doi:https://doi.org/10.5194/acp-11-2423-2011, 2011.

Dagsson-Waldhauserova, P., Renard, J.-B., Olafsson, H., Vignelles, D., Berthet, G., Verdier, N. and Duverger, V.: Vertical distribution of aerosols in dust storms during the Arctic winter, Sci. Rep., 9(1), 1–11, doi:10.1038/s41598-019-51764-y, 2019.

Devasthale, A., Tjernström, M. and Omar, A. H.: The vertical distribution of thin features over the Arctic analysed from CALIPSO observations: Part II: Aerosols, Tellus B Chem. Phys. Meteorol., 63(1), 86–95, doi:10.1111/j.1600-0889.2010.00517.x, 2011.

Engvall, A.-C., StröM, J., Tunved, P., Krejci, R., Schlager, H. and Minikin, A.: The radiative effect of an aged, internally mixed Arctic aerosol originating from lower-latitude biomass burning, Tellus B Chem. Phys. Meteorol., 61(4), 677–684, doi:10.1111/j.1600-0889.2009.00431.x, 2009.

Herber, A. B., Haas, C., Stone, R. S., Bottenheim, J. W., Liu, P., Li, S.-M., Staebler, R. M., Strapp, J. W. and Dethloff, K.: Regular airborne surveys of Arctic sea ice and atmosphere, Eos Trans. Am. Geophys. Union, 93(4), 41–42, doi:10.1029/2012EO040001, 2012.

Herenz, P., Wex, H., Henning, S., Kristensen, T. B., Rubach, F., Roth, A., Borrmann, S., Bozem, H., Schulz, H. and Stratmann, F.: Measurements of aerosol and CCN properties in the Mackenzie River delta (Canadian Arctic) during spring–summer transition in May 2014, Atmospheric Chem. Phys., 18(7), 4477–4496, doi:https://doi.org/10.5194/acp-18-4477-2018, 2018.

Jacob, D. J., Crawford, J. H., Maring, H., Clarke, A. D., Dibb, J. E., Emmons, L. K., Ferrare, R. A., Hostetler, C. A., Russell, P. B., Singh, H. B., Thompson, A. M., Shaw, G. E., McCauley, E., Pederson, J. R. and Fisher, J. A.: The Arctic Research of the Composition of the Troposphere from Aircraft and Satellites (ARCTAS) mission: design, execution, and first

8299 results, Atmospheric Chem. Phys., 10(11), 5191–5212, doi:https://doi.org/10.5194/acp-
8300 10-5191-2010, 2010.

8301 Law, K. S., Stohl, A., Quinn, P. K., Brock, C. A., Burkhart, J. F., Paris, J.-D., Ancellet, G., Singh,
8302 H. B., Roiger, A., Schlager, H., Dibb, J., Jacob, D. J., Arnold, S. R., Pelon, J. and Thomas, J.
8303 L.: Arctic Air Pollution: New Insights from POLARCAT-IPY, Bull. Am. Meteorol. Soc.,
8304 95(12), 1873–1895, doi:10.1175/BAMS-D-13-00017.1, 2014.

8305 Liu, D., Quennehen, B., Darbyshire, E., Allan, J. D., Williams, P. I., Taylor, J. W., Bauguitte, S.
8306 J.-B., Flynn, M. J., Lowe, D., Gallagher, M. W., Bower, K. N., Choularton, T. W. and Coe, H.:
8307 The importance of Asia as a source of black carbon to the European Arctic during
8308 springtime 2013, Atmospheric Chem. Phys., 15(20), 11537–11555,
8309 doi:https://doi.org/10.5194/acp-15-11537-2015, 2015.

8310 Paris, J.-D., Stohl, A., Nédélec, P., Arshinov, M. Y., Panchenko, M. V., Shmargunov, V. P., Law,
8311 K. S., Belan, B. D. and Ciais, P.: Wildfire smoke in the Siberian Arctic in summer: source
8312 characterization and plume evolution from airborne measurements, Atmospheric Chem.
8313 Phys., 9(23), 9315–9327, doi:https://doi.org/10.5194/acp-9-9315-2009, 2009.

8314 Pierro, M. D., Jaeglé, L., Eloranta, E. W. and Sharma, S.: Spatial and seasonal distribution of
8315 Arctic aerosols observed by the CALIOP satellite instrument (2006–2012), Atmospheric
8316 Chem. Phys., 13(14), 7075–7095, doi:https://doi.org/10.5194/acp-13-7075-2013, 2013.

8317 Roiger, A., Thomas, J.-L., Schlager, H., Law, K. S., Kim, J., Schäfler, A., Weinzierl, B.,
8318 Dahlkötter, F., Krisch, I., Marelle, L., Minikin, A., Raut, J.-C., Reiter, A., Rose, M., Scheibe,
8319 M., Stock, P., Baumann, R., Bouarar, I., Clerbaux, C., George, M., Onishi, T. and Flemming,
8320 J.: Quantifying Emerging Local Anthropogenic Emissions in the Arctic Region: The ACCESS
8321 Aircraft Campaign Experiment, Bull. Am. Meteorol. Soc., 96(3), 441–460,
8322 doi:10.1175/BAMS-D-13-00169.1, 2015.

8323 Schwarz, J. P., Samset, B. H., Perring, A. E., Spackman, J. R., Gao, R. S., Stier, P., Schulz, M.,
8324 Moore, F. L., Ray, E. A. and Fahey, D. W.: Global-scale seasonally resolved black carbon
8325 vertical profiles over the Pacific, Geophys. Res. Lett., 40(20), 2013GL057775,
8326 doi:10.1002/2013GL057775, 2013.

8327 Shibata, T., Shiraishi, K., Shiobara, M., Iwasaki, S. and Takano, T.: Seasonal Variations in High
8328 Arctic Free Tropospheric Aerosols Over Ny-Ålesund, Svalbard, Observed by Ground-Based

8329 Lidar, J. Geophys. Res. Atmospheres, 123(21), 12,353-12,367,
8330 doi:10.1029/2018JD028973, 2018.

8331 Stjern, C. W., Lund, M. T., Samset, B. H., Myhre, G., Forster, P. M., Andrews, T., Boucher, O.,
8332 Faluvegi, G., Fläschner, D., Iversen, T., Kasoar, M., Kharin, V., Kirkevåg, A., Lamarque, J.-F.,
8333 Olivié, D., Richardson, T., Sand, M., Shawki, D., Shindell, D., Smith, C. J., Takemura, T. and
8334 Voulgarakis, A.: Arctic Amplification Response to Individual Climate Drivers, J. Geophys.
8335 Res. Atmospheres, 124(13), 6698–6717, doi:10.1029/2018JD029726, 2019.

8336 Stone, R. S., Sharma, S., Herber, A., Eleftheriadis, K. and Nelson, D. W.: A characterization of
8337 Arctic aerosols on the basis of aerosol optical depth and black carbon measurements,
8338 Elem. Sci. Anthr., 2, 000027, doi:10.12952/journal.elementa.000027, 2014.

8339 Thomas, M. A., Devasthale, A., Tjernström, M. and Ekman, A. M. L.: The Relation Between
8340 Aerosol Vertical Distribution and Temperature Inversions in the Arctic in Winter and
8341 Spring, Geophys. Res. Lett., 46(5), 2836–2845, doi:10.1029/2018GL081624, 2019.

8342 Tomasi, C., Kokhanovsky, A. A., Lupi, A., Ritter, C., Smirnov, A., O'Neill, N. T., Stone, R. S.,
8343 Holben, B. N., Nyeki, S., Wehrli, C., Stohl, A., Mazzola, M., Lanconelli, C., Vitale, V., Stebel,
8344 K., Aaltonen, V., de Leeuw, G., Rodriguez, E., Herber, A. B., Radionov, V. F., Zielinski, T.,
8345 Petelski, T., Sakerin, S. M., Kabanov, D. M., Xue, Y., Mei, L., Istomina, L., Wagener, R.,
8346 McArthur, B., Sobolewski, P. S., Kivi, R., Courcoux, Y., Larouche, P., Broccardo, S. and
8347 Piketh, S. J.: Aerosol remote sensing in polar regions, Earth-Sci. Rev., 140, 108–157,
8348 doi:10.1016/j.earscirev.2014.11.001, 2015.

8349 Wendisch, M., Macke, A., Ehrlich, A., Lüpkes, C., Mech, M., Chechin, D., Dethloff, K.,
8350 Barientos, C., Bozem, H., Brückner, M., Clemen, H.-C., Crewell, S., Donth, T., Dupuy, R.,
8351 Ebell, K., Egerer, U., Engelmann, R., Engler, C., Eppers, O., Gehrmann, M., Gong, X.,
8352 Gottschalk, M., Gourbeyre, C., Griesche, H., Hartmann, J., Hartmann, M., Heinold, B.,
8353 Herber, A., Herrmann, H., Heygster, G., Hoor, P., Jafariserajehlou, S., Jäkel, E., Järvinen, E.,
8354 Jourdan, O., Kästner, U., Kecorius, S., Knudsen, E. M., Köllner, F., Kretzschmar, J., Lelli, L.,
8355 Leroy, D., Maturilli, M., Mei, L., Mertes, S., Mioche, G., Neuber, R., Nicolaus, M.,
8356 Nomokonova, T., Notholt, J., Palm, M., van Pinxteren, M., Quaas, J., Richter, P., Ruiz-
8357 Donoso, E., Schäfer, M., Schmieder, K., Schnaiter, M., Schneider, J., Schwarzenböck, A.,
8358 Seifert, P., Shupe, M. D., Siebert, H., Spreen, G., Stapf, J., Stratmann, F., Vogl, T., Welti, A.,

8359 Wex, H., Wiedensohler, A., Zanatta, M. and Zeppenfeld, S.: The Arctic Cloud Puzzle: Using
8360 ACLOUD/PASCAL Multi-Platform Observations to Unravel the Role of Clouds and Aerosol
8361 Particles in Arctic Amplification, Bull. Am. Meteorol. Soc., doi:10.1175/BAMS-D-18-
8362 0072.1, 2018.

8363 <BC vertical distributions>

8364 Bozem, H., Hoor, P., Kunkel, D., Köllner, F., Schneider, J., Herber, A., Schulz, H., Leaitch, W.
8365 R., Aliabadi, A. A., Willis, M. D., Burkart, J. and Abbatt, J. P. D.: Characterization of
8366 Transport Regimes and the Polar Dome during Arctic Spring and Summer using in-situ
8367 Aircraft Measurements, Atmospheric Chem. Phys. Discuss., 1–36,
8368 doi:https://doi.org/10.5194/acp-2019-70, 2019.

8369 Ferrero, L., Cappelletti, D., Busetto, M., Mazzola, M., Lupi, A., Lanconelli, C., Becagli, S.,
8370 Traversi, R., Caiazzo, L., Giardi, F., Moroni, B., Crocchianti, S., Fierz, M., Močnik, G.,
8371 Sangiorgi, G., Perrone, M. G., Maturilli, M., Vitale, V., Udisti, R. and Bolzacchini, E.:
8372 Vertical profiles of aerosol and black carbon in the Arctic: a seasonal phenomenology
8373 along 2 years (2011–2012) of field campaigns, Atmos Chem Phys, 16(19), 12601–12629,
8374 doi:10.5194/acp-16-12601-2016, 2016.

8375 Köllner, F., Schneider, J., Willis, M. D., Klimach, T., Helleis, F., Bozem, H., Kunkel, D., Hoor, P.,
8376 Burkart, J., Leaitch, W. R., Aliabadi, A. A., Abbatt, J. P. D., Herber, A. B. and Borrmann, S.:
8377 Particulate trimethylamine in the summertime Canadian high Arctic lower troposphere,
8378 Atmospheric Chem. Phys., 17(22), 13747–13766, doi:10.5194/acp-17-13747-2017, 2017.

8379 Kondo, Y., Matsui, H., Moteki, N., Sahu, L., Takegawa, N., Kajino, M., Zhao, Y., Cubison, M. J.,
8380 Jimenez, J. L., Vay, S., Diskin, G. S., Anderson, B., Wisthaler, A., Mikoviny, T., Fuelberg, H.
8381 E., Blake, D. R., Huey, G., Weinheimer, A. J., Knapp, D. J. and Brune, W. H.: Emissions of
8382 black carbon, organic, and inorganic aerosols from biomass burning in North America and
8383 Asia in 2008, J. Geophys. Res. Atmospheres, 116(D8), D08204,
8384 doi:10.1029/2010JD015152, 2011.

8385 Law, K. S., Roiger, A., Thomas, J. L., Marelle, L., Raut, J.-C., Dalsøren, S., Fuglestvedt, J.,
8386 Tuccella, P., Weinzierl, B. and Schlager, H.: Local Arctic air pollution: Sources and impacts,
8387 Ambio, 46(3), 453–463, doi:10.1007/s13280-017-0962-2, 2017.

8388 Liu, D., Quennehen, B., Darbyshire, E., Allan, J. D., Williams, P. I., Taylor, J. W., Bauguitte, S.
8389 J.-B., Flynn, M. J., Lowe, D., Gallagher, M. W., Bower, K. N., Choularton, T. W. and Coe, H.:
8390 The importance of Asia as a source of black carbon to the European Arctic during
8391 springtime 2013, Atmospheric Chem. Phys., 15(20), 11537–11555,
8392 doi:https://doi.org/10.5194/acp-15-11537-2015, 2015.

8393 Marelle, L., Raut, J.-C., Thomas, J. L., Law, K. S., Quennehen, B., Ancellet, G., Pelon, J.,
8394 Schwarzenboeck, A. and Fast, J. D.: Transport of anthropogenic and biomass burning
8395 aerosols from Europe to the Arctic during spring 2008, Atmospheric Chem. Phys., 15(7),
8396 3831–3850, doi:https://doi.org/10.5194/acp-15-3831-2015, 2015.

8397 Markowicz, K. M., Ritter, C., Lisok, J., Makuch, P., Stachlewska, I. S., Cappelletti, D., Mazzola,
8398 M. and Chilinski, M. T.: Vertical variability of aerosol single-scattering albedo and
8399 equivalent black carbon concentration based on in-situ and remote sensing techniques
8400 during the iAREA campaigns in Ny-Ålesund., Atmos. Environ., 164, 431–447,
8401 doi:Markowicz, K. M. , Ritter, C. , Lisok, J. , Makuch, P. , Stachlewska, I. S. , Cappelletti, D. ,
8402 Mazzola, M. and Chilinski, M. (2017) Vertical variability of aerosol single-scattering
8403 albedo and equivalent black carbon concentration based on in-situ and remote sensing
8404 techniques during the iAREA campaigns in Ny-Ålesund. , Atmospheric
8405 Environment, 164 , pp. 431-447 .
8406 doi:https://doi.org/10.1016/j.atmosenv.2017.06.014
8407 <https://doi.org/10.1016/j.atmosenv.2017.06.014> , hdl:10013/epic.51325, 2017.

8408 Matsui H., Kondo Y., Moteki N., Takegawa N., Sahu L. K., Zhao Y., Fuelberg H. E., Sessions W.
8409 R., Diskin G., Blake D. R., Wisthaler A. and Koike M.: Seasonal variation of the transport of
8410 black carbon aerosol from the Asian continent to the Arctic during the ARCTAS aircraft
8411 campaign, J. Geophys. Res. Atmospheres, 116(D5), doi:10.1029/2010JD015067, 2011.

8412 McNaughton, C. S., Clarke, A. D., Freitag, S., Kapustin, V. N., Kondo, Y., Moteki, N., Sahu, L.,
8413 Takegawa, N., Schwarz, J. P., Spackman, J. R., Watts, L., Diskin, G., Podolske, J., Holloway,
8414 J. S., Wisthaler, A., Mikoviny, T., de Gouw, J., Warneke, C., Jimenez, J., Cubison, M.,
8415 Howell, S. G., Middlebrook, A., Bahreini, R., Anderson, B. E., Winstead, E., Thornhill, K. L.,
8416 Lack, D., Cozic, J. and Brock, C. A.: Absorbing aerosol in the troposphere of the Western
8417 Arctic during the 2008 ARCTAS/ARCPAC airborne field campaigns, Atmos Chem Phys,
8418 11(15), 7561–7582, doi:10.5194/acp-11-7561-2011, 2011.

8419 Roiger, A., Thomas, J.-L., Schlager, H., Law, K. S., Kim, J., Schäfler, A., Weinzierl, B.,
8420 Dahlkötter, F., Krisch, I., Marelle, L., Minikin, A., Raut, J.-C., Reiter, A., Rose, M., Scheibe,
8421 M., Stock, P., Baumann, R., Bouarar, I., Clerbaux, C., George, M., Onishi, T. and Flemming,
8422 J.: Quantifying Emerging Local Anthropogenic Emissions in the Arctic Region: The ACCESS
8423 Aircraft Campaign Experiment, Bull. Am. Meteorol. Soc., 96(3), 441–460,
8424 doi:10.1175/BAMS-D-13-00169.1, 2015.

8425 Schulz, H., Zanatta, M., Bozem, H., Leaitch, W. R., Herber, A. B., Burkart, J., Willis, M. D.,
8426 Kunkel, D., Hoor, P. M., Abbatt, J. P. D. and Gerdes, R.: High Arctic aircraft measurements
8427 characterising black carbon vertical variability in spring and summer, Atmospheric Chem.
8428 Phys., 19(4), 2361–2384, doi:https://doi.org/10.5194/acp-19-2361-2019, 2019.

8429 Schwarz, J. P., Samset, B. H., Perring, A. E., Spackman, J. R., Gao, R. S., Stier, P., Schulz, M.,
8430 Moore, F. L., Ray, E. A. and Fahey, D. W.: Global-scale seasonally resolved black carbon
8431 vertical profiles over the Pacific, Geophys. Res. Lett., 40(20), 2013GL057775,
8432 doi:10.1002/2013GL057775, 2013.

8433 Sobhani, N., Kulkarni, S. and Carmichael, G. R.: Source sector and region contributions to
8434 black carbon and PM2.5 in the Arctic, Atmospheric Chem. Phys., 18(24), 18123–18148,
8435 doi:https://doi.org/10.5194/acp-18-18123-2018, 2018.

8436 Stohl A.: Characteristics of atmospheric transport into the Arctic troposphere, J. Geophys.
8437 Res. Atmospheres, 111(D11), doi:10.1029/2005JD006888, 2006.

8438 Stone, R. S., Sharma, S., Herber, A., Eleftheriadis, K. and Nelson, D. W.: A characterization of
8439 Arctic aerosols on the basis of aerosol optical depth and black carbon measurements,
8440 Elem. Sci. Anthr., 2, 000027, doi:10.12952/journal.elementa.000027, 2014.

8441 Willis, M. D., Bozem, H., Kunkel, D., Lee, A. K. Y., Schulz, H., Burkart, J., Aliabadi, A. A.,
8442 Herber, A. B., Leaitch, W. R. and Abbatt, J. P. D.: Aircraft-based measurements of High
8443 Arctic springtime aerosol show evidence for vertically varying sources, transport and
8444 composition, Atmospheric Chem. Phys., 19(1), 57–76, doi:https://doi.org/10.5194/acp-
8445 19-57-2019, 2019.

8446 Xu, J.-W., Martin, R. V., Morrow, A., Sharma, S., Huang, L., Leaitch, W. R., Burkart, J., Schulz,
8447 H., Zanatta, M., Willis, M. D., Henze, D. K., Lee, C. J., Herber, A. B. and Abbatt, J. P. D.:
8448 Source attribution of Arctic black carbon constrained by aircraft and surface

measurements, Atmospheric Chem. Phys., 17(19), 11971–11989, doi:https://doi.org/10.5194/acp-17-11971-2017, 2017.

<dust vertical distributions>

Biagio, C. D., Pelon, J., Ancellet, G., Bazureau, A. and Mariage, V.: Sources, Load, Vertical Distribution, and Fate of Wintertime Aerosols North of Svalbard From Combined V4 CALIOP Data, Ground-Based IAOOS Lidar Observations and Trajectory Analysis, J. Geophys. Res. Atmospheres, 123(2), 1363–1383, doi:10.1002/2017JD027530, 2018.

Blechschmidt, A.-M., Kristjánsson, J. E., Ólafsson, H., Burkhart, J. F., Hodnebrog, Ø. and Rosenberg, P. D.: Aircraft-based observations and high-resolution simulations of an Icelandic dust storm, Atmospheric Chem. Phys., 12(22), 10649–10666, doi:https://doi.org/10.5194/acp-12-10649-2012, 2012.

Bullard, J. E., Baddock, M., Bradwell, T., Crusius, J., Darlington, E., Gaiero, D., Gassó, S., Gisladottir, G., Hodgkins, R., McCulloch, R., McKenna-Neuman, C., Mockford, T., Stewart, H. and Thorsteinsson, T.: High-latitude dust in the Earth system, Rev. Geophys., 54(2), 447–485, doi:10.1002/2016RG000518, 2016.

Crusius, J., Schroth, A. W., Gassó, S., Moy, C. M., Levy, R. C. and Gatica, M.: Glacial flour dust storms in the Gulf of Alaska: Hydrologic and meteorological controls and their importance as a source of bioavailable iron, Geophys. Res. Lett., 38(6), doi:10.1029/2010GL046573, 2011.

Dagsson-Waldhauserova, P., Renard, J.-B., Olafsson, H., Vignelles, D., Berthet, G., Verdier, N. and Duverger, V.: Vertical distribution of aerosols in dust storms during the Arctic winter, Sci. Rep., 9(1), 1–11, doi:10.1038/s41598-019-51764-y, 2019.

Francis, D., Eayrs, C., Chaboureau, J.-P., Mote, T. and Holland, D. M.: Polar Jet Associated Circulation Triggered a Saharan Cyclone and Derived the Poleward Transport of the African Dust Generated by the Cyclone, J. Geophys. Res. Atmospheres, 123(21), 11,899-11,917, doi:10.1029/2018JD029095, 2018.

Groot Zwaaftink, C. D., Grythe, H., Skov, H. and Stohl, A.: Substantial contribution of northern high-latitude sources to mineral dust in the Arctic, J. Geophys. Res. Atmospheres, 121(22), 2016JD025482, doi:10.1002/2016JD025482, 2016.

Groot Zwaaftink, C. D., Arnalds, Ó., Dagsson-Waldhauserova, P., Eckhardt, S., Prospero, J. M. and Stohl, A.: Temporal and spatial variability of Icelandic dust emissions and atmospheric transport, Atmospheric Chem. Phys., 17(17), 10865–10878, doi:10.5194/acp-17-10865-2017, 2017.

McAuliffe, M. A. P. and Ruth, A. A.: Typical tropospheric aerosol backscatter profiles for Southern Ireland: The Cork Raman lidar, Atmospheric Res., 120–121, 334–342, doi:10.1016/j.atmosres.2012.09.020, 2013.

McNaughton, C. S., Clarke, A. D., Freitag, S., Kapustin, V. N., Kondo, Y., Moteki, N., Sahu, L., Takegawa, N., Schwarz, J. P., Spackman, J. R., Watts, L., Diskin, G., Podolske, J., Holloway, J. S., Wisthaler, A., Mikoviny, T., de Gouw, J., Warneke, C., Jimenez, J., Cubison, M., Howell, S. G., Middlebrook, A., Bahreini, R., Anderson, B. E., Winstead, E., Thornhill, K. L., Lack, D., Cozic, J. and Brock, C. A.: Absorbing aerosol in the troposphere of the Western Arctic during the 2008 ARCTAS/ARCPAC airborne field campaigns, Atmos Chem Phys, 11(15), 7561–7582, doi:10.5194/acp-11-7561-2011, 2011.

Moroni, B., Cappelletti, D., Ferrero, L., Crocchianti, S., Busetto, M., Mazzola, M., Becagli, S., Traversi, R. Udisti, R., Local vs long range sources of aerosol particles upon Ny-Alesund (Svalbard Islands):

mineral chemistry and geochemical records Rend. Fis. Acc. Lincei (2016) 27 (Suppl 1):S115–S127

DOI 10.1007/s12210-016-0533-7

Moroni, B., Arnalds, O., Dagsson-Waldhauserová, P., Crocchianti, S., Vivani, R. and Cappelletti, D.: Mineralogical and Chemical Records of Icelandic Dust Sources Upon Ny-Ålesund (Svalbard Islands), Front. Earth Sci., 6, doi:10.3389/feart.2018.00187, 2018.

<OA vertical distributions>

Abbatt, J. P. D., Leaitch, W. R., Aliabadi, A. A., Bertram, A. K., Blanchet, J.-P., Boivin-Rioux, A., Bozem, H., Burkart, J., Chang, R. Y. W., Charette, J., Chaubey, J. P., Christensen, R. J., Cirisan, A., Collins, D. B., Croft, B., Dionne, J., Evans, G. J., Fletcher, C. G., Ghahremaninezhad, R., Girard, E., Gong, W., Gosselin, M., Gourdal, M., Hanna, S. J., Hayashida, H., Herber, A. B., Hesaraki, S., Hoor, P., Huang, L., Hussherr, R., Irish, V. E.,

8507 Keita, S. A., Kodros, J. K., Köllner, F., Kolonjari, F., Kunkel, D., Ladino, L. A., Law, K.,
8508 Levasseur, M., Libois, Q., Liggio, J., Lizotte, M., Macdonald, K. M., Mahmood, R., Martin,
8509 R. V., Mason, R. H., Miller, L. A., Moravek, A., Mortenson, E., Mungall, E. L., Murphy, J. G.,
8510 Namazi, M., Norman, A.-L., O'Neill, N. T., Pierce, J. R., Russell, L. M., Schneider, J., Schulz,
8511 H., Sharma, S., Si, M., Staebler, R. M., Steiner, N. S., Galí, M., Thomas, J. L., Salzen, K. von,
8512 Wentzell, J. J. B., Willis, M. D., Wentworth, G. R., Xu, J.-W. and Yakobi-Hancock, J. D.: New
8513 insights into aerosol and climate in the Arctic, Atmospheric Chem. Phys. Discuss., 1–60,
8514 doi:https://doi.org/10.5194/acp-2018-995, 2018.

8515 Burkart, J., Willis, M. D., Bozem, H., Thomas, J. L., Law, K., Hoor, P., Aliabadi, A. A., Köllner,
8516 F., Schneider, J., Herber, A. and others: Summertime observations of elevated levels of
8517 ultrafine particles in the high Arctic marine boundary layer., Atmospheric Chem. Phys.,
8518 17(8) [online] Available from:
8519 https://www.researchgate.net/profile/Amir_A_Aliabadi/publication/316640687_Summe
8520 rtime_observations_of_elevated_levels_of_ultrafine_particles_in_the_high_Arctic_marin
8521 e_boundary_layer/links/590b284c0f7e9b1d0826fc34/Summertime-observations-of-
8522 elevated-levels-of-ultrafine-particles-in-the-high-Arctic-marine-boundary-layer.pdf
8523 (Accessed 21 May 2017), 2017.

8524 Collins, D. B., Burkart, J., Chang, R. Y.-W., Lizotte, M., Boivin-Rioux, A., Blais, M., Mungall, E.
8525 L., Boyer, M., Irish, V. E., Massé, G., Kunkel, D., Tremblay, J.-É., Papakyriakou, T., Bertram,
8526 A. K., Bozem, H., Gosselin, M., Levasseur, M. and Abbatt, J. P. D.: Frequent ultrafine
8527 particle formation and growth in Canadian Arctic marine and coastal environments,
8528 Atmospheric Chem. Phys., 17(21), 13119–13138, doi:10.5194/acp-17-13119-2017, 2017.

8529 Croft, B., Martin, R. V., Leaitch, W. R., Burkart, J., Chang, R. Y.-W., Collins, D. B., Hayes, P. L.,
8530 Hodshire, A. L., Huang, L., Kodros, J. K., Moravek, A., Mungall, E. L., Murphy, J. G.,
8531 Sharma, S., Tremblay, S., Wentworth, G. R., Willis, M. D., Abbatt, J. P. D. and Pierce, J. R.:
8532 Arctic marine secondary organic aerosol contributes significantly to summertime particle
8533 size distributions in the Canadian Arctic Archipelago, Atmospheric Chem. Phys., 19(5),
8534 2787–2812, doi:https://doi.org/10.5194/acp-19-2787-2019, 2019.

8535 Dall´Osto, M., Beddows, D. C. S., Tunved, P., Krejci, R., Ström, J., Hansson, H.-C., Yoon, Y. J.,
8536 Park, K.-T., Becagli, S., Udisti, R., Onasch, T., O´Dowd, C. D., Simó, R. and Harrison, R. M.:

8537 Arctic sea ice melt leads to atmospheric new particle formation, Sci. Rep., 7(1), 3318,
8538 doi:10.1038/s41598-017-03328-1, 2017.

8539 Dall´Osto, M., Geels, C., Beddows, D. C. S., Boertmann, D., Lange, R., Nøjgaard, J. K.,
8540 Harrison, R. M., Simo, R., Skov, H. and Massling, A.: Regions of open water and melting
8541 sea ice drive new particle formation in North East Greenland, Sci. Rep., 8(1), 1–10,
8542 doi:10.1038/s41598-018-24426-8, 2018.

8543 Ghahremaninezhad, R., Norman, A.-L., Croft, B., Martin, R. V., Pierce, J. R., Burkart, J.,
8544 Rempillo, O., Bozem, H., Kunkel, D., Thomas, J. L., Aliabadi, A. A., Wentworth, G. R.,
8545 Levasseur, M., Staebler, R. M., Sharma, S. and Leaitch, W. R.: Boundary layer and free-
8546 tropospheric dimethyl sulfide in the Arctic spring and summer, Atmospheric Chem. Phys.,
8547 17(14), 8757–8770, doi:10.5194/acp-17-8757-2017, 2017.

8548 Köllner, F., Schneider, J., Willis, M. D., Klimach, T., Helleis, F., Bozem, H., Kunkel, D., Hoor, P.,
8549 Burkart, J., Leaitch, W. R., Aliabadi, A. A., Abbatt, J. P. D., Herber, A. B. and Borrmann, S.:
8550 Particulate trimethylamine in the summertime Canadian high Arctic lower troposphere,
8551 Atmospheric Chem. Phys., 17(22), 13747–13766, doi:10.5194/acp-17-13747-2017, 2017.

8552 Leaitch, W. R., Korolev, A., Aliabadi, A. A., Burkart, J., Willis, M. D., Abbatt, J. P. D., Bozem,
8553 H., Hoor, P., Köllner, F., Schneider, J., Herber, A., Konrad, C. and Brauner, R.: Effects of
8554 20–100 nm particles on liquid clouds in the clean summertime Arctic, Atmos Chem Phys,
8555 16(17), 11107–11124, doi:10.5194/acp-16-11107-2016, 2016.

8556 Leaitch, W. R., Russell, L. M., Liu, J., Kolonjari, F., Toom, D., Huang, L., Sharma, S., Chivulescu,
8557 A., Veber, D. and Zhang, W.: Organic functional groups in the submicron aerosol at 82.5°
8558 N, 62.5° W from 2012 to 2014, Atmospheric Chem. Phys., 18(5), 3269–3287,
8559 doi:https://doi.org/10.5194/acp-18-3269-2018, 2018.

8560 Willis, M. D., Burkart, J., Thomas, J. L., Köllner, F., Schneider, J., Bozem, H., Hoor, P. M.,
8561 Aliabadi, A. A., Schulz, H., Herber, A. B., Leaitch, W. R. and Abbatt, J. P. D.: Growth of
8562 nucleation mode particles in the summertime Arctic: a case study, Atmos Chem Phys,
8563 16(12), 7663–7679, doi:10.5194/acp-16-7663-2016, 2016.

8564 Willis, M. D., Bozem, H., Kunkel, D., Lee, A. K. Y., Schulz, H., Burkart, J., Aliabadi, A. A.,
8565 Herber, A. B., Leaitch, W. R. and Abbatt, J. P. D.: Aircraft-based measurements of High
8566 Arctic springtime aerosol show evidence for vertically varying sources, transport and

composition, Atmospheric Chem. Phys., 19(1), 57–76, doi:https://doi.org/10.5194/acp-19-57-2019, 2019.

<vertical distributions of physical properties>

Brock, C. A., Cozic, J., Bahreini, R., Froyd, K. D., Middlebrook, A. M., McComiskey, A., Brioude, J., Cooper, O. R., Stohl, A., Aikin, K. C., Gouw, J. A. de, Fahey, D. W., Ferrare, R. A., Gao, R.-S., Gore, W., Holloway, J. S., Hübler, G., Jefferson, A., Lack, D. A., Lance, S., Moore, R. H., Murphy, D. M., Nenes, A., Novelli, P. C., Nowak, J. B., Ogren, J. A., Peischl, J., Pierce, R. B., Pilewskie, P., Quinn, P. K., Ryerson, T. B., Schmidt, K. S., Schwarz, J. P., Sodemann, H., Spackman, J. R., Stark, H., Thomson, D. S., Thornberry, T., Veres, P., Watts, L. A., Warneke, C. and Wollny, A. G.: Characteristics, sources, and transport of aerosols measured in spring 2008 during the aerosol, radiation, and cloud processes affecting Arctic Climate (ARCPAC) Project, Atmospheric Chem. Phys., 11(6), 2423–2453, doi:https://doi.org/10.5194/acp-11-2423-2011, 2011.

Burkart, J., Willis, M. D., Bozem, H., Thomas, J. L., Law, K., Hoor, P., Aliabadi, A. A., Köllner, F., Schneider, J., Herber, A. and others: Summertime observations of elevated levels of ultrafine particles in the high Arctic marine boundary layer., Atmospheric Chem. Phys., 17(8) [online] Available from: https://www.researchgate.net/profile/Amir_A_Aliabadi/publication/316640687_Summertime_observations_of_elevated_levels_of_ultrafine_particles_in_the_high_Arctic_marine_boundary_layer/links/590b284c0f7e9b1d0826fc34/Summertime-observations-of-elevated-levels-of-ultrafine-particles-in-the-high-Arctic-marine-boundary-layer.pdf (Accessed 21 May 2017), 2017.

Ferrero, L., Cappelletti, D., Busetto, M., Mazzola, M., Lupi, A., Lanconelli, C., Becagli, S., Traversi, R., Caiazzo, L., Giardi, F., Moroni, B., Crocchianti, S., Fierz, M., Močnik, G., Sangiorgi, G., Perrone, M. G., Maturilli, M., Vitale, V., Udisti, R. and Bolzacchini, E.: Vertical profiles of aerosol and black carbon in the Arctic: a seasonal phenomenology along 2 years (2011–2012) of field campaigns, Atmos Chem Phys, 16(19), 12601–12629, doi:10.5194/acp-16-12601-2016, 2016.

8595 Hegg, D. A., Ferek, R. J. and Hobbs, P. V.: Cloud condensation nuclei over the Arctic Ocean in
8596 early spring, J. Appl. Meteorol., 34(9), doi:10.1175/1520-
8597 0450(1995)034<2076:CCNOTA>2.0.CO;2, 1995.

8598 Kupiszewski, P., Leck, C., Tjernström, M., Sjogren, S., Sedlar, J., Graus, M., Müller, M.,
8599 Brooks, B., Swietlicki, E., Norris, S. and Hansel, A.: Vertical profiling of aerosol particles
8600 and trace gases over the central Arctic Ocean during summer, Atmospheric Chem. Phys.,
8601 13(24), 12405–12431, doi:https://doi.org/10.5194/acp-13-12405-2013, 2013.

8602 Lathem, T. L., Beyersdorf, A. J., Thornhill, K. L., Winstead, E. L., Cubison, M. J., Hecobian, A.,
8603 Jimenez, J. L., Weber, R. J., Anderson, B. E. and Nenes, A.: Analysis of CCN activity of
8604 Arctic aerosol and Canadian biomass burning during summer 2008, Atmospheric Chem.
8605 Phys., 13(5), 2735–2756, doi:10.5194/acp-13-2735-2013, 2013.

8606 Matsui, H., Kondo, Y., Moteki, N., Takegawa, N., Sahu, L. K., Koike, M., Zhao, Y., Fuelberg, H.
8607 E., Sessions, W. R., Diskin, G., Anderson, B. E., Blake, D. R., Wisthaler, A., Cubison, M. J.
8608 and Jimenez, J. L.: Accumulation-mode aerosol number concentrations in the Arctic
8609 during the ARCTAS aircraft campaign: Long-range transport of polluted and clean air from
8610 the Asian continent, J. Geophys. Res. Atmospheres, 116(D20),
8611 doi:10.1029/2011JD016189, 2011.

8612 McFarquhar, G. M., Ghan, S., Verlinde, J., Korolev, A., Strapp, J. W., Schmid, B., Tomlinson, J.
8613 M., Wolde, M., Brooks, S. D., Cziczo, D., Dubey, M. K., Fan, J., Flynn, C., Gultepe, I., Hubbe,
8614 J., Gilles, M. K., Laskin, A., Lawson, P., Leaitch, W. R., Liu, P., Liu, X., Lubin, D., Mazzoleni,
8615 C., Macdonald, A.-M., Moffet, R. C., Morrison, H., Ovchinnikov, M., Shupe, M. D., Turner,
8616 D. D., Xie, S., Zelenyuk, A., Bae, K., Freer, M. and Glen, A.: Indirect and Semi-direct
8617 Aerosol Campaign, Bull. Am. Meteorol. Soc., 92(2), 183–201,
8618 doi:10.1175/2010BAMS2935.1, 2010.

8619 Moore, R. H., Bahreini, R., Brock, C. A., Froyd, K. D., Cozic, J., Holloway, J. S., Middlebrook, A.
8620 M., Murphy, D. M. and Nenes, A.: Hygroscopicity and composition of Alaskan Arctic CCN
8621 during April 2008, Atmospheric Chem. Phys., 11(22), 11807–11825, doi:10.5194/acp-11-
8622 11807-2011, 2011.

8623 Prenni, A. J., Demott, P. J., Rogers, D. C., Kreidenweis, S. M., Mcfarquhar, G. M., Zhang, G.
8624 and Poellot, M. R.: Ice nuclei characteristics from M-PACE and their relation to ice

formation in clouds, Tellus B Chem. Phys. Meteorol., 61(2), 436–448, doi:10.1111/j.1600-0889.2008.00415.x, 2009.

Quennehen, B., Schwarzenboeck, A., Matsuki, A., Burkhart, J. F., Stohl, A., Ancellet, G. and Law, K. S.: Anthropogenic and forest fire pollution aerosol transported to the Arctic: observations from the POLARCAT-France spring campaign, Atmospheric Chem. Phys., 12(14), 6437–6454, doi:10.5194/acp-12-6437-2012, 2012.

Rogers, D. C., DeMott, P. J. and Kreidenweis, S. M.: Airborne measurements of tropospheric ice-nucleating aerosol particles in the Arctic spring, J. Geophys. Res. Atmospheres, 106(D14), 15053–15063, doi:10.1029/2000JD900790@10.1002/(ISSN)2169-8996.FIREAC1, 2001.

Schulz, H., Zanatta, M., Bozem, H., Leaitch, W. R., Herber, A. B., Burkart, J., Willis, M. D., Kunkel, D., Hoor, P. M., Abbatt, J. P. D. and Gerdes, R.: High Arctic aircraft measurements characterising black carbon vertical variability in spring and summer, Atmospheric Chem. Phys., 19(4), 2361–2384, doi:https://doi.org/10.5194/acp-19-2361-2019, 2019.

Shantz, N. C., Gultepe, I., Andrews, E., Zelenyuk, A., Earle, M. E., Macdonald, A. M., Liu, P. S. K. and Leaitch, W. R.: Optical, physical, and chemical properties of springtime aerosol over Barrow Alaska in 2008, Int. J. Climatol., 34(10), 3125–3138, doi:10.1002/joc.3898, 2014.

Shibata, T., Shiraishi, K., Shiobara, M., Iwasaki, S. and Takano, T.: Seasonal Variations in High Arctic Free Tropospheric Aerosols Over Ny-Ålesund, Svalbard, Observed by Ground-Based Lidar, J. Geophys. Res. Atmospheres, 123(21), 12,353-12,367, doi:10.1029/2018JD028973, 2018.

Yum, S. S. and Hudson, J. G.: Vertical distributions of cloud condensation nuclei spectra over the springtime Arctic Ocean, J. Geophys. Res. Atmospheres, 106(D14), 15045–15052, doi:10.1029/2000JD900357@10.1002/(ISSN)2169-8996.FIREAC1, 2001.

5.1.2.3 Observations of aerosol components in snow

8652 Aamaas, B., Bøggild, C.E., Stordal, F., Berntsen, T., Holmén, K. and Ström, J.: Elemental
8653 carbon deposition to Svalbard snow from Norwegian settlements and long-range
8654 transport, Tellus, 63B, 340–351, doi:10.1111/j.1600-0889.2011.00531.x, 2011

8655 Boy, M., Thomson, E.S., Acosta Navarro, J.-C., Arnalds, O., Batchvarova, E., Bäck et al. (2019).
8656 Interactions between the atmosphere, cryosphere, and ecosystems at northern high
8657 latitudes. Atmos. Chem. Phys. 19, 2015–2061.

8658 Dang, C., Warren, S. G., Fu, Q., Doherty, S. J., Sturm, M., and Su, J. (2017), Measurements of
8659 light-absorbing particles in snow across the Arctic, North America, and China: Effects on
8660 surface albedo, *J. Geophys. Res. Atmos.*, 122, 10,149– 10,168,
8661 doi:10.1002/2017JD027070.

8662 Dou, T., Xiao, C., Du, Z., Schauer, J.J., Ren, H., Ge, B., Xie, A., Tan, J., Fu, P. and Zhang, Y.:
8663 Sources, evolution and impacts of EC and OC in snow on sea ice: a measurement study in
8664 Barrow, Alaska, Sci. Bull. 62, 1547–1554, doi:10.1016/j.scib.2017.10.014, 2017.

8665 Evangeliou, N., Shevchenko, V. P., Yttri, K. E., Eckhardt, S., Sollum, E., Pokrovsky, O. S.,
8666 Kobelev, V. O., Korobov, V. B., Lobanov, A. A., Starodymova, D. P., Vorobiev, S. N.,
8667 Thompson, R. L., and Stohl, A.: Origin of elemental carbon in snow from western Siberia
8668 and northwestern European Russia during winter–spring 2014, 2015 and 2016, Atmos.
8669 Chem. Phys., 18, 963–977

8670 Flanner, M. G., Zender, C. S., Randerson, J. T., & Rasch, P. J. (2007). Present-day climate
8671 forcing and response from black carbon in snow. Journal of Geophysical Research:
8672 Atmospheres, 112, D11202.

8673 Forsström, S., Isaksson, E., Skeie, R. B., Ström, J., Pedersen, C. A., Hudson, S. R., Berntsen, T.
8674 K., Lihavainen, H., Godtliebsen, F. and Gerland, S. : Elemental carbon measurements in
8675 European Arctic snow packs, J. Geophys. Res. Atmos., 118, 13,614–13,627, 2013.

8676 Forsström, S., Ström, J., Pedersen, J. C. A., Isaksson, E., and Gerland, S.: Elemental carbon
8677 distribution in Svalbard snow, J. Geophys. Res. Atmos. 114, D19112, 2009.

8678 Gogoi, M.M., Babu, S.S., Pandey, S.K., Nair, V.S., Vaishya, A., Girach, A.I.A. and Koushik, N.:
8679 Scavenging ratio of black carbon in the Arctic and the Antarctic, Polar Science, 16, 10–22
8680 2018.

8681 Hagler, G. S. W., Bergin, M.H., Smith, E.A., Dibb, J.E., Anderson, C. and Steig, E.J.: Particulate
8682 and water-soluble carbon measured in recent snow at Summit, Greenland, Geophys.
8683 Res. Lett., 34, L16505, doi:10.1029/2007GL030110, 2007.

8684 Jacobi, H.-W., Obleitner, F., Da Costa, S., Ginot, P., Eleftheriadis, K., Aas, W., & Zanatta, M.
8685 (2019). Deposition of ionic species and black carbon to the Arctic snowpack: combining
8686 snow pit observations with modeling. Atmospheric Chemistry and Physics, 19, 10,361–
8687 10,377. https://doi.org/10.5194/acp-19-10361-2019

8688 Meinander Outi, Anna Kontu, Rostislav Kouznetsov and Mikhail Sofiev, Snow samples
8689 combined with long-range transport modeling to reveal the origin and temporal
8690 variability of black carbon in seasonal snow in Sodankylä (67 oN) Front. Earth Sci. | doi:
8691 10.3389/feart.2020.00153, accepted, available at
8692 https://www.frontiersin.org/articles/10.3389/feart.2020.00153/abstract, 2020.

8693 Meinander, O., Kazadzis, S., Arola, A., Riihelä, A., Räisänen, P., Kivi, R., Kontu, A.,
8694 Kouznetsov, R., Sofiev, M., Svensson, J., Suokanerva, H., Aaltonen, V., Manninen, T.,
8695 Roujean, J.-L., and Hautecoeur, O.: Spectral albedo of seasonal snow during intensive
8696 melt period at Sodankylä, beyond the Arctic Circle, Atmos. Chem. Phys., 13, 3793–3810,
8697 do:10.5194/acp-13-3793-2013, 2013.

8698 Mori, T., Goto-Azuma, K., Kondo, Y., Ogawa-Tsukagawa, Y., Miura, K., Hirabayashi, M., et al.
8699 (2019). Black carbon and inorganic aerosols in Arctic snowpack. Journal of Geophysical
8700 Research: Atmospheres, 124.

8701 Pedersen, C. A., Gallet, J. -C. ., Ström, J., Gerland, S., Hudson, S. R., Forsström, S., Isaksson, E.
8702 and Berntsen, T. K. (2015), In situ observations of black carbon in snow and the
8703 corresponding spectral surface albedo reduction. *J. Geophys. Res. Atmos.*, 120: 1476–
8704 1489. doi: 10.1002/2014JD022407

8705 Ruppel, M. M., Soares, J., Gallet, J.-C., Isaksson, E., Martma, T., Svensson, J., Kohler, J.,
8706 Pedersen, C.A., Manninen, S., Korhola, A. and Ström, J.: Do contemporary (1980–2015)
8707 emissions determine the elemental carbon deposition trend at Holtedahlfonna glacier,
8708 Svalbard? Atmos. Chem. Phys., 17, 12,779–12,795, doi:10.5194/acp-17-12779-2017,
8709 2017

8710 Svensson, J., Ström, J., Kivekäs, N., Dkhar, N. B., Tayal, S., Sharma, V. P., et al. (2018). Light-
8711 absorption of dust and elemental carbon in snow in the Indian Himalayas and the Finnish
8712 Arctic. *Atmos. Meas. Tech*. 11, 1403–1416. doi: 10.5194/amt-11-1403-2018

8713 Sinha, P. R., Kondo, Y., Goto-Azuma, K., Tsukagawa, Y., Fukuda, K., Koike, M., et al. (2018).
8714 Seasonal progression of the deposition of black carbon by snowfall at Ny-Ålesund,
8715 Spitsbergen. Journal of Geophysical Research: Atmospheres, 123, 997–1016.

8716 Spolaor, E. Barbaro, M. Mazzola, A.P. Viola, J. Lisok, F. Obleitner, K.M. Markowicz, D.
8717 Cappelletti, Determination of black carbon and nanoparticles along glaciers in the
8718 Spitsbergen (Svalbard) region exploiting a mobile platform, Atmospheric Environment,
8719 170, 184--196 (2017).

8720 Svensson, J., Ström, J., Kivekäs, N., Dkhar, N. B., Tayal, S., Sharma, V. P., Jutila, A., Backman,
8721 J., Virkkula, A., Ruppel, M., Hyvärinen, A., Kontu, A., Hannula, H.-R., Leppäranta, M.,
8722 Hooda, R. K., Korhola, A., Asmi, E., and Lihavainen, H.: Light-absorption of dust and
8723 elemental carbon in snow in the Indian Himalayas and the Finnish Arctic, Atmos. Meas.
8724 Tech., 11, 1403–1416, https://doi.org/10.5194/amt-11-1403-2018, 2018.

8725 Svensson, J. Ström, J., Hansson, M., Lihavainen, H., and Kerminen, V.-M.: Observed metre
8726 scale horizontal variability of elemental carbon in surface snow, Environ. Res. Lett., 8,
8727 034012, doi:10.1088/1748-9326/8/3/034012, 2013

8728 Svensson, J., Ström, J., and Virkkula, A.: Multiple-scattering correction factor of quartz filters
8729 and the effect of filtering particles mixed in water: implications for analyses of light
8730 absorption in snow samples, Atmos. Meas. Tech., 12, 5913–5925,
8731 https://doi.org/10.5194/amt-12-5913-2019, 2019.

8732 Zdanowicz et al., in preparation (to be submitted to ACP next weeks).

8733 <dust in snow>

8734 Boy, M., Thomson, E.S., Acosta Navarro, J.-C., Arnalds, O., Batchvarova, E., Bäck et al. (2019).
8735 Interactions between the atmosphere, cryosphere, and ecosystems at northern high
8736 latitudes. *Atmos. Chem. Phys*. 19, 2015–2061.

8737 Dagsson-Waldhauserova, P., Meinander, O., eds. Atmosphere – Cryosphere Interaction in
8738 the Arctic, at High Latitudes and Mountains With Focus on Transport, Deposition and

Effects of Dust, Black Carbon, and Other Aerosols. Lausanne: Frontiers Media SA. ISSN 1664-8714, ISBN 978-2-88963-504-7, doi: 10.3389/978-2-88963-504-7, e-book, 2020.

Dagsson-Waldhauserova P. and Meinander O. Editorial: Atmosphere - cryosphere interaction in the Arctic, at high latitudes and mountains with focus on transport, deposition and effects of dust, black carbon, and other aerosols. Front. Earth Sci., doi: 10.3389/feart.2019.00337, 2019.

Dragosics, M., Meinander, O., Jónsdóttír, T., Dürig, T., De Leeuw, G., Pálsson, F., Dagsson-Waldhauserová, P., and Thorsteinsson, T.: Insulation effects of Icelandic dust and volcanic ash on snow and ice. Arabian Journal of Geosciences, Dust special issue, 9, 126, doi: 10.1007/s12517-015-2224-6, 2016.

Dumont, M., Brun, E., Picard, G., Michou, M., Libois, Q., Petit, J. R., Morin, S., and Josse, B.: Contribution of light-absorbing impurities in snow to Greenland/'s darkening since 2009, Nat. Geosci., 7, 509–512, 2014.

Gassó , S., T. Thorsteinsson, and C. McKenna-Neuman (2018), Assessing the many influences of high-latitude dust, *Eos, 99,* https://doi.org/10.1029/2018EO090315. Published on 23 January 2018.

IPCC, 2019. *Summary for Policymakers. In: IPCC Special Report on the Ocean and Cryosphere in a Changing Climate* [H.-O. Pörtner, D.C. Roberts, V. Masson-Delmotte, P. Zhai, M. Tignor, E. Poloczanska, K. Mintenbeck, M. Nicolai, A. Okem, J. Petzold, B. Rama, N. Weyer (eds.)]. In press.

Khan, A. L., Dierssen, H., Schwarz, J. P., Schmitt, C., Chlus, A., Hermanson, M., Painter, T. H., and McKnight, D. M. (2017), Impacts of coal dust from an active mine on the spectral reflectance of Arctic surface snow in Svalbard, Norway, *J. Geophys. Res. Atmos.*, 122, 1767– 1778, doi:10.1002/2016JD025757.

Peltoniemi, J.I., Gritsevich, M., Hakala, T., Dagsson-Waldhauserová, P., Arnalds, Ó., Anttila et al. (2015). Soot on Snow experiment: bidirectional reflectance factor measurements of contaminated snow. Cryosphere 9, 2323–2337. doi.org/10.5194/tc-9-2323-2015.

Kylling, A., C. D. Groot Zwaaftink and A. Stohl, 2018: Mineral Dust Instantaneous Radiative Forcing in the Arctic.Geophysical Research Letters, 45 (9), 4290-4298, doi:10.1029/2018gl077346.

Möller, R., Möller, M., Kukla, P. A., and Schneider, C. (2016). Impact of supraglacial deposits of tephra from Grimsvötn volcano, Iceland, on glacier ablation. *J. Glaciol.* 62, 933–943. doi: 10.1017/jog.2016.82

5.1.3.1 Present day trends

Collaud Coen et al., Multidecadal trend analysis of aerosol radiative properties at a global scale, submitted.

Dutkiewicz et al., Forty-seven years of weekly atmospheric black carbon measurements in the Finnish Arctic: Decrease in black carbon measurements in the Finnish Arctic: Decrease in black carbon with declining emissions. J. Geophys. Res., 119, 12, 7667-7683, 2014. doi.ore/10.1002/2014JD021790

Sharma, S., Andrews, E., Barrie, L. A., Ogren, J. A., and Lavoué, D. (2006). Variations and sources of the Equivalent Black Carbon in the high Arctic revealed by long-term observations at Alert and Barrow: 1989-2003. *Journal of Geophysical Research-Atmosphere*, *111(D14)*, D14208. https://doi.org/10.1029/2005jd006581, 47

Sharma, S., Ishizawa, M., Chan, D., Lavoue, D., Andrews, E., Eleftheriadis, K., and Maksyutov, S. (2013). 16-year simulation of Arctic black carbon: Transport, source contribution, and sensitivity analysis on deposition. *Journal of Geophysical Research-Atmosphere*, *118 (2)*, 943-964.

Sharma, S., Barrie, L.A., Magnusson, E., Brattstrom , G., Leaitch, W. R., Steffen, A., and Landsberger, S., (2019). A factor and trends analysis of multidecadal lower tropospheric observations of arctic aerosol composition, black carbon, ozone, and mercury at Alert, Canada. J.Geophys. Res.:Atmospheres, 124, 14,133-14,161. http://doi.org/10.1029/2019JD030844.

<dust trends>

EBAS data base. Data of calcium for Villum (2008-2017), Alert (1980-1995), Ny alesund (2008-2019) and iron for Ny Alesund - Zeppelin full 2019 and Villum 2008-2012.

Dagsson-Waldhauserova, P., Arnalds, O., and Olafsson, H.: Long-term variability of dust events in Iceland (1949–2011), Atmos. Chem. Phys., 14, 13411–13422, https://doi.org/10.5194/acp-14-13411-2014, 2014.

5.1.3.2 Ice core records

McConnell et al., PNAS, 2019.

The NEEM_2011_S1 and Humboldt nssS records were published previously in Sigl et al., JGR, 2013.

The Tunu2013 nssS record was previously published in Sigl et al., Nature, 2015 (although these data are from a more recent analysis of a parallel sample from the same core).

The BC record from D4 was published in McConnell et al, Science, 2007 (although these data are from a more recent analysis of a parallel sample from the same core).

The BC record from Act2 was published in McConnell and Edwards, PNAS, 2008 (although it has been scaled by 0.65 to bring it in line with our newer analytical setup and calibration procedures).

The BC record from NEEM was published in Zennaro et al., Clim Past, 2014.

Wittmann, M., Groot Zwaaftink, C. D., Steffensen Schmidt, L., Guð*mundsson, S., Pálsson, F., Arnalds, O., et al. (2017). Impact of dust deposition on the albedo of Vatnajökull ice cap, Iceland. *Cryosphere* 11, 741–754. doi: 10.5194/tc-11-741-2017

Grieman, M. M., Aydin, M., Fritzsche, D., McConnell, J. R., Opel, T., Sigl, M. and Saltzman, E. S.: Aromatic acids in a Eurasian Arctic ice core: A 2600-year proxy record of biomass burning, Clim. Past, 13(4), 395–410, doi:10.5194/cp-13-395-2017, 2017.

Grieman, M. M., Aydin, M., Isaksson, E., Schwikowski, M. and Saltzman, E. S.: Aromatic acids in an Arctic ice core from Svalbard: A proxy record of biomass burning, Clim. Past, 14(5), 637–651, doi:10.5194/cp-14-637-2018, 2018a.

8823 Grieman, M. M., Aydin, M., McConnell, J. R. and Saltzman, E. S.: Burning-derived vanillic acid
8824 in an Arctic ice core from Tunu, northeastern Greenland, Clim. Past, 14(11), 1625–1637,
8825 doi:10.5194/cp-14-1625-2018, 2018b.

8826 Kehrwald, N., Zangrando, R., Gabrielli, P., Jaffrezo, J. L., Boutron, C., Barbante, C. and
8827 Gambaro, A.: Levoglucosan as a specific marker of fire events in Greenland snow, Tellus,
8828 Ser. B Chem. Phys. Meteorol., 64(1), 1–11, doi:10.3402/tellusb.v64i0.18196, 2012.

8829 Legrand, M., McConnell, J., Fischer, H., Wolff, E. W., Preunkert, S., Arienzo, M., Chellman, N.,
8830 Leuenberger, D., Maselli, O., Place, P., Sigl, M., Schüpbach, S. and Flannigan, M.: Boreal
8831 fire records in Northern Hemisphere ice cores: A review, Clim. Past, 12(10), 2033–2059,
8832 doi:10.5194/cp-12-2033-2016, 2016.

8833 Pokhrel, A., Kawamura, K., Kunwar, B., Ono, K., Tsushima, A., Seki, O., Matoba, S. and
8834 Shiraiwa, T.: Ice core records of levoglucosan and dehydroabietic and vanillic acids from
8835 Aurora Peak in Alaska since the 1660s: A proxy signal of biomass-burning activities in the
8836 North Pacific Rim, Atmos. Chem. Phys., 20(1), 597–612, doi:10.5194/acp-20-597-2020,
8837 2020.

8838 Rubino, M., D'Onofrio, A., Seki, O. and Bendle, J. A.: Ice-core records of biomass burning,
8839 Anthr. Rev., 3(2), 140–162, doi:10.1177/2053019615605117, 2016.

8840 Zennaro, P., Kehrwald, N., McConnell, J. R., Schuepbach, S., Maselli, O. J., Marlon, J.,
8841 Vallelonga, P., Leuenberger, D., Zangrando, R., Spolaor, A., Borrotti, M., Barbaro, E.,
8842 Gambaro, A. and Barbante, C.: Fire in ice: two millennia of boreal forest fire history from
8843 the Greenland NEEM ice core, Clim. Past, 10(5), 1905–1924, doi:10.5194/cp-10-1905-
8844 2014, 2014.

8845

8846

8847 **Supplementary material**

8848

8849 Table S1 List of in-situ aerosol measurements performed on airborne platforms including
8850 aircrafts and tethered balloons in the Arctic regions.

8851

Year	Month	Arctic region	Project	Reference
2007	Mar-Apr	European Arctic	ASTAR	(Engvall et al., 2009)
2008	Mar-Apr	Alaska	ARCTAS	(Jacob et al., 2010)
	Mar-Apr	Alaska	ARCPAC	(Brock et al., 2011)
	Mar-Aprl	European Arctic	POLARCAT	(Law et al., 2014)
	Jun-Jul	Western Greenland	POLARCAT	(Law et al., 2014)
	Jul	Siberia	YAK-AEROSIB	(Paris et al., 2009)
2009	Jan	Alaska North Pole	HIPPO-01	(Schwarz et al., 2013b)

	Apr	Svalbard Canadian Arctic Alaska	PAMARCMiP	(Herber et al., 2012)
	Nov	Alaska North Pole	HIPPO-02	(Schwarz et al., 2013b)
2010	Mar-Apr	Alaska North Pole	HIPPO-03	(Schwarz et al., 2013b)
2011	Mar-Apr	Alaska Canadian Arctic Svalbard	PAMARCMiP	(Herber et al., 2012)
	Jun-Jul	Alaska North Pole	HIPPO-04	(Schwarz et al., 2013b)
	Aug-Sep	Alaska North Pole	HIPPO-05	(Schwarz et al., 2013b)

	March-May	Svalbard	CICCI	(Ferrero et al., 2016)
2012	Mar-Apr	Svalbard Canadian Arctic	PAMARCMiP	(Herber et al., 2012)
	Jul	European Arctic Svalbard	ACCESS	(Roiger et al., 2015)
	June-July	Svalbard	CICCI	(Ferrero et al., 2016)
2013	Apr	Svalbard	PAMARCMiP	(Herber et al., 2012)
	Mar	Svalbard	ACCACIA	(Liu et al., 2015)
2014	Apr-May	Canadian Arctic	RACEPAC	(Herenz et al., 2018)
	Jul	Canadian Arctic	NETCARE	(Abbatt et al., 2018)
	Sept-Oct	Svalbard	AGAP	(Mazzola et al., 2016)

	Oct	Russian Arctic	Tu-134 2014	(Antokhina et al., 2018)
2015	Apr	Canadian Arctic	NETCARE	(Abbatt et al., 2018)
	Jun-Sep	Alaska	ACME-V	(Biraud et al., 2016)
	April-May	Svalbard	AGAP	(Moroni et al. 2016)
	April-May	Svalbard	iAREA	(Markowitz et al., 2017)
2016	Jan	Iceland	HLD-Iceland	(Dagsson-Waldhauserova et al., 2019)
	April-May	Svalbard	AGAP	(Moroni et al. 2016)
	April-May	Svalbard	iAREA	(Markowitz et al., 2017)
2017	Mar-Apr	Svalbard Northern Greenland Canadian Arctic	PAMARCMiP	(Herber et al., 2012)

		Alaska		

8852

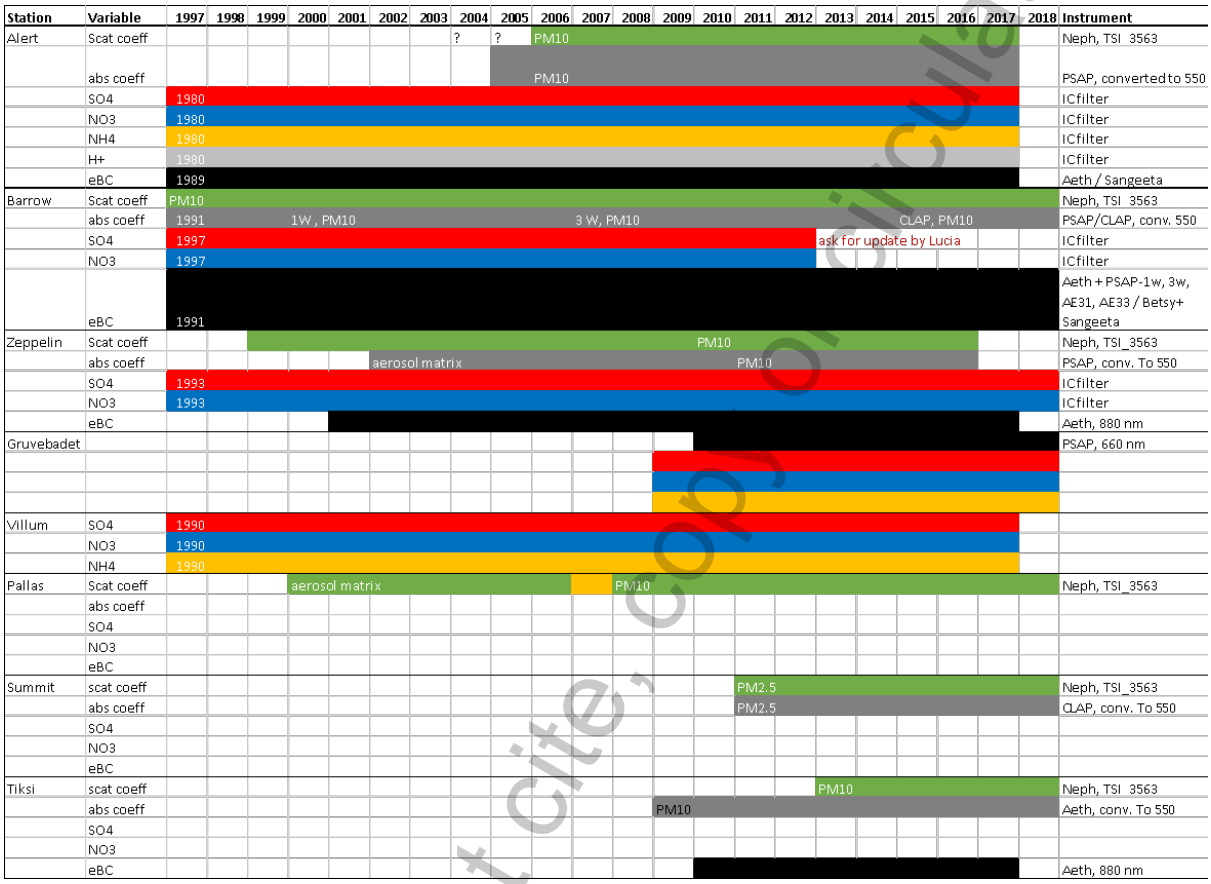

8853

8854

8855 Table: Locations of ice-cores used in this report

Core	Location
Devon Island, DV99.1 (rBC)	75.32_ N, 81.64_W Zdanowicz
Devon Island, DV98.3 (ions)	75.34 N, 82.1 W Zdanowicz
Summit 2010	72.5 N, 38.3 W from Mernild et al. 2015
ACT2	66.0 N, 45.2 W from Mernild et al. 2015

ACT11D	66.5 N, 46.3 W from Mernild et al. 2015
NGT_B19	78 N, 36.4 W link
Humboldt	78.5 N , 56.8 W from Mernild et al. 2015
D4	71.4, 44.0 W from Mernild et al. 2015
Lomo09	78°49'24'' N, 17°25'5'' E (Wendl et al., 2015)
HDF	79°80' N, 13°16' E (Wendl et al., 2015)

8856

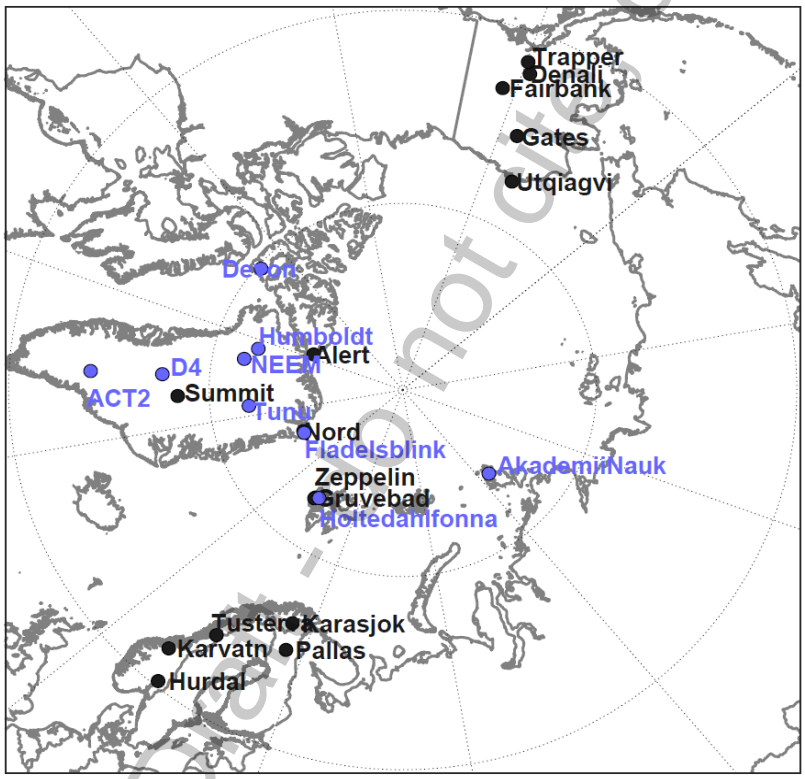

8857

8858

8859

5.3 Ozone and precursors

(total 4-5 pages including figures, 2000 words)

This section reviews recent work on the origins of Arctic O_3 including natural and anthropogenic sources and O_3 sinks and discusses observed distributions of ozone (O_3) and its precursors and observed O_3 trends in the Arctic troposphere.

5.3.1 Ozone sources and sinks

Ozone (O_3) is produced photochemically from anthropogenic and natural precursor emissions (see Section 3.X). Downward transport of O_3 from the stratosphere is a substantial direct source of O_3 to the troposphere (Shapiro et al. 1987). It is destroyed by photochemistry and by dry deposition to the Earth's surface.

5.3.1.1 Ozone sources (incomplete – missing natural sources, VOCs):

Methane oxidation is a major source of tropospheric ozone contributing ~50 Tg to the annual mean global burden (~15%) (Fiore et al., 2008), and as such makes a substantial contribution to Arctic ozone abundance (working on including numbers for this). Enhancements also result from import of ozone and its precursors from lower latitudes during episodes of long-range transport of both anthropogenic and fire plumes to the Arctic (refs – mainly same as last report?). In addition, there has been recent progress in improving knowledge of local ozone precursor sources. Surface ozone in summer is already impacted by shipping NOx emissions along the northern Norwegian coast (Marelle et al., 2016; Marelle et al., 2018) and the Northwest Passage (Aliabadi et al., 2015). Marelle et al., (2018) showed that for a 2050 scenario that includes diversion shipping in the Arctic, shipping would become the main surface ozone source. Tuccella et al. (2017) showed that background ozone is influenced by emissions downwind of oil and gas extraction platforms in the Southern Norwegian Sea. Investigation of long-range transport of ozone precursors has shown efficient export of PAN from East Asia to the North Pacific, with relative contributions to long-range O_3 transport of 35% in spring and 25% in summer (Jiang et al., 2016). Ship observations over the Arctic and Bering Seas have identified events of long-range pollution transport with enhancements in ozone, which are under-represented in

models due to simplifications in treatments of boundary layer and dry deposition (Kanaya et al., 2019).

5.3.1.2 Ozone sinks

Photochemical loss of O_3 is mainly via photolysis in the presence of water vapor or direct reaction of O_3 with hydroxy radicals (HO_2 or OH). Photochemical destruction involving the hydroperoxyl radical (HO_2) may be particularly important in the Arctic where water vapor abundances are low (Arnold et al. 2015) as well as reactions involving halogens during the Arctic spring. Dry deposition of O_3 and its precursors to ice and ocean surfaces is slower than to vegetated terrestrial surfaces. Van Dam et al. (2016) reported ozone dry deposition velocities that were 5 times higher over Arctic snow-free tundra in the summer months at Toolik Lake (n. Alaska) compared to snow covered ground. Dry deposition, combined with possible photochemical loss (e.g. involving BVOCs) producing lower ozone concentrations during stable (lower light) night conditions may explain the different diurnal cycle observed at this tundra site compared to Arctic coastal locations (see Fig. 1).

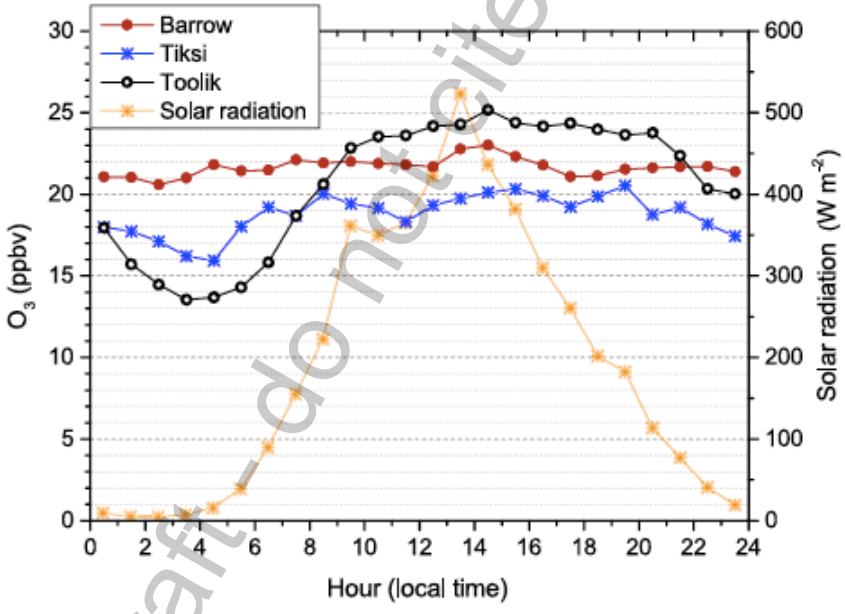

Figure 1. From Van Dam et al. (2016): Diurnal cycle in median ozone concentrations for July at different Arctic sites.

During Arctic spring, photochemical cycling of halogens in so-called 'bromine explosion' events leads to rapid depletion of surface O_3 to low or near-zero concentrations (Barrie et al. 1988; Simpson et al. 2007). This phenomenon is most commonly observed at Arctic coastal locations in March/April and attributed to bromine (halogen) sources linked to Arctic sea-ice coupled with stable surface temperature inversions (e.g. Hermann et al., 2019). Fig. 2 shows the vertical extent of low O_3 episodes observed by lidar at Eureka in northern Canada where orographic effects were also important (Seabrook et al., 2016). Peterson et al. (2018) showed that active halogen chemistry and related ozone depletion can also occur up to 200 km inland over snow-covered tundra in Alaska. Simpson et al. (2018) reported high levels of BrO at Utqiaġvik (Alaska) occurring earlier in February in air masses originating from the Arctic Ocean polar night. Their findings suggest a dark wintertime source of reactive bromine (halogens) that could feed halogen photochemistry at lower latitudes as the sun returns.

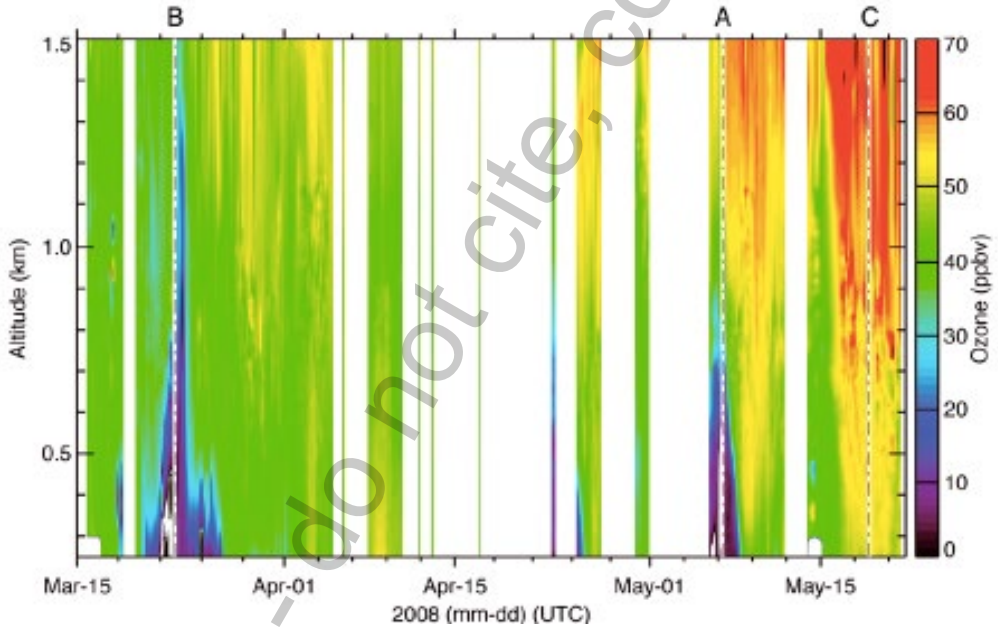

Figure 2: Fig. 3 from Seabrook and Whiteway 2016: Ozone lidar measurements from Eureka (spring 2008). Important effects of large-scale meteorology: ODEs when air from Arctic Ocean, downward transport of O_3 into ABL when flow from south over mountains.

In addition, whilst earlier studies proposed indirect evidence that ozone and Hg^0 are removed by reaction with Br atoms (e.g. Goodsite et al. 2012, Skov et al. 2004, Dastoor et al. 2008), Wang et al. (2019) have shown, for the first time a direct connection between O_3

and Hg^0 with Br during ozone and Hg^0 depletion episodes at Utqiagvik, Alaska at a site 5 km from the coast to the Arctic Ocean. (see Figure 3). Here, the Br/BrO ratio anti-correlates with O_3 concentrations and box modeling confirmed that ozone in fact is removed by Br.

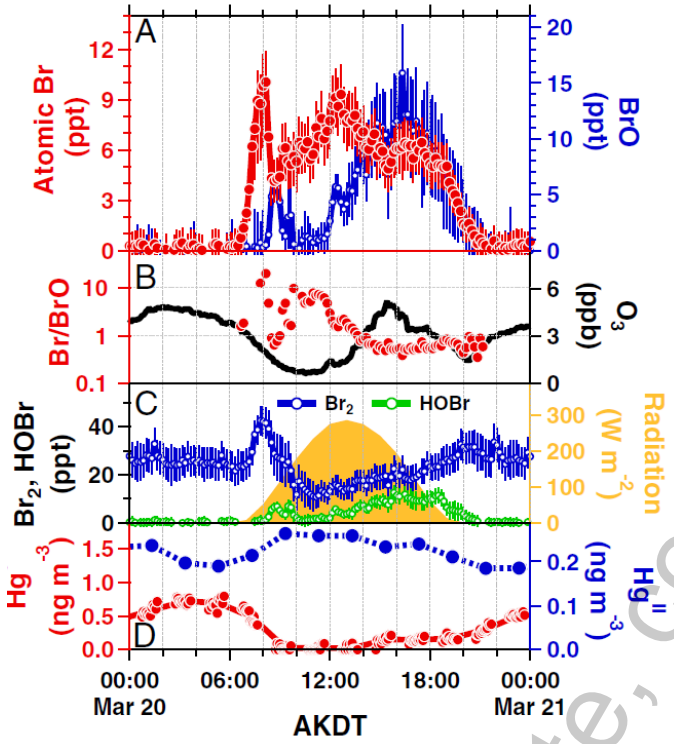

Figure 3 (caption needs simplifying): Time series on 20 March 2012 of measured (A) Br and BrO, (B) Br/BrO ratios and O3, (C) Br2, HOBr, and solar radiation, and (D) Hgo and HgII levels near Utqiagvik, Alaska. Br, BrO, Br2, HOBr, O3, and Br/BrO ratios are in 10-min resolution, while all others are 1-h averages. Hgo was measured at 5-min resolution for 1-h periods (red dots in D), during which time HgII was sampled; then the instrument shifted to offline mode for 1 h and HgII was analyzed (blue dots in D). In this case, HOBr likely played a minor role in morning Br2 production, as HOBr remained below 6 ppt in the morning (<13 ppt all day). Error bars represent propagated measurement uncertainties. (Wang et al., 2019).

This result is significant since the main source of halogens in the Arctic is release from refreezing leads and/or from snow blowing over sea ice (Petersen et al. 2016, Pratt et al. 2013; Yang et al. 2020). Burd et al. (2017) found a strong relationship between the end of the reactive bromine season and snowmelt timing. Decreases in Arctic sea ice extent or relative distributions of multi-year/seasonal sea-ice cover, and increases in the length of the

snow-free season could influence future ozone sinks via changes in halogen fluxes or increased deposition to tundra (and possibly also the ocean).

5.3.2 Observed concentrations

5.3.2.1 Surface site and ship in-situ observations

(placeholder text)

Add introduction.

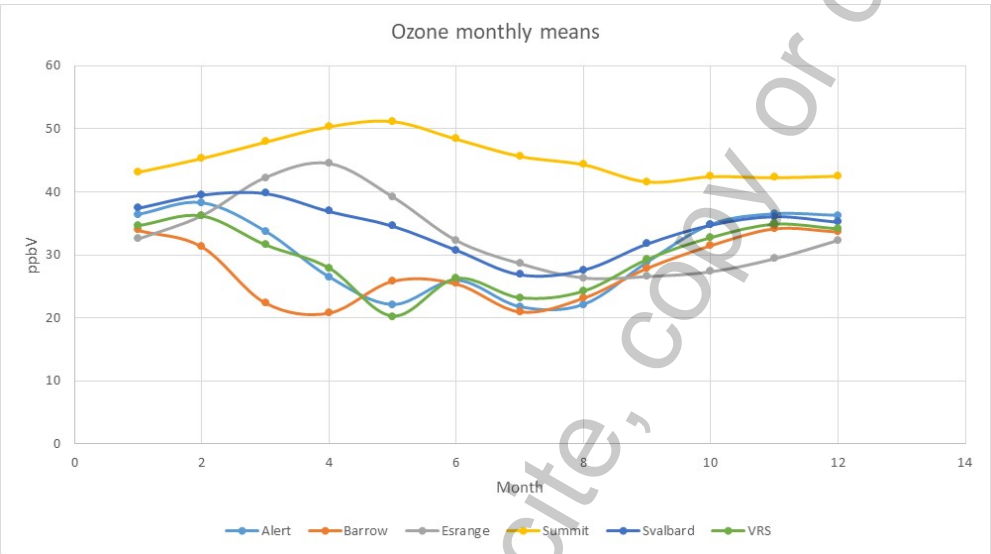

Figure 4: The seasonal behavior ozone at Arctic Stations. Monthly means are calculated for the period 2003 to 2018 except for Villum as data were not available for 2002 to 2006. The highest ozone mixing ratios are found at Summit due to influence from the free troposphere.

The seasonality at Villum and Alert is very close. The two stations are located at about the same latitude and close to sea level (see Figure 4). There is a strong seasonal behavior in the ozone mixing ratio with a minimum at 20.5 ppbv in May due to ODEs a slight increase in June and a local minimum in July at 23.8 ppbv. This minimum can be explained by surface removal of ozone and photochemical degradation. O_3 is reaching its maximum during winter where 36.6 ppbv is reached in February. In winter there is not any photochemical degradation of O_3, and the vertical mixing is low as the atmosphere during polar night is highly stratified (Reference). Summit on the Greenlandic Inland Ice located at 3212 m asl. The station is in the free troposphere and thus it is not affected by the bromine chemistry

originating from sea ice or other surface processes (Huang et al. 2017). Consequently the seasonal variation is different. A clear maximum in March and a minimum in September are observed. Short episodes of depletion has been reported (REFERENCE) but apparently they do not affect the monthly mean values substantially, see Figure 5. Zeppelin is located at about 450 m ….

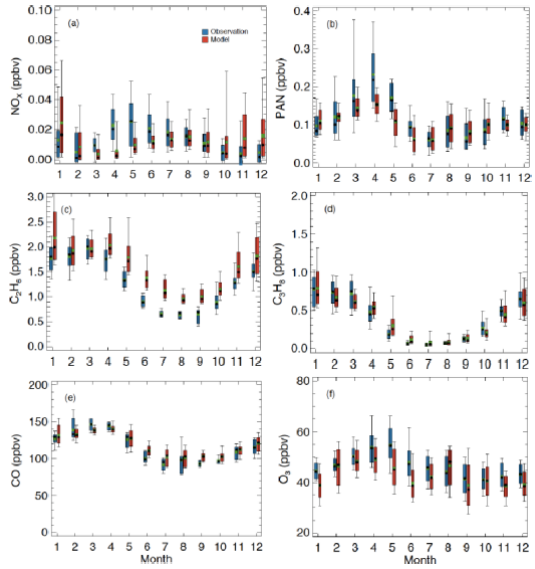

Figure 5: Huang et al 2017, Figure 1: 2 years (2008-2010) data collected at Summit compared to GEOS-CHEM. Issues with NOx (snow chem), emissions (C2H6).

The interaction of chlorine species and NO_y with ozone is discussed further in McNamara et al. 2019 (to be commented further, see Figure 6).

Barrow (McNamara 2019)

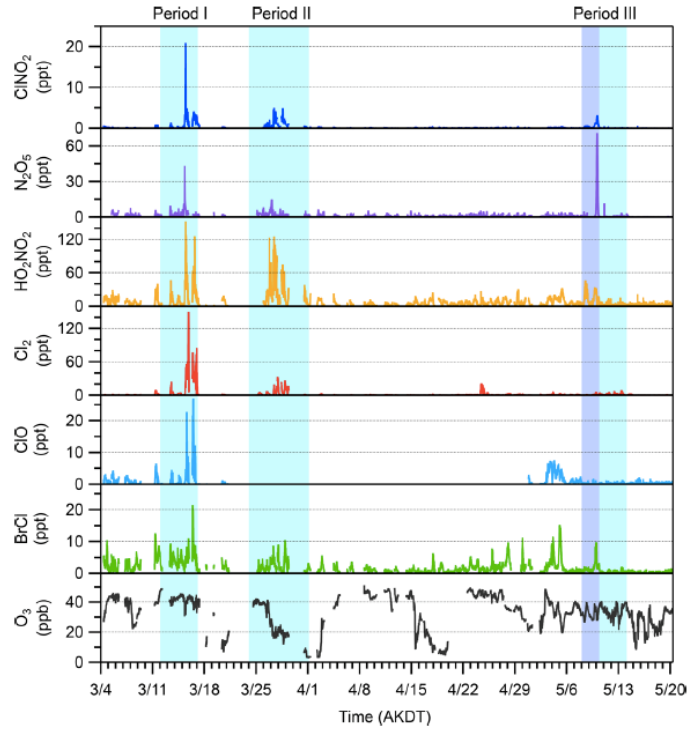

Figure 6 : McNamara et al, EST, 2019: enhanced N2O5, Cl2, CLO and HO2NO2 in air masses influenced by local Barrow or Prudhoe Bay Oilfield emissions. Important interactions between snowpack (chlorine) chemistry and anthropogenic NOx emissions.

Ship-based measurements: Observations of ozone and its precursors over the oceans are important for validation of models but there is a scarcity of such data from the Arctic. Recently two datasets from ship cruises in the Arctic have been reported. Kanaya et al. (2019) performed measurements of CO and ozone in several cruise legs over open oceans, including the Bering Sea and the Arctic Ocean; the cruise in the Arctic Ocean was in September. As a general conclusion it was found that halogen chemistry, stable boundary layers, and deposition might explain differences between measured and modeled ozone concentrations. He et al. (2016) measured ozone and black carbon on a ship cruise in the Arctic ocean in the period between June 27 and September 23 The latitudinal and longitudinal ranges of the cruise were 31.1°N–87.7°N and 9.3°E–90°E–168.4°W. Comparing the observed ozone concentrations to those measured at Barrow no statistically significant differences were found, suggesting that coastal stations between July and September may be representative for the entire Arctic.

5.3.2.2 Vertical profiles

Christiansen et al. (2017) examined long-term ozonesonde records at 7 Arctic stations reporting consistent seasonal cycles as a function of altitude between sites with later maxima in the mid-troposphere compared to the surface layers and upper troposphere. Since AMAP (2015), no new comprehensive aircraft campaigns have taken place with a focus on understanding processes affecting Arctic O_3 in the free troposphere. Ancellet et al. (2016) examined aircraft, lidar and ozonesonde data over Canada and Greenland during summer 2008 POLARCAT campaigns (described in AMAP 2015). This study shows clear latitudinal and longitudinal variations in the origins of sampled air mass origins based on back trajectories and O_3:PV correlations. While downward transport of O3 was important over Greenland, air masses with higher O_3 were attributed to North America boreal fires over Canada and polluted air masses from mid-latitudes also contributed, for example from Asia north of 80N.

The NASA AToM mission (ref) has undertaken extensive surveying of the global troposphere. This includes repeated vertical profile measurements between latitudes of 60 and 90N, which give a useful insight into the seasonal variation of ozone and its precursors through the depth of the Arctic troposphere (Fig. X). These profiles also demonstrate a springtime enhancement in ozone extending through the troposphere, with evidence of stratospheric influence in the UT. Summertime shows less ozone enhancement in the lower troposphere, but enhancement in ozone precursors (CO, PAN) in the mid-troposphere, associated with import of forest fire and anthropogenic emissions from lower latitudes. Near-surface NO2 is greatly enhanced during winter, associated with a longer NO2 lifetime and accumulation of pollution in the Arctic haze.

Placeholder figures showing NASA AToM aircraft data – text to be added (and possibly Siberian YAK aircraft data – ozone and CO).

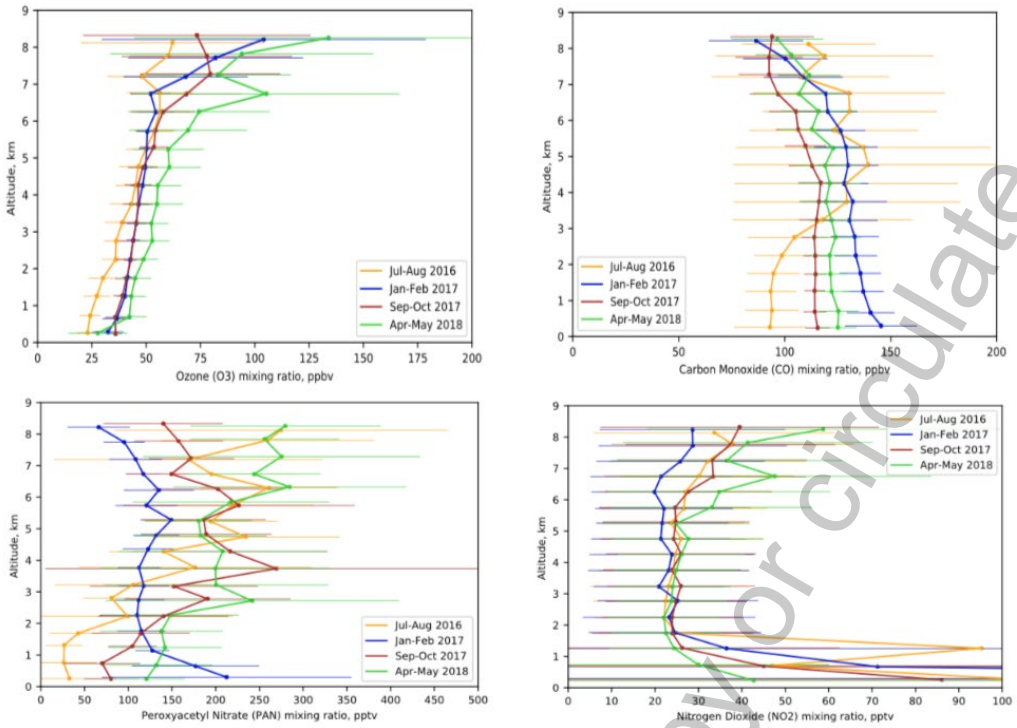

Fig X: Mean vertical profiles of (a) ozone, (b) CO, (c) PAN and (d) NO2 measured north of 60N from the NASA AToM experiment during summer 2016, winter 2017, autumn 2017 and spring 2018. Horizontal lines indicate 1 standard deviation spread around mean values at each altitude.

5.3.2.3 Satellite data

Despite the potential limitations of some satellite data products at high latitudes (see Section 2c), numerous studies have exploited satellite observations to investigate tropospheric ozone and precursor distributions and trends relevant to the Arctic. Pommier et al., (2012) presented IASI retrievals of 0-8 km and 0-12 km sub-column ozone for the Arctic in spring and summer 2008. These showed widespread enhancement in springtime (Mar-Apr) tropospheric ozone column compared with summer (Jun-Jul), particularly over NE Siberia, northern Canada and the Arctic Ocean (ADD possible figure here). Generally good agreement with in-situ aircraft profiles was demonstrated, but negative IASI bias was found compared with aircraft data in the lower troposphere, due to low thermal contrast in the Arctic boundary layer. Wespes et al., (2012) showed that IASI was able to detect enhancements in mid-latitude sourced ozone enhancements during summer at the edge of

the Arctic, but also showed a lack of sensitivity over snow and ice surfaces, potentially resulting in missing some ozone enhancements. Tropospheric NO2 columns measured from OMI have been used to detect enhancements and trends in NOx emissions due to gas flaring in high latitude (up to 67°N) areas of Russia and North America (Li et al., 2016). Sodemann et al. (2011) analysed cross-polar transport of a large pollution plume in the Arctic during summer 2008 using IASI CO retrievals. IASI was able to detect features and structures of the plume consistent with in-situ aircraft data, and provided a useful comparison for evaluation of transport model simulations.

Satellite observations are also useful in evaluating the sources and export of ozone precursors from mid-latitude source regions and their subsequent transport to the Arctic. Assessment of a suite of chemical transport models using OMI tropospheric NO2 columns for summer 2008 showed a potential overestimate in NO2 over biomass burning regions in Eastern Siberia, with lower biases over European and N American source regions, and model under-estimates over China. Monks et al., (2015) exploited limited profile information from MOPITT CO retrievals to evaluate relationships between CO seasonal cycles in the lower and upper troposphere over the Arctic and over mid-latitude source regions. Inter-annual variability in PAN retrieved by TES over Eastern Siberia for April 2006-2008 was documented by Zhu et al., (2015), and it was shown to be largely controlled by fire emissions. More recently, TES PAN data was used to help characterise Asian influence on exported PAN and downwind ozone production (Jiang et al., 2016). A temperature-dependent high bias in TES PAN was found at cold temperatures over high latitudes.

5.3.3 Observed trends in ozone

Placeholder text: Growth in anthropogenic emissions of O_3 precursors since pre-industrial times (i.e. increased emissions of CH_4, NO_X, CO and VOCs) has led to an increase in tropospheric O_3 throughout the northern hemisphere (e.g. Parrish et al. 2012). This increase in tropospheric O_3 has contributed to the observed increase in global temperature over the past century (e.g. Stevenson et al. 2013) and is likely to have made an important contribution to Arctic warming observed over this period (Shindell 2007; Shindell et al. 2006).

9229

9230 5.3.3.1 Observed trends in ozone (and precursors)

9231 Introduction to be added followed by placeholder text.

9232

9233 In Table 1 is listed trend of ozone at several Arctic stations using Mann-Kendall Test and

9234 Sen's slope.

9235

9236 *Table 1: Percentage per year increase over the years indicated. Only significant trends are*

9237 *shown*

Site	Annual	Level of significance	DJF	Level of significance	MAM	Level of significance	JJA	Level of significance	SON	Level of significance	Period
Alert	n.s.	>0.1	0.40	0.001	n.s.	>0.1	n.s.	>0.1	n.s.	>0.1	1992-2018
Barrow	0.21	0.05	031	0.001	0.35	>0.1	n.s.	>0.1	0.20	0.05	1973-2018
Summit	-0.40	0.05	-0.41	0.1	-1.02	0.01	n.s.	>0.1	-0.34	0.05	2000-2019
Villum	n.s.	>0.1	n.s.	>0.1	n.s.	>0.1	n.s.	>0.1	n.s.	>0.1	1996-2018
Zeppelin	0.28	0.05	0.45	0.01	n.s.	>0.1	n.s.	>0.1	n.s.	>0.1	1989-2018

9238

9239

9240 There is a small increase for all stations but Summit but of those only the trends at Barrow

9241 and Zeppelin are significant and the increase is 0.21% yr^{-1} and 0.28% yr^{-1}, respective. The

9242 positive trends are due to increases during winter (DJF). Only the most southern station

9243 Barrow has positive trends also in spring (MAM) and in autumn (SON). Summit is located on

9244 the Greenlandic inland Ice sheet above 3200 m and thus is measuring ozone in the free

9245 troposphere. Interestingly the largest trend is observed here. The trend is negative (-0.40 %

9246 yr^{-1}) and there is significant negative trends for all but autumn. The ozone trends at Villum

9247 are shown in Figure 7 below …

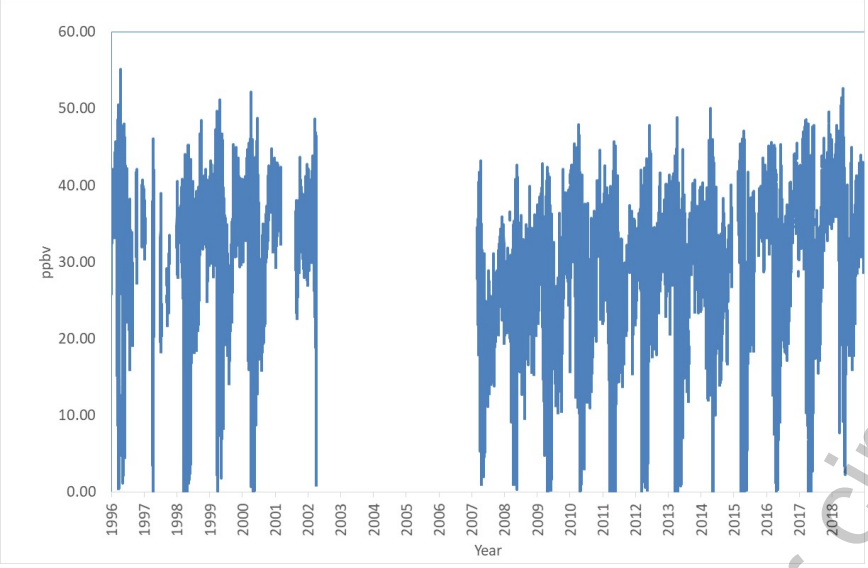

Figure 7 ….

The trend analyses are extended compared to those found in the literature. Sharma et al (2019) studied Alert ozone from 1980 to 2013 and found a positive trend of 5% for the entire period. The trend found here for was 10.4% for 1998 to 2018, so it looks that winter ozone increase is accelerating.

A general negative trend at Summit is here reported for the first time. Gaudel et al. (2018) revisited trends (2000-2014 only) including Summit (shows no significant trends except for decrease in spring, only NH mountain site) and surface sites (positive DJF trends in Alaska, weakly negative or no trend elsewhere (JJA and DJF) - see Fig. 13) (Comment on TOST dataset in Gaudel et al., 2018).

Tarasick et al. 2019: detailed comparison of different methods → surface concentrations from 1877 to 2016 – Figure 3 shows results for Northern High Latitudes (60-90N). Overall increase of 57.1% with questionable datasets omitted. Add comment on past Past tropospheric ozone trends based on oxygen isotope constraints (Yeung et al, 2019).

A shift towards an earlier peak in the seasonal cycle at the surface in northern Sweden over the period 1990-2013 was reported by Andersson et al. (2017) using a combined data and modeling approach. Changes were attributed to rising hemispheric background concentrations, meteorological variations and European emission reductions. These results

are in line with seasonal cycle shifts first reported based on surface site data at mid-latitudes (Parrish et al., 2013).

Placeholder: short paragraph on ozone precursor trends

E.g. Breider et al – historical CO trends (see figure below)

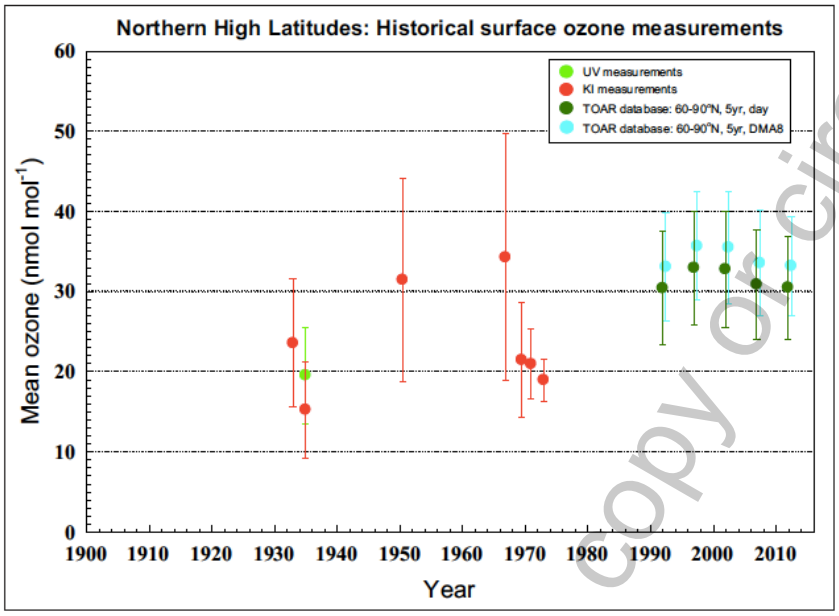

5.3.3.2 Vertical profile trends

Long-term data on the vertical distribution of tropospheric ozone in the Arctic is limited and confined to the European and North American sector of the Arctic. Tarasick et al. (2019) made a thorough review of available data and their accuracies. Ozonesondes are the only source of data that can currently be used for long-term trend analysis in the Arctic. AMAP (2015) referred to positive trends of ozone in the upper troposphere reported for the European sector of the Arctic for 1996 – 2010 (Zbinden, 2011) and showed ozonesonde data for Scoresbysund on the east coast of Greenland for the period 1989 – 2013 with positive trends at levels from 500 hPa and higher (Christiansen et al., 2015). In an extended study Christiansen et al. (2017) analysed trends and annual variability in ozonesonde data for 9 Arctic sites (including Scoresbysund) for the period 1990 – 2015 depending on location. Significant increases in free tropospheric ozone up to 2005, then decreases were found for European Arctic sector sites. For Eureka, in the Canadian sector, increases were found also from 2008. They also report evidence for a shift in the O_3 seasonal cycle at several stations

with the late May/early June summer maximum occurring earlier in the year. This could be due to increased spring-time photochemical production (from Asian sources), decreasing summertime mid-latitude emissions combined with lower dry deposition (to snow and ice) earlier in the year.

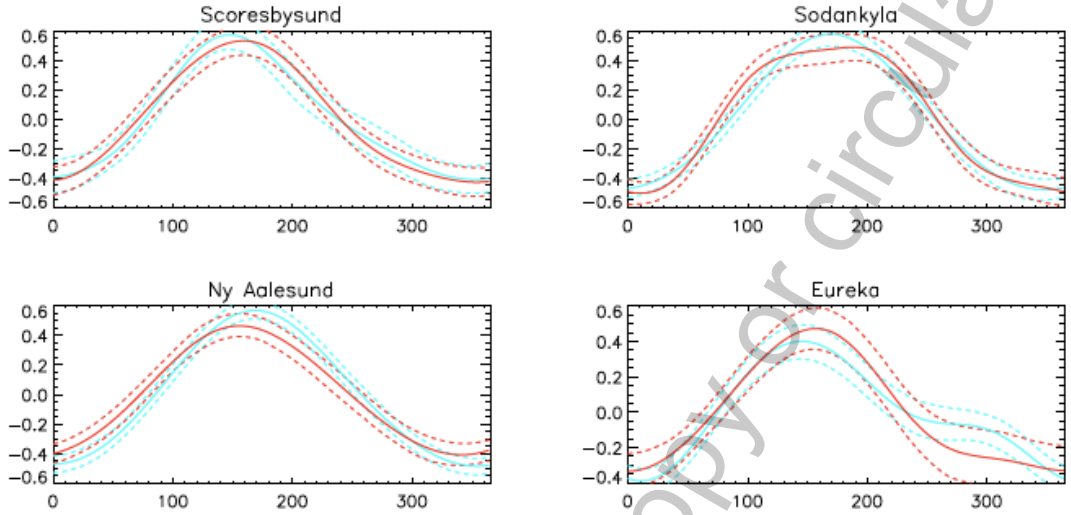

Figure …: Christiansen 2017 Figure 10: changes in Arctic ozone seasonal cycle: 2012-2007 (red) minus 1995-2000 (cyan) at 500hPa (relative to annual means)

Bahramash Shams et al (2019) analysed total and partial ozone columns by combining data from ozonesondes and the Microwave Limb Sounder on the Aura satellite for the stations Alert, Eureka, Summit and Ny Ålesund. They found no significant annual mean trends over the period 2005 -2017. Ny Ålesund was the only station showing significant trends in the troposphere with a negative trend in tropospheric column in the spring and a positive trend in summer.

5.3.4 Open questions (DRAFT): Observations, origins and trends

- Lack of data in urban/industrial, rural locations or lack of accessibility to existing data (data quality) for source attribution and emission validation. Need for data sharing.
- Lack of continuous long-term surface data to estimate trends and standardization of measurement techniques - NOx and NOy (PAN), VOC or CO trends in the Arctic.

- On-going questions related to improving understanding about ozone sources and sinks at the surface (e.g. ….) and in the free troposphere (e.g. …) in different seasons.
- Simulated ozone perturbations and associated radiative effects requires evaluation of models against observed trends estimated as a function of altitude.
- ….

5.3.5 Summary

References

(includes all references on ozone for Chapters 4 and 5):

Ancellet, G., Daskalakis, N., Raut, J. C., Tarasick, D., Hair, J., Quennehen, B., Ravetta, F., Schlager, H., Weinheimer, A. J., Thompson, A. M., Johnson, B., Thomas, J. L., and Law, K. S.: Analysis of the latitudinal variability of tropospheric ozone in the Arctic using the large number of aircraft and ozonesonde observations in early summer 2008, Atmos. Chem. Phys., 16, 13341–13358, https://doi.org/10.5194/acp-16-13341-2016, 2016.

Andersson, C., Alpfjord, H., Robertson, L., Karlsson, P. E., and Engardt, M.: Reanalysis of and attribution to near-surface ozone concentrations in Sweden during 1990–2013, Atmos. Chem. Phys., 17, 13869–13890, https://doi.org/10.5194/acp-17-13869-2017, 2017.

Arnold, S. R., Emmons, L. K., Monks, S. A., Law, K. S., Ridley, D. A., Turquety, S., Tilmes, S., Thomas, J. L., Bouarar, I., Flemming, J., Huijnen, V., Mao, J., Duncan, B. N., Steenrod, S., Yoshida, Y., Langner, J., and Long, Y., (2015), Biomass burning influence on high-latitude tropospheric ozone and reactive nitrogen in summer 2008: a multi-model analysis based on POLMIP simulations, Atmos. Chem. Phys., 15, 6047-6068, doi:10.5194/acp-15-6047-2015.

Bahramvash Shams, S., Walden, V. P., Petropavlovskikh, I., Tarasick, D., Kivi, R., Oltmans, S., Johnson, B., Cullis, P., Sterling, C. W., Thölix, L., and Errera, Q.: Variations in the vertical profile of ozone at four high-latitude Arctic sites from 2005 to 2017, Atmos. Chem. Phys., 19, 9733–9751, https://doi.org/10.5194/acp-19-9733-2019, 2019.

9344 Burd, J. A., P. K. Peterson, S. V. Nghiem, D. K. Perovich, and W. R. Simpson, Snowmelt onset
9345 hinders bromine monoxide heterogeneous recycling in the Arctic, J. Geophys. Res.
9346 Atmos., 122, 8297–8309, doi:10.1002/2017JD026906, 2017.

9347 Christiansen, B., Jepsen, N., Kivi, R., Hansen, G., Larsen, N., and Korsholm, U. S.: Trends and
9348 annual cycles in soundings of Arctic tropospheric ozone, Atmos. Chem. Phys., 17, 9347–
9349 9364, https://doi.org/10.5194/acp-17-9347-2017, 2017.

9350 Christian, K. E., Brune, W. H., and Mao, J.: Global sensitivity analysis of the GEOS-Chem
9351 chemical transport model: ozone and hydrogen oxides during ARCTAS (2008), Atmos.
9352 Chem. Phys., 17, 3769–3784, https://doi.org/10.5194/acp-17-3769-2017, 2017.

9353 Clerbaux, C., Boynard, A., Clarisse, L., George, M., Hadji-Lazaro, J., Herbin, H., Hurtmans, D.,
9354 Pommier, M., Razavi, A., Turquety, S., Wespes, C., and Coheur, P.-F.: Monitoring of
9355 atmospheric composition using the thermal infrared IASI/MetOp sounder, At- mos.
9356 Chem. Phys., 9, 6041–6054, doi:10.5194/acp-9-6041-2009, 2009.

9357 Fadnavis, S., Müller, R., Kalita, G., Rowlinson, M., Rap, A., Li, J.-L. F., Gasparini, B., and
9358 Laakso, A.: The impact of recent changes in Asian anthropogenic emissions of SO_2 on
9359 sulfate loading in the upper troposphere and lower stratosphere and the associated
9360 radiative changes, Atmos. Chem. Phys., 19, 9989–10008, https://doi.org/10.5194/acp-19-
9361 9989-2019, 2019.

9362 Fiore, A. M., J. J. West, L. W. Horowitz, V. Naik, and M. D. Schwarzkopf (2008),
9363 Characterizing the tropospheric ozone response to methane emission controls and the
9364 benefits to climate and air quality, J. Geophys. Res., 113, D08307,
9365 doi:10.1029/2007JD009162.

9366 Gaudel, A, et al. 2018. Tropospheric Ozone Assessment Report: Present-day distribution and
9367 trends of tropospheric ozone relevant to climate and global atmospheric chemistry
9368 model evaluation. Elem Sci Anth, 6: 39. DOI:
9369 https://www.elementascience.org/articles/10.1525/elementa.291

9370 Herrmann, M., L. Cao, H. Sihler, U. Platt, and E. Gutheil, On the contribution of chemical
9371 oscillations to ozone depletion events in the polar spring, Atmos. Chem. Phys., 19,
9372 10161–10190, 2019, https://doi.org/10.5194/acp-19-10161-2019

9373 Huang, Y., Wu, S., Kramer, L. J., Helmig, D., and Honrath, R. E.: Surface ozone and its
9374 precursors at Summit, Greenland: comparison between observations and model
9375 simulations, Atmos. Chem. Phys., 17, 14661–14674, https://doi.org/10.5194/acp-17-
9376 14661-2017, 2017.

9377 Kanaya, Y., Miyazaki, K., Taketani, F., Miyakawa, T., Takashima, H., Komazaki, Y., Pan, X.,
9378 Kato, S., Sudo, K., Sekiya, T., Inoue, J., Sato, K., and Oshima, K.: Ozone and carbon
9379 monoxide observations over open oceans on R/V *Mirai* from 67° S to 75° N during 2012 to
9380 2017: testing global chemical reanalysis in terms of Arctic processes, low ozone levels at
9381 low latitudes, and pollution transport, Atmos. Chem. Phys., 19, 7233–7254,
9382 https://doi.org/10.5194/acp-19-7233-2019, 2019.

9383 Jiang, Z., J. R. Worden, V. H. Payne, L. Zhu, E. Fischer, T. Walker, and D. B. A. Jones (2016),
9384 Ozone export from East Asia: The role of PAN, J. Geophys. Res. Atmos., 121, 6555–6563,
9385 doi:10.1002/2016JD024952.

9386 Kebabian, P. L., S. C. Herndon and A. Freedman (2005). "Detection of nitrogen dioxide by
9387 cavity attenuated phase shift spectroscopy." Analytical Chemistry 77(2): 724-728.

9388 Lorenzen-Schmidt, H., S. Wessel, W. Unold, S. Solberg, H. Gernandt, F. Stordal and U. Platt
9389 (1998). "Ozone measurements in the European Arctic during the ARCTOC 1995
9390 campaign." Tellus Series B-Chemical and Physical Meteorology 50(5): 416-429.

9391 Marelle, L., Raut, J.-C., Law, K., & Duclaux, O. (2018). Current and future arctic aerosols and
9392 ozone from remote emissions and emerging local sources—Modeled source
9393 contributions and radiative effects. *Journal of Geophysical Research: Atmospheres*,
9394 *123*, 12,942–12,963. https://doi.org/10.1029/2018JD028863

9395 McNamara, S. M., A. R. W. Raso, S. Y. Wang, S. Thanekar, E. J. Boone, K. R. Kolesar, P. K.
9396 Peterson, W. R. Simpson, J. D. Fuentes, P. B. Shepson and K. A. Pratt (2019). "Springtime
9397 Nitrogen Oxide-Influenced Chlorine Chemistry in the Coastal Arctic." Environmental
9398 Science & Technology 53(14): 8057-8067.

9399 Mills G, Pleijel H, Malley CS, Sinha B, Cooper OR, Schultz MG, Neufeld HS, Simpson D, Sharps
9400 K, Feng Z, Gerosa G, Harmens H, Kobayashi K, Saxena P, Paoletti E, Sinha V, Xu X,
9401 Tropospheric Ozone Assessment Report: Present-day tropospheric ozone distribution and

trends relevant to vegetation. Elem Sci Anth. 2018;6(1):47. DOI: http://doi.org/10.1525/elementa.302

Monks, S. A., Arnold, S. R., Emmons, L. K., Law, K. S., Turquety, S., Duncan, B. N., Flemming, J., Huijnen, V., Tilmes, S., Langner, J., Mao, J., Long, Y., Thomas, J. L., Steenrod, S. D., Raut, J. C., Wilson, C., Chipperfield, M. P., Diskin, G. S., Weinheimer, A., Schlager, H., and Ancellet, G., (2015), Multi-model study of chemical and physical controls on transport of anthropogenic and biomass burning pollution to the Arctic, Atmos. Chem. Phys., 15, 3575-3603, doi:10.5194/acp-15-3575-2015.

Mungall, E. L., Abbatt, J. P. D., Wentzell, J. J. B., Wentworth, G. R., Murphy, J. G., Kunkel, D., Gute, E., Tarasick, D. W., Sharma, S., Cox, C. J., Uttal, T., and Liggio, J.: High gas-phase mixing ratios of formic and acetic acid in the High Arctic, Atmos. Chem. Phys., 18, 10237–10254, https://doi.org/10.5194/acp-18-10237-2018, 2018.

Peterson, P. K., K. A. Pratt, W. R. Simpson, S. V. Nghiem, L. X. P. Perez, E. J. Boone, D. Pohler, J. Zielcke, S. General, P. B. Shepson, U. Friess, U. Platt and B. H. Stirm (2016). "The role of open lead interactions in atmospheric ozone variability between Arctic coastal and inland sites." Elementa-Science of the Anthropocene 4: 1-9, missing doi.

Peterson, P.K., D. Pöhler, J. Zielcke, S. General, U. Frieß, U. Platt, W.R. Simpson, S.V. Nghiem, P.B. Shepson, B.H. Stirm and K.A. Pratt, Springtime Bromine Activation over Coastal and Inland Arctic Snowpacks ACS Earth Space Chem. 2018, 2, 1075−1086, DOI: 10.1021/acsearthspacechem.8b00083

Pittman, J. V., L. L. Pan, J. C. Wei, F. W. Irion, X. Liu, E. S. Maddy, C. D. Barnet, K. Chance, and R.-S. Gao (2009), Evaluation of AIRS, IASI, and OMI ozone profile retrievals in the extratropical tropopause region using in situ aircraft measurements, J. Geophys. Res., 114, D24109, doi:10.1029/2009JD012493.

Pope, R. J., Richards, N. A. D., Chipperfield, M. P., Moore, D. P., Monks, S. A., Arnold, S. R., Glatthor, N., Kiefer, M., Breider, T. J., Harrison, J. J., Remedios, J. J., Warneke, C., Roberts, J. M., Diskin, G. S., Huey, L. G., Wisthaler, A., Apel, E. C., Bernath, P. F., and Feng, W., (2016), Intercomparison and evaluation of satellite peroxyacetyl nitrate observations in the upper troposphere-lower stratosphere, Atmos. Chem. Phys., 16, 13541-13559, doi:10.5194/acp-16-13541-2016.

Rap, A., N.A.D. Richards, P.M. Forster, S.A. Monks, S.R. Arnold, and M.P. Chipperfield, (2015), Satellite constraint on the tropospheric ozone radiative effect, *Geophys. Res. Lett.*, 42, 5074-5081. doi: 10.1002/2015GL064037.

Seabrook, J., and J. Whiteway (2016), Influence of mountains on Arctic tropospheric ozone, J. Geophys. Res. Atmos., 121, 1935–1942, doi:10.1002/2015JD024114.

Sharma, S., L. A. Barrie, E. Magnusson, G. Brattstrom, W. R. Leaitch, A. Steffen and S. Landsberger, "A Factor and Trends Analysis of Multidecadal Lower Tropospheric Observations of Arctic Aerosol Composition, Black Carbon, Ozone, and Mercury at Alert, Canada." Journal of Geophysical Research-Atmospheres 124(24): 14133-14161, 2019.

Skov, H. Egeløv, A.H. Granby, K. and Nielsen, T. "The Relation of ozone with other Photochemical Products at Ll. Valby, Denmark". *Atm. Environ.* 1997, vol. 31 No. 5, p 685-691.

Skov, H., J. Hjorth, C. Nordstrøm, J. B., C. C., P. M.B., L. J.B. and M. Dall'Osto (2020). "The variability in Gaseous Elemental Mercury at Villum Research Station, Station Nord in North Greenland from 1999 to 2017." ACPD doi.org/10.5194/acp-2019-912.

Simpson, W. R., Frieß, U., Thomas, J. L., Lampel, J., & Platt, U. (2018). Polar nighttime chemistry produces intense reactive bromine events. Geophysical Research Letters, 45, 9987–9994. https:// doi.org/10.1029/2018GL079444

Tarasick, D. W., Davies, J., Smit, H. G. J., and Oltmans, S. J.: A re-evaluated Canadian ozonesonde record: measurements of the vertical distribution of ozone over Canada from 1966 to 2013, Atmos. Meas. Tech., 9, 195–214, https://doi.org/10.5194/amt-9-195-2016, 2016.

Tarasick, D., I. E. Galbally, O. R. Cooper, M. G. Schultz, G. Ancellet, T. Leblanc, T. J. Wallington, J. Ziemke, X. Liu, M. Steinbacher, J. Staehelin, C. Vigouroux, J. W. Hannigan, O. Garcia, G. Foret, P. Zanis, E. Weatherhead, I. Petropavlovskikh, H. Worden, M. Osman, J. Liu, K. L. Chang, A. Gaudel, M. Y. Lin, M. Granados-Munoz, A. M. Thompson, S. J. Oltmans, J. Cuesta, G. Dufour, V. Thouret, B. Hassler, T. Trickl and J. L. Neu (2019). "Tropospheric Ozone Assessment Report: Tropospheric ozone from 1877 to 2016, observed levels, trends and uncertainties." Elementa-Science of the Anthropocene 7: 72. Missing doi.

9462 Turnock, S.T., O. Wild, A. Sellar and F.M. O'Connor, 300 years of tropospheric ozone changes
9463 using CMIP6 scenarios with a parameterised approach, Atmos. Environ.,
9464 https://doi.org/10.1016/j.atmosenv.2019.07.001, 2019.

9465 Van Dam, B., D. Helmig, P. V. Doskey,and S. J. Oltmans (2016), Summertime surface O3
9466 behavior and deposition to tundra in the Alaskan Arctic, J. Geophys. Res. Atmos., 121,
9467 8055–8066, doi:10.1002/2015JD023914.

9468 Wang, S. Y., S. M. McNamara, C. W. Moore, D. Obrist, A. Steffen, P. B. Shepson, R. M.
9469 Staebler, A. R. W. Raso and K. A. Pratt (2019). "Direct detection of atmospheric atomic
9470 bromine leading to mercury and ozone depletion." Proceedings of the National Academy
9471 of Sciences of the United States of America 116(29): 14479-14484.

9472 Wang, X., Jacob, D. J., Eastham, S. D., Sulprizio, M. P., Zhu, L., Chen, Q., Alexander, B.,
9473 Sherwen, T., Evans, M. J., Lee, B. H., Haskins, J. D., Lopez-Hilfiker, F. D., Thornton, J. A.,
9474 Huey, G. L., and Liao, H.: The role of chlorine in global tropospheric chemistry, Atmos.
9475 Chem. Phys., 19, 3981–4003, https://doi.org/10.5194/acp-19-3981-2019 , 2019.

9476 Wespes, C., Emmons, L., Edwards, D. P., Hannigan, J., Hurt- mans, D., Saunois, M., Coheur,
9477 P.-F., Clerbaux, C., Cof- fey, M. T., Batchelor, R. L., Lindenmaier, R., Strong, K., Wein-
9478 heimer, A. J., Nowak, J. B., Ryerson, T. B., Crounse, J. D., and Wennberg, P. O.: Analysis of
9479 ozone and nitric acid in spring and summer Arctic pollution using aircraft, ground-based,
9480 satellite observations and MOZART-4 model: source attribution and par- titioning, Atmos.
9481 Chem. Phys., 12, 237–259, doi:10.5194/acp- 12-237-2012, 2012.

9482 Yang, X. Blechschmidt, A.-M. Bognar, K. McClure–Begley, Morris, S. Petropavlovskikh, I.
9483 Richter, A. Skov, H. Strong, K. Tarasick, D. Uttal, T. Vestenius, M. Zhao, X. (2020) The pan-
9484 Arctic surface ozone: modelling vs measurements. *ACPD.* doi.org/10.5194/acp-2019-984.

9485 Young, P. J., V. Naik*, A. M. Fiore, A. Gaudel, J. Guo, M. Y. Lin, J. L. Neu, D. D. Parrish, H. E.
9486 Rieder, J. L. Schnell, S. Tilmes, O. Wild, L. Zhang, J. R. Ziemke, J. Brandt, A. Delcloo, R. M.
9487 Doherty, C. Geels, M. I. Hegglin, L. Hu, U. Im, R. Kumar, A. Luhar, L. Murray, D. Plummer,
9488 J. Rodriguez, A. Saiz-Lopez, M. G. Schultz, M. T. Woodhouse and G. Zeng (2018),
9489 Tropospheric Ozone Assessment Report: Assessment of global-scale model performance
9490 for global and regional ozone distributions, variability, and trends, *Elem Sci Anth.*
9491 *2018;6(1):*10. DOI: http://doi.org/10.1525/elementa.265

Yeung, L.Y., L.T. Murray, P. Martinerie, E. Witrant, H. Hu, A. Banerjee, A. Orsi and J. Chappellaz, Isotopic constraint on the twentieth-century increase in tropospheric ozone, Nature, 570 (7760) 224, doi: 10.1038/s41586-019-1277-1, 2019.

Zhu, L., E. V. Fischer, V. H. Payne, J. R. Worden, and Z. Jiang (2015), TES observations of the interannual variability of PAN over Northern Eurasia and the relationship to springtime fires, Geophys. Res. Lett., 42, 7230–7237, doi:10.1002/ 2015GL065328.

6. Modeling of short-lived climate forcers, climate, and air quality

Policy-relevant science questions we aim to answer (*preliminary* answers below):

Do the models capture the current abundance and distribution of short-lived climate forcers such as black carbon, ozone, and methane in the Arctic atmosphere?

18 models were evaluated for 2008-9 and 2014-15 time period (or a subset of those four years), and were found to have satisfactory agreement with observed black carbon, ozone, and methane (as well as sulfate, aerosol optical properties, cloud properties, and ozone precursors). This chapter quantifies the differences between the models and the observed quantities.

Are current SLCF concentrations in line with what should be expected, taking into account the Arctic Council and other efforts to reduce emissions?

Five models provided 1990-2015 timeseries (and one 1995-2015 timeseries), which simulate well the reduction in BC and SO4 in the 1990s and subsequent levelling off of those concentrations during the 2000s. Despite reductions in NOx emissions, Arctic surface O3 volume mixing ratios have no trend.

When comparing modelled 2014-15 concentrations of BC, SO4, and others SLCFs to those 2008-9, there is not a large difference (no significant reduction).

What are the trends and interannual (? seasonal?) variability in Arctic SLCFs (ozone, methane, black carbon, and other relevant pollutants) concentrations in the atmosphere, in snow and ice, (lake sediments) etc. and what are the primary drivers of the trends and (interannual) variability?

Two models simulated methane from 1990 to 2015, and these show a steadily increasing trend, which is consistent with measurements. Black carbon has been decreasing slightly from 1990 to 2015, and ozone has no trend in the Arctic ambient air.

Six models simulated BC, SO4, and O3 from 1990 to 2015. Those models capture the current abundance, including seasonal cycle, and trends of black carbon, sulfate, and ozone in the Arctic atmosphere, as compared to 18 Arctic measurement locations. The modelled and

measured trend of ambient sulfate was to decrease from 1990 to 1995 and then hold relatively steady through to 2015. Black carbon also decreased slightly over the 1990 to 2015 time period. The annual, multi-model mean bias in the Arctic was -25%, with a correlation coefficient, R^2, of 0.57 when compared to measurements from 1990-2015. The model underestimate of Arctic BC was more pronounced in the winter (-40%), than in the summer (-6%), though overall, this is an improvement in model performance in simulating Arctic BC since that 2015 AMAP assessment on black carbon and ozone as climate forcers (which had -59% negative bias in the winter, and 88% positive bias in the summer). Ground-level ozone remained steady with no discernable trend in both the model and measurements from 1990 to 2015.

These small trends are as expected given the reductions in sulfate and black carbon emissions globally and the remoteness of the Arctic from those sources. Emissions of ozone precursors has varied, thus the lack of ozone trend is expected.

10005

How useful is satellite data in monitoring Arctic concentrations of methane, black carbon, ozone or other relevant pollutants? What are the limitations?

Satellite data are very useful for monitoring Arctic concentrations of methane, ozone, and other gaseous SLCFs. These data provide better spatial coverage than the ground sites, and often have a longer time series. They also provide vertical information of the distribution of SLCFs. We utilize data from ACE-FTS, TES, and MOPITT in this report and compare those results to the modelled mixing ratios of ozone, carbon monoxide, and methane.

While black carbon cannot be measured directly from satellites, their data is also very useful for measuring the optical properties of aerosols such as aerosol optical depth, aerosol absorption optical depth, and Angstrom exponent. Again, these measurements provide excellent spatial coverage compared to ground measurement stations. We utilize data from MODIS/Aqua, MODIS/Terra, MISR, AATSR, SeaWIFS, and CALIOP in this report and compare those results to the models. The aerosol optical properties measured by satellite can also be integrated or assimilated into derived PM2.5 data products (e.g., from MERRA, Dalhousie, Global Burden of Disease, etc), which we also use in this chapter to validate modelled PM2.5 concentrations.

Satellite measurements are limited in the Arctic during polar night, as many of them require sunlight for their spectral measurements. Also, some viewing geometries also don't allow some satellites to have a good "view" of the Arctic. In some cases, clouds and high albedo (due to snow and ice cover) limit the effectiveness of satellite measurements. Some are also less sensitive to the surface concentrations of SLCFs, and their vertical information is limited to coarse resolution. Thus satellites are no substitution for ground based, and aircraft measurements, but rather an important complementary measurement.

10006

How do the modelled concentrations in the atmosphere, in snow and ice, (lake sediments) etc. relate to observations?

Modelled concentrations of SLCFs, aerosol optical properties, cloud properties, and deposition were evaluated against measurements from surface monitoring networks, ship and aircraft campaigns, satellite instruments, and ice cores. Years 2008-9 and 2014-15 were chosen for the detailed evaluation, and 18 different models provided simulations. Model performance varied depending on species, region, and time of year.

Generally, all models capture the magnitude of concentrations of SLCFs in surface ambient air. The variability of SLCFs is not as well captured for aerosols, such as black carbon and sulfate as it is for trace gases, such as ozone and carbon monoxide. Preliminary results suggest that models have similar spatial patterns in their biases.

Modelled deposition of black carbon and sulfate in Arctic were evaluated against ice core data. The modelled deposition was highly variable and generally over-predicted deposition of these SLCFs.

Methane mixing ratios are prescribed in all of these models based on box model results using ECLIPSEv6b CH4 emissions as input. Thus, simulated methane is much simpler and not as variable as observed methane at the surface. However, the modelled methane higher up in the troposphere agrees well with the long-lived and well-mixed observed methane.

10007

10008

10009 **6.1 Introduction**

10010

While observations of SLCFs in the Arctic are invaluable, they are limited in space and time, and are quite expensive and labour intensive to carry out. Models allow us to estimate the full three-dimensional distribution of SLCFs in the atmosphere as well as their radiative forcing and optical properties over any time period of interest. Models can also be useful tools to attribute SLCF sources, and to simulate what is expected of SLCFs in the future. Models can be used to predict the impacts of various emissions mitigation scenarios on the atmosphere. In order to have confidence in those results, the models must be grounded in the truth, which is done in this chapter by comparing the model simulations to observations of SLCFs. This allows us to evaluate the performance of the models and to determine the sources of uncertainty for their simulations.

Add literature review of existing model capabilities (e.g., models not used in this report) E.g., Breider et al (2014, 2017) papers on Arctic aerosols radiative effect and decadal trends. Also L. Bruhwiler will add an overview of methane modelling, which is not well represented by the current AMAP models. Could also mention results previous report.

Eighteen models provided special new simulations for the AMAP SLCF assessment report. All used the same anthropogenic emissions (ECLIPSE v6b described in Chapter 3) as inputs. They are each briefly described in Section 6.2, and then thoroughly evaluated against observations in Section 6.3. The evaluation covers SLCF concentrations, aerosol optical properties, and clouds in the Arctic and Northern Hemisphere throughout the troposphere and lower stratosphere. Section 6.4 summarizes our main findings about the models' performance.

6.2 Models for simulations of short-lived climate forcers and radiative forcing

Brief description of individual models and their characteristics (and further individual model descriptions in an appendix). Link to chapter on emissions. Insert a box with a brief summary of generic model types for policymakers and lay audience.

Model description in table format - initial information available from survey conducted in the spring - information needs to be checked, updated, and expanded, similar to table 7.1 in AMAP (2015) (everyone)

Table 6.1: Model information. CTM = chemical transport model, CCM = chemistry climate model, ESM = earth system model.

Model name	Contact person	Model type	Horizontal grid information	Vertical grid information
CanAM5-PAM	Knut von Salzen	global climate model	128x64, Gaussian grid, T63	hybrid/sigma, 49 levels to 1hPa
CESM2.0	Luca Pozzoli	ESM	1.9x2.5 lat/lon grid	32
CESM2.1.1	Mark Flanner	ESM	0.9x1.25 lat/lon grid	32
CIESM-DESS aka DESS-MAM7	Yiran Peng	global climate model	T42, finite volume dynamics	31
CMAM	David Plummer	CCM	T47 (GCM3)	
DEHM	Jesper Christensen	CTM, hemispheric	50km, >150x150 gridpoints, Polarr stereographic	sigma up to 100hPa, 29 layer
ECHAM6-SALSA	Thomas Kühn	global	T63	L47, hybrid sigma-pressure
EMEP MSC-W	Michael Gauss, Svetlana Tsyro	CTM	0.5x0.5 degree regular lon/lat	20 sigma-pressure hybrid layers from the surface and up to 100 hPa

FLEXPART	Sabine Eckhardt, Nikolaos Evangeliou	Lagrangian Transport Model	Met. input data:1 deg x 1 deg, global	Met. input: 92-138 L
GEM-MACH	Wanmin Gong	Regional on-line air quality prediction model	Rotated lat/lon at 0.1375 (or 15-km) horizontal resolution	81 hybrid levels to 0.1 hpa
GEOS-Chem	Joshua Fu, Xinyi Dong	CTM	2x2.5degree	47 sigma level, top@0.01hPa
GISS-E2.1-OMA	Ulas Im	ESM	2x2.5 degrees	40 vertical layers
MATCH	Joakim Langner	Offline chemistry, hemispheric	rotated lat/long, 186x186, 0.75 deg resolution	38 levels, hybrid
MATCH-SALSA-RCA4	Manu Thomas	Offline coupled chemistry climate, hemispheric	rotated lat/long, 188x198, 0.75 deg resolution	40 levels, hybrid upt 20 hPa
MRI-ESM2	Naga Oshima	ESM	TL159(AGCM), TL95(aerosol), T42(ozone)	80 layers up to 0.01hPa, hybrid sigma-pressure
NorESM-happi	Maria Sand, Srinath Krishnan	Global climate model (ESM and as a CTM?)	0.9x1.25 lat/lon grid	26 levels, hybrid sigma-pressure
Oslo-CTM	Ragnhild B. Skeie	CTM	~2.25°x2.25°	60 sigma level, top@0.1hPa

UKESM1	Steve Arnold	Global Chemistry/ Climate (ESM)	145x192 (1.875°x1.25°)	85 (hybrid height terrain following grid)
WRF-Chem	Kathy Law, Jean-Christophe Raut, Tatsuo Onishi	Regional-Arctic chemistry-aerosol climate model	100km	65 levels
WRF/CMAQ	Joshua Fu, Xinyi Dong	CCM	108km	34 sigma level, top@50hPa

10047
10048
10049 **6.2.1 CanAM5-PAM**
10050
10051 The Canadian Atmospheric Model version 5 (CanAM5), with Piecewise lognormal
10052 approximation (PLA; Peng et a, 2012) Aerosol Model (PAM; von Salzen, 2006) is a climate
10053 model used to simulate aerosols for this study. (*Knut to fill out more*)
10054
10055 **6.2.2 CESM (Mark and Luca)**
10056
10057 The Community Earth System Model version 2 (Danabasoglu et al., 2020) is an ESM that can
10058 be configured in many different ways. The configuration applied for this assessment utilized
10059 the Community Atmosphere Model (CAM) version 6 and Modal Aerosol Model (MAM4) with
10060 4 mixed-species aerosol modes (Liu et al., 2016). CAM6 employs a spectral element
10061 dynamical core (Lauritzen et al., 2018), Type 0 and Type 1 CESM runs were conducted at
10062 1.9x2.5 degree horizontal resolution, while Type 3 runs at 0.9x1.25 degrees, all with 32
10063 vertical layers. For Type 0 and Type 1 simulations, CESM version 2.0 was used with "CAM6-
10064 chem" representations of chemical reactions (Emmons et al., 2020), enabling prognostic
10065 simulation of tropospheric ozone concentrations, along with a volatility basis set (VBS)
10066 parameterization for the formation of secondary organic aerosols (SOA) (Tilmes et al.,

2019). CAM6-chem is coupled to the interactive Community Land Model (CLM5), which provides biogenic emissions, calculated online using the MEGANv2.1 algorithm (Guenther et al., 2012), and handles dry deposition. Tracked aerosol species simulated by MAM4 include sulphate, primary and aged black carbon and organic matter, dust, sea-salt, and secondary organic aerosols. Both sea salt and dust emissions are calculated on-line and are highly sensitive to the surface wind speed (Mahowald, Lamarque et al., 2006; Mahowald, Muhs et al., 2006). These runs were also forced with prescribed SSTs and sea-ice concentrations, created from merged Reynolds/HADISST products as in Hurrell et al. (2008). Type 3 transient runs utilized CESM version 2.1.1 without atmospheric chemistry and with fully-coupled atmosphere, ocean, land, and sea-ice components (component set "BSSP245cmip6"), as applied to simulate future scenarios for CMIP6. All CESM runs specified global-mean mixing ratios of methane and carbon dioxide.

6.2.3 CIESM-DESS

… (Yiran)

6.2.4 CMAM

The Canadian Middle Atmosphere Model (CMAM) is based on CanAM, but with an extended vertical lid and the addition of gas-phase chemistry… (*Dave to fill out more*)

6.2.5 DEHM

… (*Jesper)*

6.2.6 ECHAM-SALSA

ECHAM-SALSA is the general aerosol-climate model ECHAM-HAMMOZ (ECHAM6.3-HAM2.3-MOZ1.0) (Tegen et al., 2019, Schultz et al., 2019) using the Sectional Aerosol module for Large Scale Applications SALSA (Kokkola et al., 2019) to solve the aerosol microphysics. ECHAM6 (Stevens et al., 2013) computes the atmospheric circulation and fluxes using a

semi-Lagrangian transport scheme. In the setup used here, the large-scale meteorology (vorticity, divergence, and surface pressure; relaxation times of 24, 6, and 48 h, respectively) was nudged towards ERA-Interim reanalysis data (Berrisford et al., 2011). In SALSA the aerosol size distribution is modelled using 10 size sections (or bins), which span particle sizes between 3 nm and 10 µm. The size distribution is further divided into a soluble and an insoluble sub-population, which are treated as externally mixed. Within one size bin of one sub-population, all aerosol particles are considered internally mixed. In its standard setup, SALSA describes the aerosol compounds, black carbon (BC), organic carbon (OC), sulfate (SO_4), sea salt (SS), and mineral dust (DU). In the model, BC, OC, SS, and DU are emitted as primary particles, while sulfate is emitted as either sulfur dioxide (SO_2) or as dimethyl sulfate (DMS), which are oxidized using a simplified chemistry (Stier et al., 2005) to form sulfuric acid (H_2SO_4), which then either nucleates or condenses onto existing particles. BC, OC, and SO_2 emissions are prescribed using input files, while SS and DU emissions are computed online. All greenhouse gas concentrations are fixed to pre-defined concentrations. The model resolution for the simulations performed here was T63 (roughly 2° by 2°), further using 47 hybrid sigma-pressure levels.

6.2.7 EMEP-MSC-W

The EMEP MSC-W model is a 3-D Eulerian chemistry transport model developed at the Norwegian Meteorological Institute within the Framework of the UN Convention on Long-range Transboundary Air Pollution. It is described in detail in Simpson et al. (2012). Although the model has traditionally been aimed at simulations of acidification, eutrophication and air quality over Europe, global modelling has been performed and evaluated with observations for many years (Jonson et al., 2010; Wild et al., 2012). The model uses 20 vertical levels defined as sigma coordinates. The 10 lowest levels are within the PBL (with the bottom layer being 92 m thick), and the top of the model domain is at 100 hPa.

EMEP-modelled $PM_{2.5}$ and PM_{10} include primary and secondary aerosols, both anthropogenic and natural. The simulations used here used EclipseV6b $PM_{2.5}$ and coarse PM emissions, which were split into elementary carbon (EC), organic matter (OM) (here assumed inert) and the remaining inorganic dust. The EC and OM emissions are further

divided into fossil fuel and wood-burning compounds for each country and source sector. 80% of emitted EC is assumed to be hydrophobic, which ages to become hydrophilic at a rate of 1-1.5 day. As in Bergström et al. (2012), the Organic Matter/Organic Carbon ratio of emissions by mass is assumed to be 1.3 for fossil-fuel sources and 1.7 for wood-burning sources. The split applied to the PM emissions is the same as used in EMEP operational runs (IIASA, personal communications). Secondary aerosol consists of inorganic sulphate, nitrate and ammonium, and secondary organic aerosol (SOA); the latter is formed from both anthropogenic and biogenic emissions (anthropogenic SOA and biogenic SOA respectively), using the 'VBS' scheme detailed in Bergström et al (2012) and Simpson et al (2012). The model also calculates sea salt aerosols and windblown dust particles from soil erosion.

Model updates since Simpson et al. (2012), resulting in EMEP model version rv4.9 as used here, have been described in Simpson et al. (2016) and references cited therein. The main changes concern a new calculation of aerosol surface area used in heterogeneous reactions (e.g. formation of coarse NO_3 on sea salt and dust aerosols), revised parameterizations of N_2O_5 hydrolysis on aerosols, additional gas-aerosol loss processes for O_3, HNO_3 and HO_2, a new scheme for ship NO_x emissions, and the use of new maps for global leaf-area for calculating biogenic VOC emissions) – see Simpson et al. (2015) for details. The EMEP model, including a user guide, is publicly available as Open Source code at https://github.com/metno/emep-ctm.

The EMEP model is driven by 3-hourly meteorological data from the ECMWF IFS model at 0.5 degree resolution.

6.2.8 FLEXPART

A Lagrangian particle transport (Pisso et al., 2019) model using data from ECMWF as driving meteorology. It calculates transport, turbulent diffusion and removal for the BC aerosols. 30 days spin-up an 8 years have been simulated (2008-2015).

6.2.9 GEM-MACH

GEM-MACH (Global Environmental Multiscale model–Modelling Air quality and CHemistry) is the Environment and Climate Change Canada (ECCC) air quality prediction model. It consists of an online tropospheric chemistry module embedded within ECCC's GEM numerical weather forecast model (Côté et al., 1998a, b; Charron et al., 2012). The chemistry module includes a comprehensive representation of air quality processes, such as gas-phase, aqueous-phase, and heterogeneous chemistry and aerosol processes (e.g. Moran et al., 2013; Makar et al., 2015a, b; Gong et al., 2015). Specifically, gas-phase chemistry is represented by a modified ADOM-II mechanism with 47 species and 114 reactions (Lurmann et al., 1986; Stockwell and Lurmann, 1989); inorganic heterogeneous chemistry is parameterized by a modified version of the ISORROPIA algorithm of Nenes et al. (1999), as described in detail in Makar et al. (2003); secondary organic aerosol (SOA) formation is parameterized using a two-product, overall or instantaneous aerosol yield formation (Odum et al., 1996; Jiang, 2003; Stroud et al., 2018); aerosol microphysical processes, including nucleation and condensation (sulfate and SOA), hygroscopic growth, coagulation and dry deposition/sedimentation are parameterized as in Gong et al. (2003); the representation of cloud processing of gases and aerosols includes uptake and activation, aqueous phase chemistry, and wet removal (Gong et al., 2006, 2015).

Aerosol chemical composition is represented by eight components: sulfate, nitrate, ammonium, elemental carbon (EC), primary organic aerosol (POA), secondary organic aerosol (SOA), crustal material (CM) and sea salt; aerosol particles are assumed to be internally mixed. A sectional approach is used for representing aerosol size distribution. For the 2015 Arctic simulation, a 12-bin (between 0.01 and 40.96 µm in diameter, logarithmically spaced: 0.01– 0.02, 0.02–0.04, 0.04–0.08, 0.08–0.16, 0.16–0.32, 0.32–0.64, 0.64–1.28, 1.28–2.56, 2.56–5.12, 5.12–10.24, 10.24–20.48 and 20.48–40.96 µm) configuration is used.

Anthropogenic emissions used in the 2015 Arctic simulation are based on a combination of North American emission inventories (specifically, the 2016 US National Emission Inventories and 2015 Canadian national Air Pollution Emission Inventories) and global ECLIPSE v6b 2015 baseline emissions. Wild fire emissions are processed using the Canadian Forest Fire Emission Prediction System (CFFEPS) from satellite detected fire hotspot data

(MODIS, AVHRR, and VIIRS). CFFEPS consists of a fire growth model, a fire emissions model, and a thermodynamic-based model to predict the vertical penetration height of a smoke plume from fire energy (see Chen et al., 2019 for details). Biogenic emissions are calculated online in GEM-MACH based on the algorithm from BEIS version 3.09 with BELD3-format vegetation land cover. Sea salt emissions are computed based on Gong et al. (2003).

The GEM-MACH 2015 Arctic simulation was conducted over a limited area (LU) domain on a rotated lat-lon grid at 0.1375° x 0.1375° (or ~ 15-km) resolution covering the Arctic (> 60°N) and extending to the southern US-Canada border. The chemical lateral boundary conditions were from MOZART-4/GEOS-5 (https://www.acom.ucar.edu/wrf-chem/mozart.shtml; Emmons et al., 2010). The meteorology was initialized daily (at 00:00 UTC) using the Canadian Meteorological Centre's global objective analyses.

6.2.10 GEOS-Chem

… (*Joshua*)

6.2.11 GISS-E2.1

NASA Goddard Institute of Space Studies (GISS) Earth system model (ESM), GISS-E2.1, is a fully-coupled ESM. A full description of GISS-E2.1 and evaluation of its coupled climatology during the satellite era (1979–2014) and the historical ensemble simulation of the atmosphere and ocean component models (1850-2014) are described in Kelley et al., 2020, under review. GISS-E2.1 has a horizontal resolution of 2◦ in latitude by 2.5◦ in longitude, and 40 vertical layers extending from the surface to 0.1 hPa in the lower mesosphere. The tropospheric chemistry scheme used in GISS-E2.1 (Shindell et al., 2001, 2003) includes inorganic chemistry of Ox, NOx, HOx, CO, and organic chemistry of CH4 and higher hydrocarbons using the CBM4 scheme (Gery et al., 1999), and the stratospheric chemistry scheme (Shindell et al., 2006) which includes chlorine and bromine chemistry together with polar stratospheric clouds.

In the present work, we used the OMA, the One-Moment Aerosol scheme (Bauer, Koch, et al., 2007; Bauer, Mishchenko, et al., 2007; Bauer & Koch, 2005; Koch et al., 2006; Miller et al., 2006; Tsigaridis et al., 2013; Bauer and Tsigaridis, 2020, under review). OMA is a mass-based scheme in which aerosols are assumed to remain externally mixed and have a prescribed and constant size distribution, with the exception of sea salt that has two distinct size classes, and dust that is described by a sectional model with an option from 4 to 6 bins. The OMA scheme treats sulfate, nitrate, ammonium, carbonaceous aerosols (black carbon and organic carbon, including the NOx-dependent formation of SOA and methanesulfonic acid formation), dust and sea-salt. The model includes secondary organic aerosol production, as described by (Tsigaridis and Kanakidou, 2007). The default dust configuration that is used in this work includes 5 bins, a clay and 4 silt ones, from submicron to 16 μm in size. The first three dust size bins can be coated by sulfate and nitrate aerosols (Bauer & Koch, 2005). OMA only includes the first aerosol indirect effect. The aerosol number concentration that impacts clouds are obtained from the aerosol mass as described in (Menon & Rotstayn, 2006).

The natural emissions of sea salt, DMS, isoprene and dust are calculated interactively. Anthropogenic dust sources are not represented in ModelE2.1. Dust emissions vary spatially and temporally only with the evolution of climate variables like wind speed and soil moisture (Miller et al., 2006). The version of the model we use in this work uses prescribed sea surface temperature (SST) and sea ice thickness and extent during the historical period (Rayner et al., 2003).

6.2.12 MATCH

MATCH - Multiscale Atmospheric Transport and Chemistry [Robertson et al., 1999] is an offline, Eulerian, 3-D chemistry transport model developed at the Swedish Meteorological and Hydrological Institute. MATCH can be run on global to urban domains to study a range of atmospheric chemistry/air quality problems, but for this study model runs were performed for the ~20°N–90°N region focusing on long-transport to the Arctic.

ERA-Interim reanalysis data from the European Centre forMedium-Range Weather Forecasts (ECMWF) were used as meteorological input to the model. Six-hourly data (3-hourly for precipitation) were extracted from the ECMWF archives on a 0.75° × 0.75° rotated latitude-longitude grid. The original data had 60 levels, but the 35 lowest levels reaching about 16 km in the Arctic were used in the model.

The scheme for gas-phase tropospheric chemistry and bulk aerosols as described in Andersson et al. (2007) was used. Methane concentrations were prescribed. Boundary conditions at the top of the model and at the lateral boundaries for a range of species including ozone were based on monthly mean values from the Copernicus Atmospheric Monitoring Service. The aerosol scheme was extended with BC and OC simulated as two fractions: fresh, hydrophobic and aged, and hydrophilic. Eighty percent of anthropogenic emissions from all sectors were emitted into the hydrophobic and 20% into the hydrophilic fraction except for fire/biomass combustion where 100% was emitted into the hydrophilic component following Genberg et al. (2013). Scavenging and aging was parameterized following Liu et al. (2011), i.e., aging is proportional to OH and scavenging in mixed-phase clouds is reduced. The hydrophobic fraction is assumed to be 5% activated in the scavenging scheme, while the hydrophilic fraction is 100% activated. If the clouds are mixed phase, then the scavenging efficiency is scaled by the ratio of cloud ice water content to total cloud water content assuming zero scavenging for 100% ice clouds.

6.2.13 MATCH-SALSA-RCA4

The chemistry transport model, MATCH (Robertson et al., 1999; Andersson et al., 2007) described above is online coupled to the aerosol dynamics model, SALSA (Kokkola et al., 2008). SALSA describes the whole chain from nucleation to the growth and deposition of particles and computes the size distribution, number concentration and chemical composition of the aerosol species. A sectional representation of the aerosol size distribution is considered with three main size ranges (a: 3–50 nm, b: 50–700 nm and c: > 700 nm) and each range is again subdivided into smaller bins and into soluble and insoluble bins adding up to a total of 20 bins. A schematic of the sectional size distribution and the aerosol species considered in each bin is shown in Fig. 1. The seasonally varying emissions

10289 are based on the sector-wise ECLIPSE inventory. Isoprene emissions are modelled online
10290 depending on the meteorology based on the methodology by Simpson et al. (1995). The
10291 terpene emissions (α-pinene) are taken from the modelled fields by the EMEP model. Sea
10292 salt is parameterized following the scheme of Foltescu et al. (2005) but modified for varying
10293 particle sizes, wherein Mårtensson et al. (2003) scheme is used if the particle diameter is ≤1
10294 µm and Monahan et al. (1986) scheme is used otherwise. The coupling of MATCH with
10295 SALSA and the evaluation of this model setup is described in detail in Andersson et al.
10296 (2015). A cloud activation model that computes 3-D CDNCs (Cloud Droplet Number
10297 Concentrations) based on the prognostic parameterization scheme of Abdul-Razzak and
10298 Ghan (2002) specifically designed for aerosol representation with sectional bins is
10299 embedded in the MATCH–SALSA model. This scheme simulates the efficiency of an aerosol
10300 particle to be converted to a cloud droplet depending on the number concentration and
10301 chemical composition of the particles given the updraft velocity and supersaturation of the
10302 air parcel. The updraft velocity is computed as the sum of the grid mean vertical velocity and
10303 turbulent kinetic energy (TKE) for stratiform clouds (Lohmann et al., 1999). These CDNCs are
10304 then offline coupled to a regional climate model, RCA4 (Samuelsson et al., 2011), that
10305 provides us information on cloud properties such as cloud cover, cloud droplet radii, cloud
10306 liquid-water path as well as radiative fluxes. The schematic of the model coupling is shown
10307 in Fig. 2. RCA4 is run with 6-hourly ERA-Interim meteorology and the 3-hourly RCA4
10308 meteorological fields along with the fields needed to calculate updraft velocity are used to
10309 drive the MATCH-SALSA-cloud activation model. The CDNCs are then used to re-run the
10310 RCA4 model to obtain the cloud properties and radiative effects. The validation and more
10311 details of this model set up is described in Thomas et al., (2015).
10312

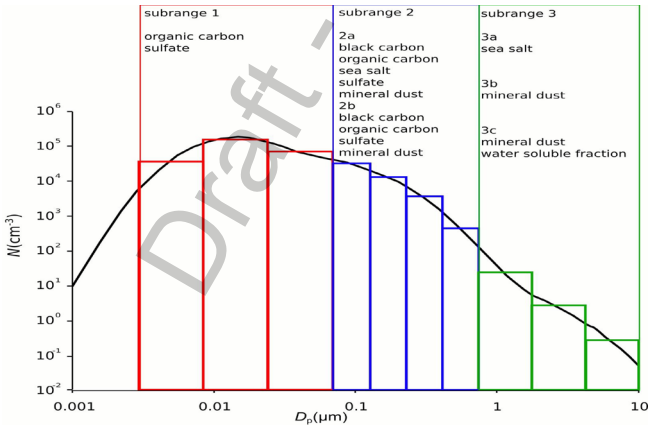

10313

Fig. 1: Schematic of sectional distribution of aerosol

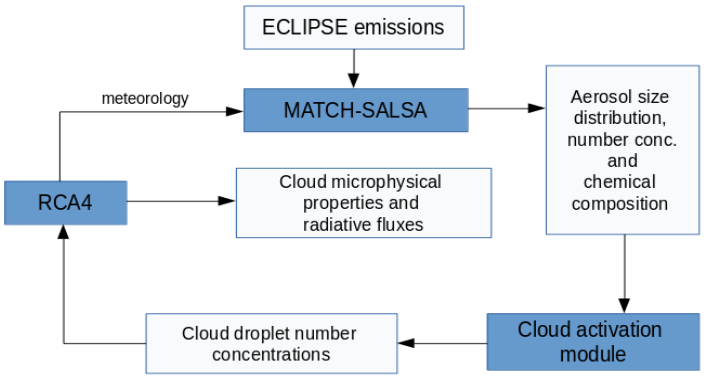

Fig.2: Schematic showing the different model components size bins and the chemical components in the bins and their couplings. (taken from Kokkola et al., 2008).

6.2.14 MRI-ESM2

MRI-ESM2 (Meteorological Research Institute Earth System Model version 2.0) consists of four major component models; an atmospheric general circulation model (AGCM) with land processes, an ocean-sea-ice general circulation model (OGCM), and aerosol and atmospheric chemistry models (Yukimoto et al., 2019), however, we do not couple OGCM in the type0, type1, and type2 simulations. MRI-ESM2 uses different horizontal resolutions but employs the same vertical resolution in each atmospheric component model as follows: TL159 (approximately 120 km), TL95 (approximately 180 km), and T42 (approximately 280 km) in the MRI-AGCM3.5, the aerosol model, and the atmospheric chemistry model, respectively, all with 80 vertical layers (from the surface to a model top of 0.01 hPa) in a hybrid sigma-pressure coordinate system. Each component model is interactively coupled by a coupler, which enables an explicit representation of the effects of gases and aerosols on the climate system.

The atmospheric chemistry component model in MRI-ESM2 is the MRI Chemistry Climate Model version 2.1 (MRI-CCM2.1), which calculates the evolution and distribution of ozone and other trace gases in the troposphere and in the middle atmosphere. The model calculates a total of 90 gas-phase chemical species and 259 chemical reactions in the atmosphere. The aerosol component model in MRI-ESM2 is the Model of Aerosol Species in

the Global Atmosphere mark-2 revision 4-climate (MASINGAR mk-2r4c) that calculates atmospheric aerosol physical and chemical processes and treats the following species; nonsea-salt sulfate, BC, OC, sea salt, mineral dust, and aerosol precursor gases (e.g., sulfur dioxide and dimethyl sulfide). The size distributions of sea salt and mineral dust are divided into 10 discrete bins and the sizes of the other aerosols are represented by lognormal size distributions. The model assumes external mixing for all aerosol species; however, in the radiation process in MRI-AGCM3.5, hydrophilic BC is assumed to be internally mixed with sulfate with a shell-to-core volume ratio of 2; the optical properties of hydrophilic BC are calculated based on Mie theory with a core-shell aerosol treatment, in which a concentric BC core is surrounded by a uniform coating shell composed of other aerosol compounds (Oshima et al. 2009a; 2009b). MRI-ESM2 employs a BC aging parameterization (Oshima and Koike, 2013) that calculates the variable conversion rate of BC from hydrophobic BC to hydrophilic BC, which generally depends on the production rate of condensable materials such as sulfate. In the radiation and cloud processes in MRI-ESM2, sulfate is assumed to be $(NH_4)_2SO_4$ and OC is assumed to be organic matter (OM) by lumping OC species using an OM-to-OC factor of 1.4. MRI-ESM2 represents the activation of aerosols into cloud droplets based on the parameterizations, and detailed descriptions and evaluations of the cloud processes and cloud representations in MRI-ESM2 are given by Kawai et al. (2019). Evaluations of the effective radiative forcing (ERF) of anthropogenic gases and aerosols in present-day conditions relative to preindustrial conditions in the global and the Arctic using MRI-ESM2 are given by Oshima et al. (submitted in 2020).

The type0 simulations were performed from January 2008 (or January 1990) to December 2015 after a 1-year spin-up run using the prescribed SST and sea ice data (provided by the AMIP experiment in CMIP6, https://www.wcrp-climate.org/modelling-wgcm-mip-catalogue/modelling-wgcm-mips-2/240-modelling-wgcm-catalogue-amip). The horizontal wind fields were nudged toward the 6-hourly Japanese 55-year Reanalysis (JRA55) data (Kobayashi et al. 2015) (https://jra.kishou.go.jp/JRA-55/index_en.html) in the simulation. We used the monthly anthropogenic emissions from the ECLIPSE V6B emission dataset and the monthly biomass burning emissions from the CMIP6 in the simulations. Major volcanic aerosols are given by the stratospheric aerosol dataset used in the CMIP6 experiments (Thomason et al. 2018). Another type0 simulation with volcanic SO_2 emission including Holuhraun eruption was also performed for 2014-2015.

The type1 simulations were performed for 4 years after a 1-year spin-up run using the prescribed SST and sea ice data provided by AMIP. The horizontal wind fields were nudged toward the 6-hourly JRA55 reanalysis in the simulations. We used the annually-repeating 2015 emissions with individually 100% perturbed (complete removal) emissions of BC and SO_2 for individual region/sector combination.

The type2 simulations were performed for 50 or 60 years after a 1-year spin-up run using the prescribed SST and sea ice data provided by AMIP. We used the annually-repeating 2015 conditions with individually 100% perturbed (complete removal) emissions of BC and SO_2 for individual region/sector combination.

The type3 simulations by the fully coupled model were performed in 2015-2050 using three time-evolving emissions (CLE, MFR, and SLCF scenarios). Five ensemble simulations were performed for each emission scenario.

6.2.15 NorESM1

NorESM1 (Bentsen et al., 2013; Iversen et al., 2013) is based on the fourth version of the Community Climate System Model (CCSM4) (Gent et al., 2011), with coupled models for the atmosphere, ocean, land and sea-ice. Here, we have used a 1° horizontal resolution in the atmosphere (0.95° latitude by 1.25° longitude, version 'NorESM1-Happi'). The model has 26 vertical levels on a hybrid sigma-pressure co-ordinate up to the model top at 2.194 hPa. The model calculates the lifecycles of a range of natural and anthropogenic aerosol components from emissions and physico-chemical processing in air and cloud droplets. The only prescribed aerosol concentrations are stratospheric sulphate from explosive volcanoes. The direct and indirect aerosol effects on climate are calculated by parameterization of aerosol interactions with schemes for radiation and warm cloud microphysics (Kirkevåg et al., 2013). The model uses a prognostic calculation of cloud droplet numbers, allowing for competition effects between aerosols of different hygroscopic property and size.

6.2.16 OsloCTM

The Oslo CTM3 is an offline global three-dimensional chemistry transport model driven by 3-hourly meteorological forecast data from the Integrated Forecast System (IFS) model at the European Centre for Medium-Range Weather Forecasts (ECMWF). The Oslo CTM3 consists of a tropospheric and stratospheric chemistry scheme (Søvde et al., 2012) as well as aerosol

modules for sulphate, nitrate, black carbon, primary organic carbon, secondary organic aerosols, mineral dust and sea salt (Lund et al. 2018).

6.2.17 UKESM1

UKESM1 (United Kingdom Earth System Model) is a fully-coupled Earth System model (Sellar et al., 2019) with a coupled atmosphere ocean physical climate model (HadGEM3-GC3.1) at its core (Kuhlbrodt et al., 2018; Williams et al., 2018). For UKESM1 various Earth system components are incorporated with the physical climate model including ocean biogeochemistry, an interactive stratosphere-troposphere chemistry and aerosol scheme and terrestrial carbon and nitrogen cycles coupled to interactive vegetation. The model has a horizontal resolution of ~135 km at the mid-latitudes (1.875° x 1.25°), with 85 levels on a terrain-following hybrid height coordinate system, ranging in height from the surface to a model top of 85 km. The combined stratosphere-troposphere United Kingdom Chemistry and Aerosol (UKCA) scheme is used within UKESM1 and is fully described and evaluated in (Archibald et al., 2019; Mulcahy et al., 2019).

The chemical scheme in UKCA is built upon on the scheme described for the stratosphere in Morgenstern et al., (2009) and that for the troposphere described in O'Connor et al., (2014). Chemical reactions are included within UKCA for odd-oxygen (Ox), nitrogen (NOy), hydrogen ($HOx = OH + HO_2$), carbon monoxide (CO), methane and short-chain non-methane volatile organic compounds (NMVOCs), including isoprene. Reactions involving NMVOCs are simulated as discrete species. UKCA includes an interactive photolysis scheme, as well as representations of both wet and dry deposition for gas and aerosol species. Additional chemical reactions for dimethyl sulphide (DMS), sulphur dioxide (SO_2) and monoterpenes ($C_{10}H_{16}$) are included to enable coupling to the aerosol scheme within UKCA. A two-moment aerosol microphysical scheme, GLOMAP (Global Model of Aerosol Processes; Mann et al., 2010, 2012), is used to simulate four aerosol components (sulphate, black carbon, organic matter, sea-salt) across five log-normal modes, ranging from sub to super micron sizes. Mineral dust is simulated separately using a 6 bin mass only scheme, ranging in size from 0.6 to 60 microns in diameter (Woodward, 2001). Ammonium nitrate is not currently included within the UKCA aerosol scheme. The formation of secondary organic aerosols (SOA) is included based on a fixed yield rate of 26% from the products of monoterpene oxidation.

The higher fixed yield value accounts for the underlying uncertainty in SOA formation and the absence of anthropogenic, marine and isoprene sources.

Precursor emission fluxes are either prescribed using specified input files or calculated interactively using online meteorological variables within UKESM1. Methane is represented by using prescribed global concentrations. Interactive emission fluxes are calculated online for sea salt, DMS, dust, lightning NOx and biogenic volatile organic compounds (BVOCs). Emissions of isoprene and monoterpenes from the natural environment are calculated online by coupling to the land surface scheme within UKESM1.

Simulations provided by UKESM1 and used in the AMAP assessment have been undertaken using different configurations. For type0 and type1 experiments UKESM1 has been set up using an atmosphere only configuration that is nudged to ECMWF reanalysis (ERA-interim) of temperature and wind fields above the boundary layer. Prescribed values of sea surface temperatures and sea ice are used for each year of simulation based on historical simulations conducted as part of CMIP6 using the fully coupled atmosphere-ocean configuration of UKESM1. For other ancillary inputs a multi-year climatology was used; equivalent to an AMIP type simulation. For type0 transient emissions were used as input whereas for type1 experiments annually repeating 2015 emissions were used for four different years to account for the influence of meteorological variability. For type3 experiments the fully coupled Earth system model configuration of UKESM1 was used with free-running meteorology, enabling feedbacks of changes in short lived climate forcers on the climate system.

6.2.18 WRF-CHEM

… (*Kathy*)

6.3 Comparison of simulated and observed short-lived climate forcers

The validation of models focuses on SLCFs black carbon (BC), sulfate (SO4), ozone (O3), and methane (CH4). We also include PM2.5 validation, as particulate matter is partially made up of some SLCFs, and PM2.5 has important implications on health. We additionally utilise measurements of aerosol optical properties to evaluate models' simulations of aerosols as a

whole (abundance, size distribution, etc). Furthermore, in the appendix, we also include model validation of organic aerosol (OA), and O3 precursor species; carbon monoxide (CO), and nitrogen oxides (NOx).

This section provides results from "type 0" model experiments, which cover four recent years; 2008-9 and 2014-15. For details regarding measurement methods and data sets, please refer to Chapters 4 & 5. Section 6.3 is split into four main parts: model results of SLCFs in the Arctic, model results in the Northern Hemisphere (which is important because of long-range transport of SLCFs to the Arctic), model results of clouds (which is a large source of variability in models, and a large factor in the radiation budgets, as will be further discussed in Chapter 7), and - from a subset of models - the 1990-2015 long-term trends of Arctic SLCFs BC, SO4, and O3.

6.3.1 Aerosols and trace gases in the Arctic

Figure X(a) below shows the measurement locations of black carbon in the Arctic. Atmospheric concentrations in surface-level air are measured at the black locations, and black carbon deposition is observed in ice cores at the brown locations. Fig X(b) shows a couple of Arctic ship-based campaigns that measured BC (and others) within the 2014-2015 model validation period.

(a) **(b)**

Fig 6.3.X (a) Location for BC deposition (black) and atmospheric BC measurements (brown) (b) ship tracks of two campaigns that measured BC.

10490

10491 ***6.3.1.1 Mean concentrations and seasonal variability at surface measurement locations***

10492

10493 *To be added here: the analysis of O3, CH4 (CO and NOx in appendix) surface maps and*
10494 *scatter plots. Surface trace gas data are from:*

10495 - *NAPS (national air pollutant surveillance; Canada)*
10496 - *CSN (chemical speciation network; US)*
10497 - *CMDL (Climate Monitoring and Diagnostics Laboratory; global)*
10498 - *China AQ (https://beijingair.sinaapp.com/)*
10499 - *Hong Kong EPA*
10500 - *EBAS (Europe; ebas.nil.no)*
10501 - *Global CH4 from the WDCGG (World Data Centre for GHGs*
10502 *https://gaw.kishou.go.jp/login/user)*

10503

10504 Figure 6.3.1.X below shows concentrations of black carbon (BC) in surface air at nine Arctic
10505 observation stations. Annual mean concentrations are of the order of less than 1 ug m^{-3} and
10506 most models tend to underestimate BC in the Arctic by about 10%.

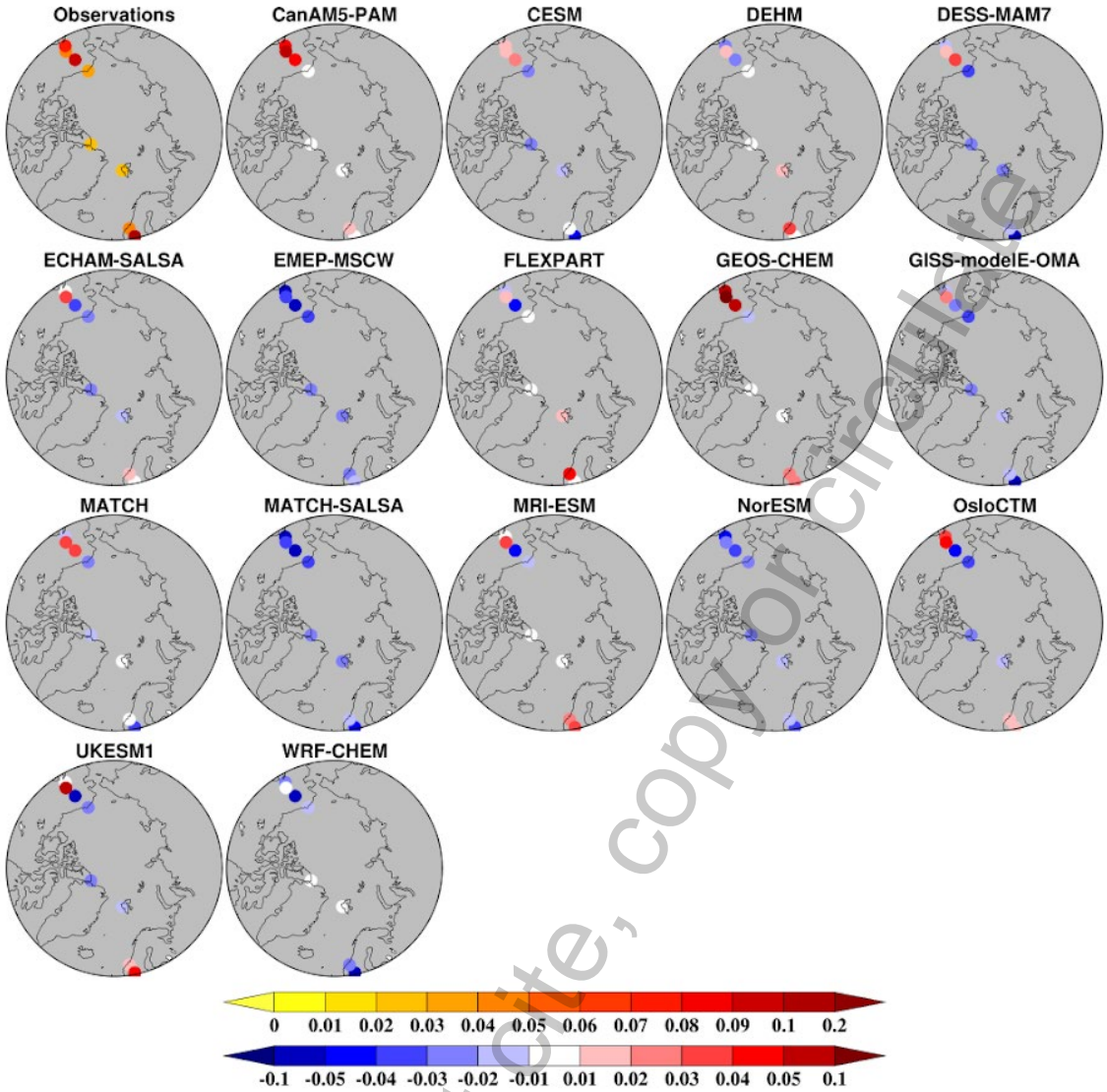

Figure 6.3.1.X Annual mean black carbon concentrations (ug m^{-3}) at surface Arctic measurement sites, and model bias in 2014-15. Results from 2008-9 are similar and not shown. Note that the annual mean is calculated for the number of available monthly mean values of each site which varies (see legend of scatter plot below).

Models have improved since the previous assessment report, in particular in their ability to capture the seasonal cycle of BC in the Arctic. Previously, models were not able to represent the higher wintertime BC concentrations (Eckhardt et al, 2015). As can be seen in Figure 6.3.1.X below, some models still underestimate wintertime BC, but most models have similar seasonality as the observations.

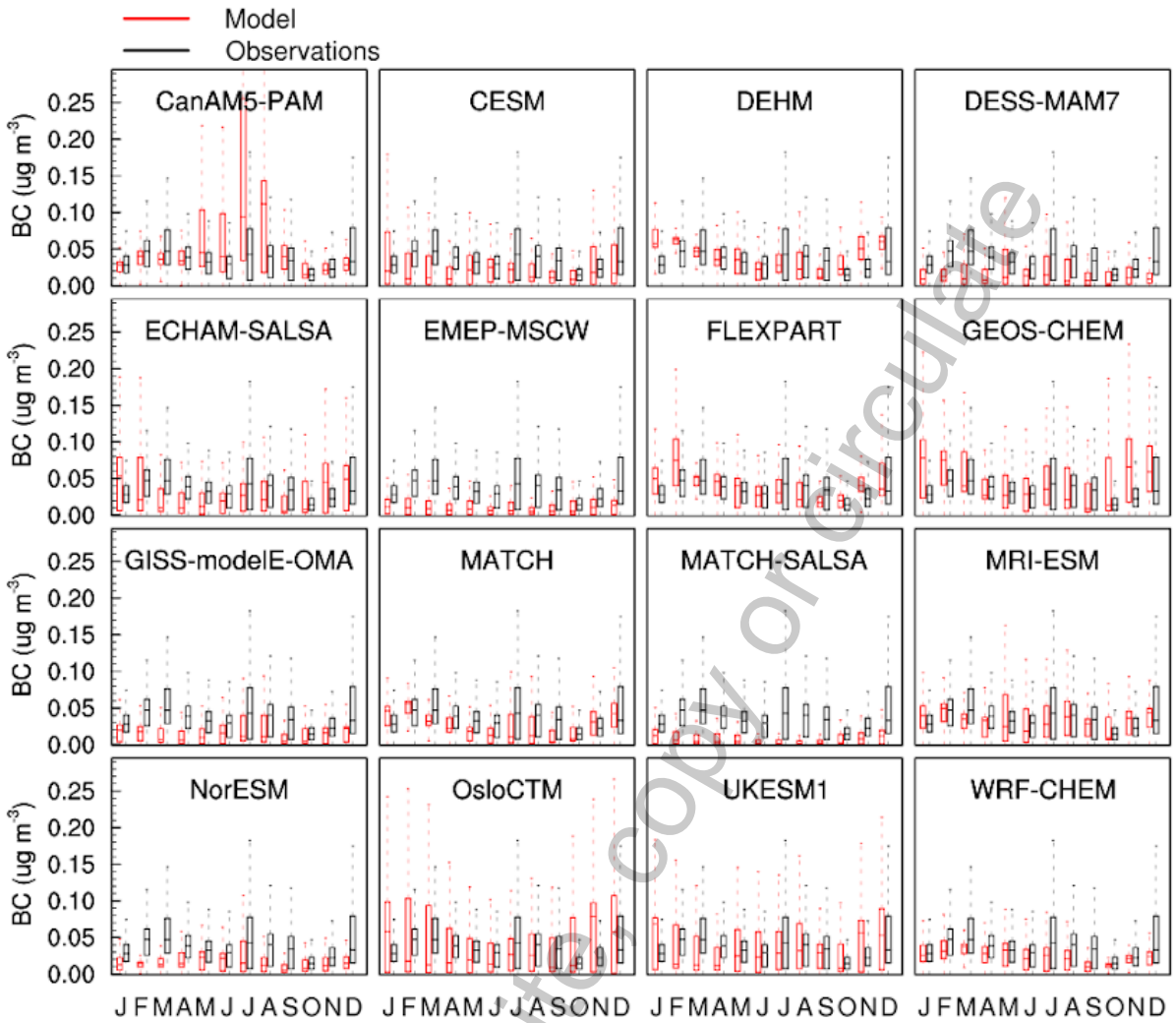

10520

10521 **Figure 6.3.1.X** Modelled and measured monthly mean black carbon concentrations at

10522 surface Arctic measurement sites in 2014-15. Results for 2008-9 are similar and not shown.

10523

10524 Most models have reasonable correlation coefficients with the measurements at various

10525 locations in the Arctic. This means that models are correctly simulating the range of BC

10526 concentrations that appear across the Arctic (e.g., higher concentrations at Hurdal, lower

10527 concentrations at Zeppelin, etc). Some statistics are shown in Figure X below.

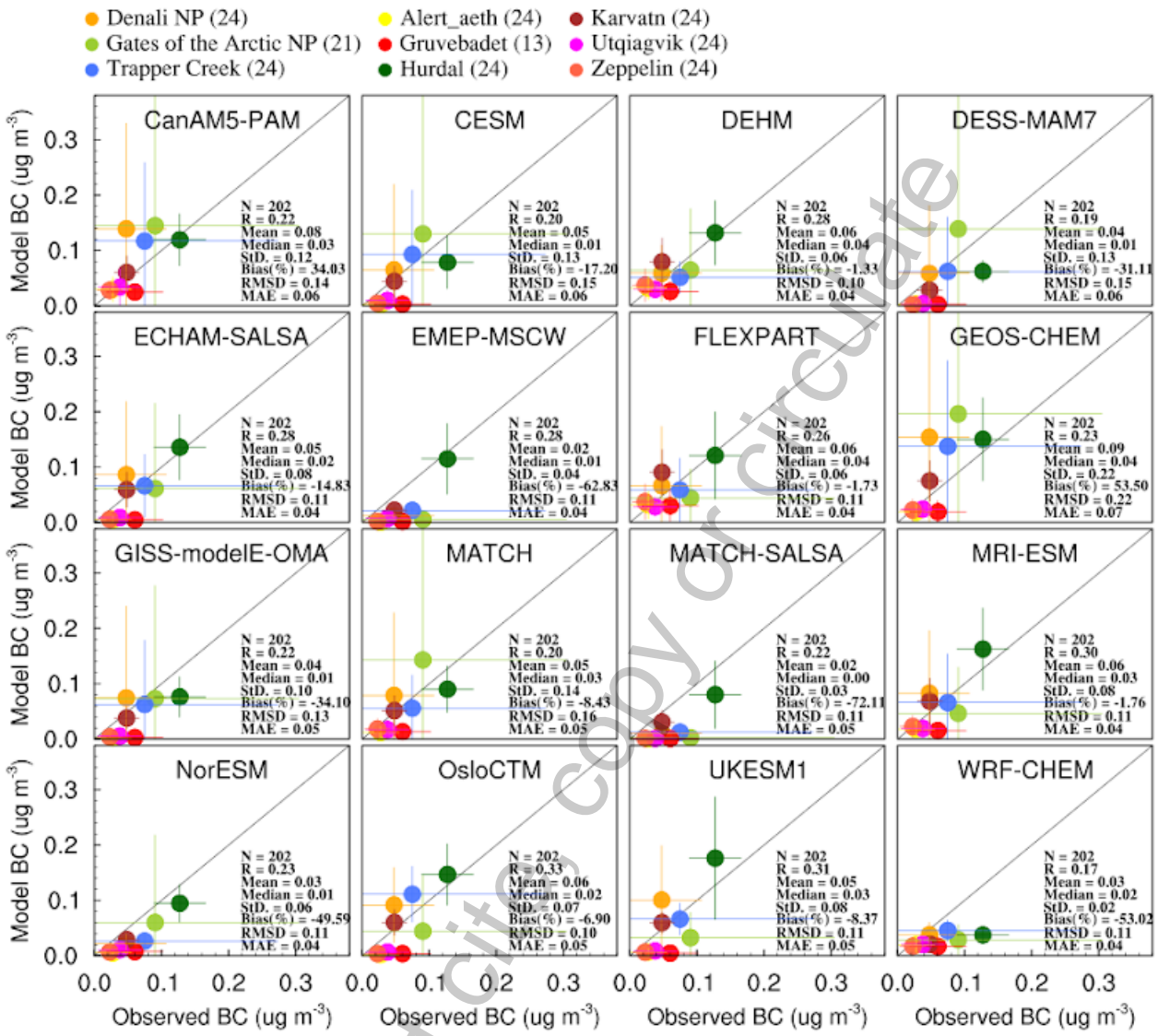

Figure 6.3.1.X Modelled vs measured black carbon concentrations at surface Arctic measurement sites in 2014-15. Results for 2008-9 (not shown) had lower correlation coefficients and higher biases.

There are quite a few more observations of sulphate in the Arctic, and Figures X-Y below show how the models perform against those measurements. Generally all models are underestimating the annual mean sulphate in the high Arctic, though some are overestimating sulphate in Scandenavia and Alaska. This could be due to not enough long-range transport of sulphate to the high Arctic.

To do: Discuss impact of Honoluran volcano in late 2014. Which models included an estimate of those emissions and does it help reduce bias?

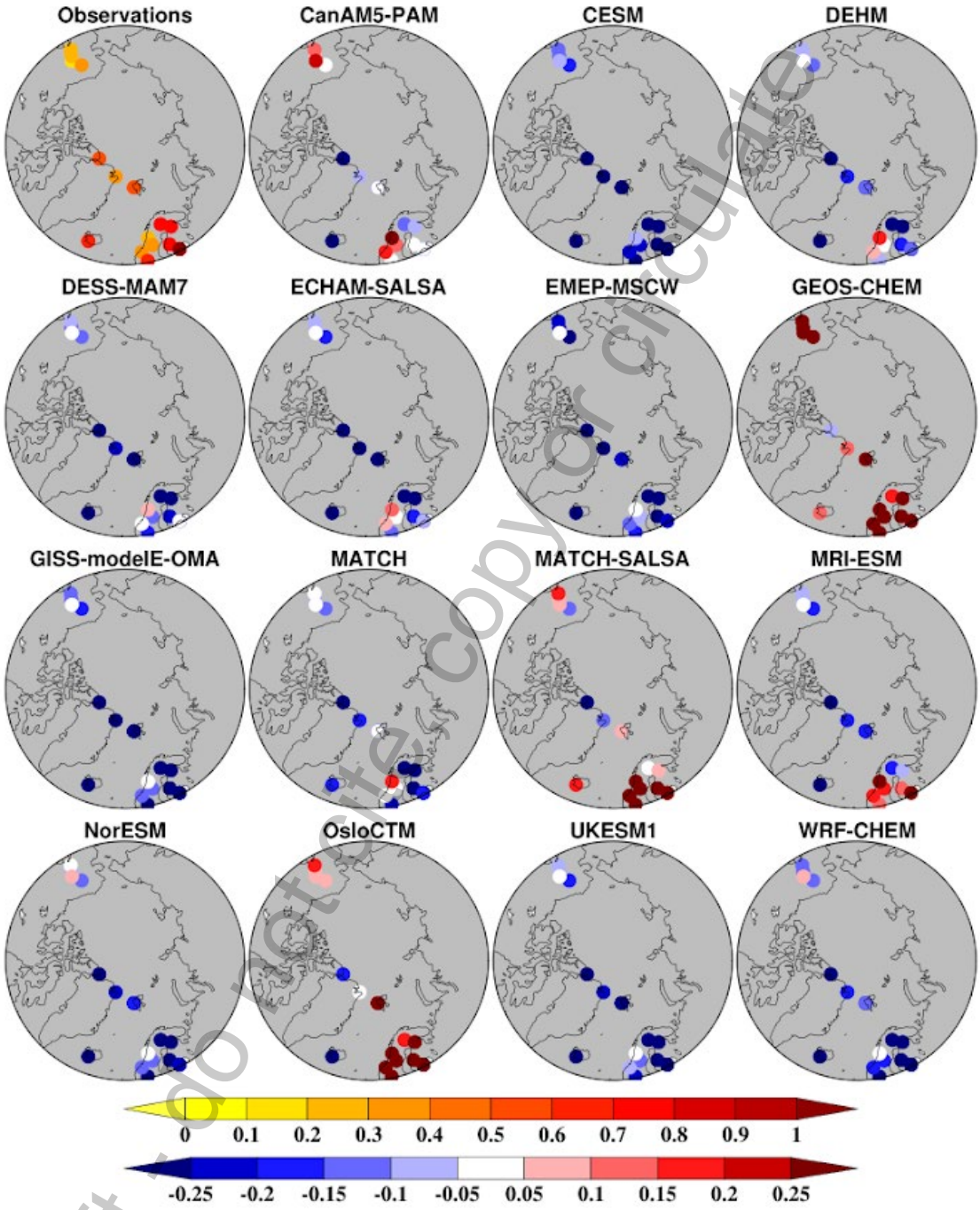

Figure 6.3.1.X Annual mean sulphate concentrations (ug m^{-3}) at surface Arctic measurement sites, and model bias in 2014-15. Results from 2008-9 are similar and not shown.

The observations show little seasonal cycle in sulphate at Arctic locations, though models show a large variation in seasonality, as shown in Figure X below.

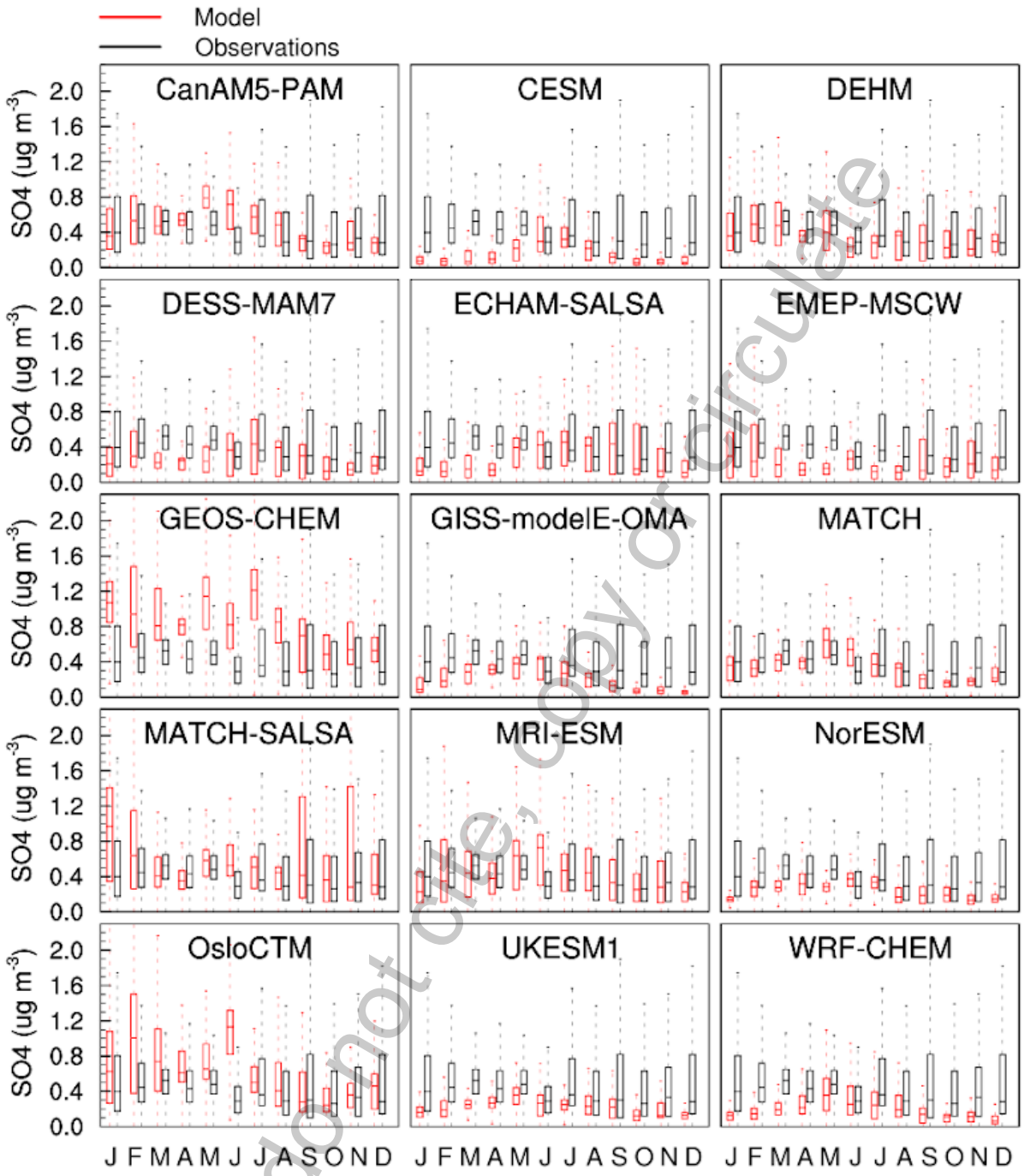

Figure 6.3.1.X Modelled and measured monthly mean sulphate concentrations at surface Arctic measurement sites in 2014-15. Results for 2008-9 are similar and not shown.

While the models capture the magnitude of sulphate well, the correlation coefficients indicate that the models are not quite capturing the spatial variability compared to the measurements. That said, all models simulate correctly the observed highest sulphate concentrations at Virolahti and Ahtari, and lowest concentrations at Fairbanks and Tustervatn.

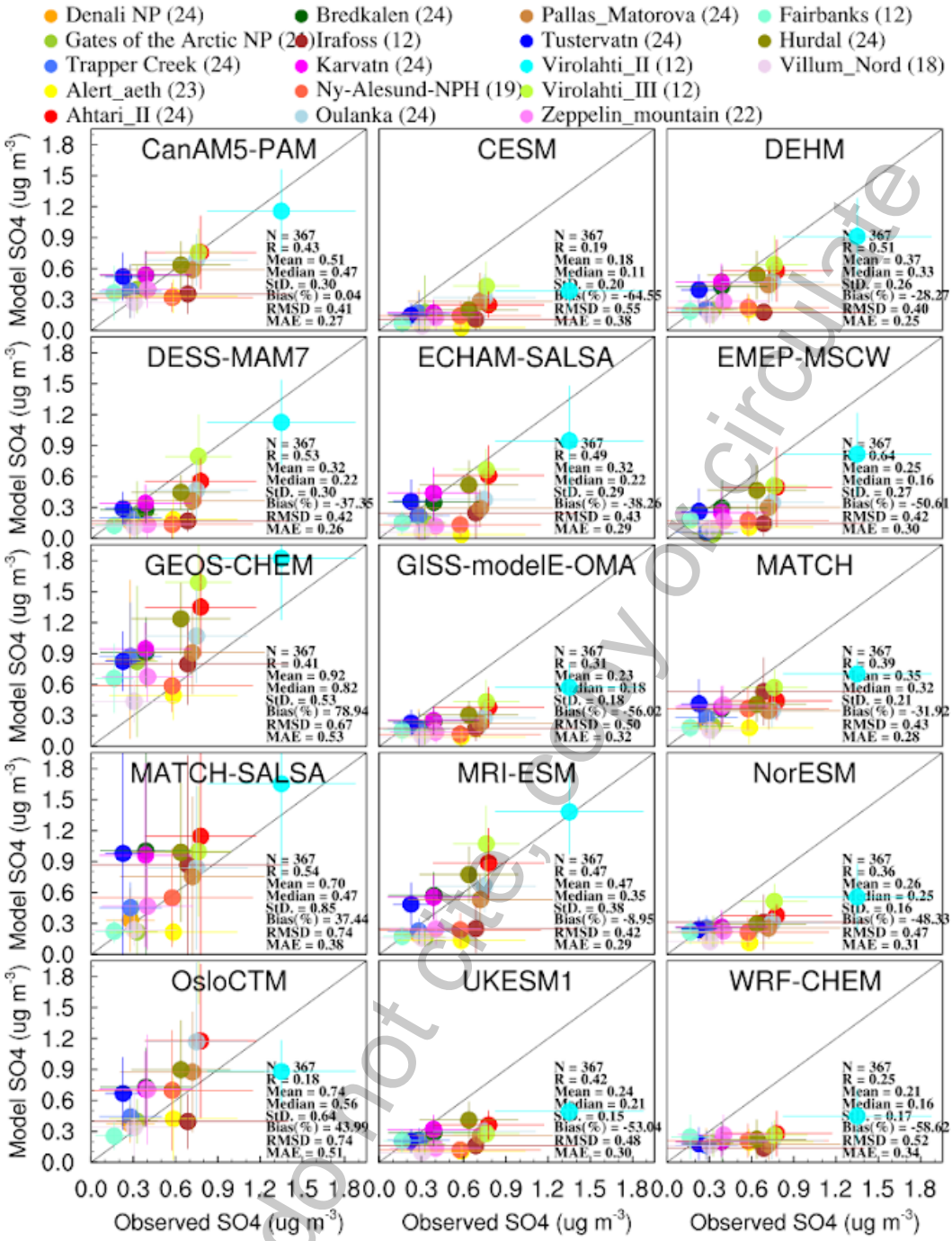

Figure 6.3.1.X Modelled vs measured sulphate concentrations at surface Arctic measurement sites in 2014-15. Results for 2008-9 (not shown) are very similar.

A similar analysis for organic aerosol was carried out (*appendix*) though fewer observation stations measure this aerosol species (only 6 stations). Organic aerosol tends to be highest in the summertime due to the large biomass burning emissions that occur then via wild fires. All models captured that seasonal cycle, although many of them overestimated

summertime concentrations, particularly in 2008-9. The models do not capture the spatial variability of organic aerosol well either.

In addition to the stationary measurement locations, there were two ship-based measurement campaigns in 2014-2015. These were the Japanese campaigns in Septembers of 2014 and 2015 (blue track in Fig 6.3.X(b) above), and the Russian campaign in October 2015 (brown track in Fig 6.3.X(b) above). Models that provided 3-hourly BC output were compared to these observations in the figure below.

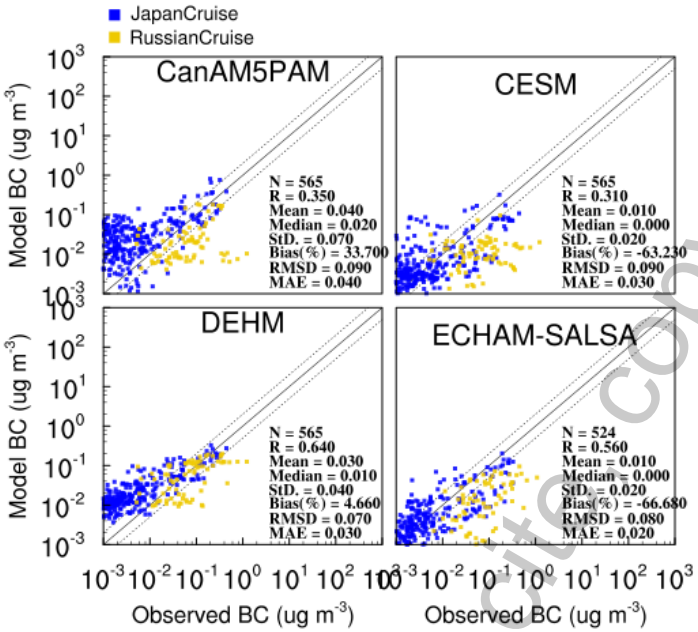

Figure 6.3.Y: Model vs measured 3-hour-average BC for the ship campaigns.

PM2.5 is particulate matter that is less than 2.5 um in diameter. At that size, particulate matter can be inhaled and pass deep into the lungs and possibly even the circulatory system. For that reason, PM2.5 is a health concern, discussed further in Chapter 8. Models simulate the processes and transport of many aerosol species (such as BC, SO4, and OA discussed above) in a number of size bins or following a size function, and calculate PM2.5 often as a sum of those species in the fine particle mode. Below we evaluate models' PM2.5 output, which is either the sum of the species in the 0-2.5 um size bin, or else a pre-calculated dry PM2.5 output.

Placeholder for Arctic PM2.5 figures

Some models, such as CESM, ECHAM-SALSA, EMEP-MSC-W, MATCH, and MATCH-SALSA underpredict PM2.5 in 2008-9, though all models simulate the magnitude of PM2.5 concentrations with more accuracy in 2014-15. The spatial variability in PM2.5 is not well captured by models with predictions of higher concentrations at sites that measure lower concentrations and vis versa.

6.3.1.2 Arctic black carbon and sulfate deposition

Ice core are valuable for investigating past emissions variation. For black carbon, the only sources, before the industrial period in 1850 have been biomass burning. After 1850 anthropogenic emission influenced the deposition on Arctic locations. Most ice cores show a decreasing trend over the years (chapter 5, Fig XX). We use the observations of the last decades to evaluate the performance of BC and Sulfate deposition in the models. For BC in the 7 ice cores used in this comparison the model mean is 2 times as high as the observations for all Greenland ice cores. Observed deposition rates mainly under 1 mg/m2/year. In NEEM the modeled mean corresponds well to the observation, at Humboldt the models give 4 times the deposition compared to the measurements. Sulfate is 4 times overestimated by the models, on average observations are 4 mg/m2/year, the models give 15 mg/m2/years.The biggest mismatch is at ACT2.

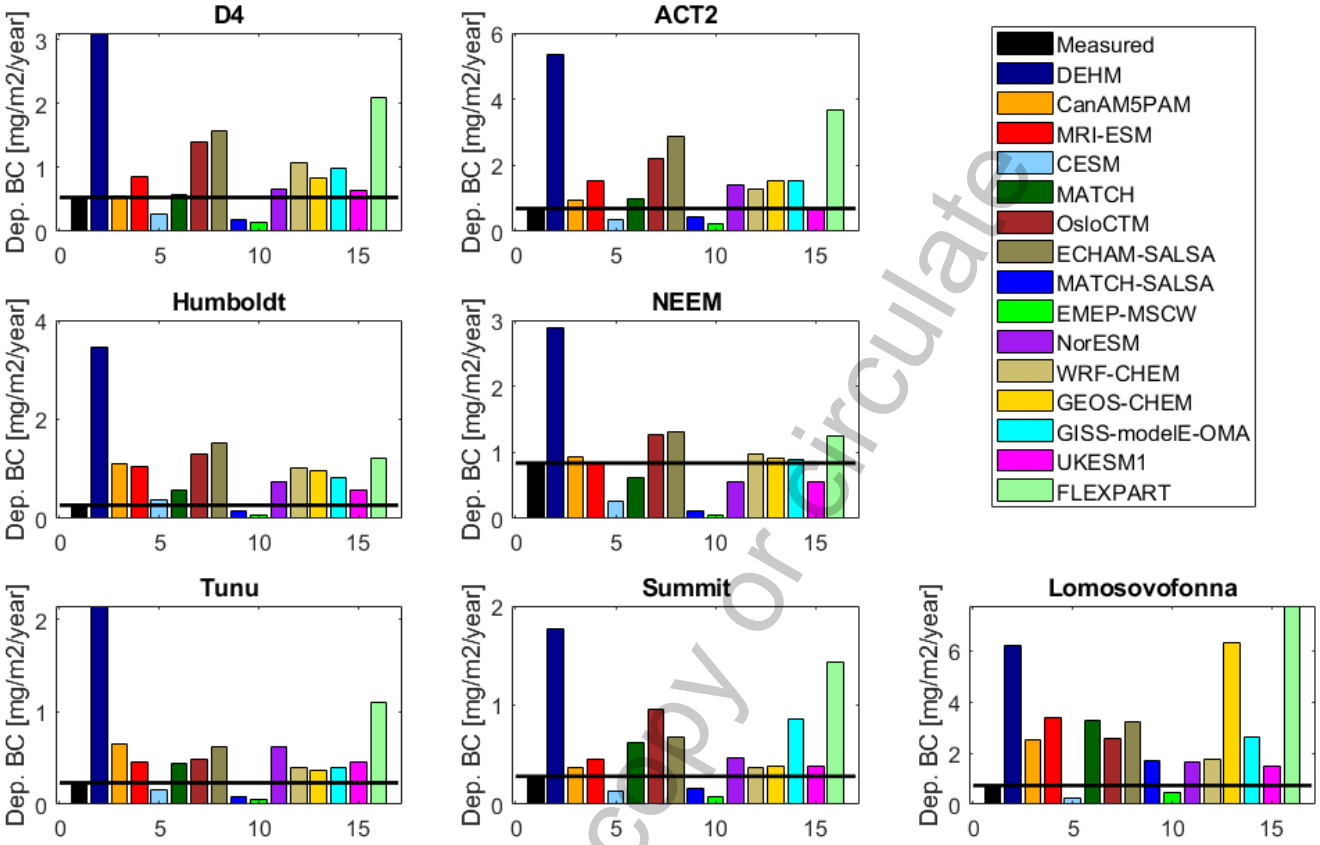

10608

10609 **Figure 6.3.1.X:** Annual average BC deposition values for the 7 ice core locations for each
10610 model. The observed concentrations are plotted in black and a black line indicates the level
10611 of the average observed concentrations. The period used for plotting are all years after
10612 1990, see table XX for which periods have been used by which model.

10613

10614

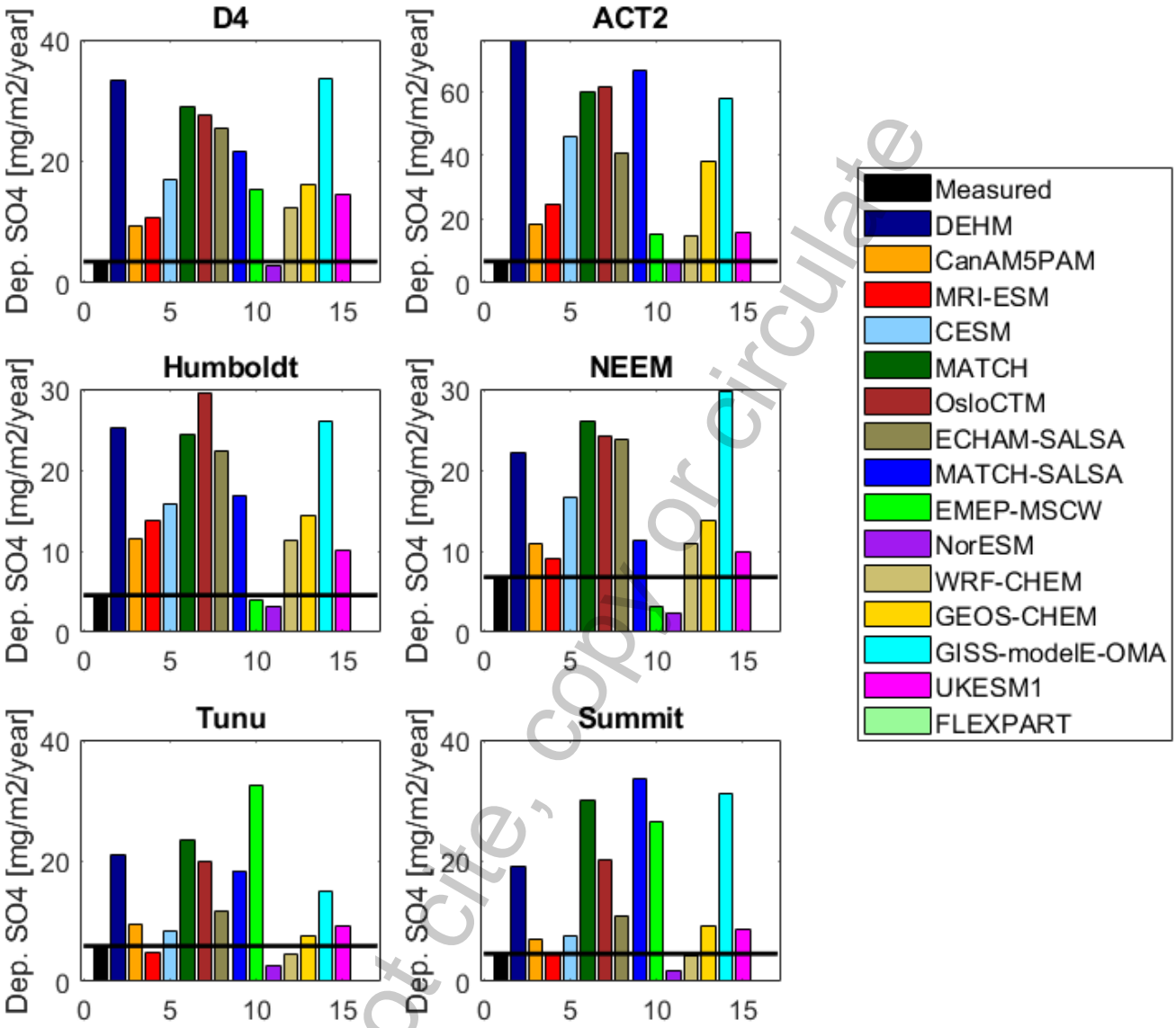

Figure 6.3.1.X: SO4 deposition for the Greenland ice core locations

6.3.1.3 Comparisons with remote sensing observations

Satellite data are very useful for monitoring Arctic concentrations of methane, ozone, and other gaseous SLCFs. These data provide better spatial coverage than the ground sites, and often have a longer timeseries. They also provide vertical information on the distribution of SLCFs. We utilize data from ACE-FTS, TES, and MOPITT in this and Section 6.3.2.2 and compare those results to the modelled mixing ratios of ozone, carbon monoxide, and methane.

Placeholder for TES O3 and CO here.

Placeholder for MOPITT CO here.

There were up to 11 models (depending on the species) that provided 3-hourly output of trace gases. These were compared to the Atmospheric Chemistry Experiment-Fourier Transform Spectrometer (ACE-FTS) satellite measurements in the upper-troposphere, lower-stratosphere (UTLS), a region where ozone is a potent greenhouse gas. ACE-FTS is a solar occultation instrument with an orbit that allows for relatively good Arctic coverage. Figure 6.3.1.X-Y shows ACE-FTS measurements and model biases for ozone, methane, carbon monoxide, and nitrogen oxides (NOx).

All models underestimate the Arctic ozone distribution in the upper stratosphere in the Arctic, as can be seen in Fig X below. In the lower stratosphere and upper troposphere, model biases of Arctic O3 are very small, at less than 10%.

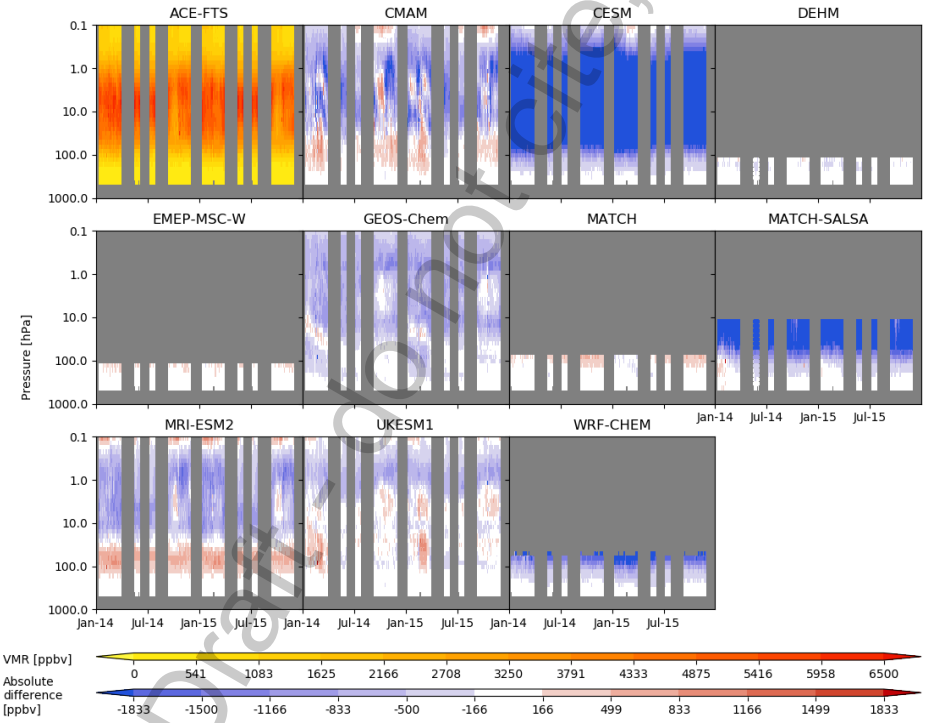

Figure 6.3.1.X Mean Arctic (60-90N) ozone from ACE-FTS and the model-measurement differences for 2014-15. Results for 2008-9 were very similar and are not shown.

Methane is prescribed in most (all?) models in different ways. It is assumed to be well-mixed in the atmosphere because of it's relatively long lifetime. Unlike at the surface, which was discussed above, in the UTLS where ACE-FTS measures, this assumption is valid, as can be seen in Fig X below, showing relatively small biases of the order of +/- <10%.

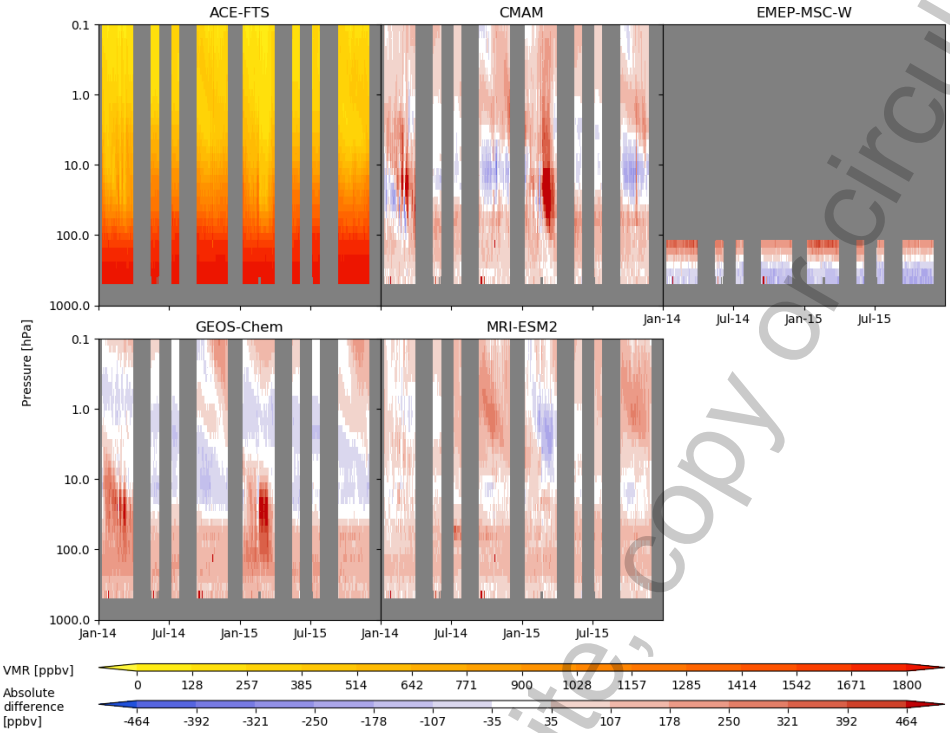

Figure 6.3.1.X Mean Arctic (60-90N) methane from ACE-FTS and the model-measurement differences for 2014-15. Results for 2008-9 were very similar and are not shown.

Carbon monoxide and NOx are precursors to O3 in the troposphere. The models show relatively small differences compared to measurements in the troposphere for both species (figures moved to appendix)

Add discussion of ACE results, particularly based on whether the model has stratospheric chemistry, or if it's prescribed and if so, from what.

6.3.1.4 Aerosol optical properties

While black carbon can not be measured directly from satellites, their data are also very useful for measuring the optical properties of aerosols such as aerosol optical depth, aerosol

absorption optical depth, and Angstrom exponent. Again, these measurements provide excellent spatial coverage compared to ground measurement stations. We utilize data from MODIS/Aqua, MODIS/Terra, MISR, AATSR, SeaWIFS, and CALIOP, as well as the ground-based ground-based Aerosol Robotic Network (AERONET) in this report and compare those results to the models.

Satellite measurements are limited in the Arctic during polar night, as many of them require sunlight for their spectral measurements. Some viewing geometries also don't allow some satellites to have a good "view" of the Arctic. In some cases, clouds and high albedo (due to snow and ice cover) limit the effectiveness of satellite measurements. Some are also less sensitive to the surface concentrations of SLCFs. Thus we don't present satellite measurements of aerosol optical depth in this section, but rather in Section 6.3.2.2 where we evaluate models on a global scale.

Here we compare modelled aerosol optical depth (AOD) - which gives indication of how much aerosol is in the atmosphere, absorption aerosol optical depth (AAOD) - which is a measure of the column aerosol loading of light-absorbing particles, and Angstrom Exponent (AE) - which gives an indication of the size of the aerosols, as it is inversely related to the average size of the particles in the aerosol to measurements.

Figure X(a) below shows AOD from ground-based AERONET observations, and the model biases, which ae relatively small in the Arctic. This means that models are capturing the amount of aerosol in the Arctic to within about 20% on average. Most models capture the seasonal cycle which has a maximum in the summertime due to biomass burning emissions (and greater secondary aerosol formation via oxidation/photolysis?).

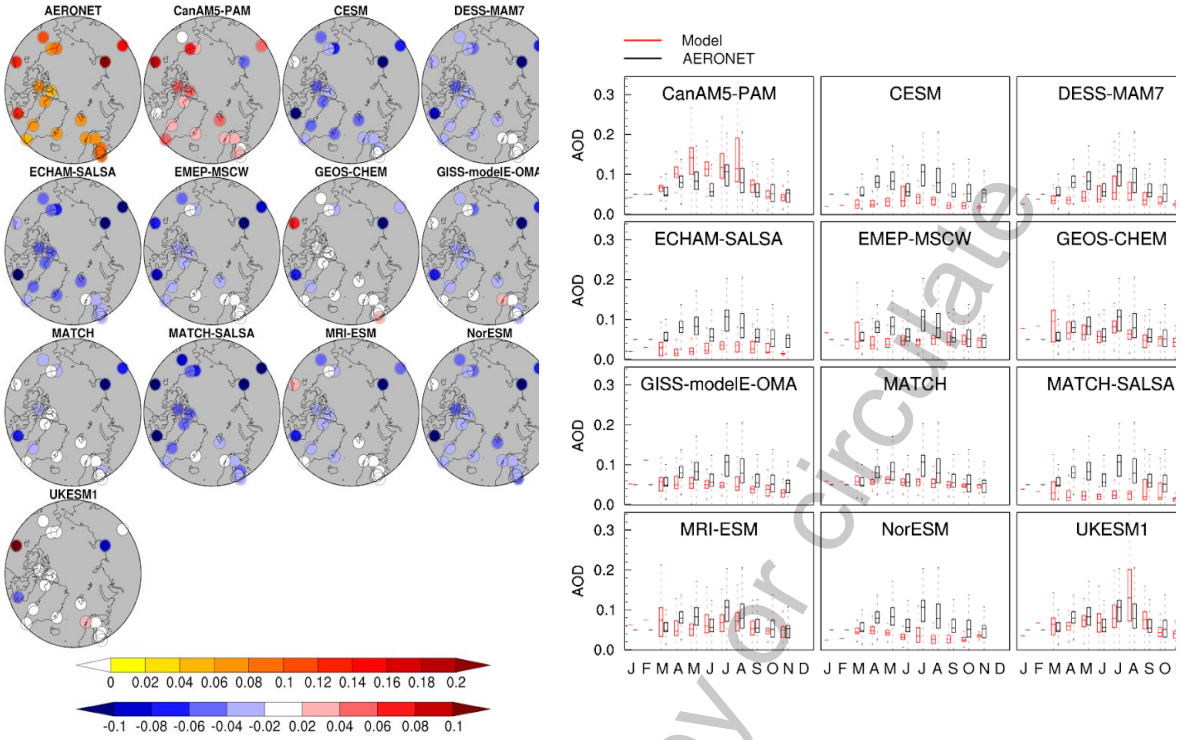

(a) **(b)**

Figure 6.3.1.X (a) Comparison of mean AOD at Arctic sites with AERONET mean values in the irst panel and model mean differences in subsequent panels. Note that mean is calculated for the number of available monthly mean values of each site which varies (see legend of scatter plot below), therefore this is not necessarily an annual mean. Results shown for 2014-15, with similar, though slightly worse results for 2008-9. (b) Comparison of AOD annual cycle at Arctic. For each month of a year the data was accumulated from all Arctic sites (i.e. sites with latitude >=60N).

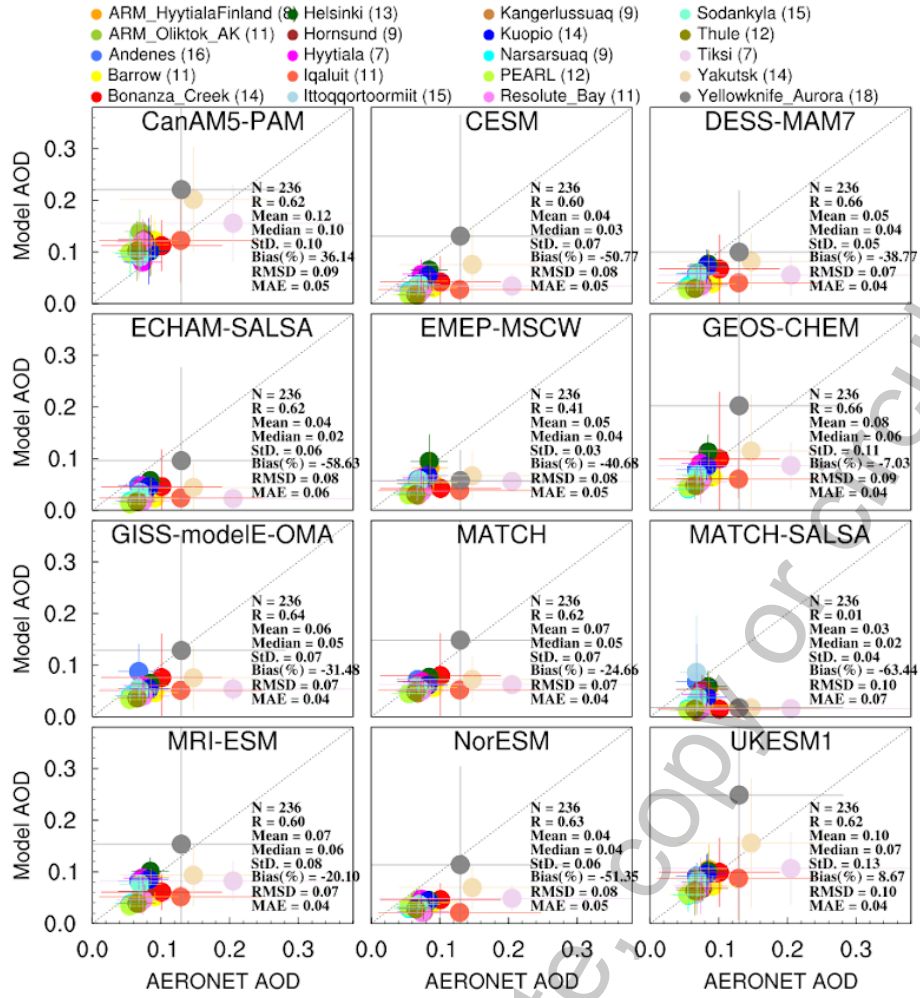

Figure 6.3.1.X Comparison of AOD at individual Arctic sites for 2014-15. Very similar 2008-9 results not shown.

AAOD from AERONET to be added

Only a smaller subset of models simulated Angstrom Exponent (AE). These are shown in Figure 6.X below with the AERONET measurements, giving an indication on whether these models are capturing the aerosol particle size accurately. Particle size is important for determining the transport and fate of aerosols, as well as their ability to absorb and scatter light. Therefore, it is important to simulate them accurately in models in order to obtain a correct distribution. MATCH and CESM greatly underestimate AE, which implies that particles are too large compared to measurements.ECHAM-SALSA and CanAM5-PAM have very low biases and accurate representation of the seasonal cycle, which peaks in the late summertime.

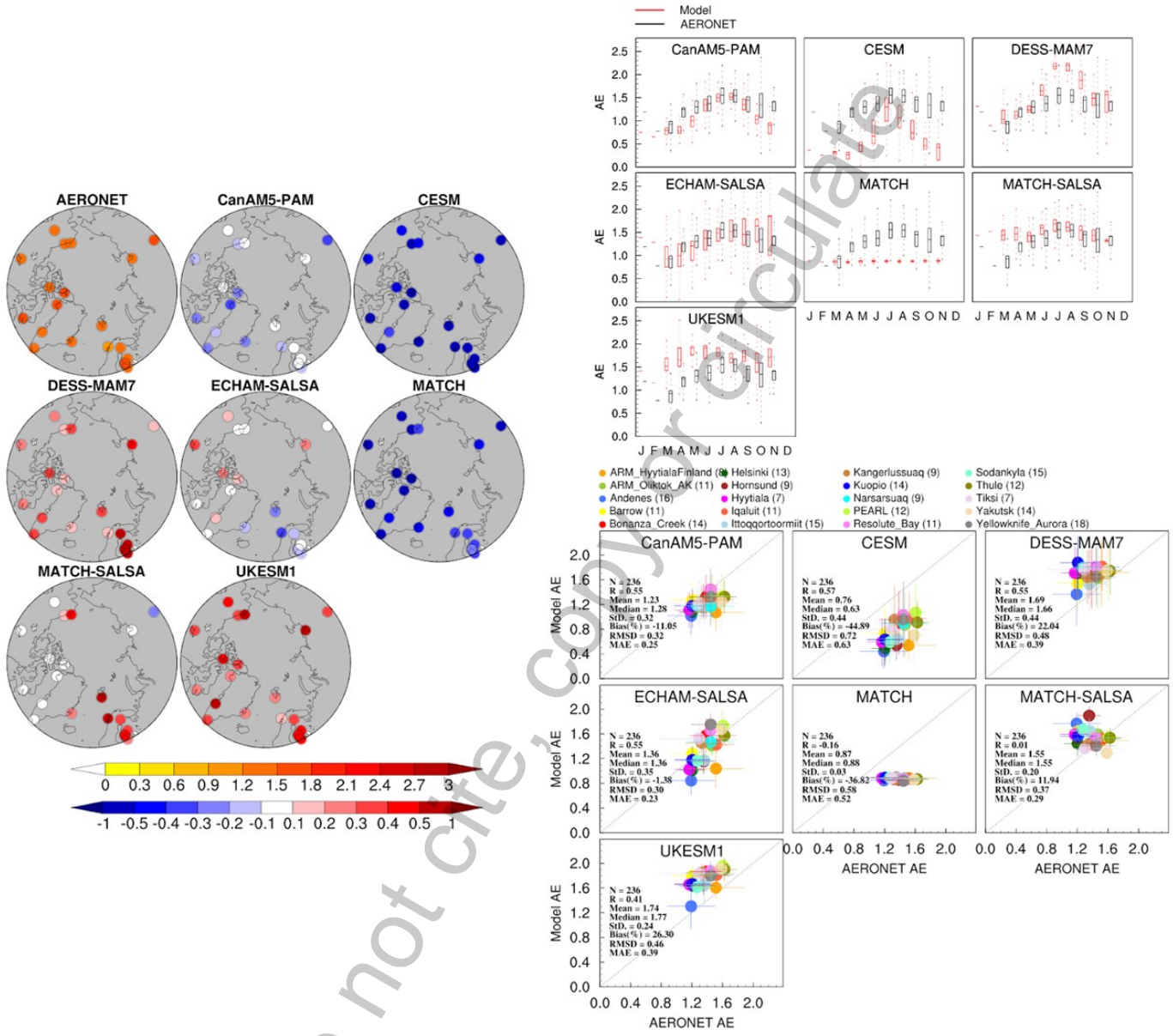

Figure 6.3.1.X: Angstrom Exponent as measured by AERONET and their model biases, seasonal cycles, and model vs measurement scatter plots. These are for 2014-15, with 2008-9 results being very similar and not shown.

6.3.2 Continental sources of short-lived climate forcers and long-range transport

Since a significant fraction of Arctic pollution comes from long-range transport, some of the model performance in the Arctic needs to be interpreted with additional information from

larger spatial scales. In this section we look at model performance throughout the Northern Hemisphere to better understand the results.

6.3.2.1 Mean concentrations and seasonal variability at surface sites

Add global plots of trace gases (O3 and CH4) and aerosols (BC, SO4, PM2.5) as measured at the surface. In appendix we can put CO, NOx, and OA.

As ground-level ozone is an important component of smog with negative impacts on health, agriculture, and ecosystems, great efforts are gone to accurately simulate surface O3 concentrations in models. Ozone creation is dependent on numerous factors, including meteorological conditions, emissions and chemistry. Ozone is measured widely in several countries' surface monitoring networks. All measurements are archived in the TOAR database, and Table X in the appendix lists the sources of the ozone measurements that are shown in Figure X.

Figure X: Measured ground-level ozone and model biases.

Carbon monoxide, a pollutant in its own right, is also an important precursor for ground-level O3. Thus, some of the model bias in O3 could be due to bias in CO. Figure Y below shows the CO measurements, and model biases.

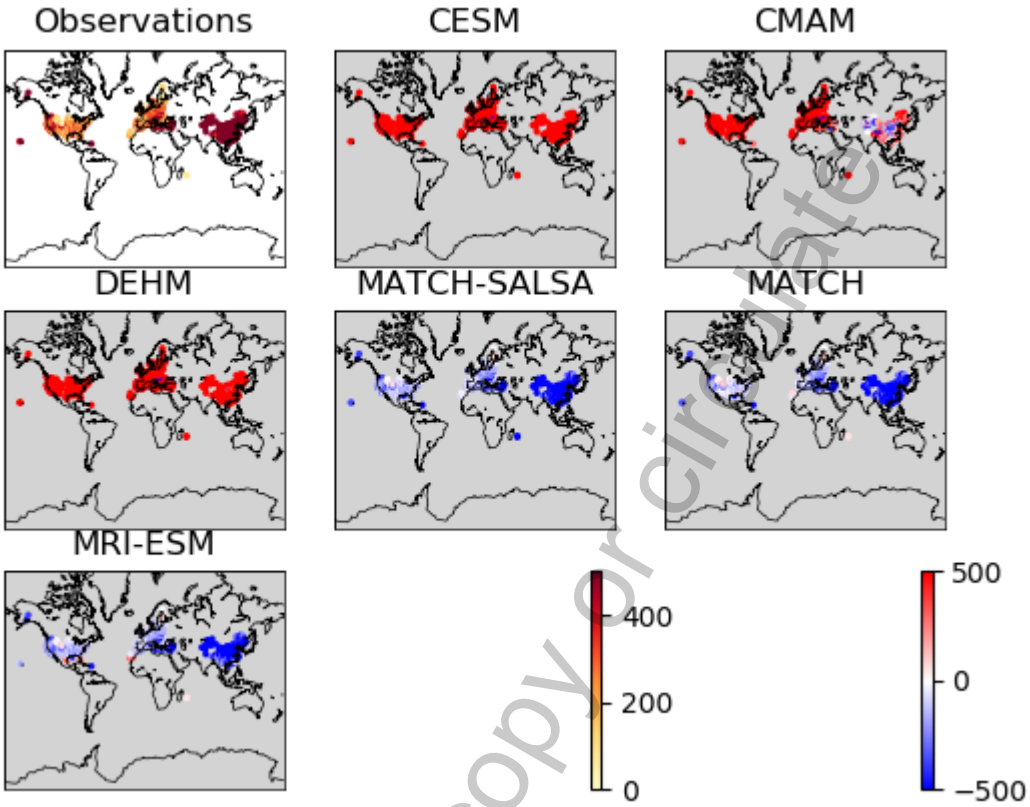

Figure Y: Measured ground-level carbon monoxide and model biases, in ppbv for 2014-15. Results for 2008-9 are similar and not shown.

Methane, a strong greenhouse gas, and important SLCF is shown in Figure Z, along with model biases. These models mainly have prognostic methane based on box model results and the ECLIPSE methane emissions. Thus, AMAP models do not have realistic variability in surface level CH4, which is quite variable in actuality. Slightly higher in the troposphere, methane is well mixed, and as shown in the next section, the simplification in the models is more realistic.

Figure Z: Measured ground-level methane and model biases.

Black carbon is measured extensively in the United States via the IMPROVE network. In Canada, there is the CABM network with six stations, and in Europe, there is the EMEP network (data obtained from the EBAS database) with approximately 16 measurement sites.

Unfortunately, we were unable to find further global measurements of BC at the surface. Figure W below shows these results along with the model biases.

Figure W: Measured ground-level black carbon concentrations and model biases.

Sulphate has more measurement locations in Europe than BC, but there is still limited publically available data for SO4 on a global scale. Figure X below shows these, along with model differences.

Figure X: Measured ground-level black carbon concentrations and model biases.

Finally, Figure Y shows the surface PM2.5 concentrations. As discussed previously, PM2.5 has important health impacts, and thus it is well measured via surface monitoring networks and campaigns.

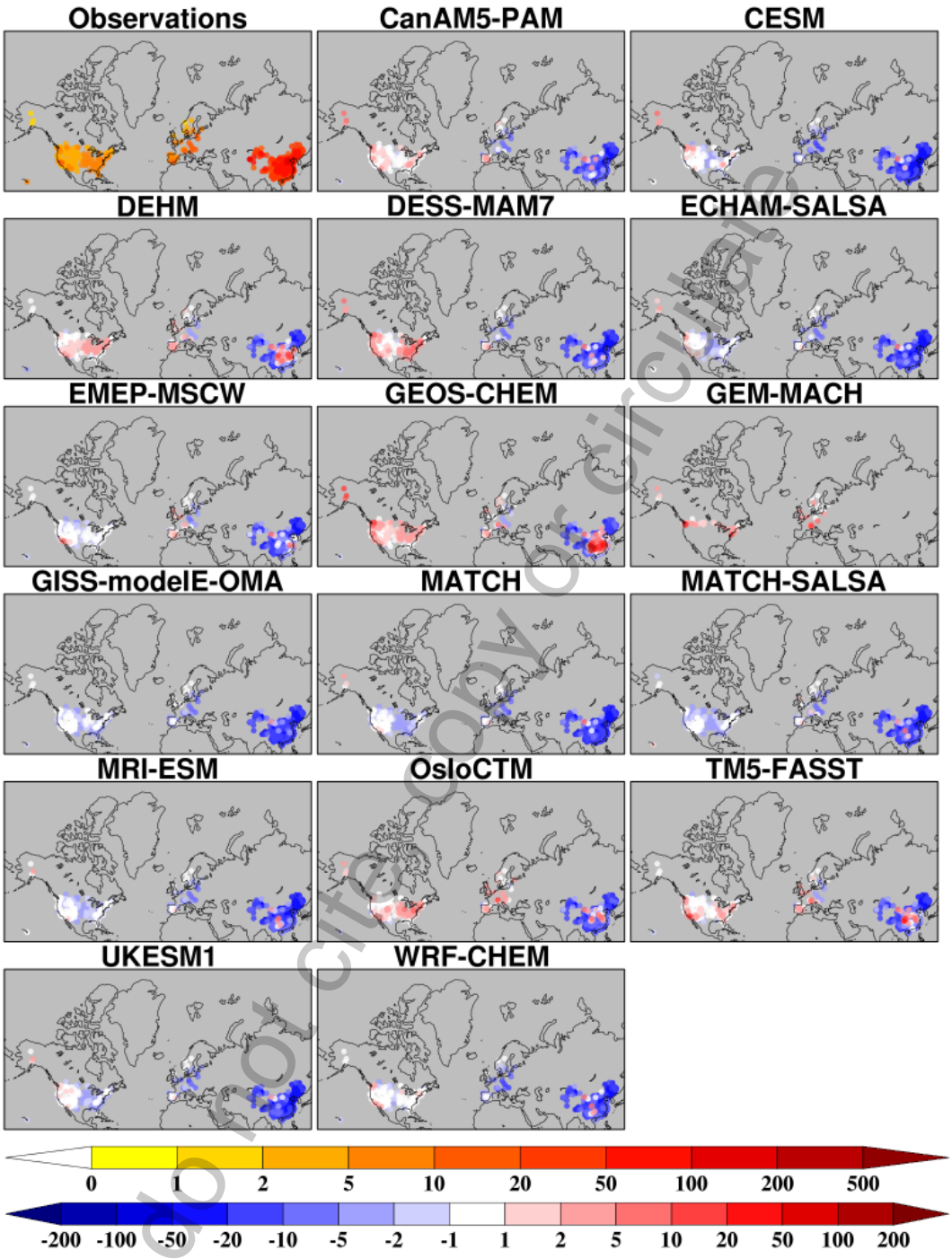

Figure Y: Measured ground-level PM2.5 concentrations and model biases for 2014-15. 2008-2009 results are similar and not shown.

6.3.2.2 Mean concentrations and seasonal variability at in the troposphere and lower stratosphere

Monthly mean modelled trace gases from X models were also compared to the Tropospheric Emission Spectrometer (TES) satellite instrument, which measures ozone and

it's precursor gases, CO, CH4, and NOx, since 2004. Similarly CO measured by the Measurements of Pollution in the Troposphere (MOPITT) satellite instrument since 2000 were compared to AMAP model output.

placeholder

Figure 6.3.2.X shows TES measurements of ozone in the lower (900 hPa) and mid (600 hPa) troposphere and model biases.

As PM2.5 is a high profile pollutant, it is also estimated globally using data assimilation techniques. There are three additional PM2.5 global estimates that are based on measurements, though also integrate models and satellite measurements of AOD to fill in the gaps. They are: the MERRA-2 reanalysis (Gelaro et al., 2017), the Global Burden of Disease (GDB) dataset, and the University of Dalhousie PM2.5 product (van Donkelaar et al., 2015). PM2.5 from all measurement sources is highly variable. Different measurement techniques are used, estimating PM2.5 with varying levels of water in them, which causes large differences, as one example. There are other sources of uncertainty in their measurements as well. The figures below show how the models compare to this different measurement-based PM2.5 products:

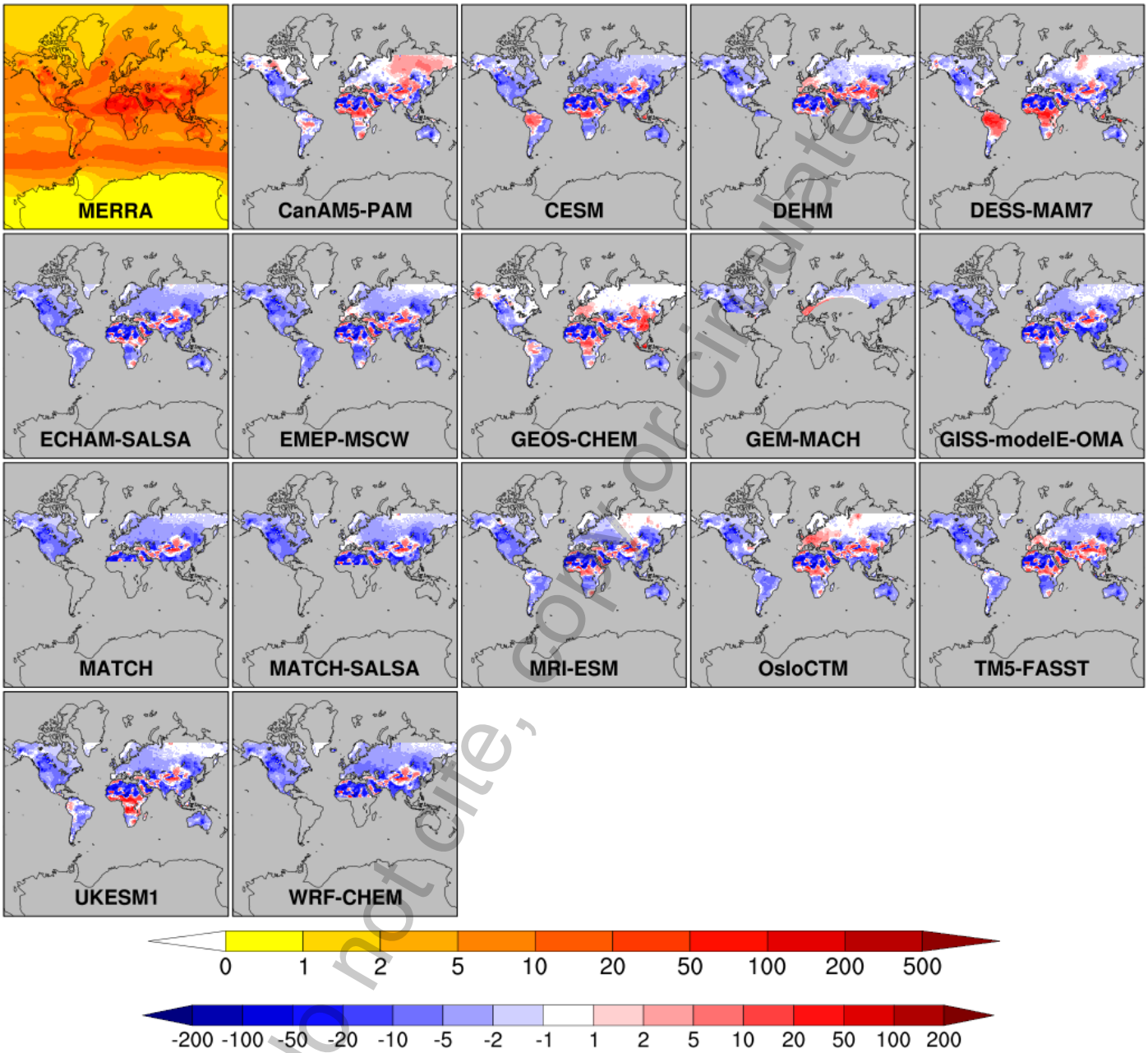

Figure 6.3.2.X: PM2.5 from MERRA reanalysis, and model biases for 2014-15.

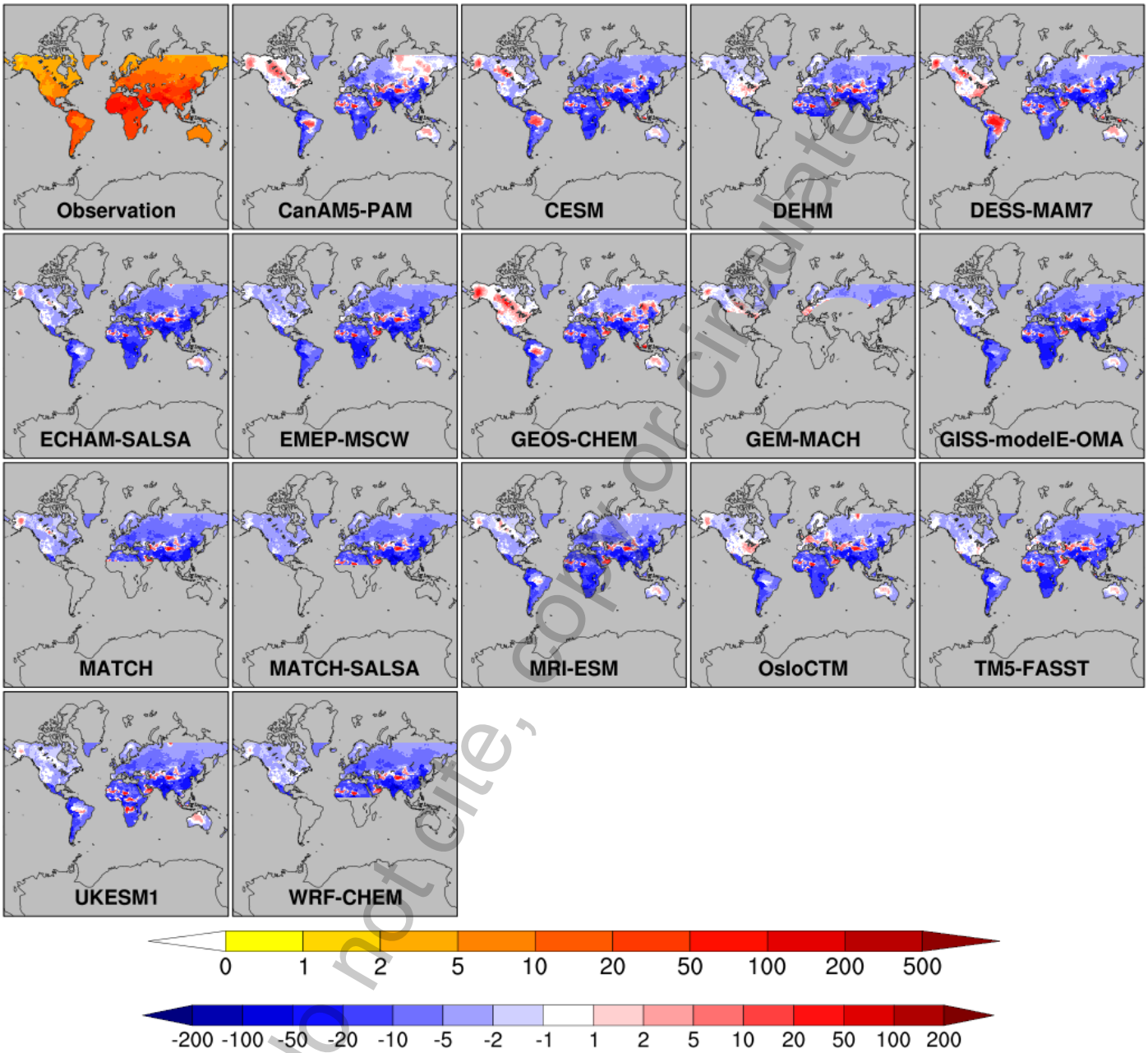

10811

10812 **Figure 6.3.2.X:** PM2.5 from GBD, and model biases for 2014-15.

10813

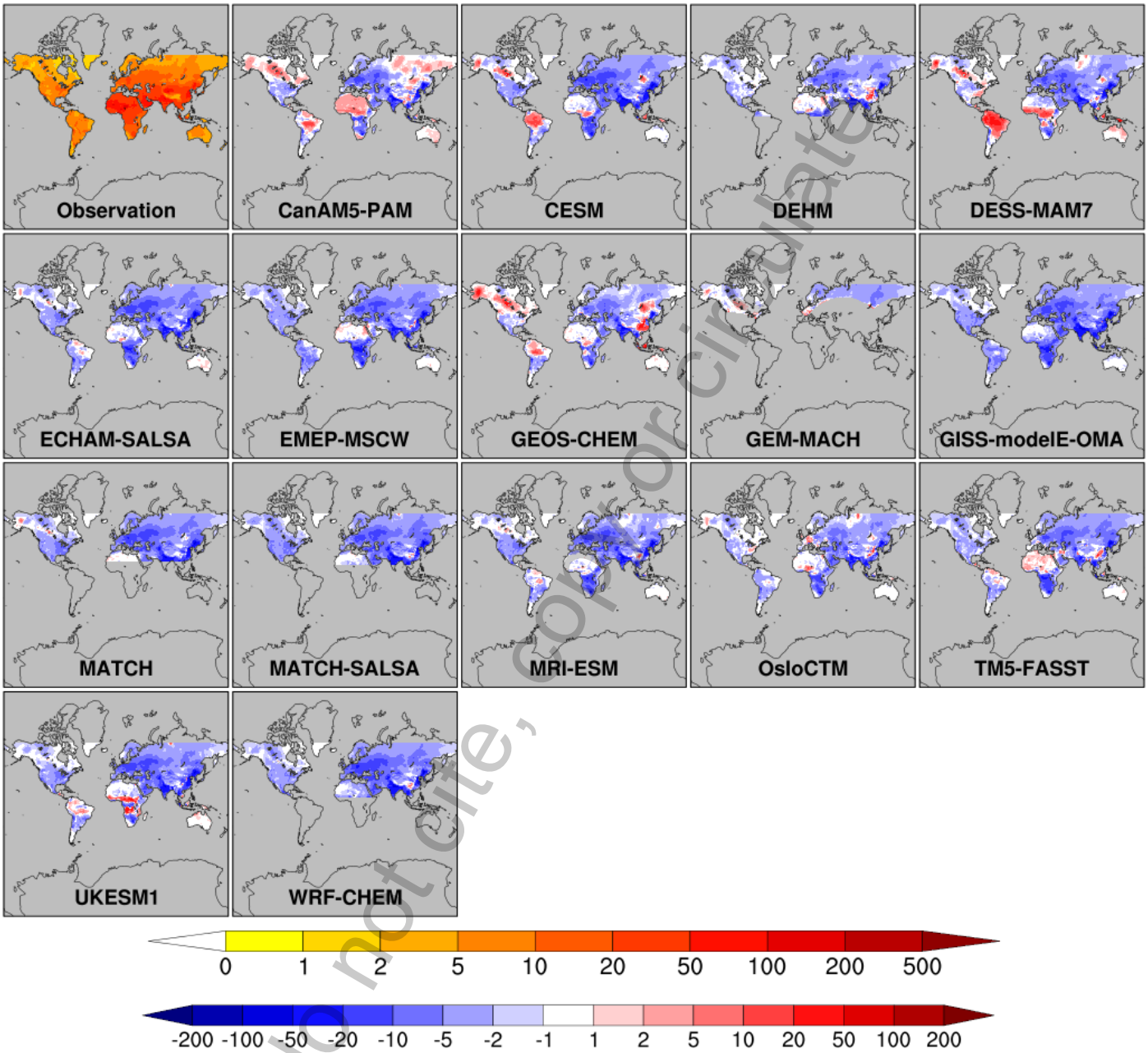

Figure 6.3.2.X: PM2.5 from University of Dalhousie, and model biases for 2014-15.

6.3.2.3 Comparisons of modelled BC vertical profiles to aircraft observations

Output at three-hourly intervals was provided to us by 14 of the participating models; 11 of these included output of black carbon concentrations in kg/m3. The purpose of this high-frequency model output is to compare the models to aircraft measurements along the track of the aircraft in the gridspace of each model. The extraction of aircraft tracks in model

space is done by tools from the Community Intercomparison Suite (CIS; cite relevant paper by Duncan Watson-Parris); the CIS consists of python-based codes which interpolate between a reference set of observations and model output. There is naturally some coarsening of information as the aircraft observations are of considerably higher spatial and temporal resolution than the model output, but this approach nonetheless provides meaningful comparisons when flight tracks are grouped over specific areas or times. The aircraft campaigns considered in our comparisons are shown on Figure 6.3.2.3.A for orientation. Note that most aircraft campaigns available to us took place in the years 2008-2009, with only the regional-scale CAST and NETCARE campaigns providing observations for 2014-2015.

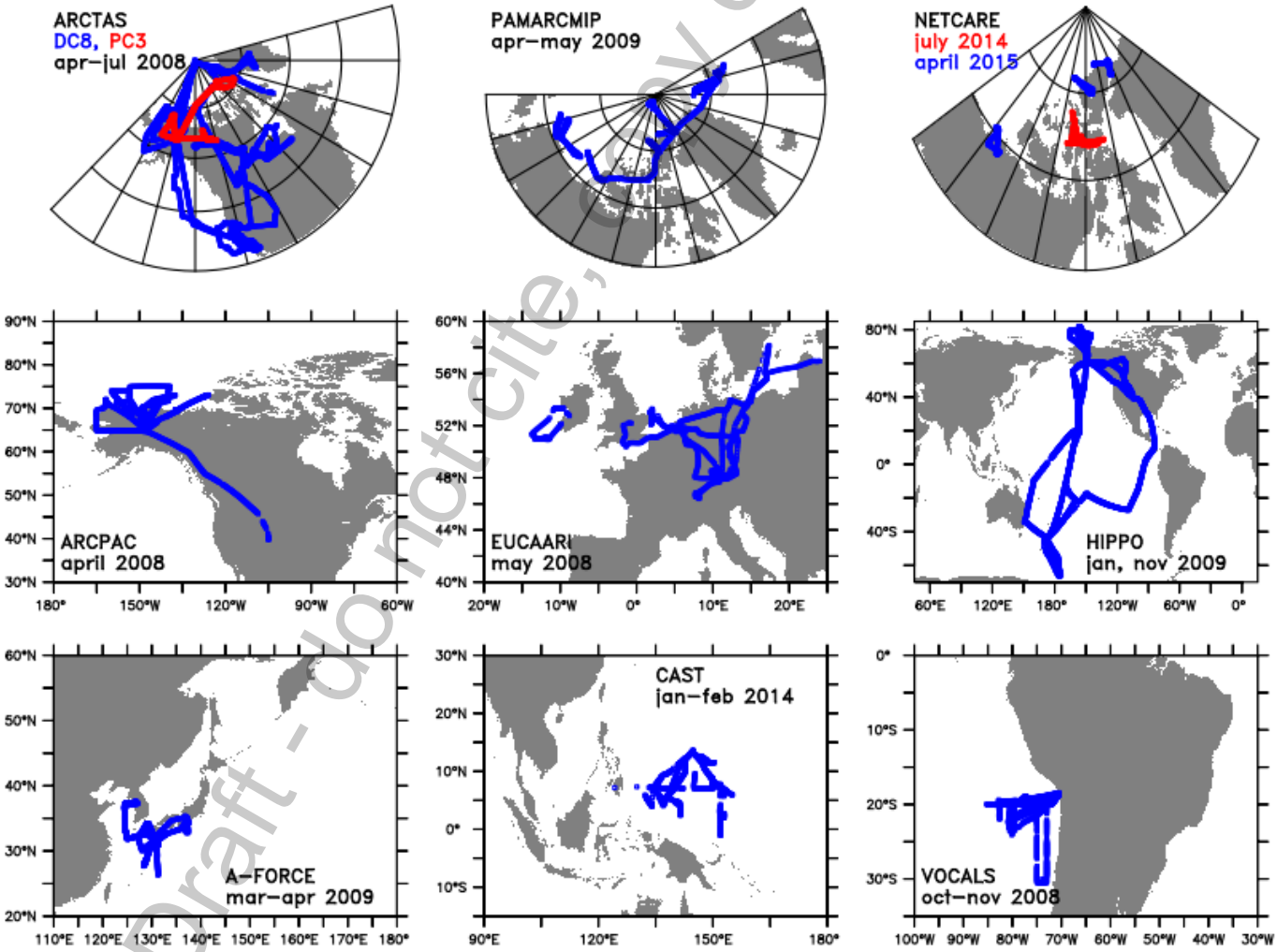

Figure 6.3.2.3.A: Maps of aircraft campaigns whose retrievals of black carbon concentrations will be compared to three-hourly output from AMAP models.

Combining all aircraft tracks onto a single map allows comparison with the corresponding tracks extracted from model output. On the following three plots constituting Figure 6.3.2.3.B, black carbon concentration in ug/m3 is shown for the aircraft observations (top left of panel of each plot), followed by each participating model. The three plots differ by altitudes; see figure legends and caption for height ranges. The colour scale is logarithmic. Models GEM-MACH, GEOS-CHEM and WRF-CHEM provided output only for years 2014 or 2015, which is reflected in the smaller areal coverage of their plots.

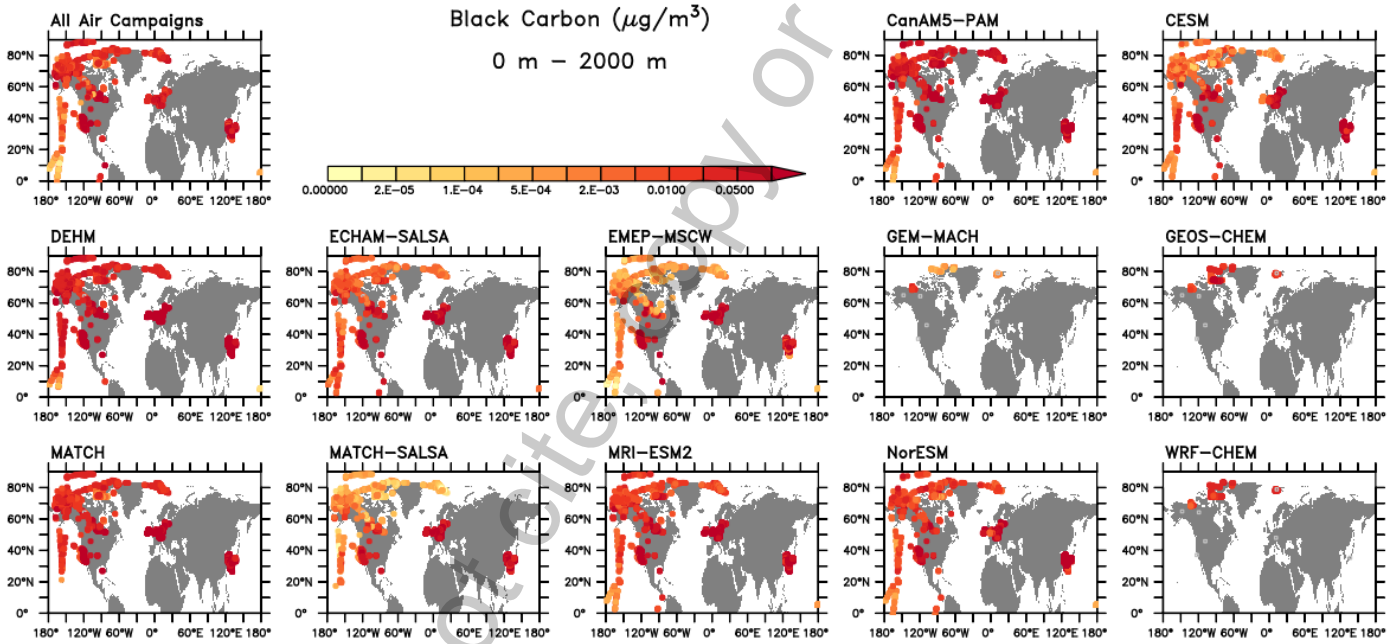

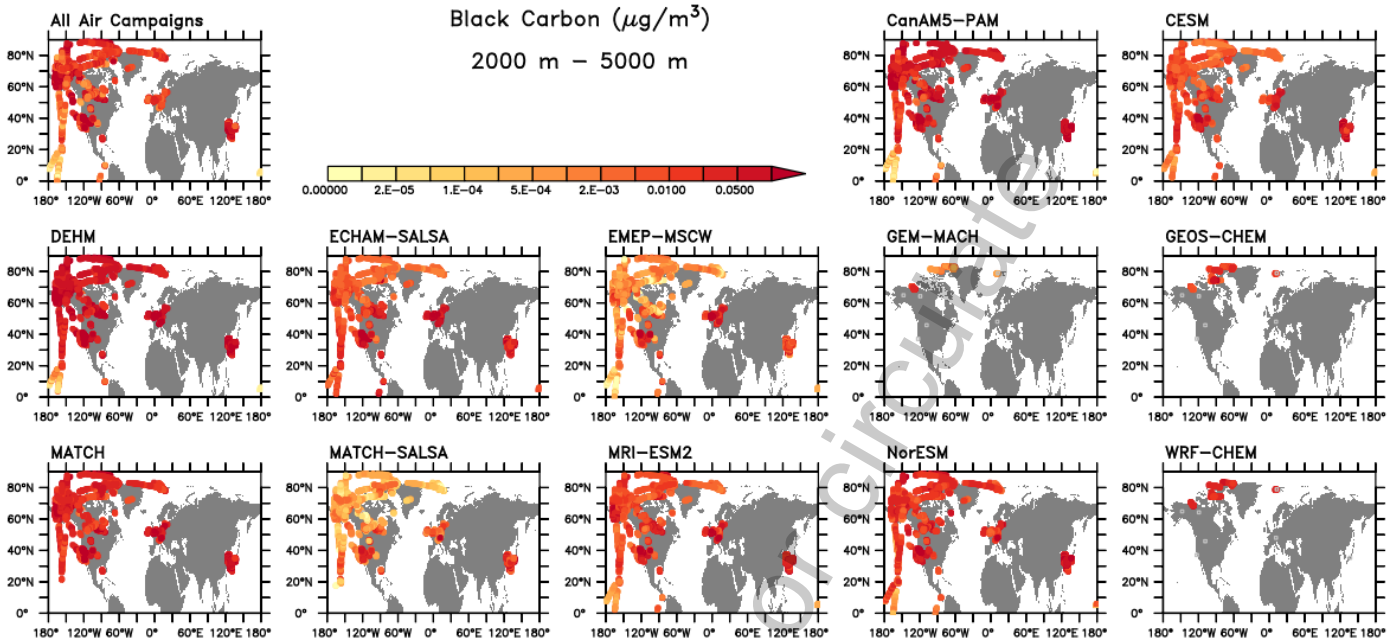

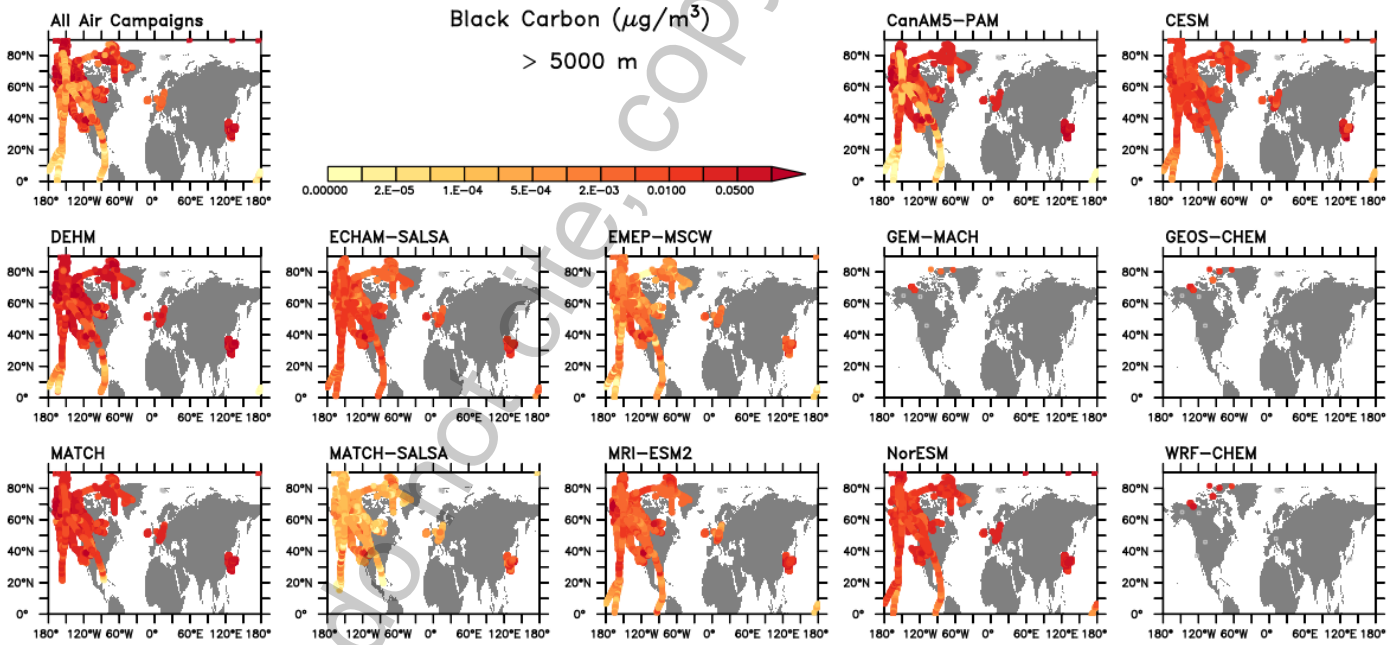

Figure 6.3.2.3.B: concentration of black carbon (ug/m3) from all aircraft campaign tracks. The top left panel of each plot shows the observations from the campaigns. The top, middle, and bottom plot differ in altitude: respectively surface to 2000m, 2000-5000m, and above 5000m. The logarithmic colour scale begins at 0.0 and the boxes are 1, 2, 5 for each decade.

To accompany the maps of black carbon concentration, the three subplots of the following Figure 6.3.2.3.C show the differences between the models and the observations. The top left panel of each plot repeats the observations from Fig. 6.3.2.3.B, for reference.

These maps of differences allow some generalizations: Models over- or underestimate the observations quite consistently, across all campaigns and largely regardless of height, i.e. skill does not depend on season, year, or altitude of the observation. Assessing the reason for each model's skill must be left to the owners of the model. The following sentence is not intended for a final version: It is interesting to note that the ECHAM-SALSA and MATCH-SALSA models consistently show similar results on the difference maps of Fig. 6.3.2.3.C, while MATCH and MATCH-SALSA do not. Which factor is more important: the aerosol model used, or the dynamics and subgrid parametrizations of the underlying GCM?

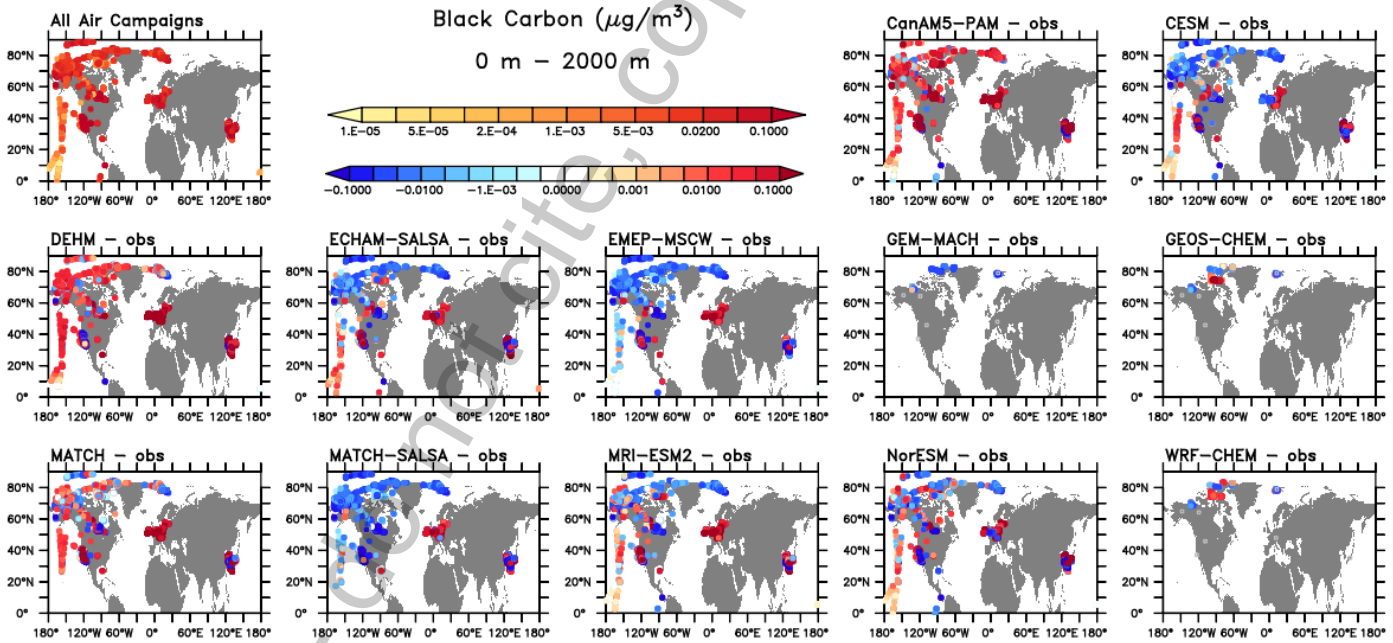

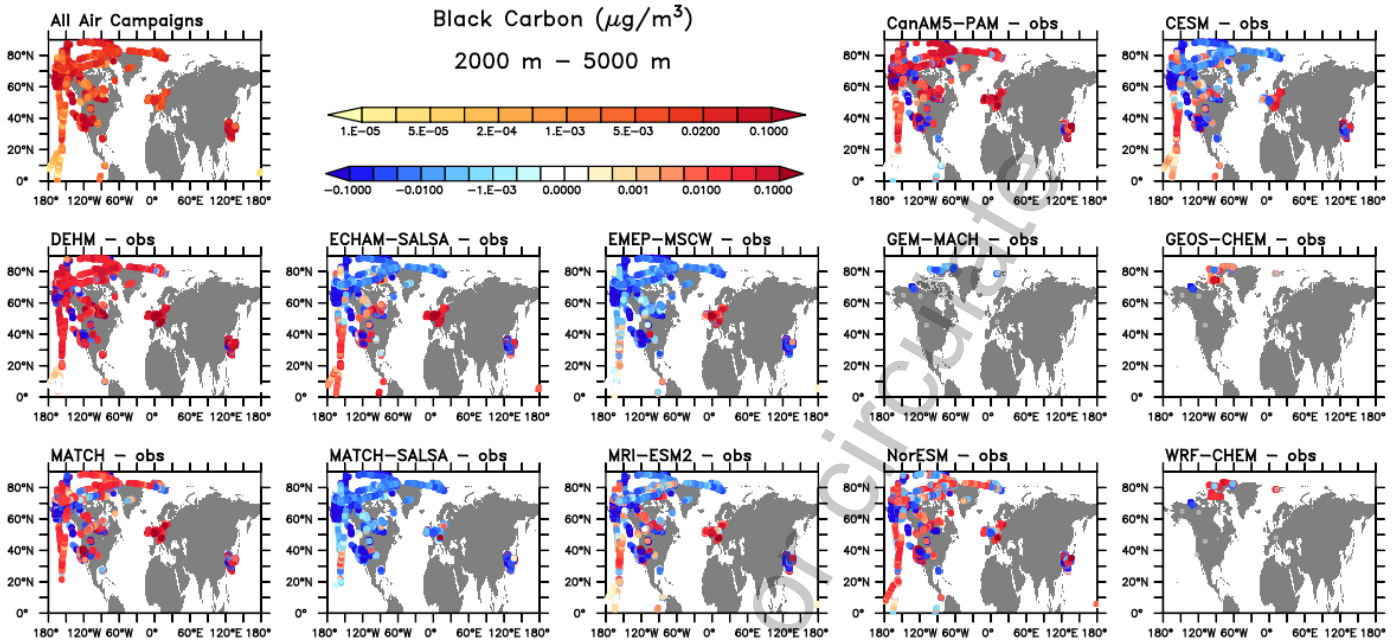

10867

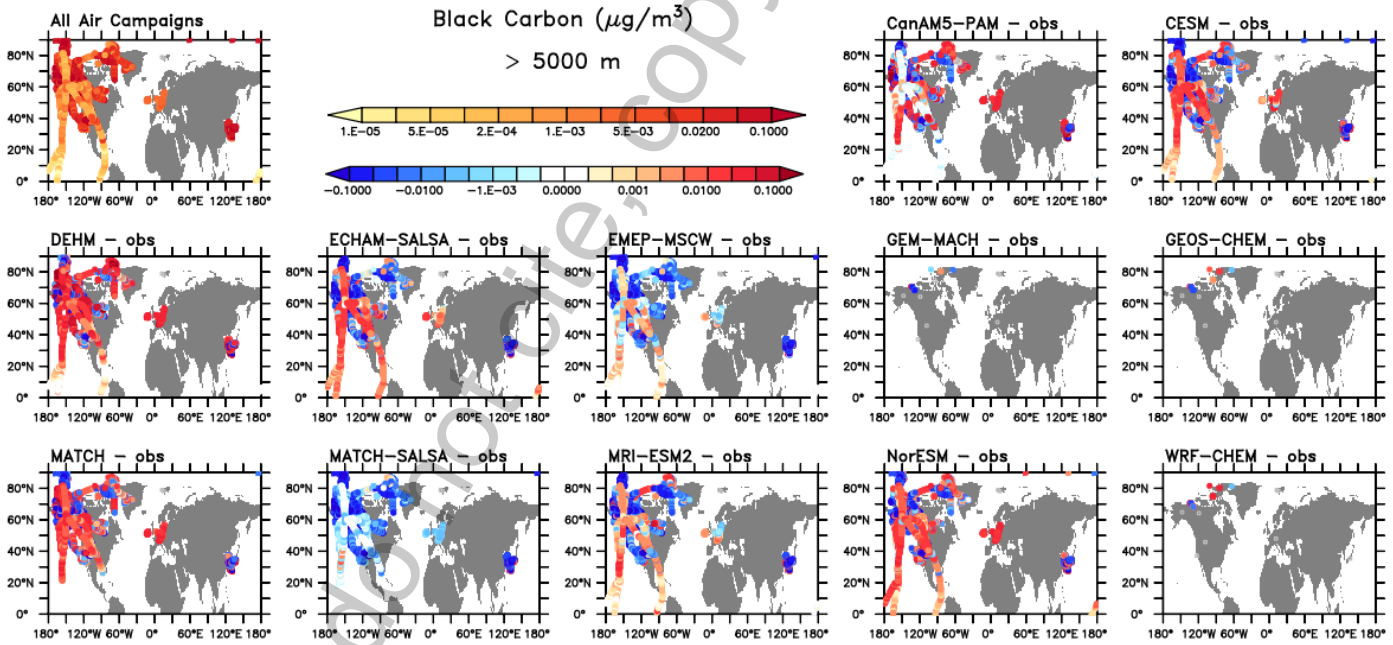

10868

10869 **Figure 6.3.2.3.C:** Differences between models and observations for the combined aircraft
10870 campaigns. The three plots making up this figure show three different altitude ranges
10871 (surface to 2000m, 2000-5000m, above 5000m). The top left panel of each plot repeats the
10872 black carbon observations from Fig. 6.3.2.3.B for reference. The difference colour scale is
10873 centred on 0.0 and extends to +- 0.1; boxes are 1, 2, 5 for each decade.

10874

To gain a better insight into the vertical distribution of black carbon concentrations, all aircraft track points from the observations and from each model were combined for each campaign, then binned by height. Bins are 500m high, beginning at 250m below the lowest observation height. Results for all campaigns are given in Figure 6.3.2.3.D. Each line represents the average value of all points falling into a given height bin. The number of points contained in each bin, their median value and standard deviation are listed for each campaign in Tables XX of Appendix Y. Because three-hourly output results in very large files, most participating modelling groups provided only Northern Hemisphere or regional data. Aircraft campaigns carried out in low latitudes (e.g. CAST) or in the Southern Hemisphere (e.g. VOCALS-C-130) are therefore compared to fewer models.

In Figure 6.3.2.3.E, the observations and the output from all campaigns were combined for each model, binned by height, and separated by latitude into points falling north of 60N, and points falling within 30N-60.

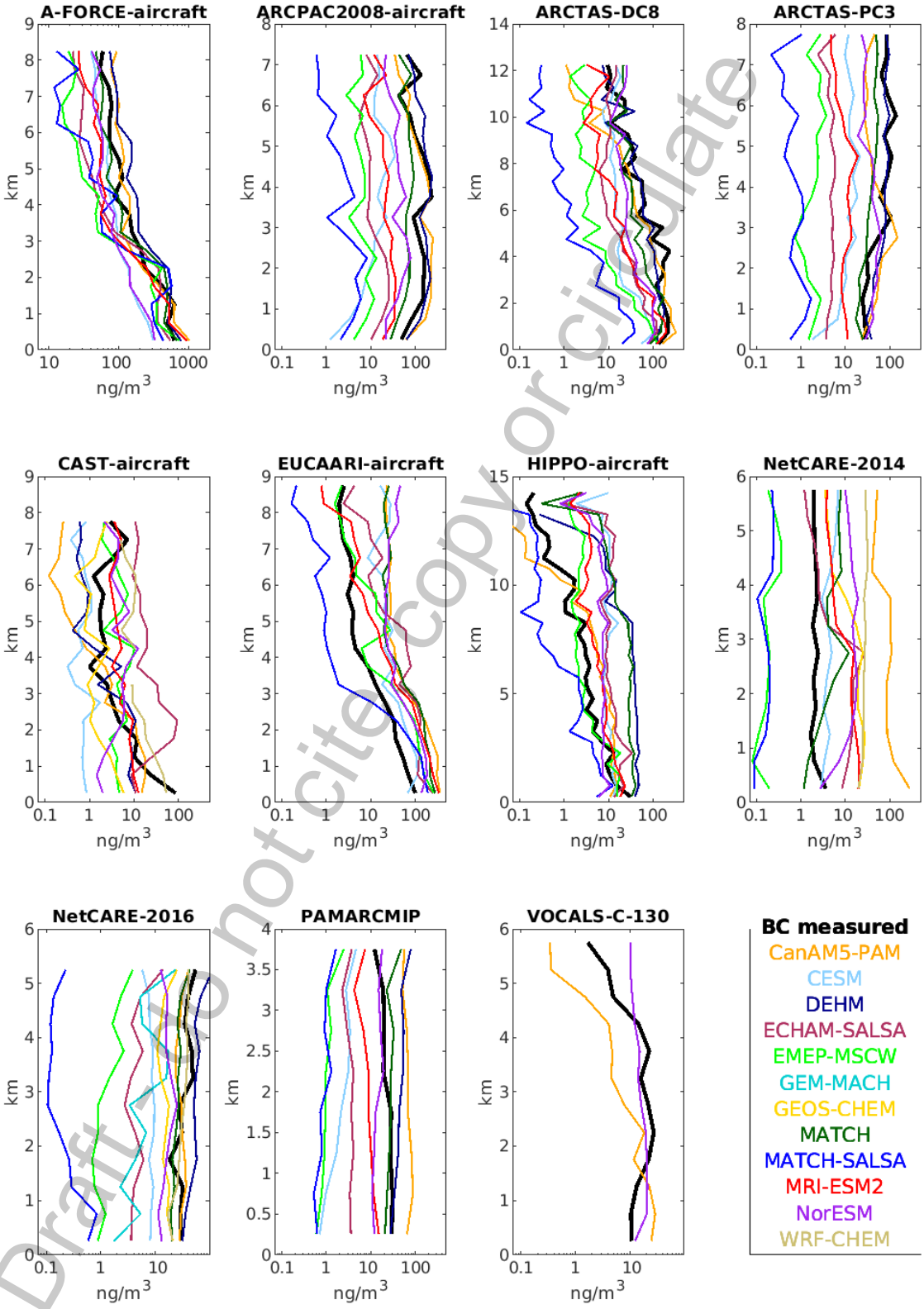

Figure 6.3.2.3.D: Profiles of observed (heavy black line) and modelled (coloured lines; see final panel for legend) black carbon concentrations (here in units of nanogrammes/m3) for

each aircraft campaign. All points falling into bins of 500m height were averaged together. Note that the horizontal axis differs between panels. Well maybe I'll change that so it doesn't.

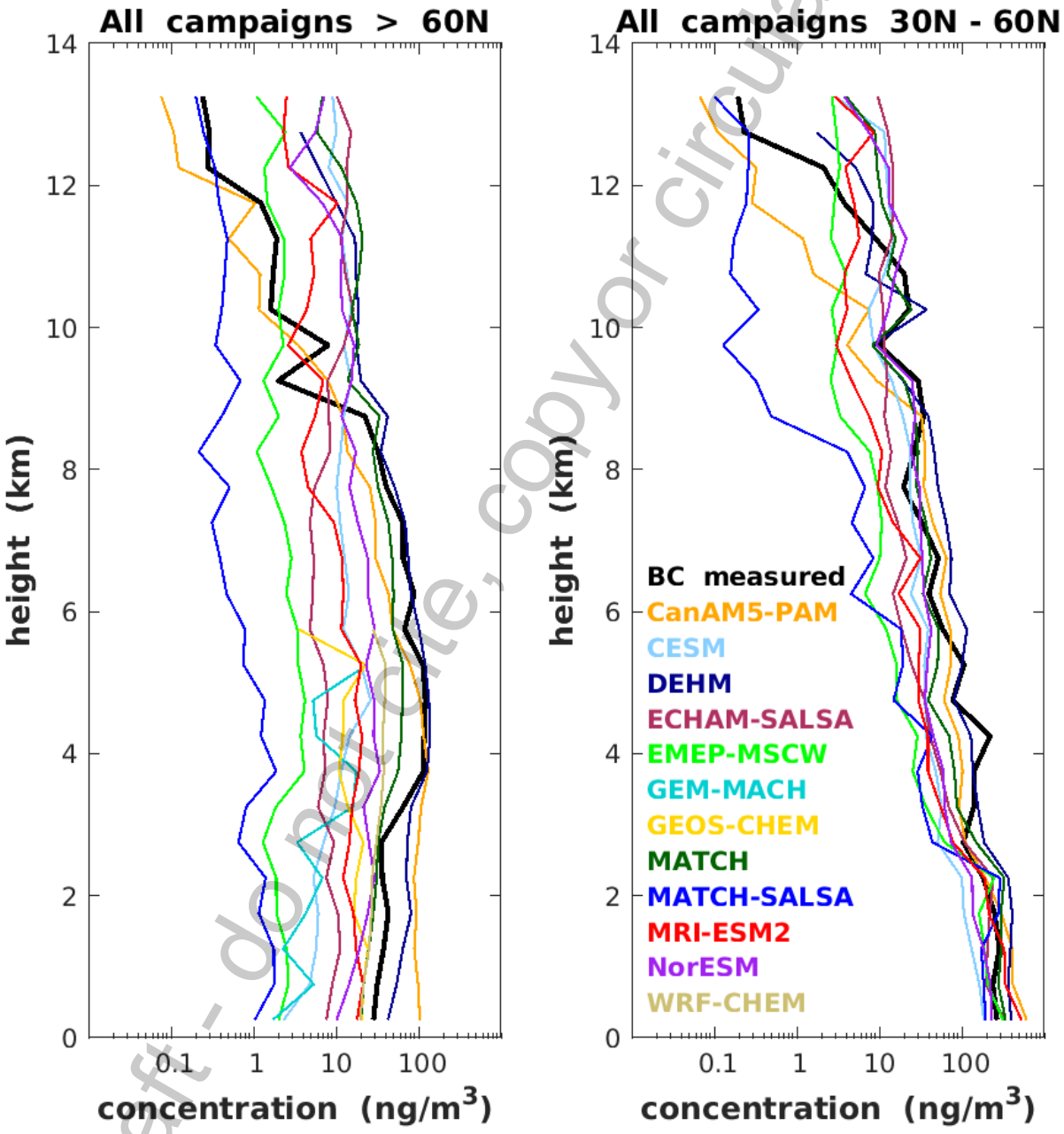

Figure 6.3.2.3.E: Profiles of observed (heavy black line) and modelled (coloured lines) black carbon concentrations for all aircraft campaigns combined, separated into mid-latitude (30N-60N, left panel) and Arctic (north of 60N) points and binned by 500m levels. All points falling into a height-latitude bin were averaged together.

Tables to accompany the profile plots, for the appendix:

- quantitative information on the average values at different vertical levels of each model's concentration, together with median, standard deviation, number of points used
- some information on the models used, if it is not already included in the overall model spec table

Possibly Stephen Arnold's work on trace gases aircraft comparisons (?)

6.3.2.4 Aerosol optical properties

We now show the global picture for aerosol optical depth (AOD), which provides an indication of model performance for aerosols globally. AOD is measured remotely from the ground-based AERONET instruments, as well as numerous satellite instruments. Figure X below shows AOD annual means as measured by MODIS, MISR, and CALIOP satellite instruments, as well as the AOD results from models, and their biases against CALIOP, which has the largest spatial coverage.

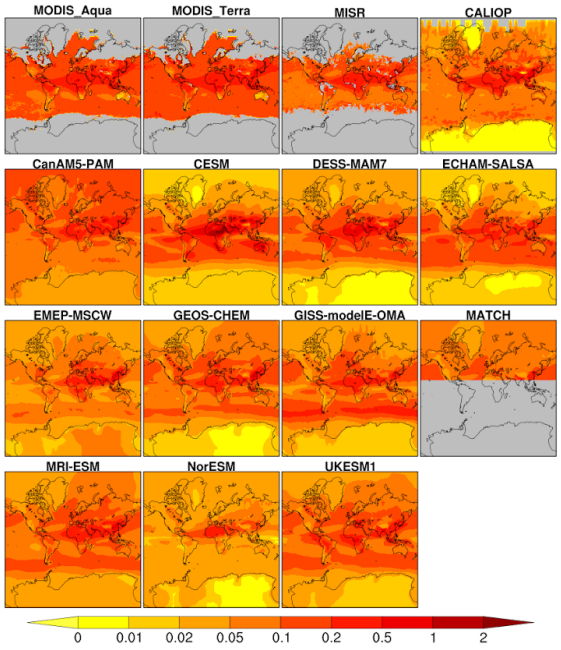

10923

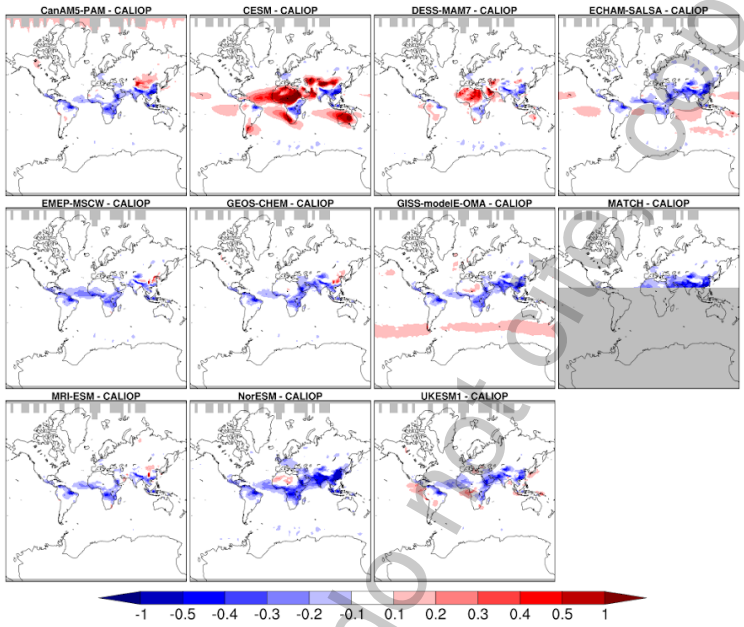

10924

10925 **Figure X:** (left) Annual mean AOD as measured by four satellite instruments (top row), and
10926 modelled. (rights) model biases compared to CALIOP.

10927

10928 Model performance can also be demonstrated via a Taylor diagram. The closer a model
10929 point is to "REF" on the x-axis, the closer it's simulation is to the measurements, taking into
10930 account correlation coefficient, standard deviation, and bias. Figure X below shows the
10931 results for AOD compared to the satellite measurements.

10932

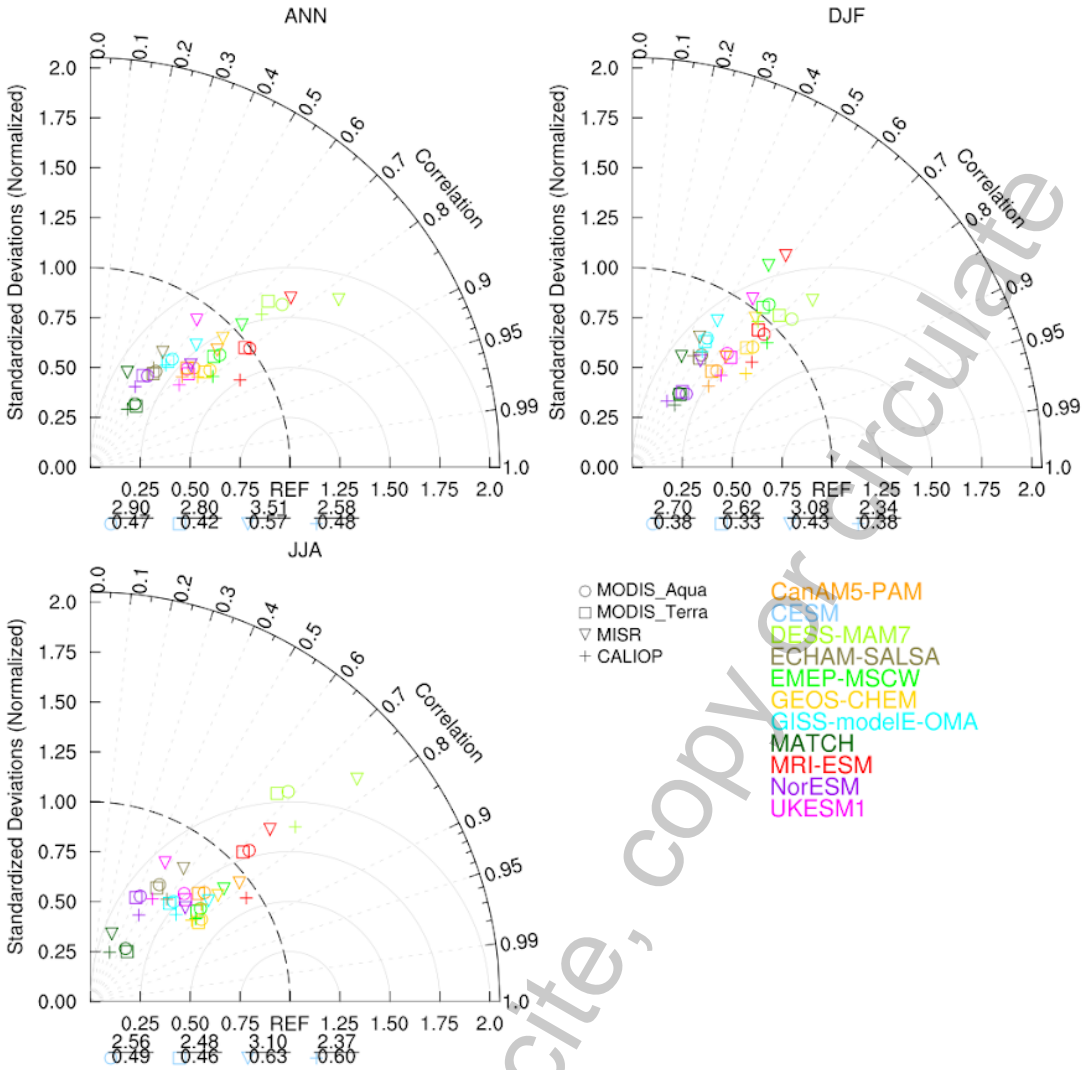

Figure X: Taylor diagram for model performance of annual mean AOD compared to satellite products for 2014-15. The results are similar for 2008-9 (not shown). The numbers outside the plotted domain represent standard deviation (numerator) and correlation (denominator).

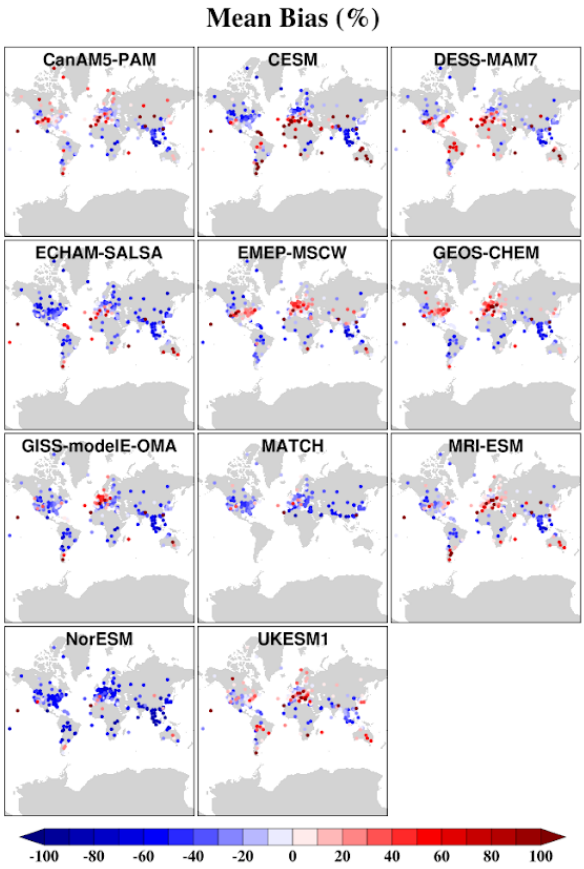

10938

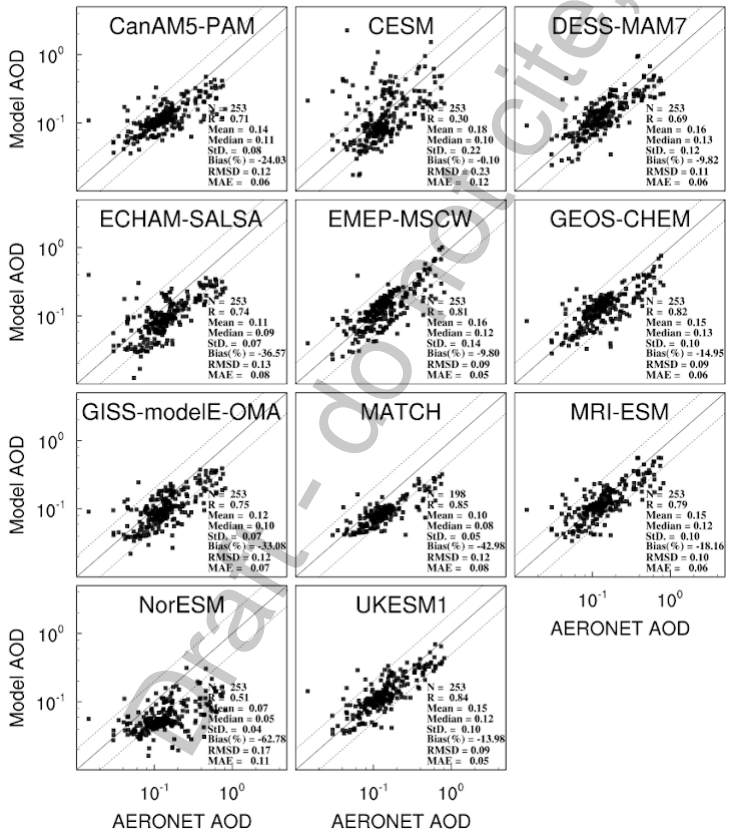

10939

Figure 6.3.2.X Comparison of mean AOD at individual AERONET sites for 2014-2015. Results for 2008-9 were similar and are not shown.

In addition to AOD and AE, in this section we can also evaluate absorption aerosol optical depth (AAOD) - which gives indication of the column aerosol loading of light-absorbing particles. The AATSR satellite instrument has global coverage of AAOD, though only over the poles during summertime.

6.3.3 Clouds and radiation in models and observations (Manu, Joakim, Rashed, Abhay)

Cloud properties from the Type 0 model simulations are evaluated against observations. Cloud liquid water path (CLWP), cloud ice water path (CIWP), cloud fraction and cloud droplet number concentrations (CDNC) are processed as a mean over the 4 years (2008, 2009, 2014 and 2015).

6.3.3.1 Cloud fraction

Evaluation of the total cloud fraction provides a first order indication of how clouds and their coupling to the large-scale thermodynamical conditions in the Arctic are simulated in the models. Cloud fraction also provides primary constraint on the cloud forcing and cloud processing of aerosols. Fig. 6.3.3.1.a and Fig. 6.3.3.1.b show intercomparison of total cloud fraction between the models and satellite products for the DJF and JJA months. Cloud fraction derived from three satellite sensors (two passive and one active) that have very different sensitivity to clouds are shown to represent variability in the observations. It is evident that, over the ice-free waters, the differences among the observations are lower, but over the ice-covered parts of the Arctic Ocean and land areas, the differences can be higher, especially during the DJF months. The differences among the models are also strong during the winter months, reaching as much as 15-20% in the Central Arctic and reaching 20-25% in some models compared to the CALIPSO observations. The differences among models and compared to the observations are also large over the polluted high latitude regions during winter, in the Eurasian as well as East Asian sectors. During summer, the differences among the models and compared to the observations over the polluted regions are much lower. Historically, better availability and quality of data from different

observational systems in polar summer compared to polar winter has led to better understanding and representation of Arctic clouds in models during summer as well. The polar winter remains a challenge in both observations and models.

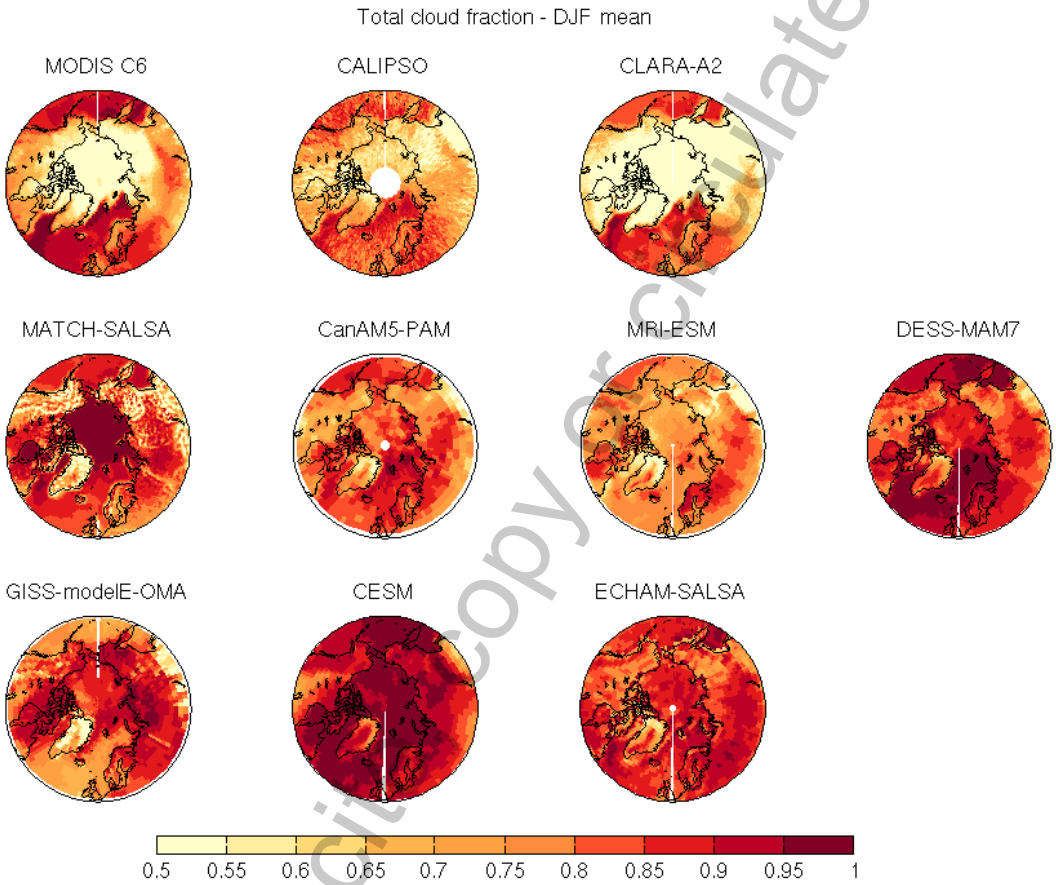

Figure 6.3.3.1.a Comparison of simulated cloud fraction (rows2-3) against observations (top row) for the mean winter months (DJF).

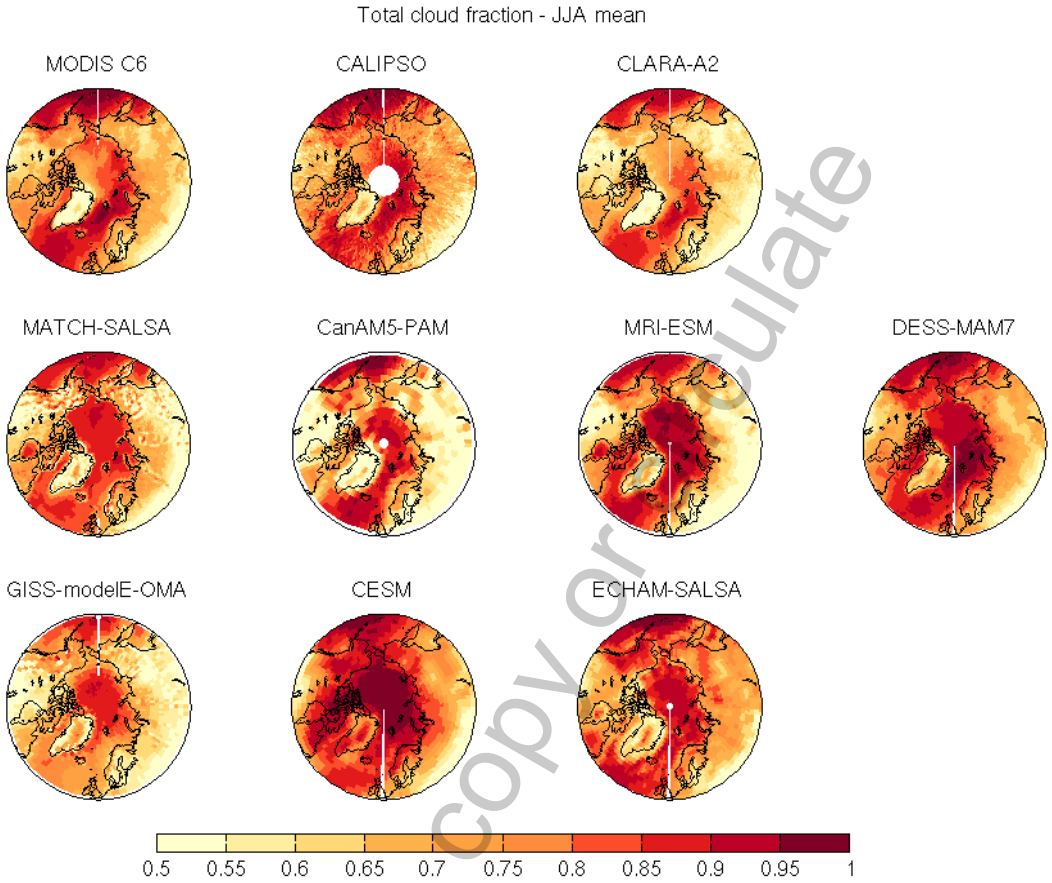

Figure 6.3.3.1.b Comparison of simulated cloud fraction (rows2-3) against observations (top row) for the mean summer months (JJA).

Figures 6.3.3.1.c and 6.3.3.1.d further show evaluation of the annual cycle of monthly mean cloud fraction over two oceanic areas, over the northern Atlantic and northern Pacific respectively. These areas are chosen as they are two important pathways of long-range transport of pollutants into the Arctic. In the northern Atlantic, the total cloud fraction in all three observational datasets remains high (above 80%) throughout the year and the annual cycle is very flat. The majority of the models also show similar features and their cloudiness estimates are within the observational variability. Few models do however overestimate or underestimate the magnitude of cloudiness, outside the variability range. In the northern Pacific, the observations differ from one another in their annual cycles. Unlike the northern Atlantic which remains ice-free throughout the year, this part of the Pacific Ocean is frozen during the winter months. The separation of ice from low level clouds becomes challenging for the passive sensors (MODIS and CLARA-A2 datasets) in the absence of information from the solar channels. As a result, the cloud conservative nature of their retrieval algorithms

leads to the underestimation of cloudiness compared to CALIPSO, which shows a very flat annual cycle. The majority of the models also show flatter annual cycles conforming to CALIPSO. The differences among the models are largest during the winter months. It is to be noted that the satellite simulators are not used here while evaluating clouds in these models. However, compared to the lower latitudes, the diurnal cycles of cloudiness are much flatter in the Arctic. The spatial coverage is also better due to multiple overpasses. Therefore, the differences arising from the different time sampling are expected to be minimal. The differences in the sensitivity remain, i.e. what constitutes a cloud in model and observation can be different. However, given the very high sensitivity of CALIOP-CALIPSO to even the subvisual clouds, its retrievals can be fairly compared with the models.

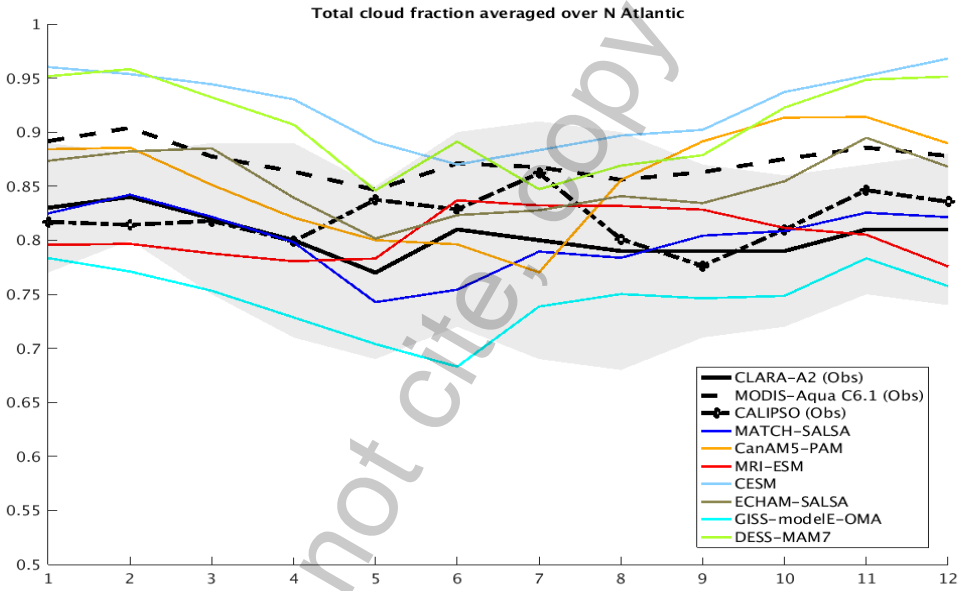

Figure 6.3.3.1.c Seasonal variability of simulated cloud fraction (rows2-3) against observations averaged over northern Atlantic. The shaded area shows the natural variability in the CLARA-A2 observations indicated by one standard deviation in the cloud fraction.

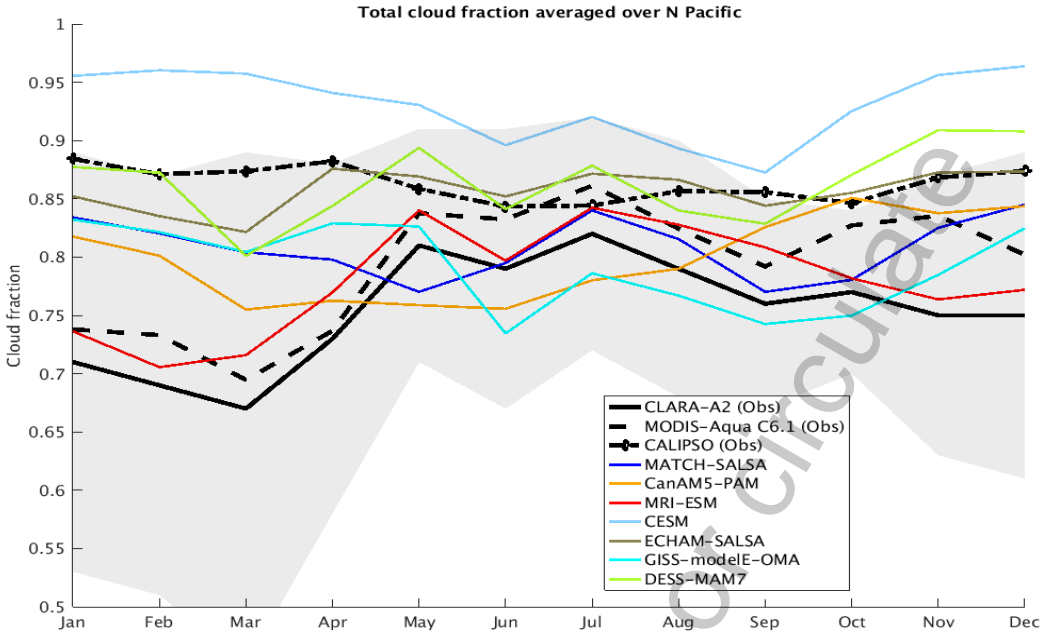

Figure 6.3.3.1.d Same as above, but, averaged over northern Pacific.

6.3.3.2 Cloud liquid water path

How much water clouds contain is an important piece of information in order to study the microphysical processes and indirect effects of aerosols, often expressed in the column integrated quantities of liquid and ice water paths. Their retrievals from passive satellite sensors depend heavily on the quality of data from the solar channels, satellite and solar geometry and the accuracy of cloud fraction over the highly reflective surfaces in the Arctic. The retrievals are therefore restricted to only a few summer months and the uncertainties among various satellite sensor datasets remain very high in the Central Arctic. This is evident in the Figure 6.3.3.2.a that shows the intercomparison of cloud liquid water paths from MODIS and CLARA-A2 as well as the models. Over the ice-free oceans MODIS and CLARA.A2 retrievals of LWP agree with one another well. However, over the permanently sea-ice covered parts of the central Arctic Ocean and over the marginal land areas, the differences between the two datasets are very high, even reaching up to 100%. The differences among the models are very strong as well and the land-sea contrast in LWP is different from model-to-model. It is difficult to find a pattern that commonly holds across all the models and observations, indicating the challenges that remain in the passive observations and representation of LWP in the Arctic. The model estimates of LWP in the Atlantic and Pacific

11030 sectors of the Arctic Ocean are qualitatively closer to the estimates derived from the
11031 combined CloudSat and CALIPSO data (e.g. Lenaerts et al., 2017).

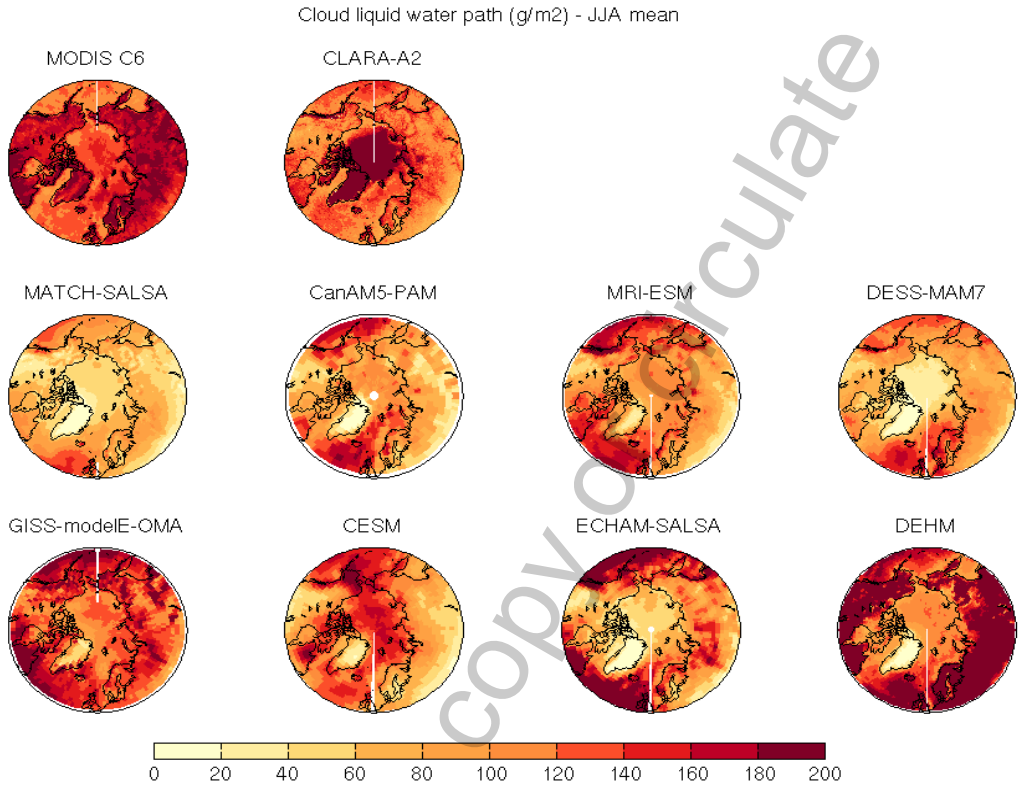

11032

11033 **Figure 6.3.3.2.a** Comparison of simulated cloud liquid water path (rows2-3) against
11034 observations (top row) for the mean summer months (JJA) (g/m2).

11035

11036 Fig. 6.3.3.2.b and 6.3.3.2.c show the histograms of CLWP over the northern Atlantic and
11037 Pacific (the same regions as in the case of annual cycle of cloud fraction) during the summer
11038 months (JJA). In the northern Atlantic, while the distribution of LWPs in CLARA-A2 and
11039 MODIS are similar, the histogram in MODIS is shifted to the higher values (by around 20
11040 g/m2). In the models, the distribution is slightly flatter compared to the observations. The
11041 majority of the models however agree well with the observations in terms of their LWP
11042 distribution. In the northern Pacific, the distributions of LWP in MODIS and CLARA-A2 agree
11043 very well with one another. Here, the modelled distributions of LWP are however even
11044 more flatter and the models show both positively and negatively skewed distributions
11045 compared to the observations.
11046 Since the retrievals of LWP from passive satellite sensors are available only during few
11047 summer months and in order to have another independent reference for the evaluation, the

retrievals available from a ARM site in Barrow, Alaska are used to evaluate the monthly mean annual cycle of LWP in the models, as shown in Fig. 6.3.3.2.d. The annual cycle of LWP unsurprisingly peaks in the late summer in the August in Barrow, while the lowest values are observed in the late winter and early spring months. The majority of the models also capture this annual cycle peaking in late summer and early autumn. The amplitude of the annual cycle is also represented well in some models. Some models however show much flatter annual cycle.

.

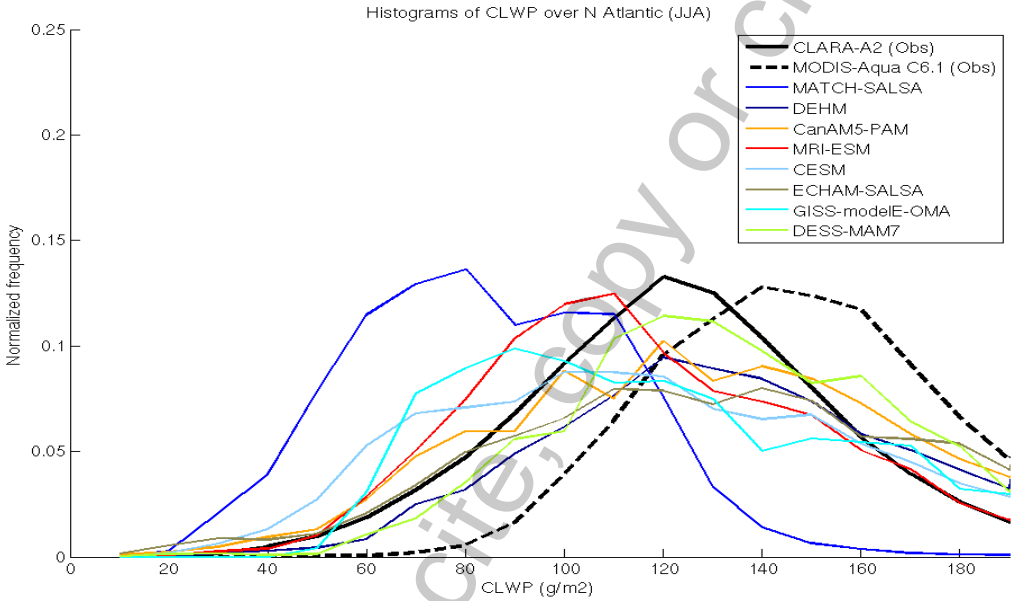

Figure 6.3.3.2.b Histograms of CLWP over N Atlantic for summer months (JJA) from models (coloured lines) and observations (black lines) (g/m2)

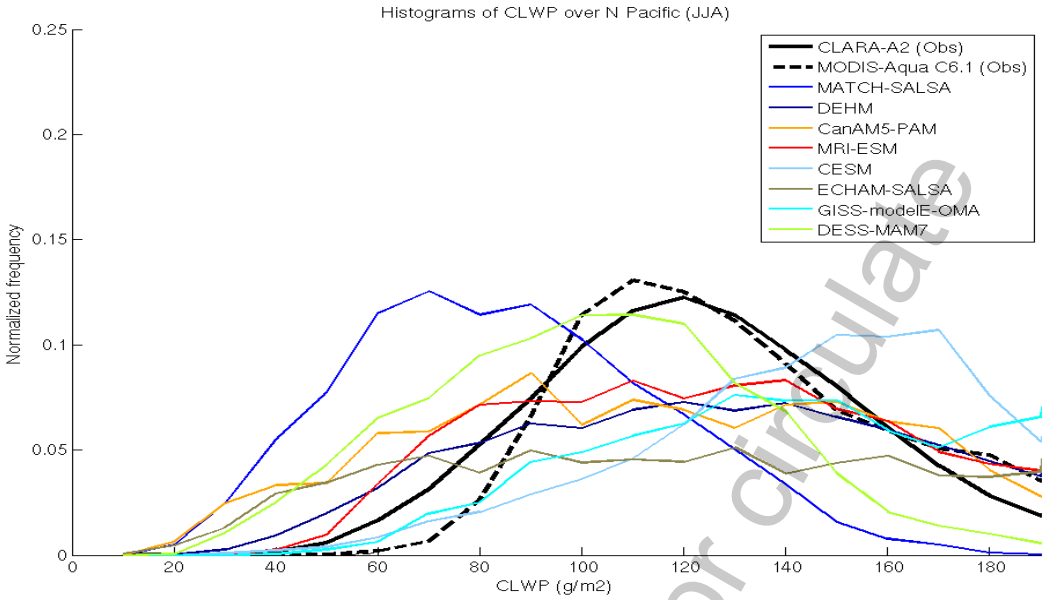

Figure 6.3.3.2.c Same as above, but, over N Pacific.

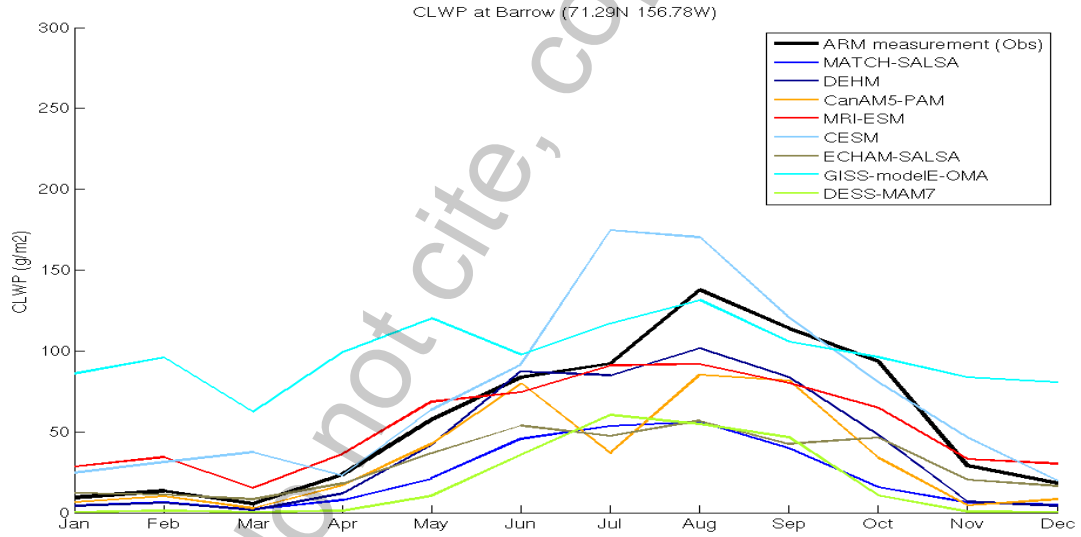

Figure 6.3.3.2.d Seasonal variability of cloud liquid water path (g/m2) at Barrow from the models selected for the study and ARM observations

6.3.3.3 Cloud ice water path

Figure 6.3.3.3.a further shows the intercomparison of cloud ice water paths. The estimates of IWPs from passive sensors disagree strongly with one another as well. The nature of the differences in LWPs seen between these two climate datasets is also similar to the differences in IWPs. The magnitudes of IWPs in the passive observations are much higher

compared to the models. The models however show very strong variability in the estimates of IWPs as well. The differences among models could reach a few hundred percentages. Once again the model estimates of IWPs in the Atlantic and Pacific sectors of the Arctic Ocean are qualitatively closer to the estimates derived from the combined CloudSat and CALIPSO data (e.g. Lenaerts et al., 2017).

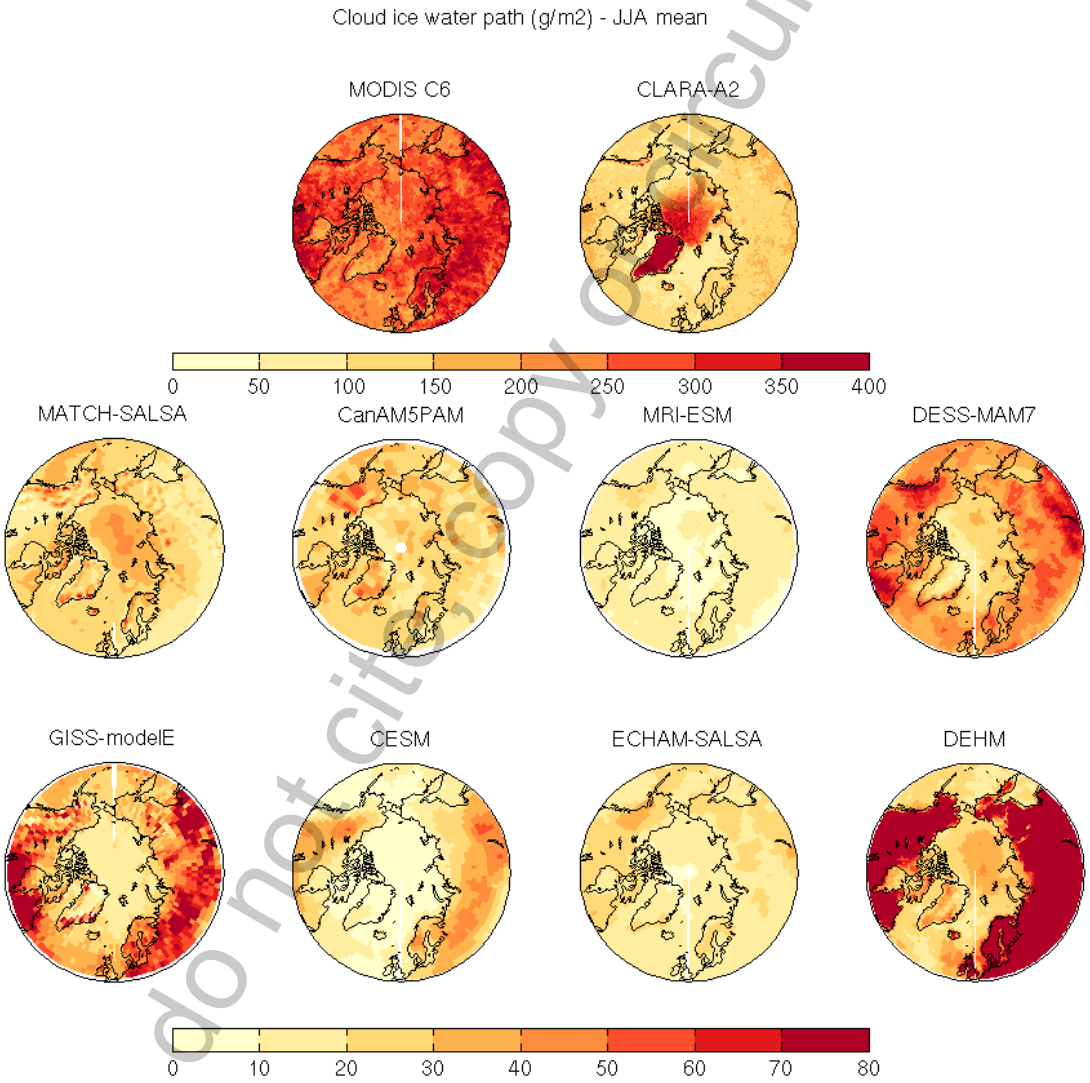

Figure 6.3.3.3.a Comparison of simulated cloud ice water path (rows2-3) against observations (top row) for the mean summer months (JJA) (g/m2).

11085 ***6.3.3.4 Cloud droplet number concentrations***

11086 Improved model simulations of cloud droplet number concentrations (CDNC) are important
11087 for reducing uncertainties in cloud radiative forcing. However evaluating model simulated
11088 CDNC remains challenging because of the limitations of direct observations over large
11089 domains and timescales. Bennartz and Rausch (2017) recently updated CDNC climatology
11090 for liquid boundary layer clouds, first published by Bennartz (2007), estimated from NASA's
11091 Aqua MODIS. Figure 6.3.3.4a compares summer (JJA) season average of observed and
11092 simulated CDNC. Similar to other cloud properties discussed above the models
11093 underestimate CDNC in most of the Arctic region. The model biases vary among the models
11094 and the region with most models underestimating MODIS based CDNC (Figure 6.3.3.4b).
11095 Match-Salsa seems to agree with MODIS better than most other models with relatively
11096 smaller biases. It is important to note that although the satellite based retrievals of cloud
11097 properties remain very important for large-scale model evaluations, these estimates can be
11098 highly uncertain especially near the polar regions.
11099

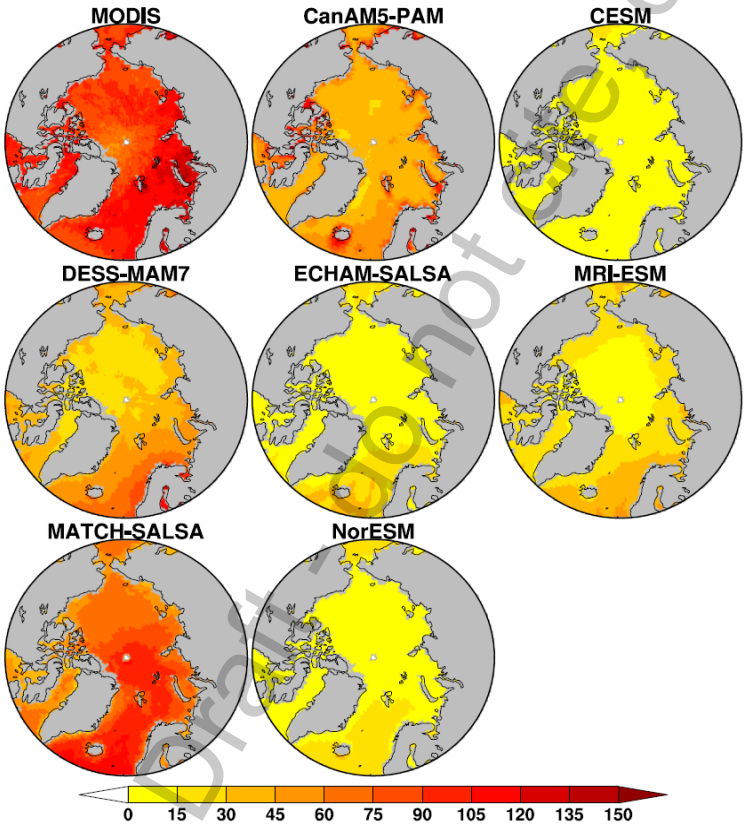

11100

11101 **Figure 6.3.3.4a:** Cloud droplet number concentration ($cm^{-3)}$ for summer months (JJA) mean
11102 of four years (i.e. 2008-09 and 2014-2015).

11103

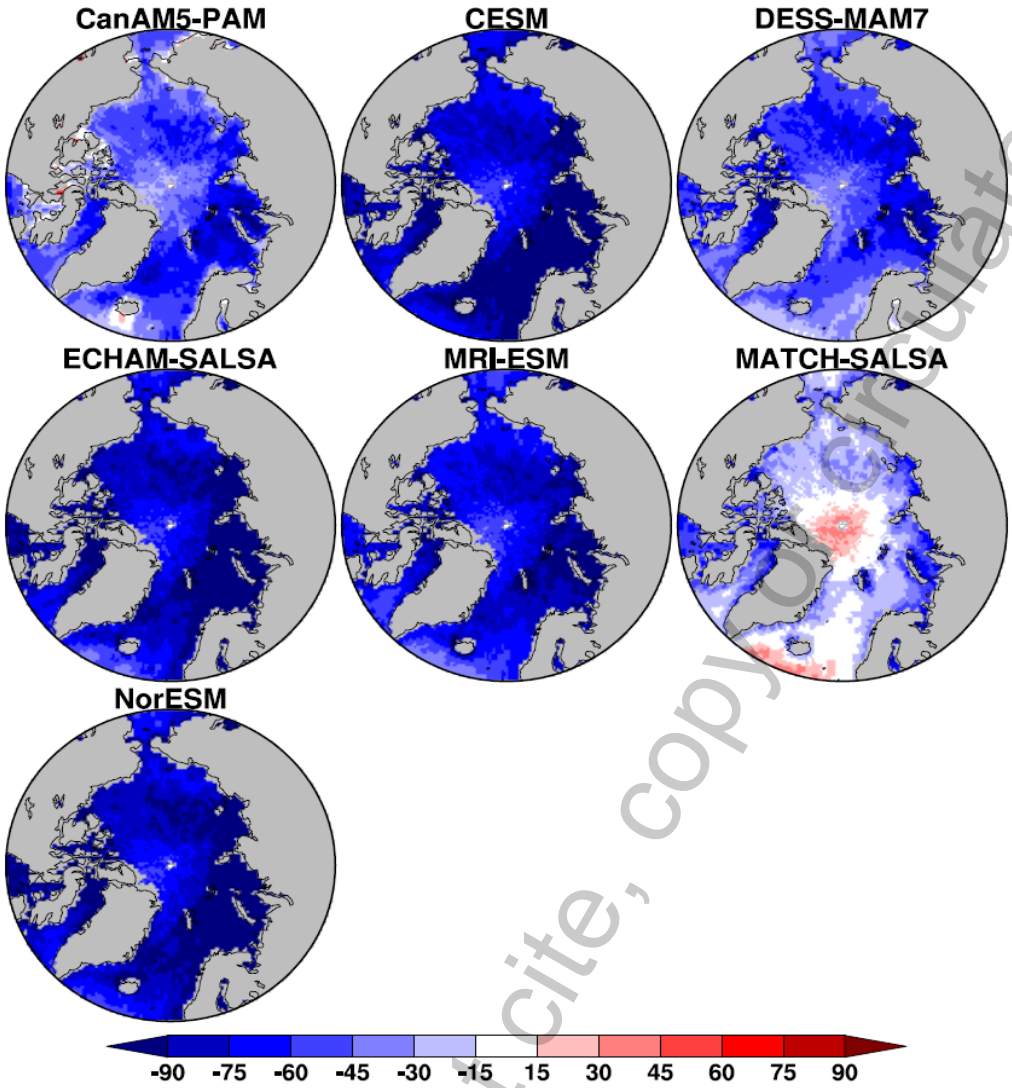

11104

11105

11106 **Figure 6.3.3.4b:** Same as **Figure 6.3.3.4a** but for difference from MODIS.

11107

11108 **6.3.4 Trend evaluation (1990-2015): observations, simulations, emissions**

11109

11110 ***6.3.4.1 Arctic trends of surface-level BC, SO4, and O3***

11111 Models (those that provided 1990-2015) were evaluated at Arctic (>60oN) ground stations

11112 that have a long time series (starting at least around the early 2000s). Model and

11113 measurement time series are plotted together, and trends discussed. (Focus only on BC,

11114 SO4, O3, CH4, and CO)

11115

Six models simulated SLCFs from 1990 to 2015. Those models capture the current abundance, including seasonal cycle, and trends of black carbon, sulfate, and ozone in the Arctic atmosphere, as compared to 18 Arctic measurement locations. The modelled and measured trend of ambient sulfate was to decrease from 1990 to 1995 and then hold relatively steady through to 2015 (Figure X). Black carbon also decreased slightly over the 1990 to 2015 time period (Figure Y). The annual, multi-model mean bias in the Arctic was -25%, with a correlation coefficient, R^2, of 0.57 when compared to measurements from 1990-2015. The model underestimate of Arctic BC was more pronounced in the winter (-40%), than in the summer (-6%), though overall, this is an improvement in model performance in simulating Arctic BC since that 2015 AMAP assessment on black carbon and ozone as climate forcers. Ground-level ozone remained steady with no discernable trend in both the model and measurements from 1990 to 2015 (Figure Z).

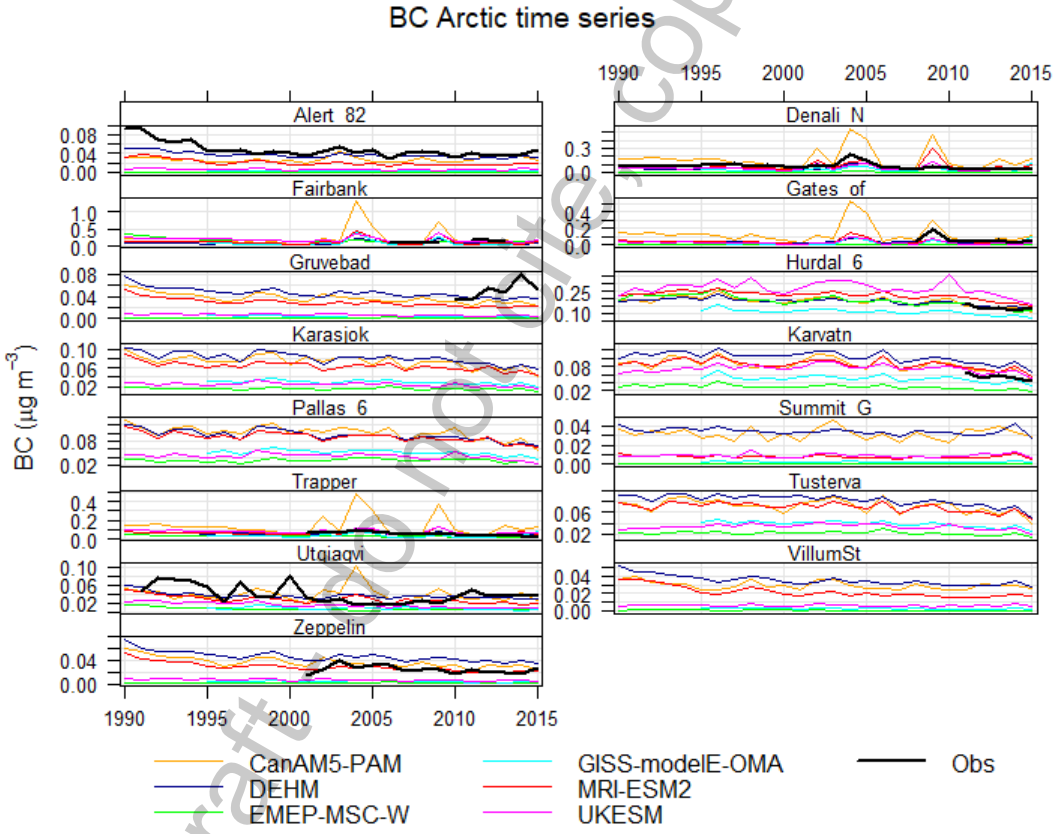

Figure 6.3.5.1.X: Measured and modelled annual mean time series of surface-level BC at 15 Arctic ground stations.

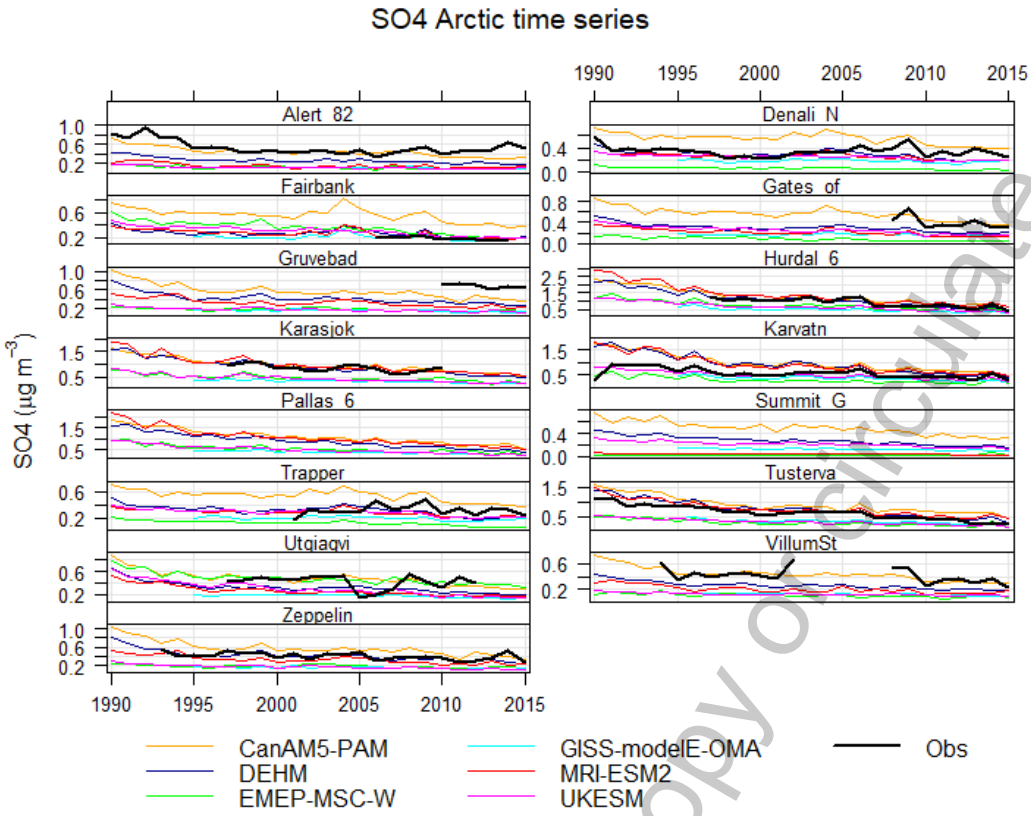

11132

11133 **Figure 6.3.5.1.X:** Measured and modelled annual mean time series of surface-level SO4 at

11134 15 Arctic ground stations.

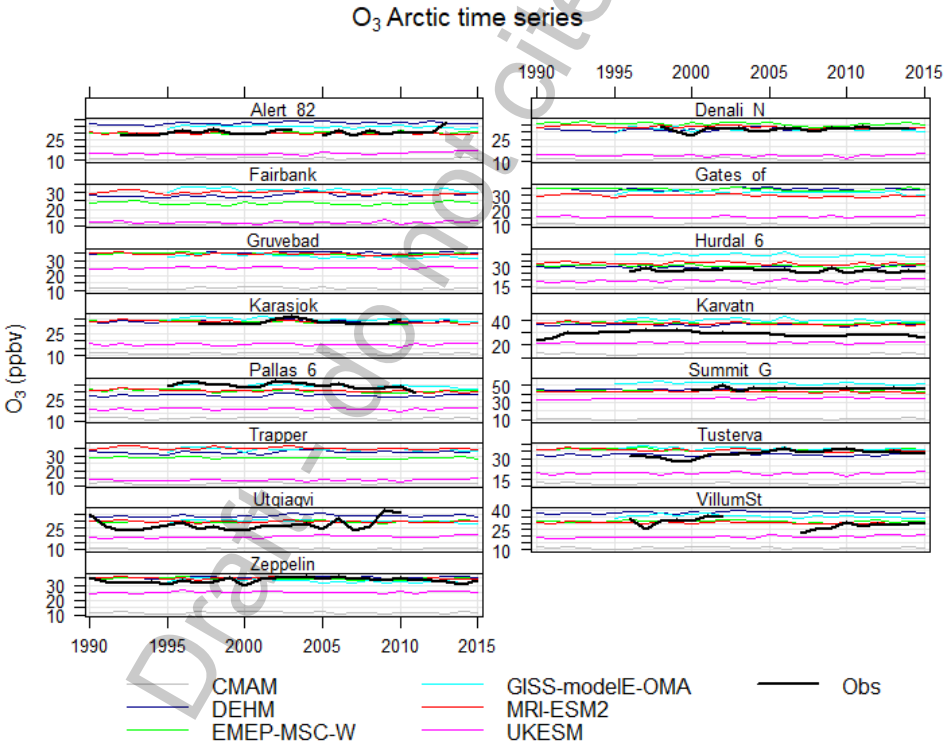

11135

11136 **Figure 6.3.5.1.X:** Measured and modelled annual mean time series of surface-level O3 at 15

11137 Arctic ground stations.

11138

11139 ***6.3.4.2 Simulated aerosol optical depth trend vs AVHRR***

11140 (Rashed) Five models provided long-term monthly mean aerosol optical depth (AOD). A
11141 common time period (i.e. 1995-2015) was chosen because of the availability of model
11142 simulation data from different models. The choice of this period, although arbitrary, can be
11143 useful because of less impacts from large volcanic eruptions of Mount Pinatubo in 1991. The
11144 AVHRR aerosol optical thickness (at 0.63 nm) data was obtained from (Zhao et al., 2013,
11145 2017). All monthly mean data sets (including model simulations and AVHRR) were
11146 remapped to a uniform 1° × 1° spatial grid before performing any analysis.

11147

11148 Figure 6.3.4.2.1 shows a negative AOD trend along eastern coasts of North America, Europe
11149 and Mediterranean region which is consistent with decreasing aerosol emissions. Over
11150 Arabian Sea, Bay of Bengal, southwest costs of Africa and East Asia the aerosol
11151 concentrations are increasing. All models reproduced the spatial distribution of dominant
11152 patterns of observed AOD trends with a varying degree of biases depending on the model.
11153 All models agree in terms of the negative AOD trend over Eastern North America and
11154 Europe and positive trends in the Northern Indian Ocean (except GISS-modelE-OMA) and
11155 southwest coasts of Africa. However most models (except GISS-modelE-OMA) failed to
11156 reproduce increasing observed AOD trends in northeast China.

11157

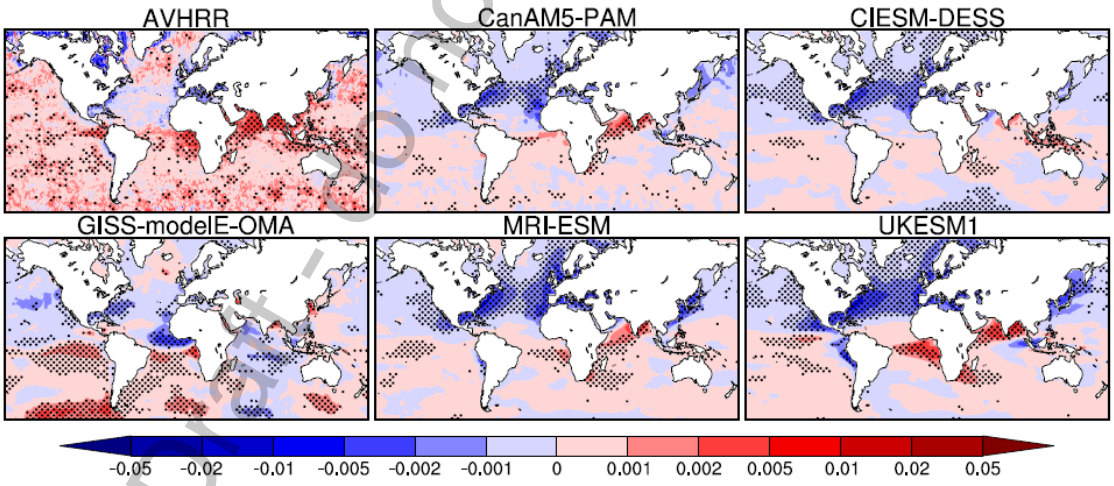

11158

11159 **Figure 6.3.4.2.1:** AOD trend comparison between AVHRR and model simulations. The trend
11160 is calculated from monthly mean AODs for the 1995-2015 time period and was multiplied by

10. Stippling represents regions where trends are statistically significant for 95% confidence level based on Student's t-test.

*****

6.4 Summary of SLCF models and their evaluation

(Cyndi, others) General conclusions about the model performance, with some multi-species summary figures. E.g.;

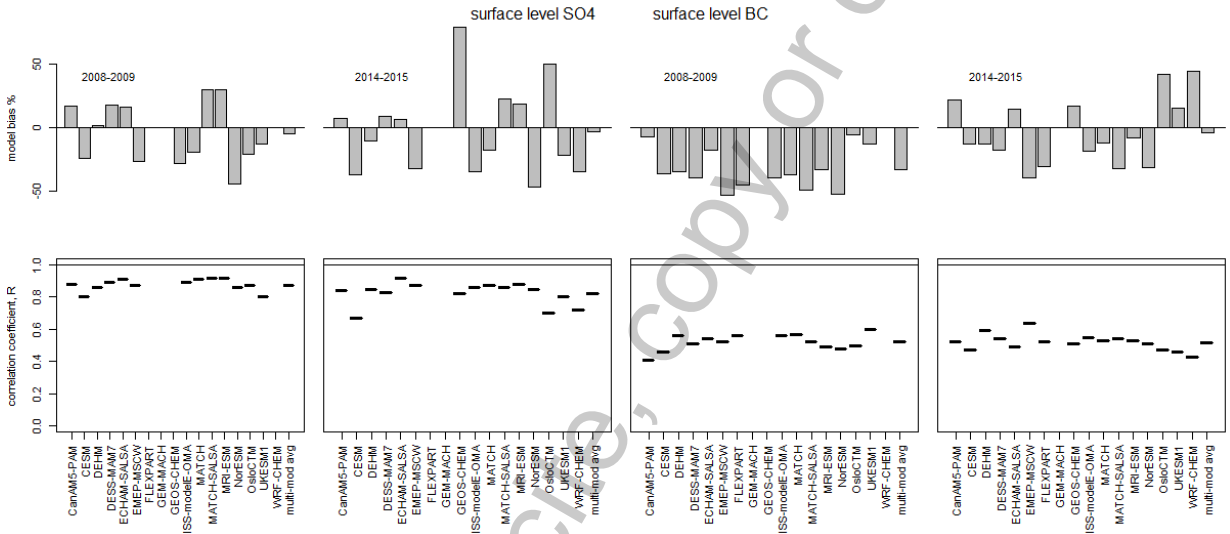

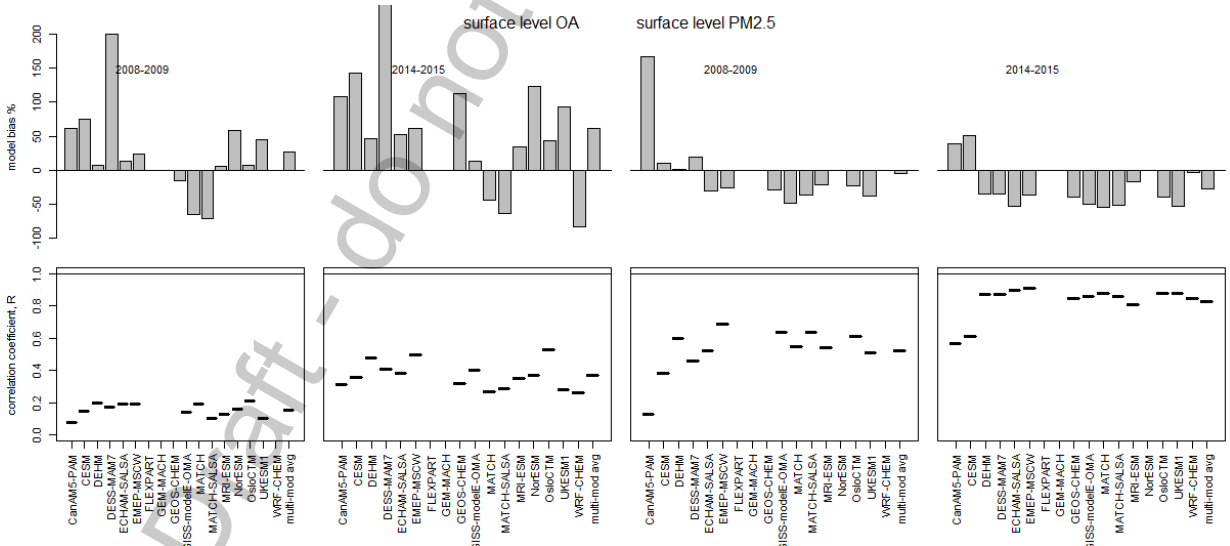

Acknowledgements

The Aerosol Optical Thickness CDR used in this study was acquired from NOAA's National Climatic Data Center (http://www.ncdc.noaa.gov). This CDR was originally developed by Xuepeng Zhao and colleagues for NOAA's CDR Program.

The MODIS, MISR, AVHRR and SeaWiFS monthly products are available at https://search.earthdata.nasa.gov/.

The AERONET measurements are available from the NASA Goddard Space Flight Center (https://aeronet.gsfc.nasa.gov/.

The ESA-CCI AATSR monthly products were obtained from the ICARE Data and Services Centre (http://www.icare.univ-lille1.fr/cci)

The surface air quality data from China (PM2.5, O3, CO, and NOx) came from China Air Quality Historical Data and Beijing Air Quality Historical data: http://beijingair.sinaapp.com/ The national air quality data comes from the national city air quality real-time publishing platform of China Environmental Monitoring Station, which is updated daily. The air quality data of Beijing comes from the website of Beijing Environmental Protection Testing Center and is updated daily.

Canada's surface AQ data is from the National Atmospheric Pollutant Surveillance network (NAPS). ...

IMPROVE is a collaborative association of state, tribal, and federal agencies, and international partners. US Environmental Protection Agency is the primary funding source, with contracting and research support from the National Park Service. The Air Quality Group at the University of California, Davis is the central analytical laboratory, with ion analysis provided by Research Triangle Institute, and carbon analysis provided by Desert Research Institute.

Russian ship-based BC was provided by Olga Popovicheva, but is also available at the EBAS database (ebas.nilo.no). Japanese ship-based BC was provided by Fumikazu Taketani.

Funding for ACE is provided by the Canadian Space Agency (CSA) and the Natural Sciences Research Council of Canada (NSERC). The ACE-FTS work was supported by NSERC.

Alert:
O3 from Alert is from
https://open.canada.ca/data/en/dataset?q=ozone+data+at+Alert&sort=
BC & SO4 from Alert is from Sangeeta Sharma (sangeeta.sharma@canada.ca) and Lin Huang (lin.huang@canada.ca)

Gruvebadet:
We acknowledge Mauro Mazzola (mauro.mazzola@cnr.it), Stefania Gilardoni (stefania.gilardoni@cnr.it), and Angelo Lupi (angelo.lupi@cnr.it) from the Institute of Polar Sciences fo Gruvabadet eBC measurements; and Rita Traversi (rita.traversi@unifi.it), Mirko Severi (mirko.severi@unifi.it), and Silvia Becagli (silvia.becagli@unifi.it) from University of Florence for the Gruvabadet SO4 measurements.
http://www.isac.cnr.it/~radiclim/CCTower/?Data:Aerosol

Zeppelin datasets from Vito Vitale Angelo Lupi (also available on http://ebas.nilu.no)

Villum Station datasets (www.villumresearchstation.dk) from Henrik Skov (hsk@envs.au.dk; also available in http://ebas.nilo.no)

NAPS (national air pollutant surveillance; Canada;
https://open.canada.ca/data/en/dataset/1b36a356-defd-4813-acea-47bc3abd859b)

CLARA-A2 dataset for cloud properties

CSN (chemical speciation network; US; https://www3.epa.gov/ttnamti1/speciepg.html)

CMDL (Climate Monitoring and Diagnostics Laboratory; global)

China AQ (https://beijingair.sinaapp.com/)

Hong Kong EPA (https://www.epd.gov.hk/epd/english/top.html)

EBAS (Europe; http://ebas.nil.no)

Global CH4 from the WDCGG (World Data Centre for GHGs https://gaw.kishou.go.jp/login/user)

TES (https://eosweb.larc.nasa.gov/project/tes/guide/TES_Lite_Products_Users_Guide.pdf)

MOPITT (https://www2.acom.ucar.edu/mopitt)

EMEP for European data (downloaded from http://ebas.nilu.no)

Fairbanks aerosol measurements from William Simpson (wrsimpson@alaska.edu) and KC Nattinger thesis https://scholarworks.alaska.edu/handle/11122/6830 can be added to the data reference list below.

The aircraft data are from multiple campaigns and provided by Duncan Watson-Parris (duncan.watson-parris@physics.ox.ac.uk)

Add more data acknowledgement here

*****

Data references

For Dalhousie pm2.5:

van Donkelaar, A., R. V. Martin, et al. (2015) Global fine particulate matter concentrations from satellite for long-term exposure assessment, *Environmental Health Perspectives*, 123, 135-143, DOI:10.1289/ehp.1408646, 2015.

For MERRA-2 pm2.5:

Gelaro, R., and Coauthors, 2017: The Modern-Era Retrospective Analysis for Research and Applications, version 2 (MERRA-2). *J. Climate*, **30**, 5419–5454, https://doi.org/10.1175/JCLI-D-16-0758.1

For IMPROVE:

Malm, W. C., Sisler, J. F., Huffman, D., Eldred, R. A., and Cahill, T. A.: Spatial and seasonal trends in particle concentration and optical extinction in the United States, J. Geophys. Res., 99, 1347–1370, 1994.

For EBAS/EMEP (Not sure how to add acknowledgement):

Tørseth, K., Aas, W., Breivik, K., Fjæraa, A. M., Fiebig, M., Hjellbrekke, A. G., Lund Myhre, C., Solberg, S., and Yttri, K. E.: Introduction to the European Monitoring and Evaluation Programme (EMEP) and observed atmospheric composition change during 1972–2009, Atmos. Chem. Phys., 12, 5447–5481, doi:10.5194/acp-12-5447-2012, 2012.

For NAPS:

Ewa Dabek-Zlotorzynska, Tom F. Dann, P. Kalyani Martinelango, Valbona Celo, Jeffrey R. Brook, David Mathieu, Luyi Ding, Claire C. Austin, Canadian National Air Pollution Surveillance (NAPS) PM2.5 speciation program: Methodology and PM2.5 chemical

composition for the years 2003–2008, Atmospheric Environment,45,3, 2011,673-686,https://doi.org/10.1016/j.atmosenv.2010.10.024.

For AVHRR AOD:

Zhao, T. X.-P., P. K. Chan, and A. K. Heidinger (2013), A global survey of the effect of cloud contamination on the aerosol optical thickness and its long-term trend derived from operational AVHRR satellite observations, J. Geophys. Res. Atmos., 118, 2849-2857, doi:10.1002/jgrd.50278.

Zhao, Xuepeng; and NOAA CDR Program (2017): NOAA Climate Data Record (CDR) of AVHRR Daily and Monthly Aerosol Optical Thickness (AOT) over Global Oceans, Version 3.0. NOAA National Centers for Environmental Information.[AOT_AVHRR_v03r00_monthly_avg] doi:10.7289/V5BZ642P [date accessed: Jan 30, 2018, last accessed on Feb 01, 2020].

For MISR AOD:

Witek, M. L., Garay, M. J., Diner, D. J., Bull, M. A., and Seidel, F. C.: New approach to the retrieval of AOD and its uncertainty from MISR observations over dark water, Atmos. Meas. Tech., 11, 429–439, https://doi.org/10.5194/amt-11-429-2018, 2018..

For MODIS:

Remer, L., Kaufman, Y., Tanre, D., Mattoo, S., Chu, D., Martins, J., Li, R.-R., Ichoku, C., Levy, R., Kleidman, R., Eck, T., Vermote, E., andHolben, B.: The MODIS Aerosol Algorithm, Products, and Validation, J. Atmospheric Sciences, 62, 947 – 973, 2005.

Hsu, N. C., Jeong, M., Bettenhausen, C., Sayer, A. M., Hansell, R., Seftor, C. S., Huang, J., and Tsay, S.: Enhanced Deep Blue aerosol retrievalalgorithm : The second generation, Journal

of Geophysical Research : Atmospheres, 118, 9296–9315, https://doi.org/10.1002/jgrd.50712,202013

Sayer, A. M., Munchak, L. A., Hsu, N. C., Levy, R. C., Bettenhausen, C., and Jeong, M. J..: MODIS collection 6 aerosol products: comparison between Aqua's e-Deep Blue, Dark Target, and "merged" datasets, and usage recommendations, J. Geophys. Res. Atmos., 119, 13965–13989, 2014.

For SeaWiFS:

Sayer, A., N. Hsu, C. Bettenhausen, Z. Ahmad, B. Holben, A. Smirnov, G.E. Thomas, and J. Zhang (2012). SeaWiFS Ocean Aerosol Retrieval (SOAR): algorithm, validation, and comparison with other datasets. J. Geophys. Res, 117, D03206. doi:10.1029/2011JD016599

Hsu, N. C., Lee, J., Sayer, A. M., Kim, W., Bettenhausen, C., and Tsay, S. C.: VIIRS Deep Blue Aerosol Products over Land: Extending the EOS Long-Term Aerosol Data Records, J. Geophys. Res.-Atmos., 124, 4026–4053, https://doi.org/10.1029/2018JD029688, 2019.

For AATSR:

North, P. R. J., Briggs, S. A., Plummer, S. E., and Settle, J. J.: Retrieval of land surface bidirectional reflectance and aerosol opacity from atsr-2 multiangle imagery, IEEE T. Geosci. Remote, 37, 526–537, 1999.

Thomas, G. E., Poulsen, C. A., Sayer, A. M., Marsh, S. H., Dean, S. M., Carboni, E., Siddans, R., Grainger, R. G., and Lawrence, B. N.: The GRAPE aerosol retrieval algorithm, Atmos. Meas. Tech., 2, 679–701, https://doi.org/10.5194/amt-2-679-2009, 2009.

Veefkind, J. P. and de Leeuw, G.: A new algorithm to determine the spectral aerosol optical depth from satellite radiometer measurements, J. Aerosol Sci., 29, 1237–1248, 1998.

Holzer-Popp, T., de Leeuw, G., Griesfeller, J., Martynenko, D., Klueser, L., Bevan, S., Davies, W., Ducos, F., Deuze, F., Graigner, R. G.,Heckel, A., von Hoyningen-Huene, W., Kolmonen, P., Litvinov, P., North, P., Poulsen, C. A., Ramin, D., Siddans, R., Sogacheva, L., Tanre,10D., Thomas, G. E., Vountas, M., Descloitres, J., Griesfeller, J., Kinne, S., Schulz, M., and Pinnock, S.: Aerosol retrieval experiments inthe ESA Aerosol cci project, Atmospheric Measurement Techniques, 6, 1919–1957, https://doi.org/10.5194/amt-6-1919-2013, 2013

For AERONET:

Holben B.N., T.F.Eck, I.Slutsker, D.Tanre, J.P.Buis, A.Setzer, E.Vermote, J.A.Reagan, Y.Kaufman, T.Nakajima, F.Lavenu, I.Jankowiak, and A.Smirnov, 1998: AERONET - A federated instrument network and data archive for aerosol characterization, Rem. Sens. Environ., 66, 1-16.

Eck, T.F., B.N.Holben, J.S.Reid, O.Dubovik, A.Smirnov, N.T.O'Neill, I.Slutsker, and S.Kinne, 1999: Wavelength dependence of the optical depth of biomass burning, urban and desert dust aerosols, J. Geophys. Res., 104, 31 333-31 350.

For CDNC:

Bennartz, R. and Rausch, J.: Global and regional estimates of warm cloud droplet number concentration based on 13 years of AQUA-MODIS observations, Atmos. Chem. Phys., 17, 9815–9836, https://doi.org/10.5194/acp-17-9815-2017, 2017

For JRA55:

Kobayashi, S., Ota, Y., Harada, Y., Ebita, A., Moriya, M., Onoda, H., Onogi, K., Kamahori, H., Kobayashi, C., Endo, H., Miyaoka, K., and Takahashi, K.: The JRA-55 Reanalysis: General Specifications and Basic Characteristics, J. Meteorol. Soc. Jpn. 93, 5–48, https://doi.org/10.2151/jmsj.2015-001, 2015.

For ship-basd BC:

Popovicheva, Olga B., N. Evangeliou, K. Eleftheriadis, A. C. kalogridis, N. Sitnikov, S. Echkardt, A. Stohl. Black carbon ources constrained by observations in the Russia high Arctic. Environmental Science and Technologiy, 51, 3871-3879, 2017, DOI: 10.1021/acs.est.6b05832.

Taketani, Fumikazu, T. Miyakawa, H. Takashima, Y. Komzaki, X. Pan, Y. Kanaya, J. Inoue. Shipborne observations of atmospheric black carbon aerosol particles over the Arctic Ocean, Bering Sea, and North Pacific, 121, 4, 1914-121, 2016, DOI:10.1002/2015JD023648.

For ACE-FTS:

Bernath, P.F. et al. (2005). Atmospheric Chemistry Experiment (ACE): Mission overview. *Geophysical Research Letters*, 32(15): 1-5.

Text References

AMAP 2015 reports

Abdul-Razzak, H. and Ghan, S. J.: A parameterization of aerosol activation 3. Sectional representation, J. Geophys. Res., 107, AAC1.1–AAC1.6, doi:10.1029/2001JD000483, 2002.

11401 Andersson, C., Langner, J., and Bergström, R.: Interannual variation and trends in air
11402 pollution over Europe due to climate variability during 1958-2001 simulated with a
11403 regional CTM coupled to the ERA-40 reanalysis, Tellus, 59B, 77–98, 2007.

11404 Andersson, C., Bergström, R., Bennet, C., Robertson, L., Thomas, M., Korhonen, H., Lehtinen,
11405 K. E. J., and Kokkola, H.: MATCH-SALSA – Multi-scale Atmospheric Transport and
11406 Chemistry model coupled to the SALSA aerosol microphysics model – Part 1: Model
11407 description and evaluation, Geosci. Model Dev., 8, 171–189, doi:10.5194/gmd-8-171-
11408 2015, 2015.

11409 Archibald, A., O'Connor, F., Archer-Nicholls, S., Chipperfield, M., Dalvi, M., Folberth, G.,
11410 Dennison, F., Dhomse, S., Griffiths, P., Hardacre, C., Hewitt, A., Hill, R., Johnson, C.,
11411 Keeble, J., Köhler, M., Morgenstern, O., Mulchay, J., Ordóñez, C., Pope, R., Rumbold, S.,
11412 Russo, M., Savage, N., Sellar, A., Stringer, M., Turnock, S., Wild, O. and Zeng, G.:
11413 Description and evaluation of the UKCA stratosphere-troposphere chemistry scheme
11414 (StratTrop vn 1.0) implemented in UKESM1, Geosci. Model Dev. Discuss., (1), 1–82,
11415 doi:10.5194/gmd-2019-246, 2019.

11416 Bauer, S. E., & Koch, D. (2005). Impact of heterogeneous sulfate formation at mineral dust
11417 surfaces on aerosol loads and radiative forcing in the Goddard Institute for Space Studies
11418 general circulation model. Journal of Geophysical Research: Atmospheres, 110(D17).
11419 https://doi.org/10.1029/2005JD005870

11420 Bauer, S. E., Koch, D., Unger, N., Metzger, S. M., Shindell, D. T., & Streets, D. G. (2007).
11421 Nitrate aerosols today and in 2030: a global simulation including aerosols and
11422 tropospheric ozone. Atmospheric Chemistry and Physics, 7(19), 5043–5059.
11423 https://doi.org/10.5194/acp-7-5043-2007

11424 Bauer, S. E., Mishchenko, M. I., Lacis, A. A., Zhang, S., Perlwitz, J., & Metzger, S. M. (2007).
11425 Do sulfate and nitrate coatings on mineral dust have important effects on radiative
11426 properties and climate modeling? Journal of Geophysical Research: Atmospheres,
11427 112(D6). https://doi.org/10.1029/2005JD006977

11428 Bauer, S. E., Wright, D. L., Koch, D., Lewis, E. R., McGraw, R., Chang, L.-S., et al. (2008).
11429 MATRIX (Multiconfiguration Aerosol TRacker of mIXing state): an aerosol microphysical

11430 module for global atmospheric models. Atmospheric Chemistry and Physics, 8(20), 6003–
11431 6035. https://doi.org/10.5194/acp-8-567 6003-2008

11432 Bauer, S. E., & Menon, S. (2012). Aerosol direct, indirect, semidirect, and surface albedo
11433 effects from sector contributions based on the IPCC AR5 emissions for preindustrial and
11434 present-day conditions. Journal of Geophysical Research: Atmospheres, 117(D1).
11435 https://doi.org/10.1029/2011JD016816

11436 Bauer, S. E., Ault, A., & Prather, K. A. (2013). Evaluation of aerosol mixing state classes in the
11437 GISS modelE MATRIX climate model using single-particle mass spectrometry
11438 measurements. Journal of Geophysical Research: Atmospheres, 118(17), 9834–9844.
11439 https://doi.org/10.1002/jgrd.50700

11440 Bauer, S.E. and K. Tsigaridis, 2020: An end to the anthropogenic emissions era? J. Adv.
11441 Model. Earth Syst., under review.

11442 Bennartz, R.: Global assessment of marine boundary layer cloud droplet number
11443 concentration from satellite, J. Geophys. Res., 112, D02201,
11444 https://doi.org/10.1029/2006jd007547, 2007.

11445 Bentsen, M., I. Bethke, J. B. Debernard, T. Iversen, A. Kirkevåg, Ø. Seland, H. Drange, C.
11446 Roelandt, I. A. Seierstad, C. Hoose, J. E. Kristjánsson: The Norwegian Earth System Model,
11447 NorESM1-M—Part 1: Description and basic evaluation of the physical climate. Geosci.
11448 Model Dev., 6, 687–720, doi:10.5194/gmd-6-687-2013.

11449 Berrisford, P., Dee, D., Poli, P., Brugge, R., Fielding, K., Fuentes, M., Kållberg, P., Kobayashi,
11450 S., Uppala, S., and Simmons, A.: The ERA-Interim archive Version 2.0, Shinfield Park,
11451 Reading, 2011.

11452 Charron, M., Polavarapu, S., Buehner, M., Vaillancourt, P. A., Charette, C., Roch, M.,
11453 Morneau, J., Garand, L., Aparicio, J. M., MacPherson, S., Pellerin, S., St-James, J., and
11454 Heilliette, S.:

11455 The Stratospheric Extension of the Canadian Global Deterministic Medium-Range Weather
11456 Forecasting System and Its Impact on Tropospheric Forecasts, Mon.Weather Rev., 140,
11457 1924–1944, https://doi.org/10.1175/MWR-D-11-00097.1, 2012.

11458

11459 Chen, J., Anderson, K., Pavlovic, R., Moran, M. D., Englefield, P., Thompson, D. K., Munoz-
11460 Alpizar, R., and Landry, H.: The FireWork v2.0 air quality forecast system with biomass
11461 burning emissions from the Canadian Forest Fire Emissions Prediction System v2.03,
11462 Geosci. Model Dev., 12, 3283–3310, https://doi.org/10.5194/gmd-12-3283-2019, 2019.

11463 Côté, J., Gravel, S., Méthot, A., Patoine, A., Roch, M., and Staniforth, A.: The operational
11464 CMC–MRB Global Environmental Multiscale (GEM) model, Part I: Design considerations
11465 and formulation, Mon. Weather Rev., 126, 1373–1395, 1998a.

11466 Côté, J., Desmarais, J.-G., Gravel, S., Méthot, A., Patoine, A., Roch, M., and Staniforth, A.:
11467 The operational CMC–MRB Global Environmental Multiscale (GEM) model, Part II:
11468 Results, Mon. Weather Rev., 126, 1397–1418, 1998b.

11469 Danabasoglu, G., Lamarque, J.-F., Bacmeister, J., Bailey, D. A., DuVivier, A. K., Edwards, J., et
11470 al. (2020). The Community Earth System Model Version 2 (CESM2). *Journal of Advances*
11471 *in Modeling Earth Systems*, 12, e2019MS001916.
11472 https://doi.org/10.1029/2019MS001916.

11473 Eckhardt, S., B. Quennehen, D. J. L. Olivié, T. K. Berntsen, R. Cherian, J. H. Christensen, W.
11474 Collins, S. Crepinsek, N. Daskalakis, M. Flanner, A. Herber, C. Heyes, Ø. Hodnebrog, L.
11475 Huang, M. Kanakidou, Z. Klimont, J. Langner, K. S. Law, M. T. Lund, R. Mahmood, A.
11476 Massling, S. Myriokefalitakis, I. E. Nielsen, J. K. Nøjgaard, J. Quaas, P. K. Quinn, J.-C. Raut,
11477 S. T. Rumbold, M. Schulz, S. Sharma, R. B. Skeie, H. Skov, T. Uttal, K. von Salzen, and A.
11478 Stohl (2015): Current model capabilities for simulating black carbon and sulfate
11479 concentrations in the Arctic atmosphere: a multi-model evaluation using a com-
11480 prehensive measurement data set. Atmos. Chem. Phys. 15, 9413-9433, doi:10.5194/acp-
11481 15-9413-2015

11482 Emmons, L. K., Schwantes, R. H., Orlando, J. J., Tyndall, G., Kinnison, D., Lamarque, J.-F., et al
11483 (2020). The Chemistry Mechanism in the Community Earth System Model version 2
11484 (CESM2). *Journal of Advances in Modeling Earth Systems*, 12, e2019MS001882.
11485 https://doi.org/10.1029/2019MS001882.

11486 Foltescu, V., Pryor, S. and Bennet, C.: Sea salt generation, dispersion and removal on the
11487 regional scale. Atmos. Env., 39. 2123-2133. 10.1016/j.atmosenv.2004.12.030, 2005.

11488

11489 Gent, P.R., G. Danabasoglu, L. J. Donner, M. M. Holland, E. C. Hunke, S. R. Jayne, D. M.
11490 Lawrence, R. B. Neale, P. J. Rasch, M. Vertenstein, P. H. Worley, Z.-L. Yang, and M. Zhang:
11491 The Community Climate System Model Version 4. J. Climate, 24, 4973–4991. doi:
11492 http://d6.doi.org/10.1175/2011JCLI4083.1 2011.

11493 Gery, M. W., Whitten, G. Z., Killus, J. P., and Dodge, M. C.: A photochemical kinetics
11494 mechanism for urban and regional scale computer modeling, J. Geophys. Res., 94, 925–
11495 956, 1989.

11496 Gong, S. L., Barrie, L. A., Blanchet, J. -P., Salzen, K. von, Lohmann, U., Lesins, G., Spacek, L.,
11497 Zhang, L. M., Girard, E., Lin, H., Leaitch, R., Leighton, H., Chylek, P., and Huang, P.:
11498 Canadian Aerosol Module: A size-segregated simulation of atmospheric aerosol
11499 processes for climate and air quality models 1. Module development, J. Geophys. Res.,
11500 108, 4007, https://doi.org/10.1029/2001JD002002, 2003.

11501 Gong, W., Makar, P. A., Zhang, J., Milbrandt, J., Gravel, S., Hayden, K. L., Macdonald, A. M.,
11502 and Leaitch, W. R.: Modelling aerosol–cloud–meteorology interaction: A case study with
11503 a fully coupled air quality model (GEM-MACH), Atmos. Environ., 115, 695–715,
11504 https://doi.org/10.1016/j.atmosenv.2015.05.062, 2015.

11505 Gong, W., Dastoor, A. P., Bouchet, V. S., Gong, S.-L., Makar, P. A., Moran, M. D., Pabla, B.,
11506 Ménard, S., Crevier, L.-P., Cousineau, S., and Venkatesh, S.: Cloud processing of gases and
11507 aerosols in a regional air quality model (AURAMS), Atmos. Res., 82, 248–275, 2006.

11508 Guenther, A. B., Jiang, X., Heald, C. L., Sakulyanontvittaya, T., Duhl, T., Emmons, L. K., &
11509 Wang, X. (2012). The Model of Emissions of Gases and Aerosols from Nature version 2.1
11510 (MEGAN2.1): An extended and updated framework for modeling biogenic emissions.
11511 Geoscientific Model Development, 5(6), 1471–1492. https://doi.org/10.5194/gmd-5-
11512 1471-2012.

11513 Horowitz, L. W., S. M. Walters, D. L. Mauzerall, L. K. Emmons, P. J. Rasch, C. Granier, X. Tie,
11514 J.-F. Lamarque, M. G. Schultz, and G. P. Brasseur: A global simulation of tropospheric
11515 ozone and related tracers: Description and evaluation of MOZART, version 2, J. Geophys.
11516 Res., 108(D24), 4784, doi:10.1029/2002JD002853, 2003.

11517 Hurrell J W, Hack J J, Shea D, Caron J M and Rosinski J 2008 A new sea surface temperature
11518 and sea ice boundary dataset for the community atmospheric model; J. Clim. 21 5145–
11519 5153.

11520 Iversen, T., Bentsen, M., Bethke, I., Debernard, J. B., Kirkevåg, A., Seland, Ø., Drange, H.,
11521 Kristjansson, J. E., Medhaug, I., Sand, M., and Seierstad, I. A.: The Norwegian Earth
11522 System Model, NorESM1-M – Part 2: Climate response and scenario projections, Geosci.
11523 Model Dev., 6, 389–415, doi:10.5194/gmd-6-389-2013, 2013.

11524 Jiang, W.: Instantaneous secondary organic aerosol yields and their comparison with overall
11525 aerosol yields for aromatic and biogenic hydrocarbons, Atmos. Environ., 37, 5439–5444,
11526 2003.

11527 Kelley, M., G.A. Schmidt, L. Nazarenko, R.L. Miller, S.E. Bauer, R. Ruedy, G.L. Russell, I.
11528 Aleinov, M. Bauer, R. Bleck, V. Canuto, G. Cesana, Y. Cheng, T.L. Clune, B. Cook, C.A. Cruz,
11529 A.D. Del Genio, G.S. Elsaesser, G. Faluvegi, N.Y. Kiang, D. Kim, A.A. Lacis, A. Leboissetier,
11530 A.N. LeGrande, K.K. Lo, J.C. Marshall, S. McDermid, E.E. Matthews, K. Mezuman, L.T.
11531 Murray, V. Oinas, C. Orbe, C. Pérez García-Pando, J.P. Perlwitz, M.J. Puma, D. Rind, A.
11532 Romanou, D.T. Shindell, S. Sun, N. Tausnev, K.

11533 Kolonjari et al (2017?)

11534 Kawai, H., S. Yukimoto, T. Koshiro, N. Oshima, T. Tanaka, H. Yoshimura, and R. Nagasawa,
11535 Significant improvement of cloud representation in the global climate model MRI-ESM2,
11536 Geosci. Model Dev., 12, 2875–2897, https://doi.org/10.5194/gmd-12-2875-2019, 2019.

11537 Kokkola, H., Kühn, T., Laakso, A., Bergman, T., Lehtinen, K. E. J., Mielonen, T., Arola, A.,
11538 Stadtler, S., Korhonen, H., Ferrachat, S., Lohmann, U., Neubauer, D., Tegen, I.,
11539 Siegenthaler-Le Drian, C., Schultz, M. G., Bey, I., Stier, P., Daskalakis, N., Heald, C. L., and
11540 Romakkaniemi, S.: SALSA2.0: The sectional aerosol module of the aerosol–chemistry–
11541 climate model ECHAM6.3.0-HAM2.3-MOZ1.0, Geosci. Model Dev., 11, 3833–3863,
11542 https://doi.org/10.5194/gmd-11-3833-2018, 2018.

11543 Tsigaridis, G. Tselioudis, E. Weng, J. Wu, and M. Yao, 2019: GISS-E2.1: Configurations and
11544 climatology. J. Adv. Model. Earth Syst., submitted.

11545 Kirkevåg, A., Iversen, T., Seland, Ø., Hoose, C., Kristjánsson, J. E., Struthers, H., Ekman, A. M.
11546 L., Ghan, S., Griesfeller, J., Nilsson, E. D., and Schulz, M.: Aerosol–climate interactions in
11547 the Norwegian Earth System Model – NorESM1-M, Geosci. Model Dev., 6, 207–244,
11548 doi:10.5194/gmd-6-207-2013, 2013.

11549 Koch, D., Schmidt, G. A., & Field, C. V. (2006). Sulfur, sea salt, and radionuclide aerosols in
11550 GISS ModelE. Journal of Geophysical Research: Atmospheres, 111(D6).
11551 https://doi.org/10.1029/2004JD005550

11552 Kokkola, H., Korhonen, H., Lehtinen, K. E. J., Makkonen, R., Asmi, A., Järvenoja, S., Anttila, T.,
11553 Partanen, A.-I., Kulmala, M., Järvinen, H., Laaksonen, A., and Kerminen, V.-M.: SALSA – a
11554 Sectional Aerosol module for Large Scale Applications, Atmos. Chem. Phys., 8, 2469–
11555 2483, doi:10.5194/acp-8-2469-2008, 2008.

11556 Kuhlbrodt, T., Jones, C. G., Sellar, A., Storkey, D., Blockley, E., Stringer, M., Hill, R., Graham,
11557 T., Ridley, J., Blaker, A., Calvert, D., Copsey, D., Ellis, R., Hewitt, H., Hyder, P., Ineson, S.,
11558 Mulcahy, J., Siahaan, A. and Walton, J.: The Low-Resolution Version of HadGEM3 GC3.1:
11559 Development and Evaluation for Global Climate, J. Adv. Model. Earth Syst., 10(11), 2865–
11560 2888, doi:10.1029/2018MS001370, 2018.

11561 Lauritzen, P, R Nair, A Herrington, P Callaghan, S Goldhaber, J Dennis, J Bacmeister, et al.
11562 (2018). NCAR Release of CAM-SE in CESM2.0: A Reformulation of the Spectral Element
11563 Dynamical Core in Dry-Mass Vertical Coordinates With Comprehensive Treatment of
11564 Condensates and Energy, *Journal of Advances in Modeling Earth Systems*,10(7): 1537-
11565 1570, doi:10.1029/2017ms001257.

11566 Liu, J., S. Fan, L. W. Horowitz, and H. Levy II (2011), Evaluation of factors controlling long-
11567 range transport of black carbon to the Arctic, J. Geophys. Res., 116, D04307,
11568 doi:10.1029/2010JD015145.

11569 Liu, X., Ma, P.-L., Wang, H., Tilmes, S., Singh, B., Easter, R. C., Ghan, S. J., and Rasch, P. J.
11570 (2016), Description and evaluation of a new four-mode version of the Modal Aerosol
11571 Module (MAM4) within version 5.3 of the Community Atmosphere Model, *Geosci. Model*
11572 *Dev.*, 9, 505–522, doi: 10.5194/gmd-9-505-2016.

11573 Lohmann, U., Feichter, J., Chuang, C. C., and Penner, J. E.: Prediction of the number of cloud
11574 droplets in the ECHAM GCM, J. Geophys. Res., 104, 9169–9198, 1999.

11575 Lund MT et al. (2018) Concentrations and radiative forcing of anthropogenic aerosols from
11576 1750 to 2014 simulated with the Oslo CTM3 and CEDS emission inventory Geosci Model
11577 Dev 11:4909-4931 doi:10.5194/gmd-11-4909-2018.

11578 Lurmann, F., Lloyd, A. C., and Atkinson, R.: A chemical mechanism for use in long-range
11579 transport/acid deposition computer modeling, J. Geophys. Res., 91, 10905–10936, 1986.

11580 Mahmood R., K. von Salzen, M. Flanner, M. Sand, J. Langner, H. Wang, L. Huang, (2016),
11581 Seasonality of global and Arctic black carbon processes in the Arctic Monitoring and
11582 Assessment Programme models, *Journal of Geophysical Research: Atmospheres,* 121 (12),
11583 7100-7116. DOI: 10.1002/2016JD024849.

11584 Mahowald, N., Lamarque, J., Tie, X., & Wolff, E. (2006). Sea-salt aerosol response to climate
11585 change: Last Glacial Maximum, preindustrial, and doubled carbon dioxide climates.
11586 Journal of Geophysical Research-Atmospheres, 111(D5).
11587 https://doi.org/10.1029/2005JD006459

11588 Mahowald, N., Muhs, D., Levis, S., Rasch, P., Yoshioka, M., Zender, C., & Luo, C. (2006).
11589 Change in atmospheric mineral aerosols in response to climate: Last glacial period,
11590 preindustrial, modern, and doubled carbon dioxide climates. Journal of Geophysical
11591 Research-Atmospheres, 111(D10). https://doi.org/10.1029/2005JD006653

11592 Makar, P., Bouchet, V., and Nenes, A.: Inorganic chemistry calculations using HETV – a
11593 vectorized solver for the SO_4^{2-}-NO_3^--NH_4^+ system based on the ISORROPIA algorithms,
11594 Atmos. Environ., 37, 2279–2294, https://doi.org/10.1016/S1352-2310(03)00074-8, 2003.

11595 Makar, P. A., Gong,W., Milbrandt, J., Hogrefe, C., Zhang, Y., Curci, G., Zabkar, R., Im, U.,
11596 Balzarini, A., Baro, R., Bianconi, R., Cheung, P., Forkel, R., Gravel, S., Hirtl, H., Honzak, L.,
11597 Hou, A., Jimenz-Guerrero, P., Langer, M., Moran, M. D., Pabla, B., Perez, J. L., Pirovano,
11598 G., San Jose, R., Tuccella, P., Werhahn, J., Zhang, J., and Galmarini, S.: Feedbacks between
11599 air pollution and weather, part 1: Effects on weather, Atmos. Environ., 115, 442–469,
11600 2015a.

11601 Makar, P. A., Gong, W., Hogrefe, C., Zhang, Y., Curci, G., Zabkar, R., Milbrandt, J., Im, U.,
11602 Balzarini, A., Baro, R., Bianconi, R., Cheung, P., Forkel, R., Gravel, S., Hirtl, H., Honzak, L.,
11603 Hou, A., Jimenz-Guerrero, P., Langer, M., Moran, M. D., Pabla, B., Perez, J. L., Pirovano,
11604 G., San Jose, R., Tuccella, P., Werhahn, J., Zhang, J., and Galmarini, S.: Feedbacks between

11605 air pollution and weather, part 2: Effects on chemistry, Atmos. Environ., 115, 499–526,
11606 2015b.

11607 Mårtensson, E. M., Nilsson, E. D., de Leeuw, G., Cohen, L. H., and Hansson, H.-C.: Laboratory
11608 simulations and parametrization of the primary marine aerosol production, J. Geophys.
11609 Res., 108, 4297, doi:10.1029/2002JD002263, 2003.

11610 Mann, G. W., Carslaw, K. S., Spracklen, D. V., Ridley, D. a., Manktelow, P. T., Chipperfield, M.
11611 P., Pickering, S. J. and Johnson, C. E.: Description and evaluation of GLOMAP-mode: a
11612 modal global aerosol microphysics model for the UKCA composition-climate model,
11613 Geosci. Model Dev., 3(2), 519–551, doi:10.5194/gmd-3-519-2010, 2010.

11614 Mann, G. W., Carslaw, K. S., Ridley, D. a., Spracklen, D. V., Pringle, K. J., Merikanto, J.,
11615 Korhonen, H., Schwarz, J. P., Lee, L. a., Manktelow, P. T., Woodhouse, M. T., Schmidt, a.,
11616 Breider, T. J., Emmerson, K. M., Reddington, C. L., Chipperfield, M. P. and Pickering, S. J.:
11617 Intercomparison of modal and sectional aerosol microphysics representations within the
11618 same 3-D global chemical transport model, Atmos. Chem. Phys., 12(10), 4449–4476,
11619 doi:10.5194/acp-12-4449-2012, 2012.

11620 Menon, S., & Rotstayn, L. (2006). The radiative influence of aerosol effects on liquid-phase
11621 cumulus and stratiform clouds based on sensitivity studies with two climate models.
11622 Climate Dynamics, 27(4), 345–356. https://doi.org/10.1007/s00382-006-0139-3

11623 Miller, R. L., Cakmur, R. V., Perlwitz, J., Geogdzhayev, I. V., Ginoux, P., Koch, D., et al. (2006).
11624 Mineral dust aerosols in the NASA Goddard Institute for Space Sciences ModelE
11625 atmospheric general circulation model. Journal of Geophysical Research: Atmospheres,
11626 111(D6). https://doi.org/10.1029/2005JD005796

11627 Monahan, E. C., Spiel, D. E., and Davidson, K. L.: A model of marine aerosol generation via
11628 whitecaps and wave disruption, in: Oceanic Whitecaps and Their Role in Air-Sea Exchange
11629 688, edited by: Monahan, E. C. and Mac Niocaill, G., D Reidel, Norwell, MA, 167–174,
11630 1986.

11631 Moran, M., Menard, S., Gravel, S., Pavlovic, R., and Anselmo, D.: RAQDPS Versions 1.5.0 and
11632 1.5.1: Upgrades to the CMC Operational Regional Air Quality Deterministic Prediction
11633 System Released in October 2012 and February 2013, Technical report, Canadian
11634 Meteorological Centre, Canadian Meteorological Centre, Dorval, Quebec, 2013.

11635 Morgenstern, O., Braesicke, P., O'Connor, F. M., Bushell, A. C., Johnson, C. E., Osprey, S. M.
11636 and Pyle, J. A.: Evaluation of the new UKCA climate-composition model – Part 1 : The
11637 stratosphere, Geosci. Model Dev., 2, 43–57 [online] Available from: www.geosci-model-
11638 dev.net/2/43/2009, 2009.

11639 Mulcahy, J. P., Johnson, C., Jones, C. G., Povey, A. C., Scott, C. E., Sellar, A., Turnock, S. T.,
11640 Woodhouse, M. T., Abraham, N. L., Andrews M., Bellouin, N., Browse, J., Carslaw, K. S.,
11641 Dalvi, M., Folberth, G., Grosvenor, D., Hardacre, C., Johnson, B., Jones, A., Kipling, Z.,
11642 Mann, G., Mollard, J., Schutgens, N., O'Connor, F., Palmieri, J., Reddington, C.,
11643 Richardson, M., Stier, P., Woodward, S. and Yool, A.: Description and evaluation of
11644 aerosol in UKESM1 and HadGEM3-GC3.1 CMIP6 historical simulations, Geosci. Model
11645 Dev., submited(March), 2019.

11646 Nenes, A., Pilinis, C., and Pandis, S. N.: Continued development and testing of a new
11647 thermodynamic aerosol module for urban and regional air quality models, Atmos.
11648 Environ., 33, 1553–1560, 1999.

11649 O'Connor, F. M., Johnson, C. E., Morgenstern, O., Abraham, N. L., Braesicke, P., Dalvi, M.,
11650 Folberth, G. A., Sanderson, M. G., Telford, P. J., Voulgarakis, A., Young, P. J., Zeng, G.,
11651 Collins, W. J. and Pyle, J. A.: Evaluation of the new UKCA climate-composition model –
11652 Part 2: The Troposphere, Geosci. Model Dev., 7(1), 41–91, doi:10.5194/gmd-7-41-2014,
11653 2014.

11654 Odum, J. R., Hoffmann, T., Bowman, F., Collins, D., Flagan, R. C., and Seinfeld, J. H.:
11655 Gas/particle partitioning and secondary organic aerosol yields, Environ. Sci. Technol., 30,
11656 2580–2585, 1996.

11657 Oshima, N., Koike, M., Zhang, Y., Kondo, Y., Moteki, N., Takegawa, N., and Miyazaki, Y.:
11658 Aging of black carbon in outflow from anthropogenic sources using a mixing state
11659 resolved model: Model development and evaluation, J. Geophys. Res., 114, D06210,
11660 doi:10.1029/2008JD010680, 2009a.

11661 Oshima, N., Koike, M., Zhang, Y., and Kondo, Y.: Aging of black carbon in outflow from
11662 anthropogenic sources using a mixing state resolved model: 2. Aerosol optical properties
11663 and cloud condensation nuclei activities, J. Geophys. Res., 114, D18202,
11664 doi:10.1029/2008JD011681, 2009b.

11665 Oshima, N., and Koike, M.: Development of a parameterization of black carbon aging for use
11666 in general circulation models, Geosci. Model Dev., 6, 263-282, doi:10.5194/gmd-6-263-
11667 2013, 2013.

11668 Oshima, N., Yukimoto, S., Deushi, M., Koshiro, T., Kawai, H., Tanaka, T. Y., and Yoshida, K.:
11669 Global and Arctic effective radiative forcing of anthropogenic gases and aerosols in MRI-
11670 ESM2.0, SPEPS, submitted.

11671 Pisso, I., E. Sollum, H. Grythe, N. I. Kristiansen, M. Cassiani, S. Eckhardt, D. Arnold, D.
11672 Morton, R. L. Thompson, C. D. Groot Zwaaftink, N. Evangeliou, H. Sodemann, L.
11673 Haimberger, S. Henne, D. Brunner, J. F. Burkhart, A. Fouilloux, J. Brioude, A. Philipp, P.
11674 Seibert, and A. Stohl (2019): The Lagrangian particle dispersion model FLEXPART version
11675 10.4. Geosci. Mod. Dev. 12, 4955-4997, doi:10.5194/gmd-12-4955-2019

11676 Rayner, N. A., Parker, D. E., Horton, E. B., Folland, C. K., Alexander, L. V., Rowell, D. P., et al.
11677 (2003). Global analyses of sea surface temperature, sea ice, and night marine air
11678 temperature since the late nineteenth century. Journal of Geophysical Research:
11679 Atmospheres, 108(D14). https://doi.org/10.1029/2002JD002670

11680 Samuelsson, P., Jones, C., Willen, U., Ullerstig, A., Gollvik, S., Hansson, U., Jansson, C.,
11681 Kjellström, E., Nikulin, G., and Wyser, K.: The Rossby Center Regional Climate model
11682 RCA3: model description and performance, Tellus A, 63, 4–23, 2011.

11683 Schmidt, G. A., Kelley, M., Nazarenko, L., Ruedy, R., Russell, G. L., Aleinov, I., et al. (2014).
11684 Configuration and assessment of the GISS ModelE2 contributions to the CMIP5 archive.
11685 Journal of Advances in Modeling Earth Systems, 6(1), 141–184.
11686 https://doi.org/10.1002/2013MS000265

11687 Robertson, L., Langner, J., and Engardt, M.: An Eulerian Limited-Area Atmospheric Transport
11688 model, J. Appl. Meteorol., 38, 190–210, 1999.

11689 Schultz, M. G., Stadtler, S., Schröder, S., Taraborrelli, D., Franco, B., Krefting, J., Henrot, A.,
11690 Ferrachat, S., Lohmann, U., Neubauer, D., Siegenthaler-Le Drian, C., Wahl, S., Kokkola, H.,
11691 Kühn, T., Rast, S., Schmidt, H., Stier, P., Kinnison, D., Tyndall, G. S., Orlando, J. J., and
11692 Wespes, C.: The chemistry–climate model ECHAM6.3-HAM2.3-MOZ1.0, Geosci. Model
11693 Dev., 11, 1695–1723, https://doi.org/10.5194/gmd-11-1695-2018, 2018.

11694 Sellar, A. A., Jones, C. G., Mulcahy, J., Tang, Y., Yool, A., Wiltshire, A., O'Connor, F. M.,
11695 Stringer, M., Hill, R., Palmieri, J., Woodward, S., Mora, L., Kuhlbrodt, T., Rumbold, S.,
11696 Kelley, D. I., Ellis, R., Johnson, C. E., Walton, J., Abraham, N. L., Andrews, M. B., Andrews,
11697 T., Archibald, A. T., Berthou, S., Burke, E., Blockley, E., Carslaw, K., Dalvi, M., Edwards, J.,
11698 Folberth, G. A., Gedney, N., Griffiths, P. T., Harper, A. B., Hendry, M. A., Hewitt, A. J.,
11699 Johnson, B., Jones, A., Jones, C. D., Keeble, J., Liddicoat, S., Morgenstern, O., Parker, R. J.,
11700 Predoi, V., Robertson, E., Siahaan, A., Smith, R. S., Swaminathan, R., Woodhouse, M. T.,
11701 Zeng, G. and Zerroukat, M.: UKESM1: Description and evaluation of the UK Earth System
11702 Model, J. Adv. Model. Earth Syst., 2019MS001739, doi:10.1029/2019MS001739, 2019.

11703 Shindell, D. T., Grenfell, J. L., Rind, D., Grewe, V., & Price, C. (2001). Chemistry-climate
11704 interactions in the Goddard Institute for Space Studies general circulation model: 1.
11705 Tropospheric chemistry model description and evaluation. Journal of Geophysical
11706 Research: Atmospheres, 106(D8), 8047–8075. https://doi.org/10.1029/2000JD900704

11707 Shindell, D. T., Faluvegi, G., & Bell, N. (2003). Preindustrial-to-present-798 day radiative
11708 forcing by tropospheric ozone from improved simulations with the GISS chemistry-
11709 climate GCM. Atmospheric Chemistry and Physics, 3(5), 1675–1702.
11710 https://doi.org/10.5194/acp-3-1675-2003

11711 Shindell, D., T, Faluvegi, G., Unger, N., Aguilar, E., Schmidt, G. , et al. (2006).
11712 Simulations of 791 preindustrial, present-day, and 2100 conditions in the NASA GISS
11713 composition and climate model G792 PUCCINI. Atmospheric Chemistry and Physics,
11714 6(12), 4427–4459. https://doi.org/10.5194/acp-6-4427-793 2006

11715 Simpson, D., Guenther, A., Hewit, C., and Steinbrecher, R.: Biogenic emissions in Europe. 1.
11716 Estimates and uncertainties, J. Geophys. Res., 100, 22875–22800, 1995.

11717 Simpson, D., A. Benedictow, H. Berge, R. Bergström, L. D. Emberson, H. Fagerli, C. R.
11718 Flechard, G. D. Hayman, M. Gauss, J. E. Jonson, M. E. Jenkin, A. Nyiri, C. Richter, V. S.
11719 Semeena, S. Tsyro, J.-P. Tuovinen, A. Valdebenito, and P. Wind, The EMEP MSC-W
11720 chemical transport model – technical description, Atmos. Chem. Phys., 12, 7825–7865,
11721 2012.

11722 Søvde OA et al. (2012) The chemical transport model Oslo CTM3 Geosci Model Dev 5:1441-
11723 1469 doi:10.5194/gmd-5-1441-2012.

11724 Stevens, B., Giorgetta, M., Esch, M., Mauritsen, T., Crueger, T., Rast, S., Salzmann, M.,
11725 Schmidt, H., Bader, J., Block, K., Brokopf, R., Fast, I., Kinne, S., Kornblueh, L., Lohmann, U.,
11726 Pincus, R., Reichler, T., and Roeckner, E. Atmospheric component of the MPI-M Earth
11727 System Model: ECHAM6, J. Adv. Model. Earth Syst., 5, 146– 172,
11728 doi:10.1002/jame.20015.

11729 Stier, P., Feichter, J., Kinne, S., Kloster, S., Vignati, E., Wilson, J., Ganzeveld, L., Tegen, I.,
11730 Werner, M., Balkanski, Y., Schulz, M., Boucher, O., Minikin, A., and Petzold, A.: The
11731 aerosol-climate model ECHAM5-HAM, Atmos. Chem. Phys., 5, 1125–1156,
11732 https://doi.org/10.5194/acp-5-1125-2005, 2005.

11733 Stockwell, W. R. and Lurmann, F. W.: Intercomparison of the ADOM and RADM gas-phase
11734 chemical mechanisms. Electrical Power Research Institute Topical Report, EPRI, 3412
11735 Hillview Avenue, Paolo Alto, CA, USA, 254 pp., 1989.

11736 Stroud, C. A., Makar, P. A., Zhang, J., Moran, M. D., Akingunola, A., Li, S.-M., Leithead, A.,
11737 Hayden, K., and Siu, M.: Improving air quality model predictions of organic species using
11738 measurement-derived organic gaseous and particle emissions in a petrochemical-
11739 dominated region, Atmos. Chem. Phys., 18, 13531–13545, https://doi.org/10.5194/acp-
11740 18-13531-2018, 2018.

11741 Tegen, I., Neubauer, D., Ferrachat, S., Siegenthaler-Le Drian, C., Bey, I., Schutgens, N., Stier,
11742 P., Watson-Parris, D., Stanelle, T., Schmidt, H., Rast, S., Kokkola, H., Schultz, M.,
11743 Schroeder, S., Daskalakis, N., Barthel, S., Heinold, B., and Lohmann, U.: The global
11744 aerosol–climate model ECHAM6.3–HAM2.3 – Part 1: Aerosol evaluation, Geosci. Model
11745 Dev., 12, 1643–1677, https://doi.org/10.5194/gmd-12-1643-2019, 2019.

11746 Thomas, M. A., Kahnert, M., Andersson, C., Kokkola, H., Hansson, U., Jones, C., Langner, J.,
11747 and Devasthale, A.: Integration of prognostic aerosol–cloud interactions in a chemistry
11748 transport model coupled offline to a regional climate model, Geosci. Model Dev., 8, 1885-
11749 1898, https://doi.org/10.5194/gmd-8-1885-2015, 2015.

11750 Thomason, L. W., N. Ernest, L. Millán, L. Rieger, A. Bourassa, J.-P. Vernier, G. Manney, B. Luo,
11751 F. Arfeuille, and T. Peter: A global space-based stratospheric aerosol climatology: 1979–
11752 2016. Earth Sys. Sci. Data, 10, 469–492, 2018.

11753 Tilmes, S., Hodzic, A., Emmons, L. K., Mills, M. J., Gettelman, A., Kinnison, D. E., et al. (2019).
11754 Climate forcing and trends of organic aerosols in the Community Earth System Model
11755 (CESM2). J. Adv. Model. Earth Sys. (CESM2 special issue), 11(12), 4323–4351.
11756 https://doi.org/10.1029/2019MS001827

11757 Tsigaridis, K., and M. Kanakidou, 2007: Secondary organic aerosol importance in the future
11758 atmosphere. Atmos. Environ., 41, 4682-4692, doi:10.1016/j.atmosenv.2007.03.045.

11759 Tsigaridis, K., Koch, D., & Menon, S. (2013). Uncertainties and importance of sea spray
11760 composition on aerosol direct and indirect effects. Journal of Geophysical Research:
11761 Atmospheres, 118(1), 220–235. https://doi.org/10.1029/2012JD018165

11762 Wiedinmyer, C., Akagi, S. K., Yokelson, R. J., Emmons, L. K., Al-Saadi, J. A., Orlando, J. J., and
11763 Soja, A. J.: The Fire INventory from NCAR (FINN): a high resolution global model to
11764 estimate the emissions from open burning, Geosci. Model Dev., 4, 625–641,
11765 doi:10.5194/gmd-4-625-2011, 2011.

11766 Williams, K. D., Copsey, D., Blockley, E. W., Bodas-Salcedo, A., Calvert, D., Comer, R., Davis,
11767 P., Graham, T., Hewitt, H. T., Hill, R., Hyder, P., Ineson, S., Johns, T. C., Keen, A. B., Lee, R.
11768 W., Megann, A., Milton, S. F., Rae, J. G. L., Roberts, M. J., Scaife, A. A., Schiemann, R.,
11769 Storkey, D., Thorpe, L., Watterson, I. G., Walters, D. N., West, A., Wood, R. A., Woollings,
11770 T. and Xavier, P. K.: The Met Office Global Coupled Model 3.0 and 3.1 (GC3.0 and GC3.1)
11771 Configurations, J. Adv. Model. Earth Syst., 10(2), 357–380, doi:10.1002/2017MS001115,
11772 2018.

11773 Woodward, S.: Modeling the atmospheric life cycle and radiative impact of mineral dust in
11774 the Hadley Centre climate model, J. Geophys. Res., 106(D16), 18155–18166,
11775 doi:10.1029/2000JD900795, 2001.

11776 Yukimoto, S., Kawai, H., Koshiro, T., Oshima, N., Yoshida, K., Urakawa, S., Tsujino, H., Deushi,
11777 M., Tanaka, T., Hosaka, M., Yabu, S., Yoshimura, H., Shindo, E., Mizuta, R., Obata, A.,
11778 Adachi, Y., and Ishii, M.: The Meteorological Research Institute Earth System Model
11779 version 2.0, MRI-ESM2.0: Description and basic evaluation of the physical component, J.
11780 Meteor. Soc. Jpn., 97, 931–965, https://doi.org/10.2151/jmsj.2019-051, 2019.

11781

11782

11783 **Appendix**

11784

11785 **Table A.X:** Emission details in models

Model name	Biogenic emissions	Volcanic emissions	Forest fire emissions	Agricultural waste burning
CanAM5-PAM	none	Specified climatological		ECLIPSE V6B
CESM2.0 (Type 0 and Type 1 runs)	MEGANv2.1	CMIP6	CMIP6	ECLIPSE V6B
CESM2.1.1 (Type 3 runs)	CMIP6 (but only affecting SOA, not ozone)	CMIP6	CMIP6	ECLIPSE V6B
CMAM				
DEHM				
ECHAM-SALSA	based on the GEIA inventory (as particulate matter only)	3D emission fields based on AeroCom III (https://wiki.met.no/aerocom/phase3-experiments); includes emissions for Holuhraun	CMIP6	ECLIPSE V6B
EMEP-MSC-W	EMEP scheme (Simpson et al.,	As reported to EMEP per year	FINN (based on Wiedinmyer et al.,	ECLIPSE V6B

	2012)	(via CEIP, www.ceip.at). For future years: 2010.	2011)	
FLEXPART	none	none	CMIP6	ECLIPSE V6B
GEOS-Chem				
GEM-MACH	BEIS v3.09	none	CFFEPS	ECLIPSE V6B
GISS-E2.1-OMA	Isoprene:Guenther et al. (2015); Terpenes: ORCHIDEE; Online DMS, Sea-salt and dust	AeroCom	CMIP6	ECLIPSE V6B
MATCH	MEGANv2	Climatological + seperate runs with and without Holuhraun eruption	CMIP6	ECLIPSE V6B
MATCH-SALSA	MEGANv2	Specified 2014-'15 + Climatological	CMIP6	ECLIPSE V6B
MRI-ESM2	Biogenic VOCs emissions are taken from	CMIP6 stratospheric aerosol	CMIP6	ECLIPSE V6B

	Horowitz et al. (2003)	dataset or specified 2014-2015 SO_2 emission with Holuhraun eruption		
NorESM				
OsloCTM				
UKESM	Isoprene and monoterpenes interactive with land surface vegetation scheme	Climatology of emissions for continually degassing volcanoes. For explosive volcanoes a zonal mean climatology of stratospheric aerosol optical properties over historical period used from CMIP6 dataset	Prescribed from CMIP6 dataset	CMIP6 emissions for Type0 but ECLIPSE V6B for all other simulations
WRF-CHEM				

11786

11787

11788 **A.2 Model validation of O3 precursors**

11789

The two figures below show the CO and NOx, respectively, in the Arctic (>60 N) UTLS region from ACE-FTS and the model biases.

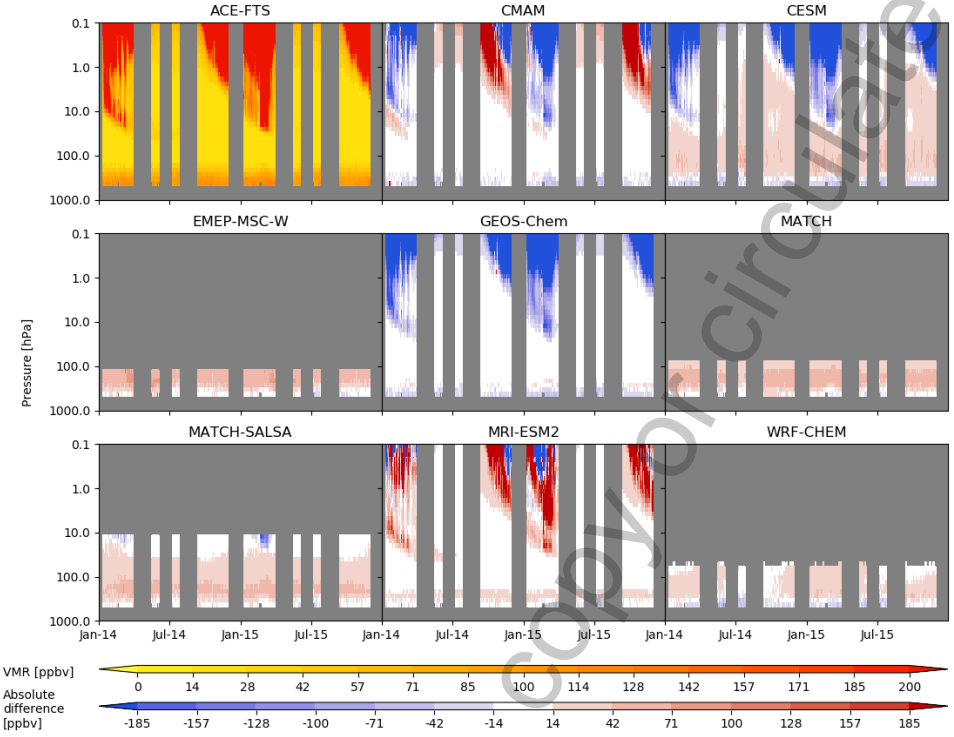

Figure A..X Mean Arctic (60-90N) carbon monoxide from ACE-FTS and the model-measurement differences for 2014-15. Results for 2008-9 were very similar and are not shown.

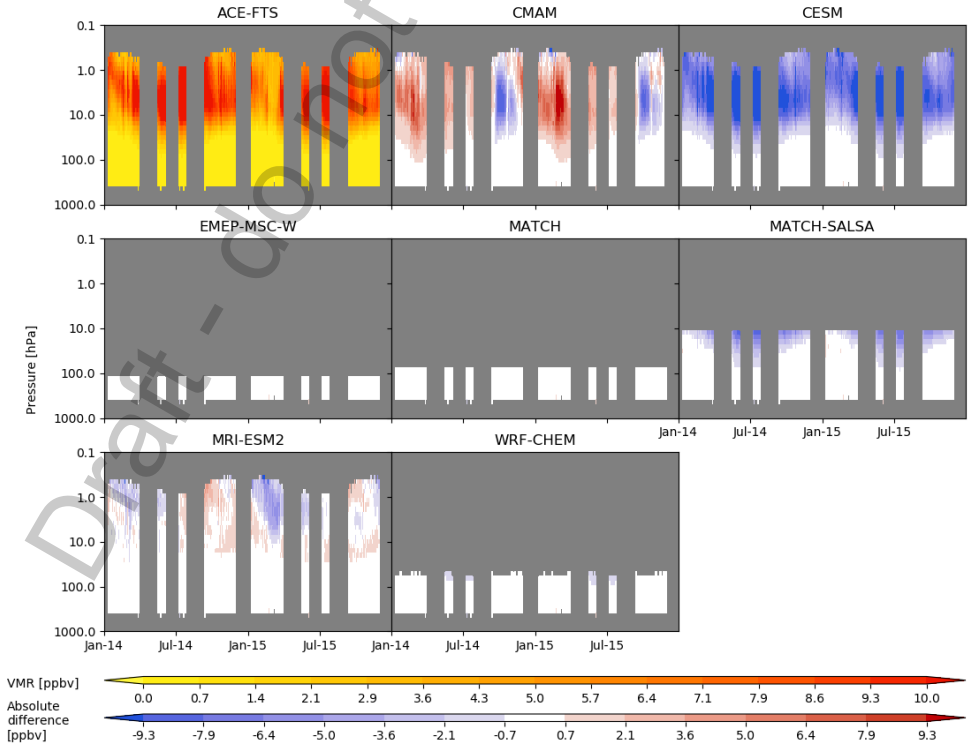

11798 **Figure A.Y:** Mean Arctic (60-90N) nitrogen oxides (NOx) from ACE-FTS and the model-
11799 measurement differences for 2014-15. Results for 2008-9 were very similar and are not
11800 shown.
11801

8. Health and Ecosystem Impacts

Policy-relevant science question:

> What are the potential present-day impacts of pollutant emissions on human health, crop yields and ecosystems and what benefits can be achieved via emission mitigation in the future?

8.1. Introduction

BC and methane emissions influence public health within Arctic communities through two pathways, whether the emissions are released in the Arctic or elsewhere in the world. First, SLCPs contribute to anthropogenic climate change, which is expected to have a variety of negative consequences for public health among cities and communities in the Arctic. Climate change can increase air pollution from wildfires, contribute to the spread of vector-borne disease, and affect natural ecosystems that sustain fish and wildlife leading to dietary risks. SLCPs are also health-damaging air pollutants that are associated with a range of health outcomes, including respiratory and cardiovascular diseases, among others. Reducing SLCPs can thus improve public health in Arctic communities by reducing the effects of both climate change and air pollution exposure.

This chapter presents an assessment of the health and environmental benefits of the SLCP policies described in Chapter 2. Understanding the health and ecosystem benefits can help inform the design and implementation of emission mitigation policies. Health and environmental impact assessment is often used for decision-making analyses, such as cost-benefit or cost-effectiveness analysis. However, quantitatively estimating the public health and environmental benefits of reduced climate change in the Arctic is challenging due to limited data and modeling approaches. Estimating health impacts from changes in air quality are more easily quantifiable and may be larger than health impacts from changes in climate in the near term. Methods also exist for estimating pollution deposition which can cause damage to crop yields and ecosystems through acidification and eutrophication. This chapter therefore focuses on how the PM2.5 and ozone changes from SLCP emission

policies could affect public health and ecosystems in the Arctic. The additional health and environmental benefits from reduced climate change are also important but are not quantified here.

Sections 8.2 and 8.3 review the evidence on air quality-related health and ecosystem impacts, including what is known from the body of scientific literature that has grown over decades of epidemiological, toxicological, environmental and other types of research studies globally. Section 8.4 presents quantitative analysis of the health and ecosystem impacts of air pollution in the Arctic, as well as the improved health and ecosystem outcomes that could come from policies reducing SLCP and other emissions. Finally Section 8.5 synthesizes the existing body of literature with the new quantitative analysis to respond to the policy-relevant question: What are the potential present-day impacts of pollutant emissions on human health, crop yields and ecosystems and what benefits can be achieved via emission mitigation in the future?

8.2 Review of evidence on air quality related health impacts

8.2.1 Health effects of PM2.5 and ozone

8.2.2. Burden of disease estimates in Arctic nations

8.2.3. Arctic and Nordic-specific emissions sources and health studies

8.2.3.1. Local emissions sources:

- Wildfires
- Wood/coal burning for home heating - PM2.5, BC, PAH
- Shipping
- Flaring

8.2.3.2 Arctic and Nordic-specific epidemiological studies

- Existing studies on Alaska & Finland epi, NordicWelfAIR (highlighted in boxes?)

- Case studies to look at local reductions in pollution sources and health

8.3. Review of evidence on air pollution impacts on ecosystems and crops

8.3.1 Deposition and Critical Loads:

8.3.2 Crop Impacts

8.4 Modeled impacts of SLCP emissions on health, depositions and crops in Arctic Council nations & observers

This section describes the new quantitative analysis of the health, ecosystem, and agricultural impacts of air pollution changes from the modeled SLCP emissions scenarios. We combine PM2.5 and ozone changes simulated from multiple chemical transport models and general circulation models described in earlier chapters with concentration-response functions from the peer-reviewed literature for health, ecosystem, and agricultural impacts.

8.4.1 Models and Methods

For the impact calculations, we use a set of health, ecosystem, and agricultural impact assessment models. These models have been developed previously and applied in multiple applications throughout the literature. They include:

The EVA system (Brandt et al., 2013a,b; Geels et al., 2015; Im et al., 2018, 2019) is based on the impact-pathway chain method (Friedrich and Bickel, 2001). With recent developments, EVAv6 can calculate all-cause acute and chronic mortality and morbidity based on linear exposure-response functions, along with cause-specific mortality based on non-linear functions following Lelieveld et al. (2019).

The EMEP MSC-W model is a 3-D Eulerian chemistry transport model developed at the Norwegian Meteorological Institute within the Framework of the UN Convention on Long-range Transboundary Air Pollution. It is described in detail in Simpson et al. (2012). Model

updates since Simpson et al. (2012), resulting in EMEP model version rv4.9 as used here, have been described in Simpson et al. (2016) and references cited therein. To assess the past trends and future scenarios of ecosystem damage by acidifying and eutrophying depositions, the results from the EMEP MSC-W model simulations have been used here.

ISTE tool, developed at the Finnish Institute for Health and Welfare (THL) has an extensible collection of available C-R functions [8] and is linked to baseline burden of disease data by WHO [38]. The ISTE tool allows for probabilistic modelling of exposure variability and calculates uncertainties using 95% CI for C-R functions and standard error for exposure when these are available.

TM5-FASST-Scenario Screening Tool a global reduced-form air quality source–receptor model that has been designed to compute ambient pollutant concentrations as well as a broad range of pollutant-related impacts on human health, agricultural crop production, and short-lived pollutant climate metrics, taking as input annual pollutant emission data aggregated at the national or regional level.

8.4.2 Data and Methods for Health Impact Analysis (HIA)

Four factors - population growth, population aging, mortality rates independent of exposure to PM2.5, and exposure to ambient PM2.5 and ozone - contribute to the total mortality attributable to ambient PM2.5 and O3 and the changes in these factors contributes to the overall change in attributable mortality. Data sources for these variables across the HIA models are described below:

<u>Input concentrations of PM2.5 and Ozone</u>

PM2.5 and O3 concentrations are derived from the suite of models described previously in Chapters 6 and 7. A wide range of different model resolutions are employed in AMAP SLCF EG models, ranging from about 0.14 degree longitude (GEM-MACH) to about 2.8 degrees longitude (CanAM5-PAM). Different methods for remapping model results onto a common grid with a resolution of 0.5 degrees have been tried in order to provide data for the analysis of population-weighted concentrations. Results of these methods were evaluated by

comparing with a range of different observational data sets for PM2.5, focussing on annual mean data for 2015. No obvious systematic relationship was found between PM2.5 concentration biases and model resolution for any of the remapping methods. Specifically, models with higher resolution do not produce systematically higher PM2.5 concentrations than models with a lower resolution. However, observations provide clear evidence for steep concentration gradients between urban and rural regions which cannot be well resolved by most of the models that are available. Given that overall model performance does not appear to depend on model resolution, it may be possible to enhance simulated concentrations simulated at low resolution by downscaling. The goal of the downscaling method is to better represent concentration gradients, with potential benefits for an analysis of health impacts.

For O3, the HIA models used the sum of ozone means over 35 ppb (SOMO35) which is based on the daily maximum of 8-hour mean O3 concentrations.

Population Data

For the population weighted concentrations and scenarios, population projections were derived from the SSP2 scenario as part of Shared Socioeconomic Pathways (KC et al 2017). The EVA model further used the global population density from Socioeconomic Data and Applications Center (SEDAC: (http://sedac.ciesin.columbia.edu/data/collection/gpw-v4/sets/browse) on a 2.5-minute spatial resolution.

Baseline Mortality and Morbidity

Data across the models are based on a number of sources including WHO 2019.

Risk Functions

A range of concentration response (C-R) functions are used across the different HIA models to calculate mortality and morbidity end-points. These include:

i) Non-linear functions: These are used to estimate cause-specific mortality due to O3 and PM2.5. This method uses the Global Exposure Mortality Model (GEMM: Burnett et al., 2018), where relative risks (RR) are calculated through the hazard ratios functions. This

13155 method can calculate cause-specific mortality due to exposure to ambient PM2.5, including
13156 lung cancer (LC), chronic obstructive pulmonary disease (COPD), cerebrovascular disease
13157 (CEV), ischemic heart disease (IHD) and lower respiratory infection (LRI). These functions
13158 have further been sampled in Lelieveld et al. (2019) for European cohorts and these
13159 updated versions are used in the EVA model.
13160
13161 ii) Linear Functions: The linear exposure-response functions (ERFs) used in the EVA model to
13162 calculate different morbidity end-points (bronchitis, asthmatic children and lung cancer) are
13163 derived from (Héroux et al, 2015; WHO, 2013).
13164
13165 8.4.3 Present-day (2015) impacts of air quality on health, critical loads and crops
13166
13167 This section describes impacts estimated from the present-day model simulations:
13168 - Contributions to Arctic burden of disease (from region/sector emissions)
13169 - Contribution of SLCPs to health impacts (relative impacts across scenarios,
13170 region/sector emissions)
13171 - Sulfur and Nitrogen deposition and critical loads
13172 - Crop impacts
13173
13174 8.4.3.1 PM2.5 and ozone health impacts
13175
13176 8.4.3.2. Sulfur and Nitrogen deposition and Critical loads
13177
13178 8.4.3.3. Crop impacts
13179
13180 8.4.4. Future benefits of emission mitigation on health, deposition and crops (2030, 2050)
13181 This section describes the future changes in PM2.5 and ozone-related health impacts,
13182 impacts of nitrogen deposition of acidification and eutrophication of ecosystems, and ozone
13183 impacts on crop yields for the years 2030 and 2050 under the SLCP emissions scenarios.
13184
13185 8.4.4.1 PM2.5 and ozone health Impacts
13186

13187 8.4.4.2 Acidifying and eutrophying depositions

13188

13189 8.4.4.3 Crop Impacts

13190

13191 8.4.5 Uncertainties and sensitivity analyses

13192 This section describes the various uncertainties involved in estimating health, ecosystem,
13193 and crop impacts from the simulated PM2.5 and ozone concentration changes, as well as
13194 sensitivity analyses that explore the influence of impact model inputs (e.g. spatial
13195 distributions of pollution, risk functions) on results.

13196

13197 **8.5. Conclusion**

13198 - Health effects of air pollution - e.g. Arctic-specific studies support large body of
13199 evidence globally linking PM2.5 and ozone exposure to a range of health outcomes
13200 - Key findings from Section 8.4
13201 - Policy relevant statements
13202 - Response to policy relevant question: What are the potential present-day impacts of
13203 pollutant emissions on human health, crop yields and ecosystems and what benefits
13204 can be achieved via emission mitigation in the future?
13205 - Possibly some statements on pollutant-specific and sector-specific impacts
13206 depending on results from section 8.4
13207 - Summary of uncertainty
13208 - Recommendations:

13209

13210 **References**

13211

13212